



**Direct Drive Wind Generators  
with Superconducting Excitation  
in the Multi-MW Class**

Zur Erlangung des akademischen Grades  
Doktor-Ingenieur (Dr.-Ing.)  
genehmigte Dissertation

von

Robin Köster, M.Sc., M.Sc., M.Sc.

Referent:	Univ.-Prof. Dr.-Ing. habil. Dr. h.c. Andreas Binder
Korreferentin:	Univ.-Prof. Dr. rer. nat. Tabea Arndt
Tag der Einreichung:	27.06.2023
Tag der mündlichen Prüfung:	16.10.2023

D17  
Darmstadt 2023



---

Köster, Robin:

Direct Drive Wind Generators with Superconducting Excitation in the Multi-MW Class  
Darmstadt, Technische Universität Darmstadt

Jahr der Veröffentlichung der Dissertation auf TUPrints: 2023

URN: urn:nbn:de:tuda-tuprints-247287

URI: <https://tuprints.ulb.tu-darmstadt.de/id/eprint/24728>

Tag der mündlichen Prüfung: 16.10.2023

Veröffentlicht unter CC BY-SA 4.0 International

<https://creativecommons.org/licenses/>

---

# Erklärungen laut Promotionsordnung

## **§ 8 Abs. 1 lit. c PromO**

Ich versichere hiermit, dass die elektronische Version meiner Dissertation mit der schriftlichen Version übereinstimmt.

## **§ 8 Abs. 1 lit. d PromO**

Ich versichere hiermit, dass zu einem vorherigen Zeitpunkt noch keine Promotion versucht wurde.

## **§ 9 Abs. 1**

Ich versichere hiermit, dass die vorliegende Dissertation selbstständig und nur unter Verwendung der angegebenen Quellen verfasst wurde.

## **§ 9 Abs. 2**

Die Arbeit hat bisher noch nicht zu Prüfungszwecken gedient.

Robin Köster

Darmstadt, den 27.06.2023

---

## Vorwort -

Die vorliegende Arbeit ist im Rahmen meiner Tätigkeit als wissenschaftlicher Mitarbeiter am *Institut für Elektrische Energiewandlung* an der *Technischen Universität Darmstadt* in den Jahren 2019 bis 2023 entstanden. Im Folgenden möchte ich mich bei allen bedanken, die mein Promotionsvorhaben in dieser Zeit unterstützt und schließlich zu dessen Gelingen beigetragen haben.

Meinem Doktorvater, *Univ.-Prof. Dr.-Ing. habil. Dr. h.c. Andreas Binder*, möchte ich herzlich dafür danken, dass er mir - seinen breit gefächerten Interessen entsprechend - ermöglicht hat, eine Doktorarbeit an der Schnittstelle von elektrischer Energietechnik und Physik zu verfassen. Diese Arbeit wurde möglich, weil er mir frühzeitig zugetraut hat, mir auch ohne unmittelbare Vorgängerprojekte am Institut ein neues Wissenschaftsfeld zu erschließen, und er mir zugleich viel Freiraum für die Entfaltung eigener Ideen ließ. Nicht selbstverständlich und gleichzeitig sehr wichtig für das Gelingen des Promotionsvorhabens war, dass mein Doktorvater fortlaufend und auch kurzfristig für einen Austausch zur Verfügung stand. Darüber hinaus möchte ich ihm für die Unterstützung beim Abfassen von wissenschaftlichen Veröffentlichungen und für deren kritische Durchsicht danken.

Herzlich danken möchte ich Frau *Univ.-Prof. Dr. rer. nat. Tabea Arndt* für die Übernahme des Korreferats. Der Austausch mit ihr und mit dem *Institut für Technische Physik* am *KIT* während meiner Tätigkeit als wissenschaftlicher Mitarbeiter und die hieraus hervorgegangenen Impulse, auch ausgehend von Herrn *Univ.-Prof. Dr.-Ing. Mathias Noe*, waren eine große Bereicherung, haben mich in der Wahl des Forschungsthemas bestärkt und haben bei der Eingrenzung der Forschungsfragen sehr geholfen. Wichtige Anregungen in Hinblick auf industrielle Anwendbar- und Verwertbarkeit habe ich zudem *Dr. Andreas Jöckel* und *Dr. Roland Zeichfußl* von der *Flender GmbH* zu verdanken. Für die finanzielle Unterstützung möchte ich der *Stiftung Energieforschung Baden-Württemberg* danken, die das Forschungsvorhaben unter der Projektnummer A 337 19 gefördert hat. Mein Dank gilt zudem *Univ.-Prof. Dr.-Ing. Yves Burkhardt* für den wertvollen Rat und die Unterstützung in der Schlussphase der Promotion.

An der fachlich und persönlich bereichernden Zeit am *Institut für Elektrische Energiewandlung* hatte der Austausch mit meinen Kollegen einen sehr wesentlichen Anteil.

---

Im Einzelnen möchte ich mich bei *Nicolas Erd* bedanken, der mich im Rahmen meiner Masterarbeit nachhaltig für elektrische Maschinen im Allgemeinen und Großgeneratoren im Speziellen begeistert hat. *Dr. Björn Deusinger* bin ich dankbar für seine unaufgeregte Hilfe bei so vielen Dingen im Institutsalltag. Der Austausch mit meinen Kollegen *Dr. Daniel Dietz*, *Alexander Möller*, *Laurenz Ziegler*, *Maximilian Clauer*, *Dr. Sascha Neusius*, *Dr. Martin Weicker*, *Omid Safdarzadeh* und *Dr. Xing Li* war wesentlich für meine fachliche Weiterentwicklung während der Promotion. Hierfür bin ich ebenso dankbar wie für das durchweg freundschaftliche, wertschätzende Miteinander, das mich auch mit den technischen und administrativen Mitarbeitern *Klaus Gütlisch*, *Andreas Fehringer* und *Sabine Waldhaus* verbindet. Sehr dankbar bin ich zudem *Prof. Dr. techn. habil. Georg Traxler-Samek* für seinen wiederholten, freundschaftlichen und fachlichen Rat in den letzten Jahren.

Allen Studierenden, die ihre Abschlussarbeit unter meiner Betreuung verfasst haben, danke ich für die tatkräftige Unterstützung. Im Einzelnen sind dies: *Steffen Koch*, *Julian Bergmann*, *Daniel Leißner*, *Aida Wirth*, *Linus Diessner*, *Tim Fößner*, *Benno Sommer*, *Dominik Fabrig* und *Sven Schumm*. Der intensive Austausch hat zu einer fortwährenden Reflexion des Dissertationsthemas beigetragen und war Grundlage vieler Ideen.

Schließlich bin ich meinen Eltern, *Patricia* und *Tilmann*, sehr dankbar für den Rückhalt, die immerwährende Bestärkung und die vielfältige Förderung, die maßgeblich dazu beigetragen hat, dass ich meine bisherigen Ziele erreicht habe. *Sebastian*, *Kersti*, *Dirk*, *Lieselotte*, *Ekkehard*, *Magda* und *Jürgen* danke ich für das andauernde Interesse und die Anteilnahme an meinem Promotionsprojekt. Meinem Bruder *Marco* bin ich dankbar für die tiefe Verbundenheit und die klugen Gespräche, die mich durch die Promotionszeit getragen haben. Von Herzen danke ich meiner Verlobten *Fiona*, die mich auf dem gemeinsamen Weg uneingeschränkt unterstützt hat und damit den Freiraum für die intensive Arbeit schuf, deren Ergebnis die vorliegende Dissertationsschrift ist. Ohne ihre Geduld und ihr Verständnis für wenig gemeinsame Zeit und so manche Einschränkung wäre mein Promotionsprojekt in dieser Form nicht möglich gewesen.

---

## Kurzfassung -

Gegenstand der vorliegenden Dissertation ist die Potentialanalyse supraleitender Wicklungen für den Einsatz in getriebelosen Windgeneratoren. Derzeit eingesetzte Synchrongeneratoren werden überwiegend mit Seltenen-Erden-Permanentmagneten erregt. Der allgemein hohe und volatile Preis der Seltenen-Erden-Metalle einerseits und die Markt-dominanz der Volksrepublik China andererseits veranlassen führende Hersteller von Windkraftanlagen derzeit, nach Technologiealternativen zu suchen. Für Generatoren mit Nennleistung von  $\approx 5$  MW kann die Supraleiter-Technologie neben einer Reduktion der Rohstoffabhängigkeit Vorteile in Hinblick auf eine reduzierte Aktivmasse, einen gesteigerten Wirkungsgrad und eine gesteigerte Generatorleistung ermöglichen.

Im Rahmen der vorliegenden Arbeit werden direktangetriebene, dreiphasige, umrichter gespeiste, supraleitende Generatoren untersucht. Auf eine analytische und feldnumerische Modellbildung sowie eine thermische Modellierung für dieses Generatorkonzept folgt der Vergleich verschiedener Generator topologien (Drehstrom-Wicklung in Nuten in Kombination mit (i) ferromagnetischem Rotor, (ii) nicht-magnetischen Rotorpolen, (iii) nicht-magnetischem Rotor sowie (iv) eine Luftspaltwicklung in Kombination mit einem ferromagnetischen Rotor) und ein Vergleich verschiedener Supraleiter (Hochtemperatur-supraleiter der 2. Generation mit/ohne künstliche Haftzentren sowie  $MgB_2$ ) hinsichtlich ihrer Eignung für den Einsatz in Windgeneratoren. Im Rahmen von Parameterstudien und multikriteriellen, numerischen Optimierungen werden exemplarisch Generatoren für die verschiedenen Topologien (i) - (iv) ausgelegt. Zu Vergleichszwecken erfolgt analog eine Auslegung von getriebelosen, permanentmagneterregten Windgeneratoren, weil detaillierte Parameterstudien zu industriell gefertigten, permanentmagneterregten Generatoren nicht verfügbar sind.

Die Untersuchung der ein-, zwei- und dreiphasigen Klemmenkurzschlüsse und des Betriebs bei teilweiser Statorspeisung sowie die Verluste im Kaltteil zeigen keine grundsätzlichen Schwierigkeiten, die der Kommerzialisierung der Supraleiter-Technologie bei Windgeneratoren entgegenstehen könnten. Es wird gezeigt, dass derzeit erhältliche  $MgB_2$ -Leiter unter technischen und ökonomischen Gesichtspunkten schlechter für den Einsatz in supraleitenden Feldwicklungen geeignet sind, als Hochtemperatursupraleiter der zweiten Generation ( $GdBCO$ ,  $EuBCO$ ). Die zwangsläufig niedrigere Betriebstemper-

---

atur und der deutlich niedrigere kritische Strom im Magnetfeld können nicht durch die deutlich niedrigeren Kosten von MgB<sub>2</sub>-Leitern aufgewogen werden. Für Generatoren mit Hochtemperatur-Supraleiter-Feldwicklung werden die niedrigsten Investitionskosten (Aktivteile des Generators, Umrichter, kryogenes Kühlsystem) erreicht, wenn die normaleitende Statorwicklung in Nuten liegt und Rotor-Polkerne sowie das Rotorjoch ferromagnetisch sind. Mit dieser Topologie kann die gravimetrische Leistungsdichte um  $\approx 33\%$  gegenüber permanentmagneterregten Generatoren gesteigert werden. Gegenüber permanentmagneterregten Generatoren ermöglicht die supraleitende Feldwicklung zudem eine Steigerung des Leistungsfaktors in Höhe von  $\approx +0.2$  auf  $|\cos \varphi_{sN}| \gtrsim 0.97$ . Für getriebe-lose, teil-supraleitende Generatoren wird basierend auf einer numerischen Optimierung gezeigt, dass jedoch eine Preisreduktion für Hochtemperatursupraleiter auf etwa  $1/3$  des derzeitigen Werts erforderlich ist, um die Wettbewerbsfähigkeit herzustellen.

**Abstract** - The main objective of this thesis is the evaluation of superconducting windings for the use in large-power direct drive wind generators. State-of-the-art synchronous wind generators feature rare-earth permanent magnets for the rotor field excitation. Currently, the investigation of alternative excitation technologies is triggered by the generally high and volatile price of rare-earth elements and the market dominance of the People's Republic of China. When economically competitive, superconducting windings offer the potentials of reduced generator active mass, higher efficiency and simplified up-scaling of the generator power. The effort for the cryogenic cooling generally limits the application of the superconductor technology to rated powers larger than  $\gtrsim 5$  MW.

In this thesis, direct drive generators with superconducting field winding and normal conducting three-phase AC stator winding are considered. Analytical and field-numerical, electromagnetic models for this generator type are developed and complemented by a thermal model. Different magnetic generator topologies, i.e. a three-phase AC winding in slots in combination with (i) a ferromagnetic rotor, (ii) non-magnetic rotor poles, (iii) a non-magnetic rotor as well as (iv) a three-phase AC air gap winding with ferromagnetic rotor, and different superconductors, i.e. second generation high-temperature superconductors with/ without artificial pinning and MgB<sub>2</sub>, are compared. Exemplary designs for direct drive generators with superconducting excitation are derived based on parameter studies and multi-objective, numerical optimizations. For comparison, permanent magnet synchronous generators for gearless drive trains are analysed, since no detailed parameter studies on commercially available permanent magnet excited generators are publicly



---

available.

The theoretical investigation of the operating behaviour under single-, two- and three-phase short circuits and under partial stator feeding as well as the calculated loss in the cryogenic section reveal no deal-breaker, which could hamper the commercialization of superconducting generators. Regarding the use in field windings,  $\text{MgB}_2$  conductors are technically and economically inferior to high-temperature superconductor tapes of the second generation (GdBCO, EuBCO). The much lower conductor cost of  $\text{MgB}_2$  wires is overcompensated by the necessarily lower operating temperature and the much lower in-field critical current. For high-temperature superconducting excited generators, the all-iron topology, i.e. with a stator copper winding in slots and ferromagnetic rotor poles and yoke, yields the lowest overall component costs (generator active parts, converter and cryogenic cooling system). An increase in gravimetric power density by  $\approx 33\%$  compared to permanent magnet excited generators can be achieved with this topology. The superconducting field winding allows rated power factors of  $|\cos \varphi_{\text{SN}}| \gtrsim 0.97$ , which is by  $\approx 0.2$  higher compared to typical gearless permanent magnet excited generators. However, a price reduction of the high-temperature superconductor to about 1/3 of the current value is required in order to achieve economical competitiveness with respect to the PM excitation.

---

# Contents

<b>1</b>	<b>Introduction and Fundamentals</b>	<b>1</b>
1.1	Wind Generator Systems . . . . .	5
1.2	Superconductivity: Fundamentals and Applications in Power Engineering	16
1.3	Superconducting Rotating Electrical Machines . . . . .	25
1.4	Research Questions and Methodological Approach . . . . .	32
<b>2</b>	<b>Electromagnetic Modelling of Superconducting Electrical Machines</b>	<b>35</b>
2.1	Analytical Multi-Layer Model . . . . .	36
2.1.1	Periodicity and Ansatz . . . . .	38
2.1.2	Solution for the Magnetic Vector Potential . . . . .	40
2.1.3	Magnetic Flux Density and Field Strength . . . . .	40
2.1.4	Continuity and Boundary Equations . . . . .	42
2.1.5	Relative Movement of Layers . . . . .	44
2.1.6	System of Equations and Solution . . . . .	45
2.1.7	Power Transfer Between Layers and Torque . . . . .	46
2.1.8	Flux Linkage and Induced Voltage . . . . .	48
2.1.9	Model Limitations and Circumferential Variation of Material Properties . . . . .	50
2.2	Numerical Models of Rotating Electrical Machines with Superconducting Windings . . . . .	50
2.2.1	Finite Element Method for Electromagnetic Problems Involving Superconductors . . . . .	51
2.2.1.1	<i>H-A</i> -Formulation . . . . .	53
2.2.1.2	<i>T-A</i> -Formulation . . . . .	55
2.2.1.3	Meshing and Implementation of Boundary Conditions	60
2.2.2	Induced Voltage . . . . .	61

2.2.3	Electromagnetic Torque . . . . .	64
2.2.4	Modelling of Superconducting Windings and AC Loss Calculation	66
2.3	Modelling of the End-Winding of Racetrack Coils . . . . .	70
2.4	Modelling of the End-Winding of Distributed Stator Windings . . . . .	73
2.5	Modelling of Superconductor Material Properties . . . . .	79
2.5.1	Current Carrying Capacity of 2G HTS Tapes . . . . .	84
2.5.2	Current Carrying Capacity of MgB <sub>2</sub> Wires . . . . .	91
<b>3</b>	<b>Permanent Magnet Excited Direct Drive Wind Turbine Generators</b>	<b>94</b>
3.1	General Properties . . . . .	94
3.2	Parameter Study . . . . .	96
3.3	Exemplary Designs . . . . .	103
<b>4</b>	<b>General Properties and Design of Direct Drive Synchronous Generators with Superconducting Field Winding</b>	<b>105</b>
4.1	General Properties and Iron Topologies . . . . .	106
4.2	Design of Partially Superconducting Direct Drive Generators . . . . .	112
4.2.1	Geometry Parametrization . . . . .	112
4.2.2	Iterative Electromagnetic Design . . . . .	116
4.2.2.1	Iteration Scheme . . . . .	116
4.2.2.2	Geometrical Simplifications and Meshing . . . . .	119
4.2.2.3	Influence of 3D Effects . . . . .	121
4.2.3	Parameter Identification and Phasor Diagram . . . . .	123
4.2.4	Thermal Design . . . . .	125
4.3	Parametric Design Study of Partially Superconducting Direct Drive Generators . . . . .	130
4.3.1	Comparison of ReBCO HTS and MgB <sub>2</sub> Field Windings . . . . .	130
4.3.2	Design of an Electromagnetic Damper . . . . .	136
4.3.3	Selection of the AC Stator Winding . . . . .	149
4.3.4	AC Loss in the DC Field Winding . . . . .	152
<b>5</b>	<b>Numerical Optimization of HTS Excited Direct Drive Wind Generators</b>	<b>158</b>
5.1	Comparison of Iron Topologies . . . . .	159
5.2	Influence of Installation Space and Outer Diameter . . . . .	166

5.3	Comparison of HTS Materials and Cryogenic Temperatures in the Field Winding . . . . .	171
5.4	Exemplary Final Design of a Partially Superconducting Direct Drive Generator . . . . .	175
<b>6</b>	<b>Basic Considerations on Redundancy Operation and Dynamics of HTS Excited Direct Drive Wind Generators</b>	<b>179</b>
6.1	Redundancy Operation . . . . .	180
6.2	Sudden Short Circuit Faults . . . . .	197
<b>7</b>	<b>Alternative Superconducting Wind Generator Concepts</b>	<b>216</b>
7.1	HTS Medium Speed Generators with Rectifier Feeding . . . . .	216
7.2	Fully Superconducting All-HTS Direct Drive Generators . . . . .	220
7.3	Fully Superconducting Direct Drive Generators with HTS Excitation and MgB <sub>2</sub> AC Stator Winding . . . . .	224
<b>8</b>	<b>Summary of Main Findings and Conclusions</b>	<b>227</b>
8.1	Conclusions on HTS Excited Direct Drive Generators . . . . .	227
8.2	Summary and Outlook . . . . .	233
	<b>Bibliography</b>	<b>235</b>
	<b>Own Publications</b>	<b>261</b>
	<b>Supervised Student Theses and Seminar Topics</b>	<b>264</b>

---

<b>Appendix A</b>	<b>Appendix</b>	<b>267</b>
A.1	Grid Connection Topologies for Wind Turbine Systems . . . . .	267
A.2	Overview of Superconducting Machine Projects . . . . .	268
A.3	Material Data . . . . .	271
A.3.1	Material Data of Ferromagnetic Materials . . . . .	271
A.3.1.1	Iron-Nickel Alloy FeNi9 . . . . .	271
A.3.1.2	Lamination Steel . . . . .	272
A.3.1.3	Nickel . . . . .	273
A.3.1.4	Magnetic Slot Wedges . . . . .	274
A.3.2	Material Properties of Permanent Magnets . . . . .	274
A.3.3	Thermal Material Properties . . . . .	275
A.3.3.1	Thermal Conductivity of Copper . . . . .	275
A.3.3.2	Thermal Conductivity of G-10CR . . . . .	275
A.3.4	Electrical Material Properties . . . . .	276
A.3.4.1	Copper . . . . .	276
A.3.4.2	Indium . . . . .	277
A.3.4.3	Iron Nickel Alloys . . . . .	278
A.3.5	Alternative Parametrization of the Lift Factor of ReBCO Coated Conductors . . . . .	278
A.4	Analytical Models . . . . .	279
A.4.1	Derivation of Current Loading Spectra . . . . .	279
A.4.2	Derivation of the Transformation Relation for Time Orders . . . . .	281
A.4.3	Loss Reduction Factor for Eddy Current Losses due to Grooves . . . . .	282
A.5	AC Loss in the Field Winding in Presence of Stator Current Harmonics . . . . .	283
A.6	Slot Plans and Spectra of Stator Windings . . . . .	286
A.7	Parameter Identification . . . . .	290
A.8	Eddy Current Loss Calculation . . . . .	294
A.8.1	Eddy Current Loss in the Damper Screen for Varied Damper Temperature . . . . .	294
A.8.2	Eddy Current Loss for Sudden Single-Phase and Three-Phase Short Circuits of Partially Superconducting Direct Drive Generators	295
A.9	Thermal Model of Partially Superconducting Generators . . . . .	297
A.9.1	Multi Layer Insulation System . . . . .	297
A.9.2	Modelling of Thermal Resistances . . . . .	297

A.9.3 Approximate Dimensioning of the Rotor Support Structure . . . 309  
A.10 Overview of Considered Direct Drive Generators . . . . . 310

---

# Abbreviations and Symbols

## Abbreviations

AC	Alternating Current
AFE	Active Front End
APC	Artificial Pinning Center(s)
<i>BCS</i>	<i>Bardeen-Cooper-Schrieffer</i>
BSCCO	Bismuth Strontium Calcium Copper Oxide (also BiSCCO)
B6, B12	B6, B12 Three- / Six-Phase Rectifier Bridge (uncontrolled)
CAPEX	Capital Expenditures
COP	Coefficient of Performance
CSM	Critical State Model
DC	Direct Current
DFIG	Doubly-Fed Induction Generator
DoF	Degrees of Freedom
EESG	Electrically Excited Synchronous Generator
EMF	Electromotive Force
FEM	Finite Element Method
GA	Genetic Algorithm
GFRP	Glass Fiber Reinforced Plastic / Polymer
<i>GL</i>	<i>Ginzburg-Landau</i> (theory)
<i>GM</i>	<i>Gifford-McMahon</i> (cryo-cooler)
HTC	Heat Transfer Coefficient
HTS, HTSC	High-Temperature Superconductor
HVAC	High Voltage Alternating Current
HVDC	High Voltage Direct Current
IG	Induction Generator
IGBT	Insulated-Gate Bipolar Transistor

## Abbreviations and Symbols

---

IMD	Internal Magnesium Diffusion
LCoE	Levelized Cost of Electricity
LHe, LH <sub>2</sub> ,	Liquid Helium, Hydrogen, Neon, Nitrogen
LNe, LN <sub>2</sub>	
LTSC	Low-Temperature Superconductor
LVAC	Low Voltage Alternating Current
MLI	Multilayer Insulation, Superinsulation
MMF	Magneto-Motive Force
MRI	Magnetic Resonance Imaging
MTBF	Mean Time Between Failure
MTPA	Maximum Torque per Ampere
MVAC	Medium Voltage Alternating Current
NMR	Nuclear Magnetic Resonance
NPV	Net Present Value
NSGA	Non-Dominated Sorting Genetic Algorithm
OFHC	Oxygen-Free High Thermal Conductivity (Copper)
PDE	Partial Differential Equation
PM	Permanent Magnet
PMSG	Permanent Magnet Excited Synchronous Generator
PR	People's Republic
USD	United States Dollar (\$)
Re	Rare-Earth (Metals)
ReBCO	Rare-Earth Barium Copper Oxide (Re = Y, Gd, Eu)
RRR	Residual Resistance Ratio
RVB	Resonating Valence Bond
SC	Superconductor
S.C.	Short Circuit
SCIG	Squirrel Cage Induction Generator
s.f.	self field
SM	Synchronous Machine
SQUID	Superconducting Quantum Interference Device
TRL	Technology Readiness Level
w. r. t.	with respect to
1D, 2D, 3D	One-, Two-, Three-Dimensional



1G, 2G	First, Second Generation (High-Temperature Superconductor)
1ph, 2ph, 3ph	One-, Two-, Three-Phase (Short Circuit)

## Notations

<b>test</b>	program code
$(\cdot)^*$	complex conjugate
$(\cdot)'$	transient
$(\cdot)''$	subtransient
$\equiv$	equivalent
$\vec{a}$	vector
$\underline{z}$	complex number
$\angle \underline{z}$	phase angle of complex number $\underline{z}$
$\underline{\underline{A}}$	tensor
$\mathbf{A}$	matrix
$\hat{A}$	peak value of quantity $A$
$\bar{A}$	average of quantity $A$
$\mathbb{I}$	identity matrix
$\delta_{ij}, \delta(t)$	<i>Kronecker delta, Dirac delta distribution</i>
$ \cdot\rangle,  0\rangle$	ket in <i>Dirac</i> notation, vacuum state in second quantization
$\partial\Omega$	boundary of domain $\Omega$
$\perp, \parallel$	perpendicular, parallel
$a \cdot b$	ordinary multiplication of scalars $a$ and $b$
$\vec{a} \cdot \vec{b}$	scalar product of vectors $\vec{a}$ and $\vec{b}$
$\vec{a} \times \vec{b}$	vector product of vectors $\vec{a}$ and $\vec{b}$
$\vec{a} \otimes \vec{b}$	dyadic product of vectors $\vec{a}$ and $\vec{b}$
$A * B$	convolution of quantities $A$ and $B$
$\nabla \vec{A}$	divergence of vector field $\vec{A}$
$\nabla A$	gradient of scalar field $A$
$\nabla \times \vec{A}$	rotation of vector field $\vec{A}$

$\Delta A, \Delta \vec{B}$	<i>Laplacian</i> , acting on scalar field $A$ or vector field $\vec{B}$
$\partial_x f, f'(x)$	partial derivative of function $f$ with respect to variable $x$
$d_x f$	total derivative of function $f$ with respect to variable $x$
$\hat{a}^\dagger, \hat{a}$	creation, annihilation operator

## Greek Letters

$\alpha$	spin state, parameter in <i>GL</i> theory, exponent in <i>Kim</i> -model, slot angle
$\beta$	angular coordinate for end winding parametrization, spin state, parameter in <i>GL</i> theory
$\Gamma$	Gamma function, boundary of domain
$\gamma$	lead angle, mass density
$\Delta$	distance, energy gap
$\delta$	air gap width
$\varepsilon$	permittivity (relative: subscript r), energy, absorption coefficient
$\eta$	efficiency
$\Theta$	magneto-motive force (MMF)
$\theta$	orientation angle of the magnetic flux density (w.r.t critical axis)
$\vartheta$	complex-valued parameter in analytical multi-layer models
$\bar{\vartheta}$	test function
$\vartheta$	temperature (degree centigrade)
$\kappa$	electrical conductivity, <i>GL</i> parameter
$\lambda$	length (scale), wave length, permeance, thermal conductivity, slimness factor (subscript d), scale, tip-speed-ratio
$\mu$	permeability
$\nu$	absolute space order (w. r. t. entire circumference), reluctivity
$\nu'$	relative space order (w. r. t. electromagnetic period)
$\xi$	length scale, coherence length, parameter in calculation of current displacement
$\rho$	electrical resistivity, electric charge density
$\sigma$	stress, thrust
$\underline{\sigma}$	stress tensor
$\tau$	time constant, per unit time, mean time of collisions, pitch

$\Phi$	magnetic flux
$\phi$	electric (scalar) potential
$\varphi$	polar angle, general phase angle, parameter in calculation of current displacement
$\chi$	loss reduction factor
$\Psi$	flux linkage (peak)
$\psi$	flux linkage (time dependent), wave function, parameter in calculation of current displacement
$\Omega$	(mech.) angular speed, domain
$\omega$	angular frequency (el.)

## Latin Letters

$\vec{A}, A$	vector potential, current loading
$a$	number of parallel branches, parameter in <i>Weibull</i> distribution
$ab$	in-plane direction of anisotropic superconductors
$\vec{B}, B$	magnetic flux density (absolute)
$C$	cost, capacitance, <i>Esson's</i> number (subscript e)
$C'$	specific cost (e.g. w. r. t. power)
$\vec{c}$	general solution vector of linear systems
$c$	critical axis of superconductor, power coefficient (subscript P), curve
$c'$	specific heat capacity
$\vec{D}, D$	electric induction (absolute)
$D$	diffusion coefficient
$d$	diameter, thickness
$\vec{E}, E$	electric field strength (absolute)
$e$	electrical charge
$\underline{e}$	general matrix in field problem formulations
$F$	force
$f$	frequency, fraction (general), non-dimensional scaling parameter
$G$	inductance coefficient
$g$	general integer number
$\vec{H}, H$	magnetic field strength (absolute)
$h$	height

## Abbreviations and Symbols

---

$\hbar$	reduced <i>Planck</i> constant
$i$	current (time dependent), interest rate, gear ratio
$I$	current (effective)
$\underline{I}$	modified <i>Bessel</i> function of the first kind
$\vec{J}, J$	electrical current density (absolute)
$J$	inertia, magnetic polarization, exchange coupling
$j$	imaginary unit
$K$	constant in diode characteristic
$\underline{K}$	modified <i>Bessel</i> function of the second kind
$k$	time order, general factor (loss increase, slot fill), parameter in <i>Kim</i> -model, parameter in <i>Weibull</i> distribution
$\vec{k}$	wave vector
$L$	lift factor of critical current (density), (axial) length, inductance
$l$	length
$M$	torque
$M'$	(gravimetric) torque density
$m$	number of phases, per unit torque, ratio between transport & critical current, mass
$N$	number of turns (winding), number of equations
$n$	rotational speed, number of winding layers, exponent in $E(J)$ -power law of superconductors, number density
$\hat{n}$	normal unit vector
Nu	<i>Nusselt</i> number
$o$	number of adjacent winding schemes fed by the same converter
$P$	power
$p$	number of pole pairs, probability density, volumetric loss density (subscript d), radial coordinate for end-winding parametrization
$p'$	specific price
Pr	<i>Prandtl</i> number
$Q$	number of slots, heat, loss per cycle (hysteresis, subscript: h), full-load hours (annual)
$\dot{Q}$	heat flow
$Q'$	number of slots per basic winding scheme
$q$	no. of slots per pole per phase, loss density per cycle (hysteresis)
$R$	resistance, strength (yield, tensile)
$\underline{R}, \tilde{R}$	complex-valued solution functions in analytical multi-layer models

$\vec{r}$	position
$r$	radius, per unit resistance
Re	<i>Reynolds</i> number
$\vec{S}$	<i>Poynting</i> vector
$S$	apparent power, spin, surface
$s$	slip, shift of rotor pole
$T$	absolute temperature, time period
$\vec{T}$	current vector potential
$t$	time, hopping integral
$\hat{t}$	tangential unit vector
$U$	voltage (effective), $z$ -component of magnetic vector potential
$u$	voltage (time dependent), per unit voltage, no. of full converters in parallel, probability
$v$	velocity, probability
$W$	coil span
$w, \underline{W}, w'$	window function, spectrum
$w$	width
$X$	reactance
$x$	per unit reactance
$x, y, z$	<i>Cartesian</i> coordinates
$Z$	impedance
$\underline{\underline{Z}}$	incidence matrix

## Subscripts and Superscripts

0	no-load, zero-sequence, zero external field, prescribed
1	fundamental
A, B, C, D, E, F	phases of six-phase stator winding
act	(electromagnetically) active parts
ax	axial
B	reference (German: <u>B</u> ezug), boiling
B6, B12	quantities for generator operation with rectifier bridge

b	brushes, winding overhang
c	critical (phase transition), cold, coil
c1, c2	critical value for leaving the <i>Shubnikov- / Meißner</i> -phase
CH	cold head
Cu	copper
ch	cooling channel
cl	current lead
compr	compressor
coupl	coupling
conv	converter, convection
cond	conductive
cp	cooling plate
cryo	cryogenic (cooling system)
cw	cryostat wall
d	dissipated, distribution
d, q	components in the dq-frame of reference
damp	damper (screen)
demag	demagnetization
dt	drive train
e	electromagnetic, engineering
el	electric
eff	effective
exc	excitation
F	<i>Fermi</i>
Fe	iron
Ft	<i>Foucault</i>
f	field winding
fr+w	friction & windage
GL	<i>Ginzburg-Landau</i>
g	generator
geom	geometrical
h	hot
hyst	hysteresis
IL	inter-layer

i	induced, equivalent (iron length)
ip	inter-pole
iso	insulated
k	(sudden) short circuit
L	layer
LL	line-to-line
M	magnet
mag	magnetic
main	main insulation
mech	mechanical
min, max	minimum, maximum
N	rated
n	normal
o	upper
u	lower
p	pole (core), pitch, penetration
ph	phase
pp	peak-to-peak, pressure plate
Q	slot
r	remanence, radial, rotor, relative (permeance, permittivity)
rad	radiation
rcc	radial cooling channel
rel	reluctance
rot	rotation
s	saturation, stator
sc	superconducting
sec	section
si, so	stator inner, outer
sin	sinusoidal
syn	synchronous
sp	side of pole (core)
sup	support
surr	surrounding
src	source

sw	slot wedge
T	single conductor (German: <u>T</u> eilleiter)
t	tooth, total, tape, tangential, transport (current)
th	thermal
U, V, W	phases of three-phase stator winding
vac	vacuum
vM	<i>von Mises</i>
W	wind
w	winding
x, y, z	components in global <i>Cartesian</i> coordinate system
X, Y, Z	components in <i>Cartesian</i> system of the material's rest frame
y	yoke
$\delta$	air gap
$\eta$	efficiency related
$\sigma$	stray (field, inductance . . .)
$\varphi$	circumferential
$\infty$	infinity, e.g. limit $t \rightarrow \infty$
$\sim$	alternating



---

# 1. Introduction and Fundamentals

This thesis is organized in eight chapters. Chapter 1 introduces the topic and summarizes underlying fundamentals in the fields of wind power and superconductivity. Chapter 2 contains descriptions and derivations of applied models and has a methodological scope. The results of design studies on direct drive PM generators for benchmarking are the content of chapter 3. Chapter 4 is on general properties of partially superconducting direct drive generators with main focus on design considerations. The numerical optimization of HTS excited direct drive wind generators is covered by chapter 5. The following chapter 6 contains the analyses of the operation with partially fed stator winding and the dynamic operating characteristics after short circuit faults. Chapter 7 gives an overview of alternative superconducting generator concepts and defines the scope of potential future work. The results are summarized in chapter 8.

Supplementary information, which this thesis builds on, is documented in technical reports [O14, O15] for the sake of brevity. These reports are available upon request at the Institute of Electrical Energy Conversion, Technical University Darmstadt. Owing to the large set of considered generator variants, Tab. A.4 in App. A.10 gives an overview of the generator design characteristics, sorted by section.

The transformation towards a resource-efficient world economy with greatly reduced greenhouse gas emissions is the major challenge faced today. This objective manifests in various national and international political agendas. The European *Green Deal* is a prominent example for such ambitious strategies, according to which the European Union intends to be the first climate-neutral continent by 2050 [60]. The German Federal Climate Change Act even goes beyond this target by striving for a 65 % reduction of greenhouse gas emissions by 2030 compared to 1990 and for climate neutrality by 2045 [74]. With the *Inflation Reduction Act* of 2022 [170], the United States, which are responsible for the second largest greenhouse gas emissions after the PR of China [173], also underlined the global demand for climate change mitigation measures.

---

## Current State and Development Pathway of the Wind Energy Sector

The timely achievement of the envisaged reduction of emissions requires far-reaching transitions, mainly in the transportation and energy sectors. Together with sector coupling and new energy storage concepts, e.g. by means of hydrogen, an unprecedented expansion of renewable energy sources is vital for a realistic chance to limit the global warming to 1.5°C (*Paris agreement* [212]). The need for a much larger installed capacity of renewable sources is aggravated by the ever increasing global electrical energy demand [86], which is driven by both the global population growth and energy-intensive technological developments. Since today's share of renewables in the global electrical energy production is only slightly less than 30 % ([89], including hydro power), fossil energy sources must be replaced on a large scale in the next years. Among renewable sources, wind power features the second largest share ( $\approx 23\%$  in 2021 globally [88]) behind hydro-power ( $> 52\%$  in 2021 globally [88]), for which further expansion is limited by the lack of suitable installation sites. The increase of wind power's installed capacity to many times of its current level is therefore an essential pillar of a successful climate change strategy.

The global, combined installed capacity of onshore and offshore wind power reached about 900 GW in 2022 [90]. In this regard, the PR of China is in the lead with about 365 GW installed capacity, followed by the European Union with 190 GW and the United States with 141 GW [92]. The global, newly installed capacity of 75 GW in 2022 fell short of the all time high of 94 GW in the preceding year 2021 [92]. To date, offshore wind parks account for only 6.4 % ( $\approx 58$  GW [229]) of the total capacity, while providing substantial potential for up-scaling to more than one GW per wind farm. The *Net Zero by 2050* pathway, which has been developed by the *International Energy Agency (IEA)*, requires a total installed wind power capacity of about 3100 GW by 2030 [87], which implies a newly installed capacity of 275 GW per year from now. Based on average powers of newly installed wind turbines in Europe in 2019, 3.1 MW onshore and 7.2 MW offshore [225], the globally required number of newly installed turbines per year must be in the order of 50000 units. To date, the largest production capacities of wind turbines exist in the PR of China (58 %), followed by the European Union (18.5 %) and the United States (10 %) [77].

In Germany, wind power had the overall largest share in the total electricity production in 2022 [68]. This was achieved with an installed onshore capacity of 58 GW and an offshore capacity of about 8 GW by the end of 2022 [68]. The national wind power strategy targets

---

an installed onshore capacity of 115 GW by 2030 and an even stronger relative expansion of offshore wind to 30 GW in the same time period [75].

### **Onshore and Offshore Wind Power**

All scenarios have in common that both on- and offshore wind power are considered. Compared to onshore wind turbines, offshore installations differ regarding the following aspects:

- ⊕ More continuous and stronger winds at sea imply a higher number of full load hours compared to onshore sites, e.g. [79]. Therefore, more energy is harvested per installed capacity.
- ⊕ There are less restrictions regarding the installation site with less lengthy approval procedures.
- ⊕ Lower hub heights suffice to reach suitable wind conditions for wind energy production due to a lower wind shear at offshore sites [195].
- ⊕ Scalability to larger powers is a major requirement for offshore wind turbine systems, while the maximum turbine size for onshore installations is limited for several reasons, e.g. public acceptance and local nature conservation.
- ⊖ The worse accessibility of offshore wind turbines increases the importance of low maintenance solutions with low system complexity [81].
- ⊖ The installation effort is significantly higher offshore and results in a larger cost share of transport and on-site assembly. In case of the generator for offshore installations, the ratio between the cost for infrastructure and transport and the cost for the generator itself is about 50:50 [81]. In contrast, onshore projects exhibit a cost allocation with a ratio transportation/infrastructure:generator of about 20:80 [81].
- ⊖ The overall CAPEX per installed capacity is by a factor of 2 ... 3 higher for offshore wind turbines [226].
- ⊖ A higher number of energy conversion stages is required for offshore wind farms that are located at larger distances from the coast [187], Fig. 1.7. This involves additional transmission losses and a substantial cost overhead for the grid connection equipment.

The high CAPEX for the infrastructure results in a strong demand for higher turbine powers, which is reflected by the evolution of newly introduced wind turbine models from leading manufacturers, Fig. 1.1. The increase in turbine power by a factor of 2 in the

last decade is accompanied by a significant increase in turbine rotor diameters beyond 200 m. While the average nameplate capacity of installed offshore turbines in the North and Baltic Sea is currently about 5 MW, offshore wind turbines with a rated capacity of 15 MW are expected to enter the commercialization stage by 2025 [81]. A linear extrapolation of the trend predicts capacities of 20 MW by 2030 at turbine rotor diameters of more than 250 m. This trend is less pronounced for onshore wind turbines, Fig. 1.2, even though an increase in the maximum power up to about 7 MW also manifests. However, the pressure to achieve a larger power per unit is higher in the offshore market, since the cost of the turbine accounts only for one third to one half of the total cost [81]. The share moreover decreases rapidly with distance to coast and increasing water depth. Wind turbine concepts, which help to reduce the grid connection complexity and enable a cheaper foundation and tower construction, can be most cost-effective, even if the turbine itself is more expensive.

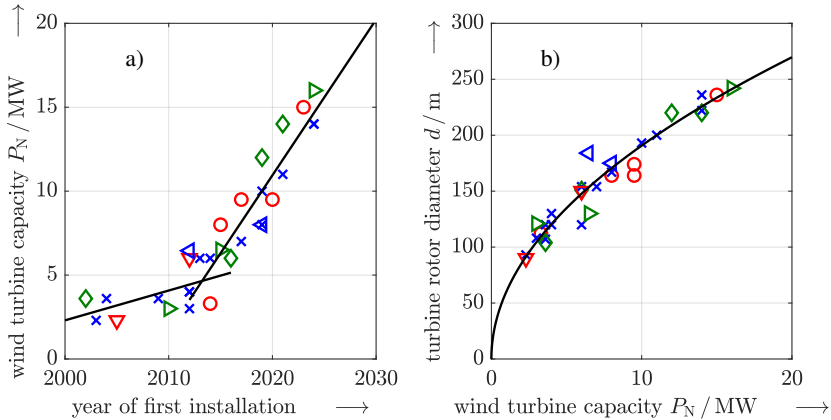
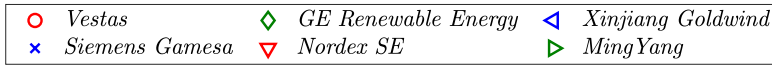


Figure 1.1.: a) Rated wind turbine capacity of newly introduced offshore wind turbines by year. The black lines represent linear fits as guide for the eye. b) Turbine rotor diameter versus rated wind turbine capacity for the same set of offshore wind turbines. The black line features the proportionality  $d \sim \sqrt{P_N}$ . The data is collected from [13], manufacturers' websites and product brochures.

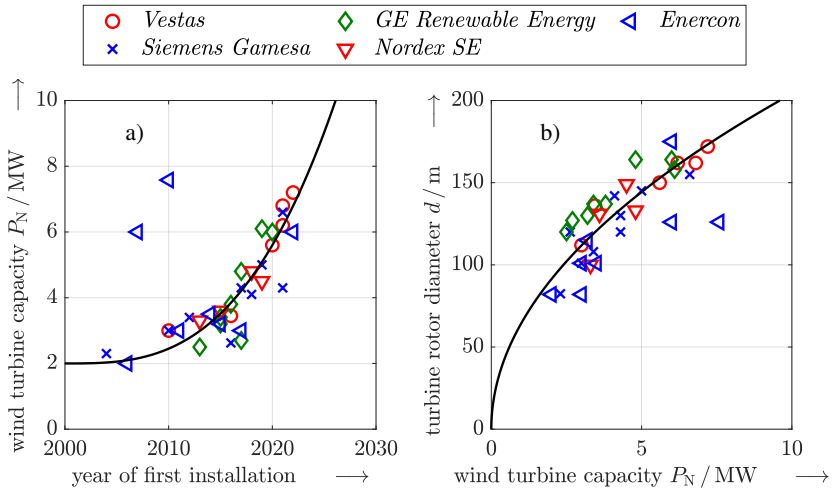


Figure 1.2.: As Fig. 1.1, but for onshore wind turbines. Less clearly pronounced trends are attributed to a larger variety of wind conditions at onshore installation sites. Both strong wind and weak wind turbines are included. The data is collected from [13], manufacturers' websites and product brochures.

## 1.1. Wind Generator Systems

The intended increase in global wind power capacity translates to the following main challenges for wind generator systems:

1. *Availability of critical resources:* Besides concrete and steel for the tower and foundation, costly raw materials can represent a bottleneck for a further up-scaling of production. High energy density magnets contain about 30% of the „rare-earth“ metal neodymium [73] and are used in permanent magnet (PM) synchronous wind generators, but also in electric motors of electric vehicles. However, the required quantities differ by orders of magnitude since a typical traction motor for e-cars contains a few kilograms of NdFeB, whereas PM wind generators require  $10^2 \dots 5 \cdot 10^3$  kg of NdFeB magnets depending on generator type and power. The global demand for neodymium is predicted to increase by at least a factor of 5 until 2030 due to the simultaneous expansion of renewable energy sources and e-mobility [91]. This competition together with the dominance of the PR of China as

supplier of neodymium (> 85% of global production [214]) leads to a substantial resource risk, faced by the wind energy sector.

2. *Cost reduction:* The expansion of wind power can only occur within the limits of economical feasibility. In this regard, wind power competes with other renewable sources. Highly volatile raw material prices of key resources, Fig. 1.3, intensify cost oriented improvements of existing generator systems, e.g. by means of increased modularity, cheaper manufacturing and optimized usage of critical materials. The large fluctuations of the neodymium price in the last years triggered new and intensified ongoing development and research activities towards rare-earth free alternatives. A cost reduction can indirectly be achieved by a lightweight generator design, reducing the nacelle's head mass to get a cheaper tower and foundation, and by improved generators, which allow for a reduced converter rating and a less complex grid connection.
3. *Increase in power and torque density:* The scaling of generator systems to power ratings above 15...20MW for offshore wind turbines is hampered for practical reasons that relate to the generator size and mass. The transportation on wheels of generators with diameters exceeding 5 m is commonly not possible [183], such that modules are manufactured separately with subsequent costly on-site assembly. High lifting capacities during installation moreover strongly increase the associated cost. Reaching highest power levels therefore requires an increase of power and torque density, where values in the order of 200Nm/kg are considered in wind industry as realistic targets in the medium-term [81].
4. *Efficiency improvements:* The overall objective of developments consists in the reduction of the levelized cost of electricity (LCoE), which can be significantly reduced over a wind turbine's lifespan of typically 20...25 years by even small reductions of the generator's loss power [136]. To some extent, larger efficiencies outweigh increased investment costs.
5. *Improvement of robustness and reliability:* Fault induced idle time of wind turbines causes considerable opportunity costs. Robust and low maintenance drive trains are therefore vital for a low LCoE [124]. This applies particularly to offshore installations, where faults often result in long times of inactivity. Gears with high-speed stage and full converters for the grid connection are particularly prone to faults [144, 63]. Future wind generator technologies are required to maintain at least the reliability level of current solutions.

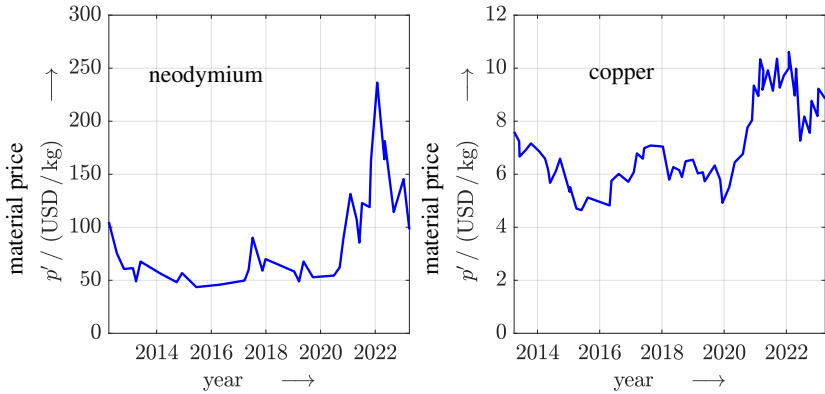


Figure 1.3.: Historical price development of neodymium (left) and copper (right) as key resources used in today's wind generator systems. Data source: [44]

### State of the Art Wind Turbine Drive Trains

The use of superconducting windings is the proposed approach in this thesis to meet these challenges. Before the potentials of superconductivity for generators are discussed in detail in Sec. 1.3, the state-of-the art of wind turbine drive train technologies is summarized. Three main synchronous and induction generator types have been established for speed variable operation at larger power ratings  $P > 1.5\text{MW}$ :

#### *Fully geared drive trains with direct grid connection*

Geared drive trains with doubly-fed induction generators (DFIG) allow for a speed variable operation, while the generator is directly connected to the grid via a generator transformer, Fig. 1.4. The induction generator features typically pole counts of  $2p = 4$  or  $6$ , while the speed of  $n = 1000 \dots 1800\text{rpm}$  requires a high-speed gear stage [177]. The wound rotor is fed via brushes and three slip rings with a three phase current system of slip frequency  $f_r = s \cdot f_s$ . Both the brushes and the rotor side converter are rated for  $20 \dots 30\%$  of the generator's nominal power [171] due to a limited speed variation.

Advantages of DFIG-based drive trains are:

- ⊕ The smaller rating of the converter reduces the cost and yields a higher reliability compared to fully-rated converters. The higher reliability of the power electronics

partially outweighs the higher failure rate of the gearbox.

- ⊕ The high speed  $n = 1000 \dots 1800 \text{ rpm}$  yields compact, lightweight generators. The reduced mass is only partially counteracted by the mass of the three-stage gear.
- ⊕ No costly permanent magnets are used, eliminating the resource risk and resulting in a comparably cheap generator.

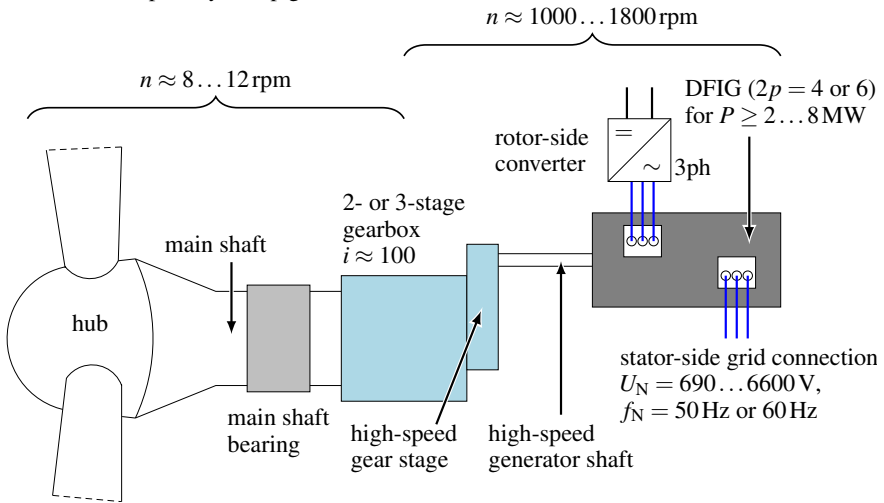


Figure 1.4.: Schematic of a fully geared wind turbine drive train with a grid-connected doubly-fed induction generator (DFIG).

Major disadvantages are:

- ⊖ The maintenance effort and the failure rate are elevated due to the high-speed gear stage and the brush contact. The overall failure rate of the drive train is by about 40 % higher than for permanent magnet excited generators [35].
- ⊖ The brushes inherently cause an increased maintenance effort. Brushless DFIGs, which were in the focus of several research projects, e.g. the EU funded *windrive* project [198], could potentially eliminate this disadvantage.
- ⊖ The annual power production is lower than for PM generators due to the more restricted speed range.
- ⊖ The sensitivity with respect to grid faults requires additional measures, like the „crow-bar“, to enhance the grid ride-through capabilities [223].



In spite of the shortcomings, the geared DFIG drive train is the dominating concept for onshore wind power. Here, its market share is stable in the order of 50 % in the past years with no evidence for a decline [34]. In contrast, DFIG are not used for offshore wind power for reliability and maintenance reasons.

#### *Geared drive trains with full-scale power converters*

Fully geared squirrel cage induction generators with fully-rated converter for grid connection rather represent an alternative for offshore installations with a global market share of about 17 %. With this approach, the maintenance effort of the brush system is eliminated, while the generally low power factor implies a rather high converter rating. A higher pole count and a lower speed are not feasible due to the decreasing power factor. Induction generators are not suitable for the application of superconducting windings and are therefore not considered in this thesis.

The medium speed concept features a two- or three-stage gear without high-speed stage [237]. The much lower rotational speeds of the generator compared to DFIGs or squirrel cage IGs greatly reduce the gear-related reliability issues, Fig. 1.5. To date, permanent magnet synchronous generators are the preferred choice for medium speed wind power applications with compact generator designs. The comparably small generator size facilitates the transport and the installation and allows for a simple implementation of an intense stator cooling. A fully-rated converter is used for the grid connection.

Advantages of the medium speed drive train are:

- ⊕ The medium speed generator is compact with a strongly reduced amount of NdFeB magnets compared to the gearless solution [81].
- ⊕ The efficiency is high due to higher rotational speeds (compared to the direct drive concept) and due to low rotor losses (compared to DFIGs and SCIGs).
- ⊕ The reliability is increased, as the vulnerable high-speed gear stage is eliminated.

The major challenge of the medium speed concept relates to the converter:

- ⊖ The PM excitation limits the power factor to  $|\cos \varphi| \lesssim 0.8$  and yields a higher converter rating, i.e. compared to unity power factor by  $\approx 0.8^{-1} = 1.25$ .
- ⊖ The fully-rated converter is costly and exhibits higher rates of failure.

- ⊖ In spite of the reduced amount of NdFeB magnets, a residual raw-material resource risk remains.

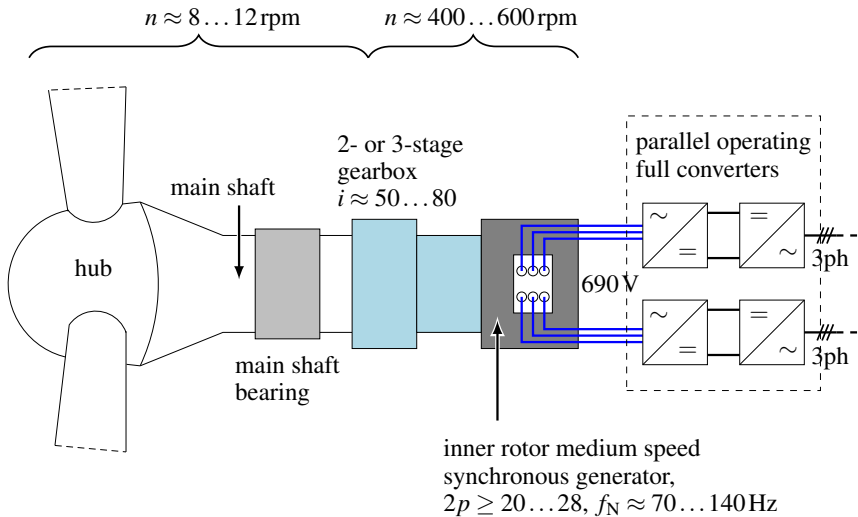


Figure 1.5.: Schematic of a medium speed wind turbine drive train. The high-speed gear stage is eliminated in favour of a higher reliability compared to the fully geared alternative in Fig. 1.4. Simultaneously, the generator size and mass is reduced by about one order of magnitude compared to the direct drive alternative in Fig. 1.6. The gear and the generator may be fully integrated, semi-integrated or modular.

To date, the onshore market share of medium speed drive trains is rather small with 13 % globally [34]. However, the offshore market share has increased to about 20 % already by the end of 2018 with predictions, according to which medium speed PMSGs can account for half of all newly installed offshore wind generators in 2030 [81].

Superconducting, electrically excited medium speed machines have not been considered in the context of wind power applications so far. The potential analysis of superconducting windings to overcome the challenges for medium speed drive trains will be part of future work, while preliminary analyses are discussed in Ch. 7.

#### *Gearless drive trains with full-scale power converter*

The gearless and hence direct drive concept features a minimum number of drive train components in the nacelle and the lowest system complexity. A fully-rated converter is

used for the grid connection of the synchronous generator, Fig. 1.6. Both PM excited generators and electrically excited gearless generators are in use for wind power conversion. In case of PMSGs, the power factor is generally lower in order to save costly magnets, which increases the converter rating. For electrical excitation, the current is commonly transferred to the rotor via brushes and two slip rings with a rating that is much lower than for DFIGs. The low rotational speed implies a high torque and a correspondingly large generator size due to the scaling  $M \sim d^2 \cdot L$  ( $d$ : generator rotor diameter,  $L$ : generator rotor axial length).

The main advantages of this drive train concept are:

- ⊕ The system complexity is low. The reliability and robustness are high. This drive train features the lowest maintenance effort.
- ⊕ Losses in the gear are eliminated.
- ⊕ In case of PM excitation, the rotor losses are very small, compared to the total losses.
- ⊕ The up-scaling to larger turbine power ratings is simple in case of modular manufacturing.

Following disadvantages limit the use of gearless drive trains, particularly for onshore wind power:

- ⊖ The generators are very large and heavy with diameters  $d > 5$  m for higher power levels  $\geq 7$  MW. Correspondingly, the cost of transportation and assembly are high.
- ⊖ In case of PM excitation, direct drive generators require the largest amount of NdFeB magnets, i.e.  $\geq 3$  t per generator with power rating of  $P \geq 5 \dots 7$  MW [59].
- ⊖ The nominal efficiency is generally low due to the lower rotational speed and the dominating *ohmic* loss in the stator winding [59], caused by the high stator current loading  $A_s$ . The high value of  $A_s$  is necessary to achieve the required torque density. In case of an electrical excitation, the additional excitation loss further reduces the efficiency. This holds particularly true, if a high power factor close to unity is required in order to limit the converter rating.
- ⊖ The fully-rated converter is costly and exhibits higher rates of failure.

Due to the low complexity and the simple up-scaling, direct drive synchronous generators dominate offshore wind applications, with a global market share of about 54 % for perma-

ment magnet excitation and 7 % for electrically excited generators by the end of 2018 [34]. The gearless concept plays a minor role in the onshore market with global market shares of only 17 % and 9 % for PMSGs and EESGs, respectively [34].

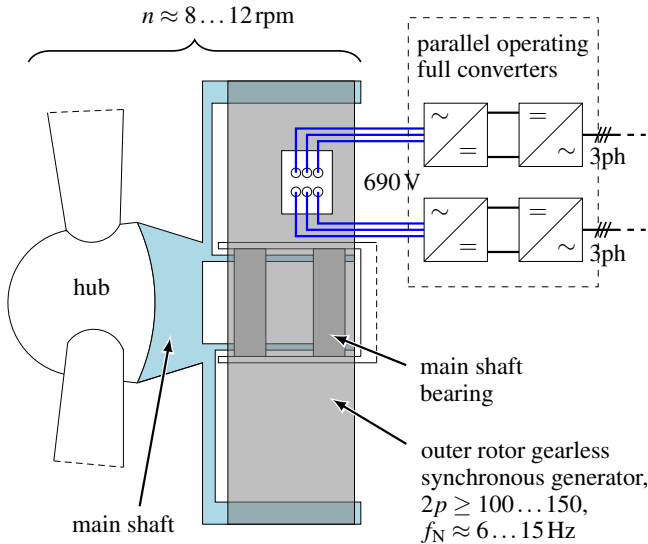


Figure 1.6.: Schematic of a gearless wind turbine drive train with a direct drive outer rotor synchronous generator. The stator winding is fed by fully-rated converters for speed variable operation.

To date, the electrically excited direct drive synchronous generator is the major wind generator type that is considered for the application of superconducting windings, Sec. 1.3. Superconducting field windings are within the scope of this thesis, Ch. 4 - 6, while preliminary analyses of superconducting AC poly-phase stator windings are discussed in Ch. 7.

Besides the currently used wind generators, alternative machine types have been investigated as potential candidates for superconducting wind generators. DC machines and synchronous machines with rotating armature (fed by brushes and three slip rings) are examples for approaches that are motivated by the simpler, stationary cryogenic system [182, 208]. In these cases, it must be proven in the future that the advantages gained by superconducting windings overcompensate the shortcomings, for which these machine types are not used in conventional generators to date.

### Potentials of Superconducting Windings in Wind Generators

Technical superconductors enable a nearly loss free DC current operation and feature reduced losses under suitable AC operating conditions, Sec. 1.2. In the context of rotating electrical machines, mainly superconducting windings are considered, while superconducting stacks and bulks are also discussed as an alternative to high energy density permanent magnets. The very low electrical resistance of conductors in the superconducting state allows for increased „engineering“ current densities that are by one to two orders of magnitude higher than achievable with conventional copper windings. This generally allows to increase the current loadings and / or the air gap flux densities in rotating electrical machines.

Regarding the aforementioned challenges of currently used wind turbine drive trains, the unique properties of superconductors offer following potentials for synchronous wind generators:

- The significantly larger magneto-motive force (MMF) of a superconducting field winding  $\Theta_f$  can be used to increase the power factor, e.g. to  $|\cos \varphi_s| = 1$ . This minimizes the converter rating for both direct drive and medium speed drive trains. Moreover, the reduced stator current at an increased flux density for a given torque implies a decrease of the *ohmic* loss in the stator winding. The latter advantage typically overcompensates the additional compressor power that is required for the cryogenic cooling of the superconductor, Ch. 4.
- The higher MMF  $\Theta_f$  allows to eliminate heavy iron parts completely or to reduce their flux guiding cross sections. This enables more lightweight magnetic topologies, which would not be feasible with a PM excitation or copper field windings.
- Generators with superconducting field winding profit from the variable excitation by eliminating the excitation losses. This yields efficiency improvements, particularly at partial load.
- The electromagnetic utilization, as product of stator current loading  $A_s$  and fundamental, radial air gap flux density amplitude  $B_{\delta,1}$ , e.g. measured by *Esson's* number  $C_e \sim A_s \cdot B_{\delta,1}$ , can be increased by a factor of two or more. This is achieved by
  - an increased rotor field radial amplitude  $B_r$ , which results in a higher air gap field fundamental amplitude  $B_{\delta,1}$ , and / or
  - a higher stator current loading  $A_s$ , if wider slots (narrow teeth) or even stator

air gap windings, either normal- or superconducting, are used. This allows the up-scaling of the wind turbine powers beyond limits, which PM excited generator experience regarding the feasibility of transports and the tower head mass.

- The use of superconducting AC stator windings is particularly promising for direct drive generators, where very low stator frequencies allow reduced AC losses. The high current carrying capacity allows to achieve superior stator current loadings  $A_s$ . Moreover, the potential for efficiency improvements is large in this case, since the *ohmic* loss in the stator winding is by far the dominating loss group for this generator type.

Besides improvements of existing concepts, superconducting windings can serve as enabler for innovative grid connection topologies. A typical offshore grid connection topology with medium voltage collection grid and high voltage DC transmission is shown in Fig. 1.7 [187]. Grid connections for offshore installations near the coast as well as for onshore wind power are shown in App. A.1. Based on these topologies, superconducting windings could offer following alternatives:

- The adjustment of the fundamental power factor to  $|\cos \varphi_s| = 1$  allows to replace the generator side active front end (AFE) of the fully-rated converter with a passive rectifier, e.g. B6 or B12 diode rectifier bridges in case of 3-phase or 6-phase stator AC windings. This requires however a unity power factor for constant stator voltage in the entire turbine speed range, which increases the excitation MMF at low speeds and hence the required amount of superconductors. It therefore implies a primary application to medium speed generators, Ch. 7.
- A sufficiently dynamic, variable, nearly loss free excitation could enable a connection of medium speed generators to a DC collector grid. If passive power electronic devices, such as diode rectifiers, replace the active front end, which typically employs IGBTs, a higher voltage level is feasible. If the stator terminals are directly connected to the generator transformer with subsequent rectification, the transformer operates at elevated frequency in the order of 100 Hz, Fig. 1.5. The doubled frequency compared to generator transformers feeding into conventional collector AC grids would yield a reduction of the transformer mass by about 1/2. This size reduction would greatly simplify the installation in the nacelle or tower and, if installed in the nacelle, reduces the tower head mass.

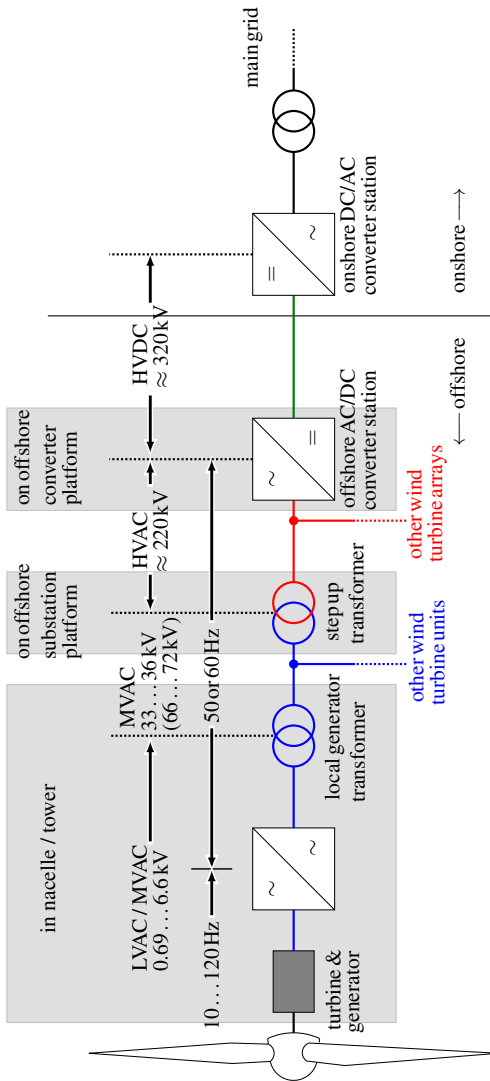


Figure 1.7.: Schematic of a grid connection topology for wind farms at larger distance of several kilometres to the coast. In this case, high voltage DC (HVDC) transmission is economical. Recently, a trend towards an increased voltage in collection grids of 66...72 kV manifests [166]. The fully-rated converter and the generator frequencies are shown under the assumption of direct drive ( $\approx 10$  Hz) or geared ( $\approx 120$  Hz) PM excited synchronous generators.

## 1.2. Superconductivity: Fundamentals and Applications in Power Engineering

### Discovery and First Phenomenological Description

The existence of a superconducting phase is known for more than 100 years since its discovery for mercury by *H. K. Onnes* in 1911 [165]. Superconductivity was first discovered for several chemical elements, before also alloys and ceramics were shown to possess superconducting phases [184]. The superconducting *Meissner* phase is characterized by two physical properties:

1. The electrical resistance of the material drops abruptly to a not measurable value („zero“ resistance) below a material dependent critical temperature  $T_c$  [10].
2. An external magnetic field is completely expelled from the interior of the superconducting sample. This is known as *Meissner-Ochsenfeld* effect, which was discovered in 1933 by *W. Meissner* and *R. Ochsenfeld* [150]. The superconducting phase persists up to a material dependent critical magnetic field, above which an abrupt transition to the normal conducting phase occurs.

An early phenomenological model of superconductivity has been proposed by *F. and H. London* in 1935. It comprises the *London* equations (1.1), (1.2) [143]. The first *London* equation can be derived from *Drude's* electronic equation of motion for infinite mean time between particle collisions  $\tau \rightarrow \infty$ , which reflects the zero resistance nature of superconductors. The second *London* equation is a direct consequence of *Faraday's* law, where  $\vec{J}_s$  is the superconductor current density,  $n_s$  is the volumetric charge carrier density, and  $e_s$ ,  $m_s$  are the charge carriers' electrical charge and effective mass, respectively.

$$\frac{d\vec{J}_s}{dt} = \frac{n_s \cdot e_s^2}{m_s} \cdot \vec{E} \quad \text{first London equation} \quad (1.1)$$

$$\nabla \times \vec{J}_s = -\frac{n_s \cdot e_s^2}{m_s} \cdot \vec{B} \quad \text{second London equation} \quad (1.2)$$

The model predicts that screening currents flow in a thin surface layer of the superconducting sample and screen the interior from any external magnetic field. Both, the screening current density and the magnetic field decay exponentially towards the inner of the sample with the so-called *London* penetration depth  $\lambda_L$  [83]. Since the model is phenomenological, it gives no explanation of the mechanism leading to zero resistance. The discovery



of the isotope effect on critical temperature in 1950 pointed to the important role of the lattice for the underlying physics [149].

### Microscopic Perspective

Existing concepts, such as the (mean field) *Fermi* liquid theory of electrons and the *Jellium* model, were not able to explain the existence of a state with zero resistance [84]. However, within the scope of a quantum mechanical treatment, it can be shown that the *fermionic* electronic ground state is unstable with respect to an (arbitrarily small) attractive interaction between electrons. In this case, pairs of electrons condensate in a bound state with an energy, which is by the energy gap width  $\Delta$  lower than two times the *Fermi* level  $2\varepsilon_F$ . These pairs of electrons are called *Cooper* pairs, named after *L. N. Cooper*, who discovered the instability in 1956 [39]. The idea of *Cooper* pairs led to the *BCS* theory, which is based on the (variable particle number) product state (1.3) of several electron pairs with opposing momentum  $\{\vec{k}, -\vec{k}\}$  and spin  $\{\alpha, \beta\}$ .  $v_{\vec{k}}$  denotes the probability that a *Cooper* pair  $(\vec{k}\alpha, -\vec{k}\beta)$  exists and is determined by calculus of variations [11].  $\hat{a}^\dagger$  denote the creation operators and  $|0\rangle$  the vacuum state in second quantization.

$$|\psi\rangle_{\text{BCS}} = \prod_{\vec{k}} \left( u_{\vec{k}} + v_{\vec{k}} \cdot \hat{a}_{\vec{k}\alpha}^\dagger \hat{a}_{-\vec{k}\beta}^\dagger \right) |0\rangle \quad (1.3)$$

For conventional superconductors, the attraction between electrons is phonon-mediated due to lattice deformations by *Coulomb* interaction [84]. The *Cooper* pairs behave like bosons, such that a common quantum mechanical state is attained. While conventional superconductors feature spin  $S = 0$  (singulets), the anisotropy in high-temperature superconductors (HTS) yields *d-waves* for *Cooper* pairs [83]. The origin of the attractive interaction in high-temperature superconductors is not fully clear to date. The first approach of a theoretical description in form of the resonating valence bond (RVB) theory by *P. W. Anderson* dates back to 1987 and is based on the *Hubbard* hamiltonian of *Mott* insulators and on the *t-J*-model [7].

### Type-II Superconductors and Ginzburg-Landau Theory

From a power engineering perspective, superconductors, which are either in the normal conducting or in the *Meissner* phase (type-I superconductors), are not useful due to their low critical magnetic fields. Therefore, the existence of a mixed state (*Shubnikov* phase) with both normal conducting and superconducting regions in so-called type-II supercon-

ductors is vital for technological applications with high currents and/or high magnetic fields [120]. The co-existence of the superconducting and normal conducting phase within one solid implies that the formation of the surface in between must be energetically favourable, in spite of a reduced *Cooper* pair density in the vicinity of the surface. The *Ginzburg-Landau* theory of superconductors is a phenomenological theory, which explains the difference between type-I and type-II superconductors [76]. It is applicable to (largely isotropic, i.e. metallic) conventional superconductors but also to the highly anisotropic high temperature superconductors, if direction dependent effective masses of the charge carriers are introduced [83]. The theory is based on the finding that the transition from the normal to the superconducting state is of second order (latent heat at transition  $\Delta Q = 0$ ). The governing order parameter is the macroscopic wave function  $\psi(\vec{r})$  of the superconducting state, where  $|\psi(\vec{r})|^2$  is the *Cooper* pair density. The minimization of the free enthalpy with respect to  $\psi(\vec{r})$  and the magnetic vector potential  $\vec{A}$  leads to the *Ginzburg-Landau* equations (1.4), (1.5) [76] with the superconducting current density  $\vec{J}_s$  and the parameters  $\alpha$ ,  $\beta$ , that originate from an expansion of the enthalpy with respect to even powers of the order parameter  $\psi(\vec{r})$ .

$$0 = \alpha \cdot \psi(\vec{r}) + \beta \cdot |\psi(\vec{r})|^2 \cdot \psi(\vec{r}) + \frac{1}{2m} \cdot \left( -j\hbar\nabla + 2e\vec{A} \right)^2 \psi(\vec{r}) \quad (1.4)$$

$$\vec{J}_s = \frac{je\hbar}{m} \cdot (\psi^*(\vec{r}) \cdot \nabla \psi(\vec{r}) - \psi(\vec{r}) \cdot \nabla \psi^*(\vec{r})) - \frac{4e^2}{m} \cdot |\psi(\vec{r})|^2 \cdot \vec{A} \quad (1.5)$$

The solution of (1.4), (1.5) yields two characteristic length scales  $\lambda_L$  (*London* penetration depth),  $\xi_{GL}$  (*Ginzburg-Landau* coherence length), which determine the decay of the magnetic field and the variation of the *Cooper* pair density, respectively. It is the ratio of these length scales, which determines whether the superconductor is of type I or II, (1.6), (1.7) [120] ( $\kappa$ : *Ginzburg-Landau* parameter).

$$\kappa = \frac{\lambda_L}{\xi_{GL}} \lesssim \frac{1}{\sqrt{2}} : \quad \text{type-I SC } \textit{Meissner} \text{ phase only} \quad (1.6)$$

$$\kappa = \frac{\lambda_L}{\xi_{GL}} \gtrsim \frac{1}{\sqrt{2}} : \quad \text{type-II SC with } \textit{Meissner} \text{ and } \textit{Shubnikov} \text{ phase} \quad (1.7)$$

The *Shubnikov* phase persists up to considerably higher magnetic flux densities (e.g.  $B_{c2} = 24$  T for Nb<sub>3</sub>Sn, 16 T for NbTi at  $T = 0$  K [184]). In this phase, the magnetic flux enters the solid in the form of flux vortices with a quantized amount of magnetic flux. The vortices arrange in a regular pattern (*Abrikosov* lattice [3]). Every movement of vortices

results in the presence of an electric field. If a transport current is impressed, the *Lorentz* force drives the flux lattice by dissipating an amount of energy, which inhibits any technical use. However, the (artificial or manufacturing-induced) creation of crystallographic defects yields local potential wells („pinning centres“), which pin the flux vortices up to sufficiently high transport currents and magnetic fields, yielding „hard“ superconductors [29]. Most prominent low-temperature „hard“ superconductors are NbTi (ductile alloy) and Nb<sub>3</sub>Sn (brittle inter-metallic compound, used for highest magnetic field applications). Besides, high-temperature superconductors were discovered in 1986 by *J. G. Bednorz* and *K. A. Müller* [18]. The superconducting phase of MgB<sub>2</sub> was discovered in 2001 by *Nagamatsu* et al. [155], Fig. 1.8. In high-temperature cuprate superconductors (e.g. Tab. 1.1), the layered architecture yields an „intrinsic“ anisotropic pinning. Artificial pinning (e.g. doping with BaZrO<sub>3</sub> or BHfO) of ReBCO (Re = Y, Gd, Eu, rare-earth barium copper oxide) conductors has recently led to a significant increase of the in-field current carrying capacity [183]. The pinning centres allow for a loss free DC current transport, apart from some residual loss due to thermally activated flux creeping.

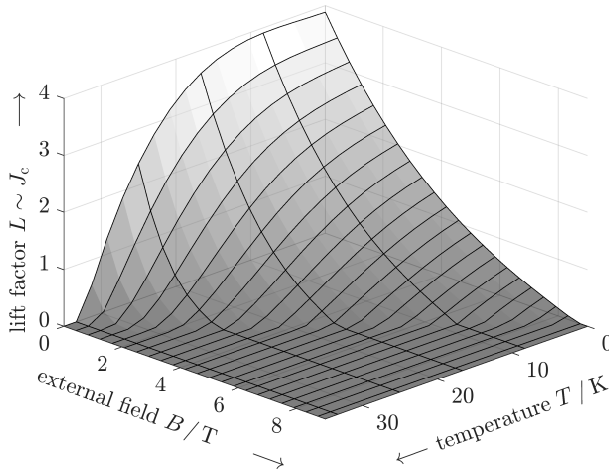


Figure 1.8.: Exemplary critical surface  $(T, B, J)$  of a MgB<sub>2</sub> superconductor from *ASG Columbus* [148]. Here, the lift factor  $L$  is defined as the ratio between the critical current density for operating conditions  $(T, B)$  and the value of  $J_c$  at  $T = 30\text{K}$  and no external magnetic field/only self field (s.f.).

In contrast, both an AC transport current and a sufficiently high magnetic AC field result in a significant periodic escaping and re-entering of flux vortices. In „hard“ superconductors, this is accompanied by a periodic process, in which vortices break loose from the potential

well by dissipating power. The produced AC loss as „hysteresis loss“ is hence a major design restriction for AC applications [78], e.g. for stator windings in fully superconducting generators.

This hysteretic behaviour of „hard“ superconductors can approximately be described with the critical state model (CSM), which was introduced by *C. P. Bean* in 1962 [16, 17]. It assumes a sharp, step-like transition between current carrying and current free regions and allows for an analytical treatment of several geometries and combinations of transport current and applied external field [78]. This model was extended to a magnetic field dependent critical current density  $J_c(B)$  by *Kim* [116]. Extensive early work on the calculation of the superconducting state and the AC loss was moreover carried out by *Clem*, *Brandt* and *Norris* [38, 28, 162, 163]. Calculations based on critical state models generally neglect any flux creeping effects, which arise due to the thermal activation of flux vortices leaving the pinning center induced potential wells, especially in HTS. These effects can be incorporated in numerical models by introducing a highly non-linear power law relation  $E(J)$ , see (2.127) in Sec. 2.5. *Barrett* and *Prighozhin* showed that the critical state model represents the limiting case of power-law models for diverging exponent  $n \rightarrow \infty$  [12].

### Technical Superconductors

Tab. 1.1 summarizes low- and high-temperature superconductors that are used for technical applications. The energy gap  $\Delta$  is typically in the order of a few meV for low-temperature superconductors and exceeds 15...20meV in case of highly anisotropic high-temperature superconductors (crystallographic *ab*-plane) [184]. For the anisotropic superconductors (HTS,  $\text{MgB}_2$ ), significantly lower critical magnetic fields in the crystallographic *c*-axis occur.

For all power engineering applications, the power consumption for maintaining the superconducting phase during operation is crucial and must be lower than the saved  $I^2R$  loss of normal conducting alternatives. Compared to the low-temperature superconductors (LTSC) NbTi and Nb<sub>3</sub>Sn, high-temperature superconductors and  $\text{MgB}_2$  offer the large advantage of a strongly increased coefficient of performance (COP) of commercial cryogenic cooling systems. Therefore, the main focus is recently on these materials for power engineering applications, while LTSCs remain the leading technology for research applications, where high and ultra-high fields must be excited in rather large volumes.

Table 1.1.: Properties of technically used type-II superconductors [184].  $\kappa = \lambda_L/\xi_{GL}$  denotes the ratio of characteristic length scales (*Ginzburg-Landau* parameter: (1.6), (1.7)).

	$T_c$	$B_c, B_{c2}$	$\xi_{GL}$	$\lambda_L$	$\sqrt{2}\kappa$
NbTi	9.6 K	16 T	4 nm	60 nm	21
Nb <sub>3</sub> Sn	18 K	24 T	4 nm	80 nm	28
MgB <sub>2</sub>	39 K	15 T (ab), 3 T (c)	10 nm (ab), 2 nm (c)	110 nm (ab), 280 nm (c)	> 15
Bi <sub>2</sub> Sr <sub>2</sub> CaCu <sub>2</sub> O <sub>8</sub> (Bi-2212)	94 K	> 60T (ab), > 250T (c)	2 nm (ab), 0.1 nm (c)	>200 nm (ab), >15000 nm (c)	> 140
Bi <sub>2</sub> Sr <sub>2</sub> Ca <sub>2</sub> Cu <sub>3</sub> O <sub>8</sub> (Bi-2223)	110 K	40 T (ab), >250 T (c)	3 nm (ab), 0.1 nm (c)	150 nm (ab), >1000 nm (c)	≥ 70
YBa <sub>2</sub> Cu <sub>3</sub> O <sub>7</sub> (YBCO) <sup>a)</sup>	92 K	240 T (ab), 110 T (c)	1.6 nm (ab), 0.3 nm (c)	150 nm (ab), 800 nm (c)	> 127

<sup>a)</sup> GdBCO/EuBCO exhibit similar properties with slightly higher in-field crit. current densities  $J_c$  [57, 230, 85].

Comparing high-temperature superconductors of the first generation (1G, BSCCO: Bi-2212, Bi-2223) and second generation (2G, ReBCO coated conductors, Re = Y, Gd, Eu), the conductor composition implies a larger cost decrease potential for 2G HTS conductors. BSCCO conductors require a costly silver matrix with a volume fraction of about 70 % (Fig. 1.9, [14]), while ReBCO coated conductors consist mainly of much cheaper stainless steel substrates (Fig. 2.25) with only small fractions of silver and a copper fraction that depends on the stabilization requirements. Therefore, only 2<sup>nd</sup> generation (2G) conductors are considered in this thesis, as a significant cost reduction can be expected in the next years, induced by increasing production capacities.



Figure 1.9.: Exemplary cross section of a multifilamentary 1<sup>st</sup> generation HTS BSCCO wire [15]. The silver matrix is a main cost factor and restricts the cost reduction potential of 1<sup>st</sup> generation HTS conductors.

MgB<sub>2</sub> conductors exhibit an inferior in-field current carrying capacity and require lower temperatures  $T \leq 20$  K, Fig. 1.8, but outweigh these drawbacks partially by a much lower price. No costly materials are required for the production and the manufacturing (adapted from the LTSC production) is simpler compared to ReBCO coated conductors. Cost-

neutral improvements of the performance have been achieved recently and are expected to continue, so that, at present,  $\text{MgB}_2$  conductors are regarded as the main competitor for 2G HTS conductors in the field of superconducting power applications [183]. A selection of manufacturers of HTS and  $\text{MgB}_2$  conductors is listed in Tab. 1.2.

To date, iron-based superconductors, discovered in 2006 [107], have not reached readiness for technical applications. This material class may however yield promising future candidates, due to the comparably high critical temperatures in the range 25 ... 55 K [184]. This material class is not considered in this thesis.

Table 1.2.: Selection of commercial manufacturers of 1G/2G HTS conductors and of  $\text{MgB}_2$  wires.

manufacturer	country	conductors
<i>SuperPower (Furukawa)</i>	US	ReBCO
<i>American Superconductors (AMSC)</i>	US	ReBCO ( <i>Amprium</i> )
<i>SuNAM</i>	Korea	GdBCO
<i>Sumitomo Electric Industries (SEI)</i>	Japan	Bi-2223
<i>THEVA</i>	Germany	GdBCO
<i>deutsche nanoschicht / BASF</i>	Germany	YBCO
<i>Fujikura</i>	Japan	EuBCO, GdBCO
<i>Bruker</i>	i.a. US, Germany	Bi-2212
<i>SuperOx</i>	Japan / Russia	ReBCO
<i>Shanghai Superconductor</i>	China	YBCO
<i>Hypertech Research</i>	US	$\text{MgB}_2$
<i>ASG Columbus</i>	Italy	$\text{MgB}_2$

Sec. 1.3 summarizes approaches for the application of „hard“ superconductors in rotating electrical machines.

### Cooling of Superconducting Windings

In spite of the much higher critical temperatures, typical operating temperatures of HTSCs are in the order of 30 K in order to achieve a sufficient utilization of the costly material and in order to ensure sufficient temperature and current margins.  $\text{MgB}_2$  windings must be operated at 20 K in order to realize technically reasonable critical engineering current densities, see Sec. 2.5.2. These temperatures can be achieved by cooling with commercially available „off-the-shelf“ cryo-coolers, which are available from several suppliers,

e.g. *Sumitomo Heavy Industries*, *Cryomech* or *ARS*, Fig. 1.10 ( $\dot{Q}$ : removed heat per time). The cooling system, Fig. 1.11, comprises a compressor unit and a cold head with either one or two cooling stages.

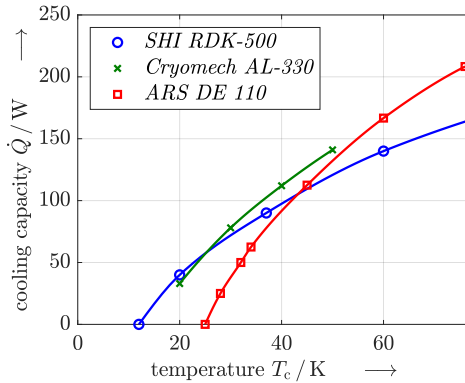


Figure 1.10.: Cooling capacities of commercially available cryocooler systems as function of the cold side temperature (at a warm side temperature  $T_h = 293$  K). Single stage *Gifford-McMahon* (GM) cryo-coolers are considered with sufficient capacity at  $T_c = 30$  K. Sources and data sheets: [200], [42], [9].

In the latter case, heat is removed at two different temperature levels, which generally allows to pre-cool e.g. radiation shields or current leads at elevated temperatures in the range of 50...60 K. High-capacity single stage GM cryo-coolers are suited for cooling the windings of rotating electrical machines. They can remove about  $\dot{Q} \approx 75$  W at 30 K, if operated with a compressor at the 50 Hz grid, Fig. 1.10. However, the minimum achievable temperature and the maximum removed heat  $\dot{Q}$  at 20 K differ considerably among the commercially available coolers, depending on the primarily intended operating range. The mean time between failures (MTBF) of the cryo-cooler system exceeds typically 9 years, while maintenance service intervals are typically 2 years [183].

Three main cooling methods exist for achieving the operating temperatures in the range 20...30 K for ReBCO and MgB<sub>2</sub> windings [184]:

- Direct cooling: Heat is removed from the superconductor in direct contact with a coolant fluid. In case of bath cooling, the device is immersed in a pool of fluid, where natural convection (evaporation/boiling) governs the heat exchange. Alternatively, the coolant flows through channels and removes heat by natural or forced convection (internal cooling). ReBCO windings at 30 K can be gas-cooled with hydrogen ( $T_B = 20.3$  K at 1 atm), neon ( $T_B = 27.1$  K at 1 atm) and helium ( $T_B = 4.2$  K at 1 atm). For necessarily lower temperatures of MgB<sub>2</sub> windings, a cooling with hydrogen or helium is possible.

- Fluid-mediated cooling: The removed heat is transferred from the winding to a cold „anchor“ by conduction [184]. A coolant fluid is used to transfer the heat from the cold anchor to the cold stage of the cold head by convection. The same restrictions on applicable coolants as for direct cooling apply.
- Conduction cooling: The heat is transferred from the HTS or  $MgB_2$  winding entirely by conduction to the cold stage of cold heads via oxygen-free high thermal conductivity copper bars (OFHC). This cryogen-free cooling system reduces the system complexity but requires large cross sections of the OFHC bars to prevent an excessive temperature difference between cold stage and winding. In case of rotating superconducting windings, the cold heads must rotate too, while the compressor is stationary and the working gas (i.e. helium in Fig. 1.11) is transferred to the rotor by a rotary coupling with ferro-fluidic seals. Since the cold heads cannot withstand large centrifugal loads, this cooling method is limited to slowly rotating machines, i.e. direct drive wind generators at  $n \approx 10$ rpm. This cooling system has been successfully applied in the *EcoSwing* generator to cool GdBCO field windings to  $\approx 30$  K [20], Fig. 1.13 a). The compressor must be installed either in the nacelle or at the base of the tower [183].

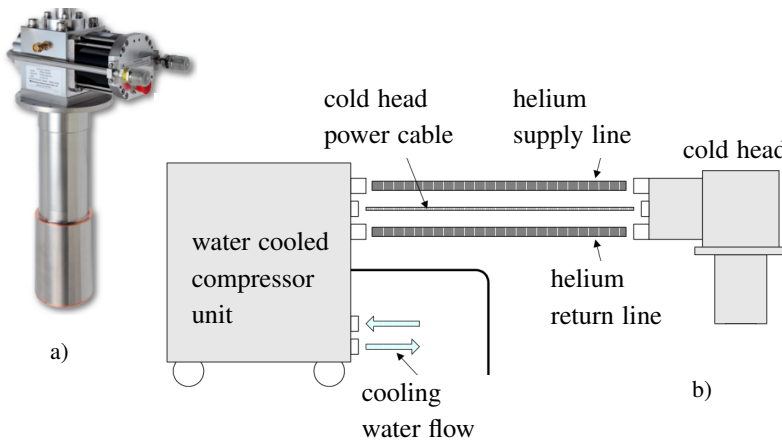


Figure 1.11.: a) Single-stage *Gifford-McMahon* cold head *RDK-500b* from *Sumitomo Heavy Industries*, b) schematic of the cryocooling system including the compressor unit and He gas lines [199].



### 1.3. Superconducting Rotating Electrical Machines

Earliest work on superconducting electrical machines dates back to 1971. In several projects, Tab. A.1 in App. A.2, LTSC field windings with LHe cooling were considered, with increasing demonstrator power ratings over about two decades. Depending on grid frequency, rotational speeds of 3000 rpm and 3600 rpm are common to the 2-pole generators. Together with the rotor diameters of  $d \approx 1.2\text{m}$ , this led to very high centrifugal loads, which the cryostat assembly must withstand. The main objective consisted in a shift of the maximum generator powers beyond 2...3 GW, which are not possible with normal conducting turbo generators in spite of strongest cooling systems [30]. These largest turbo generators, Fig. 1.12 a) were intended for use in nuclear power plants. But the expected trend towards ever increasing unit powers did not manifest, and most projects were stopped in the late 1980s. The Japanese project with 70 MW generators represented an exception from this trend.

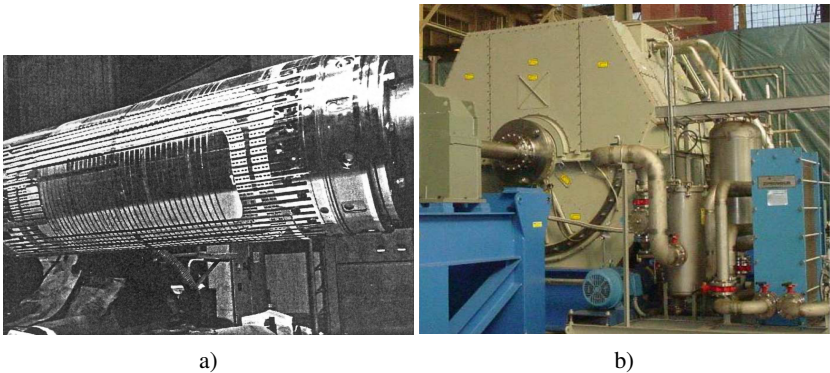


Figure 1.12.: a) Rotor of the 3000rpm, 400 MVA demonstrator with mounted LTSC winding built by *Siemens* [178]. b) 36.5 MW, 120 rpm, 2.9 MNm ship propulsion motor with HTSC excitation winding and stator oil cooling, built by *Northrop Grumman* and *AMSC* [71].

A second boom of superconducting machine projects started in the late 1990s, about one decade after the discovery of high-temperature superconductors, Tab. A.2 in App. A.2. 1<sup>st</sup> generation high temperature superconductors, i.e. BSCCO, were used. The considerably higher critical temperature of  $T_c \approx 108\text{K}$  for Bi-2223 offered multiple cooling concepts, reaching from gaseous helium over neon closed-cycle thermosiphons to liq-

### 1.3. Superconducting Rotating Electrical Machines

---

uid nitrogen bath cooling. Research projects mostly focused on weight-critical marine applications as propulsion motors and on-board generators, on aerospace generators and, to a lesser extent, on stationary generator systems. The 36.5 MW ship propulsion motor, Fig. 1.12 b), which was designed and full load tested in the late 2000s, is a prominent example. It combines a HTS field winding with intense oil cooling of the copper stator winding [71], as considered for medium speed wind generators in Ch. 7.

Superconducting machines with 2G HTS windings have come into focus since about 15 years. Several demonstrators of 2G HTS machines at reduced scale have been constructed and tested for wind power, marine and aerospace applications, Tab. A.3 in App. A.2. Generally, today's research activities on 2G HTS machines focus on applications, where machine weight and installation space are critical [40]. The latter may particularly profit from a „cooling for free“, if combined with cryogenic hydrogen storage [24, 80], which shifts the efficiency related and economical thresholds significantly in favour of the HTS technology.  $MgB_2$  conductors have been considered as promising low cost alternative, soon after its discovery in 2001. Also low temperature concepts are still under investigation [208] as a result of the to date still expensive HTS conductors, Fig. 1.13 b). The potentials listed in Sec. 1.2 make wind generators one of the most intensely investigated applications of superconducting windings today.

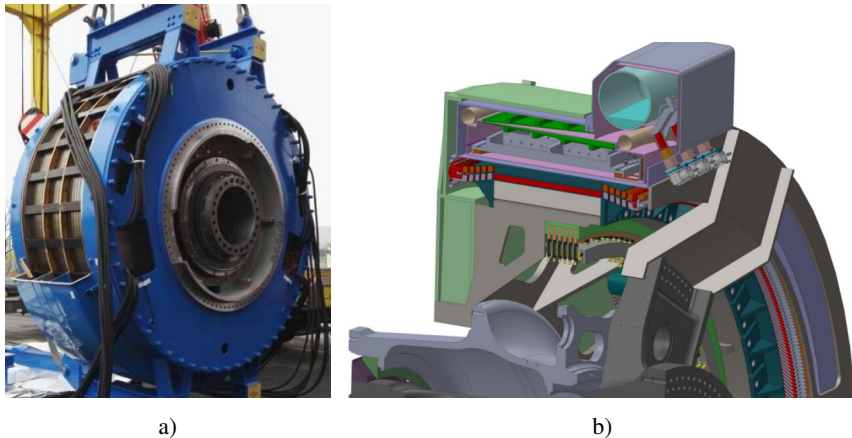


Figure 1.13.: a) Fully assembled *EcoSwing* 3.6 MW wind generator with 2G HTS field windings [196]. b) Concept drawing of the 15 MW wind generator with stationary LTSC field windings and rotating armature, designed by *General Electric* [208].

The successful construction and testing of a full-scale 3.6 MW generator in the *EcoSwing* project, Fig. 1.13 a), can be regarded as a milestone towards commercialization of superconducting wind generators. Within the project, a rotor with 2G HTS field coils was retrofitted into an existing, air-cooled stator. The generator was tested in 2018/2019 with a continuous operation of the cryogenic systems over 6 months under on-site conditions [20]. However, the cooling effort and the high investment cost for the cooling system and the HTS field windings require typically a minimum unit power of about 5 MW to be economically competitive. This precondition is well aligned with the general trend towards larger power ratings of wind generators, as discussed in the beginning of this section. Therefore, a large variety of theoretical studies and conceptual designs targets wind generators with a rated power of 10 MW and above, Tab. 1.3.

Several full-scale field coils have been built and tested, while the on-site load test of a superconducting wind generator is so far unique to the *EcoSwing* project. Many key components of partially and fully superconducting wind generators exhibit currently a technology readiness level (TRL) of 3 or 4. Successful experimental proofs cover several coil winding techniques and cryogenic cooling systems, while full-scale system tests are so far rare. In case of partially superconducting 2G HTS wind generators, the *EcoSwing* project has advanced several key technologies to a TRL of 6 or 7.

Most of the published work on partially superconducting generators focuses on direct drive concepts with rotational speeds of about 10 rpm, since the need for size and weight reduction is most urgent in this case. The large pole counts however require large quantities of superconductors, which represents the main challenge in terms of cost competitiveness.

Besides conventional synchronous generator topologies, different approaches with a stationary cryogenic cooling system are under investigation for wind turbine generators. A 10 MW DC machine with ReBCO field coils has been designed by *Liu* as part of a PhD project at *KIT* until 2018 [140, 142]. Here, a numerical optimization based on analytical models is applied, yielding a  $2p = 28$  pole generator with a speed of 10 rpm. The required ReBCO tape length ( $w_t = 4$  mm) is estimated to  $l_t \approx 230$  km and the armature current loading is in the order of 100 kA/m. The estimated mass is about  $m \approx 110$  t, including also inactive parts, while the active generator mass is about  $m_{\text{act}} \approx 80$  t, corresponding to a torque density of 120 Nm/kg. The calculated reduction in total loss is reported to be small compared to PM excited synchronous generators. A downsized demonstrator with 10 kW was manufactured and tested [182]. Another approach with stationary cryogenic

### 1.3. Superconducting Rotating Electrical Machines

system consists in an inverted synchronous generator with stationary DC excited poles and rotating armature, which is fed by a 3-phase brush/slip ring system. This concept is currently under investigation in a project of *General Electric* [208], Fig. 1.13 b).

Table 1.3.: Overview of recent projects on the application of superconducting windings to wind generator systems.

project name	consortium	main objectives	years
<i>WINDSPEED</i> [55]	<i>Eco 5</i>	design and proof of concept of direct drive MgB <sub>2</sub> -excited wind generators	2014/2015
<i>EcoSwing</i> [196, 20, 227]	coordinator: <i>Envision</i> ; 9 partners from industry and academia	design, built first MW-class direct drive wind generator rotor with 2G HTS field winding; in-field test with retrofit to existing stator	2015 - 2019
<i>UpWind</i> [53]	coordinator: <i>DTU wind</i> ; 40 partners	design and proof of concept of wind conversion systems in the power range 8...10MW	2006 - 2011
<i>INNWIND.EU</i> [52]	coordinator: <i>DTU wind</i> ; 27 partners	conceptual design of wind conversion systems in the power range 10...20MW; demonstration of critical hardware components, i.e. MgB <sub>2</sub> field coils for a direct drive 10 MW generator	2012 - 2017
<i>SUPRAPOWER</i> [203]	coordinator: <i>Tecnalia Research</i> ; 8 partners from industry and academia	design and proof of concept of a MgB <sub>2</sub> -excited 10 MW direct drive offshore wind generator	2012 - 2017
<i>SupraGenSys</i> [217]	<i>KIT, Fraunhofer IEE, Siemens, Krämer Energietechnik</i>	design of a fully superconducting 10 MW direct drive wind generator with 2G HTS windings, investigation of innovative HTS coil geometries	2019 - 2022
<i>High Efficiency Ultra-Light Superconducting Generator</i> [208]	<i>GE</i>	design and construction of a 15 MW LTSC direct drive wind turbine generator; in-lab test of a demonstrator and up-tower demonstration	2019 - 2025

Partially superconducting synchronous generators with rotating superconducting field winding are however the dominating approach and have been investigated in several studies, Tab. 1.4.

Table 1.4.: Examples for investigations of synchronous generators with superconducting field winding for wind power applications ( $P_N / n_N$ : rated power / speed,  $T_{SC}$ : operating temperature of SC, AG: air gap (winding)).

author / ref.	year	$P_N, n_N$	SC, $T_{SC}$	topology	details
<i>Müller &amp; Lewis</i> [131]	2004	8 MW, 12 rpm	2G HTS, 30 K	stator AG winding, non-magn. poles	study for <i>Alstom, Converteam</i> ; predicted price drop to less than 20Euro / (kA · m) by 2010 did not manifest
<i>Karmaker et al.</i> [109, 194]	2012	8 MW, 12 rpm	2G HTS, 30 K	stator AG winding	single pole tested; weak orientation dependence of <i>GM</i> cold head performance reported
<i>Ohsaki et al.</i> [164]	2013	10 MW, 10 rpm	2G HTS	comparison of topologies	comparison to fully SC generator with MgB <sub>2</sub> AC winding; loss reduction by $\approx -40\%$ w. r. t. PM generator
<i>Karmaker et al.</i> [110, 108]	2015	10 MW, 8 rpm	2G HTS, 30 K	comparison of topologies	exemplary designs reported; heaviest all-iron topology is cheapest; no details available for cost calculation and thermal model; minimum SC length $l_t = 10.7$ km
<i>Marino et al.</i> [146]	2016	10 MW, 8.1 rpm	MgB <sub>2</sub> , 20 K	ferromagnetic poles, stator AG winding	part of the <i>SUPRAPOWER</i> project; conductors from <i>ASG Columbus</i> ; air gap diameter $d_\delta = 10.1$ m; $2p = 48$ poles; modular cryostats; assumed price 3Euro / m leads to cost estimate of 307kEuro / MW; weight reduction of $\approx -26\%$ compared to PM generator
<i>Liu</i> [136]	2017	10 MW	MgB <sub>2</sub> , 20 K	12 different topologies	part of the <i>INWWIND.EU</i> project; assumed price: 4Euro / m; numerical optimization with genetic algorithm: variation of pole count at fixed diameter; lowest LCoE for heaviest designs; torque density 100... 235 Nm / kg

Some studies consider also superconducting AC stator windings in fully superconducting generators or in combination with a permanent magnet excitation. Both 2G HTS conductors and MgB<sub>2</sub> wires are considered for AC windings. A selection of design studies with AC superconducting windings is summarized in Tab. 1.5.

Besides the development of concepts and the testing of critical hardware components, recently, the numerical models of superconductors have evolved quickly. The modelling approaches were thoroughly tested against experimental results and analytical formulas for a variety of geometries and operating conditions, e.g. [168, 78, 185, 4]. The model implementation is to date rather complicated, compared to commercial software for standard, normal conducting, electromagnetic devices. However, these advanced models are characterized by a high computational efficiency and consequently allow for the prediction of superconductors' properties within full-scale non-linear models. Technical details are described in chapter 2, while two important developments are mentioned here:

- *Brambilla* et al. developed a framework for the application of the  $H$ - $A$ -formulation to rotating electrical machines in 2018 [27], after the  $H$ -formulation has been applied successfully to superconductors in several previous studies. The coupled  $H$ - $A$ -formulation has also been successfully applied to a variety of other large-scale applications, e.g. for the analysis of transients in HTS magnets [25]. In case of rotating electrical machines, the well established modelling techniques of the usually applied  $A$ -formulation can be adopted. *Grilli* et al. give an extensive overview of numerical models to determine the state of superconductors in [78].
- *Zhang* et al. introduced the  $T$ - $A$ -formulation in 2017 together with the thin sheet approximation for electromagnetic finite element models of 2G HTS tapes [238]. This approach allows a considerably reduced computational effort for large scale models, e.g. of coils with  $> 100$  turns employing tapes with high aspect ratio  $w_t/d_t$  ( $w_t$ : width of tape,  $d_t$ : thickness of tape). In the following, this formulation was successfully applied to some full-scale electrical machine models [19, 82, 216].

Table 1.5.: Examples for investigations of wind generators with superconducting stator winding ( $P_N / n_N$ ; rated power / speed).

author / ref.	year	$P_N, n_N$	rotor excit.	stator winding	details
<i>Terao et al.</i> [204]	2012	10 MW, 10 rpm	1G/2G HTS, 20 K	MgB <sub>2</sub> , 20 K	non-magnetic rotor; stator AG winding; stator back iron; active generator mass $m_{act} \approx 35$ t; gravimetric torque density $\approx 270$ Nm/kg; HTS tape length $l_t \approx 250$ km (tape width not specified); MgB <sub>2</sub> conductor length $\approx 150$ km; analytical AC loss estimate $\approx 1.5$ kW
<i>Liang et al.</i> [133]	2013	10 MW, 10 rpm	YBCO, 20 K	MgB <sub>2</sub> , 20 K	only stator yoke ferromagnetic; details on loss calculation & electromagnetic design missing; active mass reduction by $\approx -16\%$ predicted compared to generator with copper stator winding
<i>Kalsi</i> [104]	2013	10 MW, 10 rpm	MgB <sub>2</sub> , 20 K	MgB <sub>2</sub> , 20 K	conductor from <i>HyperTech Research</i> ; $2p = 24$ poles; active mass $m_{act} \approx 52$ t; gravimetric torque density $\approx 184$ Nm/kg; single-layer stator AG winding; non-magnetic rotor poles; assumed price of conductor 4\$/m; low AC loss reported for optimized conductors
<i>Song et al.</i> [197]	2015	10 MW, 10 rpm	2G HTS, 30 K	MgB <sub>2</sub> , 20 K	non-magnetic coil supports; stator and rotor back iron; analytical AC loss estimate $\approx 1.1$ kW; 36 cryo-coolers; comparison to MgB <sub>2</sub> rotor: calculated cost of ReBCO rotor is $\approx 5$ times higher
<i>Saruwatari et al.</i> [180]	2016	15 MW, 10 rpm	2G HTS, 40 K	2G HTS, 40 K	non-magn. rotor; stator AG winding; stator back iron; AC loss estimates of 4...12 kW with scribing and transposition; details of AC loss calculation not available; active mass $m_{act} = 80 \dots 100$ t; gravimetric torque density $\approx 160$ Nm/kg
<i>Lin et al.</i> [134]	2018	13.2 MW, 9 rpm	NbTi, 4.2 K	MgB <sub>2</sub> , 20 K	very high eddy current loss of $\approx 230$ kW in electromagnetic shield; gravimetric torque density $\approx 82$ Nm/kg, not competitive to state-of-the-art generators; analytical AC loss estimate $\approx 3$ kW; low SC material cost, but expensive cooling system
<i>Vargas-Llanos et al.</i> [217]	2021	10 MW, 10 rpm	PM ex-citation	2G HTS, 65 K	part of the <i>SupraGenSys</i> project; $2p = 40$ poles; air gap diameter of $d_\delta \approx 6.2$ m; active length $l_{Fe} = 2.4$ m; volumetric torque density lower than for state-of-the-art generators with copper winding; minimum AC loss estimates of $\approx 4 \dots 5$ kW for optimized coil geometries / positions; efficiency increase w. r. t. normal conducting winding predicted

### 1.4. Research Questions and Methodological Approach

Following conclusions are drawn from the overview of the current state of the wind power sector and of recent projects on superconducting wind generators:

- It is not clear, which drive train, i.e. direct drive or medium speed, will dominate offshore wind power in the medium-term. The offshore market is dominated by synchronous generators. The share of synchronous generators in the onshore wind market is to date rather small but increases steadily.
- The resource risk of high energy density permanent magnets, i.e. NdFeB, causes an urgent need for alternative excitation concepts. This brings electrically excited synchronous generators back into the focus of recent development programs.
- Today's generator concepts must allow for a simple up-scaling to power ratings in the range of 15...20MW per turbine.
- Superconducting windings are considered as a promising technology for wind turbine generators in the highest power class, i.e. > 5MW.
- Partially superconducting 2G HTS gearless synchronous generators have reached the highest TRL among superconducting wind generator concepts so far. Numerical optimizations of partially superconducting MgB<sub>2</sub> generators were carried out, while similar studies for 2G HTS (ReBCO) windings are to be done.
- Early work on fully superconducting wind generators indicates a considerable potential regarding key requirements, e.g. an increased gravimetric torque density  $M'$  in Nm/kg. A systematic treatment based on approved generator components is to be done.
- Studies on partially superconducting 2G HTS (ReBCO) medium speed wind generators have not been published so far. Still, substantial potential is expected since the advantages of superconducting windings can be achieved with a comparably low amount of superconductors.
- The competition between MgB<sub>2</sub> and 2G HTS (ReBCO) is not decided yet. A comprehensive study on the potentials of superconducting wind generators must therefore cover both alternatives.

Generally, wind power, especially off-shore, will be a fundamental energy source for a future energy supply without fossil energy sources. It must be reliable with minimum maintenance requirements, which favours gearless generator concepts. In order to be



independent from large quantities of rare earth magnets, the superconducting excitation with a minimum amount of SC per generator might be the future solution. Therefore, this thesis covers only direct drive generators in order to keep the adequate page limit. First investigations of alternative SC generator concepts are reviewed in Ch. 7.

Four main research questions are derived, which define the scope of this thesis:

- Q1 Are optimized, partially superconducting gearless wind generators economically competitive with respect to state-of-the-art, optimized PM generators? If not, which technological and economical developments could establish competitiveness?
- Q2 Which role will  $\text{MgB}_2$  superconducting windings play for future gearless wind generator systems? Are commercially available  $\text{MgB}_2$  conductors useful alternatives for ReBCO tapes regarding the use in DC field windings?
- Q3 Which superconducting generator topology is most promising? Which improvements regarding key characteristics of gearless wind generators, e.g. specific thrust and efficiency, can be achieved, if superconducting excitation windings are employed?
- Q4 Which characteristics feature direct drive wind generators with SC excitation under fault conditions? Are dynamic operating conditions or a redundancy operation, which is required for offshore wind generators, problematic?

The major approach in this thesis consists in numerical simulations of gearless synchronous wind generators with SC field winding. The calculation results are compared to analytical models and, if available, with experimental data from literature. This approach is motivated by two aspects:

1. The main objective is to derive general conclusions, which intrinsically require a large number of considered designs. This is not achievable with experimental investigations of singular designs. Of course, future experimental demonstrations will be vital for a potential commercialization.
2. Sophisticated modelling approaches for SC electrical machines exist, which cover all relevant phenomena and allow for the evaluation of the required level of detail, e.g. the importance of end effects. The applied work flow always starts with an exemplary quantification of relevant effects, before a broad range of variants is covered with an accurate and computationally efficient model.

Direct drive generators are analyzed for a rated power of 7 MW throughout this thesis, based on reference data of commercially available PM generators. The close contact to a well-known generator manufacturer was used to base the analyses on state-of-the-art PM synchronous generator designs and manufacturing methods. Numerical optimizations are carried out for partially superconducting gearless generators in order to advance already existing systematic parameter studies. Based on data from the above mentioned industry partner for commercially available generators, design studies on direct drive PM generators are conducted. The aim is to generate reliable benchmarks within the employed modelling framework. From the large sets of gearless generator designs, advantageous exemplary variants are derived, which allow for a final overall comparison.

---

## 2. Electromagnetic Modelling of Superconducting Electrical Machines

This chapter is on the models, which are used to analyse direct drive wind generators in Ch. 3 to 7. Analytical models for eddy current loss calculations and for a preliminary design of superconducting generators are described in Sec. 2.1. The following Sec. 2.2 is on numerical electromagnetic models and applied formulations. End-winding models for concentrated windings and distributed armature windings are described in Sec. 2.3 and 2.4. The last Sec. 2.5 summarizes the relations that are used to describe superconducting material properties.

The starting point of any modelling approach are *Maxwell's* equations in non-moving media and in differential form [96], (2.1) - (2.4). Throughout this thesis, SI units are used.

$$\nabla \vec{D} = \rho \quad \text{Gauss's law of electrostatics} \quad (2.1)$$

$$\nabla \times \vec{H} - \partial_t \vec{D} = \vec{J} \quad \text{Ampère-Maxwell law} \quad (2.2)$$

$$\nabla \times \vec{E} + \partial_t \vec{B} = 0 \quad \text{Faraday's law of induction} \quad (2.3)$$

$$\nabla \vec{B} = 0 \quad \text{Gauss's law of magnetism} \quad (2.4)$$

In the following, due to  $|\partial_t \vec{D}| \ll J$ , only *Ampère's* law (2.5) is used instead of (2.2). The displacement current densities  $\partial_t \vec{D}$  are neglected, since all quantities vary slowly in the considered generators (order of magnitude  $f \approx 10^0 \dots 10^3$  Hz).

$$\nabla \times \vec{H} = \vec{J} \quad \text{Ampère's law} \quad (2.5)$$

These quantities are supplemented by the constituting material relations (2.6), (2.7), which are non-linear, anisotropic and inhomogeneous in the most general case.

$$\vec{D} = \underline{\underline{\epsilon}} \left( \vec{E}, \vec{r} \right) \cdot \vec{E} \quad (2.6)$$

$$\vec{B} = \underline{\underline{\mu}} \left( \vec{H}, \vec{r} \right) \cdot \vec{H} \quad (2.7)$$

## 2.1. Analytical Multi-Layer Model

Analytical models of rotating electrical machines generally feature two main advantages compared to numerical models:

- The calculation by analytical models is faster, particularly if eddy current problems are considered.
- The analytical expressions allow to trace effects back to their origin in terms of space and time harmonics. These insights are hardly achievable by means of integral numerical solutions.

The disadvantages of analytical approaches consist in a limited degree of detail and in inaccuracies, as discussed in Sec. 2.1.9.

Most analytical models of rotating electrical machines are based on either the magnetic scalar potential  $\phi_M$  or the magnetic vector potential  $\vec{A}$ . Models based on the scalar potential allow for a simple modelling of permanent magnets. The magnetic vector potential approach is the preferred choice for eddy current calculations and if windings are explicitly modelled. Therefore, the latter approach is used for the superconducting generators in this thesis. Analytical models based on  $\vec{A}$  were extensively applied to superconducting turbo generators, since the magnetic topology without ferromagnetic teeth and pole cores features rotational symmetry [30]. The magnetic potential is defined by (2.8) and directly incorporates the divergence-free nature of the magnetic field.

$$\nabla \times \vec{A} = \vec{B} \quad (2.8)$$

Together with the material law  $\vec{B} = \mu \cdot \vec{H}$  for isotropic, linear material properties, where  $\mu$  is a  $B$ -independent scalar, (2.9) is derived from *Ampère's* law (2.5).

$$\nabla \times \vec{H} = \vec{J} \quad \rightarrow \quad \nabla \times \left( \mu^{-1} \cdot \nabla \times \vec{A} \right) = \vec{J} \quad (2.9)$$

Applying the definition (2.8) to *Faraday's* law, yields (2.10) and (2.11), since the time and spatial derivatives commute.

$$\nabla \times \vec{E} = -\partial_t \vec{B} = -\partial_t \left( \nabla \times \vec{A} \right) \quad (2.10)$$

$$= \nabla \times \left( -\partial_t \vec{A} \right) \quad (2.11)$$

The electric field strength can be written as (2.12) with an electric scalar potential  $\phi$ .

$$\vec{E} = -\partial_t \vec{A} + \nabla\phi \quad (2.12)$$

If only eddy currents occur in the considered domains, except from boundaries with impressed stator current loadings, the electric potential can be chosen as  $\phi = 0$ . Then, the eddy current density  $\vec{J}$  is written as (2.13). If a linear, isotropic conductivity is assumed,  $\kappa$  is a  $J$ -independent scalar, allowing for a further analytical treatment. This impedes an explicit modelling of superconductors within this model framework.

$$\vec{J} = \kappa \cdot \vec{E} = -\kappa \cdot \partial_t \vec{A} \quad (2.13)$$

The combination of (2.9) and (2.13) results in the second order differential equation (2.14).

$$\nabla \times (\mu^{-1} \cdot \nabla \times \vec{A}) = -\kappa \cdot \partial_t \vec{A} \quad (2.14)$$

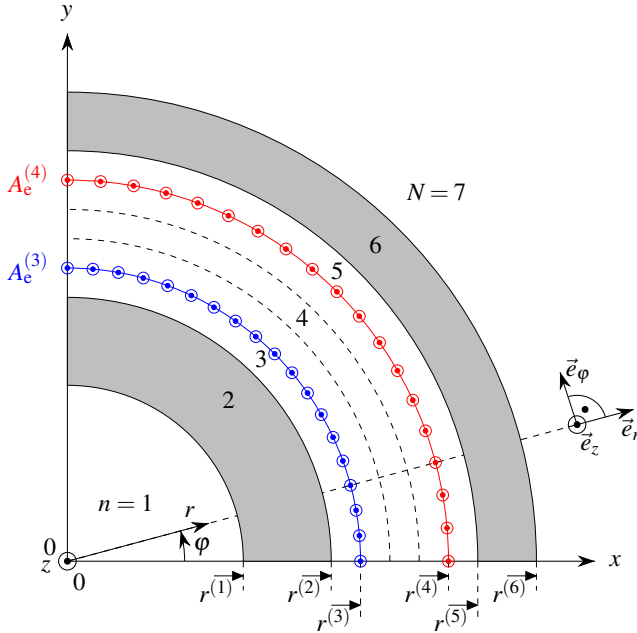


Figure 2.1.: Schematic of one quadrant of an exemplary multi-layer model with  $N = 7$  layers and two current loadings, e.g. representing the field winding  $A_e^{(3)}$  (blue) and the stator winding  $A_e^{(4)}$  (red) for an inner rotor topology.

The remaining ambiguity of the definition for  $\vec{A}$  is eliminated by introducing the *Coulomb* gauge  $\nabla \vec{A} = 0$ . Only 2D geometries in the cross section of the generators, Fig. 2.1, are considered in the following. In this section, the electrical current loading is denoted by  $A_e$  with subscript „e“ in order to distinguish from the vector potential. In the subsequent sections, the subscript is omitted due to the unambiguous meaning.

The translational invariance in  $z$ -direction implies that the sources of the magnetic field, i.e. current loadings at layer boundaries  $\vec{A}_e$  and eddy current densities  $\vec{J}$  inside layers, exhibit only a  $z$ -component, (2.15). Because of (2.13), the same holds for the magnetic vector potential  $\vec{A} = A_z \cdot \vec{e}_z \equiv A \cdot \vec{e}_z$ , yielding only one unknown scalar  $A_{e,z}$ .

$$\vec{J} = J_z \cdot \vec{e}_z, \quad \vec{A}_e = A_{e,z} \cdot \vec{e}_z \quad (2.15)$$

The magnetic flux density  $\vec{B}$  and the magnetic field strength  $\vec{H}$  exhibit consequently only in-plane  $x$ - and  $y$ -components with respect to the generator cross section. These are expressed in terms of the basis vectors in the (curvilinear) polar coordinate system, (2.16).

$$\vec{B} = B_r \cdot \vec{e}_r + B_\varphi \cdot \vec{e}_\varphi, \quad \vec{H} = H_r \cdot \vec{e}_r + H_\varphi \cdot \vec{e}_\varphi \quad (2.16)$$

For this 2D problem, the  $z$ -component of (2.14) reads (2.17), whereas the  $r$ - and  $\varphi$ -components vanish.

$$-\frac{1}{r} \cdot \left[ \partial_r \left( \frac{r}{\mu} \cdot \partial_r A \right) + \frac{1}{r} \cdot \partial_\varphi \left( \frac{1}{\mu} \cdot \partial_\varphi A \right) \right] = -\kappa \cdot \partial_t A \quad (2.17)$$

### 2.1.1. Periodicity and Ansatz

For constant  $\mu$ ,  $\kappa$  the diffusion equation (2.18) is derived from (2.17) and  $D = (\mu \cdot \kappa)^{-1}$  plays the role of the diffusion coefficient. In case of ferromagnetic teeth and pole cores, the actual conditions in the generator deviate significantly from this simplified model, as discussed in Sec. 2.1.9.

$$\Delta A = \frac{1}{r} \cdot \partial_r (r \cdot \partial_r A) + \frac{1}{r^2} \cdot \partial_\varphi^2 A = \mu \cdot \kappa \cdot \partial_t A \quad (2.18)$$

Since the geometry of the considered two-dimensional problem exhibits cylindrical symmetry and since the model is linear, the occurring space orders  $\nu$  and time orders  $k$  are

entirely determined by the field exciting source, i.e. the current loadings  $A_e^{(3)}$  and  $A_e^{(4)}$  at the layer boundaries, Fig. 2.1. At this point, the model is further restricted to current loadings (and hence field problems) obeying the following conditions:

- The current loading  $A_e \equiv A_{e,z}$  is periodic along the circumference with a period of at most  $2\pi$  (mechanical angle). This condition is trivially fulfilled for all current loadings.
- The time evolution of the current loading  $A_e$  is periodic, containing frequencies that are integer multiples of the fundamental frequency  $f_s = \omega_s/(2\pi)$ . Transients, like short circuit faults or load steps, do not meet this condition.

With these restrictions on  $A_e(\varphi, t)$ , (2.18) can be solved for each time order  $k$  and space order  $\nu$  separately without loss of generality. The field exciting component for the pair of orders  $\{\nu, k\}$  is obtained from an infinite 2D *Fourier* series representation of the actual current loading wave, while resulting field solutions are subsequently superimposed for all considered pairs  $\{\nu, k\}$ . In favour of a simple calculation scheme, the complex valued *Fourier* series, (2.19), is used.

$$A(r, \varphi, t) = \sum_{k=-\infty}^{\infty} \underline{A}_k(r, \varphi) \cdot e^{jk \cdot \omega_s \cdot t} = \sum_{k=-\infty}^{\infty} \sum_{\nu=-\infty}^{\infty} \underline{A}_{\nu,k}(r) \cdot e^{j(\nu \cdot \varphi + k \cdot \omega_s \cdot t)} \quad (2.19)$$

By exploiting the time harmonic nature of the magnetic vector potential, the *Helmholtz* equation (2.20) for a single time order  $k$  is obtained from (2.18).

$$\Delta \underline{A}_k(r, \varphi) = j(k \cdot \omega_s) \cdot \boldsymbol{\mu} \cdot \boldsymbol{\kappa} \cdot \underline{A}_k(r, \varphi), \quad k = -\infty, \dots, \infty \quad (2.20)$$

The ansatz (2.19) reflects that the dependence of the magnetic vector potential  $A$  on  $r$  and  $\varphi$  can be factorized for each space order  $\nu$ . This yields the differential equation (2.21) for the 2D *Fourier* coefficients belonging to the pair of orders  $\{\nu, k\}$ . These coefficients depend only on the radius  $r$ .

$$\frac{1}{r} \cdot \partial_r (r \cdot \partial_r \underline{A}_{\nu,k}(r)) - \frac{\nu^2}{r^2} \cdot \underline{A}_{\nu,k}(r) = j(k \cdot \omega_s) \cdot \boldsymbol{\kappa} \cdot \boldsymbol{\mu} \cdot \underline{A}_{\nu,k}(r), \quad \nu, k = -\infty, \dots, \infty \quad (2.21)$$

### 2.1.2. Solution for the Magnetic Vector Potential

For non-zero conductivity  $\kappa \neq 0$ , the differential equations (2.21) are of modified *Bessel* type. The standard form (2.22) is obtained by multiplying with  $r^2$  and substituting  $\underline{u} := r \cdot \underline{\vartheta}_k$  with (2.23).

$$\underline{u}^2 \cdot \partial_{\underline{u}}^2 \underline{A}_{v,k}(\underline{u}) + \underline{u} \cdot \partial_{\underline{u}} \underline{A}_{v,k}(\underline{u}) - \left( v^2 + \underline{u}^2 \right) \cdot \underline{A}_{v,k}(\underline{u}) = 0 \quad (2.22)$$

$$\underline{\vartheta}_k = r \cdot \sqrt{j(k \cdot \omega_s) \cdot \kappa \cdot \mu} \quad (2.23)$$

The general solution for the 2D *Fourier* coefficients  $\underline{A}_{v,k}(r)$  is (2.24), where  $\underline{C}_{v,k}$  and  $\underline{D}_{v,k}$  are complex-valued coefficients that are determined by the boundary and continuity conditions in Sec. 2.1.4.  $I_v(\underline{\zeta})$  and  $\underline{K}_v(\underline{\zeta})$  denote the modified *Bessel* functions of the first and second kind of order  $v$ , which are defined for complex-valued arguments  $\underline{\zeta}_k = \underline{\vartheta}_k \cdot r$ .

$$\underline{A}_{v,k}(r) = \underline{C}_{v,k} \cdot I_v(\underline{\vartheta}_k \cdot r) + \underline{D}_{v,k} \cdot \underline{K}_v(\underline{\vartheta}_k \cdot r) \quad (2.24)$$

For non-conductive layers with  $\kappa = 0$ , the resulting second order differential equation (2.25) is solved by the general solution (2.26) with coefficients  $\underline{C}_{v,k}$ ,  $\underline{D}_{v,k}$ , obeying continuity and boundary conditions.

$$r^2 \cdot \partial_r^2 \underline{A}_{v,k}(r) + r \cdot \partial_r \underline{A}_{v,k}(r) - v^2 \cdot \underline{A}_{v,k}(r) = 0 \quad (2.25)$$

$$\underline{A}_{v,k}(r) = \underline{C}_{v,k} \cdot r^v + \underline{D}_{v,k} \cdot r^{-v} \quad (2.26)$$

### 2.1.3. Magnetic Flux Density and Field Strength

The magnetic flux density is obtained as rotation of the magnetic vector potential with  $\vec{A} = A \cdot \vec{e}_z$ ,  $A_r = A_\varphi = 0$ . Similar to the magnetic vector potential, the  $r$ - and  $\varphi$ -components of the magnetic flux density  $B$  and the magnetic field strength  $H$  can also be represented by their complex 2D *Fourier* series, (2.27) and (2.28).

$$B_i(r, \varphi, t) = \sum_{k=-\infty}^{\infty} \underline{B}_{i,k}(r, \varphi) \cdot e^{jk \cdot \omega_s t} = \sum_{k=-\infty}^{\infty} \sum_{v=-\infty}^{\infty} \underline{B}_{i,v,k}(r) \cdot e^{j(v \cdot \varphi + k \cdot \omega_s t)}, \quad i \in \{r, \varphi\} \quad (2.27)$$



$$H_i(r, \varphi, t) = \sum_{k=-\infty}^{\infty} \underline{H}_{i,k}(r, \varphi) \cdot e^{jk \cdot \omega_s t} = \sum_{k=-\infty}^{\infty} \sum_{v=-\infty}^{\infty} \underline{H}_{i,v,k}(r) \cdot e^{j(v \cdot \varphi + k \cdot \omega_s t)}, \quad i \in \{r, \varphi\} \quad (2.28)$$

Therefore, the differential operators  $\partial_r(\cdot)$ ,  $\partial_\varphi(\cdot)$  can be applied separately for each harmonic component. With (2.27) and (2.28), this yields (2.29), (2.31) for the  $r$ - and  $\varphi$ -components of the magnetic flux density and the magnetic field strength.

$$\underline{B}_{r,v,k}(r) \cdot e^{jv \cdot \varphi} = \frac{1}{r} \cdot \partial_\varphi \left( \underline{A}_{v,k}(r) \cdot e^{jv \cdot \varphi} \right) = \frac{jv}{r} \cdot \underline{A}_{v,k}(r) \cdot e^{jv \cdot \varphi} \quad (2.29)$$

$$\implies \underline{B}_{r,v,k}(r) = \frac{jv}{r} \cdot \underline{A}_{v,k}(r), \quad \underline{H}_{r,v,k}(r) = \frac{jv}{\mu \cdot r} \cdot \underline{A}_{v,k}(r) \quad (2.30)$$

$$\underline{B}_{\varphi,v,k}(r) \cdot e^{jv \cdot \varphi} = -\partial_r \left( \underline{A}_{v,k}(r) \cdot e^{jv \cdot \varphi} \right) \quad (2.31)$$

$$\implies \underline{B}_{\varphi,v,k}(r) = -\partial_r \underline{A}_{v,k}(r), \quad \underline{H}_{\varphi,v,k}(r) = \frac{-1}{\mu} \cdot \partial_r \underline{A}_{v,k}(r) \quad (2.32)$$

The radial components of the flux density  $B_r$  and the magnetic field strength  $H_r$  are hence obtained from the vector potential by scaling with a  $r$ -dependent pre-factor. The explicit expression for  $B_r$ , which enters the continuity relations, is (2.33).

$$\underline{B}_{r,v,k}(r) = \begin{cases} \frac{jv}{r} \cdot (\underline{C}_{v,k} \cdot r^v + \underline{D}_{v,k} \cdot r^{-v}) & \kappa = 0 \\ \frac{jv}{r} \cdot (\underline{C}_{v,k} \cdot I_v(\vartheta_k \cdot r) + \underline{D}_{v,k} \cdot K_v(\vartheta_k \cdot r)) & \kappa \neq 0 \end{cases} \quad (2.33)$$

The calculation of the tangential components involves the calculation of the first derivative with respect to  $r$ . Since the tangential magnetic field strength  $H_\varphi$  enters the continuity relations, the explicit expression is given in (2.34). The derivatives of the modified *Bessel* functions can be expressed in terms of the respective functions for neighbouring orders, (2.35).

$$\underline{H}_{\varphi,v,k}(r) = \begin{cases} -\frac{v}{\mu \cdot r} \cdot (\underline{C}_{v,k} \cdot r^v - \underline{D}_{v,k} \cdot r^{-v}) & \kappa = 0 \\ -\frac{\vartheta_k}{\mu} \cdot (\underline{C}_{v,k} \cdot I'_v(\vartheta_k \cdot r) + \underline{D}_{v,k} \cdot K'_v(\vartheta_k \cdot r)) & \kappa \neq 0 \end{cases} \quad (2.34)$$

$$I'_v(z) = \frac{1}{2} \cdot [I_{(v-1)}(z) + I_{(v+1)}(z)], \quad K'_v(z) = -\frac{1}{2} \cdot [K_{(v-1)}(z) + K_{(v+1)}(z)] \quad (2.35)$$

### 2.1.4. Continuity and Boundary Equations

The derived expressions hold in all layers of the multi-layer model, while the coefficients  $\underline{C}_{v,k}$ ,  $\underline{D}_{v,k}$ , as well as the material properties  $\kappa$ ,  $\mu$  and hence the value of  $\underline{\vartheta}_k$ , (2.23), may differ from layer to layer. In the following, the layers are numbered by the index  $n = 1, \dots, N$  in ascending order radially outwards, Fig. 2.1. The quantities in layer  $n$  are labelled by an additional superscript ( $n$ ). The innermost layer  $n = 1$  represents the interior of the generators, which is not conductive for the considered generators and has the same magnetic properties as air or vacuum with  $\mu = \mu_0$ ,  $\kappa = 0$ . The outermost layer  $n = N$  represents the surrounding with the same material properties. The boundary conditions must reflect that the field quantities are finite for both  $r \rightarrow 0$  and  $r \rightarrow \infty$ . The general solutions for the vector potential in conductive and non-conductive layers are linear combinations of two functions, of which one diverges for  $r \rightarrow 0$  and one does for  $r \rightarrow \infty$ . The requirement for finite values in the limiting cases therefore implies vanishing coefficients (2.36), (2.37). It is important to mention that the boundary conditions would be different if the inner- or outermost layer were conductive, since  $L_v(\underline{\zeta}) = \underline{L}_{-v}(\underline{\zeta})$  and  $\underline{K}_v(\underline{\zeta}) = \underline{K}_{-v}(\underline{\zeta})$  for  $v \in \mathbb{Z}$ .

$$\kappa = 0: \quad v > 0: \quad \underline{D}_{v,k}^{(1)} = 0, \quad \underline{C}_{v,k}^{(N)} = 0 \quad (2.36)$$

$$v < 0: \quad \underline{C}_{v,k}^{(1)} = 0, \quad \underline{D}_{v,k}^{(N)} = 0 \quad (2.37)$$

The  $2 \cdot (N - 1)$  continuity conditions for the normal component of the flux density ( $r$ -component) and the tangential component of the magnetic field strength ( $\varphi$ -component) at the layer boundaries are (2.38), (2.39).  $r_n$  denotes the outer radius of layer  $n$ , and  $\underline{A}_{e,v,k}^{(n)}$  is the 2D *Fourier* coefficient of the current loading at the boundary between layers  $n$  and  $(n + 1)$ . Fig. 2.2 visualizes the relation (2.39) between  $H_\varphi$  and the current loading  $A_{e,z}$ . Together with the two boundary conditions, a unique solution for the  $2N$  coefficients  $\{\underline{C}_{v,k}^{(n)}, \underline{D}_{v,k}^{(n)}\}$ ,  $n = 1, \dots, N$  is obtained.

$$\underline{B}_{r,v,k}^{(n)}(r = r_n) = \underline{B}_{r,v,k}^{(n+1)}(r = r_n), \quad n = 1, \dots, (N - 1) \quad (2.38)$$

$$\underline{H}_{\varphi,v,k}^{(n)}(r = r_n) = \underline{H}_{\varphi,v,k}^{(n+1)}(r = r_n) + \underline{A}_{e,v,k}^{(n)}, \quad n = 1, \dots, (N - 1) \quad (2.39)$$

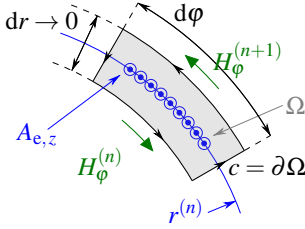


Figure 2.2.: Schematic of a boundary section between layers  $n$  and  $n+1$ , which features a current loading  $A_{e,z}$ . The integration of *Ampère's law* (2.5) along the boundary curve  $c = \partial\Omega$  of the domain  $\Omega$ , together with *Stokes' theorem*, yields the continuity relation (2.39).

By introducing the generalized expressions  $\underline{R}$  (2.40) - (2.43), the continuity conditions are directly expressed in terms of the unknown coefficients  $\{\underline{C}_{v,k}^{(n)}, \underline{D}_{v,k}^{(n)}\}$ ,  $n = 1, \dots, N$ , (2.44) and (2.45).

$$\underline{R}_{1,v,k}^{(n)} = \begin{cases} j\mathbf{v} \cdot r_{n-1}^{(v-1)} & \kappa = 0 \\ \frac{j\mathbf{v}}{r_{n-1}} \cdot \underline{I}_v(\vartheta_k^{(n)}) r_{n-1} & \kappa \neq 0 \end{cases} \quad \underline{\tilde{R}}_{1,v,k}^{(n)} = \begin{cases} j\mathbf{v} \cdot r_n^{(v-1)} & \kappa = 0 \\ \frac{j\mathbf{v}}{r_n} \cdot \underline{I}_v(\vartheta_k^{(n)}) r_n & \kappa \neq 0 \end{cases} \quad (2.40)$$

$$\underline{R}_{2,v,k}^{(n)} = \begin{cases} j\mathbf{v} \cdot r_{n-1}^{-(v+1)} & \kappa = 0 \\ \frac{j\mathbf{v}}{r_{n-1}} \cdot \underline{K}_v(\vartheta_k^{(n)}) \cdot r_{n-1} & \kappa \neq 0 \end{cases} \quad \underline{\tilde{R}}_{2,v,k}^{(n)} = \begin{cases} j\mathbf{v} \cdot r_n^{-(v+1)} & \kappa = 0 \\ \frac{j\mathbf{v}}{r_n} \cdot \underline{K}_v(\vartheta_k^{(n)}) \cdot r_n & \kappa \neq 0 \end{cases} \quad (2.41)$$

$$\underline{R}_{3,v,k}^{(n)} = \begin{cases} -\frac{\nu}{\mu^{(n)}} \cdot r_{n-1}^{(v-1)} & \kappa = 0 \\ -\frac{\vartheta_k^{(n)}}{\mu^{(n)}} \cdot \underline{I}'_v(\vartheta_k^{(n)}) r_{n-1} & \kappa \neq 0 \end{cases} \quad \underline{\tilde{R}}_{3,v,k}^{(n)} = \begin{cases} -\frac{\nu}{\mu^{(n)}} \cdot r_n^{(v-1)} & \kappa = 0 \\ -\frac{\vartheta_k^{(n)}}{\mu^{(n)}} \cdot \underline{I}'_v(\vartheta_k^{(n)}) r_n & \kappa \neq 0 \end{cases} \quad (2.42)$$

$$\underline{R}_{4,v,k}^{(n)} = \begin{cases} +\frac{\nu}{\mu^{(n)}} \cdot r_{n-1}^{-(v+1)} & \kappa = 0 \\ -\frac{\vartheta_k^{(n)}}{\mu^{(n)}} \cdot \underline{K}'_v(\vartheta_k^{(n)}) r_{n-1} & \kappa \neq 0 \end{cases} \quad \underline{\tilde{R}}_{4,v,k}^{(n)} = \begin{cases} +\frac{\nu}{\mu^{(n)}} \cdot r_n^{-(v+1)} & \kappa = 0 \\ -\frac{\vartheta_k^{(n)}}{\mu^{(n)}} \cdot \underline{K}'_v(\vartheta_k^{(n)}) r_n & \kappa \neq 0 \end{cases} \quad (2.43)$$

$$\underline{C}_{v,k}^{(n)} \cdot \underline{R}_{1,v,k}^{(n)} + \underline{D}_{v,k}^{(n)} \cdot \underline{R}_{2,v,k}^{(n)} - \underline{C}_{v,k}^{(n+1)} \cdot \underline{\tilde{R}}_{1,v,k}^{(n+1)} - \underline{D}_{v,k}^{(n+1)} \cdot \underline{\tilde{R}}_{2,v,k}^{(n+1)} = 0, \quad n = 1, \dots, (N-1) \quad (2.44)$$

$$\begin{aligned} & \underline{C}_{v,k}^{(n)} \cdot \underline{R}_{3,v,k}^{(n)} + \underline{D}_{v,k}^{(n)} \cdot \underline{R}_{4,v,k}^{(n)} \\ & - \underline{C}_{v,k}^{(n+1)} \cdot \underline{\tilde{R}}_{3,v,k}^{(n+1)} - \underline{D}_{v,k}^{(n+1)} \cdot \underline{\tilde{R}}_{4,v,k}^{(n+1)} = \underline{A}_{e,v,k}^{(n)}, \quad n = 1, \dots, (N-1) \end{aligned} \quad (2.45)$$

### 2.1.5. Relative Movement of Layers

The derived relations hold also in case of a relative movement between the layers, if the effective time order, and thus the effective frequency, in rotating layers is considered. Here, the slow motion, compared to the velocity of light, allows the use of the *Galilei* transform instead of the *Lorentz* transform. If several current loadings exist in the model, it is convenient to solve the field equations for each current loading separately and superimpose the separate results thereafter by exploiting the linearity. In this case, the reference system, in which the calculation is carried out, is suitably chosen such that the winding of the exciting current loading is at rest (layer with index  $\tilde{n}$ ). If only the time fundamental of the impressed current is considered, the only occurring time order in all layers with equal rotational speed is  $k^{(\tilde{n})} = 1$ . Higher time orders  $k^{(\tilde{n})} > 1$  may play a role in case of inverter feeding, causing significant current harmonics.

Without loss of generality, the rotational speed of layer  $\tilde{n}$  can be set to zero,  $n^{(\tilde{n})} = 0$ . Regardless of the relative speed of other layers with respect to layer  $\tilde{n}$ , the time evolution of all quantities, as seen from the reference layer  $\tilde{n}$ , is characterized by the time order  $k^{(\tilde{n})}$ , e.g. for the vector potential in the form (2.46).

$$A^{(n)}(r, \varphi, t) = \sum_{k=\pm k^{(\tilde{n})}} \underline{A}_k^{(n)}(r, \varphi) \cdot e^{jk \cdot \omega_s \cdot t}, \quad n = 1, \dots, N \quad (2.46)$$

However, the effective time order  $k_v^{(n)}$ , as seen from the rotating layer  $n \neq \tilde{n}$  with speed  $n^{(n)} \neq 0$ , is different and depends on  $k^{(\tilde{n})}$ , the layer's speed  $n^{(n)}$  and the considered space order  $v$ , (2.47). The derivation of this relation can be found in App. A.4.2.

$$k_v^{(n)} = k^{(\tilde{n})} + v \cdot \frac{2\pi \cdot n^{(n)}}{\omega_s} \quad (2.47)$$

This plays a role in case of conductive layers ( $\kappa^{(n)} \neq 0$ ), where the time evolution of the magnetic field *in the rest system of the respective layer* determines via *Faraday's* law the magnitude of eddy currents. Here, the influence of the relative movement is reflected in the model by the parameter  $\underline{\vartheta}$ , in which the layer-dependent, effective time order  $k_v^{(n)}$  must be used instead of  $k^{(\tilde{n})}$ , (2.48). As  $k_v^{(n)}$  depends on the space order, the same holds for  $\underline{\vartheta}$ , such that it also features the index  $v$  in case of rotating layers.

$$\underline{\vartheta}_{v,k}^{(n)} = \sqrt{j \left( k_v^{(n)} \cdot \omega_s \right) \cdot \kappa^{(n)} \cdot \mu^{(n)}} \quad (2.48)$$

As an example, the stator current loading in a  $2p$ -pole generator, e.g.  $A_e^{(4)}$  in Fig. 2.1, is considered. The rotor rotates synchronously with the stator field at feeding with frequency  $f_s$ . The synchronously rotating stator field fundamental is characterized by the order pairs  $\{v = +p, k^{(s)} = -1\}$  and  $\{v = -p, k^{(s)} = +1\}$ , which yield the synchronous rotational velocity (2.49) in the stator frame of reference.

$$\dot{\phi}^{(s)} = -\frac{k^{(s)} \cdot \omega_s}{v} = -\frac{(-1) \cdot \omega_s}{p} = -\frac{1 \cdot \omega_s}{(-p)} = 2\pi \cdot \frac{f_s}{p} = 2\pi \cdot n_{\text{syn}} = \Omega_{\text{syn}} \quad (2.49)$$

Based on (2.47), the time order of the stator field fundamental in the rotor frame of reference evaluates to zero, (2.50).

$$k_{v=\mp p}^{(r)} = k^{(s)} + v \cdot \frac{2\pi \cdot n^{(r)}}{\omega_s} = \pm 1 \mp p \cdot \frac{2\pi \cdot \frac{f_s}{p}}{2\pi \cdot f_s} = 0 \quad (2.50)$$

For synchronous rotation, the effective time orders of asynchronously rotating stator field harmonics with  $|v| \neq p$  are given by (2.51) with  $k^{(s)} = \pm 1$  for the stator current fundamental.

$$k_v^{(r)} = k^{(s)} + \frac{v}{p} \quad (2.51)$$

### 2.1.6. System of Equations and Solution

The resulting set of linear algebraic equations for the unknown quantities per layer  $n$ , (2.53), can either be solved at once [O12] or iteratively by translating solutions from layer to layer [176]. The latter approach makes use of transfer matrices and is computationally favourable, since only the inverse of small matrices must be calculated. However, the transfer matrix approach is not possible if a circumferential variation of material properties is considered, Sec. 2.1.9. Therefore, one global system of equations is assembled and solved. The system of equations for the pair of orders  $\{v, k\}$  is of the form (2.52). For  $v > 0$ , the  $2(N-1) \times 2(N-1)$ -system matrix is (2.55), the coefficient vector is (2.53) and the inhomogeneity, which contains the current loadings, is (2.54).

$$\mathbf{M} \cdot \vec{c} = \vec{s} \quad (2.52)$$

$$\vec{c} = \left( \underline{C}_{v,k}^{(1)} \quad \dots \quad \underline{C}_{v,k}^{(N-1)} \quad \underline{D}_{v,k}^{(2)} \quad \dots \quad \underline{D}_{v,k}^{(N)} \right)' \quad (2.53)$$

$$\vec{s} = \left( 0 \quad \underline{A}_{e,v,k}^{(1)} \quad 0 \quad \underline{A}_{e,v,k}^{(2)} \quad \dots \right)' \quad (2.54)$$

$$\mathbf{M} = \begin{pmatrix} \tilde{R}_{1,v,k}^{(1)} & -\tilde{R}_{1,v,k}^{(2)} & 0 & 0 & \cdots & 0 & -\tilde{R}_{2,v,k}^{(2)} & 0 & 0 & \cdots \\ \tilde{R}_{3,v,k}^{(1)} & -\tilde{R}_{3,v,k}^{(2)} & 0 & 0 & \cdots & 0 & -\tilde{R}_{4,v,k}^{(2)} & 0 & 0 & \cdots \\ 0 & \tilde{R}_{1,v,k}^{(2)} & -\tilde{R}_{1,v,k}^{(3)} & 0 & \cdots & 0 & \tilde{R}_{2,v,k}^{(2)} & -\tilde{R}_{2,v,k}^{(3)} & 0 & \cdots \\ 0 & \tilde{R}_{3,v,k}^{(2)} & -\tilde{R}_{3,v,k}^{(3)} & 0 & \cdots & 0 & \tilde{R}_{4,v,k}^{(2)} & -\tilde{R}_{4,v,k}^{(3)} & 0 & \cdots \\ \vdots & \ddots & \ddots & \ddots & & & \ddots & \ddots & \ddots & \ddots \end{pmatrix} \quad (2.55)$$

The solution vector  $\vec{c}_{\text{sol}}$  directly contains all non-zero coefficients, from which the field quantities are calculated for the pair of orders  $\{v, k\}$ . Solving the large linear system of equations requires computational software. Both a script-based implementation in *MATLAB* and an object-oriented software package in *Python 3.9* have been developed and are used in parallel for the calculations. If solved with a numerical scheme, the precision of the solution is limited by the data type's maximum number of digits. Alternatively, a computationally expensive, symbolic calculation, e.g. with *MATLAB*, can be carried out for small models. The comparison of both solutions reveals negligible inaccuracies of numerically obtained solutions (maximum order of magnitude for relative deviation of coefficients:  $10^{-16}$ ).

### 2.1.7. Power Transfer Between Layers and Torque

The radial power transfer between and within layers is calculated by means of the *Poynting* vector  $\vec{S} = \vec{E} \times \vec{H}$ , which locally characterises the power density's magnitude and the direction of the power flow. The *Poynting* vector can be evaluated along an arbitrary curve  $c$ , while the choice of  $c$  as circle is appropriate for the cylindrical model, Fig. 2.1. Since the electric field  $\vec{E}$  has only a  $z$ -component, it is only the circumferential component of the magnetic field strength that contributes to the radial power transfer, (2.56).

$$S_r = \vec{S} \cdot \vec{e}_r = [E \cdot \vec{e}_z \times (H_r \cdot \vec{e}_r + H_\phi \cdot \vec{e}_\phi)] \cdot \vec{e}_r = -E \cdot H_\phi \quad (2.56)$$

Both field strengths can be expressed in terms of the vector potential  $A$  based on (2.12), (2.31). In terms of the *Fourier* series representations, the radial component  $S_r$  of the *Poynting* vector evaluates to (2.57).

$$\begin{aligned}
 S_r(r, \varphi, t) &= -\frac{1}{\mu} \cdot \partial_r A(r, \varphi, t) \cdot \partial_r A(r, \varphi, t) \\
 &= -\frac{1}{\mu} \cdot \sum_{k, k'=-\infty}^{\infty} \sum_{v, v'=-\infty}^{\infty} [jk \cdot \omega_s \cdot \underline{A}_{v, k}(r)] \cdot [\partial_r \underline{A}_{v', k'}(r)] \cdot e^{j[(v+v')\varphi + (k+k')\omega_s t]}
 \end{aligned} \tag{2.57}$$

The radial power transfer through a cylindrical surface with axial length  $L$  involves the integration over the entire circumferential angle, where relation (2.58) can be used.  $\delta_{i, j}$  is the *Kronecker delta*.

$$\int_0^{2\pi} e^{j(v+v')\varphi} d\varphi = 2\pi \cdot \delta_{v', -v} \tag{2.58}$$

The instantaneous power transfer through the surface at radius  $r$  is then calculated as (2.59).

$$\begin{aligned}
 P_r(r, t) &= \int_0^{l_i} dz \int_0^{2\pi} d\varphi r \cdot S_r(r, \varphi, t) \\
 &= -\frac{2\pi r \cdot l_i}{\mu} \cdot \sum_{k, k'=-\infty}^{\infty} \sum_{v=-\infty}^{\infty} [jk \cdot \omega_s \cdot \underline{A}_{v, k}(r)] \cdot [\partial_r \underline{A}_{-v, k'}(r)] \cdot e^{j(k+k')\omega_s t}
 \end{aligned} \tag{2.59}$$

The expression can be further simplified if the time averaged power  $\bar{P}$  is considered. Here, (2.60) is used to eliminate the time order  $k'$ .

$$\frac{1}{T} \cdot \int_0^T e^{j(k+k')\omega_s t} dt = \delta_{k', -k} \tag{2.60}$$

The average power  $\bar{P}$  is calculated as (2.61).

$$\begin{aligned}
 \bar{P}(r) &= \frac{1}{T} \cdot \int_0^T P(r, t) dt \\
 &= -\frac{2\pi r \cdot l_i}{\mu} \cdot \sum_{k=-\infty}^{\infty} \sum_{v=-\infty}^{\infty} [jk \cdot \omega_s \cdot \underline{A}_{v, k}(r)] \cdot [\partial_r \underline{A}_{-v, -k}(r)] \\
 &= -\frac{2\pi r \cdot l_i \cdot \omega_s}{\mu} \cdot \sum_{k=-\infty}^{\infty} \sum_{v=-\infty}^{\infty} \frac{-k}{2j} \cdot \left[ \underline{A}_{v, k}(r) \cdot \underbrace{(\partial_r \underline{A}_{-v, -k}(r))}_{=\partial_r \underline{A}_{v, k}^*(r)} - \underbrace{\underline{A}_{-v, -k}(r)}_{=\underline{A}_{v, k}^*(r)} \cdot (\partial_r \underline{A}_{v, k}(r)) \right] \\
 &= \frac{2\pi r \cdot l_i \cdot \omega_s}{\mu} \cdot \sum_{k=-\infty}^{\infty} \sum_{v=-\infty}^{\infty} k \cdot \text{Im}\{\underline{A}_{v, k}(r) \cdot (\partial_r \underline{A}_{v, k}(r))^*\}
 \end{aligned} \tag{2.61}$$

The dissipated power within one layer with index  $n$  due to eddy currents is calculated as the difference of the transferred power at the inner and outer radii  $r^{(n-1)}$  and  $r^{(n)}$  of the layer, (2.62).

$$P_{d, \text{Ft}}^{(n)} = |\bar{P}(r^{(n)}) - \bar{P}(r^{(n-1)})| \quad (2.62)$$

The calculation of the electromagnetic torque for only two current loadings (e.g.  $A_e^{(3)}$  representing the field winding's fundamental,  $A_e^{(4)}$  the stator winding's fundamental in Fig. 2.1) is suitably calculated by means of the *Lorentz* force acting on one of the current loadings. The tangential force on current loading  $A_{e,z}^{(n)}$  at radius  $r_n$  is (2.64). Here,  $\sigma_t$  is the local specific thrust, (2.63), and  $A^{(n)}$  denotes the cylindrical surface of the layer boundary with current loading  $A_{e,z}^{(n)}$ . The electromagnetic torque is then calculated as  $M_e = r^{(n)} \cdot F_\varphi^{(n)}$ .

$$\sigma_t^{(n)}(\varphi) = A_{e,z}^{(n)}(\varphi) \cdot B_r(r^{(n)}, \varphi) \quad (2.63)$$

$$F_\varphi^{(n)} = \int_{A^{(n)}} \sigma_t^{(n)}(\varphi) dA = l_i \cdot r^{(n)} \cdot \int_0^{2\pi} A_{e,z}^{(n)}(\varphi) \cdot B_r(r^{(n)}, \varphi) d\varphi \quad (2.64)$$

The average specific thrust  $\sigma_t$  is defined as (2.65) and is a measure for the electromagnetic utilization.

$$\sigma_t = \frac{M_e}{2\pi \cdot r_{\text{ro}}^2 \cdot l_i} \sim A_{e,s} \cdot B_{\delta,1} \quad (2.65)$$

The number of current loadings generally becomes high if both rotor and stator windings are represented by several layers, and if more space orders apart from the fundamental are considered. In this case, the air gap torque is suitably calculated based on the *Maxwell* stress tensor, similar to the calculation for numerically obtained results in Sec. 2.2.3. The integration is approximated by the evaluation of the circumferential force density,  $f_\varphi = B_r \cdot H_\varphi$  in (2.101), for  $N > 100$  points at the average air gap radius  $r_\delta$ , Fig. 2.3 a).

### 2.1.8. Flux Linkage and Induced Voltage

The flux linkage in the analytical layer model is calculated from the vector potential  $A$ , as discussed in Sec. 2.2.2 for the *H-A*-formulation. Since the representation of the winding by  $n_{\text{split}}$  current loadings is just an approximation, Fig. 2.3 b), the averaged value of the vector potential across the actual extent of the winding window  $\bar{A}(t)$  is used for the calculation, (2.66).



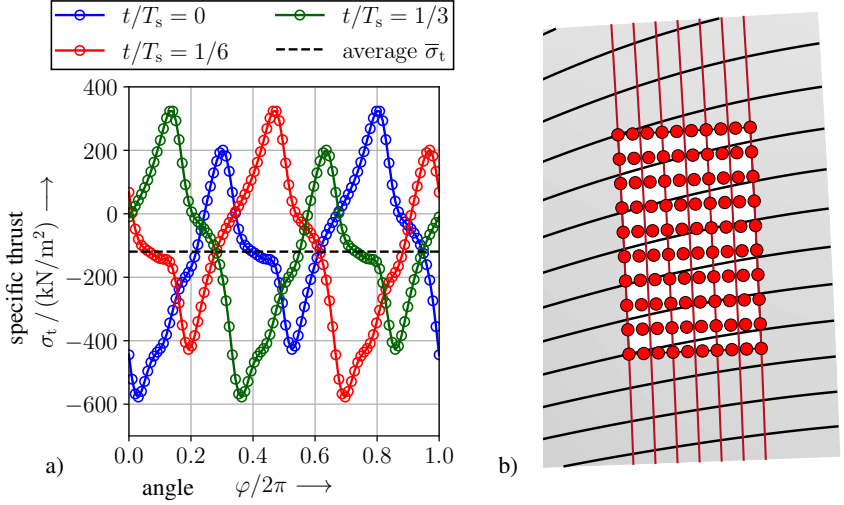


Figure 2.3.: a) Exemplary visualization of the analytically calculated specific thrust over two poles (one basic winding scheme) for several time instants. The dashed line represents the average braking (negative) specific thrust of  $\bar{\sigma}_t \approx -125 \text{ kN/m}^2$ . b) Visualization of the grid in one stator coil side, which is used for the evaluation of the flux linkage  $\psi$ , Sec. 2.2.2. The cross section of the coil side is indicated by the white shaded region. Black lines represent field lines, red lines represent seven layer boundaries with current loadings.

The vector potential is evaluated at  $N_w$  points (Fig. 2.3 b):  $N_w = 100$ ) within the coil side's cross section.

$$\psi(t) = \bar{A}(t) \cdot l_i \approx \frac{l_i}{N_w} \cdot \sum_{i=1}^{N_w} A_i(t) \quad (2.66)$$

The flux linkage is calculated for  $n_T$  time steps after solving the multi-layer model (2.52) by propagating the solution coefficients in time. From the set  $\{\psi(t_n)\}$ ,  $n = 1, \dots, n_T$ , the discrete *Fourier* transform  $\underline{\Psi}_k$  is calculated. The spectral representation of the induced voltage is obtained via (2.67). The inverse DFT yields the inner induced voltage in the time domain.

$$\underline{U}_{i,k} = jk \cdot \omega_s \cdot \underline{\Psi}_k \quad (2.67)$$

### 2.1.9. Model Limitations and Circumferential Variation of Material Properties

The major limitations of the analytical multi-layer model are:

- The non-linearity of the  $B(H)$ -relation of the ferromagnetic parts is not included. Local flux densities in ferromagnetic regions and in their near vicinity are not correctly predicted in presence of significant iron saturation. Regarding preliminary design considerations, this shortcoming is not of major importance if sufficiently low *average* flux densities are ensured.
- In presence of ferromagnetic teeth and/or ferromagnetic pole cores, both the permeability  $\mu$  and the conductivity  $\kappa$  vary in circumferential direction. Highly saturated iron pole cores, which are typical in case of superconducting field windings, justify an approximation with  $\mu_r \approx 1$  for eddy current loss calculations. However, the variation of  $\kappa$  between the pole core and the inter-pole gap yields large deviations of the calculated eddy current loss, if not incorporated in the analytical model.

Two approaches for a partial relief of these limitations are considered:

- An equivalent stator current loading can be extracted from a series of magnetostatic, non-linear finite element simulations, Sec. 4.3.2. This current loading includes the effect of the iron saturation and the circumferentially varying reluctance to some extent.
- The variation of  $\mu$  and  $\kappa$  can be included in the analytical multi-layer model if their *Fourier* series representation is used. This leads to a set of coupled differential equations, which can be decoupled, if a planar approximation, i.e. neglect of any curvature effects, is applied. This approximation is justified for large direct drive generators with comparably high pole count and, hence, small curvature effects per pole pair. Details of this model extension are described in [O14].

## 2.2. Numerical Models of Rotating Electrical Machines with Superconducting Windings

In numerical models, both complicated geometries with low degree of symmetry and non-linear material properties can be incorporated. The commonly applied technique to solve

for electromagnetic field quantities is the finite element method (FEM), Sec. 2.2.1. From the field solution, aggregated quantities, e.g. the electromagnetic torque and induced voltages, can be derived, Sec. 2.2.2, 2.2.3. The calculation schemes are already implemented in software solutions for standard applications, e.g. *JMAG* and *FEMM*. However, in order to explicitly model superconductors' material properties, FEM models are built based on fundamental equations as part of this thesis. In these cases, any of the calculation procedures must be implemented manually, e.g. in *COMSOL Multiphysics*. These models are i.a. used for the calculation of the AC loss in superconductors, Sec. 2.2.4.

### 2.2.1. Finite Element Method for Electromagnetic Problems Involving Superconductors

In finite element models, the calculation domain is divided in a set of elements, in which the field quantities are described by a linear combination of basis functions. The accuracy of the spatial discretization is determined by the number of elements as well as the kind and order of the basis functions. Sec. 2.2.1.3 summarizes the element types that are used in this thesis. The problem of determining the field solution in the calculation domain is reduced to finding a solution for a finite number of variables per element. This is done by assembling a global stiffness matrix representing the system of equations. In case of transient analyses, the evolution in time is discretized by time stepping with finite step width  $\Delta t$ . A sufficiently small time step is crucial for an accurate calculation of eddy currents and of the superconducting current density distribution.

Several formulations for electromagnetic problems exist, which differ with respect to the quantity to be solved (state variables). One choice consists in a direct solution for the field quantity of interest, e.g.  $\vec{H}$ . Alternatively, potentials can be introduced and solved for [31]. This approach involves a subsequent calculation of the field quantities from the respective potential.

Most of the software solutions for electromagnetic standard applications, e.g. *JMAG* and *FEMM*, employ a vector potential approach. In case of problems with eddy currents, a combination of the vector potential  $\vec{A}$  and the electrostatic potential  $\phi$  is required ( $A$ - $\phi$ -formulation [O15]). For constant conductivities  $\kappa$  in the conductive region, an approach based on a modified vector potential  $\vec{A}_{\text{mod}}$  alone is also possible [31]. Details can be found in [O15]. The vector potential based approach is computationally efficient in presence of non-linear iron, but exhibits poor convergence behaviour in case of non-linear

$E(J)$ -relations of superconductors, Sec. 2.5. Moreover, the  $A$ -formulation allows for a simple incorporation of rotation periodic boundary conditions, which are required for the simulation of generator sector models. In this thesis, this formulation is used for models, where superconducting windings are approximated with a homogenized, impressed current density  $J$ .

For an explicit modelling of superconductors, the  $H$ -formulation has been applied successfully in various cases, e.g. in [218]. Here, the specific resistance  $\rho = \kappa^{-1}$  enters the equations rather than the conductivity  $\kappa$ , as is the case for the  $A$ -formulation. For  $J = 0$  in the superconducting region, the specific resistance is finite, i.e.  $\rho = 0$ , whereas the conductivity diverges, i.e.  $\kappa \rightarrow \infty$ , which hampers the convergence significantly. The advantages of both  $A$ - and  $H$ -formulations can be exploited if combined in a coupled  $H$ - $A$ -formulation, Sec. 2.2.1.1.

An alternative approach, which also circumvents the use of  $\kappa$  in the constituting equations, is based on the current vector potential  $\vec{T}$  [82]. It is suitably coupled with the  $A$ -formulation of the normal conducting part of the calculation domain, yielding the  $T$ - $A$ -formulation, Sec. 2.2.1.2. If the  $T$ -formulation is employed in conjunction with a thin-sheet approximation for high aspect ratio HTS conductors, it enables a simple coupling together with a significant reduction of degrees of freedom (DoFs).

The choice of the formulation determines, whether the non-linear magnetization behaviour of ferromagnetic materials is incorporated by either a  $B$ -dependent reluctivity  $\nu(B)$  ( $A$ -formulation) or an  $H$ -dependent permeability  $\mu(H)$  ( $H$ -formulation). The material specific, characteristic curves of relevant materials are summarized in App. A.3.1. Available data from data sheets and measurements typically cover only the range up to  $B \approx 2\text{ T}$ , which is generally exceeded in superconducting generators up to  $B \geq 5\text{ T}$ . Therefore, an extrapolation scheme with correct behaviour in the limiting case  $B, H \rightarrow \infty$  is required, as described in App. A.3.1. An important restriction on the accuracy of the numerical solutions is that the hysteresis in ferromagnetic parts is not directly incorporated, such that any phase shift between  $H$  and  $B$  is neglected. Instead, an iron loss estimate including hysteresis losses is obtained as part of the post-processing via appropriate loss formulas.

Here, irrespective of the used software, the iron loss is calculated from the (empirical) *Jordan* model (2.68) for the gravimetric loss density  $p_{d, \text{Fe}}$  [98]. The coefficients are extracted from fits to manufacturer data [221] as  $k_{\text{hyst}} = 1.353\text{ W/kg}$  and  $k_{\text{Fe}} = 0.528\text{ W/kg}$ . The

empirical pre-factor is chosen as  $k_V = 1.6$  and accounts for manufacturing related effects at the edges of steel sheets, which increase the overall iron loss [23]. A model with an additional contribution due to the movement of magnetic domain boundaries was proposed by *Bertotti* [21]. It is especially useful for grain-oriented steel sheets. In case of rotational fields, like in the considered generators, no grain-oriented steel sheets are used and the *Bertotti* loss effect is rather small ( $< 10\%$ ). Further, this model extension does not relieve the main model limitations, i.e. the neglect of hysteresis and the uncertainties regarding the manufacturing induced degradation. For these reasons, the simpler *Jordan* approach is used, since it fits well to manufacturer data. Generally, the iron loss is of minor importance in direct drive generators due to the low frequency  $f_s \approx 5 \dots 10\text{Hz}$ , and does also play a subordinate role in medium speed generators with normal conducting stator winding.

$$p_{d,Fe} = k_V \cdot \left[ k_{\text{hyst}} \cdot \left( \frac{B}{1\text{T}} \right)^2 \cdot \left( \frac{f}{50\text{Hz}} \right) + k_{\text{Ft}} \cdot \left( \frac{B}{1\text{T}} \right)^2 \cdot \left( \frac{f}{50\text{Hz}} \right)^2 \right] \quad (2.68)$$

The fundamentals of the *A*-formulation and the *H*-formulation are summarized in [O15]. Based on this, the *H-A*-formulation and the *T-A*-formulation are discussed in the following subsections.

### 2.2.1.1. *H-A*-Formulation

The general concept of the coupled *H-A*-formulation is visualized in Fig. 2.4 for 2D models. Within the sub-domain  $\Omega_1$ , the *A*-formulation equations [O15] for two dimensions are solved. In  $\Omega_2$ , the *H*-formulation equations [O15] are solved. The coupling between the problems is achieved by imposing weak contributions at the coupling boundary  $\Gamma_{\text{coupl}}$ . In the following,  $x$ ,  $y$  and  $z$  denote the *Cartesian* coordinates in the laboratory frame of reference.  $X$ ,  $Y$  and  $Z$  denote the *Cartesian* coordinates in the rest frame of the coupling boundary, which rotates with an angular frequency  $\Omega$  in the general case.

The tangential magnetic field  $H_t$  is evaluated on  $\Gamma_{\text{coupl}}$  and prescribed for the *A*-formulation part. It is determined by using the tangential vector to the coupling boundary  $\vec{t}$ , (2.69).

$$H_t = \vec{t} \cdot \vec{H}, \quad \vec{H} = \nu(B) \cdot \vec{B}, \quad \vec{B} = \nabla \times \vec{A} \quad (2.69)$$

Based on the weak form of the *A*-formulation [O15], the weak contribution (2.70) with  $K = H_t$  and scalar weighting functions  $\vartheta$  is imposed. Here,  $\Gamma_{\text{coupl}}$  is part of the generalized

boundary section  $\Gamma_H$  with prescribed magnetic field.

$$\int_{\Gamma_{\text{coupl}}} \vartheta \cdot H_t \, d\Gamma \quad \text{in } A\text{-formulation part} \quad (2.70)$$

In the  $H$ -formulation part, the tangential electric field is prescribed on  $\Gamma_{\text{coupl}}$ . The electric field  $E_Z$  on  $\Gamma_{\text{coupl}}$  is obtained from (2.71) in the boundary's frame of reference, which is rotating in the general case. The magnetic flux density is obtained from  $B_X = \partial_Y A_z$  and  $B_Y = -\partial_X A_z$  in the rest system of  $\Gamma_{\text{coupl}}$ . The contribution  $E_{\text{rot}}$  is zero for sub-domains that are stationary in the laboratory frame ( $\Omega = 0$ ). In rotating regions, subtracting  $E_{\text{rot}}$  ensures that the proper electric field in the rest system of the rotating boundary is imposed [27].

$$\begin{aligned} E_Z &= -\partial_t A_Z - E_{\text{rot}} \\ &= -\partial_t A_Z - \mu \cdot \Omega \cdot (X \cdot B_X + Y \cdot B_Y) \end{aligned} \quad (2.71)$$

Based on [O15], the electric field is imposed in the  $H$ -formulation part as weak contribution (2.72) on the coupling boundary.  $\vec{\vartheta}_t = \vartheta_t \cdot \vec{t} = (\vec{\vartheta} \cdot \vec{t}) \cdot \vec{t}$  denotes the part of the testing functions, which is tangential to the coupling boundary.

$$\int_{\Gamma_{\text{coupl}}} \vec{\vartheta} \cdot \underbrace{(\vec{n} \times \vec{E})}_{\text{in tangent plane}} \, d\Gamma = \int_{\Gamma_{\text{coupl}}} \vec{\vartheta}_t \cdot (-E_Z \cdot \vec{t}) \, d\Gamma = - \int_{\Gamma_{\text{coupl}}} E_Z \cdot \vartheta_t \, d\Gamma \quad (2.72)$$

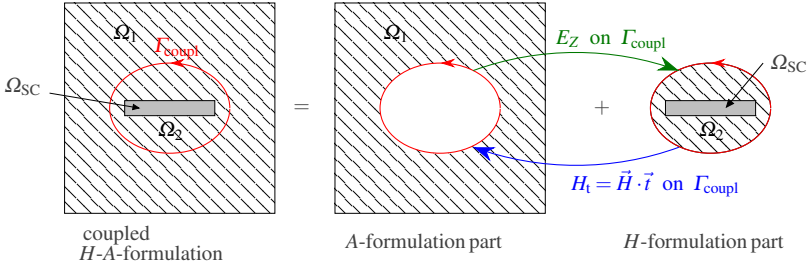


Figure 2.4.: Schematic of the coupling between the  $A$ -formulation and the  $H$ -formulation parts. The  $H$ -formulation part comprises the superconducting region, whereas the  $A$ -formulation part contains the ferromagnetic regions and the sliding boundary between stator and rotor in time stepping simulations. ( $\Omega_{\text{SC}}$ : superconducting domain,  $\Omega_1, \Omega_2$ : normal conducting domains)

Integral constraints of the form (2.73) [27] are used to impress a transport current in the su-

perconductor, while allowing for an inhomogeneous current density distribution  $J_z(x, y, t)$ .

$$I_{sc} = \int_{\Omega_{sc}} J_z(x, y, t) d\Omega \quad (2.73)$$

A sufficiently fine space and time discretization together with comparably strict convergence criteria are required in order to achieve a proper coupling. In case of larger models, this increases the required computation time significantly.

### 2.2.1.2. *T-A-Formulation*

An alternative approach for the numerical simulation of problems involving superconductors consists in the *T-A*-formulation, first introduced in [238, 132]. Since then, the *T-A*-formulation has been successfully applied to a variety of 2D and 3D problems and was successfully validated against experimental data [216, 82, 19, 167]. However, there is an ongoing discussion on the differences between the *T-A*- and the *H-A*-formulation and on the applicability of the *T-A*-formulation for high frequency problems. Since the latter point does not affect the applicability of the *T-A*-approach to electrical wind generators with  $f_s \approx 10^0 \dots 10^3$  Hz, the studies based on the *H-A*-formulation, Sec. 2.2.1.1, are supplemented by analyses that use the *T-A*-formulation.

The motivation for the *T-A*-formulation consists again in the need to exclude the highly non-linear  $E(J)$ -relation from the *A*-formulation part while solving for the vector potential  $A$  in non-superconducting regions to improve computational efficiency and the ease of implementation. The system of equations must therefore rely on the specific resistance  $\rho_{sc}$  with  $\rho_{sc} \rightarrow 0$  for  $J \rightarrow 0$ . In case of the *H-A*-formulation, the domains with different state variables (either  $A$  or  $H$ ) are spatially separated and coupled via their common boundary, Sec. 2.2.1.1. In contrast, the *T-A*-formulation requires to solve for the vector potential  $A$  in the entire model domain. The current vector potential  $T$  is additionally solved for in the superconducting sub-domain and is coupled to the *A*-formulation part. The non-linear  $E(J)$ -relation can therefore be „outsourced“ from the *A*-formulation part to the *T*-formulation part, while the field exciting effect of the superconducting currents enters the *A*-formulation part by the mutual coupling.

In the following, the entire model domain is denoted by  $\Omega$  and the superconducting domain is  $\Omega_{sc} \subset \Omega$ . The equation to solve for  $\vec{A}$  is Ampère's law (2.74), while the current density  $\vec{J}$  enters as „external“ source term, whose connection to the electric field strength

$\vec{E}$  is not defined within the  $A$ -formulation part in the superconductor.

$$\nabla \times \left( \nu(B) \cdot \nabla \times \vec{A} \right) = \vec{J} \quad (2.74)$$

The current vector potential  $\vec{T}$  is defined by (2.75) in the superconducting model domain.

$$\nabla \times \vec{T} = \vec{J} \quad (2.75)$$

Together with the numerically manageable material relation  $\vec{E} = \rho_{\text{SC}}(J, \vec{B}) \cdot \vec{J}$ , the equation to solve for  $T$  is *Faraday's law* (2.76). The magnetic flux density (and its derivative with respect to time  $t$ ) enter as „external“ source terms that are obtained from the  $A$ -formulation part.

$$\nabla \times \left( \rho_{\text{SC}}(J, \vec{B}) \cdot \nabla \times \vec{T} \right) = -\partial_t \vec{B} \quad \text{in } \Omega_{\text{SC}} \quad (2.76)$$

Given the solution  $\vec{A}$ , the magnetic flux density is obtained from  $\vec{B} = \nabla \times \vec{A}$  while the solution of the  $T$ -formulation part yields the current density  $\vec{J} = \nabla \times \vec{T}$  in turn. In this sense, the  $A$ - and  $T$ -formulation parts exchange the current density  $\vec{J}$  and the magnetic flux density  $\vec{B}$ , Fig. 2.5. The consistent solution  $\{\vec{A}, \vec{T}\}$  can be obtained by coupling the partial models, which was done here in *COMSOL Multiphysics*. The field-dependent, non-linear resistance characteristic  $\rho_{\text{SC}}(J, \vec{B})$  of superconductors is described by means of the relations in Sec. 2.5.

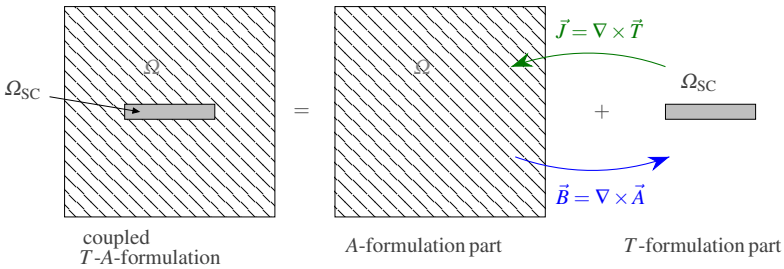


Figure 2.5.: Schematic of the simulation domains for the coupled  $T$ - $A$ -formulation. The numerical scheme solves for the magnetic vector potential  $\vec{A}$  in the entire domain  $\Omega$  and for the current vector potential  $\vec{T}$  in the superconducting sub-domain  $\Omega_{\text{SC}}$ .

The  $T$ - $A$ -formulation is usually used for HTS tapes in combination with the *thin sheet approximation* in the limit of zero cuprate layer thickness  $d_{\text{HTS}} \rightarrow 0$ . This approximation is motivated by the typically large aspect ratios  $w_t/d_{\text{HTS}} \approx 10^3 \dots 10^4$ . It is simple to



implement and computationally efficient, if the current vector potential  $\vec{T}$  is used. If the cuprate layer is modelled without finite thickness ( $d_{\text{HTS}} \rightarrow 0$ ), the current density  $\vec{J}$  cannot exhibit any component that is normal to the tape's wide face with width  $w_t$ . Therefore, the current vector potential  $\vec{T}$  is normal to the current carrying sheet, so that (2.77) holds with  $\vec{n}$  as normal unit vector of the tape's wide face, Fig. 2.6.

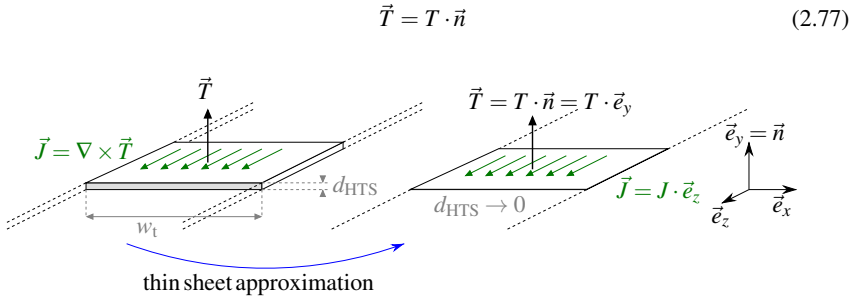


Figure 2.6.: Schematic of the section of a HTS tape with infinite length in  $z$ -direction: The thin sheet approximation  $d_{\text{HTS}} \rightarrow 0$  reduces the dimensionality of the modelled tape. For 2D problems, the current vector potential must be calculated on a line and is scalar-valued.

The task to solve for the vector field  $\vec{T}$  in a finite volume is therefore reduced to the determination of one scalar-valued unknown variable  $T$  in the sheet. In the following, 2D cross sectional models are considered, where the components of the current vector potential in *Cartesian* coordinates are defined by (2.78).

$$\begin{aligned} T_x &= \vec{T} \cdot \vec{e}_x = T \cdot (\vec{n} \cdot \vec{e}_x) = T \cdot n_x \\ T_y &= \vec{T} \cdot \vec{e}_y = T \cdot (\vec{n} \cdot \vec{e}_y) = T \cdot n_y \end{aligned} \quad (2.78)$$

The restriction of  $\vec{T}$  to a normal component in the *thin sheet approximation* implies that the current density in the superconductor cannot change in the direction that is perpendicular to the tape's wide face with width  $w_t$ . Therefore, the  $T$ -formulation sub-model receives only the normal component of the flux density from the  $A$ -formulation part for the purpose of coupling. Still, the actual flux density  $\vec{B} = (B_n, B_t)'$ , including also the tangential component  $B_t$ , is used for the determination of the critical current density  $J_c = f(T, \vec{B})$ , Sec. 2.5. The excitation of the tangential field component  $B_t$  by the superconducting currents in the exterior of the superconducting sub-domain (which is the domain with  $A$ -formulation only) is represented by a surface current boundary condition.

## 2.2. Numerical Models of Rotating Electrical Machines with Superconducting Windings

For the 2D model with  $\vec{E} = E_z \cdot \vec{e}_z$  and  $B_z = 0$ , the projection of *Faraday's* law to the wide side's normal direction is (2.79) [238] ( $n_x = \vec{n} \cdot \vec{e}_x$ ,  $n_y = \vec{n} \cdot \vec{e}_y$ ).

$$(\partial_y E_z) \cdot n_x - (\partial_x E_z) \cdot n_y = -\mu \cdot \partial_t [H_x \cdot n_x + H_y \cdot n_y] \quad (2.79)$$

Based on (2.75), the current density  $J_z$  and the electric field strength  $E_z$  in (2.79) can be written in terms of the current vector potential  $T$ , (2.81), using  $\rho_{SC} = \rho_{HTS}$ .

$$J_z = \partial_x T_y - \partial_y T_x = \partial_x (T \cdot n_y) - \partial_y (T \cdot n_x) \quad (2.80)$$

$$E_z = \rho_{HTS} (|J_z|, \vec{B}) \cdot J_z = \rho_{HTS} (|J_z|, \vec{B}) \cdot (\partial_x (T \cdot n_y) - \partial_y (T \cdot n_x)) \quad (2.81)$$

The derivatives in (2.80) and (2.81) reduce to the tangential derivatives due to the thin sheet approximation. In this case, the  $T$ -formulation part involves boundary partial differential equations. For the implementation, it is convenient to introduce the tangential derivative operator of vector-valued functions (2.82), where  $\vec{n}$  is the normal unit vector of a boundary.

$$\nabla_T(\cdot) = (\mathbb{I} - \vec{n} \otimes \vec{n}) \cdot \nabla(\cdot) = (\vec{t} \otimes \vec{t}) \cdot \nabla(\cdot) \quad (2.82)$$

For the considered 2D problem and a *Cartesian* coordinate system, the tangential derivative operator is (2.83).

$$\nabla_T(\cdot) = \begin{pmatrix} n_y^2 \cdot \partial_x - n_x \cdot n_y \cdot \partial_y \\ -n_x \cdot n_y \cdot \partial_x + n_x^2 \cdot \partial_y \end{pmatrix} (\cdot) \quad (2.83)$$

In *COMSOL Multiphysics*, the general form of boundary partial differential equations of the *Coefficient Form Boundary PDE* module for a scalar-valued state variable  $u$  is (2.84).

$$e_a \cdot \partial_t^2 u + d_a \cdot \partial_t u + \nabla_T \left( -c \cdot \nabla_T u - \vec{\alpha} \cdot u + \vec{\Gamma} \right) + \vec{\beta} \cdot \nabla_T u + a \cdot u = f \quad (2.84)$$

Equation (2.79) can therefore be implemented by specifying (2.84) to (2.85). The variable section contains the definition of  $E_z$  in terms of the current vector potential  $T$ .

$$e_a = d_a = c = a = 0, \quad \vec{\alpha} = \vec{\beta} = 0 \quad (2.85)$$

$$\vec{\Gamma} = \begin{pmatrix} -E_z \cdot n_y \\ E_z \cdot n_x \end{pmatrix}, \quad f = -\mu \partial_t [H_x \cdot n_x + H_y \cdot n_y]$$

The surface current densities  $A_{e,z}$  at the edges  $\Gamma_{HTS}$ , which represent HTS tapes, are impressed in the  $A$ -formulation part by means of weak contributions (2.86), based on the

weak formulation described in [O15].  $\vartheta$  denotes the scalar valued test functions.

$$\int_{\Gamma_{\text{HTS}}} \vartheta \cdot A_{e,z} d\Gamma \quad (2.86)$$

The value of the surface current density  $A_{e,z}$  is the current per unit length along the tape's wide side with width  $w_t$ , (2.87).

$$A_{e,z} = d_{\text{HTS}} \cdot J_z, \quad \text{with } J_z \text{ from (2.80)} \quad (2.87)$$

The impressed transport current in the superconducting tape  $I_t$  is expressed in terms of the current vector potential  $\vec{T}$ , (2.88). The net transport current is only related to the current vector potential's values at either end of the tape, Fig. 2.7. Equation (2.88) is implemented by means of *Dirichlet* boundary conditions for the  $T$ -formulation sub-domain, i.e. for each HTS line segment separately. This is a significant simplification compared to the integral boundary condition (2.73), that is applied in the  $H$ -formulation.

$$\begin{aligned} I_t &= \int_{\Omega_{\text{HTS}}} \vec{J} \cdot \vec{n}_{\Omega} d\Omega = \int_{\Omega_{\text{HTS}}} (\nabla \times \vec{T}) \cdot \vec{n}_{\Omega} d\Omega \\ &= \int_{\partial\Omega_{\text{HTS}}} \vec{T} \cdot \vec{t}_{\Gamma} d\Gamma = \int_{c_2+c_4} \vec{T}_t \cdot \vec{t}_{\Gamma} d\Gamma + \int_{c_1+c_3} \vec{T}_n \cdot \vec{t}_{\Gamma} d\Gamma \quad (2.88) \\ &= (T_1 - T_2) \cdot d_{\text{HTS}} \end{aligned}$$

The cuprate layer thickness  $d_{\text{HTS}}$  in (2.88) is not a meaningful quantity for models involving the thin sheet approximation  $d_{\text{HTS}} \rightarrow 0$ . However, (2.88) implies  $T \sim d_{\text{HTS}}^{-1}$  and therefore  $J_z \sim d_{\text{HTS}}^{-1}$  for fixed transport current  $I_t$ . Together with (2.87), this yields a field-exciting surface current density  $A_{e,z}$ , that is independent from  $d_{\text{HTS}}$ . The proportionality of the AC loss  $P_{d,\text{HTS}} \sim d_{\text{HTS}} \cdot J_z$ , (2.111), also reflects the arbitrariness of the considered value of  $d_{\text{HTS}}$ .

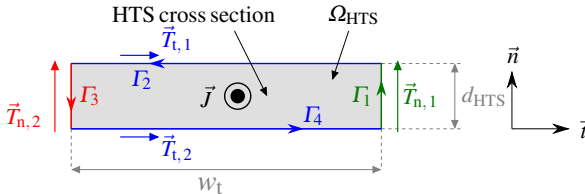


Figure 2.7.: Schematic cross section of one HTS tape with current vector potential  $\vec{T}$  and superconducting current density  $\vec{J}$ . The net transport current is fixed by the specification of  $T \equiv T_n$  at either end of the tape in the thin sheet approximation.

2.2.1.3. Meshing and Implementation of Boundary Conditions

The basis (resp., shape) functions for the interpolation within elements are chosen in accordance with the state variables to solve for. For the  $A$ -formulation part, first- or second-order nodal *Lagrange* elements [125, 32, 31] are used. First-order nodal elements are the default in *FEMM* and *JMAG* and cannot be changed here. In the 2D  $H$ -formulation part, which involves the superconducting domains, first-order *Nédélec* edge elements [154, 33] are used, Fig. 2.8. Edge elements are particularly suitable to model discontinuities and strong non-linearities in material properties [154] and obey by definition  $\nabla \vec{H} = 0$  within the elements [26]. As an example, the basis functions are visualized in Fig. 2.8 for a triangular 2D element.

Table 2.1.: Summary of used FEM software, formulations and of element types.

software	state variable	element type
<i>JMAG 20 &amp; 21</i>	$A$	first-order nodal
<i>FEMM 4.2</i> <sup>a)</sup>	$A$	first-order nodal
<i>COMSOL Multiphysics 6.0</i>	$A$	first- or second-order nodal
	$H$	first-order edge
	$T$	second-order nodal

<sup>a)</sup> A customized version with implementation of additional boundary conditions is used.

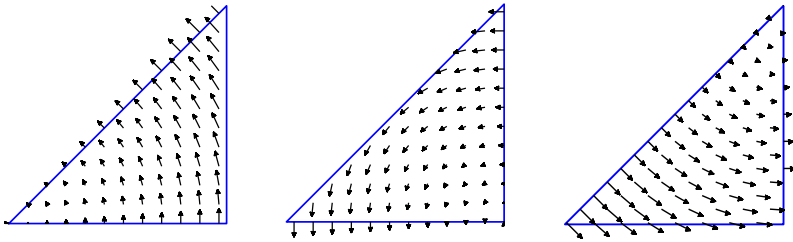


Figure 2.8.: Exemplary visualization of the basis functions in first-order edge elements, which are used for the  $H$ -formulation part of 2D FEM models.

The element types and the used software in this thesis are summarized in Tab. 2.1. Convergence analyses towards a finer mesh and shorter time steps in case of transient models are carried out with respect to the torque, the eddy current loss and the AC loss in superconductors (convergence limit of  $10^{-3}$  for relative change).

All boundary conditions are applied in terms of the vector potential  $A$ . Periodic (resp., anti-periodic) boundary conditions are applied for generator sector models comprising an even (resp., uneven) number of magnetic poles, ( $1 \rightarrow 1'$ ,  $2 \rightarrow 2'$  in Fig. 2.9). The sector models comprise one pole in case of integer slot windings and symmetric rotor poles, Fig. 2.9, and more poles for fractional slot windings, e.g. two poles for  $q = 1/2$  slots per pole per phase, or magnetic asymmetries, i.e. shifted (resp., rotated) rotor poles or redundant feeding (Ch. 6). *Dirichlet* boundary conditions  $A_z = 0$  are assigned to the radially inner and outer model boundaries, which eliminate the ambiguity of the solution for  $A_z$ . In order to cover the continuity, periodicity and anti-periodicity of  $A_z$  across the rotation line ( $3 \rightarrow 3'$ ,  $4 \rightarrow 4'$  in Fig. 2.9), a mapping function is implemented, which selects the appropriate condition per node, based on the rotational angle.

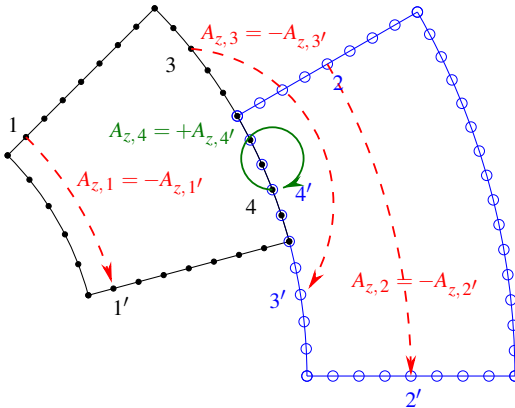


Figure 2.9.: Schematic of the boundary equations in case of a sector model of the generator, which comprises one pole in case of an integer slot stator winding, see e.g. App. A.6. Both boundary conditions and continuity equations on the rotation line are implemented in the  $A$ -formulation part.

### 2.2.2. Induced Voltage

In standard FEM models, e.g. models in *FEMM* and *JMAG*, pre-implemented calculation routines for the flux linkage  $\psi$ , the „inner“ or outer induced voltages  $u_i$ , the electromagnetic torque  $M_e$  and the *ohmic* loss exist. In contrast, custom implementations, which allow for an explicit modelling of superconductors, e.g. in *COMSOL Multiphysics*, require a manual implementation of these calculations, which are described in this and the following subsections 2.2.3, 2.2.4.

The flux linkage  $\psi$  of one region, i.e. the cross section of a conductor, is computed from the vector potential  $\vec{A}$ , which is however only defined in the  $A$ -formulation model

parts. In case of the  $H$ - $A$ -formulation, the calculation of the flux linkage for superconducting winding turns requires an additional determination of  $A_z$  in the sub-domains with  $H$ -formulation. For this purpose, an additional state variable  $U$  with governing equation (2.89) is defined. The current density  $J_z$  is known from the solution of the  $H$ - $A$ -formulation problem in the entire model domain. The boundary conditions and continuity conditions of the  $A$ -formulation part apply similarly for the problem with state variable  $U$ . The solution for  $U$  is the  $z$ -component of the magnetic vector potential in the entire model domain.

$$-\left(\partial_x(v(B) \cdot \partial_x U) + \partial_y(v(B) \cdot \partial_y U)\right) = J_z \quad (2.89)$$

The flux linkage of any point in the modelled domain can be defined by considering a conductor loop  $\Gamma$ , Fig. 2.10, with returning conductor at radius  $r \rightarrow \infty$ . For  $r \rightarrow \infty$ , both the potential  $U$  and its spatial derivatives vanish, (2.90).

$$\lim_{r \rightarrow \infty} U = 0, \quad \lim_{r \rightarrow \infty} \partial_i U = 0, \quad i \in \{x, y\} \quad (2.90)$$

The flux linkage of the loop  $\Gamma$  ( $N = 1$  turn) with some magnetic flux density  $\vec{B}$  in the modelled domain can be expressed in terms of the vector potential  $\vec{U} = U \cdot \vec{e}_z$ , (2.91), where  $\Omega$  is the surface that is bounded by  $\Gamma$ .

$$\psi = \int_{\Omega} \vec{B} \cdot \vec{n}_{\Omega} \, d\Omega = \int_{\Omega} (\nabla \times \vec{U}) \cdot \vec{n}_{\Omega} \, d\Omega \stackrel{\text{Stokes' theorem}}{=} \int_{\Gamma=\partial\Omega} \vec{U} \cdot \vec{t}_{\Gamma} \, d\Gamma = U \cdot l_i \quad (2.91)$$

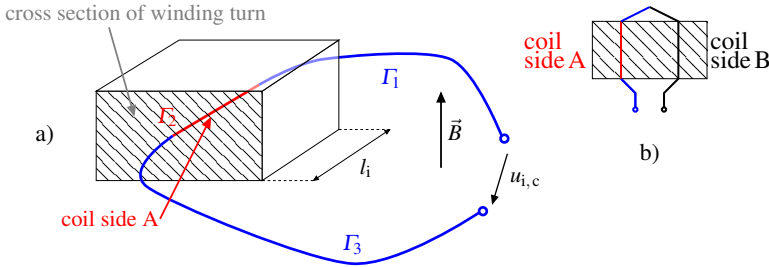


Figure 2.10.: a) Schematic of the curve for the calculation of a conductor's flux linkage  $\psi$  and the „outer“ induced voltage  $u_i = -\partial_t \psi(t)$  after solving for the vector potential  $A$ . b) Schematic of the considered coil.

If conductors with finite cross section  $A_c$  are considered, the flux linkage is suitably aver-

aged as  $\bar{\psi}(t)$  over the respective region (index  $k$ ), similar to Fig. 2.3 b). Applying the time derivative yields the „outer“ induced voltage, (2.92).

$$u_{i,c,k}(t) = -\partial_t \bar{\psi}_k(t) = -l_i \cdot \partial_t \left( \frac{1}{A_c} \cdot \int_{A_c} U(\vec{r}, t) dA \right) \quad (2.92)$$

The induced voltage in a coil side, Fig. 2.10 a), with  $N_c$  turns is calculated as the sum over the induced voltages in all associated regions  $k = 1, \dots, N_c$ , (2.93).

$$u_{i,c}(t) = \sum_{k=1}^{N_c} u_{i,c,k}(t) = u_{i,c}^{\text{A or B}}(t) \quad (2.93)$$

The induced voltage in the entire coil, comprising coil sides A and B, Fig. 2.10 b), is calculated as the difference of the induced voltages (2.93) for A and B. If the actual coil with  $N_c$  turns is approximated with an equivalent coil with  $n$  turns, a scaling according to (2.94) is applied for the induced voltage and the flux linkage.

$$u_{i,c}(t) = \frac{N_c}{n} \cdot \left( u_{i,c}^{\text{A}}(t) - u_{i,c}^{\text{B}}(t) \right) \quad (2.94)$$

In order to validate the calculation scheme, the stator flux linkages of a fully superconducting generator (Ch. 7) are compared to a magnetostatic model with a pre-implemented calculation scheme and without explicit modelling of the superconductor, Fig. 2.11. The differences are very small, i.e. relative deviation of  $< 0.03\%$  for the peak value.

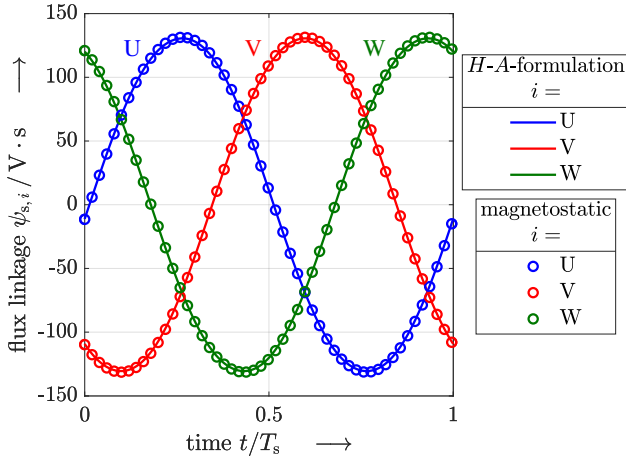


Figure 2.11.: Comparison of the calculated flux linkages of phases U, V, W, obtained from a series of magnetostatic simulations (*FEMM*) and by means of (2.91) for the manually implemented, coupled *H-A*-formulation (*COMSOL Multiphysics*).

In case of the coupled  $T$ - $A$ -formulation, the magnetic vector potential  $A_z$  is directly obtained in the entire model domain. The flux linkage of one turn in one coil side A of the superconducting coil  $\psi_c^A$  can be obtained by averaging the magnetic vector potential  $\bar{A}_z$  along the edge  $\Gamma_{\text{HTS}}$ , which represents the tape of width  $w_t$ . Multiplying with the magnetically effective model length in the out-of-plane direction yields the flux linkage of the straight conductor section  $\psi$ , (2.95). The induced voltage is again calculated as  $u_i = -\partial_t \psi$ .

$$\psi = l_i \cdot \bar{A}_z = l_i \cdot \frac{1}{w_t} \cdot \int_{\Gamma_{\text{HTS}}} A_z \cdot d\Gamma \quad (2.95)$$

### 2.2.3. Electromagnetic Torque

Two frequently used methods for the calculation of the electromagnetic torque in the air gap consist in

1. the integration of the *Maxwell* stress tensor over a surface surrounding either the stator or the rotor [169] and
2. the computation of nodal forces by applying the virtual work principle [41].

The evaluation of nodal forces is difficult in the present case, where the covered domain comprises two different types of elements, i.e. nodal and edge elements. Therefore, the surface integration method 1. is applied. The *Maxwell* stress tensor in the general form for  $N_M$  dimensions, (2.96a), (2.96b), comprises contributions from both electric and magnetic fields.

$$\underline{\underline{\sigma}} = \varepsilon_0 \cdot \left( \vec{E} \otimes \vec{E} - \frac{1}{2} \cdot E^2 \cdot \mathbb{I} \right) + \frac{1}{\mu_0} \cdot \left( \vec{B} \otimes \vec{B} - \frac{1}{2} \cdot B^2 \cdot \mathbb{I} \right) \quad (2.96a)$$

$$\sigma_{ij} = \varepsilon_0 \cdot \left( E_i \cdot E_j - \frac{1}{2} \cdot E^2 \cdot \delta_{ij} \right) + \frac{1}{\mu_0} \cdot \left( B_i \cdot B_j - \frac{1}{2} \cdot B^2 \cdot \delta_{ij} \right), \quad i, j \in \{1, \dots, N_M\} \quad (2.96b)$$

The volumetric, electromagnetic force density can be written in terms of the *Maxwell* tensor's divergence and the *Poynting* vector  $\vec{S} = \vec{E} \times \vec{H}$ , (2.97).

$$\vec{f} = \nabla \underline{\underline{\sigma}} - \varepsilon_0 \cdot \mu_0 \cdot \partial_t \vec{S} \quad (2.97)$$

Since the forces due to magnetic fields dominate those of electric fields (influence of  $\vec{E}$ ) and all field quantities vary slowly (influence of  $\vec{S}$ ), the approximation (2.98) holds with



sufficient accuracy.

$$\vec{f} \approx \nabla \underline{\underline{\sigma}}, \quad \underline{\underline{\sigma}} \approx \frac{1}{\mu_0} \cdot \left( \vec{B} \otimes \vec{B} - \frac{1}{2} \cdot B^2 \cdot \mathbb{I} \right) \quad (2.98)$$

For the application to electrical machines,  $\underline{\underline{\sigma}}$  is suitably written in cylindrical coordinates  $(r, \varphi, z)$ , (2.99).

$$\underline{\underline{\sigma}} \approx \frac{1}{\mu_0} \cdot \left[ \frac{1}{2} \cdot (B_r^2 - B_\varphi^2) \cdot \vec{e}_r \otimes \vec{e}_r + \frac{1}{2} \cdot (B_\varphi^2 - B_r^2) \cdot \vec{e}_\varphi \otimes \vec{e}_\varphi + B_r \cdot B_\varphi \cdot (\vec{e}_r \otimes \vec{e}_\varphi + \vec{e}_\varphi \otimes \vec{e}_r) \right] \quad (2.99)$$

The closed surface area of the considered volume corresponds to the closed curve  $\Gamma$  in the cross-sectional 2D model with axial length  $l_i$ . Therefore, the curve  $\Gamma$  in Fig. 2.12 is considered for the integration to get the resulting force per volume. For the cross-sectional model, the integration along the path  $\Gamma_1 + \Gamma_2 + \Gamma_3 + \Gamma_4$  yields the electromagnetic force per unit length (axial length  $l_i$ ), which acts on the stator section. The total force is calculated as (2.100).

$$\vec{F}_e = \int_{A=\partial V} \underline{\underline{\sigma}} \cdot \vec{n} \, dA \quad (2.100)$$

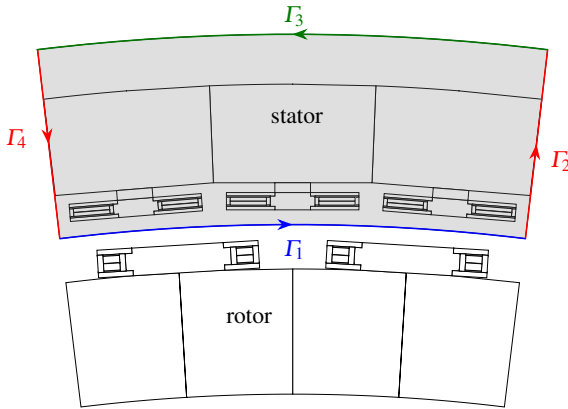


Figure 2.12.: Schematic cross-sectional view of one pole pair of an exemplary fully superconducting generator with integration path used for the derivation of the electromagnetic torque  $M_e$ .

As the contributions along the curves  $\Gamma_2$  and  $\Gamma_4$  cancel out for symmetry reasons, only the last summand in (2.99) contributes to the circumferential force component  $F_{e,\varphi}$ . Moreover, the contribution along  $\Gamma_3$  is zero, since  $\Gamma_3$  coincides with the outer model boundary, where  $B_r = 0$  due to the *Dirichlet* boundary condition. This results in the expression (2.101) for the torque producing force component  $F_{e,\varphi}$  with  $\varphi$  counted in mechanical

degrees. The force with opposite sign acts on the rotor:

$$F_{e,\varphi} \approx \frac{1}{\mu_0} \cdot l_i \cdot \int_0^{2\pi} (B_r \cdot B_\varphi) \cdot r d\varphi = p \cdot l_i \cdot \int_0^{2\pi/p} (B_r \cdot H_\varphi) \cdot r d\varphi \quad (2.101)$$

The electromagnetic air gap torque is obtained by multiplication with the radius  $r$ , (2.102).

$$M_e = -p \cdot l_i \cdot r^2 \cdot \int_0^{2\pi/p} (B_r \cdot H_\varphi) d\varphi \quad (2.102)$$

To validate the calculation scheme, the torque from (2.102) is compared with the pre-implemented method in *FEMM*, Fig. 2.13.

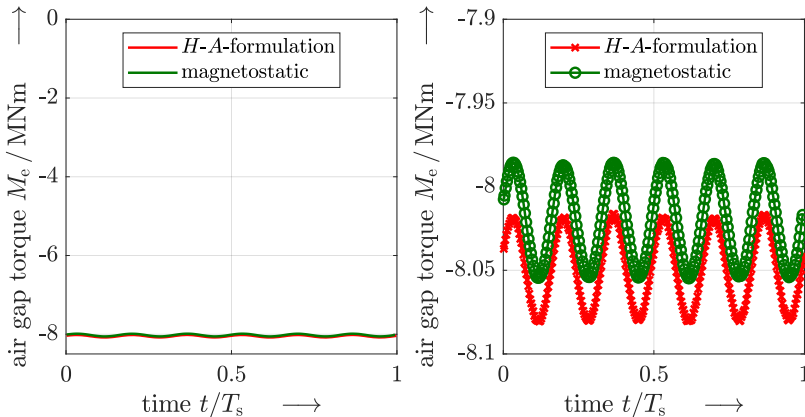


Figure 2.13.: Comparison of the numerically calculated electromagnetic torque obtained from the magnetostatic simulations (*FEMM*) and by means of the manual implementation, (2.102), for the coupled *H-A*-formulation (*COMSOL Multiphysics*).

The average torque  $\overline{M}_e$  differs by less than 0.25%, while the torque ripple is nearly identical. The deviation in  $\overline{M}_e$  is caused by the eddy current loss in the cryostat wall and the damper, which is neglected in the magnetostatic *FEMM* model.

#### 2.2.4. Modelling of Superconducting Windings and AC Loss Calculation

Technical 2G HTS (ReBCO) and  $MgB_2$  conductors feature a composite structure. Models with a high level of geometrical detail imply a large number of DoFs, which inhibits

full-scale models of coils with many turns. In case of multifilamentary  $\text{MgB}_2$  wires, the required level of detail is high, as shown in Ch. 7. The surrounding metallic matrix and the outer sheath must be modelled in the FEM model in order to obtain sufficiently accurate AC loss estimates. In case of HTS coated conductors, accurate results for the typical operating conditions in wind generators can be obtained, if only the very thin cuprate layer ( $d_{\text{HTS}} \approx 2 \dots 3 \mu\text{m}$ ) is explicitly modelled:

- Under normal operating conditions, the fraction of transport current, which is not carried by the cuprate layer, is negligible.
- The AC hysteresis loss in the cuprate layer largely dominates the entire AC loss in the coated conductor for the considered frequency range [138]. The loss contributions were examined in preliminary analyses for a detailed tape model (not shown here).

In the following, the modelling approach for ReBCO winding stacks is described. If the  $T$ - $A$ -formulation is used for the description of coated conductors together with the thin sheet approximation, even large numbers of turns  $N_c \geq 100 \dots 1000$  can be explicitly modelled with manageable computational effort. In case of the  $H$ -formulation, two approximations are commonly applied in order to decrease the DoFs:

1. *Artificial expansion*: In contrast to the thin sheet approximation ( $d_{\text{HTS}} \rightarrow 0$ ), the thickness of the modelled cuprate layer  $h_{\text{sec}}$  is artificially increased by up to one order of magnitude compared to the actual thickness  $d_{\text{HTS}}$ . This reduces the aspect ratio  $w_t/h_{\text{sec}}$  ( $w_t$ : width of tape,  $d_{\text{HTS}}$ : thickness of the cuprate layer), Fig. 2.14, and the required number of elements, if only one element in the normal direction of the cuprate plane is used. The artificially expanded tape model yields an overestimation of the actual AC loss if  $h_{\text{sec}}/d_{\text{HTS}}$  gets too large.
2. *Homogenized coil models*: Based on the assumption, that the current density distribution varies little from turn to turn within one SC winding stack, several turns are combined in one modelled region of an equivalent coil with  $n_{\text{sec}}$  turns. The AC loss deviates little, even for small ratios  $n_{\text{sec}}/N'_c = n_{\text{sec}} \cdot n_L/N_c$ , and is only inaccurate for very low numbers of modelled regions.

These approximations are commonly combined, as schematically visualized in Fig. 2.14.

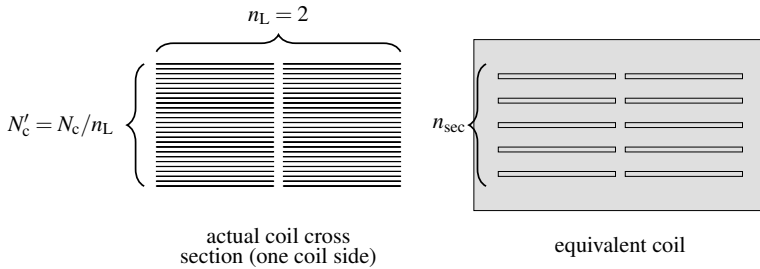


Figure 2.14.: Schematic of a simplified model of a coil made from ReBCO coated conductors. The cuprate layer height  $d_{HTS}$  is artificially increased to  $h_{sec}$  and the modelled number of turns  $n_{sec}$  is considerably lower than the actual number of turns  $N'_c$  per layer.

In this thesis, equivalent coil models are used for both ReBCO field windings and for ReBCO AC stator windings in fully superconducting generators with  $n_{sec}/N'_c \approx 1/5$ . The impressed currents as well as the critical current density must be adapted to the equivalent coil model. The height of the winding stack  $w$ , which is common to the actual and the equivalent coil, is calculated as (2.103).  $d_{t,iso}$  is the thickness of the tape, including an insulation layer, e.g. *Kapton* insulation:  $d_{t,iso} = d_t + d_{iso}$ , where  $d_{iso}$  is the insulation thickness with typically  $d_{iso} \approx 0.1$  mm.

$$w = N'_c \cdot d_{t,iso} \quad (2.103)$$

The width of the modelled superconducting region is the same as of the actual width of the cuprate layer:  $w_{sec} = w_t$ . The height of the modelled HTS sections  $h_{sec}$  is determined as fraction  $d_T \in (0, 1]$  of the inter-turn distance  $\Delta_{sec}$  of the equivalent coil, (2.104).

$$\Delta_{sec} = \frac{w}{N'_c}, \quad h_{sec} = d_T \cdot \Delta_{sec} \quad (2.104)$$

In order to preserve the MMF per coil side and layer, the impressed current per modelled region is (2.105).  $i_{orig}(t)$  denotes the original current in the real tape ( $w_t$ ,  $d_{HTS}$ ).

$$i_{sec}(t) = \frac{N'_c}{n_{sec}} \cdot i_{orig}(t) \quad (2.105)$$

The cross sections of the actual cuprate layer  $A_{HTS}$  and the modelled superconducting region  $A_{sec}$  are determined by (2.106).

$$A_{HTS} = d_{HTS} \cdot w_t, \quad A_{sec} = h_{sec} \cdot w_t \quad (2.106)$$

In order to assure the same relative loading with respect to the critical current carrying capacity, the assigned critical current density  $J_{c0}$  is scaled to  $J_{c0,sec}$ , (2.107).  $J_{c0}$  is the actual critical current density of the cuprate layer in absence of any external field ( $B = 0$ ). Besides the scaling of the critical current density, the same  $E(J)$ -relation is used as for the actual conductor. The magnetic field dependent critical current density  $J_c(\vec{B})$  is determined based on the local value of  $\vec{B}$ .

$$J_{c0,sec} = \frac{A_{HTS} \cdot J_{c0}}{A_{sec}} \cdot \frac{N'_c}{n_{sec}} \quad (2.107)$$

If the  $H$ -formulation is used, the AC loss in the  $k$ -th explicitly modelled superconducting region of the equivalent coil model is calculated from the expression for the volumetric *ohmic* loss density  $p_d = \vec{E} \cdot \vec{J}$ , (2.108).  $L$  is the out-of-plane length of the straight conductor section. The AC loss contribution in the winding overhang is generally small due to the smaller magnetic field.

$$P_{d,AC,k}(t) = \int_{V_k} p_{AC}(t) dV = L \cdot \int_{A_{sec,k}} (E_z \cdot J_z) dA = L \cdot \int_{A_{sec,k}} \rho(|J_z|) \cdot J_z^2 dA \quad (2.108)$$

The total AC loss in the winding stack is obtained as sum over the  $n_{sec}$  modelled regions, (2.109).

$$P_{d,AC}(t) = \sum_{k=1}^{n_{sec}} P_{d,AC,k}(t) \quad (2.109)$$

Besides locally different current density distributions, inter-turn coupling effects and locally differing magnetic flux densities, the use of an equivalent coil model with reduced number of turns  $n_{sec}$  does not change the AC loss, since based on (2.106), the AC loss scales as  $P_{d,AC} \sim n_{sec} \cdot A_{sec} \sim n_{sec} \cdot n_{sec}^{-1} = n_{sec}^0$  according to (2.108), (2.109). The average current density  $\bar{J}_z$  is not changed, since  $\bar{J}_z = I_{sec}/A_{sec} \sim n_{sec}^{-1}/n_{sec}^{-1} = n_{sec}^0$ .

The artificial expansion leads also only via local effects to deviations for the AC loss estimate. In terms of average quantities, the AC loss scales as  $P_{d,AC} \sim A_{sec} \cdot \bar{E}_z \cdot \bar{J}_z$ . For the same relative current loading  $\bar{J}_z/J_c$ , the electric field does not depend on  $d_T$ , (2.104). The relations  $A_{sec} \sim d_T$  and  $J_z \sim d_T^{-1}$  yield therefore  $P_{d,AC} \sim d_T^0$ . The highly non-linear  $E(J)$ -relation generally leads to a high sensitivity with respect to locally differing current density distributions, which manifests in an upper bound of  $d_T$  and a lower limit of  $n_{sec}$  regarding sufficient accuracy. The entire AC loss in the field winding or the stator AC winding is obtained as sum over all turns per coil and all coils. This loss can be represented

by an equivalent resistance, which is defined by the equality (2.110).

$$R_{AC}(t) \cdot i^2(t) = P_{d,AC}(t) \quad (2.110)$$

If the  $T$ - $A$ -formulation is used, the instantaneous loss power is directly calculated from the current density, (2.111).  $J_z$  is defined by (2.80) on the edge that represents the tape. The electric field strength  $E_z$  is also defined on the superconducting edge by (2.81).

$$P_{d,AC}(t) = L \cdot d_{HTS} \cdot \int_{\Gamma_{sc}} (E_z \cdot J_z) d\Gamma \quad (2.111)$$

### 2.3. Modelling of the End-Winding of Racetrack Coils

The racetrack coil geometry, Fig. 2.15, is considered in this thesis for superconducting rotor field windings and for preliminary analyses of superconducting AC stator windings of fully superconducting generators, Ch. 7. The calculation of large-scale generators by means of 3D FEM models is computationally expensive and therefore limited to singular analyses, mainly in order to validate approximate calculations by 2D models. Parametric analyses and numerical optimizations require computationally efficient analytical or numerical 2D models, where the influence of the end-winding section is included by analytical formulas.

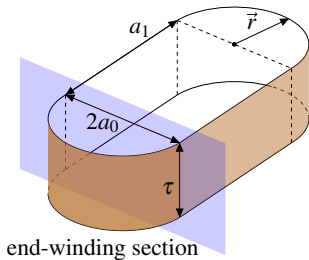


Figure 2.15.: Schematic sketch of the equivalent geometry of a (multi-layer) racetrack coil that is considered for the analytical calculation of the self inductance. The straight coil sides feature the axial length  $a_1$ . For  $a_1 \rightarrow 0$ , a solenoid coil is obtained, which is used for the analytical calculation of the end-winding leakage inductance  $L_{\sigma b}$  of either field coils or stator coils in case of HTS concentrated windings in fully superconducting machines.

Due to the simple geometry, the conductor length per turn is calculated with the average curvature radius  $\bar{r}$  in the end-winding section as  $l_b = \pi \cdot \bar{r}$ . In case of superconducting stator windings, the AC loss in the end-winding section is low, mainly since the external field experienced in the winding overhangs is small. The relative contribution to the entire coil inductance is however significant, particularly in case of short axial lengths  $a_1$ , in case of non-magnetic pole cores and for large coil spans  $2a_0$ , e.g. due to a low number  $q$  of

slots per pole and phase. An accurate estimate for the end-winding stray inductance  $L_{\sigma_b}$  is particularly essential for

- the calculation and adjustment of the power factor and the estimation of the inverter rating for a superconducting stator winding,
- the calculation of the voltage requirements for the variation of the field current and
- transient analyses, where  $L_{\sigma_b}$  contributes to a limitation of sudden field current changes (Ch. 6).

The end-winding inductance per coil is calculated by the analytical expression (2.112) [94].  $a_0$  and  $\tau$  are defined according to Fig. 2.15.

$$L_{\sigma_{bc}} = \frac{\mu_0 \cdot \pi \cdot a_0^2 \cdot N_c^2}{\tau} \cdot G \quad (2.112)$$

The inductance coefficient  $G$ , (2.113), is valid for a solenoid coil, which is equivalent to the union of the winding overhangs at either end [94, 156]. The calculation is based on the assumption that approximately no magnetic flux in axial direction in the planes at either end of the straight section occurs.  $G$  depends on the coil span  $2a_0$  and on the height of the coil sides, which can be approximated by  $\tau \approx n_L \cdot w_l$  for the racetrack coil. The separation into  $n_L$  layers is not incorporated with only minor reduction of accuracy. The integral in (2.113) contains the *Bessel* function of first kind  $J_\nu(x)$  (order  $\nu = 1$ ) and is calculated numerically (*MATLAB & Python*).

$$G(a_0, \tau) = 2 \cdot \int_0^\infty J_1^2(a_0 \cdot \xi) \cdot \left( \frac{1}{\xi} - \frac{1}{\tau \cdot \xi^2} + \frac{e^{-\tau \cdot \xi}}{\tau \cdot \xi^2} \right) d\xi \quad (2.113)$$

In order to determine the relative contribution of the end-winding inductance and in order to obtain a reference value for numerical calculations, the entire self inductance of an air-cored racetrack coil is calculated analytically. This estimate represents a lower bound to the actual inductance of the racetrack coil in presence of ferromagnetic parts. This approximate estimate is meaningful, since the iron parts saturate significantly, if exposed to the high rotor field. The analytically calculated value of  $L_c$ , (2.114), can therefore be used to estimate the ratio  $L_{\sigma_b}/L_c$  [94].

$$L_c = \frac{\mu_0 \cdot a_0 \cdot N^2}{\tau} \cdot (4a_1 + \pi \cdot a_0) - \frac{4\mu_0 \cdot a_0^2 \cdot N^2}{\pi^2 \cdot \tau^2} \cdot \tilde{G}(a_0, a_1, \tau) \quad (2.114)$$

### 2.3. Modelling of the End-Winding of Racetrack Coils

The inductance coefficient  $\tilde{G}$  is defined as (2.115).

$$\tilde{G}(a_0, a_1, \tau) = \int_0^\infty \int_0^{\frac{\pi}{2}} \frac{S^2(a_0, a_1, \xi, \varphi)}{\xi^2} \cdot (1 - e^{-\tau \cdot \xi}) d\varphi d\xi \quad (2.115)$$

The integrals are evaluated numerically by means of *MATLAB & Python*, where the integrand comprises the expressions (2.116), (2.117).

$$S(a_0, a_1, \xi, \varphi) = \pi \cdot J_1(a_0 \cdot \xi) \cdot \cos(a_1 \cdot \xi \cdot \sin(\varphi)) + F(a_0, \xi, \varphi) \cdot \frac{\sin(a_1 \cdot \xi \cdot \sin(\varphi))}{\sin(\varphi)} \quad (2.116)$$

$$F(a_0, \xi, \varphi) = 2 \cdot \int_0^{\frac{\pi}{2}} [\cos(\alpha) \cdot \cos(a_0 \cdot \xi \cdot \sin(\varphi) \cdot \cos(\alpha)) \cdot \cos(a_0 \cdot \xi \cdot \cos(\varphi) \cdot \sin(\alpha))] d\alpha \quad (2.117)$$

The total number of turns  $N_c$ , which is determined by the tape width  $w_t$  for a fixed MMF, has major influence on the end-winding inductance  $L_{\sigma b}$ , Fig. 2.16 a).

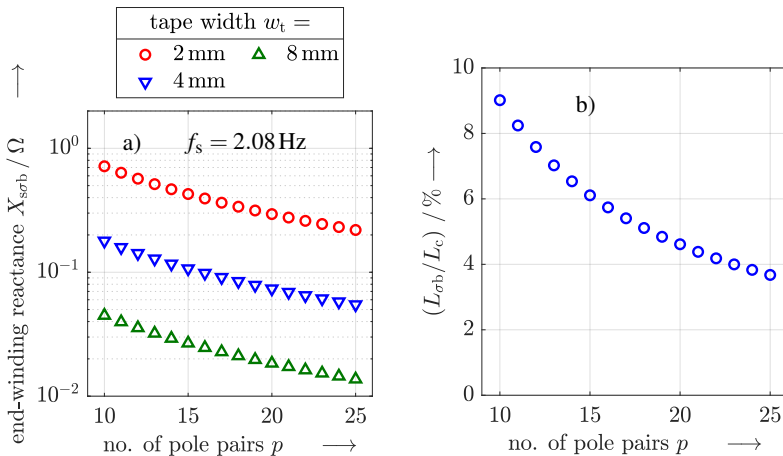


Figure 2.16.: a) Analytically calculated end-winding reactance  $X_{\sigma b}$  for AC HTS racetrack coils. Results are shown for different numbers of pole pairs  $p$  and different widths of the tape  $w_t$ , where  $\tau = w_t \cdot n_{Ls} = 16 \text{ mm}$  is fixed. b) Share of the end-winding inductance in the total coil inductance versus number of pole pairs. Narrow tapes imply higher numbers of winding layers and an accordingly increased number of turns  $N_c$ . The results in b) are shown for the stator winding of an exemplary generator with  $P_N = 7 \text{ MW}$ ,  $8.33 \text{ rpm}$ ,  $r_{si} = 2.2 \text{ m}$ ,  $p = a$ ,  $N_c = 512$  for  $w_{\text{tape}} = 4 \text{ mm}$ ,  $I_N \approx 740 \text{ A}$ .



For an exemplary 7MW direct drive, fully superconducting wind generator, the contribution of the end-winding stray inductance to the entire stator inductance is in the order of 4...9%, based on the analytical formulas (2.112), (2.114), Fig. 2.16 b). For a fixed bore diameter,  $L_{\sigma b}/L_c$  decreases towards higher pole counts, since the ratio  $l_b/L$  decreases.

A comparison with a non-linear 3D FEM model of a partially superconducting medium speed generator, Fig. 7.4 in Ch. 7 (HTS field winding), reveals a very good agreement with the analytical calculation. The numerically calculated value of  $L_{\sigma b}$  shows a strong decrease due to iron saturation, while matching for rated field current approximately the analytical estimate for an air-cored coil. As a main finding, the end-winding inductance plays an important role and must be incorporated, even for the short end-winding length in case of racetrack coils.

## 2.4. Modelling of the End-Winding of Distributed Stator Windings

All normal conducting stator windings of wind generators, that are considered in this thesis, are made from copper bars with rectangular profile in order to increase the slot fill factor  $k_{Cu}$ . Therefore, the geometry of the end-winding section of the coils is well defined. In this case, approximate analytical formulas exist for the end-winding stray inductance  $L_{s\sigma b}$ , (2.118) and (2.119) [23].

$$\lambda_{bs} = 0.075 \cdot \left( 1 + \frac{l_{bs}}{\tau_p} \right) \quad (2.118)$$

$$L_{s\sigma b} = \mu_0 \cdot N_s^2 \cdot \frac{2}{p} \cdot \lambda_{bs} \cdot l_{bs} \quad (2.119)$$

The explicit 3D modelling of the stator end-winding section is difficult and requires a custom implementation of the end-winding path. Still, a parametrized 3D model of the stator end-winding is implemented for following reasons:

- The magnetic flux densities in the considered generators with superconducting field winding imply strong saturation effects in the axial iron end regions. The end-winding inductance shows therefore a dependence on the excitation state of the generator, which cannot be easily covered by analytical techniques.
- A detailed 3D model of the actual geometry allows to quantify the relevance of end effects in terms of the magnetic field distribution. This question is of particular

interest due to the large magnetic air gap and in presence of the cryostat wall and the damper in the axial end sections. A complete end-winding model moreover allows to analyse the magnetic field conditions experienced by the end-winding sections of the superconducting field coils.

The parametrized model is implemented in *Python* with an interface for a transfer to the *JMAG Designer*, where the detailed 3D model is built. A general implementation for arbitrary two-layer windings is used, based on [209]. The winding is specified by the pole count  $2p$ , the number of slots per pole and phase  $q$  and the coil pitch  $W/\tau_p$  with coil span  $W$  and pole pitch  $\tau_p$ . The computationally expensive 3D modelling approach is used in following cases:

- The analytical calculation is validated for selected designs of direct drive and medium speed partially superconducting generators, Sec. 4.2.2.3 and Ch. 7.
- An accurate value for the end-winding leakage inductance is required as preliminary for dynamic analyses, i.e. sudden short circuit calculations by means of 2D models, Ch. 6.
- The preliminary analyses of a medium speed generator connected to a passive diode rectifier, i.e. by means of a 2D FEM model with voltage feeding, Ch. 7, require an accurate incorporation of the end-winding, since the end-winding leakage inductance directly influences the commutation process and hence the stator current harmonics.

The parametrized end-winding paths of a three-phase, distributed, two-layer winding are shown in Fig. 2.17 as an example.

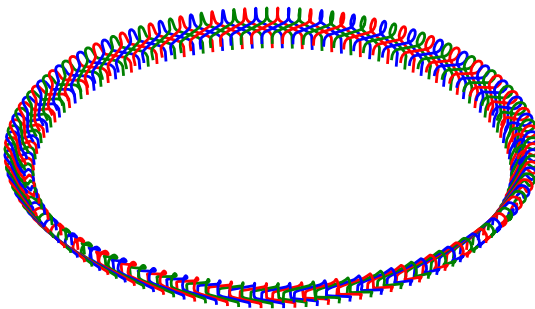


Figure 2.17.: Exemplary visualization of the entire stator winding overhang of a generator with  $2p = 24$ ,  $Q_s = 144$ ,  $m = 3$ ,  $W/\tau_p = 5/6$  (two-layer winding). The colours alternate in favour of a better visibility and are not associated with the three stator phases.

The entire path in the end-winding section is split into several path sections, as shown in Fig. 2.18. The largest part of the path sections lies on involutes of cones with differing half-angle  $\alpha_o$  for the upper layer and  $\alpha_u$  for the lower layer, Fig. 2.18 a). These sections correspond to straight lines in the  $p$ - $\beta$ -plane, which results from the development of the cone, Fig. 2.20 a) and b) [209]. As the map from the curved surface to the development of the cone preserves lengths, i.e. it is an isometry, this geometry yields the shortest path on the cones' curved surfaces. The mathematical details of the parametrized model are not described here, but the general calculation procedure is summarized.

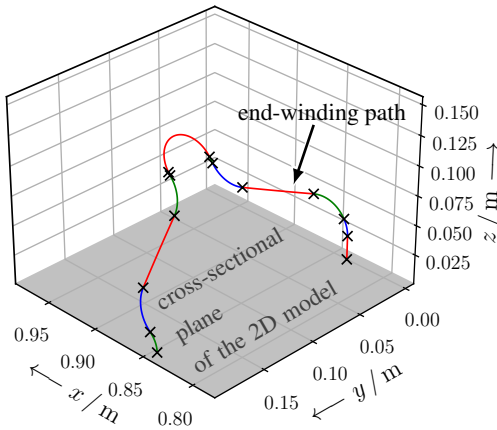


Figure 2.18.: Detailed view of the parametrized end-winding path of one form-wound coil from the end-winding in Fig. 2.17 at one axial end. The colors indicate path sections with separate parametrizations. The black crosses represent start/end points of these sections.

The 3D geometry is specified in two planes:

- The  $y$ - $z$ -plane represents a longitudinal cutting plane of the generator, Fig. 2.19.
- The  $p$ - $\beta$ -planes, Fig. 2.20, result from the development of the cones (flattened tangential surfaces) and are therefore separately defined for the upper and the lower layer, a) and b) in Fig. 2.20.

The general transformation from the radius  $r$  and the polar angle  $\varphi$  in the cross sectional plane of the generator to the radius and the angle in the  $p$ - $\beta$ -plane is (2.120) [209].

$$\begin{pmatrix} p^{(i)} \\ \beta^{(i)} \end{pmatrix} = \mathbf{T}^{(i)} \cdot \begin{pmatrix} r \\ \varphi \end{pmatrix}, \quad \mathbf{T}^{(i)} = \begin{pmatrix} \sin^{-1}(\alpha_i) & 0 \\ 0 & \sin(\alpha_i) \end{pmatrix} \quad i \in \{o, u\} \quad (2.120)$$

The parameters, which are used for the parametrization of the end-winding, are listed

in Tab. 2.2, where several parameters are directly obtained from the 2D cross-sectional generator geometry.

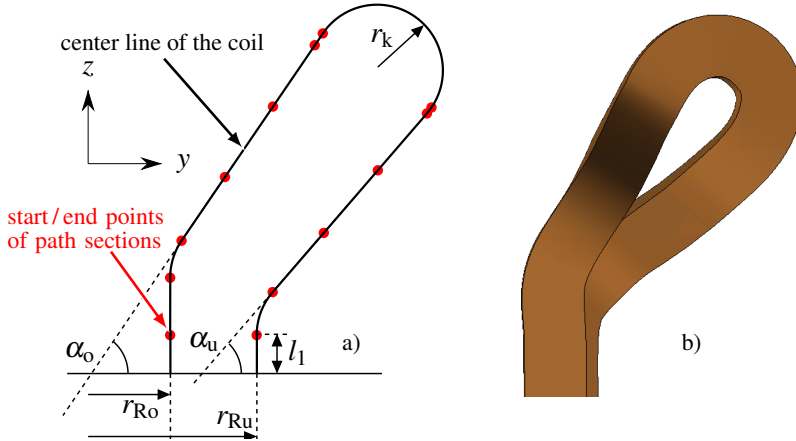


Figure 2.19.: a) Center line of the coil's end-winding section in the projection to the  $y$ - $z$ -plane. The red points indicate start / end points of path sections with separate parametrization. b) End-winding section in the *JMAG Designer*, obtained by extrusion along the parametrized path.

First, the winding section in the  $p$ - $\beta$ -plane of the lower layer, Fig. 2.20 b), is calculated by requiring that the minimum distance  $d_{\min}$  between the center lines of neighbouring coil sides is met. The second condition is that the path section covers half of the coil span in circumferential direction, before the transition to the  $p$ - $\beta$ -plane of the upper layer occurs. Based on this, the dimensions in the  $y$ - $z$ -plane are calculated by requiring that the start and end points of the winding path feature the same axial coordinate  $z$ . Here, the second condition is that the radial difference  $\Delta r = r_{Ro} - r_{Ru}$  must be covered. The section in the  $p$ - $\beta$ -plane of the upper layer is then fixed by the half-angle  $\alpha_o$ , Fig. 2.20 a).

A very good agreement of the analytical and numerical calculations is found for the end-winding inductance, as shown for an exemplary medium speed generator design in Ch. 7. In general, the end-winding can be optimized regarding

1. a minimum conductor length in the winding overhang  $l_{bs}$  or
2. a minimum axial outreach in favour of more compact generators.

Since the end-winding parametrization relies on a large set of parameters, Tab. 2.2, the optimization is carried out by applying a genetic algorithm in *Python* for individual designs. The *DEAP* framework [65] is used with the pre-implemented functions `cxTwoPoint()`, `mutFlipBit()` and `selTournament()` for the mating, mutation and selection of individuals. The minimum conductor length (objective 1) is chosen as criterion in order to increase the efficiency.

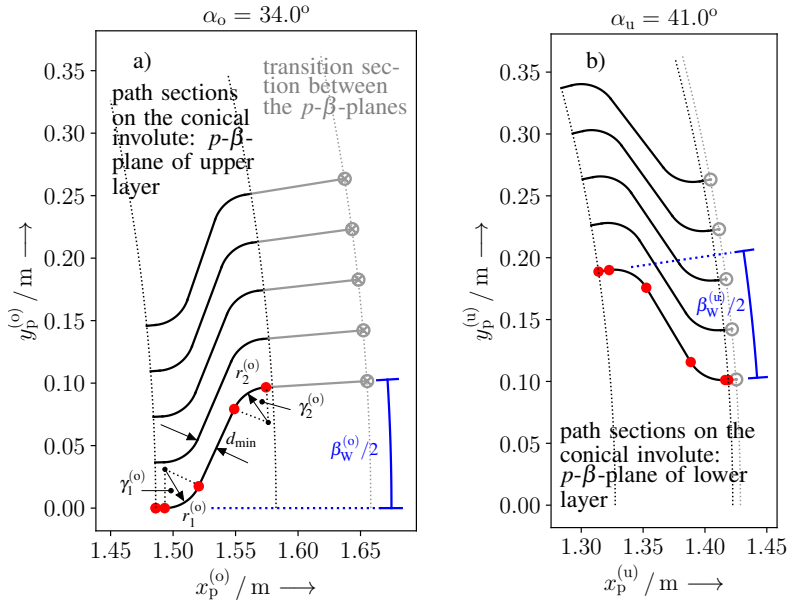


Figure 2.20.: Developed reference path of the end-winding section for a) the upper layer and b) the lower layer in the respective  $p$ - $\beta$ -planes for cone angles  $\alpha_o = 34^\circ$  and  $\alpha_u = 41^\circ$ . The red dots indicate the start/end points of the sections with separate parametrization. The gray sections are not located in any of the  $p$ - $\beta$ -planes, but represent the transition between the cones, that are associated with the layers.

The simulation of sector models yields intermittent coils in the end-winding section, Fig. 2.21 a), where the continuity of the impressed current is ensured by similar boundary conditions as discussed in Sec. 2.2.1.3. Compared to other sub-domains, the stator winding features a coarse mesh, Fig. 2.21 b), in favour of a reduction of the DoFs. This is valid, because a homogeneous current density is impressed, without explicit modelling

of individual conductors or the winding insulation. The current displacement is therefore not directly taken into account, but approximately included by the formulas of *Field* and *Emde* [22]. The average factor of the increase in resistance is (2.121), which accounts for the two-sided current displacement in a stack of  $N_T$  conductors. The loss functions  $\varphi(\xi)$  and  $\psi(\xi)$  [22] are defined in (2.122), (2.123) and depend on the ratio between the conductor height  $h_T$  and the current penetration depth, (2.124).

$$k_m = N_T^{-1} \cdot \sum_{p=1}^{N_T} k_p = \varphi(\xi) + \frac{N_T^2 - 1}{3} \cdot \psi(\xi) \quad (2.121)$$

$$\varphi(\xi) = \xi \cdot \frac{\sinh(2\xi) + \sin(2\xi)}{\cosh(2\xi) - \cos(2\xi)} \quad (2.122)$$

$$\psi(\xi) = 2\xi \cdot \frac{\sinh(\xi) - \sin(\xi)}{\cosh(\xi) + \cos(\xi)} \quad (2.123)$$

$$\xi = \frac{h_T}{d_E} = h_T \cdot \sqrt{\pi \cdot f_s \cdot \mu_0 \cdot \kappa_{Cu} \cdot \frac{b_T}{b_Q}} \quad (2.124)$$

These analytical formulas are validated against detailed 2D FEM models with an explicit modelling of individual conductor cross sections, e.g. in Ch. 4. A good agreement in the considered range of the fundamental frequency is found.

Table 2.2.: Fixed parameters for the specification of the end-winding section in 3D models. Parameters in the upper section are required for the end-winding alone. Parameters in the lower section are determined from the cross-sectional 2D model.

$l_1$	axial straight path length in the lower layer, Fig. 2.19 a)
$r_k$	curvature radius at the turning point in the end-winding, Fig. 2.19 a)
$\alpha_o$	half-angle of the truncated cone of the upper layer, Fig. 2.19 a)
$\alpha_u$	half-angle of the truncated cone of the lower layer, Fig. 2.19 a)
$r_1$	curvature radius in the $p$ - $\beta$ -plane next to the iron stack, Fig. 2.20 a)
$r_2$	curvature radius in the $p$ - $\beta$ -plane next to the turning point, Fig. 2.20 a)
$d_{\min}$	minimum distance between the center line of neighbouring coil sides in the winding overhang, Fig. 2.20 a)
$r_{Ru}$	average radius of the lower layer in the $y$ - $z$ -plane, Fig. 2.19 a)
$r_{Ro}$	average radius of the upper layer in the $y$ - $z$ -plane, Fig. 2.19 a)
$h_c$	height of the coil side in the $y$ - $z$ -plane, including the insulation, Fig. 2.19 a)
$d_{\text{IL}}$	distance between upper & lower layers, straight coil section, Fig. 2.19 a)
$\varphi_W$	polar angle of the coil span in mechanical degrees
$\varphi_Q$	polar angle of the slot pitch in mechanical degrees

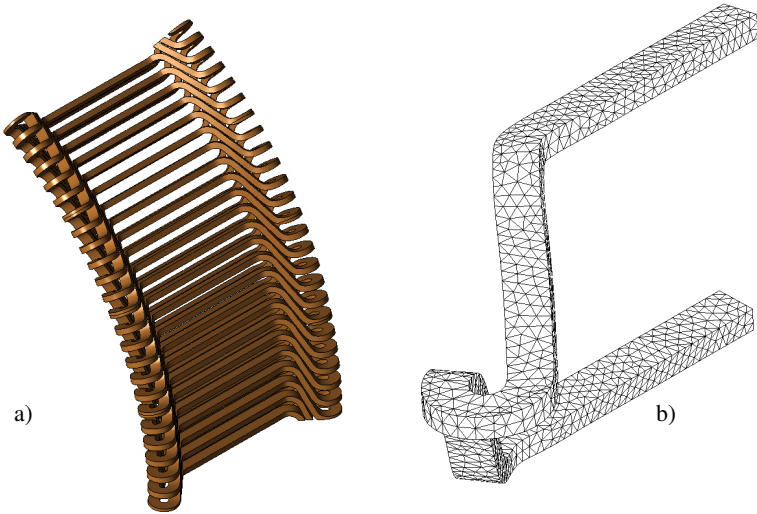


Figure 2.21.: a) Normal conducting stator winding of four poles of a partially superconducting generator: Extrusion along the parametrized path in *JMAG Designer*. b) Detailed view of a single half stator coil of the generator, implemented and meshed in *JMAG Designer*. A rather coarse mesh is used since a homogeneous current density is impressed and current displacement effects are not directly incorporated.

## 2.5. Modelling of Superconductor Material Properties

From a microscopic perspective, the behaviour of hard type-II superconductors is governed by the dynamics and the pinning of magnetic flux vortices. The description in terms of flux vortices is however not suitable for calculations of problems, which exhibit technically relevant length scales. However, well established and experimentally validated calculations have been carried out based on critical state models (CSMs) with equivalent formulations (2.125), (2.126) [78]. The critical state model with  $B$ -independent critical current density  $J_c$  is called *Bean* model [16]. The incorporation of the  $B$ -dependence  $J_c(B)$  is commonly called *Kim* extension [78].

$$J(t) = \begin{cases} 0 & \text{if } E(t') = 0 \forall t' \leq t \\ J_c & \text{else} \end{cases} \quad (2.125)$$

$$J(t) = \begin{cases} 0 & \text{if } B(t) = 0 \\ J_c & \text{else} \end{cases} \quad (2.126)$$

Key aspects of critical state models are:

- Most analytical calculations are based on CSMs. In particular, most AC loss formulas are based on CSMs.
- CSMs lead to free boundary problems, which require numerical „front tracking“ algorithms in case of complex sample geometries. The formulation with variational inequalities is one approach to determine the superconducting current density distributions [172].
- There is a sharp transition between superconducting and normal conducting regions. The thermally activated flux flow and the directed flux creep, which play a significant role in HTS materials, are not represented. The same holds for the corresponding relaxation effects, i.e. a redistribution of the superconducting current over time. The contribution to the AC loss by the flux flow, before the *Lorentz* force exceeds pinning forces, can be significant and is not covered.

The latter shortcoming can be circumvented with numerical models, where the sudden transition between the superconducting and the normal conducting state is described with a power law for the non-linear electrical resistance, (2.127).  $E_c$  is a small reference electric field strength, i.e. typically  $E_c = 10^{-4} \text{ V/m} = 1 \mu\text{V/cm}$ .  $B$ -dependent critical current densities are usually used, while the exponent is in the range  $n \approx 10 \dots 25$ , depending on the material. For large exponents  $n \rightarrow \infty$ , the power law relation approaches the critical state model, Fig. 2.22.

$$\vec{E} = \rho(|\vec{J}|) \cdot \vec{J} = E_c \cdot \left( \frac{|\vec{J}|}{J_c} \right)^n \cdot \frac{\vec{J}}{|\vec{J}|}, \quad \rho(|\vec{J}|) = \left( \frac{E_c}{J_c} \right) \cdot \left( \frac{|\vec{J}|}{J_c} \right)^{(n-1)} \quad (2.127)$$

The exponent  $n$  in the power law relation (2.127), which characterizes the transition to the normal conducting state, is generally a function of the temperature and the magnetic field:  $n = f(T, \vec{B})$ .

The power law relation yields a non-zero loss density  $p_{d,AC} = E \cdot J$  also for  $J < J_c$ , which is associated with the thermally activated flux flow and the directed flux creep. In this model, inhomogeneous current density profiles, e.g. after a ramping of the transport current,



experience a (slow) transition towards a homogeneous current density over time. The  $E(J)$  material law is well established, validated against experimental loss data, e.g. in [236], and yields a comparably good convergence behaviour in numerical models due to the differentiability. A generalization of both, the CSM and the power law model, extend the relations in Fig. 2.22 by a linear increase of  $E$  with  $J$  in the normal conducting state.

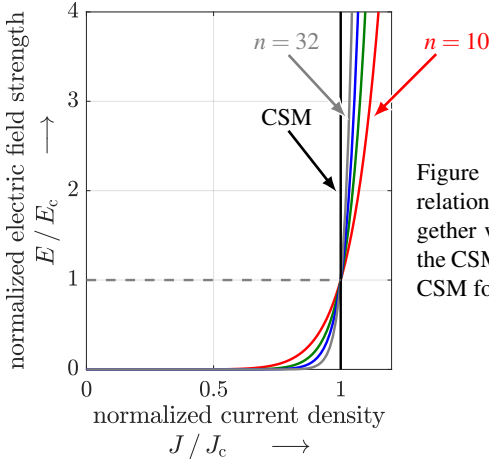


Figure 2.22.: Normalized  $E(J)$  power law relations for superconducting materials, together with the non-differentiable relation of the CSM. The  $E(J)$  power law approaches the CSM for  $n \rightarrow \infty$ .

A comparison between numerically and analytically calculated, one-dimensional current density profiles in a coated conductor, Fig. 2.23, shows similar results. In contrast to the analytical model, the power law relation also allows for current densities exceeding  $J_c$ , which generally leads to higher estimates for the AC loss. The analytical result is approached for (advantageously) high exponents  $n$ .

The 2G HTS tapes and the  $\text{MgB}_2$  wires, which are considered in this thesis, differ considerably with respect to

- the absolute values of the achievable in-field critical current densities  $J_c(\vec{B})$  and
- the functional form, which characterizes the impact of the external magnetic flux density  $\vec{B}$  on  $J_c(\vec{B})$ .

One main challenge regarding a commercialization of the superconducting winding technology in wind generators consists in a competitive low cost level. In this regard, ReBCO coated conductors compete with  $\text{MgB}_2$  wires, Sec. 1.3. Fig. 2.24 shows a comparison of the conductor price per unit length and critical current  $I_c$ .

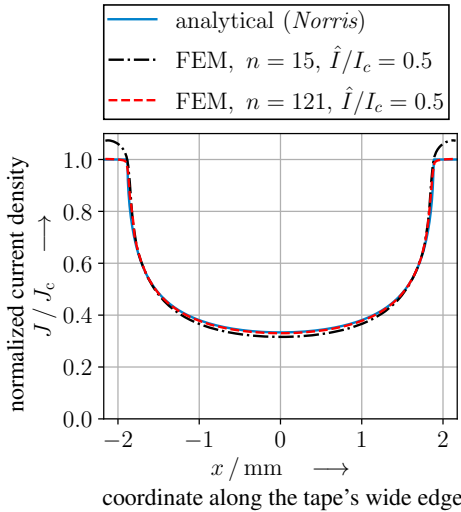


Figure 2.23.: Analytically and numerically calculated current density profile along the wide edge of a HTS tape, normalized by a (uniform) critical current density  $J_c$ . The amplitude of the applied AC current amounts to half the critical current  $I_c$  of the tape. The numerical results are calculated in *JMAG*, where the convergence in the *A*-formulation is limited to simple geometries. The analytical expression is derived in [162]. (tape width:  $w_t = 4.2\text{mm}$ )

Since the MMF scales as  $\Theta = I \cdot N \sim I_c \cdot l$ , the relative price  $p'$  is a measure for the price per MMF of a field coil. The determination of the analytical expressions for the critical current  $I_c(T, \vec{B})$  as function of the operating temperature  $T$  and of the external field  $\vec{B}$  enables a comparison in a wide range of operating conditions. As of today, sufficient conductor lengths per piece of  $l \geq 300 \dots 500\text{m}$  can be manufactured for both ReBCO tapes and MgB<sub>2</sub> wires. The typical prices are listed in Tab. 2.3.

From the comparison, three main findings are derived:

1. MgB<sub>2</sub> wires must be operated at temperatures  $T \leq 20\text{K}$  in order to achieve a useful relative price  $p'$  at technically relevant magnetic field conditions  $B \geq 1.5\text{T}$ . Otherwise, the maximum magnetic flux density experienced by the conductors must not exceed about  $B \lesssim 1 \dots 1.5\text{T}$ . At  $T = 30\text{K}$ , there is no alternative to HTS conductors.
2. At  $T \leq 3\text{T}$  the MgB<sub>2</sub> wires outperform the ReBCO tapes in terms of material costs at  $T = 20\text{K}$ . The lower operating temperature increases however the cost of the cryogenic cooling system.
3. The cost/performance ratio in case of intermediate external flux densities  $B \approx 2\text{T}$  is similar for ReBCO tapes from different manufacturers, even though the tapes differ considerably with respect to the current carrying capacity. Higher  $I_c$ -values are equalized by the higher price. Larger differences are observed towards higher

external magnetic fields.

Since the comparison reveals no clear favourite for wind generator designs, expressions for the current carrying capacity are derived for two ReBCO tapes and two  $\text{MgB}_2$  wire types. This allows for a subsequent comparison at actual field conditions in the different wind generators, discussed in Sec. 4.3.1.

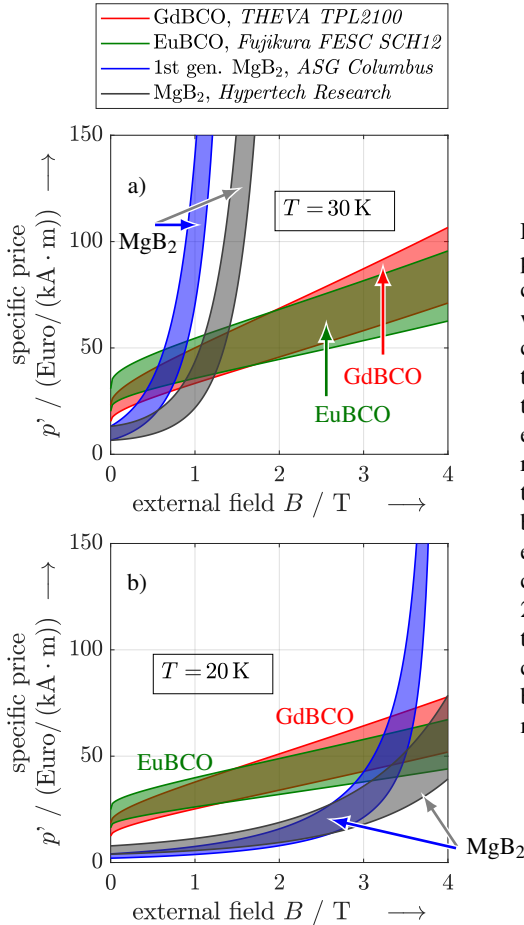


Figure 2.24.: Comparison of the price per unit length of ReBCO coated conductors and  $\text{MgB}_2$  wires, normalized by the critical current  $I_c$ .  $p'$  is a measure for the price per MMF and, thus, for the price of a field coil at fixed excitation requirements. The results are shown for operating temperatures of a)  $T = 30$  K and b)  $T = 20$  K as a function of the external field  $B$  (in case of ReBCO coated conductors:  $\vec{B}||c$ , Sec. 2.5.1). The underlying prices of the conductors, Tab. 2.3, and the current carrying capacities are based on information provided by manufacturers.

Table 2.3.: Price range for commercially available superconducting wires, resp. tapes, based on manufacturer information. The in-field performance is not reflected by the listed prices, which are given for the self field (s.f.) only. The field-dependence varies significantly among the different types of conductors.

tape / wire	price $p'$
ReBCO tapes ( $T = 77\text{K}$ , s.f.)	100...150 (...300) (Euro/(kA · m))
ReBCO tapes ( $T = 30\text{K}$ , s.f.)	16...24 (...35) (Euro/(kA · m))
MgB <sub>2</sub> wire (1 <sup>st</sup> generation, $T = 20\text{K}$ , s.f.)	2.0...4.1 (Euro/(kA · m))

In the following, the properties of 2G HTS conductors are discussed in Sec. 2.5.1 and those of MgB<sub>2</sub> conductors follow in Sec. 2.5.2. The critical engineering current density  $J_{ce}$ , (2.128), is used for the dimensioning of the winding pack and relates the superconducting current  $I_{SC}$  to the total conductor, resp. tape, cross section  $A_t$ , i.e. including all conductor constituents except for the insulation.

$$J_{ce} = \frac{I_c}{A_t} \quad (2.128)$$

The critical current density  $J_c$ , (2.129), refers to the superconductor's cross section  $A_{SC}$  alone, and is used for the AC loss calculations.

$$J_c = \frac{I_c}{A_{SC}} \quad (2.129)$$

The temperature and magnetic field dependence of both,  $J_c$  and  $J_{ce}$ , is described with the same lift factor  $L(T, \vec{B})$ , as discussed in the following.

### 2.5.1. Current Carrying Capacity of 2G HTS Tapes

2G HTS coated conductors exhibit a layered architecture with biaxially textured cuprate planes, Fig. 2.25 a). The biaxial texture is achieved during the deposition of buffer layers on the polycrystalline substrate with random crystallographic orientation. The anisotropic crystallographic properties of the ReBCO layer translate to a strong anisotropy of the macroscopic properties, i.e. the sensitivity of the current carrying capacity with respect to external magnetic fields. To describe this directional dependence, the  $c$ -axis, perpendicular to the cuprate planes, is defined, Fig. 2.25 b). It is not necessarily perpendicular to the tape's wide side, but may show an inclination with the angle  $\theta_0$  as a result of the production process. If an external magnetic field is locally aligned with the  $c$ -axis (notation:

$\vec{B} \parallel c$ ), the strongest decrease of the critical current density  $J_c$  occurs.

By introducing the lift factor  $L(\vec{B})$ , the critical current density can be expressed as (2.130) with reference to the current density at zero field, i.e. self field only, for the respective temperature  $J_{c0}(T)$ .

$$J_c(T, \vec{B}) = L(\vec{B}) \cdot J_{c0}(T) \quad (2.130)$$

One approach to model the dependence on the magnetic flux density is a *Kim* model with an elliptical form  $L(\vec{B})$  according to (2.131) [78, 215].  $B_{\parallel}$  denotes the component of the magnetic flux density that is parallel to the cuprate planes, whereas  $B_{\perp}$  denotes the component that is perpendicular to the planes and hence aligned with the  $c$ -axis, Fig. 2.25 b).

$$L(\vec{B}) = \frac{1}{\left[ 1 + \frac{\sqrt{(k \cdot B_{\parallel})^2 + B_{\perp}^2}}{B_0} \right]} \alpha \quad (2.131)$$

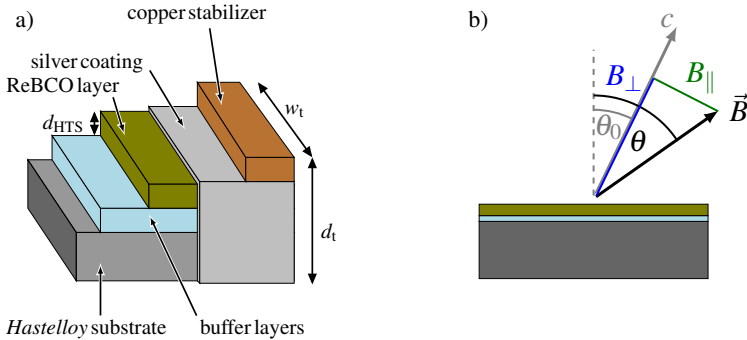


Figure 2.25.: a) Schematic of a typical, layered tape architecture of 2G ReBCO coated conductors (not to scale). b) Definition of the  $c$ -axis for coated conductors and of the perpendicular and parallel magnetic flux density components. The  $c$ -axis is not necessarily perpendicular to the tape's wide side (width  $w_t$ ), depending on the production process.

The coefficients  $k(T)$ ,  $B_0(T)$  and  $\alpha(T)$  are obtained from fits to manufacturer data, e.g. Fig. 2.26, and generally show a dependence on temperature  $T$ . Since the flux density component  $B_{\perp}$ , which is aligned with the  $c$ -axis, yields a much stronger critical current degradation compared to flux density components in the cuprate plane,  $k < 1$  holds for all HTS tapes. To obtain the parameters  $J_{c0}$ ,  $\alpha$ ,  $k$  and  $B_0$ , a two-step fitting procedure is applied:

1. Analysis for  $B_{\parallel} = 0$ : Fits to manufacturer data (Fig. 2.28) with a lift factor according to (2.132) yield parameters  $J_{c0}(T)$ ,  $\alpha(T)$  and  $B_0(T)$  as functions of the temperature.

$$L(B_{\perp}) = \frac{1}{\left[1 + \frac{B_{\perp}}{B_0}\right]^{\alpha}} \quad (2.132)$$

The parameters  $J_{c0}$ ,  $B_0$  and  $\alpha$  are interpolated by a cubic spline interpolation in order to obtain relations for all temperatures in the relevant range.

2. By comparing the lift factors for either an entirely parallel or entirely perpendicular flux density, the parameter  $k(T)$  can be computed as a function of temperature. The lift factor for a flux density  $B_{\parallel}$  that is aligned entirely with the cuprate ab-planes is (2.133).

$$L(B_{\parallel}) = \frac{1}{\left[1 + \frac{k \cdot B_{\parallel}}{B_0}\right]^{\alpha}} \quad (2.133)$$

Dividing (2.132) by (2.133) and solving for  $k$  yields (2.134).  $r_L = L(B_{\perp})/L(B_{\parallel})$  is the ratio of the lift factors, where same magnitudes of the flux density  $B = B_{\perp} = B_{\parallel}$  are considered.

$$k = \left(\frac{B + B_0}{B}\right) \cdot \sqrt[r_L]{\frac{B_0}{B}} \quad (2.134)$$

The parameter  $k(T)$ , (2.134), is evaluated in the considered temperature range for flux densities  $B = 3\text{ T}$  and  $B = 5\text{ T}$ . As an example, results are shown in Fig. 2.29 and reveal a weak  $B$ -dependence. In favour of a simple model, in which the  $B$ -dependence is entirely described by the elliptical functional form (2.131), the average value of  $k$  for both flux densities is used in the calculations. This approximation can be justified by the small values of  $k = 0.1 \dots 0.45$ , which imply a subordinate role of the parallel field component  $B_{\parallel}$ . The  $T$ -dependence is again described by means of a cubic spline interpolation in the relevant temperature range. In order to simplify the model, the rather weak  $B$ -dependence of the exponent  $n(T, \vec{B}) \approx n(T)$  is neglected and the exponent is fixed at its mean value over the set of parameters for different  $B_{\perp} = 0.5 \dots 6\text{ T}$ . The  $T$ -dependence of  $n(T)$  is again incorporated by means of a cubic spline interpolation in the considered temperature range, see Fig. 2.27 b) as an example.

An alternative approach to parametrize the lift factor  $L$  more accurately is described in App. A.3.5. This parametrization is used in the design stage to account for the maximum current in superconducting coils, whereas the (modified) *Kim*-relation (2.131) is used for

AC loss calculations for its simplicity and its good numerical convergence behaviour. The original *Kim-Relation* incorporates only the absolute value of the local magnetic flux density  $B$  and is not appropriate for the anisotropic ReBCO coated conductors.

In this thesis, two ReBCO tapes are considered for the superconducting windings of wind generators. The material data is provided by manufacturers or is publicly available. The tapes mainly differ with respect to the production process and the presence of artificial pinning centres (APCs).

#### *Fujikura FESC SCH12*

In case of the tape *FESC SCH12* manufactured by *Fujikura*, the EuBCO layer is produced by pulsed laser deposition. The texturing of the buffer layer is achieved with ion beam assisted deposition. This tape features artificial pinning centres. For this EuBCO tape, the  $c$ -axis is normal to the tape's wide side ( $\theta_0 = 0$ ). The angular dependence of the critical engineering current density in presence of an external field is shown in Fig. 2.26 together with the critical engineering current density  $J_{ce}$  as a function of temperature.

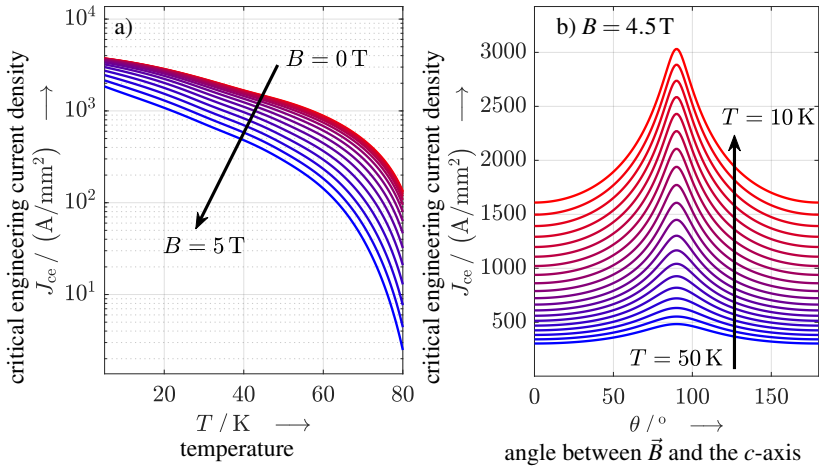


Figure 2.26.: Critical engineering current density of the EuBCO tape *Fujikura FESC SCH12* a) as a function of temperature for different magnetic flux densities ( $\vec{B}||c$ ) and b) as a function of the orientation angle of the external magnetic flux density, Fig. 2.25.

## 2.5. Modelling of Superconductor Material Properties

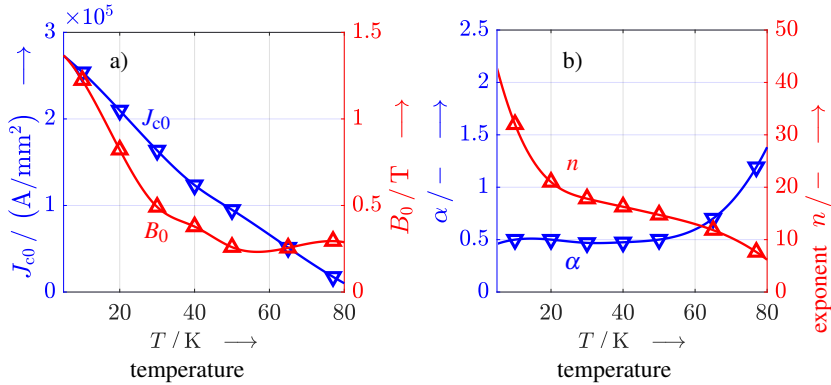


Figure 2.27.: Fit parameters a)  $J_{c0}$ ,  $B_0$  and b)  $\alpha$ ,  $n$  as a function of temperature (EuBCO tape *Fujikura FESC SCH12*).

The  $B$ -dependence according to a fit with (2.131) is shown in Fig. 2.28 a). The critical engineering current density, i.e. the current density with respect to the entire tape cross section excluding insulation, is shown in Fig. 2.28 b).

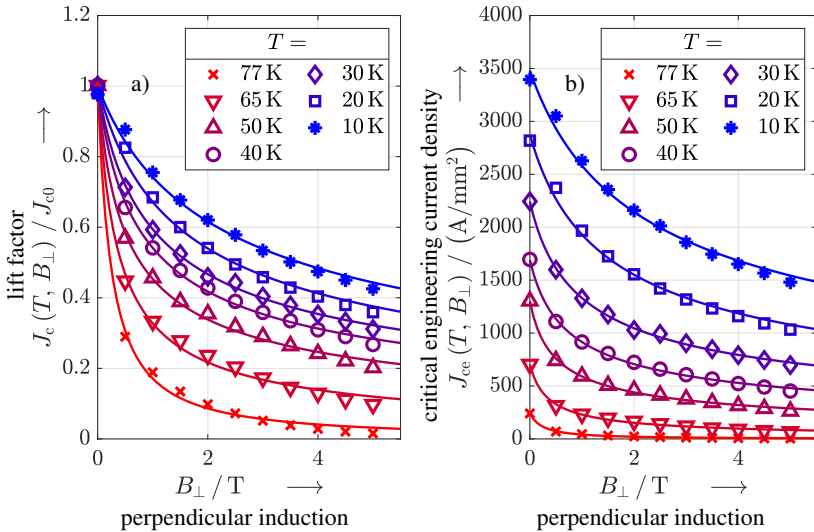


Figure 2.28.: a)  $B$ -dependent part of the lift factor (EuBCO tape: *Fujikura FESC SCH12*) for several temperatures  $T$  and  $\vec{B} \parallel c$ . b) Critical engineering current density as a function of the external magnetic flux density for the same tape.

The fit parameters  $J_{c0}$ ,  $B_0$ ,  $\alpha$  and  $k$  are plotted in Fig. 2.27, Fig. 2.29 versus temperature.



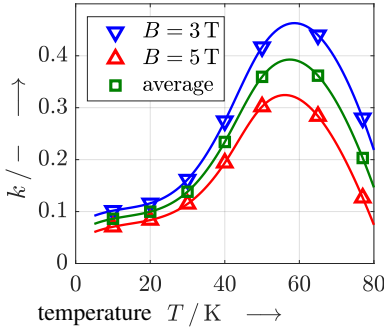


Figure 2.29.: Fit parameter  $k$ , which is a measure of the relative impact of a parallel magnetic field component  $B_{\parallel}$  on  $J_c$ , as a function of temperature based on (2.134). Results are shown for the EuBCO tape *Fujikura FESC SCH12* with  $B = 3$  T and  $B = 5$  T. The average curve is used for simulations in order to prevent further model complexity.

### THEVA TPL2100

The tape *TPL2100*, manufactured by *THEVA*, features a textured buffer layer, which is achieved by inclined substrate deposition. Electron-beam vapour deposition is used for the GdBCO layer. Material data for a tape without APCs, as available in the beginning of 2021, is used for the analyses, while *THEVA* offers also APC-enhanced tapes in the meantime. The GdBCO tape *TPL2100* manufactured by *THEVA* features a  $c$ -axis with an inclination of  $\theta_0 = 30^\circ$  with respect to the normal of the tape's wide face. The critical engineering current density and its  $B$ -dependence are visualized in Fig. 2.30.

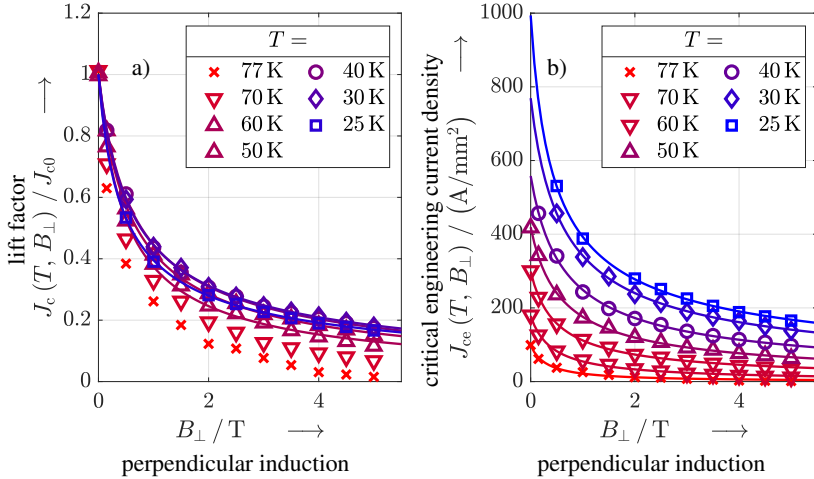


Figure 2.30.: a)  $B$ -dependent part of the lift factor and b) critical engineering current density as a function of  $B_{\parallel}|c$  for the GdBCO tape *THEVA TPL2100*.

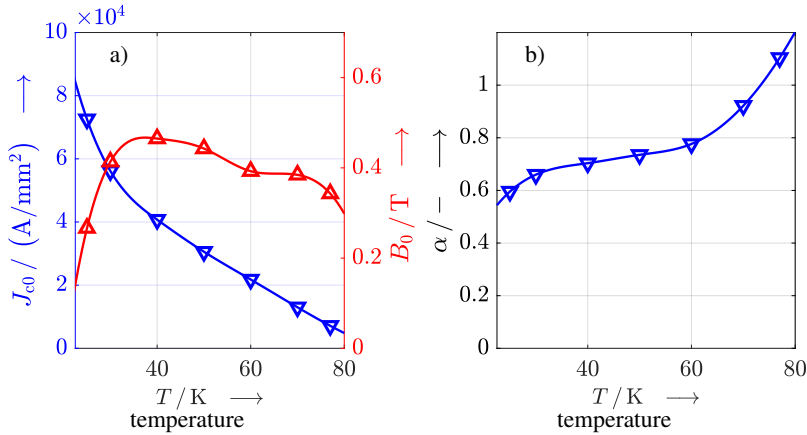


Figure 2.31.: Fit parameters according to (2.130), (2.131) for the GdBCO tape *THEVA TPL2100*: a)  $J_{c0}$  and  $B_0$ , b)  $\alpha$  versus temperature  $T$ .

The fit parameters  $J_{c0}$ ,  $B_0$  and  $\alpha$  are shown in Fig. 2.31. Compared to the *Fujikura FESC SCH12* tape, similar values for  $\alpha$  are found. In contrast, the absence of APCs leads to significantly lower values of  $B_0$  for  $T \gtrsim 40$  K. The dependence of  $J_{c0}$  on temperature is visualized in Fig. 2.32.

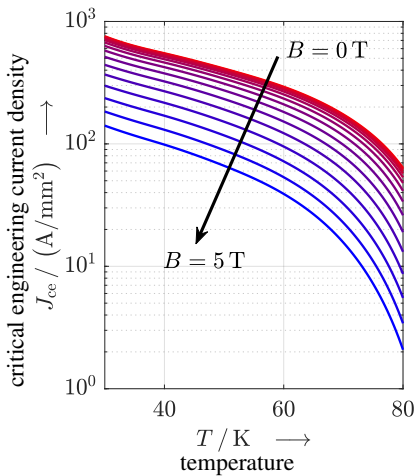


Figure 2.32.: Critical engineering current density versus temperature for the tape *THEVA TPL2100*. The results are shown for different magnetic flux densities, where  $\vec{B} \parallel c$ .

### 2.5.2. Current Carrying Capacity of MgB<sub>2</sub> Wires

As of today, two main commercial suppliers of MgB<sub>2</sub> wires exist, i.e. *ASG Superconductors* and *Hypertech Research*. In this thesis, material data of both suppliers are considered for MgB<sub>2</sub> coils in superconducting wind generators. Rectangular wire profiles are considered, Fig. 2.33.

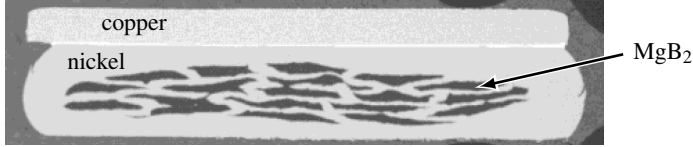


Figure 2.33.: Actual cross section of an exemplary MgB<sub>2</sub> wire with 19 filaments, nickel matrix and copper stabilizer [210].

#### *ASG Superconductors*

Material data for a round wire with a diameter of  $d = 1.5$  mm and 37 filaments in a nickel matrix is available [148, 210]. According to manufacturer information, the  $T$ - and  $B$ -dependence of wires with rectangular cross section is similar. The parametrization of the lift factor is based on the formulas that are used by *ASG Superconductors*. The  $B$ -dependence is parametrized with three temperature dependent parameters  $a(T)$ ,  $b(T)$ ,  $c(T)$ , (2.135). MgB<sub>2</sub> exhibits only a weak anisotropy, Tab. 1.1, such that no dependence on the orientation of the flux density but only on the absolute value  $B = |\vec{B}|$  is considered.

$$L(T, B) = \max \left\{ 0, a(T) \cdot \left( 1 - \frac{B}{b(T)} \right) + c(T) \cdot \left( 1 - \frac{B}{b(T)} \right)^3 \right\} \quad (2.135)$$

The temperature dependence of the parameters is described by polynomial relations (2.136) - (2.138).

$$a(T) = c_1 \cdot T^2 + d_1 \cdot T + e_1 \quad (2.136)$$

$$b(T) = c_2 \cdot T^3 + d_2 \cdot T^2 + e_2 \cdot T + f_3 \quad (2.137)$$

$$c(T) = c_3 \cdot T + d_3 \quad (2.138)$$

The critical engineering current density obtained by (2.135) is visualized in Fig. 2.34 as a function of temperature  $T$  for different external magnetic fields.

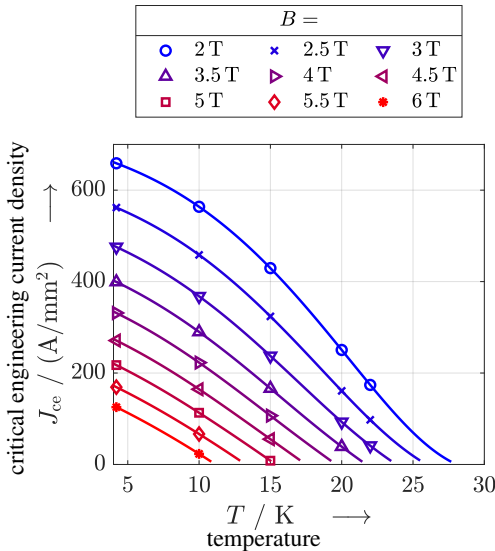


Figure 2.34.: Critical engineering current density of a multifilamentary MgB<sub>2</sub> wire from *ASG Superconductors* as a function of temperature for different magnetic flux densities. The relevant operating range for superconducting windings in wind generators is  $B \approx 2 \dots 3$  T. In this thesis, only an operating temperature of  $T = 20$  K is considered.

This lift factor (2.135) is also applied to conductors with tape-like geometry. A comparison of the critical current based on (2.135) with available material data for multifilamentary MgB<sub>2</sub> tapes shows a good agreement. The transferability may be restricted in case of a ferromagnetic matrix material, where the local flux density at the filaments' positions is affected by the cross sectional geometry. In view of the uncertainties regarding the actual position of the filaments, the analyses are still based on (2.135), while a sufficient current margin  $I_c/I \approx 1.3 \dots 2$  ensures that the  $I_c$ -limit of the wires is kept.

For AC loss calculations, an  $E(J)$ -power law exponent of  $n = 20$  is assumed in accordance with the typical range reported in literature, e.g. [52].

### HyperTech Research

Material data of a first generation MgB<sub>2</sub> round wire with a copper matrix is considered [207], which is fabricated by the PIT method and is commercially available in kilometre-long piece lengths. The critical engineering current density is similar to the wire from *ASG Superconductors*, Fig. 2.35. An empirical fit function (2.139) is used for  $L(T, B)$ . A similar  $T$ - and  $B$ -dependence of the critical current for wires with rectangular profile is assumed. The temperature dependent parameters  $a(T)$ ,  $b(T)$ ,  $c(T)$  are defined in (2.140), (2.141).

$$\log_{10}(L(T, B)) = a(T) \cdot B^2 + b \cdot B + c(T) \quad (2.139)$$

$$a(T) = c_1 \cdot \exp \left\{ - \left( \frac{T}{d_1} \right)^{e_1} \right\} + f_1 \quad (2.140)$$

$$c(T) = c_3 \cdot T + d_3 \quad (2.141)$$

As in case of the  $\text{MgB}_2$  wires produced by *ASG Superconductors*, an exponent of  $n = 20$  is used for the AC loss calculations. It should be mentioned, that several successful approaches recently led to a significant increase in the achievable critical current densities  $J_{ce}$ , e.g. by improved magnesium diffusion (IMD). This group of wires is called the „second generation“ of  $\text{MgB}_2$  conductors. Since many of the production techniques are to date still at an experimental stage and the scope of the thesis is the short- and medium-term potential of superconducting wind generators, only wires of the first generation are considered.

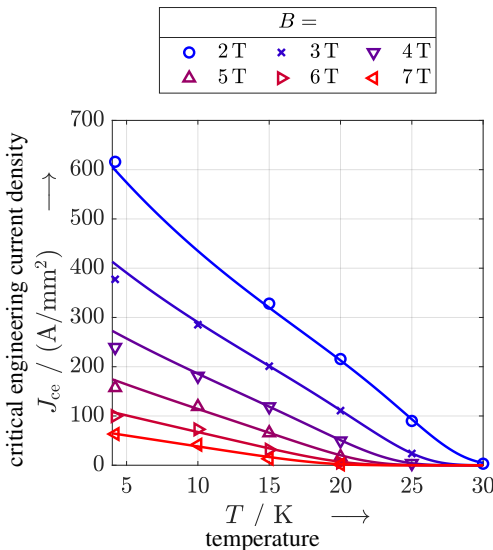


Figure 2.35.: Critical engineering current density of a  $\text{MgB}_2$  wire from *HyperTech Research*, together with a fit based on (2.139).  $J_{ce}$  is plotted versus temperature  $T$  for different external magnetic flux densities. The relevant operating conditions  $T = 20\text{ K}$ ,  $B \approx 2 \dots 3\text{ T}$  yield critical engineering current densities of  $J_{ce} \approx 100 \dots 200\text{ A/mm}^2$ .

---

## 3. Permanent Magnet Excited Direct Drive Wind Turbine Generators

Synchronous generators with permanent magnet (PM) excitation are the state-of-the-art solution of wind generator systems with largest power up to  $\approx 15$  MW, Sec. 1.1. In order to get a consistent benchmark for the evaluation of superconducting wind generators in Ch. 4 - 7, design studies of PM excited generators are carried out in the same modelling framework. The design studies are based on today's commercially available generators from leading manufacturers.

### 3.1. General Properties

Large PM excited direct drive generators for wind applications typically feature surface mounted NdFeB magnets. They employ low-voltage AC windings, i.e.  $U_N < 1000$  V, to avoid the high test-voltage regulations, to use low-voltage converters and to enable a small insulation thickness in the slots. They are advantageously designed with an outer rotor topology [59] for following reasons:

- The outer rotor leads to a thermal decoupling of the stator, where the highest losses occur, and the temperature sensitive PM rotor. The cooling at the outer housing reduces the operating temperature of the NdFeB magnets.
- A flux concentration effect of typically  $\approx 1.005$  for the PM excited rotor field is achieved. This effect is however very small due to the large radii and the small curvature.
- The rotor yoke can simultaneously serve as outer housing, except from struts and a casing for protection purpose. This reduces the overall outer diameter for the same size of active parts. Generally, the high-torque nature of this generator type yields a high sensitivity with respect to variations in diameter.

A schematic of the considered geometry is visualized in Fig. 3.1. Distributed stator windings are considered, App. A.6, since concentrated windings suffer from a low fundamen-

tal winding factor and/or significant additional losses due to stator field harmonics [58]. Consistent with commercially available generators, a forced air cooling is considered.

General features of PM excited direct drive generators are:

- The magnetically effective air gap  $\delta_{\text{mag}} \approx 30 \text{ mm}$  is large due to the surface mounted magnets.
- The rated power factor  $\cos \varphi_{\text{sN}} \approx -0.7 \dots -0.8$  is comparably low due to the limited excitation capabilities of the permanent magnets and the typically high stator current loading  $A_s \approx 1300 \dots 1500 \text{ A/cm}$ .
- The overall loss is dominated by the *ohmic* loss  $P_{\text{d,Cu}}$  in the stator winding (typically  $> 90\%$  of the total generator loss) due to the very low speeds  $n \approx 10 \text{ rpm}$  and the low fundamental frequencies  $f_s = 5 \dots 15 \text{ Hz}$ . The applied MTPA strategy coincides therefore largely with a loss minimum operation.

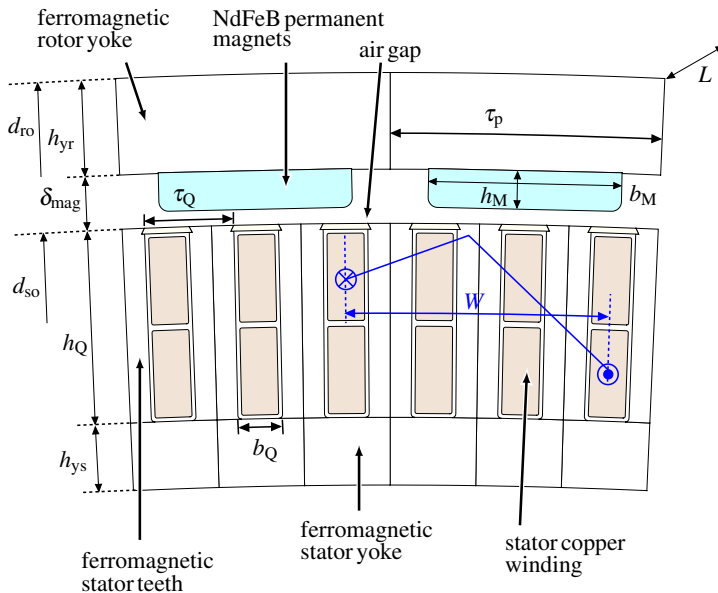


Figure 3.1.: Schematic of four poles of a 7 MW, 8.33 rpm outer rotor direct drive generator with surface mounted PMs (segmentation not shown). The generator features a distributed winding in slots (here:  $q = 1$  slots per pole per phase) and is excited by high energy density NdFeB magnets (height  $h_M$ , width  $b_M$ ).

## 3.2. Parameter Study

The fixed specifications for the parameter study on 7 MW direct drive generators are listed in Tab. 3.1. The rated voltage of  $U_{LL} = 690$  V (rms) is a design target. The rated speed  $n_N = 8.33$  rpm is typical for wind generator systems in this power range and is limited by the mechanical load and the aerodynamic noise of the glass fibre-reinforced rotor blades.

Table 3.1.: Fixed specifications for the parameter study on direct drive PM generators. The consumer reference frame is used.

$P_{el,N}$	-7 MW
$n_N, f_s$	8.33 rpm, 10 Hz
$U_{LL}$	690 V
$2p$	144
$r_{ro}$	3.257 m
$\delta_{geom}$	8 mm
$f_{bQ, \tau_Q}$	0.5
$h_Q$	100 mm
$J_{Cu}$	3.8 A/mm <sup>2</sup>
$k_{Cu}$	0.75
$m, q, W/\tau_p$	3, 1, 1
$A_s$	142 kA/m

Table 3.2.: Variables of the design study of PM excited direct drive generators.

$b_M$	70...140 mm
$h_M$	15...25 mm

Table 3.3.: Operating conditions and limits of NdFeB magnets (details in App. A.3.2) and the copper stator winding.

$\vartheta_{Cu,s}$	100°C
$B_{r,NdFeB}$ @80°C	1.25 T
$H_{demag}$	1440 kA/m

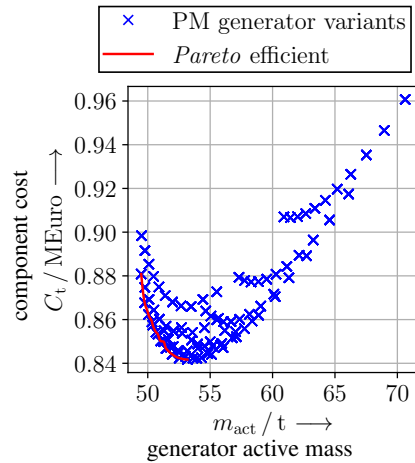


Figure 3.2.: Calculated total generator material and converter cost versus the generator active mass for the variants of PM excited direct drive generators. The red line indicates *Pareto* efficient variants.

The high pole count  $2p = 144$  allows for small yoke heights  $h_{ys}, h_{yr} \approx 35 \dots 50$  mm, while a further increase of  $2p$  is not possible for manufacturing reasons, i.e. a too high number of slots and coils. The geometrical air gap width  $\delta_{geom}$  cannot be decreased for mechanical yoke ovalization reasons in case of the very large diameters  $d_{ro} > 6$  m. Sufficiently wide



iron teeth, i.e.  $f_{b_Q, \tau_Q} = b_Q / \tau_Q \lesssim 0.5$ , are required for flux guidance due to the limited excitation capabilities of the PMs. The high slot fill factor  $k_{Cu} = 0.75$  refers to the actual winding window of the low-voltage winding, excluding the inter layer insulation and the slot wedge. The thermal utilization is calculated as (3.1) and is in the typical range for intense air cooling.  $\alpha$  denotes the effective heat transfer coefficient (HTC), which governs the cooling.

$$A_s \cdot J_{Cu} = 5396 \frac{\text{A}^2}{\text{cm} \cdot \text{mm}^2} \sim \frac{P_{d, Cu}}{d_{si} \cdot \pi \cdot (L + l_{bs})} \sim \alpha \cdot \Delta\vartheta \quad (3.1)$$

An operating temperature of the stator winding of  $\vartheta_{Cu} = 100^\circ\text{C}$  is assumed. This would keep the limits of thermal class B ( $\Delta\vartheta \leq 80\text{K}$ , standard IEC 60034-1 [50]) at  $\vartheta_{surr} = 40^\circ\text{C}$  ambient, although insulation materials for thermal class F ( $\Delta\vartheta \leq 105\text{K}$ ) are usually employed. High energy density NdFeB magnets of grade G44EH from *Arnold Magnetics*, App. A.3.2, are considered. The thermal stability of these magnets is enhanced with the grain boundary diffusion method. The operating temperature is estimated as  $\vartheta_{NdFeB} = 80^\circ\text{C}$  in the sense of a worst case scenario. A stator winding without pitching  $W / \tau_p = 1$  is chosen in order to prevent a reduction of the fundamental winding factor of  $k_{w,1} = 1$ . This choice leads to higher stator field harmonics with space orders  $\nu = -5, +7$  and anticipates a limited impact of these stator field harmonics due to the large magnetically effective air gap width  $\delta_{mag} \approx 30\text{mm}$ . Based on these considerations, the variable space for adjustments is limited. As the trade-off between the generator performance (high efficiency and high power factor) and the cost of the rotor excitation system is of primary interest in this thesis, the magnet shape alone is varied: The magnet mass is scaled by the height  $h_M$  and the width per magnet  $b_M$ , Fig. 3.1 and Tab. 3.2. Depending on the PM rotor field, the rotor yoke height is adjusted to yield always a reasonable maximum flux densities of  $B_{Yr, max} \approx 1.7\text{T}$ .

The electromagnetic design follows a similar scheme as visualized in Fig. 4.8 for HTS excited generators. The losses and the mechanical input power per axial unit length are first calculated by means of a parametric 2D FEM model in *JMAG*. Since the number of turns per coil  $N_c$  is yet to be determined, the MMF per slot  $\Theta_{Qs}$  is impressed for the time stepping transient simulations.  $\Theta_{Qs}$  is calculated from the available cross section in the slot  $A_Q \lesssim b_Q \cdot h_Q$  and the admissible current density  $J_{Cu} = 3.8\text{A} / \text{mm}^2$  in the copper conductors, (3.2).

$$\Theta_{Qs} = N_c \cdot I_s = J_{Cu} \cdot \frac{A_Q \cdot k_{Cu}}{2} \quad (3.2)$$

### 3.2. Parameter Study

---

In the following, the calculation scheme for the determination of the two unknowns  $l_i$ , axial length, and  $N_s$ , number of turns per phase, is described. The mechanical input power  $P'_{\text{mech}}$  per unit length is calculated from the torque per unit length  $\overline{M}'_e$ , (3.3). In generator mode,  $P'_{\text{mech}} < 0$  holds in the consumer reference frame due to the braking torque  $\overline{M}'_e < 0$ .

$$P'_{\text{mech}} = 2\pi \cdot n_{\text{syn}} \cdot \overline{M}'_e \quad (3.3)$$

The iron loss per unit length  $P'_{d,\text{Fe}} > 0$  and the *Foucault* eddy current loss in the magnets  $P'_{d,\text{Ft}} > 0$  are also extracted from the 2D FEM simulation. The influence of end effects on  $P'_{d,\text{Ft}}$  is approximately included by a reduced electric conductivity  $\kappa_{\text{PM}}$  of the magnets, as in [O1]. The net electrical power  $P'_{\text{net,FEM}} < 0$  per unit length, excluding the *ohmic* loss in the stator winding, is (3.4). Due to the large magnetically effective air gap width, *Carter's* coefficient for the incorporation of radial cooling ducts [23] is near unity, i.e.  $k'_{\text{C}} \approx 1.002 \approx 1$  for an axial duct width of  $l = 5$  mm,  $\delta_{\text{mag}} \approx 30$  mm and an iron stack segment length of  $l'_{\text{Fe}} \approx 60$  mm. Therefore,  $l_i \approx L$  holds, so that  $l_i$  is used in the following without loss of accuracy.

$$P'_{\text{net,FEM}} = P'_{\text{mech}} + P'_{d,\text{Fe}} + P'_{d,\text{Ft}} \equiv \frac{P_{\text{FEM}}}{l_i} \quad (3.4)$$

By introducing the ratio between the number of turns per coil  $N_c$  and the number of parallel branches  $a$  as  $\gamma := N_c/a$ , the r.m.s. stator current  $I_s$  per phase is written as (3.5) for the considered two-layer winding, Fig. 3.1.

$$I_s = \frac{k_{\text{Cu}} \cdot A_{\text{Q}} \cdot J_{\text{Cu}}}{2 \cdot \gamma} \quad (3.5)$$

Based on the resistance  $R_c$  per turn, the stator resistance per phase  $R_s$  is written in terms of  $\gamma$ , (3.6).  $A_{\text{T}}$  is the non-insulated copper cross section of one conductor without any subdivision in strands due to the low frequency  $f_s$ .

$$R_s = \frac{N_s}{a} \cdot R_c = \frac{2p \cdot q \cdot N_c}{a^2} \cdot \frac{2 \cdot (l_i \cdot k_m + l_{\text{bs}})}{A_{\text{T}} \cdot \kappa_{\text{Cu}}} \quad (3.6)$$

$$= \frac{2p \cdot q \cdot N_c}{a^2} \cdot \frac{4 \cdot N_c}{A_{\text{Q}} \cdot k_{\text{Cu}} \cdot \kappa_{\text{Cu}}} \cdot (l_i \cdot k_m + l_{\text{bs}}) \quad (3.7)$$

$$= \frac{4 \cdot 2p \cdot q}{\underbrace{A_{\text{Q}} \cdot k_{\text{Cu}} \cdot \kappa_{\text{Cu}}}_{=: \tilde{R}}} \cdot \gamma^2 \cdot (l_i \cdot k_m + l_{\text{bs}}) = \tilde{R} \cdot \gamma^2 \cdot (l_i \cdot k_m + l_{\text{bs}}) \quad (3.8)$$

In (3.6),  $l_{bs}$  denotes the length per half-turn in the winding overhang. The electrical output power  $P_{el,out} < 0$  is then obtained as a function of the axial length  $l_i$  alone, (3.9). This expression is essentially independent from the number of turns per phase  $N_s$ , except for the resistance increase factor  $k_m$ , Sec. 2.4, which depends on  $N_c$ .

$$P_{el,out} = l_i \cdot P'_{net,FEM} + 3 \cdot I_s^2 \cdot \tilde{R} \cdot \gamma^2 \cdot (k_m \cdot l_i + l_{bs}) \quad (3.9)$$

$$= l_i \cdot P'_{net,FEM} + 3 \cdot (2 \cdot k_{Cu} \cdot A_Q \cdot J_{Cu})^2 \cdot \tilde{R} \cdot (l_i \cdot k_m + l_{bs}) \quad (3.10)$$

From (3.10), the generator active length  $l_i$  is calculated by specifying  $P_{el,out} \stackrel{!}{=} -7\text{MW}$ . At the first stage, an estimate of  $k_m = 1$  is used, while the actual value  $k_m \approx 1$  (small due to the low frequency  $f_s$ ) is finally obtained as self consistent solution by iteration.

The second equation for the determination of the two unknowns  $\{\gamma, l_i\}$  is derived from the stator voltage equation. From the 2D FEM model, the induced voltage per pole and unit length  $\underline{U}'_{i,c}$  of a single turn coil is extracted. The induced voltage (3.11) is caused by the entire flux linkage in the 2D FEM model, i.e. the flux linkage with the rotor field, the flux linkage with the stator main field and all stray fluxes in the cross-sectional plane.

$$\underline{U}_{i,2D} = \frac{2p}{a} \cdot (l_i \cdot N_c \cdot \underline{U}'_{i,c}) = 2p \cdot l_i \cdot \gamma \cdot \underline{U}'_{i,c} \quad (3.11)$$

After a validation against a 3D FEM model, the analytical equations in Sec. 2.4 are used to calculate the end-winding stray inductance.  $L_{s\sigma b}$  is written in terms of  $\gamma$ , (3.12).

$$L_{s\sigma b} = \mu_0 \cdot 4 \cdot 2p \cdot q^2 \cdot 0.075 \cdot l_{bs} \cdot \left(1 + \frac{l_{bs}}{\tau_p}\right) \cdot \gamma^2 \equiv \tilde{L}_{s\sigma b} \cdot \gamma^2 \quad (3.12)$$

With (3.11) and (3.12), the complex valued stator terminal voltage per phase (3.13) for sinusoidal stator current depends only on  $L$  and  $\gamma$ . The phase angle of  $\underline{L}_s$  with respect to  $\underline{U}'_{i,c}$  is known from the applied MTPA strategy.

$$\underline{U}_s = \underline{L}_s \cdot \left[ \tilde{R} \cdot (k_m \cdot l_i + l_{bs}) \cdot \gamma^2 + j\omega_s \cdot \tilde{L}_{s\sigma b} \cdot \gamma \right] + 2p \cdot l_i \cdot \gamma \cdot \underline{U}'_{i,c}, \quad \sqrt{-1} = j \quad (3.13)$$

By specifying  $\sqrt{3} \cdot |\underline{U}_s| \stackrel{!}{=} U_N = 690\text{V}$ , a unique solution for  $\gamma$  and  $l_i$  is found. The actual number of turns per phase  $N_s$  is determined by choosing  $\{N_c, a\}$  from the set of possible combinations, so that the best approximation of the required value of  $\gamma$  is achieved. For  $2p = 144$  and two converters in parallel, the number of parallel branches can attain

### 3.2. Parameter Study

---

$a = 144, 72, 36, \dots$

About 2000 generator variants are designed, Fig. 3.3. Based on the electromagnetic design, the active mass  $m_{\text{act}}$  and the system cost  $C_t$ , including the material cost of the generator components and of the converter, are calculated. The mass densities and costs are listed in Tab. 3.4, 3.5.

Table 3.4.: Assumed prices for the design study on PM excited direct drive generators.

$p'_{\text{NdFeB}}$	70€/kg
$p'_{\text{Fe}}$	3€/kg
$p'_{\text{Cu}}$	13.5€/kg
$p'_{\text{conv}}$	30€/kVA

Table 3.5.: Mass densities of materials, that are used in PM excited direct drive generators.

$\gamma_{\text{NdFeB}}$	7600kg/m <sup>3</sup>
$\gamma_{\text{Fe}}$	7760kg/m <sup>3</sup>
$\gamma_{\text{Cu}}$	8900kg/m <sup>3</sup>

Following findings are derived from the relation between the total component cost  $C_t$  and the generator active mass  $m_{\text{act}}$ , Fig. 3.2:

- An active mass, which is significantly below  $m_{\text{act}} < 50\text{t}$ , is hardly achievable. The maximum rated gravimetric torque density  $M' = \overline{M}_e/m_{\text{act}}$  is therefore about 175Nm/kg. All *Pareto* efficient designs with respect to  $\{C_t, m_{\text{act}}\}$  feature torque densities of  $M' \gtrsim 160\text{Nm/kg}$ .
- The system material cost, including the converter, is less than 900kEuro for 7MW, which corresponds to a relative cost of less than 0.129MEuro/MW.

The rated generator efficiency  $\eta_N = |P_{\text{el},N}|/P_{\text{mech}}$  increases monotonically towards higher absolute power factors  $|\cos \varphi_{sN}|$ , Fig. 3.3 a), since for a fixed stator voltage  $U_{sN}$ , a higher  $|\cos \varphi_{sN}|$  implies lower *ohmic* losses in the stator winding. The higher power factor is enabled by a higher magnet mass  $m_M$ , which yields a higher rotor field and a shorter axial length  $l_i$ . The maximum efficiencies are in the order of  $\eta_N = 92.8\%$  and the maximum absolute power factor is in the range of  $|\cos \varphi_{sN}| \approx 0.8 \dots 0.85$  (inductive, current lags voltage). These upper limits are a direct consequence of the limited excitation capability of the PM rotor. This is evident from the plot of the required NdFeB magnet mass  $m_M$  versus the efficiency  $\eta_N$ , Fig. 3.3 b). Even for low efficiency designs, more than  $m_M \approx 2.5\text{t}$  of NdFeB magnets are required. The bounding approximation to the *Pareto* frontier features a considerably increasing steepness for  $\eta_N \gtrsim 92\%$ . The increase in rated efficiency from  $\eta_N = 91\%$  to  $\eta_N = 92\%$  requires an additional magnet mass of  $\Delta m_M = 0.76\text{t}$ . Roughly

the same additional amount of NdFeB magnets is required for an increase of efficiency from  $\eta_N = 92.6\%$  to  $\eta_N = 92.7\%$ . Since the considered NdFeB magnet type already features a comparably high energy density of  $(B \cdot H)_{\max} \approx 340 \text{ kJ/m}^3$  [8], the derived limitations in terms of  $|\cos \varphi_{sN}|$  and  $\eta_N$  are considered to be generic for this type of PM excited generators.

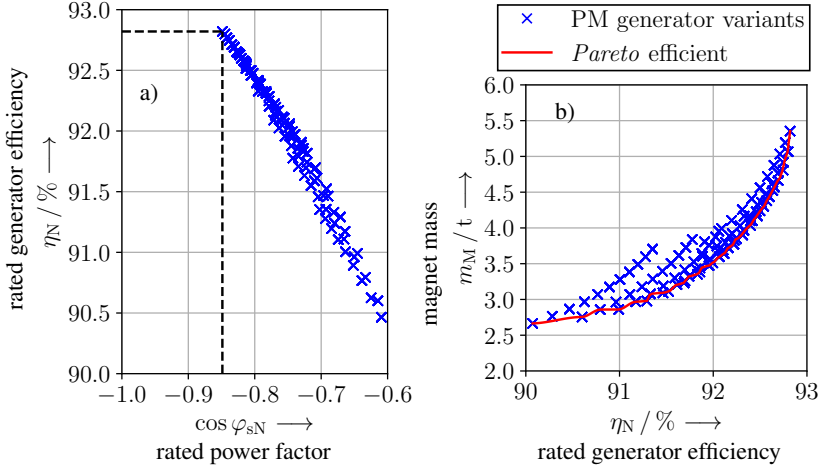


Figure 3.3.: a) Numerically calculated generator efficiency  $\eta_N$  versus power factor  $\cos \varphi_{sN}$  for the variants of PM excited direct drive generators in Fig. 3.2. b) Calculated magnet mass  $m_M$  versus generator efficiency  $\eta_N$  for the same set of designs. The red line indicates *Pareto* efficient designs with respect to minimum  $m_M$  and maximum  $\eta_N$ .

The dynamic development of the neodymium price, Fig. 1.3, requires, that the sensitivity of  $C_t$  with respect to price increases is quantified. The calculated relation  $m_M(\eta_N)$  allows to estimate the relative impact of the price fluctuations. Based on the assumption that the relative price of  $p'_{\text{NdFeB}} = 70 \text{ Euro/kg}$  relies on an average neodymium price of  $p'_{\text{Nd}} \approx 75 \text{ Euro/kg}$ , Fig. 1.3, the neodymium's cost contribution to  $C_t$  is about 34%. An increase of the neodymium price to 225 Euro/kg, which is in the range of the historical short term maximum, yields a price increase of the NdFeB magnets to about 113 Euro/kg, i.e. by 62.1%. For the generator design with maximum efficiency, the total material cost of NdFeB magnets increases to about 600 kEuro, which yields a total component cost of  $C_t \approx 1.13 \text{ MEuro}$ . Even the component costs of designs with intermediate efficiency, e.g. design ② in Sec. 3.3, exceed 1 MEuro for an elevated neodymium price.

### 3.2. Parameter Study

The specific thrust  $\sigma_t$  increases monotonically with efficiency, since the *ohmic* loss  $P_{d,Cu}$  is reduced for axially shorter generators, Fig. 3.4 a). Efficiencies beyond 92% are accompanied by  $\sigma_t \gtrsim 80 \text{ kN/m}^2$  and  $|\cos \varphi_{sN}| \gtrsim 0.75$ , Fig. 3.3 a). This is achieved with a magnet mass of at least  $m_M \approx 3.5 \text{ t}$ , Fig. 3.4 b), which corresponds to about  $0.5 \text{ t/MW}$ , if related to the rated power. An extrapolation to  $P_{el,out} = -10 \text{ MW}$  implies a minimum total NdFeB magnet mass of  $m_M \approx 5 \text{ t}$ , in order to achieve a technically reasonable efficiency.

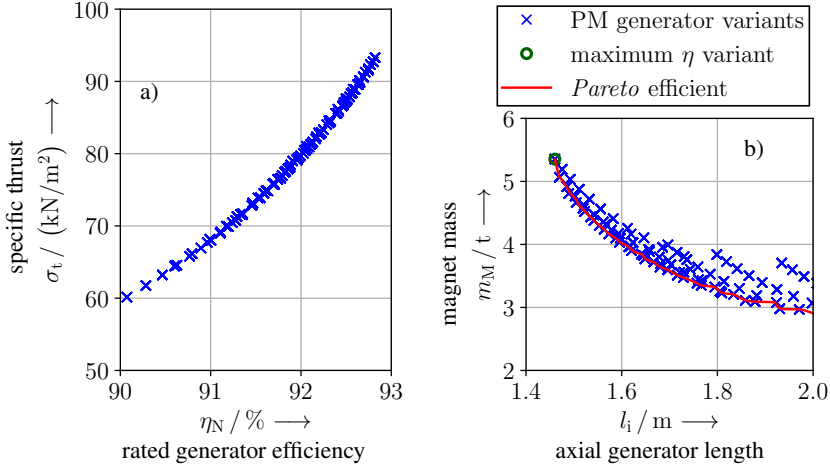


Figure 3.4.: a) Calculated specific thrust versus efficiency for the variants of PM excited direct drive generators. b) Magnet mass versus axial generator length for the same set of designs. The red line indicates *Pareto* efficient designs with respect to minimum  $m_M$  and minimum  $l_i$ , i.e. most compact generators.

The axial length for generator designs with  $\eta_N \geq 92\%$  is less than  $l_i \leq 1.7 \text{ m}$ , which corresponds to a circumscribing generator active volume of  $V_g \leq 57 \text{ m}^3$ . For the same electromagnetic utilization  $C_e \sim A_s \cdot B_{\delta,1}$ , similar rated speed  $n_N$  and the same slimness factor  $\lambda_d = l_i/d_{ro}$ , 10 MW (20 MW) generators with reasonable efficiency  $\eta_N$  must feature an active length of 1.9 m (2.4 m) and an outer diameter of 7.3 m (9.2 m). These large dimensions constitute a major incentive for a technological shift to medium speed generator systems, as employed for example in the 16 MW offshore wind turbine announced by *MingYang* in 2021 [45].

### 3.3. Exemplary Designs

For further comparisons, Ch. 8, two exemplary designs are summarized. As the considerations in Sec. 4.3.1 reveal the strong impact of efficiency on the net present value (NPV, (4.20)) of investments in wind turbine systems, the first design ① is selected for its maximum rated efficiency of  $\eta_N = 92.82\%$ . The second design ② exhibits a  $\approx -0.6\%$  lower efficiency, but requires only  $\approx 70\%$  of the magnet mass of design ①. The selection of design ② is motivated by the disproportionate increase in magnet mass  $m_M$  for increasing the efficiency beyond  $\eta_N \approx 92.2 \dots 92.3\%$ . The calculated magnetic field lines at rated operation and the magnetic field strength  $H$  after a sudden short circuit from no-load are shown in Fig. 3.5 for design ②. Fig. 3.5 b) shows that the magnets are safe from irreversible demagnetization with a safety margin of  $H_{\text{demag}}/H_{m,\text{max}} \approx 1.6 \dots 1.7$ . Generally, the demagnetization of the surface mounted permanent magnets is a minor issue for this generator type, due to the large magnetic air gap.

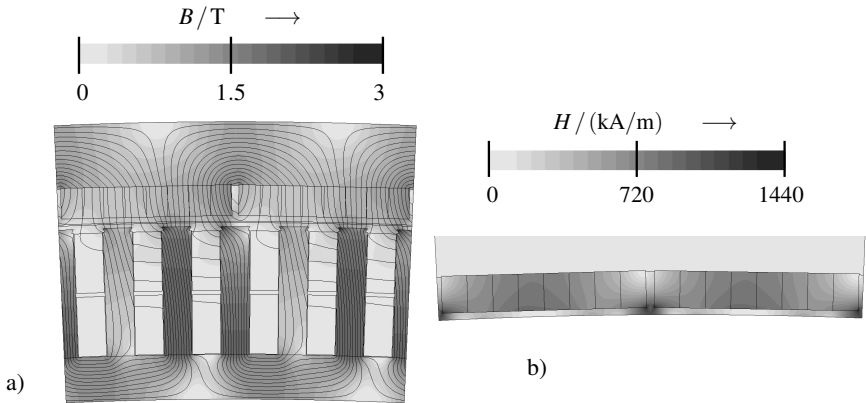


Figure 3.5.: Numerically calculated results: a) Flux density and magnetic field lines at rated load for the exemplary design ②. b) Magnetic field strength  $H$  after a sudden three-phase short circuit from no-load in the two magnets of one pole pair for the exemplary design ②. The results are shown for the time instant, when the maximum magnetic field strength in the PMs occurs. (software: *JMAG*)

The main characteristics of both variants are listed in Tab. 3.6. The difference in converter rating  $\Delta S \approx 828 \text{ kVA}$ , and, hence, the higher converter costs, for design ② are largely overcompensated by the decreased NdFeB magnet mass, i.e. lower magnet costs, from a cost oriented perspective. The circumscribing active generator volume is calculated

### 3.3. Exemplary Designs

from (3.14).

$$V_g = \frac{\pi}{4} \cdot d_o^2 \cdot l_i, \quad d_o = \begin{cases} d_{so} & \text{inner rotor} \\ d_{ro} & \text{outer rotor} \end{cases} \quad (3.14)$$

Table 3.6.: Characteristics of exemplary PM excited direct drive wind generator designs, selected from the variants in Fig. 3.2. Design ① features maximum efficiency among the considered variants. Design ② features intermediate efficiency at a considerably reduced NdFeB magnet mass to reduce the material cost.

	① maximum efficiency	② intermediate efficiency (Pareto efficient w. r. t. $\{m_M, \eta_N\}$ )
$S_N$	8.248 MVA	9.076 MVA
$U_N$	694 V	685 V
$I_{sN}$	6.86 kA	7.65 kA
$M_N$		-8.645 MNm
$\cos \varphi_{sN}$	-0.849	-0.771
$\eta_N$	92.82 %	92.22 %
$A_{sN}$		142.6 kA/m
$\sigma_t$	94.9 kN/m <sup>2</sup>	84.4 kN/m <sup>2</sup>
$C_e$	16.83 kVA · min/m <sup>3</sup>	16.34 kVA · min/m <sup>3</sup>
$V_g$	48.7 m <sup>3</sup>	54.95 m <sup>3</sup>
$H_{M,max}$	1409 kA/m	1233 kA/m
$P_{d,Cu}$	502.0 kW	549.4 kW
$P_{d,Fe}$	32.8 kW	34.8 kW
$P_{d,Fe}$	6.3 kW	5.8 kW
$l_i$	1.460 m	1.648 m
$m_M$	5.355 t	3.770 t
$N_c, N_s, a$	69, 69, 144	62, 62, 144
$h_M$	25 mm	19 mm
$b_M$	134 mm	110 mm
$m_{act}$	54.9 t	53.2 t
$m_{Cu,s}$	13.7 t	15.0 t
$m_{ys}$	7.6 t	8.6 t
$m_{ts}$	11.3 t	12.8 t
$m_{yr}$	11.5 t	13.0 t
$M'$	157 Nm/kg	163 Nm/kg
$C_t$	898.3 kEuro	841.7 kEuro
$C_M$	374.9 kEuro	263.9 kEuro
$C_{Fe}$	91.4 kEuro	103.3 kEuro
$C_{Cu}$	184.8 kEuro	202.2 kEuro
$C_{conv}$	247.4 kEuro	272.3 kEuro
$C'_t$	0.128 MEuro/MW	0.120 MEuro/MW



---

## 4. General Properties and Design of Direct Drive Synchronous Generators with Superconducting Field Winding

The scope of this chapter covers the design of synchronous direct drive wind generators with superconducting field winding and normal conducting stator winding. The principal aim is to evaluate the potential of this generator type regarding low costs, high efficiency and low converter rating. Different magnetic topologies and different superconductors are considered, Sec. 4.1 and 4.3.1. Parasitic effects, which are unique to synchronous generators with superconducting field winding, e.g. the AC loss in the superconductor and the necessity of a damper screen, are investigated with regard to their technological criticality. Throughout the chapter, generators with a power rating of 7 MW are considered. Generally, the high excitation capability of superconducting field windings enables a large variability among the generator designs, Fig. 4.1.

The chapter is organized in three sections, starting with an introduction of the general generator layout and the considered magnetic topologies in Sec. 4.1. Different operating strategies for partially superconducting generators are discussed in this preliminary section. The modelling approach is described in Sec. 4.2. It comprises a parametric, electromagnetic design model, the parameter identification and a thermal model. These models are used in Sec. 4.3 for parametric studies on fundamental design aspects, i.e. a comparison of  $\text{MgB}_2$  and  $\text{ReBCO}$  HTS field windings, the damper design and the evaluation of different stator windings.

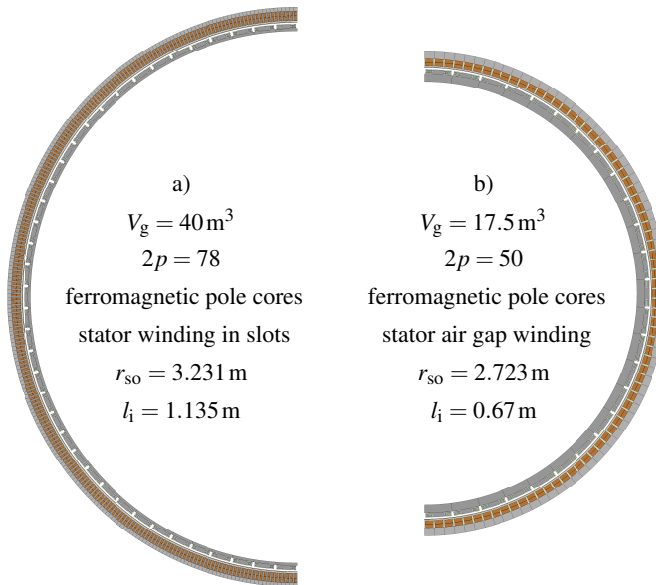


Figure 4.1.: Schematics of 7 MW, 8.33 rpm partially superconducting direct drive generator halves: a) variant with stator winding in slots, b) variant with stator air gap winding, very high electromagnetic utilization and small installation space (software: *JMAG Designer*). For details see Fig. 4.4 (A) for a) and (D) for b).

## 4.1. General Properties and Iron Topologies

All superconducting field windings, that are considered in this chapter, feature a racetrack coil geometry, Fig. 4.2 a). This layout is the simplest form of superconducting coils with a well established winding technique. Coils with this geometry were produced in larger numbers, e.g. for the *EcoSwing* generator [196]. The geometry enables a comparably simple cryogen-free cooling via heat conduction and was used for both ReBCO and MgB<sub>2</sub> field coils. The conductive cooling is achieved via oxygen-free high thermal conductivity (OFHC) copper plates that are connected to a cold bus. Generally, different numbers of winding layers of the SC field winding  $n_{Lf}$  are considered, depending on the excitation requirements and on the used superconductor tape, i.e. its width  $w_t$  and critical current  $I_c$ .

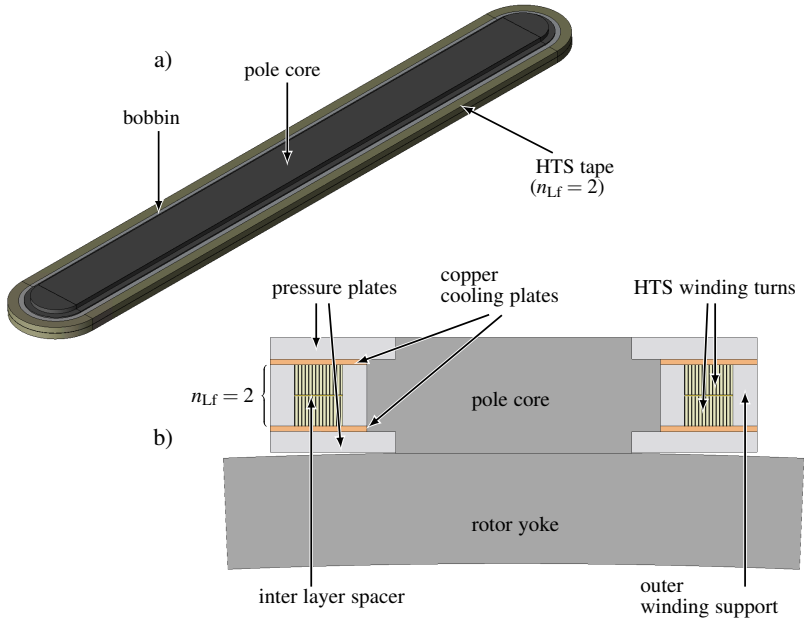


Figure 4.2.: Exemplary double racetrack HTS coil ( $n_{Lf} = 2$ ), which serves as field winding in partially superconducting synchronous generators: a) 3D view of the coil with end-windings, pressure and cooling plates are omitted, b) cross section, assuming a conductive cooling via OFHC copper plates. (software: *JMAG Designer*)

The thermal insulation is established with a single vacuum chamber, which is attached to a warm rotor rim and covers all cold rotor poles as well as a cold rotor yoke. The stationary cryostat wall is made from non-magnetic stainless steel, e.g. AISI 304L or AISI 316, and contributes to the magnetically effective air gap  $\delta_{\text{mag}}$ . The general assembly is shown in Fig. 4.3. The mechanical support structure between the cold rotor yoke and the warm rotor rim is made from glass fibre reinforced plastic (GFRP). This material is best suited to provide sufficient mechanical strength at maximum thermal resistance [20]. The cold rotor yoke and poles facilitate the cold to warm support, since the major temperature gradient occurs favourably along large structural components and not across the coil to pole core or pole core to yoke connections with strict spatial limitations. This simplifies the extension of the conductive heat path through the support elements, which accounts for the major share in the overall heat load. Details of the thermal design are described in Sec. 4.2.4

and App. A.9. The cold rotor parts are wrapped by several layers of super insulation foil as multilayer insulation (MLI) in order to limit the heat leakage by radiation. The entire vacuum chamber is evacuated to limit the convective heat transfer. An electrical series connection of all SC field coils is considered. The field current is supplied by a slip ring-brush system, while a brushless exciter is alternatively also possible. Hybrid current leads are used, as described in Sec. 4.2.4. Generally, the damper screen is attached to the cryostat wall (not shown in Fig. 4.3), while details are discussed in Sec. 4.3.2.

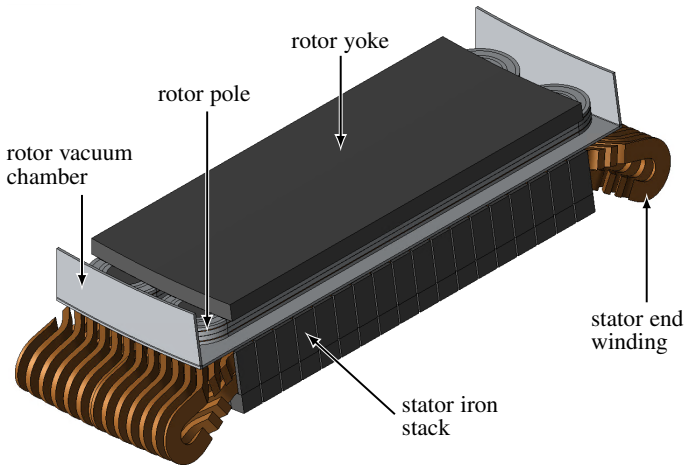


Figure 4.3.: Pole pair of an inner rotor, partially superconducting direct drive generator with distributed two-layer stator winding in slots. Generator specifications:  $P_{el,N} = -7\text{ MW}$ ,  $n = 8.33\text{ rpm}$ ,  $2p = 78$ ,  $V_g = 40\text{ m}^3$ , ferromagnetic yokes and pole cores, HTS tape width  $w_t = 12\text{ mm}$ , two field winding layers  $n_{Lf} = 2$ ,  $n_r = 17$  radial cooling ducts in the stator iron core, axial length of stator core segments  $l_{seg,ax} = 63\text{ mm}$ . (software: *JMAG Designer*)

Distributed integer slot stator windings are considered, Fig. 4.3, in order to limit the stator field harmonics, which yield additional eddy current losses in the cryostat wall and the damper screen and can reach the cold rotor parts. A segmented stator iron core with radial cooling ducts for an intense air cooling is considered for generator topologies with an air-cooled stator winding in slots.

As enabled by the high superconducting excitation MMF, four iron topologies are considered for partially superconducting generators, Fig. 4.4. In ascending order of the excitation

requirement, the considered topologies are:

- Ⓐ Ferromagnetic rotor pole and yoke, stator winding in slots: The cold rotor yoke and the cold rotor poles are made from magnetic FeNi9 (material data in App. A.3.1). The segmented stator iron core is made from M470-65A electrical steel sheets (material data in App. A.3.1). The pressure plates and the coil side support are made from stainless steel AISI 316, which is suitable for cryogenic temperatures.
- Ⓑ Ferromagnetic rotor yoke, non-magnetic pole core, stator winding in slots: Stator core and rotor yoke as for topology Ⓐ. The magnetic iron-nickel pole core in Ⓐ is locally highly saturated, e.g. at  $B \gtrsim 3$  T, such that the use of a more lightweight, non-magnetic pole core is generally reasonable. This pole core can be made from stainless steel, which is however susceptible for additional eddy current loss, or from GFRP.
- Ⓒ Non-magnetic rotor, stator winding in slots: Stator core as for topologies Ⓐ and Ⓑ. The large rotor field yields generally a high induction  $B_{yr} \gtrsim 1.8$  T in the rotor yoke, whose height  $h_{yr}$  is limited for mass reduction. In view of the considerable saturation in the magnetic yoke, the use of a non-magnetic rotor yoke, made from a lighter material, is therefore reasonable. The consequently increased excitation requirement in terms of the MMF per pole  $\Theta_{f,p}$  must however be compensated by larger SC winding packs and a correspondingly larger amount of superconductor material.
- Ⓓ Ferromagnetic rotor poles and yoke, stator air gap winding: The elimination of flux guiding iron teeth enables an increase of the stator winding's copper cross section. A non-magnetic structure is needed to support the *Lorentz* force acting on the stator conductors. The absence of ferromagnetic teeth hampers the heat removal, such that e.g. an indirect conductor water cooling via cooling channels is required. Copper litz wires must be used to prevent excessive load-independent eddy current losses due to the high rotor field. The presence of the cooling channels and the use of litz wires manifest in a reduced copper fill factor in the given winding window. The absence of ferromagnetic teeth increases the required excitation MMF considerably. In order to limit  $\Theta_{f,p}$ , a ferromagnetic rotor structure is employed. The shielding of the surrounding from magnetic fields is achieved with the ferromagnetic stator back iron.

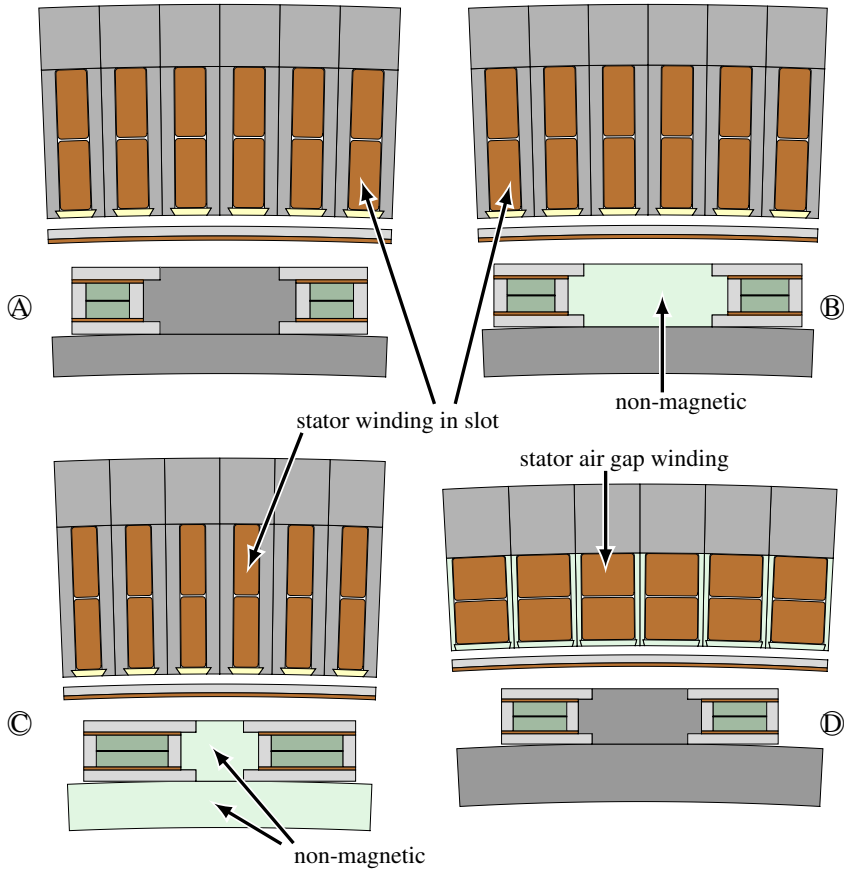


Figure 4.4.: Considered topologies of partially superconducting direct drive synchronous generators with superconducting field winding: **A**) ferromagnetic pole core and rotor yoke, copper AC stator winding in slots, **B**) ferromagnetic rotor yoke, non-magnetic rotor pole cores, copper AC stator winding in slots, **C**) non-magnetic rotor, copper AC stator winding in slots, **D**) ferromagnetic rotor, copper AC stator air gap winding with non-magnetic support structure. The dimensions are shown in Fig. 4.6.

The evaluation of generator variants is focussed on the operation at rated load. In contrast to the PM excited generators in Ch. 3, the variable excitation in superconducting, electrically excited synchronous generators generally allows an adjustment of the rated power factor  $\cos \varphi_{sN}$ , e.g. to unity, within the limits of the current carrying capacity of the

superconductor. This enables two operating strategies for rated operation:

1.  $|\cos \varphi_{sN}| = 1$ : This corresponds to a minimum apparent power  $S_N$  for a fixed output power  $P_N$  and consequently allows for a lower rating of the feeding converter. The increase in exciting MMF  $\Theta_{f,p}$  requires a higher amount of superconductor.
2. Maximum torque per ampere (MTPA): For fixed stator current  $I_s$ , which is prescribed by the thermally admissible stator current density  $J_{Cu}$  at continuous operation and the available stator conductor copper cross section  $A_{Cu}$ , this corresponds to an adjustment of the lead angle  $\gamma$  to achieve maximum torque. The lead angle is counted from the back-EMF  $\underline{U}_p$  to the stator current  $\underline{I}_s$ . The excitation MMF is adjusted, so that the torque for optimum  $\gamma$  matches the required rated torque  $M_N$ . If the stator current attains its thermal upper limit, this strategy consequently corresponds to a maximum utilization of the employed superconductor material and therefore minimizes the cost of the excitation winding.

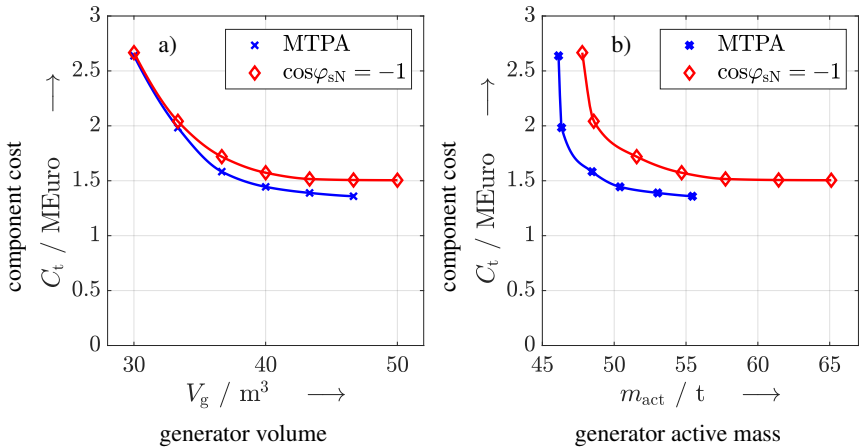


Figure 4.5.: Topology  $\textcircled{A}$ : Component cost  $C_t$  (generator active parts + converter + cryogenic cooling system) versus a) the generator volume and b) the generator active mass under variation of the axial generator length  $l_i = 900 \dots 1400 \text{ mm}$  for the two operating strategies 1 & 2. 7 MW, 8.33 rpm generator, pole count  $2p = 72$ , stator outer radius  $r_{so} = 3258 \text{ mm}$ , *THEVA TPL2100* GdBCO tape with width  $w_t = 12 \text{ mm}$  in the  $n_{Lf} = 2$  layer field winding, cryogenic operating temperature  $T_{HTS} = 30 \text{ K}$ , 9 *GM* cold heads with a price of 25 kEuro per-unit (MTPA: maximum torque per ampere).

To evaluate the operating strategies from a cost oriented perspective, exemplary 7 MW

generator variants of topology ① are analysed under variation of the axial length  $l_i$ , Fig. 4.5. A specific cost of the converter of 30Euro/kVA is assumed, which is typical for low voltage wind power full-converters according to manufacturers' information. The assumed price of the GdBCO tape is 100Euro / (kA · m) (77 K, s.f.). The variation of the variants' active length  $l_i$  corresponds to a variation of the generators' electromagnetic utilization, e.g. measured by *Esson's* number  $C_e$ , and hence the iron saturation state. For short active lengths, i.e. small generator volumes  $V_g$  and highest electromagnetic utilization, the component cost  $C_t$  of generator material, converter and cryogenic cooling system is similar for the two operating strategies 1 and 2. This finding is attributed to the highly saturated iron, which leads to a decrease of the stator winding reactances  $X_d, X_q$ , implying a successively increased power factor in case of MTPA operating strategy 2. In general, the comparison reveals an advantage of the MTPA strategy from a cost-oriented perspective. For this strategy, the component costs  $C_t$  can be reduced by up to 20 % for the same generator active mass  $m_{act} \approx 48 \dots 55$  t. The cost reductions due to the reduced inverter rating are overcompensated by the higher amount of expensive superconductor to enable a unity power factor. The following analyses and the comparison of topologies ① ... ④, Fig. 4.1, are consequently restricted to an operation with MTPA strategy.

## 4.2. Design of Partially Superconducting Direct Drive Generators

The focus of the design is on electromagnetic properties, Sec. 4.2.2, by incorporating design restrictions due to mechanical and thermal requirements. A thermal model is necessary for the determination of the cryogenic cooling power, from which the size and the cost of the cooling system are calculated. These quantities are vital for a meaningful comparison with the PM excitation technology.

### 4.2.1. Geometry Parametrization

The generator's geometry, Fig. 4.6, is specified by eight non-dimensional variables with equal range, Tab. 4.1. The number of pole pairs  $p$  as well as the excitation winding's number of layers  $n_{Lf}$  are continuously scaled between prescribed minimum and maximum values, (4.1) and (4.2), and subsequently rounded to integers (denoted by  $\lfloor \dots \rfloor$ ).



$$p = \lfloor p_{\min} + f_p \cdot (p_{\max} - p_{\min}) \rfloor \quad (4.1)$$

$$n_{Lf} = \lfloor n_{Lf, \min} + f_{n_{Lf}} \cdot (n_{Lf, \max} - n_{Lf, \min}) \rfloor \quad (4.2)$$

The stator outer radius  $r_{so}$  and accordingly the axial length  $l_i$  of the generator are fixed by the prescribed value of  $V_g$  and the slimness factor  $\lambda_d$ , (4.3).

$$r_{so} = \sqrt[3]{\frac{V_g}{2\pi \cdot \lambda_d}} \quad (4.3)$$

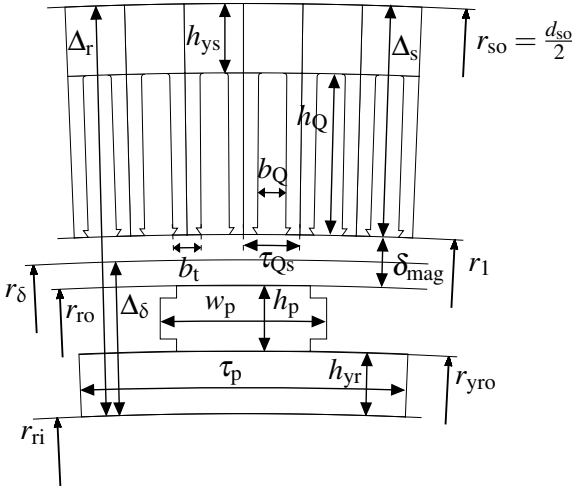


Figure 4.6.: Cross section of the stator and rotor parts for one pole of a partially superconducting 7MW direct drive generator. The visualized radii are scaled by the non-dimensional variables, which determine the overall radial extension of the active parts as well as the split into rotor and stator. The geometry parameters are listed in Tab. 4.1.

Based on the stator outer radius  $r_{so}$ , (4.4) - (4.7) determine the radial extension of the stator and the rotor by scaling with  $f_{r_{ri}, r_{so}}$  and  $f_{\Delta_r, \Delta_\delta}$ .

$$r_{ri} = f_{r_{ri}, r_{so}} \cdot r_{so} \quad (4.4)$$

$$r_\delta = r_{ri} + f_{\Delta_r, \Delta_\delta} \cdot (r_{so} - r_{ri}) \quad (4.5)$$

$$r_1 = r_\delta + \frac{\delta_{\text{mag}}}{2} \quad (4.6)$$

$$r_{si} = \frac{r_l}{\sqrt{1 - \sin^2 \left( \frac{(1 - f_{b_Q, \tau_Q}) \cdot \pi}{Q} \right)}} \quad (4.7)$$

The stator yoke height is specified by its share in the total radial extension of the stator, (4.8).

$$h_{ys} = f_{h_{ys}} \cdot (r_{so} - r_{si}) \quad (4.8)$$

The pole pitch  $\tau_p$  and the slot pitch  $\tau_Q$  at the stator bore are calculated as (4.9).

$$\tau_Q = \frac{2\pi \cdot r_{si}}{Q}, \quad \tau_p = \frac{\pi \cdot r_{si}}{p} \quad (4.9)$$

Table 4.1.: Summary of non-dimensional variables that are used for the parametrization of the geometry of partially superconducting direct drive generators, Fig. 4.6.

parameter	explanation (see also Fig. 4.6)
$f_p$	scaling of the number of pole pairs in a specified range $[p_{\min}, \dots, p_{\max}]$ , rounded to integers
$f_{n_{Lf}}$	scaling of the number of layers of the field winding as racetrack coils in the specified range $[n_{Lf, \min}, \dots, n_{Lf, \max}]$ , rounded to integers
$\lambda_d$	slimness factor $l_i/d_{so}$ , determining the aspect ratio of axial length and generator outer diameter ( $d_{so} = 2r_{so}$ )
$f_{r_{ri}, r_{so}}$	ratio between the inner radius of the inner rotor and the outer radius of the outer stator
$f_{\Delta_r, \Delta_\delta}$	ratio between the radial extension of the rotor $\Delta_\delta$ (inner rotor radius to middle of the magnetic air gap) and the overall radial extension $\Delta_r$ of active parts (stator and rotor together)
$f_{h_{ys}}$	ratio between the stator yoke height $h_{ys}$ and the radial extension of the stator $\Delta_s$
$f_{w_p, \tau_p}$	ratio between the width of the rotor pole core $w'_p$ (arc length) and the pole pitch $\tau_p$ at the rotor outer diameter
$f_{b_Q, \tau_Q}$	ratio between the stator slot width $b'_Q$ (arc length) and the slot pitch $\tau_Q$ at the stator bore

This allows to determine the width of the stator slots  $b'_Q$ , (4.10), and of the stator teeth  $b'_l$ ,

(4.11), as arc length and secant line length.

$$b'_Q = f_{b_Q, \tau_Q} \cdot \tau_Q, \quad b_Q = 2r_{si} \cdot \sin\left(\frac{b'_Q}{2r_{si}}\right) \quad (4.10)$$

$$b'_t = \tau_Q - b'_Q, \quad b_t = 2r_{si} \cdot \sin\left(\frac{b'_t}{2r_{si}}\right) \quad (4.11)$$

The remaining space, i.e. without stator yoke, is available for the teeth and slots, whose height  $h_Q$  is calculated from (4.12).

$$h_Q = (r_{so} - h_{ys}) \cdot \sqrt{1 - \left(\frac{b_Q/2}{(r_{so} - h_{ys})}\right)^2} - r_{si} \cdot \sqrt{1 - \left(\frac{b_Q/2}{r_{si}}\right)^2} \quad (4.12)$$

The rotor outer radius  $r_{ro}$  is derived from the average air gap radius, (4.13).

$$r_{ro} = r_\delta - \frac{\delta_{mag}}{2} \quad (4.13)$$

The height of the rotor pole core  $h_p$  is determined by the field winding's number of layers  $n_{Lf}$  and the prescribed width of the superconductor tapes  $w_t$ , (4.14). The radial height per winding layer  $h_{pLf}$  exceeds the tape width  $w_t$  due to the insulation thickness and some variation of the tape position:  $h_{pLf} \approx w_t + 0.5$  mm. An inter-layer insulation with thickness  $w_{spf} = 0.5$  mm, a thickness of the cooling plates of  $h_{cp} = 2 \cdot 2.3 = 4.6$  mm and a thickness of the pressure plates of  $h_{pp} = 2 \cdot 9 = 18$  mm are considered. The width of the pole core sides, Fig. 4.7, is designed as  $w_{p,side} = 12$  mm, while the side support structure features a width of  $w_{sp,side} = 10$  mm.

$$h_p = n_{Lf} \cdot h_{pLf} + w_{spf} \cdot (n_{Lf} - 1) + h_{cp} + h_{pp} \quad (4.14)$$

As the pole count is known, the radii characterizing the rotor can be determined, (4.15).

This directly yields the rotor yoke height  $h_{yr}$ , (4.16), via (4.17).

$$r'_r = r_{ro} \cdot \sqrt{1 - \left(\frac{w_p}{2r_{ro}}\right)^2} - h_p, \quad r_{yro} = \sqrt{(r'_r)^2 + \left(\frac{w_p}{2}\right)^2} \quad (4.15)$$

$$h_{yr} = r_{yro} - r_{ri} \quad (4.16)$$

The schematic geometry of one rotor pole is shown in Fig. 4.7. The width of the pole core  $w_p$  is calculated from (4.17), while the dimensions of the side support, of the pressure

plates and of the cooling plates are fixed to meet mechanical and thermal requirements.

$$w'_p = f_{w_p, \tau_p} \cdot \frac{\pi \cdot r_{ro}}{p}, \quad w_p = 2r_{ro} \cdot \sin\left(\frac{w'_p}{2r_{ro}}\right) \quad (4.17)$$

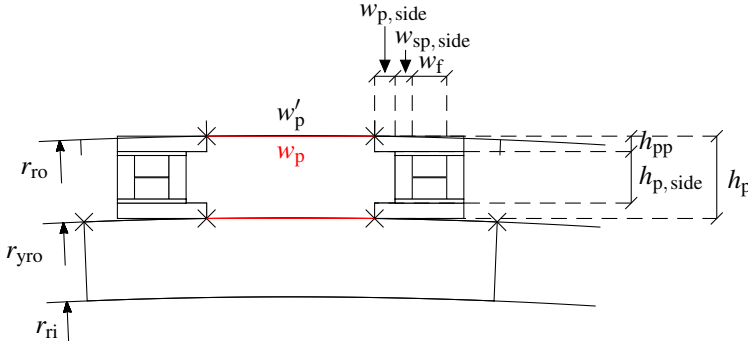


Figure 4.7.: One rotor pole with superconducting field winding as double racetrack coil ( $n_{Lf} = 2$ ) with geometry variables that are used for the parametrization. See Fig. 4.2 for the explanation of the different components.

The minimum double bending diameter  $d_{HTS, \min}$  of HTS tapes is not explicitly considered for ReBCO field windings in the design process. This is valid, since the width of the pole cores  $w_p$  is more than two times larger than  $d_{HTS, \min} \approx 40$  mm, e.g. [205], for resulting stator bore radii in the order of  $r_{si} \approx 3000$  mm, even if a very high pole count of  $2p \approx 160$  is assumed.

### 4.2.2. Iterative Electromagnetic Design

The high magnetic flux densities lead to a major influence of iron saturation effects on the electromagnetic design, such that numerical models must be used. The underlying formulations are described in Sec. 2.1.9 and [O15], while Sec. 4.2.2.1 - 4.2.2.3 summarize major aspects of the design process.

#### 4.2.2.1. Iteration Scheme

The electromagnetic design of the HTS generator is based on non-linear 2D FEM models, which employ the geometry parametrization in Sec. 4.2.1. Magnetostatic simulations by means of the free software *FEMM* are chosen for their computational speed. The number of finite elements per model is in the order of  $N_e \approx 25000 \dots 30000$  and is large enough

to meet convergence criteria. Sinusoidal three-phase AC currents are impressed, so that all stator current harmonics due to the converter feeding are neglected. The large current-smoothing inductances  $L_d$ ,  $L_q$  justify this approximation.

The generator's performance is evaluated by a series of magnetostatic simulations (neglect of any eddy current reaction), where the rotor is successively shifted in finite steps over one electrical period  $T_s = f_s^{-1}$ . After each series of magnetostatic simulations, the flux density in the cross section of the field winding is evaluated, while an iteration loop ensures a self-consistent adjustment of the field current  $I_f$  based on the most critical conditions in terms of  $\vec{B}$ , Sec. 2.5. The SC excitation winding is composed of  $N_f$  insulated turns in each of the  $n_{L_f}$  layers. Non-magnetic parts, e.g. the coil support, the cooling plates and slot wedges, are not explicitly modelled in favour of an improved computational efficiency with only minor lack of accuracy.

The entire, automated design process is visualised in Fig. 4.8. It ensures that the prescribed output power  $P_{el,N}$ , the rated voltage  $U_N$  (rms line-to-line value) and the field-dependent maximum DC excitation current  $I_f$  are set with a maximum relative deviation of 1.5%. A subordinate iteration loop adjusts the lead angle  $\gamma$  in order to achieve the maximum torque per excited rotor field and, thus, per used superconductor material.

Each iteration involves several series of 2D FEM simulations, where the *Newton-Raphson* method is used to adjust the lead angle  $\gamma$ , the excitation current  $I_f$ , the excitation winding's number of turns per layer  $N_f$ , and the stator winding's number of turns per phase  $N_s$ .  $N_f$  determines the dimensions of the field winding, Fig. 4.7, so that large numbers of turns require larger inter-pole gaps to accommodate the field winding. The number of turns per phase  $N_s$  does not determine the stator slot cross section, but the ratio between the number of turns per coil  $N_c$  and the number of parallel branches  $a$ . The slot cross section is fixed by the variable  $f_{b_Q, \tau_Q}$ , Sec. 4.2.1, while the stator current loading  $A_s$  scales linearly with the available cross-sectional area at a fixed  $J_{Cu}$ . Transient, time stepping 2D FEM simulations are carried out for the final designs with the software *JMAG*, in order to incorporate the eddy current reaction field. The calculation of the AC loss  $P_{d,AC}$  in the DC field winding due to air gap field harmonics is not part of the automated design procedure, since  $P_{d,AC}$  is very small and can be neglected without loss of accuracy regarding the total cryogenic heat load estimate, Sec. 4.3.4.

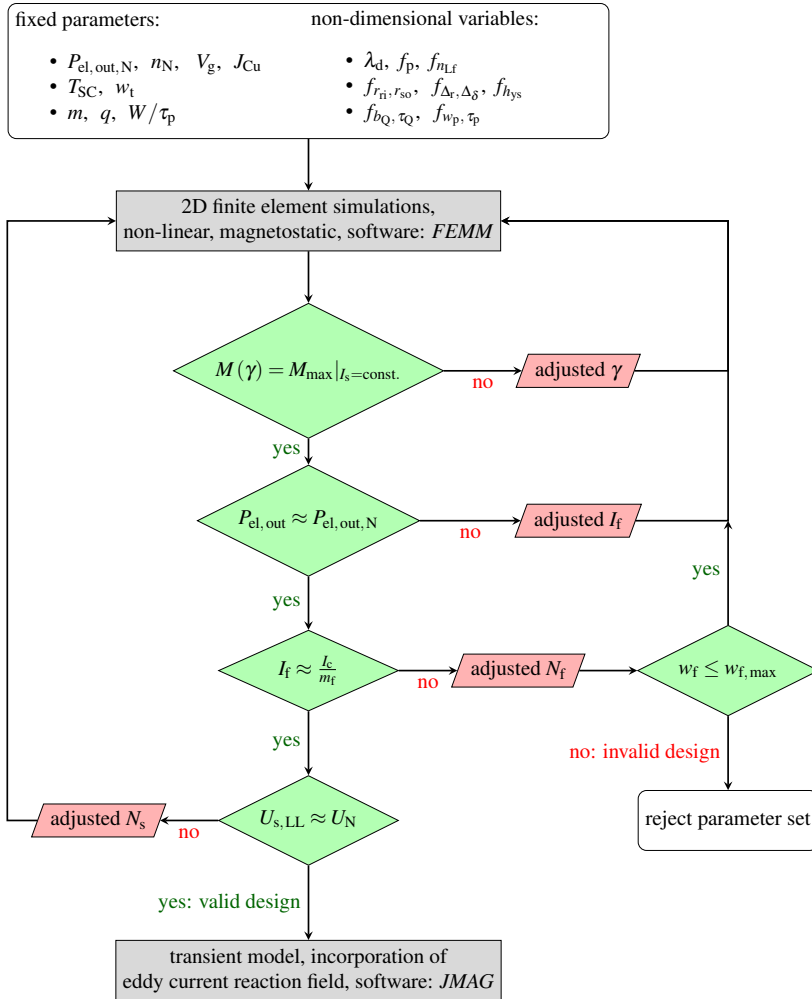


Figure 4.8.: Flow chart of the iterative design process of partially superconducting synchronous generators with superconducting field winding. The process is aborted, if the SC field winding is incapable of providing the required MMF, given  $T_{SC}$  and  $n_{Lf}$ . ( $m_f$ : current margin w. r. t. the critical current  $I_c$  in the SC field winding)

#### 4.2.2.2. Geometrical Simplifications and Meshing

The 2D FEM models in *FEMM* and *JMAG* feature following major geometrical simplifications in order to decrease the degrees of freedom (DOFs):

- The stator winding is modelled by conductors with homogeneous current density. The increase of the stator resistance due to AC current displacement effects is considered in addition by analytical calculation with (2.121). A comparison between the analytically and numerically calculated AC resistances in Sec. 4.3.3 shows a good agreement. The effect of the AC current displacement on the slot stray reactance is neglected, since it is small for low frequencies  $f_s \approx 5\text{ Hz}$ . The stator winding insulation is not explicitly modelled in the 2D FEM models.
- The superconducting field winding is modelled with a homogeneously distributed current density. This generally differs from the actual superconducting current density due to the  $\vec{B}$ -dependence of the local critical current density  $J_c$ , Sec. 2.5. However, the impact of the spatial variation of  $J$  is mostly restricted to the magnetic fields inside the winding window and the nearest vicinity. A subordinate impact on the torque producing air gap field is found by comparison to numerical calculations with detailed coil models (*H-A*-formulation).
- Non-magnetic, non-conductive stator slot wedges are used and are therefore not explicitly modelled.
- Any 3D effects are approximated by analytical calculations. This includes the estimation of the inductance  $L_{s\sigma b}$  and resistance  $R_b$  of the stator end-winding section, the equivalent iron length  $l_i$  in presence of radial cooling ducts and the reduced electrical conductivities for all conductive parts, which are effective for eddy currents. The relevance of 3D effects is discussed in Sec. 4.2.2.3.

The 2D mesh for a transient model of an exemplary generator variant with topology  $\textcircled{A}$  (Sec. 4.1) is visualized in Fig. 4.9. A custom meshing procedure is used for models in *JMAG*. An object oriented *Python* interface is developed to mesh the domains manually by accounting for following requirements:

- A rectangular mesh is used in conductive parts to resolve eddy currents more accurately. The mesh is adapted to provide sufficient spatial resolution at length scales of the skin depth, i.e. with  $\gtrsim 20$  layers per skin depth of the first pair of slot harmonics in the different materials.

- The mesh in the air gap must be sufficiently fine with homogeneous element size. This is achieved by  $\approx 11$  layers in the geometrical air gap, Fig. 4.9.
- A fine mesh in the cross section of the field winding is required in order to incorporate the local magnetic field conditions with sufficient accuracy. A rectangular mesh with at least  $15 \times 18$  mesh elements per layer in case of a  $w_t = 12$  mm wide tape are used, i.e. with element dimensions in the order of  $\lesssim 1$  mm. This is vital for the determination of the current carrying capacity  $I_c(\vec{B})$  of the superconductor.
- A sufficient resolution in highly saturated iron parts, Fig. 4.9 c), is required in order to cover the actual excitation requirements accurately. For example, 60 mesh elements along the radial height of one stator tooth are used and 12 elements across the tooth width at the stator bore. The mesh size in the rotor pole cores is mainly determined by the need for an accurate modelling of eddy currents. In all non-linear iron parts, the element dimensions do not exceed  $\approx 2$  mm, while the magnetic flux density largely varies on length scales of  $\approx 5$  mm in the direct drive generators.

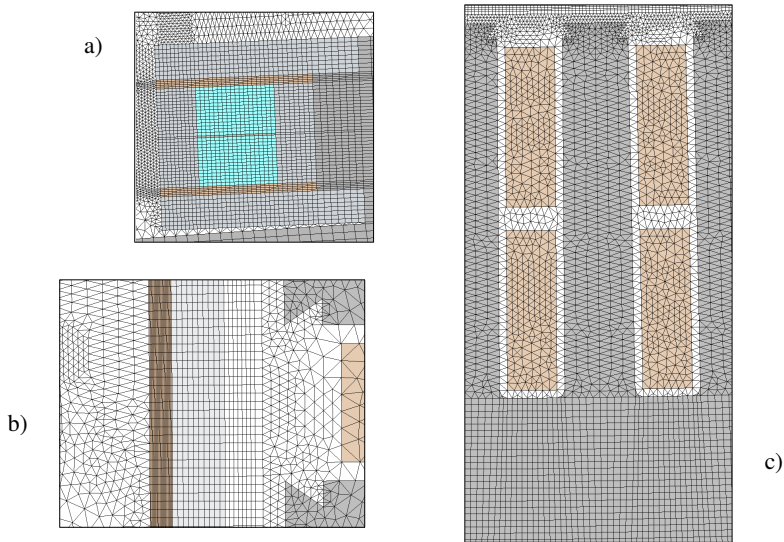


Figure 4.9.: Topology  $\textcircled{A}$  (Fig. 4.4): Detailed views of the parametrized custom mesh. The mesh uses both triangular and quadrilateral linear elements, depending on the geometry of the respective region. a) Coil side of the superconducting field winding with homogenized current density, b) air gap with slot opening, cryostat wall and damper screen, c) stator iron core with slots and copper stator winding. (software: *JMAG Designer*)



### 4.2.2.3. Influence of 3D Effects

The large magnetically effective air gap width  $\delta_{\text{mag}} \approx 30 \dots 40 \text{ mm}$  and the strong iron saturation in ferromagnetic parts, i.e.  $B > 2 \text{ T}$ , Fig. 4.10, lead to a situation, where 3D effects for the generator performance and for the local magnetic field conditions may become important. Therefore, 3D FEM models are implemented for all four considered magnetic topologies ① - ④, Fig. 4.4. As an example, the calculated 3D flux density distribution at rated load in a generator with topology ① is shown in Fig. 4.10.

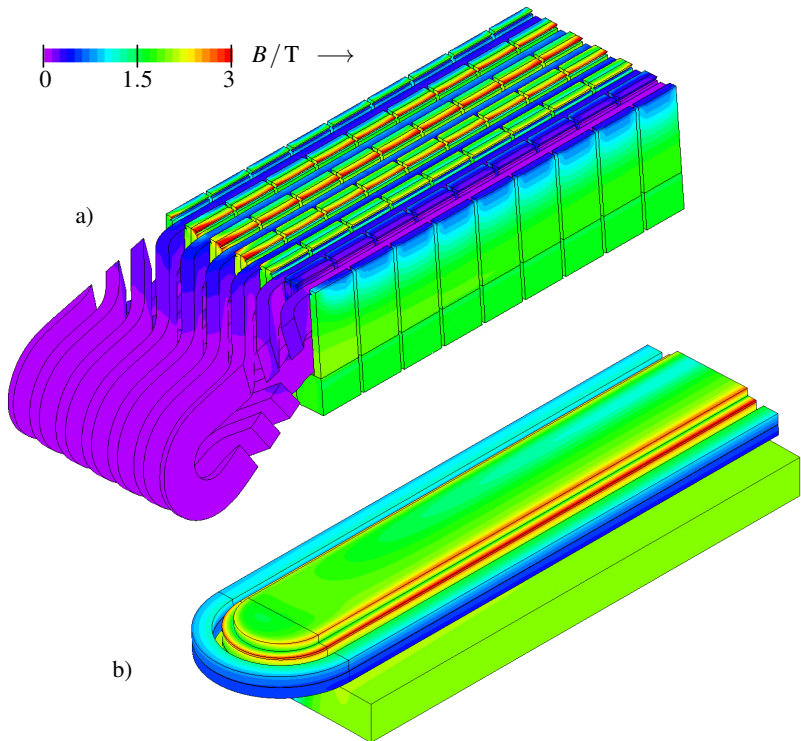


Figure 4.10.: Topology ①: Numerically calculated absolute value of the 3D magnetic flux density  $B$  in one pole of a partially superconducting direct drive synchronous generator at rated load of 7 MW. a) Stator copper winding in stator iron stack, b) HTS field winding with ferromagnetic pole core and ferromagnetic iron yoke. The cooling and pressure plates are omitted for the visibility of the SC winding. (software: *JMAG Designer*)

In order to quantify inherently three-dimensional effects, the radial flux density  $B_r$  is evaluated along axial lines with radial positions according to Fig. 4.11.

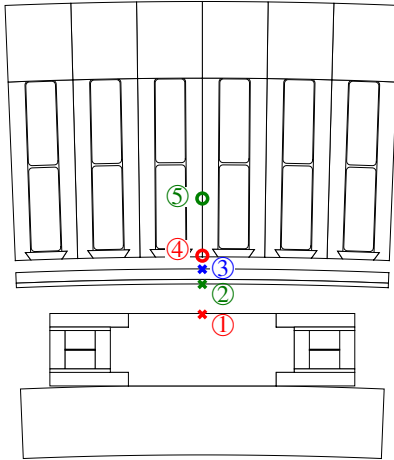


Figure 4.11.: Positions for the evaluation of the radial magnetic flux density in the cross section of one pole of a partially superconducting direct drive wind generator with topology  $\textcircled{A}$ , Fig. 4.12. All points are located in the  $d$ -axis. ①: middle of the pole surface, ②: inner side of the damper screen, ③: outer surface of the cryostat wall, ④: stator bore, ⑤: stator iron core at a distance of  $h_Q/3$  from the stator bore.

The results are shown in Fig. 4.12 and lead to following main findings:

- The magnetic flux density in the end-winding section of the field coil is generally lower than in the straight section, in spite of the curvature related flux concentration, Fig. 4.10. The highest flux density, e.g.  $B \approx 1.8\text{ T}$  in Fig. 4.10, is experienced by the straight, leading coil side of the field winding. This justifies, that the superconductor's current carrying capacity  $I_c$  is determined by means of the 2D models.
- The stray field in the end-winding section of the stator winding is very small, i.e. mostly  $B \lesssim 0.5\text{ T}$ , Fig. 4.10. The stator end-winding has no influence on the external field, experienced by the field winding. The other way around, the field of the rotor excitation winding does not reach out to the stator winding overhang, Fig. 4.12.
- Any flux concentration effects due to the segmented stator iron core do not reach out to the rotor pole, Fig. 4.12, so that the magnetic field conditions in the rotor can be accurately covered by 2D models.
- In spite of the saturated stator iron teeth ( $B \gtrsim 2\text{ T}$ ), the axial end effects in the stator, i.e. the increased magnetic flux density  $B \approx 2 \dots 3\text{ T}$ , and an axially oriented magnetic flux density component  $B_z \lesssim 1.5\text{ T}$ , are restricted to the first stack segment of the stator iron core, Fig. 4.12. The locally higher hysteresis loss there and the

additional eddy current loss in the iron stack have minor influence on the calculation accuracy, due to the low fundamental frequency  $f_s \approx 5\text{Hz}$  and the small share of  $P_{d,\text{Fe}}/P_{d,t} \lesssim 3\%$  of these loss components in the total loss  $P_{d,t}$ .

- 2D models with reduced electrical conductivity allow for the calculation of the eddy current loss in the damper screen, the cryostat wall and cold rotor parts with sufficient accuracy. This is discussed in detail in Sec. 4.3.2.
- The torque calculated by a) 2D models with equivalent iron length  $l_i$  and b) 3D models differs by less than 0.1% for the considered generator variants.

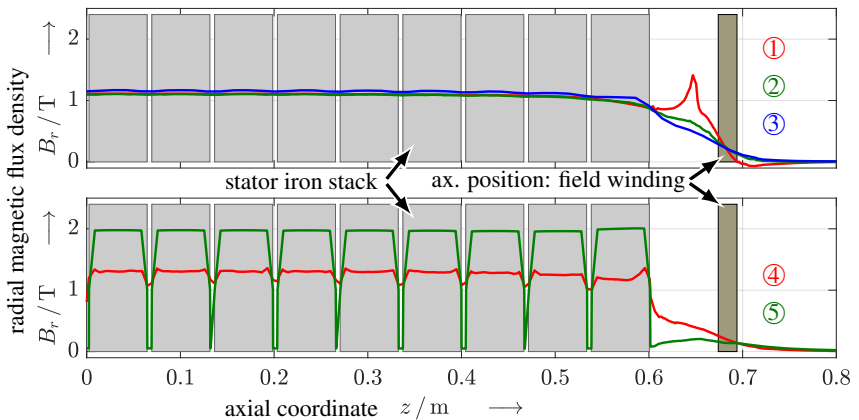


Figure 4.12.: Topology **(A)**: Numerically calculated (3D model) radial flux density component along axial lines with radial positions according to Fig. 4.11. The axial positions of the stator iron stack segments, separated by radial cooling ducts, are indicated by gray shaded regions, the axial position in the middle of the field winding overhang, i.e. in the  $d$ -axis, is indicated by the brown shaded region. Since also the tangential and axial components of the flux density are significant, depending on position, the absolute value of the flux density is larger:  $B \approx 1.8 \dots 2.1\text{T}$  at the pole surface,  $B \approx 2 \dots 3\text{T}$  in the stator teeth.

### 4.2.3. Parameter Identification and Phasor Diagram

The construction of the voltage and current phasor diagram per phase requires the extraction of equivalent circuit parameters from the numerical simulations. Due to the sensitivity with respect to saturation, these parameters characterize the generator only for one operating point, i.e. operation at rated field current  $I_{fN}$  and rated stator current  $I_{sN}$ . The

calculation procedure is described in App. A.7 for a symmetrical three-phase winding. The consumer reference frame is used.

Exemplary phasor diagrams for a generator with all-iron topology **(A)** and stator air gap winding topology **(D)** are shown in Fig. 4.13. The corresponding parameters of the equivalent circuit are listed in Tab. 4.2.

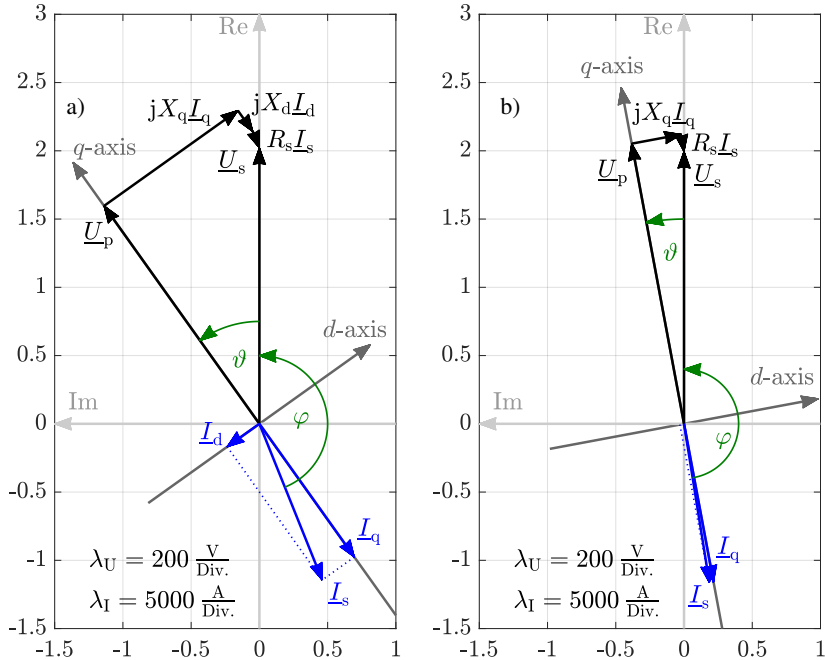


Figure 4.13.: Exemplary phasor diagrams of 7MW, 8.33 rpm partially superconducting generators with HTS field winding: a) generator variant **(A)** with ferromagnetic rotor poles and yoke, copper stator winding in slots, b) generator topology as a) but with stator copper air gap winding and non-magnetic winding support **(D)**. The very short phasors of the  $d$ -current and  $jX_d I_d$  are not shown in b) for better visibility.

The exemplary phasor diagrams show the large electromagnetic variability among the variants of partially superconducting generators. The exemplary generator variant with all-iron topology **(A)** features similar characteristics as conventional generators, e.g. with PM excitation. In contrast, the variant with stator air gap winding exhibits much smaller inductances and a significantly smaller load angle  $\vartheta_N$  at rated operation.

Table 4.2.: Exemplary equivalent circuit parameters of the 7MW, 8.33 rpm generator variants with phasor diagrams in Fig. 4.13. The generator variants feature a HTS field winding and a copper stator winding.

	a) stator winding in slots (A)	b) stator air gap winding (D)
$U_{sN}$	404 V	399 V
$U_{s,d}$	235 V	73 V
$U_{s,q}$	329 V	392 V
$U_{LL}$	700 V	691 V
$U_p$	392 V	418 V
$U_{i,2D,FEM}$	425 V	420 V
$\vartheta_{2D}$	32.8°	7.3°
$\vartheta$	35.5°	10.6°
$\gamma$	166.4°	178.5°
$I_s$	6165 A	5895 A
$I_d$	-1449 A	-155 A
$I_q$	-5993 A	-5893 A
$Z_N$	65.5 mΩ	67.7 mΩ
$X_{d,2D}$	24.3 mΩ	7.0 mΩ
$X_{q,2D}$	38.4 mΩ	9.0 mΩ
$X_{s\sigma b}$	1.8 mΩ	3.5 mΩ
$X_d$	26.1 mΩ	10.5 mΩ
$X_q$	40.2 mΩ	12.5 mΩ
$R_s$	4.2 mΩ	4.0 mΩ
$x_d$	0.398 p.u.	0.156 p.u.
$x_q$	0.613 p.u.	0.185 p.u.
$r_s$	0.064 p.u.	0.059 p.u.
$\cos \varphi_{sN}$	-0.928	-0.988
$M_{e,2D,rel}$	-419.5 kNm	-6.3 kNm
$M_{e,2D,rel}/M_{e,2D}$	4.93 %	0.07 %

#### 4.2.4. Thermal Design

The purpose of the thermal model is the quantification of the cost of the cooling system and of the efficiency decrease due to the required cooling power. A lumped element thermal model is derived, which incorporates major heat transfer paths. The simplified schematic of the stator section is shown in Fig. 4.14, a corresponding schematic of the rotor part is shown in Fig. 4.15. The details of the model, i.e. the expressions for the thermal resistances, are listed in App. A.9, while the major model properties are listed here:

- Non-linear, temperature dependent thermal conductivities are used. The material properties are listed in App. A.3.3. To solve the resulting system of equations, a non-linear solver in *MATLAB* is used.
- The mechanical support structure between the warm rotor rim and the cold rotor yoke („cold-warm support“) of the rotor yoke accounts for a significant share in the total heat load of the cryogenic cooling system. Therefore, a preliminary mechanical design of the support structure is required. The cold-warm support is designed to withstand as a maximum short circuit torque of three times rated torque. Details are listed in App. A.9. This estimate of the maximum torque is reasonable based on the analysis of different sudden short circuit faults in Sec. 6.2.

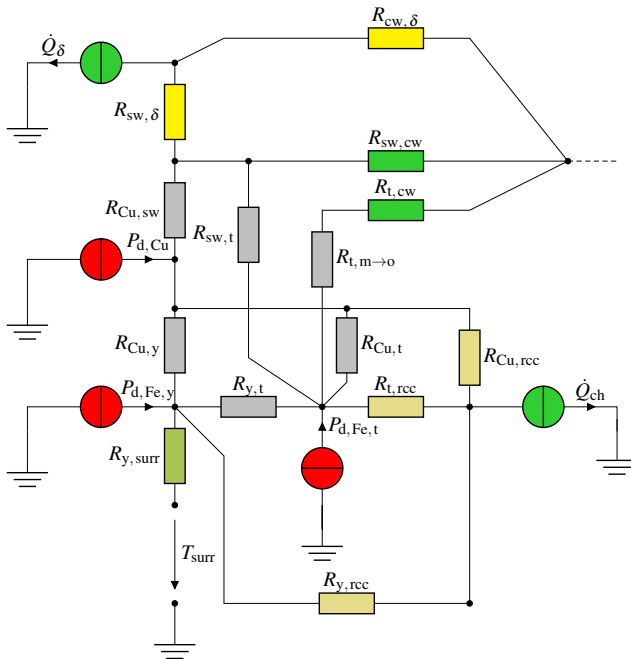


Figure 4.14.: Thermal network representing the stator of the partially superconducting generator. Colours:  conductive heat transfer,  radiative heat transfer,  convective heat transfer,  combination of radiative and convective heat transfer,  combination of conductive and convective heat transfer.

- An ambient temperature of  $40^{\circ}\text{C}$  is considered in the sense of a worst case scenario. The warm temperature  $T_h$  faced by the cryogenic cooling system is  $20^{\circ}\text{C}$ , as an air-conditioned nacelle is assumed.
- A material with zero electrical conductivity, i.e. GFRP, is assumed for the non-magnetic pole cores of topologies **B** and **C**. This prevents additional eddy current losses in the cryogenic section.
- The model is only valid for a stator winding in slots with air cooling. In case of the stator air gap winding (topology **D**), the necessarily more powerful cooling system ensures that the heat transfer from stator to rotor is small and, hence, neglected here. Based on this assumption of a thermal decoupling, a simplified model of the rotor alone, Fig. 4.15, is used for the estimation of the cryogenic heat load in this case.

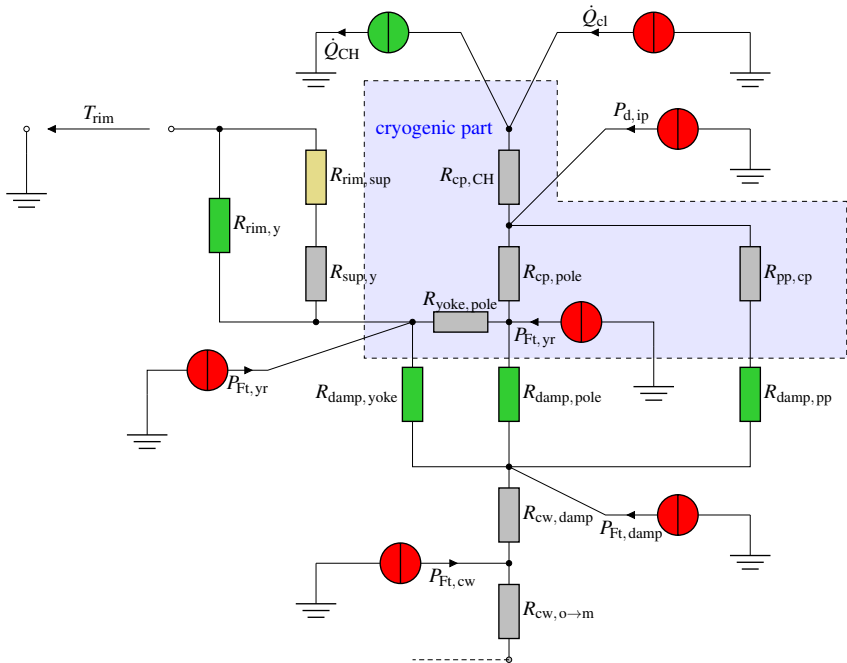


Figure 4.15.: Thermal network representing the rotor of the partially superconducting generator. The cryogenic section of the rotor is highlighted in blue. Colours:  conductive heat transfer,  radiative heat transfer,  combination of radiative and convective heat transfer,  combination of conductive and convective heat transfer.

Following loss contributions to the overall heat load are included:

- *ohmic* loss in the copper stator winding
- iron loss in the ferromagnetic stator yoke (all) and stator teeth (topologies Ⓐ - Ⓒ)
- eddy current loss in the cryostat wall  $P_{d, Ft, cw}$  and the warm damper screen  $P_{d, Ft, damp}$  (not at cryogenic temperatures)
- eddy current loss in the cold massive pole core  $P_{d, Ft, rp}$  (topologies Ⓐ, Ⓓ) and in the massive rotor yoke  $P_{d, Ft, yr}$  (topologies Ⓐ, Ⓑ, Ⓓ)
- conductive heat flow through high-current leads  $\dot{Q}_{cl}$
- *ohmic* loss in the normal-conducting inter-pole connections in the excitation circuit  $P_{d, ip}$

The considered cooling mechanisms are:

- forced air cooling with convective heat transfer in cooling ducts  $\dot{Q}_{ch}$  and air gap  $\dot{Q}_{\delta}$
- heat transfer from the stator yoke to the surrounding via air convection (thermal resistance  $R_{y, surr}$ )
- cooling in the cryogenic section by means of *GM* cryocoolers  $\dot{Q}_{CH}$

The loss power together with the heat flows and the calculated temperatures are listed in Tab. 4.3 for an exemplary partially superconducting generator with topology Ⓐ. Based on the exemplary results, following findings can be generalized:

- The mostly conductive heat transfer through the cold-warm support accounts for about 70 % of the total cryogenic heat load. The mostly radiative heat transfer from the damper and cryostat wall to cold parts and the eddy current loss in the cold iron feature a minor share, i.e.  $\lesssim 10\%$ .
- The estimated average stator winding temperature at 40°C ambient differs from the initially assumed temperature of  $\vartheta_{Cu, s} = 100^{\circ}\text{C}$  by  $\Delta\vartheta \approx 19\text{ K}$ . A self consistent solution is obtained by iterative adjustment of the calculated, temperature-dependent stator resistance  $R_s$ .
- A significant temperature difference of  $\Delta T \approx 4\text{ K}$  between the SC winding, resp. the OFHC cooling plates, and the cold stage of the cold head occurs along the cold bus connection. The increase of the cross section of the OFHC bars is limited for cost reasons and due to spatial restrictions. This temperature difference ( $T_{SC} - T_{CH}$ ) is an inherent disadvantage of the cryogen-free, conductive cooling system.



- The heat load at the 30K stage through the current leads is very small because a „thermal anchoring“ at 70K, i.e. a pre-cooling of the current leads at elevated temperature, is considered. HTS current leads are used for the connection to the  $T = 30\text{K}$  stage. The heat load at the 70K stage is calculated for a rated excitation current of  $I_{fN} \approx 417\text{A}$ . By using the optimum copper cross section, the characteristic ratio  $L \cdot I/A$  ( $L$ : conductor length,  $I$ : current,  $A$ : conductor cross section) at  $T_c = 70\text{K}$  and  $T_h = 290\text{K}$  ( $\vartheta \approx 20^\circ\text{C}$ ) is  $L \cdot I/A \approx 3.8 \cdot 10^6\text{A/m}$  [56]. For a conductor length of  $L = 1\text{m}$ , spanning the temperature difference of  $\Delta T = T_h - T_c = 290 - 70 = 220\text{K}$ , the optimum conductor cross section is calculated as (4.18).

$$A_{\text{Cu,cl}} = \frac{1 \cdot 417}{3.8 \cdot 10^6} \approx 110\text{mm}^2 \quad (4.18)$$

The heat flux through the current leads is (4.19) [120].

$$\dot{Q} = 2 \cdot I \cdot \sqrt{L_0 \cdot (T_h^2 - T_c^2)} = 2 \cdot 417 \cdot \sqrt{2.445 \cdot 10^{-8} \cdot (290^2 - 70^2)} \approx 36.7\text{W} \quad (4.19)$$

This value is well below the capacity of commercially available *GM* cryocoolers at 70K, Fig. 1.10, so that a single cold head is sufficient for cooling the current lead. Based on a typical COP at 70K of  $\approx 2.5\%$  for the *GM* cryo-cooler, the required compressor power for the pre-cooling is in the order of 1.6kW, which is less than 0.02% of the rated generator electric power.

The cryogenic heat load  $\dot{Q}_{\text{CH}}$  is used to calculate the required compressor input power  $P_{\text{compr}}$ . The required number of cryo-coolers is calculated based on  $\dot{Q}_{\text{CH}}$ , on the capacities in Fig. 1.10 and on the cold stage temperature  $T_{\text{CH}}$ .

As the cryogenic heat load is mainly determined by the torque  $M$  of the generator via the cold-warm support, a linear scaling of the cooling system capacity with  $M_N \sim \hat{M}_{k,\text{max}}$  is reasonable. For similar rotating speeds, this implies the proportionality  $\dot{Q}_{\text{CH}} \sim P_N$ . Generators with larger rated power may profit from an increase of the cooling system's COP towards higher cooling capacity. Apart from this effect, no size-dependent influence of the cryogenic cooling on the overall efficiency is expected.

### 4.3. Parametric Design Study of Partially Superconducting Direct Drive Generators

Table 4.3.: Exemplary heat loads/fluxes in a partially superconducting 7 MW direct drive generator (topol.  $\text{\textcircled{A}}$ ) with HTS field winding at  $T_{\text{HTS}} = 30\text{K}$ . The equivalent circuits in Fig. 4.14, 4.15 are used. An ambient temperature of  $T_{\text{surr}} = 313.15\text{K}$  ( $\vartheta_{\text{surr}} = 40^\circ\text{C}$ ) is assumed.

$P_{\text{d,Cu}}$	476.5 kW
$P_{\text{d,Fe,y}}$	10.3 kW
$P_{\text{d,Fe,t}}$	12.4 kW
$P_{\text{d,Ft,damp}}$	7.1 kW
$P_{\text{d,Ft,cw}}$	2.9 kW
$P_{\text{d,Ft,pr}}$	65 W
$P_{\text{d,Ft,yr}}$	12 W
$P_{\text{d,ip}}$	22.2 W
$\dot{Q}_{\text{cl}}$	0.3 W
$\dot{Q}_{\text{rim}}$	358.9 W
$\dot{Q}_{\text{damp,rad}}$	37.0 W
$\dot{Q}_{\text{CH}}$	495 W
$\dot{Q}_{\text{surr}}$	126.1 kW
$\dot{Q}_{\text{ch}}$	298.1 kW
$\dot{Q}_{\delta}$	84.0 kW

Table 4.4.: Exemplary, calculated temperatures in a partially superconducting 7 MW direct drive generator. The same operating conditions as in Tab. 4.3 are considered. An average air flow velocity of  $\bar{v}_{\delta} = 55\text{m/s}$  in the air gap is assumed.

$\vartheta_{\text{surr}}$	40°C
$\vartheta_{\text{Cu,s}}$	119°C
$\vartheta_{\text{Fe,s,t}}$	112°C
$\vartheta_{\text{Fe,s,y}}$	92°C
$\vartheta_{\text{cw}}$	75°C
$\vartheta_{\text{damp}}$	76°C
$\vartheta_{\text{rim}}$	40°C
$\bar{\vartheta}_{\delta,\text{in}}$	69°C
$\bar{\vartheta}_{\text{ch}}$	54°C
$\vartheta_{\text{air,out}}$	77°C
$T_{\text{HTS}}$	30 K
$T_{\text{CH}}$	25.8 K
$T_{\text{pp}}$	30.1 K
$T_{\text{cp}}$	30.0 K
$T_{\text{rp}}$	36.2 K
$T_{\text{yr}}$	33.4 K

### 4.3. Parametric Design Study of Partially Superconducting Direct Drive Generators

The aim of the parametric design studies in this section is to narrow the scope for the numerical optimization in the following Ch. 5. A comparison between  $\text{MgB}_2$  and ReBCO excitation windings in Sec. 4.3.1 is followed by a systematic investigation of different stator windings and damper designs in Sec. 4.3.2, 4.3.3. The relevance of the AC loss in the superconducting field winding is discussed in Sec. 4.3.4.

#### 4.3.1. Comparison of ReBCO HTS and $\text{MgB}_2$ Field Windings

Compared to ReBCO coated conductors,  $\text{MgB}_2$  wires feature following advantages and disadvantages regarding a use in field windings of direct drive wind generators:

- ⊕ MgB<sub>2</sub> wires are generally cheaper, due to a much simpler manufacturing. The wires exhibit a lower cost per length and critical current compared to 2G HTS conductors at  $T = 20\text{K}$  and relevant flux densities of up to  $B \approx 3\text{T}$ , Sec. 2.5.
- ⊕ MgB<sub>2</sub> wires are available in long piece lengths, while the production of long piece lengths is more challenging for ReBCO conductors. This difference is partially eliminated, since HTS conductor lengths of up to  $l_t = 300 \dots 500\text{m}$  are commercially available today. The required conductor length per rotor pole rarely exceeds this range for reasonable generator designs.
- ⊖ The MgB<sub>2</sub> wires require an operating temperature of at most 20K. In contrast, an operating temperature of  $T = 30\text{K}$  is reasonable for ReBCO tapes, Sec. 2.5.1. For commercially available cryo-coolers, the higher operating temperature leads to an increase of the COP by a factor of about  $\approx 1.8$ . The lower temperature in case of MgB<sub>2</sub> wires affects the overall efficiency and the cost:
  - A  $\approx 80\%$  higher compressor power is required to remove the same heat, e.g. Fig. 1.10.
  - The larger cooling system is more expensive, which counteracts the lower superconductor price.
- ⊖ The thermal margin is smaller for MgB<sub>2</sub> wires, i.e.  $\approx 19\text{K}$  in contrast to  $\approx 60\text{K}$  for ReBCO windings with respect to  $T_c (B = 0)$ . This is relevant for thermal transients. This disadvantage is aggravated for magnetic topologies with less cold iron parts, which contribute to the thermal inertia.
- ⊖ MgB<sub>2</sub> wires feature a  $-25 \dots -70\%$  lower engineering current density  $J_e$ , which implies less compact windings and makes the cooling more difficult, e.g. in case of conductive, cryogen-free cooling. With regard to field windings in synchronous generators, the larger coil cross section is challenging for following reasons:
  - The space in the inter-pole gap is limited in order to provide sufficient magnetic flux guiding cross section in the pole cores and to achieve a high fundamental winding factor.
  - Poles with small radial outreach reduce the inter-pole stray flux, which is necessary for following reasons:
    - \* The stray flux magnetically increases the flux density in the pole core and the rotor yoke without contribution to the torque generation.

- \* The inter-pole stray flux penetrates the SC field winding's coil sides and reduces the critical current  $I_c$ .

A meaningful comparison of the two superconductors from a cost-oriented perspective must incorporate the cost of the superconductor, the cost of the cryogenic cooling system and the opportunity cost, i.e. the missed returns of the missed energy production, due to an efficiency decrease as a result of a lower operating temperature. For this purpose, three generator variants, Tab. 4.5, are compared.

Two ReBCO tapes with and without APCs are considered in order to cover the variety among available conductors regarding the in-field critical current  $I_c(\vec{B})$ . An intermediate  $\text{MgB}_2$  price of 5.25Euro/m is assumed for ①. The assumed ReBCO prices are 250Euro / (kA · m) for type ② and 100Euro / (kA · m) for type ③ ( $T = 77\text{K}$ , s.f.). Type ② features a much higher in-field lift-factor  $L(\vec{B})$ , which equalizes the price difference depending on operating conditions, see Sec. 2.5.

Table 4.5.: Variants of partially superconducting direct drive wind generators for the comparison between  $\text{MgB}_2$  and ReBCO field windings. All generators feature the topology ④ in Fig. 4.1 and an identical active generator volume  $V_g = (\pi/4) \cdot d_{\text{so}}^2 \cdot l_i$ . Generator specifications: 7MW, 8.33rpm,  $d_{\text{so}}^{\text{max}} = 6.5\text{m}$ ,  $U_N = 690\text{V}$ .

	①	②	③
superconductor	$\text{MgB}_2$	EuBCO	GdBCO
manufacturer	<i>ASG Superconductors</i>	<i>Fujikura</i>	<i>THEVA</i>
$T_{\text{SC}}$	20 K	30 K	30 K
$V_g$	40m <sup>3</sup>		
topology	— ferromagnetic rotor yoke & poles, stator winding in slots —		

Following findings are derived from the comparison in Fig. 4.16 and 4.17:

- Based on current prices,  $\text{MgB}_2$  excited partially superconducting direct drive generators feature the lowest capital expenditures (CAPEX), Fig. 4.16 a). However, only a small active mass reduction by about  $-10\%$  is possible compared to PM excited generators. The system cost  $C_i$  is by 20...35% higher than for PM generators (assuming  $p'_{\text{NdFeB}} = 70\text{Euro/kg}$ , Fig. 3.2).
- With ReBCO field windings, a larger mass reduction by  $\approx 25\%$  for type ③ and by even  $> 30\%$  for type ② is possible.

- The investment cost  $C_t$  is by  $\approx -2 \dots 17\%$  lower for both ReBCO field winding types than for the  $\text{MgB}_2$  field winding, if a ReBCO price reduction to about  $1/3$  of the current value is achieved, Fig. 4.16 b). This price reduction is considered as realistic in the medium term by manufacturers. The higher  $C_t$  of  $\text{MgB}_2$  excited generators is mainly caused by the necessarily more powerful cooling system. The material cost of the superconductor alone is similar for  $(1/3) \cdot p'_{\text{ReBCO}}$ , Fig. 4.17 a).
- The generator types in Tab. 4.5 differ regarding the rated efficiency:  $\text{MgB}_2$  excited generators feature only a slightly higher efficiency (including cooling power) compared to PM generators, i.e.  $\eta_N = 92 \dots 93\%$ , Fig. 4.17 b). Both ReBCO excited generator types exhibit an efficiency increase by  $0.8 \dots 1.2\%$  compared to PM and  $\text{MgB}_2$  excited generators for a reasonable total ReBCO conductor length, i.e.  $l_t \lesssim 30\text{km}$  ( $w_t = 12\text{mm}$ ).
- The absolute fundamental power factor  $|\cos \varphi_{sN}|$  is generally much higher compared to the PM excited generator with only minor difference between the different generator types with superconducting excitation. This reduces the converter rating, i.e. by  $\approx -20\%$  from  $\cos \varphi_{sN} \approx -0.76$ , Fig. 3.3 a), to  $\cos \varphi_{sN} \approx -0.95$ , Fig. 4.17 b).

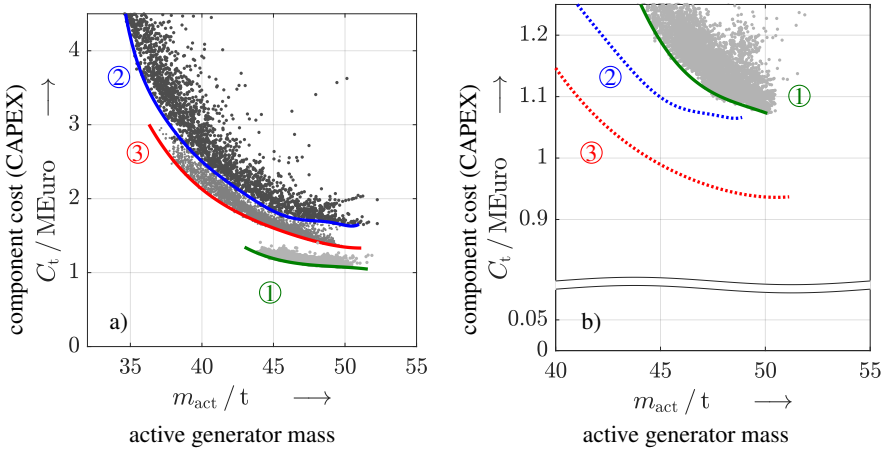


Figure 4.16.: a) Calculated component cost (generator material + converter + cryogenic cooling system) versus generator active mass for generator variants ① - ③ in Tab. 4.5. b) Same as a), but with a ReBCO price reduction to  $1/3$  of its current value.

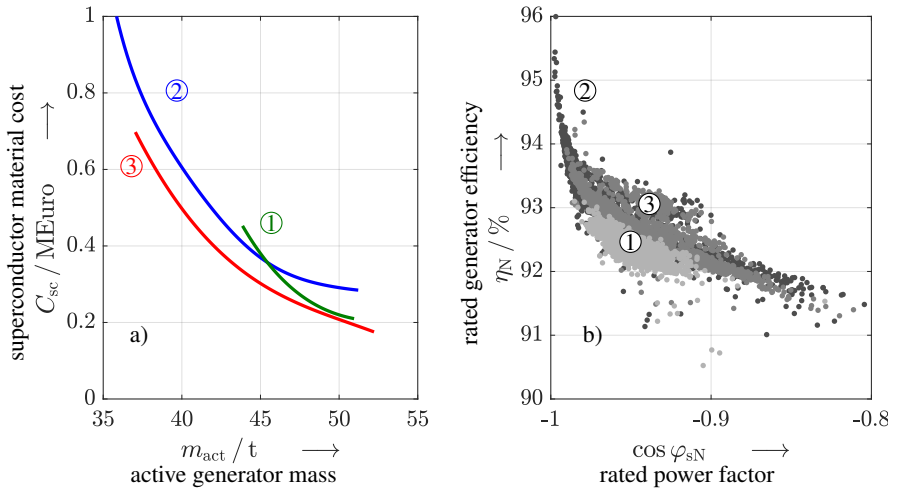


Figure 4.17.: a) Calculated material costs of the superconductor for *Pareto* efficient designs for generator types ① - ③ in Tab. 4.5. A ReBCO price reduction to 1/3 of its current value is considered. b) Calculated generator efficiency versus fundamental power factor for the generator variants of generator types ① - ③ in Tab. 4.5.

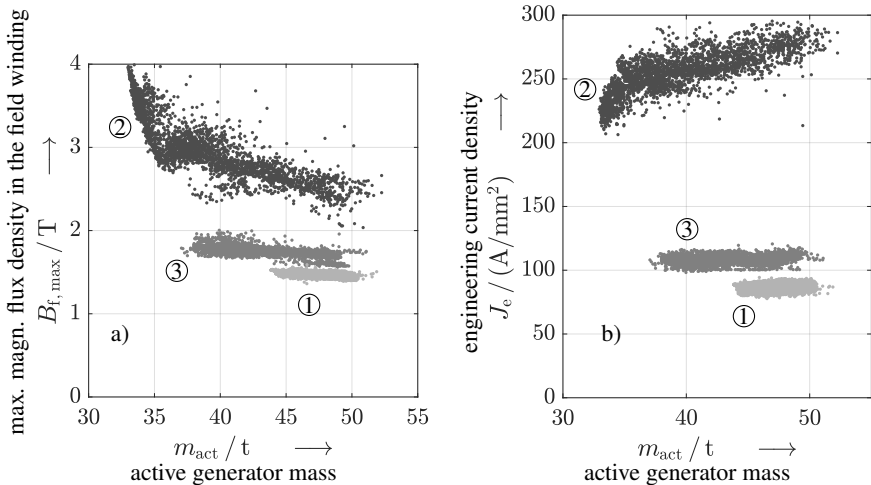


Figure 4.18.: a) Calculated maximum magnetic flux density  $B_{f,max}$  in the excitation winding ( $|B|_c$ ) versus the generator active mass for generator variants ① - ③ in Tab. 4.5. b) Engineering current density  $J_e$  in the field winding versus the generator active mass  $m_{act}$  for the same set of generator variants.

The considered SC generator types differ strongly regarding the achievable superconducting in-field engineering current density  $J_e$ , Fig. 4.18 b). In spite of the lower operating temperature  $T = 20\text{K}$ , the values of  $J_e$  in the  $\text{MgB}_2$  winding are lower by  $\approx 25 \dots 30\%$  compared to ③ and by  $\approx 70\%$  lower compared to ②. The high in-field current carrying capacity of ② is caused by APCs. As a result of the more compact winding, considerably higher local magnetic flux densities in the excitation winding occur, Fig. 4.18 a). The presence of APCs yields however a reduced sensitivity with respect to magnetic flux densities  $B > 2\text{T}$  ( $\vec{B} \parallel c$ ).

Table 4.6.: Assumptions for the calculation of a cost equivalent for efficiency differences in terms of the net present value (NPV).

feed-in tariff $p'$	12 ... 18 Ct/kWh
full load	3750h
hours p.a. $Q$	
interest rate $i$	2 ... 5%
rated mechanical	7MW
power $P_{\text{mech},N}$	
service life $T$	20y

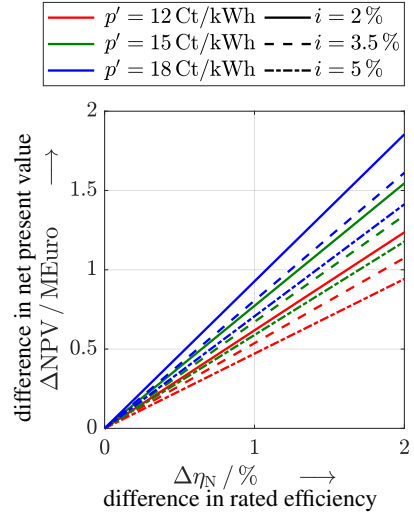


Figure 4.19.: Difference in the NPV due to an efficiency difference.

An approximate cost equivalent of the efficiency difference is obtained, if the loss power is priced with the current feed-in tariff  $p'$ , Tab. 4.6. The influence on the net present value (NPV) of an investment in wind power is calculated from (4.20). This calculation is based on the assumption, that all generator types share the same turbine availability.  $Q$  is the number of full load hours per year. The discussion is restricted to the rated operation here, as the primary cause of  $\Delta\eta_N$ , i.e. the cryogenic cooling, is largely independent from load.

$$\Delta\text{NPV} \approx (Q \cdot P_{\text{mech},N} \cdot \Delta\eta_N) \cdot p' \cdot \sum_{k=1}^T (1+i)^{-k} \quad (4.20)$$

The increase in  $\Delta NPV$  due to a higher rated efficiency  $\eta_N$  is strongly dependent on the feed-in tariff  $p'$  and the interest rate  $i$ , Fig. 4.19. An increased rated efficiency by  $\Delta\eta_N = 1\%$  offers a margin of 0.5...0.9MEuro for an increase in CAPEX (50...90kEuro for  $\Delta\eta_N = 0.1\%$ ). This overcompensates the to date lower investment costs  $C_i$  of MgB<sub>2</sub> excited generators, Fig. 4.16 a). In view of the additional cost reduction potential, ReBCO conductors are considered to be more promising for the application in SC field windings of synchronous wind generators. Therefore, only ReBCO HTS field coils are analysed in the following. The difference in efficiency nearly compensates the higher  $C_i$  of ReBCO HTS generators compared to PM generators, Ch. 3, even at today's HTS cost level, see also Ch. 8.

#### 4.3.2. Design of an Electromagnetic Damper

In spite of the large magnetically effective air gap width, the possibly large content of stator field harmonics at stationary operation, mainly due to slotting, imply the requirement for an electromagnetic damper screen [196]. It ensures a reduction of the AC loss in the HTS winding to sufficiently low values, improves the generator's transient stability and leads to a reduction of the eddy current loss in massive cold rotor parts, which must be removed by the cryogenic cooling system. These requirements must be fulfilled at a limited loss in the damper screen and in the conductive cryostat wall. The damper screen is made from copper for its high electrical conductivity. Generally, the electrical conductivity can be increased by at least one order of magnitude, if the damper is cooled to cryogenic temperatures to  $T_{\text{damp}} < 30\text{K}$ , depending on the RRR. A preliminary analysis, based on analytical calculations for a 7MW generator with a three-phase stator winding ( $q = 1$ ,  $W/\tau_p = 1$ ), revealed that the eddy current loss in the damper screen at rated load increases towards lower  $T_{\text{damp}}$ , App. A.8.1. In spite of the much better screening properties, the cryogenic cooling of the damper is therefore not reasonable.

Therefore, a warm damper screen is exclusively considered in the following. A forced air cooling of the damper via the air gap is considered, which yields temperatures in the order of  $\vartheta_{\text{damp}} \approx 70 \dots 80^\circ\text{C}$  [O4].

Three modelling approaches with increasing degree of detail and accuracy from 1. to 3. are pursued:

1. *Semi-analytical multi-layer model*: The computation of the eddy current loss in



large FEM models is time consuming, already in case of 2D models: Eddy currents pose challenges in terms of sufficiently fine meshes, short time steps and long settling times. Therefore, the linear analytical model in Sec. 2.1 is used. Since saturation effects are important and must be incorporated, an equivalent stator current loading  $A_e$  is extracted from non-linear magnetostatic 2D FEM models, Fig. 4.20, which relieves the restrictions due to settling times and the approximation of time derivatives. The air gap field harmonics, causing the eddy current loss, comprise both stator field harmonics and rotor field modulations due to the slotted stator. In this sense, the origin of harmful field harmonics is geometrically located at the stator bore. To approximately reproduce the field configuration in the analytical model, it is suitable to impress the tangential magnetic field strength  $H_\varphi$  at the stator bore. For infinitely high stator permeability, (4.21) holds ( $A_e$ : electrical current loading as in Ch. 2).

$$H_\varphi(r = r_{si}^-, \varphi, t) = A_{e,z}(r = r_{si}, \varphi, t) \quad (4.21)$$

The tangential component  $H_\varphi$  is extracted from a series of magnetostatic 2D FEM simulations with the free software *FEMM*, Fig. 4.20. The magnetostatic model comprises an entire basic winding scheme corresponding to  $\varphi = 2\pi$  (el.). Several simulations for  $N_t$  time steps (e.g.  $N_t = 201$ ) within one fundamental period  $T_s = 1/f_s$  are carried out, where the rotor is successively moved. Four integer-slot and two fractional-slot three-phase stator windings are considered, Tab. 4.7. The tangential magnetic field strength  $H_\varphi$  is evaluated along the contour in Fig. 4.20 and is visualised in Fig. 4.22, 4.23 and 4.24 in a two-dimensional representation (stator frame of reference). The moving rotor poles, as well as the stationary modulation due to the stator slotting, can be observed.

2. *2D FEM time-stepping transient model (JMAG)*: The 2D FEM model is used to validate the semi-analytical calculation approach (1.). The model is used to investigate all six stator winding types, Tab. 4.7, for a selected damper screen thickness  $d_{\text{damp}}$ . Reduced effective conductivities are used in order to approximate the influence of 3D effects.
3. *3D FEM time-stepping transient model (JMAG)*: The 3D FEM model is used for a single generator design ( $q = 2$ ,  $W/\tau_p = 5/6$ ,  $d_{\text{damp}} = 7$  mm) in order to validate the 2D calculation approaches (1. and 2.). The very high computational effort ( $> 30$  days on 48 cores) impedes any variation of stator winding type or geometry.

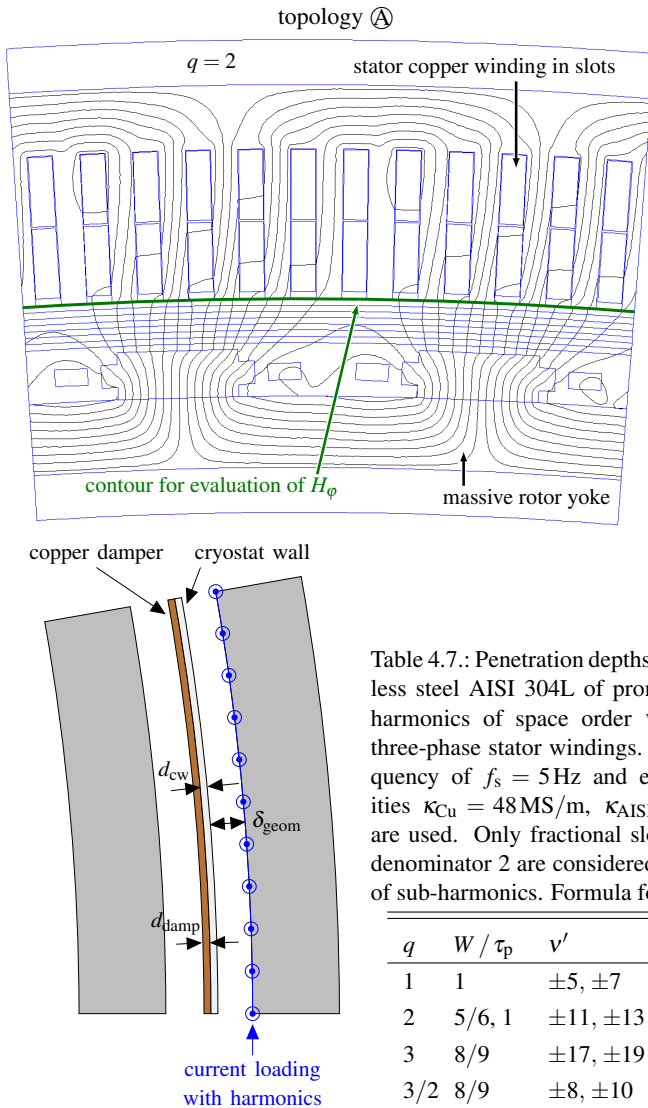


Figure 4.20.: Non-linear, magnetostatic model, implemented in the software *FEMM*, that is used for the calculation of an equivalent current loading  $A_e$  from  $H_\varphi$ , (4.21). The tangential magnetic field component  $H_\varphi$  is evaluated at the stator bore (green line). Field lines are shown for rated field and stator currents.

Table 4.7.: Penetration depths in copper and stainless steel AISI 304L of prominent air gap field harmonics of space order  $\nu'$  for six different three-phase stator windings. A fundamental frequency of  $f_s = 5\text{Hz}$  and electrical conductivities  $\kappa_{\text{Cu}} = 48\text{MS/m}$ ,  $\kappa_{\text{AISI304L}} = 1.31\text{MS/m}$  are used. Only fractional slot windings with  $q$ -denominator 2 are considered due to the absence of sub-harmonics. Formula for  $k^{(r)}$ : (2.51).

$q$	$W / \tau_p$	$\nu'$	$k^{(r)}$	$\frac{d_E^{(\text{Cu})}}{\text{mm}}$	$\frac{d_E^{(\text{SiSt})}}{\text{mm}}$
1	1	$\pm 5, \pm 7$	6	13.3	80
2	5/6, 1	$\pm 11, \pm 13$	12	9.4	57
3	8/9	$\pm 17, \pm 19$	18	7.7	47
3/2	8/9	$\pm 8, \pm 10$	9	10.8	66
5/2	4/5	$\pm 14, \pm 16$	15	8.4	51

Figure 4.21.: Geometry of the simplified analytical eddy current model, in which the numerically calculated current loading is impressed.

The approximation of an impressed current loading in the stator bore (model 1.) is reasonable, since the eddy currents are „resistance-limited“. Hence, the eddy current reaction field can be neglected. This corresponds to a unidirectional coupling. The penetration depths  $d_E$  of prominent air gap field harmonics of space order  $\nu'$  for the six different stator windings are listed in Tab. 4.7. Based on this and the  $A_e$ -spectra in Fig. 4.22, 4.23 and 4.24, following results are derived:

- Only a partial screening can be achieved for a reasonably limited copper screen thickness of  $d_{\text{damp}} \approx 5 \dots 10 \text{ mm}$ . The cryostat wall has minor influence on the electromagnetic screening.
- Short pitched ( $W/\tau_p < 1$ ) integer-slot windings with  $q > 1$  reduce low order field harmonics and greatly improve the overall screening, since the lowest relevant space orders  $\nu'$  belong to the first pair of well damped slot harmonics. The higher time order in the rotor frame of reference leads advantageously to a reduction of the skin depth.
- Significant „saturation harmonics“ occur, mainly with space order  $|\nu'| = 3$ . These are mainly caused by the rotor field saturation and exist therefore for all six considered stator windings. Due to the low space order of  $|\nu'| = 3$ , these harmonics in the stator current loading manifest also in a significant contribution to the air gap field,  $|B_{\nu'}| \sim |A_{e, \nu'}| / \nu'$ . The main contributions with  $k^{(s)} = -\nu' = \pm 3$  rotate synchronously and do not induce the rotating damper screen and cryostat wall. Besides, field harmonics with  $k^{(s)} = \nu' = \pm 3$  occur, which rotate asynchronously and contribute to the rotor eddy current loss.
- For fractional slot windings, two contrary effects occur in terms of loss producing harmonics: On one hand, higher numbers of slots per pole per phase  $q = 3/2, 5/2$  with  $q > 1$  advantageously increase the space orders  $\nu'$  of the slot harmonics. On the other hand, additional asynchronously rotating stator field harmonics with lower space orders contribute to the air gap field. This effect is only partially reduced by the short pitched coils.

### 4.3. Parametric Design Study of Partially Superconducting Direct Drive Generators

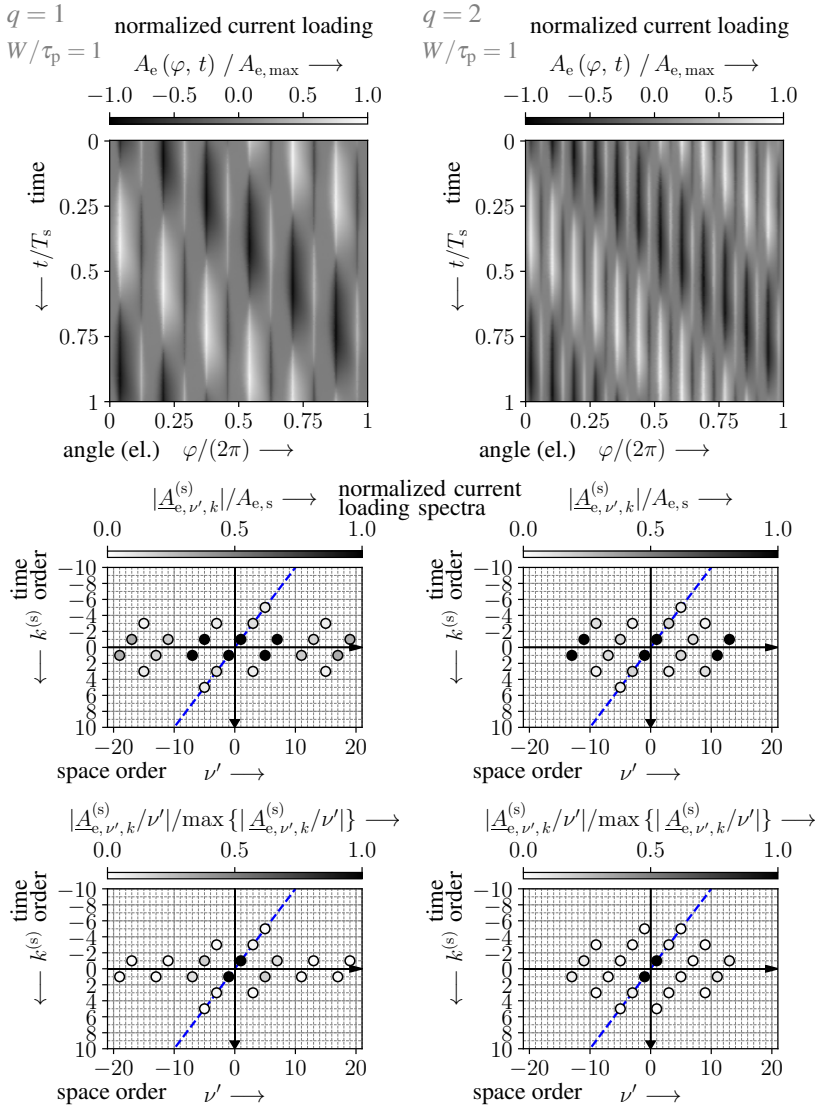


Figure 4.22.: Equivalent current loading, which is extracted from the 2D FEM model in Fig. 4.20. *Top*: Current loading in the original domain over one basic winding scheme and one electrical period. *Middle*: Normalized 2D spectrum of the current loading. *Bottom*: Normalized 2D spectrum of  $|A_{e,\nu',k}/\nu'| \sim |B_{\nu'}|$ . *Left*: Stator winding with  $m = 3$ ,  $q = 1$ ,  $W = \tau_p$ . *Right*:  $m = 3$ ,  $q = 2$ ,  $W = \tau_p$ . The dashed blue line indicates synchronously rotating harmonics. In this example, an all-iron topology  $\textcircled{A}$  is considered.

### 4.3. Parametric Design Study of Partially Superconducting Direct Drive Generators

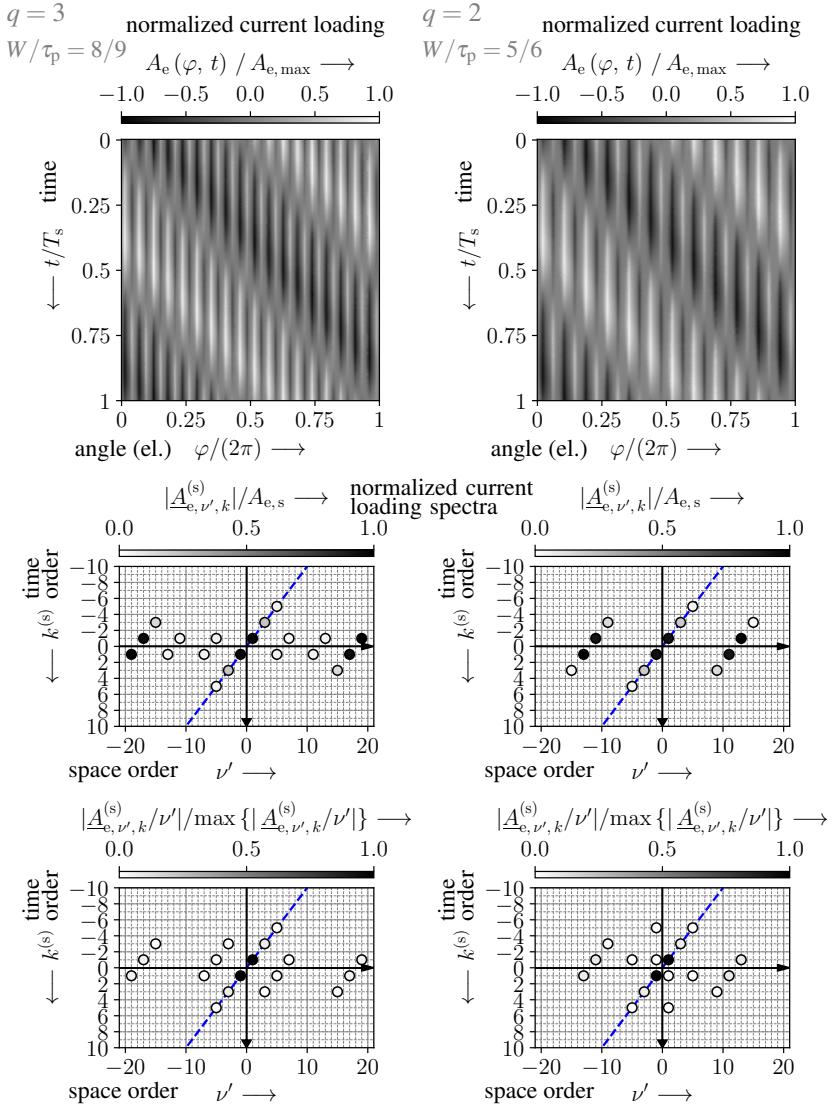


Figure 4.23.: As Fig. 4.22, but: *Left:* Stator winding with  $m = 3$ ,  $q = 3$ ,  $W/\tau_p = 8/9$ . *Right:*  $m = 3$ ,  $q = 2$ ,  $W/\tau_p = 5/6$ .

### 4.3. Parametric Design Study of Partially Superconducting Direct Drive Generators

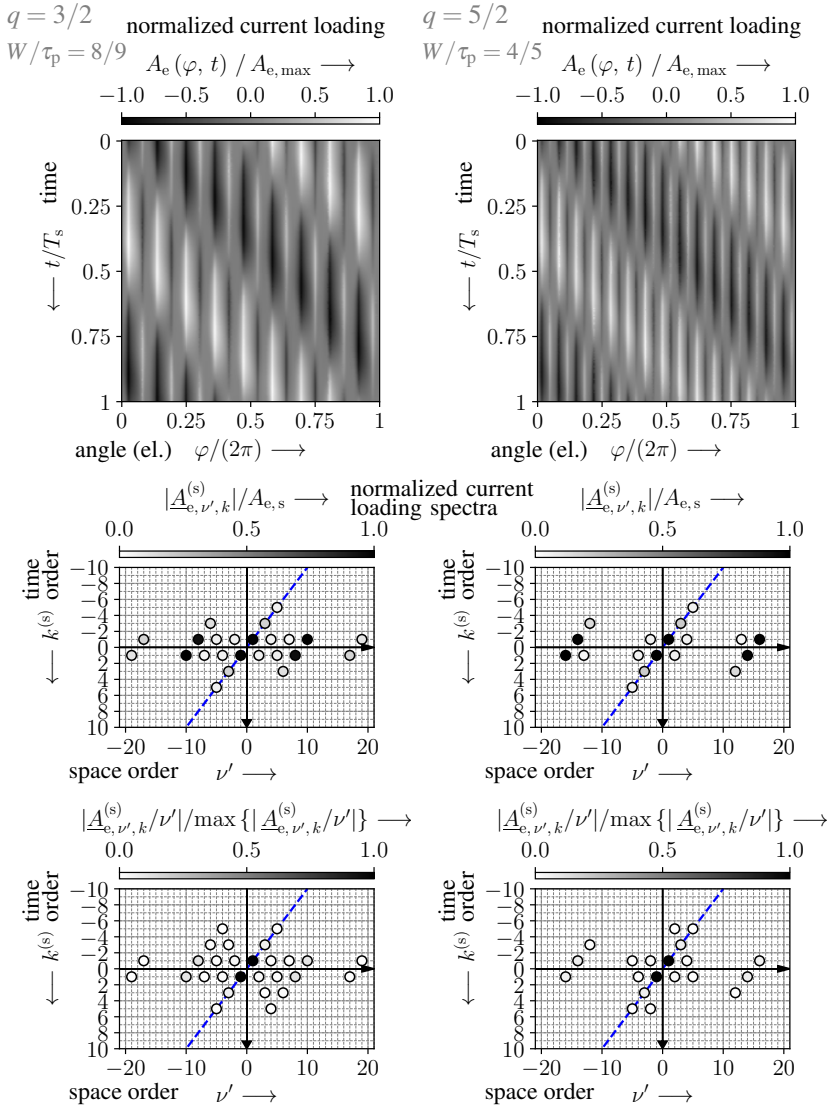


Figure 4.24.: As Fig. 4.22, but: *Left*: Stator winding with  $m = 3$ ,  $q = 3/2$ ,  $W/\tau_p = 8/9$ . *Right*:  $m = 3$ ,  $q = 5/2$ ,  $W/\tau_p = 4/5$ .

Since the AC loss in the field winding due to air gap field harmonics is very low, Sec. 4.3.4, only the eddy current loss in the rotor, i.e. the damper, the cryostat wall and the rotor

poles and yoke, is considered in the following. In order to validate the 2D eddy current loss calculation approach (models 1. and 2.), the numerically calculated losses from the 2D transient FEM model 2. are compared for exemplary generator variants with the 3D FEM model 3. for a generator with topology  $\textcircled{A}$ , Fig. 4.25. This all-iron topology is most susceptible for eddy current losses in the cold part. A warm damper, which is attached to the inner side of the cryostat wall („inner damper“) is considered. A good agreement for full and half rated stator current  $I_{\text{SN}}$  is found regarding the calculated eddy current loss in both warm and cold parts, Tab. 4.8. Based on this finding, the following analyses use and compare the 2D FEM model 2. (*JMAG*) and the semi-analytical model 1. (multi-layer model).

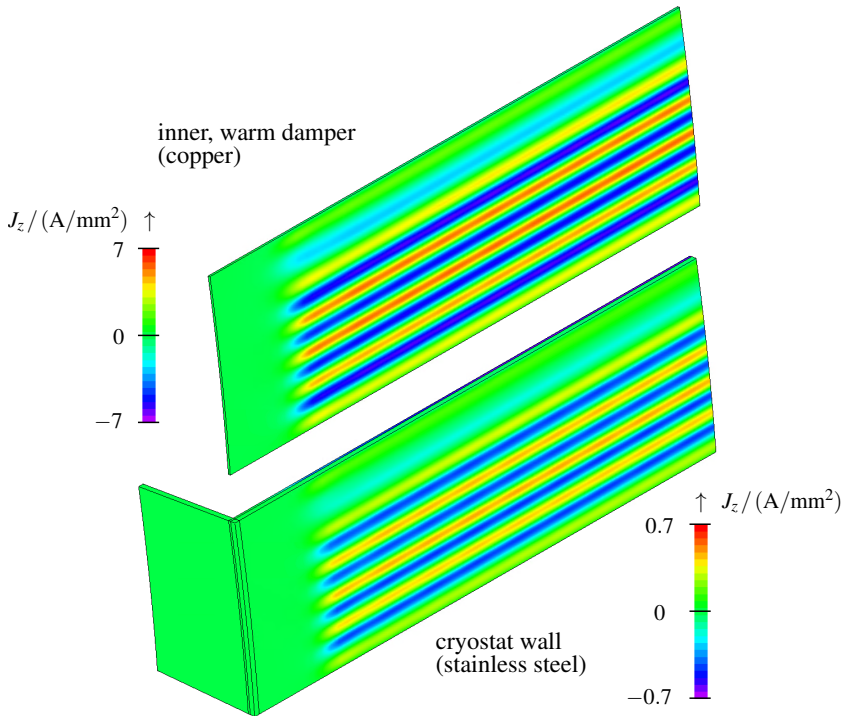


Figure 4.25.: Exemplary visualization of the numerically calculated  $z$ -component of the eddy current density  $J_z$  in the inner, warm damper screen and the cryostat wall for a 7 MW, 8.33 rpm direct drive generator at rated load (software: *JMAG*). This corresponds to variant  $\textcircled{A}$  in Tab. 4.9.

Table 4.8.: Comparison of the numerically calculated eddy current loss in the inner, warm damper, the cryostat wall and the cold rotor iron. Results are compared for 2D and 3D non-linear, transient models, both implemented in the software *JMAG*. Generator specifications:  $P_{el,N} = -7\text{MW}$ ,  $2p = 72$ ,  $V_g = 40\text{m}^3$ ,  $m = 3$ ,  $q = 2$ ,  $W/\tau_p = 5/6$ ,  $f_s = 5.41\text{Hz}$ ,  $n = 8.33\text{rpm}$ ,  $\delta_{geom} = 8\text{mm}$ ,  $d_{damp} = 3\text{mm}$ ,  $d_{cw} = 7\text{mm}$ . The results are calculated for variant  $\textcircled{A}$  in Tab. 4.9.

	load	3D FEM ( <i>JMAG</i> )	2D FEM ( <i>JMAG</i> )
eddy current loss in	$I_{sN}$	10833 W	11334 W (+4.6%)
copper damper $P_{d,Ft,damp}$	$I_{sN}/2$	8941 W	9216 W (+3.1%)
eddy current loss in	$I_{sN}$	4042 W	3979 W (-1.6%)
cryostat wall $P_{d,Ft,cw}$	$I_{sN}/2$	3445 W	3340 W (-3.0%)
eddy current loss in	$I_{sN}$	16.6 W	15.3 W (-7.9%)
cold rotor iron $P_{d,Ft,c}$	$I_{sN}/2$	8.1 W	8.0 W (-1.6%)

Before analysing the influence of the damper screen thickness, the 2D FEM model 2. is used to calculate the eddy current loss for four combinations of damper arrangements and stator winding types, i.e.  $\textcircled{A}$  -  $\textcircled{D}$  in Tab. 4.9. Here, a three-phase stator winding with  $q = 2$  and  $W/\tau_p = 5/6$  is considered to examine the influence of following design options:

- presence of ferromagnetic teeth in comparison to a stator air gap winding
- use of magnetic slot wedges
- attachment of the copper damper screen at the radially inner or outer side of the cryostat wall, i.e. „inner damper“ or „outer damper“ arrangement

The losses are calculated for rated load  $I_{sN}$  and no-load in order to quantify the rotor field related loss and the load-dependent loss. As the damper screen is in direct contact with the cryostat wall, only designs with warm damper are considered. The calculated losses are listed in Tab. 4.9 and the eddy current density distributions are shown in Fig. 4.26.



Table 4.9.: Numerically calculated (2D model, *JMAG*) eddy current loss in the copper damper, the stainless steel cryostat wall and the FeNi9 cold massive rotor parts for four partially superconducting generator variants. Results are listed for rated stator current and no-load operation at rated field current  $I_{fN}$ . All variants feature the same specifications:  $P_{el,N} = -7\text{MW}$ ,  $2p = 88$ ,  $\delta_{geom} = 8\text{mm}$ ,  $m = 3$ ,  $q = 2$ ,  $W/\tau_p = 5/6$ . The  $B(H)$ -relation of the magnetic slot wedge material *vetroferrit* is shown in App. A.3.1.4.

variant	load	$P_{d,Ft,damp}/\text{kW}$	$P_{d,Ft,cw}/\text{kW}$	$P_{d,Ft,c}/\text{W}$
Ⓐ stator winding in slots; non-magnetic slot wedge; inner, warm damper	$I_s = I_{sN}$	4.75	4.6	10.95
	$I_s = 0$	4.18	4.16	2.6
Ⓑ stator winding in slots; magnetic slot wedges; inner, warm damper	$I_s = I_{sN}$	0.99	0.70	9.15
	$I_s = 0$	0.31	0.26	0.71
Ⓒ stator air gap winding; inner, warm damper	$I_s = I_{sN}$	0.02	0.01	1.29
	$I_s = 0$	0	0	0.72
Ⓓ stator winding in slots; non-magnetic slot wedge; outer, warm damper	$I_s = I_{sN}$	109.50	1.59	9.32
	$I_s = 0$	99.77	1.44	3.56

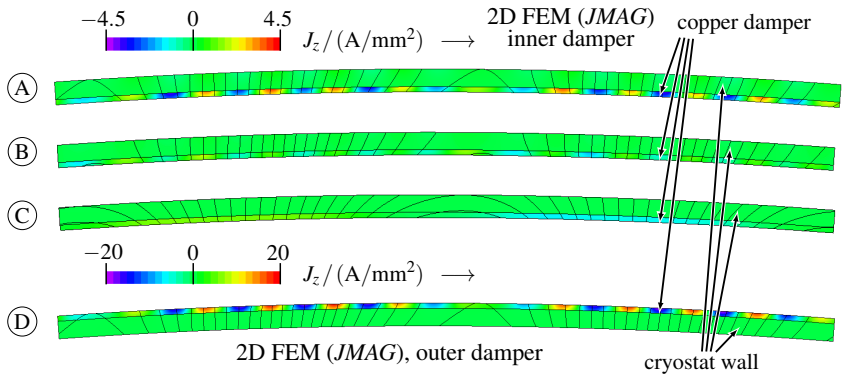


Figure 4.26.: Numerically calculated (2D model, *JMAG*) eddy current density in the inner, warm copper damper and the cryostat wall, made from stainless steel AISI 304L. Results are shown for the variants Ⓐ - Ⓓ in Tab. 4.9. As the maximum eddy current densities are by nearly one order of magnitude higher for the outer damper geometry, a separate color scheme is used.

The numerically calculated eddy current density distributions for the variants in Tab. 4.9 are visualized in Fig. 4.26. Following main findings are derived:

- The eddy current loss in warm and cold rotor parts for the three-phase stator winding in slots with  $q = 2$ ,  $W/\tau_p = 5/6$  is reasonably low in the inner damper arrangement, even without additional mitigation measures.
- In case of a slotted stator (variants ①, ② and ④ in Tab. 4.9), the slot pulsations due to the permeance modulation account for the major part of the total eddy current loss. Therefore, the eddy current loss at no-load  $I_s = 0$  is only little lower than for rated stator current  $I_{sN}$ .
- The lowest eddy current loss in warm and cold parts is produced for stator air gap windings (variant ③ in Tab. 4.9). In this case, the damper is not required for stationary operation but for the protection of the SC field winding during transients.
- For a stator winding in slots, an outer damper screen (variant ⑤ in Tab. 4.9) experiences significantly higher losses due to the proximity to the slotted stator. The eddy current loss in the cold part is however similar compared to an inner damper assembly.
- The use of magnetic slot wedges (variant ② in Tab. 4.9, non-linear material data of *vetroferrit* in App. A.3.1.4) is a suitable measure to reduce the eddy current loss in the copper damper and the cryostat wall. The eddy current loss in the cold parts is little changed compared to non-magnetic slot wedges.

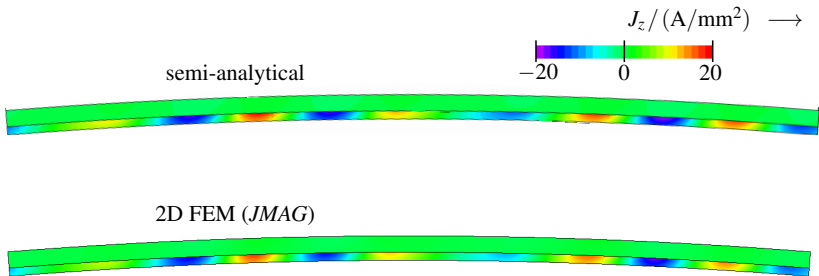


Figure 4.27.: Comparison of the analytically and numerically calculated eddy current densities in the inner, warm damper screen and the cryostat wall for an exemplary HTS excited 7 MW, 8.33 rpm direct drive generator with all-iron topology ① (software: *JMAG*).

Based on these findings, only the configuration with warm, inner damper, i.e. an attachment of the copper damper screen to the inner side of cryostat wall, is considered in the

following.

The influence of the inner copper screen thickness  $d_{\text{damp}}$  and the cryostat wall thickness  $d_{\text{cw}}$  on the eddy current loss is analysed by means of the semi-analytical model 1. in Fig. 4.21 for the stator windings in Tab. 4.7. The model is validated against the 2D FEM model 2. for exemplary generator variants, Fig. 4.27.

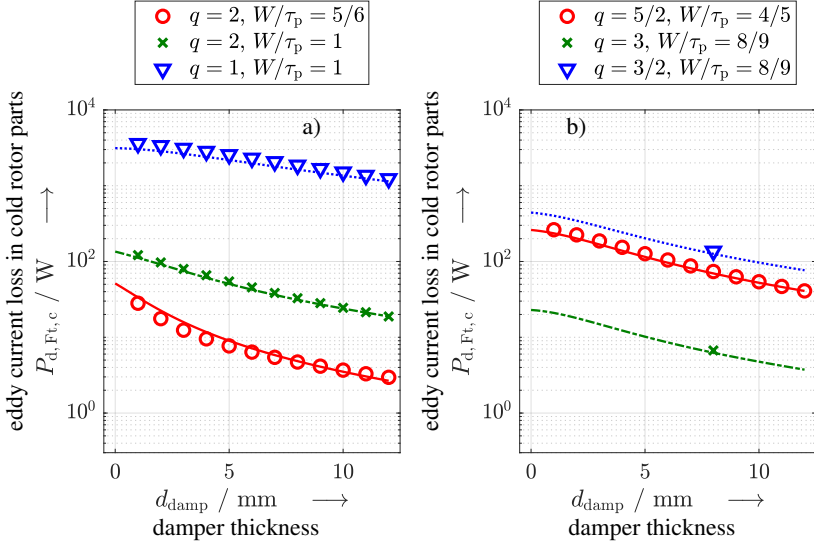


Figure 4.28.: Analytically and numerically (2D model, *JMAG*) calculated eddy current loss in the cold rotor iron parts (topology  $\textcircled{A}$ ) for a varied thickness of the warm, inner copper damper screen and fixed  $d_{\text{cw}} = 10\text{mm}$ . The lines represent the results obtained by the semi-analytical model, while the symbols represent exemplary numerical results. Stator windings in slots are considered: a) Integer slot stator windings with  $q = 1$  and  $q = 2$ , b) integer slot winding with  $q = 3$  and two fractional slot windings with  $q = 3/2$  and  $q = 5/2$ .

In the following, the eddy current loss in the warm parts is denoted by  $P_{d,Ft,h} = P_{d,Ft,\text{damp}} + P_{d,Ft,\text{cw}}$ , i.e. the sum of the loss in the warm damper screen  $P_{d,Ft,\text{damp}}$  and the cryostat wall  $P_{d,Ft,\text{cw}}$ . The eddy current loss in the cold parts is denoted by  $P_{d,Ft,c} = P_{d,Ft,\text{rp}} + P_{d,Ft,\text{yr}}$ , i.e. the sum of the loss in the conductive, ferromagnetic FeNi9 rotor poles  $P_{d,Ft,\text{rp}}$  and the FeNi9 rotor yoke  $P_{d,Ft,\text{yr}}$  (all-iron topology  $\textcircled{A}$ ). The calculated eddy current loss, Fig. 4.28 - 4.30, points to following main findings:

- The eddy current loss in the cold parts varies by up to 2.5...3 orders of magnitude for the same damper thickness, depending on the stator winding type.
- The reduction of the eddy current loss in cold parts with increasing  $d_{\text{damp}}$  differs among the stator windings due to the different relevant space orders  $v'$ . The largest reduction is achieved for the short pitched winding with  $q = 2$ ,  $W/\tau_p = 5/6$ .
- The eddy current loss in the warm parts, i.e. the damper and the cryostat wall, generally increases for  $d_{\text{damp}} \leq 4$  mm, but changes only little for thicker damper screens. It varies by two orders of magnitude among the windings in Tab. 4.7 and decreases monotonically towards higher  $q$ . As the eddy current loss due to the slot pulsation dominates, reasonably low losses  $\approx 10 \dots 15$  kW can only be achieved with  $q \geq 2$ .
- The eddy current loss in the cryostat wall is only little affected by its thickness, Fig. 4.30. However, the loss in the damper screen increases by a factor of up to 4...5, as the thickness of the cryostat wall is reduced. This effect reflects the high sensitivity of the loss in the damper with respect to its distance to the slotted stator.

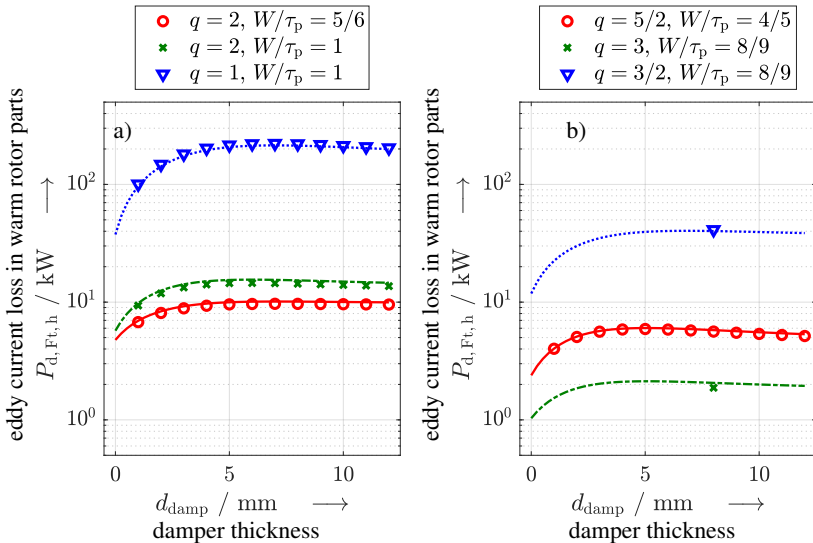


Figure 4.29.: As Fig. 4.28 but for the eddy current loss in the warm, inner damper screen and in the cryostat wall.

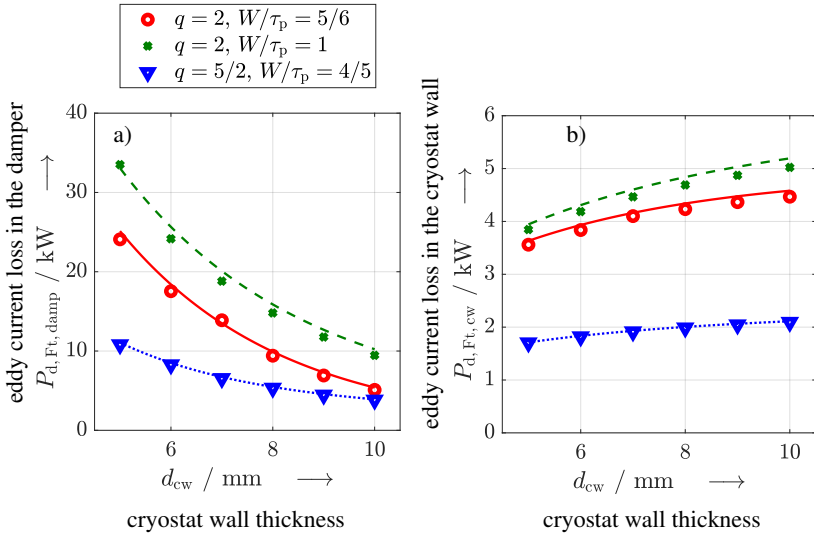


Figure 4.30.: As Fig. 4.29 but for fixed  $d_{\text{damp}} = 5$  mm and varied thickness of the cryostat wall. The losses are separately shown for a) the warm, inner damper screen and b) the cryostat wall.

### 4.3.3. Selection of the AC Stator Winding

All considered stator windings in Tab. 4.7 do not excite any sub-harmonic stator field waves with  $\nu < p$  and wave lengths  $\lambda_\nu > 2\tau_p$ , which more easily reach out to the cold rotor and build up a larger magnetic flux, inducing eddy currents. The use of fractional slot windings, e.g. concentrated windings, is therefore problematic, if the basic winding scheme covers more than two poles. In case of a stator air gap winding, there is no need for short-pitched coils regarding the mitigation of air gap field harmonics. The only criterion consists in a high fundamental winding factor, which is unity and, hence, maximum for  $q = 1, W = \tau_p$ . In case of a stator winding in slots, following criteria must be fulfilled:

- low eddy current loss in cold and warm parts, Sec. 4.3.2,
- high fundamental winding factor  $k_{w,1}$  in order to reduce the required excitation MMF and consequently the required amount of HTS,
- low torque ripple and low content of harmonics of the induced stator voltage.

### 4.3. Parametric Design Study of Partially Superconducting Direct Drive Generators

The fundamental winding factors are listed for the considered stator windings in Tab. 4.10. The numerically calculated torque ripple (2D model, *JMAG*) and the eddy current loss for exemplary generator variants are summarized in Tab. 4.11. The slot plans and analytically calculated spectra of the current loading are shown in App. A.6. The exemplary spectra of the electromagnetic torque and the no-load voltage for a generator with all-iron topology  $\textcircled{A}$  are also compared in App. A.6 for the stator windings in Tab. 4.7.

Table 4.10.: Fundamental winding factors of considered three-phase stator windings. The slot harmonics with lowest space order, which are critical regarding rotor eddy current losses, are listed.

$q$	$W/\tau_p$	$k_{d,1}$	$k_{p,1}$	$k_{w,1}$	$( K'_v /v')/ K'_1 $
1	1	1	1	1	0.19 ( $v' = \pm 5$ )
2	1	0.966	1	0.966	0.09 ( $v' = \pm 11$ )
2	5/6	0.966	0.966	0.933	0.09 ( $v' = \pm 11$ )
3	8/9	0.960	0.985	0.945	0.06 ( $v' = \pm 17$ )
3/2	8/9	0.960	0.985	0.945	0.12 ( $v' = \pm 8$ )
5/2	4/5	0.957	0.951	0.910	0.07 ( $v' = \pm 14$ )

A reasonable AC loss in cold iron parts of at most 10 W can only be achieved with two windings, i.e.  $q = 2$ ,  $W/\tau_p = 5/6$  and  $q = 3$ ,  $W/\tau_p = 8/9$ . For the  $q = 2$  winding, a copper screen thickness of at least  $d_{\text{damp,min}} = 4$  mm is required, while the  $q = 3$  winding requires at least a thickness of  $d_{\text{damp,min}} = 5$  mm, Fig. 4.28.

Table 4.11.: Numerically calculated (2D model, *JMAG*) torque ripple and eddy current loss in warm and cold parts at rated load and excitation for the considered stator windings. An exemplary generator with all-iron topology is considered. A warm, inner damper with a thickness of  $d_{\text{damp}} = 8$  mm is considered.

$q$	$W/\tau_p$	$(M_{pp}/2)/\bar{M}$	$P_{d,\text{Ft,h}}/\text{kW}$	$P_{d,\text{Ft,c}}/\text{W}$
1	1	4.71%	221.2	1864.7
2	1	0.64%	14.3	32.8
2	5/6	0.77%	9.7	4.7
3	8/9	0.17%	5.6	6.7
3/2	8/9	0.27%	41.2	136.6
5/2	4/5	0.57%	1.9	73.8

Among these alternatives, the winding with  $q = 3$  is superior with regard to a higher fundamental winding factor, a lower amplitude of the stator slot harmonics as well as a low torque ripple. The advantages of the  $q = 2$  winding consist in a reduced manufacturing effort due to the lower number of stator coils and in a slightly lower eddy current loss in the cold parts. Therefore, the  $q = 2$ ,  $W/\tau_p = 5/6$  winding is selected for all further analyses on partially superconducting generators with a stator winding in slots.

For this stator winding, the influence of the current displacement is analysed for an exemplary 7 MW generator variant with characteristics according to Tab. 4.12. The open slots, together with the highly saturated iron teeth, lead to a considerable penetration of the rotor field into the slots, Fig. 4.31. This causes additional eddy current losses in the slot conductors, which are not included in an analytical treatment of the current displacement.

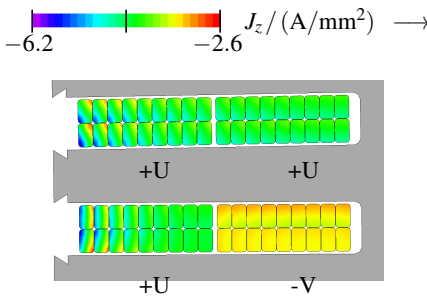


Figure 4.31.: Current density distribution  $J_z$  in the stator winding of a partially superconducting generator with a detailed conductor model at rated stator current and rated excitation (software: *JMAG*).

The eddy current loss due to the penetrating rotor field is nearly load-independent and occurs therefore already at no-load, Tab. 4.12, with an increase of losses by  $k_m \approx 1.033$  (eq. 2.121) or  $\approx 2.16$  kW, Tab. 4.13. Generally, the efficiency decrease due to the total current displacement effect in the stator slot conductors is in the order of  $\approx 0.15\%$  for the considered direct drive generators. The comparison of the analytically and numerically calculated stator *ohmic* losses in the conductors, including the load-dependent current displacement, reveals a small deviation of less than 1%. This corresponds to a difference in the calculated efficiency of about 0.035%. Since this deviation is sufficiently small, the analytical formulas in Sec. 2.4 are applied for further analyses.

Table 4.12.: Specifications of the stator winding in Fig. 4.31. The DC stator resistance is calculated analytically.

$I_{sN}$	6180 A
$J_{Cu}$	3.5 A/mm <sup>2</sup>
$f_s$	7.33 Hz
$a$	22
$N_c$	9
$n_{T,n}$	2
$l_{bs}$	446 mm
$\kappa_{Cu, 100^\circ C}$	44.269 MS/m
$A_{Cu,T}$	43.99 mm <sup>2</sup>
$k_m$	1.033
$R_{s,DC}$	2.661 m $\Omega$

 Table 4.13.: Comparison of the analytically and numerically (*JMAG*) calculated loss in the stator winding of a 7MW partially superconducting generator with specifications in Tab. 4.12 and all-iron topology (A). Losses without current displacement, based on  $R_{s,DC}$ :  $P_{d,Cu} = 304.9$  kW.

	analytical	2D FEM
rated power	312.22 kW	314.67 kW
$(I_{fN}, I_{sN})$		(+0.78%)
no load	0	2.16 kW
$(I_{fN}, I_s = 0)$		
no excitation	312.22 kW	313.09 kW
$(I_f = 0, I_{sN})$		(+0.28%)
$R_{s,AC}$	2.725 m $\Omega$	2.746 m $\Omega$

#### 4.3.4. AC Loss in the DC Field Winding

The AC loss in the SC field winding is caused by asynchronously rotating air gap field harmonics. It is generally small and can be neglected. To validate the neglect of this loss component for the thermal calculations, Sec. 4.2.4, and for the sizing of the cryogenic cooling system, the AC loss in the double layer HTS field winding with upper layer (UL) and lower layer (LL) is calculated with a 2D FEM model in the coupled *H-A*-formulation, Fig. 4.32. These results are validated against a model with *T-A*-formulation with good agreement. The calculation of very small loss quantities is generally difficult, since a superimposed loss contribution occurs, which is caused by the up-ramping of the excitation current from zero to the final DC value in the beginning of the simulation. An equilibration run with artificially increased SC resistance, but the same  $\vec{B}$ -dependent lift factor  $L(\vec{B})$  helps to damp this „switch-on“ transient and to reduce the settling times until the steady state superconducting current distribution is attained. Thereafter, an evaluation run with the actual SC resistance characteristic is used for the AC loss calculation.



A homogenized, equivalent coil model is used for the HTS field winding, Sec. 2.2.4, with  $n_{\text{sec}} = 11$  regions per layer (UL or LL) and coil side ( $\oplus$  or  $\ominus$ ), and  $d_T = h_{\text{sec}}/\Delta_{\text{sec}} = 1$ .

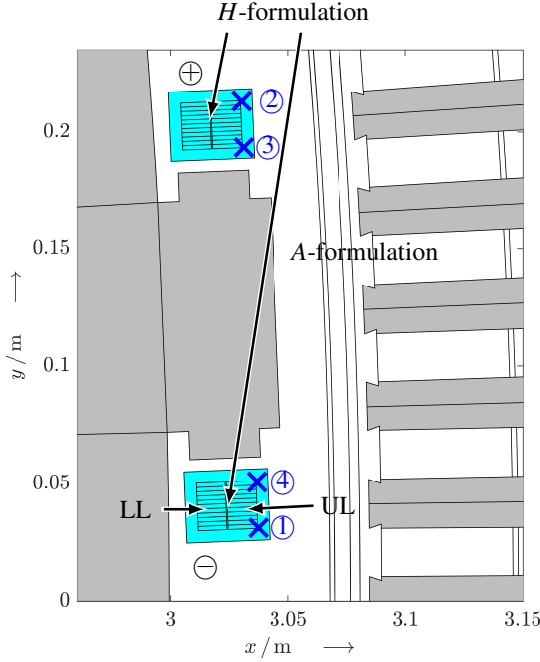


Figure 4.32.: 2D model of an exemplary HTS excited 7 MW, 8.33 rpm generator with all-iron topology  $\textcircled{A}$  in *COMSOL Multiphysics* for the calculation of the AC loss in the SC field winding. ① - ④ enumerate points, for which the magnetic flux density is evaluated.  $\oplus$  and  $\ominus$  are used to label the coil sides. Stator winding:  $m = 3$ ,  $q = 2$ ,  $W/\tau_p = 5/6$ ,  $2p = 76$ ,  $f_s = 5.3 \text{ Hz}$ .

Table 4.14.: Numerically calculated (*H-A*-formulation, *COMSOL Multiphysics*) AC loss in the GdBCO field winding for different three-phase stator windings. Results are listed for rated stator current  $I_{sN}$  at stationary operation. No damper screen is modelled as a worst-case scenario in terms of AC losses.

stator winding	$P_{d,AC,f}$
$q = 1, W/\tau_p = 1$	0.24 W
$q = 2, W/\tau_p = 1$	0.52 mW
$q = 2, W/\tau_p = 5/6$	0.04 mW
$q = 3, W/\tau_p = 8/9$	0.78 mW
$q = 3/2, W/\tau_p = 8/9$	6.96 mW
$q = 5/2, W/\tau_p = 4/5$	6.22 mW

Table 4.15.: Numerically calculated (*H-A*-formulation, *COMSOL Multiphysics*) AC loss in the GdBCO field winding for different magnitudes of stator current harmonics with time orders  $k = -5, +7$ . Results are listed for  $m = 3$ ,  $q = 2$ ,  $W/\tau_p = 5/6$ .

scaling factor $s$	$P_{d,AC,f}$
1	0.4 mW
2	59.8 mW
3	0.8 W
5	7.5 W
10	208.0 W

The calculated AC loss in the HTS field winding for the all-iron topology  $\textcircled{A}$  is summarized in Tab. 4.14 for the different stator windings, without damper screen as a worst-case scenario. The instantaneous loss  $P_{d,AC,f}(t)$  is shown in Fig. 4.33 a). The time-averaged loss per layer (LL, UL), coil side ( $\oplus$ ,  $\ominus$ ) and all regions  $i = 1, \dots, 11$  (homogenized coil, Sec. 2.2.4) are shown in Fig. 4.33 b). For all considered stator windings, Tab. 4.14, this AC loss is negligibly small compared to the typical cryogenic heat load, Sec. 4.2.4. Similar to the eddy current loss in the cold rotor iron in Tab. 4.9, the lowest AC loss in the HTS occurs for  $q = 2$ ,  $W/\tau_p = 5/6$ , Tab. 4.14.

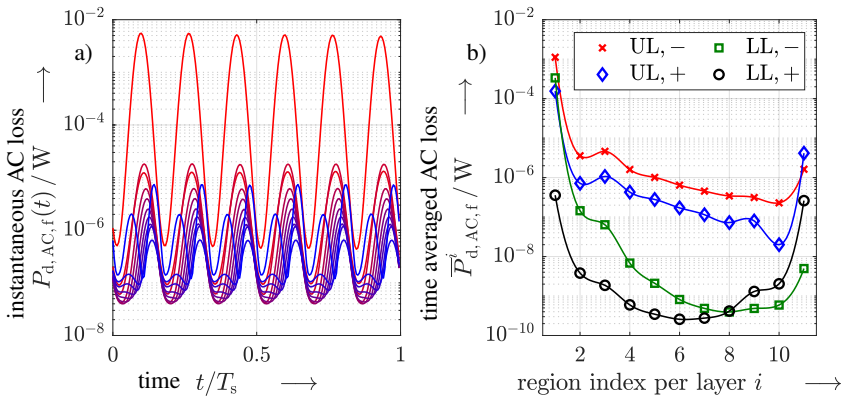


Figure 4.33.: a) Numerically calculated instantaneous AC loss power  $P_{d,AC,f}(t)$  per pole in the HTS winding for a stator winding with  $q = 1$ ,  $W/\tau_p = 1$ ,  $T_s = 0.19$  s at rated load. The generator features the all-iron topology  $\textcircled{A}$ . The loss is shown for all regions of the homogenized coil model in the UL of coil side  $\ominus$ . b) Layer and region resolved, time averaged AC loss per pole for the same exemplary generator. (software: *COMSOL Multiphysics*)

The flux density in the most exposed points in the field winding are shown in Fig. 4.34 ( $q = 1$ ,  $W = \tau_p$ ). The maximum amplitudes of the perpendicular and parallel slot-frequent ( $f = n \cdot Q \approx 31.7$  Hz) AC fields are in the order of  $\hat{B}_\perp \approx 35$  mT and  $\hat{B}_\parallel \approx 37.5$  mT. One major reason for the low AC loss consists in the high margin with respect to the critical current of  $I_c/I_f = 1.7$ , while higher AC losses are expected as this ratio approaches  $I_c/I_f \approx 1$ . The calculated AC loss in presence of significant stator current harmonics (scaling factor  $s = 1$ , App. A.5) is also low, i.e.  $P_{d,AC,f} \approx 0.4$  mW, Tab. 4.15 (all-iron topology  $\textcircled{A}$ , stator winding with  $q = 2$ ,  $W/\tau_p = 5/6$ , six-step mode at rated stator current). Details are discussed in App. A.5.

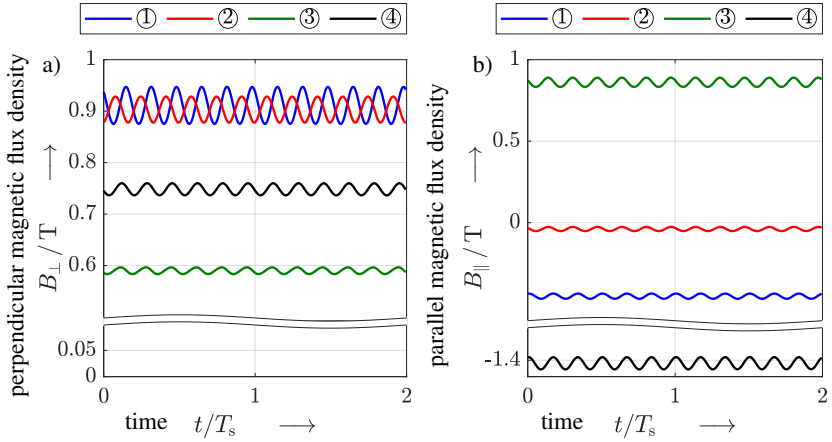


Figure 4.34.: Parallel and normal component of the calculated flux density for points ① - ④ in Fig. 4.32. A stator winding with  $q = 1$ ,  $W/\tau_p = 1$  for all-iron topology ④ is considered as worst case scenario. The AC field ripple features slot frequency  $f = n \cdot Q_s = 6 \cdot f_s$ . ( $f_s = 5.3$  Hz, no damper screen as worst case scenario)

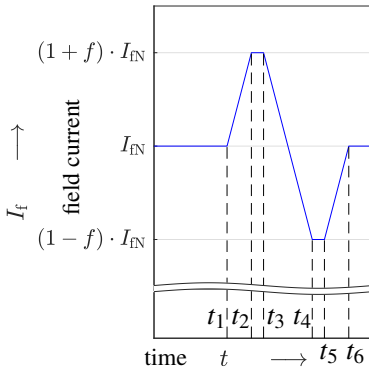


Figure 4.35.: Schematic of the considered field current variation. The deviations from  $I_{FN}$  are specified as fraction  $f$  of the rated field current. The steepness of the current ramps is set with  $t_i$ ,  $i = 1, \dots, 6$ .

Table 4.16.: Calculated, maximum AC loss power in the field winding of a 7MW partially superconducting direct drive generator for different field current ramps according to Fig. 4.35.

$f \downarrow$	$d_t I_f / (\text{A/s}) \rightarrow$			
	10	50	100	500
0.05	6.0 mW	6.0 mW	6.0 mW	6.0 mW
0.10	1.6 W	2.9 W	3.6 W	4.7 W
0.15	17.8 W	41.6 W	56.4 W	113.5 W
0.20	42.0 W	178.2 W	310.0 W	805.1 W

The AC loss for varying  $I_f$  is of interest regarding transients after faults and regarding

an intentional field variation, i.e. for minimum loss operation. In order to quantify the AC loss in a general scheme, the variation of  $I_f$  in Fig. 4.35 is considered. The deviation from the rated excitation current is expressed by the fraction  $f > 0$ . The steepness of the current ramps is varied by specifying the rise times  $t_i, i = 1, \dots, 6$ . The maximum loss power occurs after the first ramp-up of the SC current, Fig. 4.36, primarily at the outer edges of the SC field winding stack, Fig. 4.37. Tab. 4.16 summarizes the maximum loss power values. For variations  $\Delta I_f \lesssim 0.1 \cdot I_{fN}$ , the AC loss is low in the entire considered range of slopes  $d_t I_f \leq 500 \text{ A/s}$ .

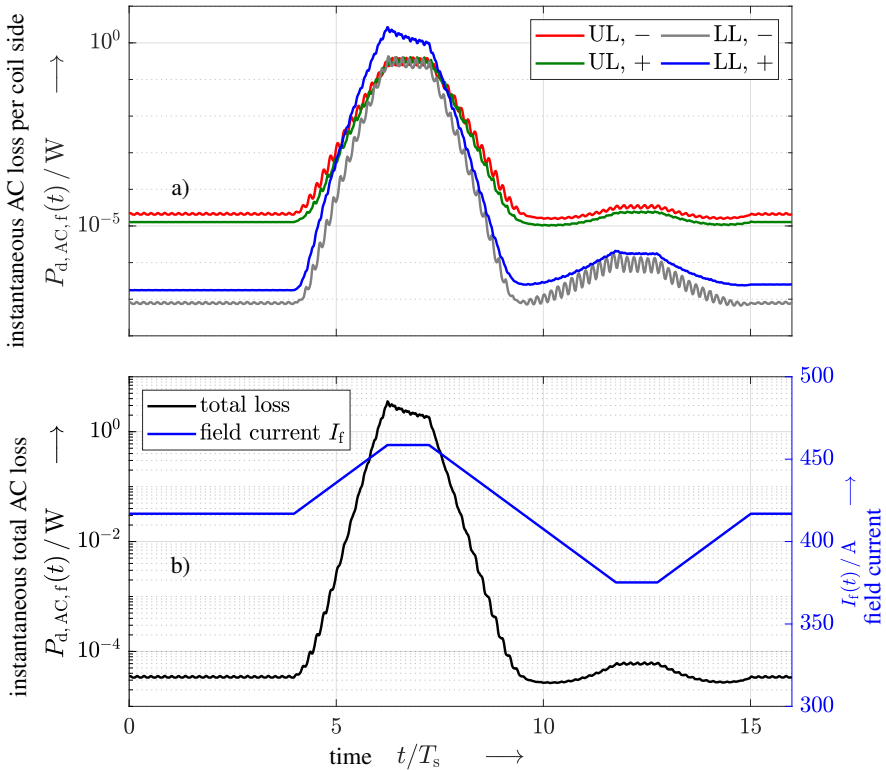


Figure 4.36.: a) Calculated instantaneous total loss power (all  $2p = 76$  poles) in the two layers (LL, UL) and in the two coil sides ( $\oplus$ ,  $\ominus$ ) during a variation of the field current by  $f \cdot I_{fN} = 0.1 \cdot I_{fN} \approx 42 \text{ A}$  with a ramp of  $d_t I_f = 100 \text{ A/s}$ . b) Total calculated AC loss power (all  $2p = 76$  poles) and excitation current for the same scenario.

The maximum AC loss exceeds  $P_{d,AC,max} \approx 40\text{ W}$  for variations  $f \geq 0.15$  with current ramps  $d_t I_f \geq 50\text{ A/s}$  and for variations  $f \geq 0.2$ , irrespective of the positive or negative slope. This loss power is in the order of 10% of the total cryogenic heat load, Sec. 4.2.4, with a certain influence on the operating temperature. However, if this heating occurs only over short time spans, e.g. during transients after short circuit faults, Ch. 6, no significant temperature increase occurs. The calculated loss power values in Tab. 4.16 constitute upper limits to the maximum periodic variation of the excitation current, i.e. as a reaction to wind speed turbulences.

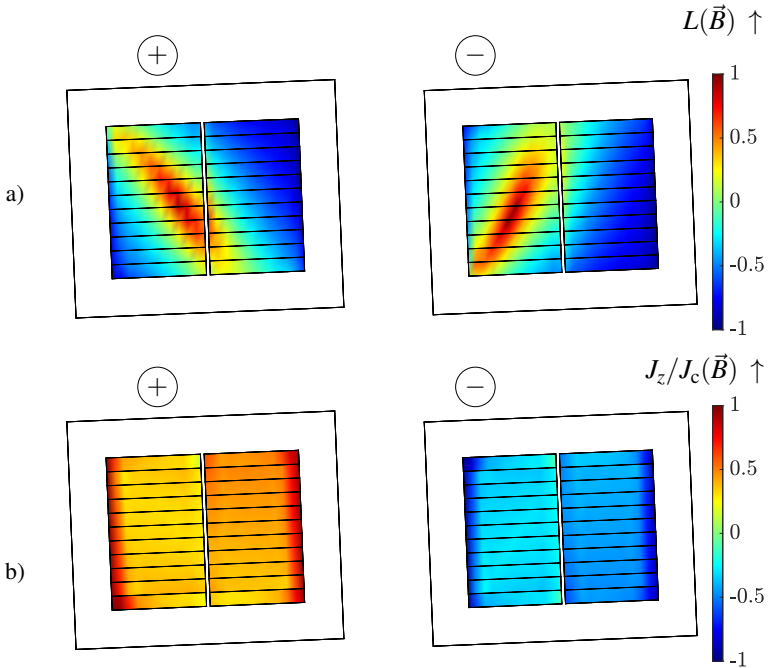


Figure 4.37.: a) Varying lift factor  $L = I_c(\vec{B})/I_c(B = 0)$  in both coil sides of the field winding at time instant  $t_2$  after a ramp with  $f = 0.2$  and  $d_t I_f = 10\text{ A/s}$  (calculated with a homogenized coil model, Fig. 4.32). b) Ratio between the superconducting current density  $J_z$  and the critical current density  $J_c$  in the two coil sides ( $\oplus$ ,  $\ominus$ ) for the same scenario as in a).

## 5. Numerical Optimization of HTS Excited Direct Drive Wind Generators

Based on the preliminary analyses in Ch. 4, the multi-objective numerical optimizations for different iron topologies, Sec. 5.1, different geometrical constraints, Sec. 5.2, and different ReBCO tape materials, Sec. 5.3, define the scope of this chapter. Among the large set of designed generator variants, exemplary designs are selected and described in Sec. 5.4.

The considered 7 MW, 8.33 rpm HTS synchronous generator designs are generated during a numerical optimization by means of a genetic algorithm (GA), separately for each of the topologies  $\textcircled{A}$  -  $\textcircled{D}$  in Fig. 4.4, each set of fixed specifications  $T_{\text{HTS}}$ ,  $V_g$ , and for two different HTS tapes, Tab. 5.1. A genetic algorithm allows to explore a high-dimensional variable space efficiently, which is not possible with a conventional grid search. The eight non-dimensional parameters  $f_i$  in Sec. 4.2.1 represent the optimization variables, while the investment costs  $C_t$  and the active generator mass  $m_{\text{act}}$  (excluding inactive parts like frame structures) serve as competing objectives. The price assumptions, Tab. 5.2, are based on manufacturer information or publicly available data.

Table 5.1.: Fixed generator specifications for the different optimization runs.

$P_{\text{el},N}$	-7 MW
$U_N$	690 V
$n_N$	8.33 rpm
$T_{\text{HTS}}$	20 K, 25 K, 30 K
$V_g$	25 m <sup>3</sup> , 30 m <sup>3</sup> , 35 m <sup>3</sup> , 40 m <sup>3</sup>
$d_{\text{so}}^{\text{max}}$	6.5 m
operation	MTPA
HTS tape	<i>THEVA TPL2100</i> (i), <i>Fujikura FESC-SCH12</i> (ii)
topology	$\textcircled{A}$ - $\textcircled{D}$ (Fig. 4.4)

Table 5.2.: Specific prices of material and components, based on information provided by manufacturers (s.f.: self field)

tape (i) (77 K, s.f.)	100 €/ (kA · m)
tape (ii) (77 K, s.f.)	250 €/ (kA · m)
AC / AC converter	30 €/kVA
cold head	25000 €/unit
copper	13.5 €/kg
stainless steel	3 €/kg
steel sheets	3 €/kg
FeNi9	3 €/kg
G10CR	15 €/kg

The pre-implemented GA `gamultiobj()` of the commercial software *MATLAB* is used with parameters `ParetoFraction=0.35` and `CrossoverFraction=0.8`. This is a variant of a controlled non-dominated sorting genetic algorithm (NSGA-II), which was originally developed by *Deb* et al. [46]. Individual designs are selected based on their rank, while the diversity among the selected individuals is maintained by including a distance function during the selection process.

### 5.1. Comparison of Iron Topologies

The topologies  $\textcircled{A}$ ,  $\textcircled{B}$ , Fig. 4.4, are compared for the same volume  $V_g = 40\text{m}^3$ , the same cryogenic operating temperature  $T_{\text{HTS}} = 30\text{K}$  of the GdBCO tape, manufactured by *THEVA*, and a maximum stator outer diameter of  $d_{\text{so}}^{\text{max}} = 6.5\text{m}$ . Topology  $\textcircled{C}$  is considered for the same specifications, except for a reduced operating temperature of the HTS winding to  $T_{\text{HTS}} = 20\text{K}$ . This choice is motivated by the strongly increased excitation requirement.

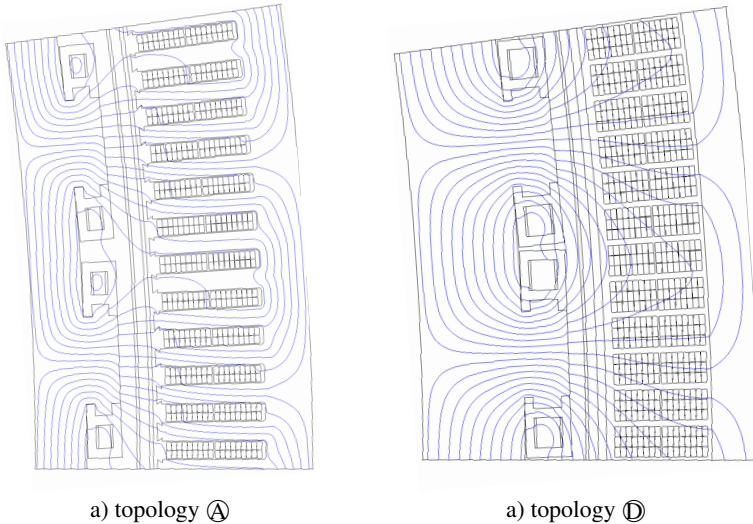


Figure 5.1.: a) Calculated field lines per pole pair at rated load  $I_{\text{SN}}$  and rated excitation  $I_{\text{FN}}$  for an exemplary 7MW generator, Tab. 5.1), featuring topology  $\textcircled{A}$  ( $T_{\text{HTS}} = 30\text{K}$ ,  $V_g = 40\text{m}^3$ ). b) As a), but for topology  $\textcircled{D}$  in Fig. 4.4 ( $T_{\text{HTS}} = 20\text{K}$ ,  $V_g = 25\text{m}^3$ ). (software: *JMAG*)

For topology  $\textcircled{D}$  with stator air gap winding and consequently increased stator current loading  $A_s$ , a smaller volume  $V_g = 25\text{m}^3$ , but also  $d_{\text{so}}^{\text{max}} = 6.5\text{m}$  are considered. In this

## 5.1. Comparison of Iron Topologies

case, the EuBCO tape from *Fujikura* is used, operated at  $T_{\text{HTS}} = 20\text{K}$ . This choice is motivated by the better in-field performance as a reaction to the increased inter-pole stray flux for topology ④, Fig. 5.1. The glass fibre-reinforced plastic G10CR is used as material for non-magnetic rotor parts (topologies ② and ③).

In all four cases, the required total HTS tape length  $l_t$  increases with decreasing generator active mass, Fig. 5.2 b), since the heavy iron parts with large cross section reduce the required excitation MMF per pole  $\Theta_{f,p}$ .

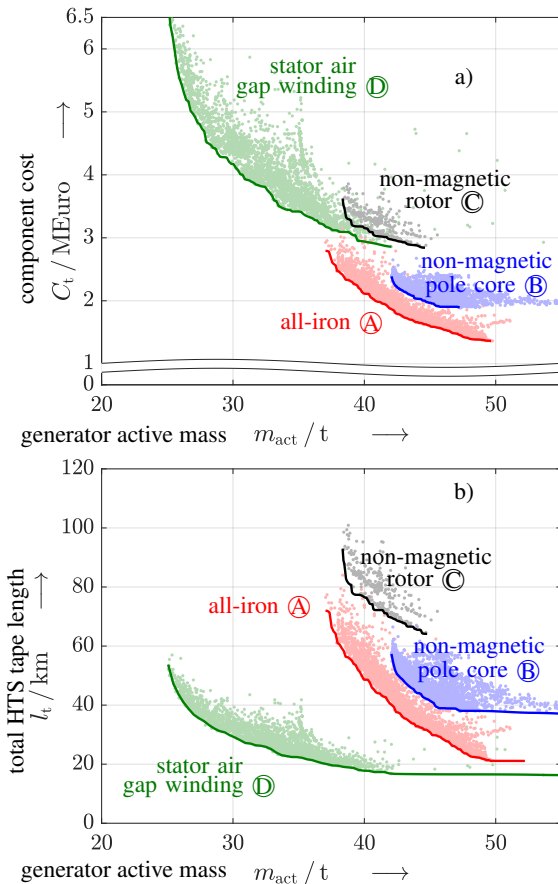


Figure 5.2.: Numerically calculated generator variants for different topologies ① - ④, Fig. 4.4. The lines represent *Pareto* efficient variants. a) Component cost  $C_t$ : generator material + fully-rated converter + cryogenic cooling system, versus generator active mass  $m_{\text{act}}$ . b) Total tape length  $l_t$  (tape width  $w_t = 12\text{mm}$ ) versus generator active mass  $m_{\text{act}}$ . Not all variants are plotted for a better visibility.

The comparison between topologies ① - ③ with the same HTS tape shows that topology



Ⓐ with ferromagnetic rotor pole core and rotor yoke dominates the generator designs with partially or completely non-magnetic rotor, Fig. 5.2 a). The mass reduction for Ⓑ, Ⓒ due to the lighter composite material comes at the cost of a disproportionate increase in the required HTS material amount.

A similar result has been reported in [110] for a comparison of single designs. The limited space in the rotor inter-pole gap restricts geometrically the design options for the topologies Ⓑ and Ⓒ, which require larger excitation coils. Moreover, the lack of flux guidance in case of non-magnetic rotor poles Ⓑ increases the rotor inter-pole stray flux, which additionally loads the rotor iron yoke magnetically. The rotor yoke height  $h_{yr}$  must be accordingly increased in order to achieve the specified power.

The variants with stator air gap winding topology Ⓓ dominate the other designs Ⓐ - Ⓒ regarding a reduced active mass at similar total HTS tape length for following reasons:

1. The tape with APCs (ii) in Tab. 5.2 has a higher in-field critical current  $I_c$ , allowing for considerably higher excitation currents  $I_f$  (Sec. 2.5.1), particularly at the reduced operating temperature  $T_{HTS} = 20\text{K}$ . This choice anticipates the increased excitation requirement  $\Theta_{f,p}$  due to the air gap winding. The reduced amount of required HTS material does not necessarily yield reduced material costs, since the tape (ii) features a higher price per-unit length, Tab. 5.2.
2. The reduced circumscribing generator volume in case Ⓓ accounts for the increased electromagnetic utilisation  $C_e \sim A_s \cdot B_{\delta,1}$  and implies a reduced mass of all active parts. Preliminary studies (not shown here) revealed, that the stator air gap winding only provides benefits, if a more compact design with a smaller generator active volume  $V_g$  is considered.

The comparison to the gearless PM generators in Ch. 3 leads to following findings:

- The all-iron topology Ⓐ enables a reduction of the generator active mass by  $\approx 10 \dots 25\%$  compared to most lightweight PM generators. A reduction by  $20\%$  is achieved with a reasonable total tape length of  $\approx 47\text{km}$ , which is comparable to the *EcoSwing* generator in terms of tape length per output power of  $\approx 6.7\text{km}/\text{MW}$  [196] (width of tape  $w_t = 12\text{mm}$ ).
- The active mass can be reduced by  $\approx 50\%$  compared to PM generators, if the air gap winding topology Ⓓ is employed. The very large excitation requirement yields

however an increase in CAPEX by a factor  $> 6$  compared to the PM generators.

- For the current cost level, even variants of HTS excited generators with lowest costs require a CAPEX that is by  $\approx 25\%$  higher compared to the PM excitation. This relation can however change to some extent due to the volatility of NdFeB magnet prices, Fig. 1.3, and the potential economies of scale in the HTS production.

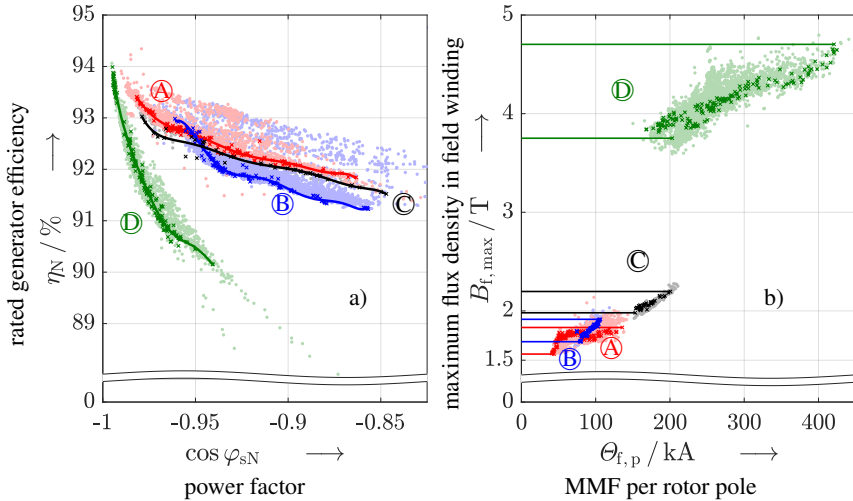


Figure 5.3.: Numerically calculated generator variants for different topologies  $\textcircled{A}$  -  $\textcircled{D}$ , Fig. 4.4. a) Rated generator efficiency  $\eta_N$  versus fundamental power factor  $\cos \varphi_{sN}$ . b) Maximum magnetic flux density in the excitation winding ( $\vec{B}|_c$ ) versus the excitation MMF per pole  $\Theta_{f,p}$ . Opaque symbols indicate *Pareto* efficient variants.

The absolute power factor  $|\cos \varphi_{sN}| \approx 0.85 \dots 1.0$  is high for each of the considered topologies  $\textcircled{A}$  -  $\textcircled{D}$ , Fig. 5.3 a), particularly in comparison with PM excited direct drive generators with  $|\cos \varphi_{sN}| \approx 0.7 \dots 0.85$ . This is attributed to the high rotor field and the reduced stator inductance due to the large magnetic air gap width  $\delta_{mag}$ , Fig. 4.4. Designs with low HTS material consumption feature the lowest absolute values  $|\cos \varphi_{sN}| \approx 0.85$ . Most efficient designs are enabled by a high rotor field and are therefore also characterised by  $|\cos \varphi_{sN}| > 0.975$ , so that a high efficiency and a high power factor are aligned objectives.

Among the topologies  $\textcircled{A}$  -  $\textcircled{C}$  with a stator winding in slots, all-iron designs  $\textcircled{A}$  with high magnetic utilization feature the highest efficiency, i.e.  $\eta_N > 93\%$  Fig. 5.3 a). Similar

results are achieved for an entirely non-magnetic rotor structure ③ in spite of the reduced operating temperature of  $T_{\text{HTS}} = 20\text{K}$ . *Pareto* efficient variants for topology ② with non-magnetic pole core are mostly dominated by the other topologies regarding  $\eta_{\text{N}}$  and  $\cos \varphi_{\text{sN}}$ . The HTS design ④ with stator air gap winding outperforms the alternatives with slotted stator in case of highest electromagnetic utilisation, i.e.  $\eta_{\text{N}} \approx 94\%$  and  $|\cos \varphi_{\text{sN}}| \approx 0.99$ . Similar findings based on single designs have been reported by *Liu et al.* [139]. In case of topology ④, the overall efficiency suffers from the larger stator current loading  $A_{\text{s}}$  and the associated *ohmic* loss.

Following results are obtained regarding the magnetic flux density experienced by the HTS tape and the required MMF of the excitation winding, Fig. 5.3 b)

- The flux density in the critical axis is in a similar range of  $B \approx 1.6 \dots 2.4\text{T}$  for the topologies ① - ③ with a stator winding in slots. This corresponds to a lift-factor in the range of  $L \approx 2.0 \dots 2.4$  at 30K with respect to 77K/LN<sub>2</sub>, s.f., Sec. 2.5. Consistent with most designs reported in literature, e.g. [20, 141], this range of  $\vec{B}|_c$  corresponds to the maximum admissible value in order to prevent an excessive HTS tape requirement in absence of APCs. The flux density of *Pareto* efficient variants increases, if iron parts are eliminated in the rotor. This is caused by a larger fraction of meandering field, which penetrates the excitation winding.
- Similar excitation requirements for *Pareto* efficient designs with ferromagnetic and non-magnetic pole core are found. However, larger rotor yoke heights  $h_{\text{yT}}$  are required for topology ② in order to compensate the increased excitation requirement of the non-magnetic pole cores. The required MMF per pole is by a factor of 1.5 ... 2 higher for an entirely non-magnetic rotor ③, compared to the other topologies ①, ② with ferromagnetic rotor yoke.
- For a stator air gap winding in topology ④, the flux density in the critical axis is in the range 3.8 ... 4.7T, which corresponds to an increase by a factor of 2 ... 3 compared to the other topologies ① - ③. Following effects cause the high values of  $\vec{B}|_c$ :
  - For the same excitation MMF, the higher critical current  $I_{\text{c}}$  of the tape with APCs implies a smaller width  $w_{\text{f}}$  of the coil sides. This leads inherently to a larger local flux density, since, to the first order, the scaling  $B \sim \Theta_{\text{f,p}}/w_{\text{f}}$  applies.
  - The increase of the MMF by a factor of 2 ... 4 is reflected by an according

increase of the inter-pole stray flux.

The rated field current  $I_{fN}$ , Fig. 5.4 a), is in the range of  $I_{fN} \approx 400 \dots 450$  A for *Pareto* efficient variants of topology (A) and (B). Only a small increase to about  $I_{fN} \approx 500$  A is achieved with the lower operating temperature in case of topology (C). The higher rotor inter-pole stray flux  $\Phi_{p\sigma}$  in this case reduces the critical current  $I_c$ . The difference in the field dependent lift factor  $L$  between non-magnetic ((B)) and ferromagnetic pole cores ((A)) is not significant, because the iron rotor yoke permeability mainly determines the reluctance of the relevant stray flux path. The excitation current for topology (D) with stator air gap winding and APC-enhanced HTS tapes (ii) in Tab. 5.2 is in the range of  $I_f \approx 1150 \dots 1250$  A for *Pareto* efficient designs. The much better in-field performance in combination with the lower operating temperature yield lift factors in the range of  $L \approx 4.2 \dots 4.8$ , in spite of the higher flux densities, Fig. 5.3 b).

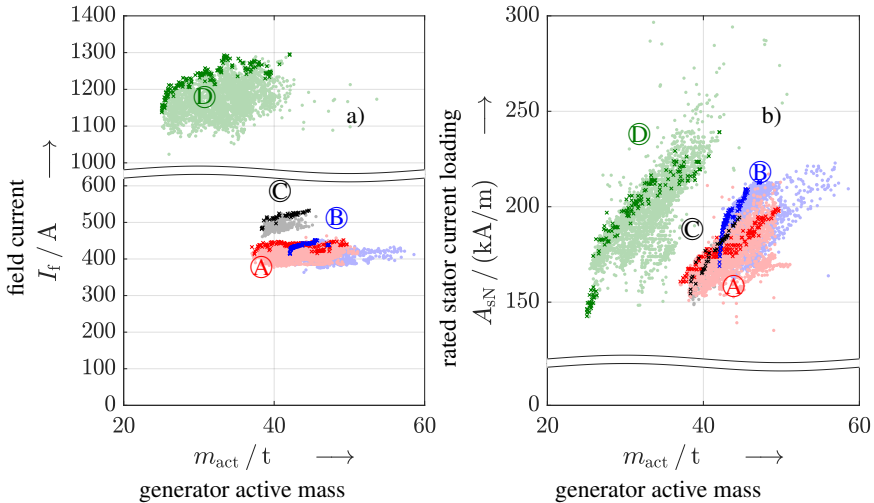


Figure 5.4.: Numerically calculated generator variants for different topologies (A) - (D), Fig. 4.4. a) Rated field current  $I_{fN}$  versus active generator mass  $m_{act}$ . b) Rated stator current loading  $A_{sN}$  versus generator active mass  $m_{act}$ . Opaque symbols indicate *Pareto* efficient variants.

The stator current loading  $A_{sN}$  increases with the generator active mass  $m_{act}$ : The armature field  $B_s$  loads the stator iron yoke magnetically and requires a larger stator yoke height  $h_{ys}$ . Moreover, high stator current loadings  $A_s$  are enabled by a large radial extent of the stator winding, which increases the required excitation MMF. This implies an additional

magnetic loading of the rotor yoke, requiring a larger rotor yoke height  $h_{yr}$ . These effects overcompensate the reduction of the required air gap field fundamental  $B_{\delta,1}$  for similar electromagnetic utilization  $B_{\delta,1} \cdot A_s$ . The differences between the topologies ① - ③ are small with current loadings in the range  $A_{sN} \approx 150 \dots 200 \text{ kA/m}$ . The rated stator current loadings of *Pareto* efficient designs with topology ④ lie also mostly in the range  $A_s \approx 150 \dots 220 \text{ kA/m}$ , even though much higher values of  $A_s$  are generally possible. The higher electromagnetic utilization in case of  $V_g = 25 \text{ m}^3$  is therefore mainly achieved by an increase in  $B_{\delta,1}$ . Compared to the PM excited generators in Ch. 3, all optimum HTS generators feature  $\approx 10 \dots 50\%$  higher stator current loadings  $A_s$ , as the need for comparably wide iron stator teeth is relieved due to the better excitation capabilities. This leads to the more general finding, that superconducting field windings must be combined with a high stator current loading  $A_s$  in order to profit optimally from the higher excitation MMF.

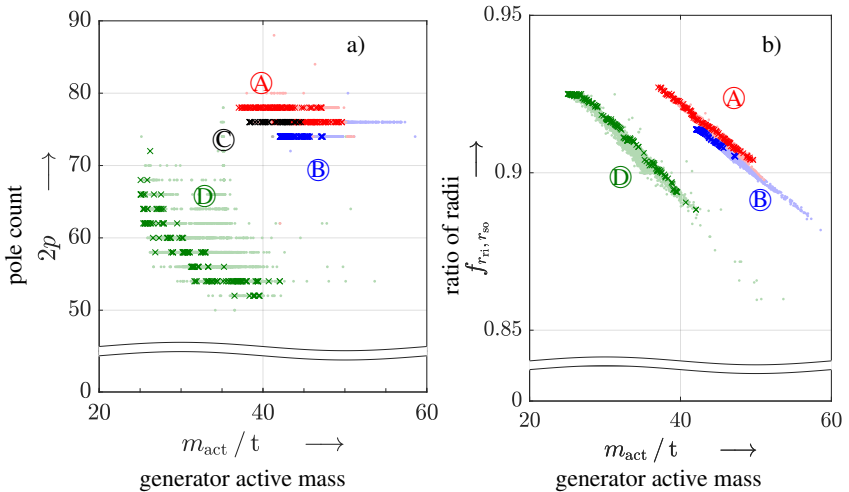


Figure 5.5.: Numerically calculated generator variants for different topologies ① - ④, Fig. 4.4. a) Pole count  $2p$  versus active generator mass  $m_{act}$ . b) Ratio between stator outer radius  $r_{so}$  and rotor inner radius  $r_{ri}$  versus generator active mass  $m_{act}$ . Opaque symbols indicate *Pareto* efficient variants.  $f_{r_{ri}, r_{so}} = r_{ri}/r_{so}$  is not a meaningful variable from an electromagnetic point of view in case of an entirely non-magnetic rotor structure ③.

The comparison of the pole count  $2p$  of the *Pareto* efficient individuals, Fig. 5.5 a), reveals only small differences between the topologies ① - ③ with slotted stator. For topologies ② and ③ with non-magnetic rotor parts, all *Pareto* efficient generator designs feature an

identical pole count, i.e.  $2p = 74$  and  $2p = 76$ . Higher pole counts  $2p$  would reduce the required yoke heights, but come at the cost of additional HTS material requirements and are excluded due to the limited space in the inter-pole gaps for the SC field winding.

Efficient designs with stator air gap winding topology ④ are characterised by considerably smaller pole counts  $2p = 52 \dots 70$ , which decrease towards heavier designs with larger iron cross sections. This result is attributed to a minimum ratio between the magnetically effective air gap width and the pole pitch  $\delta_{\text{mag}}/\tau_p$ , which must be kept in order to obtain a sufficiently high torque-producing main flux linkage. Compared to the PM excited generators, the optimum pole count is by a factor of  $\approx 0.5$  lower for all topologies of partially superconducting generators. The low pole counts are mainly caused by the increase of the total HTS length towards higher  $p$  and limit the potential for stronger active mass reductions.

The relation between the radial extent of the generator in terms of the ratio  $f_{r_{\text{ri}}, r_{\text{so}}} = r_{\text{ri}}/r_{\text{so}}$  and the generator active mass  $m_{\text{act}}$  differs among the topologies ①, ②, ④, Fig. 5.5 b). For the same ratio  $f_{r_{\text{ri}}, r_{\text{so}}}$ , generator variants with non-magnetic pole core feature just a slightly lower active mass. Even though the generators' main dimensions can generally vary during the optimization, all *Pareto* efficient variants feature the same maximum outer diameter  $d_{\text{so}} \approx 6.5\text{m}$ , irrespective of the topology. The lower active mass of generators with topology ④ for the same  $f_{r_{\text{ri}}, r_{\text{so}}} \approx 0.89 \dots 0.925$  is therefore caused by a shorter axial length  $l_i$  in case of  $V_g = 25\text{m}^3$ .

## 5.2. Influence of Installation Space and Outer Diameter

Besides the choice of the topology ① - ④, the generators' main dimensions  $d_{\text{so}} = 2r_{\text{so}}$ ,  $l_i$  determine the electromagnetic utilisation  $C_e \sim P_N/(d_{\text{so}}^2 \cdot l_i) \sim A_s \cdot B_{\delta,1}$  and hence the magnetic conditions inside the generator. The installation space in the nacelle usually restricts the maximum outer diameter  $d_{\text{so}}$ . Small circumscribing active volumes  $V_g$  are an advantage that is supported by the HTS DC excitation. Smaller values of  $V_g$  yield however not necessarily more lightweight generators, so that this section compares *Pareto* efficient generator designs with all-iron topology ① for different main dimension limits. Two optimization runs with the APC-free HTS tape (tape (i) in Tab. 5.2, GdBCO), the same active volume  $V_g = 40\text{m}^3$  (Tab. 5.1) and the same cryogenic operating temperature  $T_{\text{HTS}} = 30\text{K}$  are considered for the following two cases:

1.  $d_{\text{so}}^{\text{max}} = 6.5\text{ m}$ : The stator outer diameter is restricted according to typical dimensions of commercially available wind generators with 7 MW power rating. The outer diameter is typically restricted due to on-road transport restrictions.
2.  $d_{\text{so}}^{\text{max}}$  is not restricted: For fixed volume  $V_{\text{g}}$ , the diameter is essentially restricted by a disproportionate increase of the stator and rotor end-winding length. This increases the corresponding *ohmic* loss in the stator winding, where Thermal Class F (IEC 60034-1, [50]) is assumed with  $\Delta\vartheta = 105\text{ K}$  winding temperature rise over  $40^\circ\text{C}$  ambient. The limit is checked by means of the thermal model, Sec. 4.2.4. This scenario is considered in order to evaluate the impact of the restricted diameter  $d_{\text{so}}^{\text{max}}$  in 1. for HTS excited generators.

In addition, two optimization runs for topology  $\textcircled{\text{A}}$  with the same maximum outer diameter  $d_{\text{so}}^{\text{max}} = 6.5\text{ m}$ , but reduced circumscribing volume  $V_{\text{g}}$  are considered. Even though the stator outer diameter can generally differ from its maximum value due to the scaling with the slimness factor  $\lambda_{\text{d}} = l_{\text{i}}/d_{\text{so}}$ , also here all *Pareto* efficient individuals feature approximately  $d_{\text{so}} \approx d_{\text{so}}^{\text{max}}$ , as expected from the approximate scaling of the torque  $M|_{C_{\text{c}}=\text{const.}} \sim d_{\text{so}}^2 \cdot l_{\text{i}}$ .

The minimum generator active mass  $m_{\text{act}}$  is obtained for HTS generator designs without upper limit on the outer diameter, Fig. 5.6 a). In this case, the stator outer diameter is in the range  $d_{\text{so}} \approx 6.65 \dots 10.3\text{ m}$ . The reduced generator active mass originates from the approximate scaling of both stator and rotor yoke masses (5.1), (5.2) for  $d_{\text{so}}^2 \cdot l_{\text{i}} \sim V_{\text{g}} \sim M_{\text{e}} = \text{const.}$  and similar air gap flux densities  $B_{\delta,1}$ .

$$h_{\text{y}} \sim (B_{\delta,1} \cdot \tau_{\text{p}}) \Big|_{B_{\delta,1}=\text{const.}} \sim \frac{d_{\text{so}}}{p} \quad \Rightarrow \quad (5.1)$$

$$m_{\text{y}} \sim l_{\text{i}} \cdot h_{\text{y}} \cdot d_{\text{so}} \sim \frac{d_{\text{so}}^2}{p} \cdot l_{\text{i}} \Big|_{d_{\text{so}}^2 \cdot l_{\text{i}}=\text{const.}} \sim \frac{1}{p} \Big|_{\tau_{\text{p}} \approx \text{const.}} \sim \frac{1}{d_{\text{so}}} \quad (5.2)$$

The significant contribution of the yoke masses to the total active mass is therefore considerably reduced. In order to achieve the same active mass  $m_{\text{act}} \approx 37 \dots 43\text{ t}$  with finite maximum stator outer diameter  $d_{\text{so}}^{\text{max}} = 6.5\text{ m}$ , an about three times higher amount of HTS material is required, Fig. 5.6 b). For similar local magnetic field conditions in the field winding and correspondingly similar critical currents, the total SC tape length scales ap-

## 5.2. Influence of Installation Space and Outer Diameter

proximately as (5.3) for constant pole pitch  $\tau_p$  and  $d_{so}^2 \cdot l_i = \text{const.} \equiv C_2$ .

$$l_t \sim p \cdot (\tau_p + l_i) \sim p \cdot \left( C_1 + \frac{C_2}{d_{so}^2} \right) \Big|_{\tau_p = \text{const.}} \sim d_{so} \cdot \left( C_1 + \frac{C_2}{d_{so}^2} \right), \quad C_1, C_2 = \text{const.} \quad (5.3)$$

The approximate scaling reflects the trade-off between an axially shorter coil and a longer total conductor length in the winding overhangs for larger diameters. The required HTS conductor length  $l_t$  for  $m_{\text{act}} \approx 37 \dots 43 \text{ t}$  is reduced for  $d_{so}^{\text{max}} \rightarrow \infty$ , since the reduction of the axial length dominates.

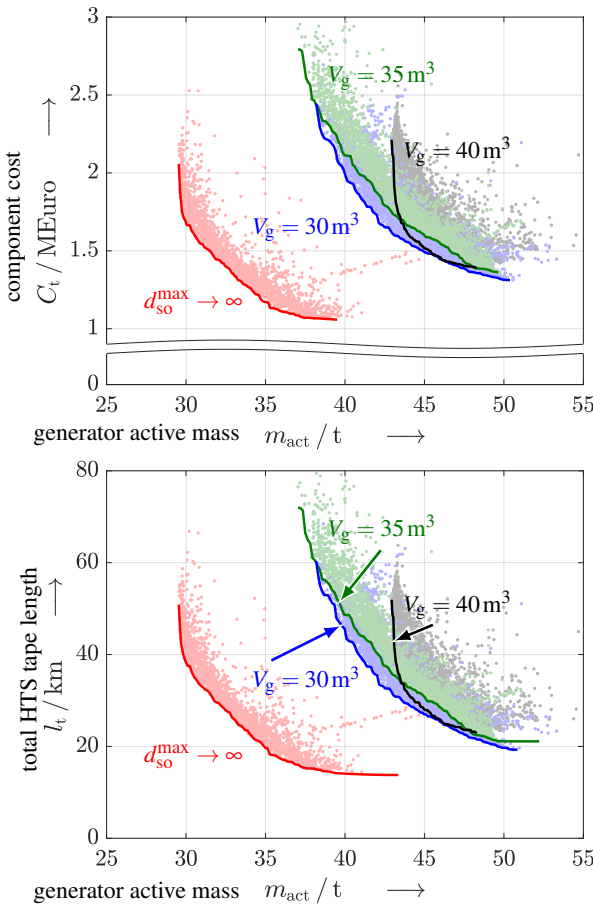


Figure 5.6.: Numerically calculated generator variants with all-iron topology  $\textcircled{A}$ , Fig. 4.4, for different volumes  $V_g = 30, 35, 40 \text{ m}^3$  and a restriction of the outer diameter, Tab. 5.1. For  $V_g = 40 \text{ m}^3$ , a separate optimization run for an unrestricted outer diameter  $d_{so}^{\text{max}} \rightarrow \infty$  is carried out. The lines represent *Pareto* efficient variants. a) Component cost  $C_t$ : generator material + fully-rated converter + cryogenic cooling system, versus generator active mass  $m_{\text{act}}$ . b) Total tape length  $l_t$  (tape width  $w_t = 12 \text{ mm}$ ) versus generator active mass  $m_{\text{act}}$ . Not all variants are shown for a better visibility.



Compared to the case of a maximum outer diameter  $d_{so}^{\max} = 6.5$  m, the prescribed, circumscribing volume  $V_g$  has only little influence on the relation between  $l_i$  and  $m_{act}$ , Fig. 5.6 b). Opposing effects of a volume reduction are:

1. The reduced generator axial length  $l_i$  implies axially shorter poles with shorter tape lengths per pole. The shorter axial length directly reduces the size and the mass of active parts.
2. For fixed stator apparent power  $S$  and fixed speed  $n$ , the electromagnetic utilization  $C_e \sim A_s \cdot B_{\delta,1} \sim S/(n \cdot V_g) \sim 1/V_g$  increases for reduced circumscribing active volume  $V_g$ . The SC field winding experiences accordingly a higher magnetic field, Fig. 5.7 b), which reduces the critical current  $I_c$  and increases the total HTS conductor length. The higher magnetic fluxes require moreover larger iron cross sections for the flux guidance, which lead to an increase in generator active mass  $m_{act}$ .

The comparison, Fig. 5.6 b), reveals that these effects nearly cancel out for  $V_g = 30$  m<sup>3</sup> and  $V_g = 35$  m<sup>3</sup>, so that a reduction of  $V_g$  has only limited potential to decrease the active mass and the HTS material consumption in the studied range. Still, the shorter axial length  $l_i$  implies lower *ohmic* losses in the stator winding, even if  $A_s$  is increased, Fig. 5.8 a). The lower stator *ohmic* loss, which dominates for low speed direct drive generators, manifests in efficiency advantages towards smaller  $V_g$ , Fig. 5.7 a). For a given power factor, the larger stator outer diameter  $d_{so}^{\max} \rightarrow \infty$  proves advantageous in terms of a higher generator efficiency  $\eta_N$  due to the reduced stator current loading  $A_{sN}$ , Fig. 5.8 a). With a restricted outer diameter  $d_{so}^{\max} = 6.5$  m, the maximum efficiency for a power factor in the range  $|\cos \varphi_{sN}| \approx 0.9 \dots 0.96$  is achieved with the most compact generator design, featuring  $V_g = 30$  m<sup>3</sup>, Fig. 5.7 a).

In all considered cases, the high stator current loadings  $A_{sN}$  of *Pareto* efficient designs, Fig. 5.8 a), are accompanied by a high thermal utilisation  $\alpha \cdot \Delta\vartheta \sim A_{sN} \cdot J_{Cu}$ , which requires a powerful stator cooling system (high heat transfer coefficient  $\alpha$ ) to limit  $\Delta\vartheta$ . Regardless of the considered installation space  $V_g$  and the maximum diameter  $d_{so}^{\max}$ , the share of the reluctance torque in the overall rated air gap torque is small, Fig. 5.8 b): The reluctance torque contributes always less than 10% for *Pareto* efficient variants, featuring the all-iron topology **A**. This share decreases moreover towards highly-saturated, lightweight variants **B**, **C** and **D**.

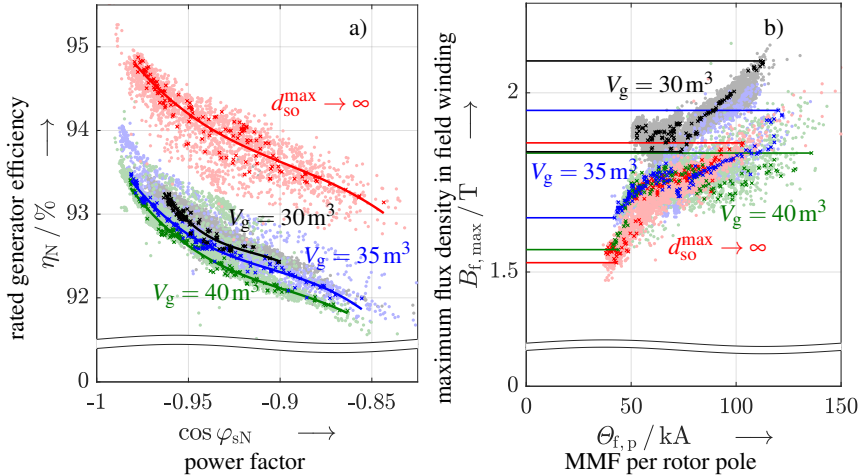


Figure 5.7.: Numerically calculated variants for different volumes  $V_g = 30/35/40\text{ m}^3$  and a restriction of the outer diameter  $d_{so}^{\max} = 6.5\text{ m}$ , Tab. 5.1. For  $V_g = 40\text{ m}^3$ , a separate optimization run for an unrestricted outer diameter  $d_{so}^{\max} \rightarrow \infty$  is carried out. Opaque symbols indicate *Pareto* efficient variants. The lines represent polynomial fits to the *Pareto* efficient variants. a) Rated generator efficiency versus fundamental power factor. b) Maximum magnetic flux density ( $\vec{B}||c$ ) in the winding versus the excitation MMF per pole.

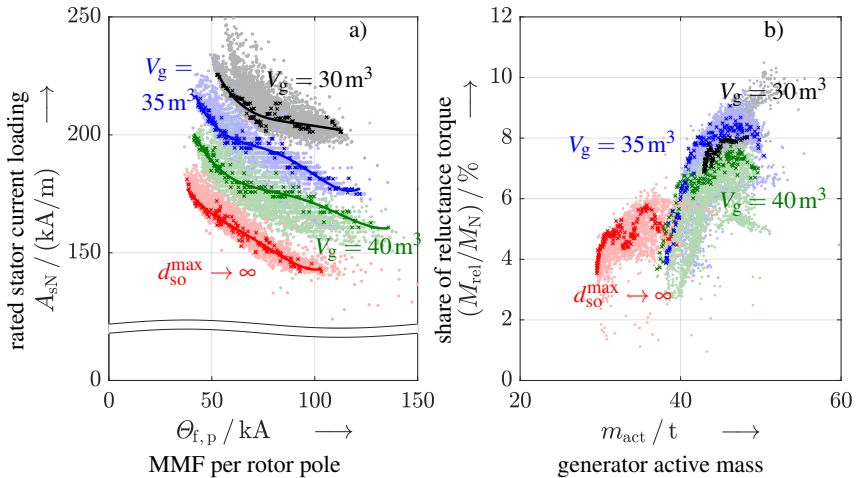


Figure 5.8.: As Fig. 5.7, but: a) Stator current loading versus the excitation MMF. b) Share of the reluctance torque in the total electromagnetic torque versus generator active mass. Not all variants are shown for better visibility.

### 5.3. Comparison of HTS Materials and Cryogenic Temperatures in the Field Winding

The choice of the HTS tape and of the cryogenic operating temperature  $T_{\text{HTS}}$  determines the number of turns  $N_f$  and consequently the dimensions of the excitation winding window, which are required to provide the necessary MMF  $\Theta_{f,p}$ . It also affects the inductance of the excitation winding  $L_f$ . In this section, generator variants with two different tapes, (i) and (ii) in Tab. 5.1, but the same volume  $V_g = 40 \text{ m}^3$ , the same maximum outer diameter  $d_{\text{so}}^{\text{max}} = 6.5 \text{ m}$  and the same operating temperature  $T_{\text{HTS}} = 30 \text{ K}$  are compared. The generators feature the all-iron topology  $\textcircled{A}$ . The higher critical current of the tape (ii) with APCs influences the electromagnetic design in following ways:

- With a higher  $I_c$ , larger widths  $w_p$  of the pole cores are possible for the same excitation  $\Theta_{f,p}$ , which relieves one potential magnetic bottleneck of iron saturation.
- Higher flux densities in the excitation winding are admissible due to the better in-field performance, so that a higher saturation of the rotor parts (particularly the rotor yoke) are tolerable.
- Higher rotor fields can be achieved for fixed space requirements in the inter-pole gap. This allows for a smaller stator current loading  $A_{sN}$  in order to obtain the same electromagnetic utilisation  $C_e$ .

From an investment cost-oriented perspective, the tape (i) without APCs is favoured for its lower cost at fixed generator active mass, Fig. 5.9 a). The much higher critical current  $I_c$  of tape (ii) is overcompensated by the considerably higher price. There is no significant difference between the tapes (i) and (ii) with respect to the rated generator efficiency  $\eta_N$  and the rated power factor  $\cos \varphi_{sN}$ , Fig. 5.9 b): For the considered topology  $\textcircled{A}$ , the power factor can be regarded as a measure for the saturation state, whereas the efficiency is mainly determined by the stator current loading  $A_{sN}$ , as *Pareto* efficient designs almost always exhibit outer diameters  $d_{\text{so}} \approx d_{\text{so}}^{\text{max}} = 6.5 \text{ m}$ . Since the electromagnetic utilisation  $C_e$  is determined by  $V_g$ ,  $n_N$  and  $P_N$ , the designs are characterised by a trade-off between high rotor field  $B_r \sim B_{\delta,1}$  (and, thus, saturated iron with higher power factor  $|\cos \varphi_{sN}|$ ) and high stator current loading  $A_s$  (and, thus, reduced efficiency  $\eta_N$ ). As expected, this relation turns out to be generic, while the tape (ii) with higher in-field critical current  $I_c(\vec{B})$  allows to extend the achievable range towards even higher absolute values of the power factor  $|\cos \varphi_{sN}|$  and generator efficiencies  $\eta_N$ .

### 5.3. Comparison of HTS Materials and Cryogenic Temperatures in the Field Winding

The choice of the operating temperature  $T_{\text{HTS}}$  is characterised by the balance between

1. a high utilisation of the HTS tape material in terms of high admissible excitation currents  $I_f$  and
2. a limited compressor power  $P_{\text{comp}}$  for the cryogenic cooling, which scales with the cooling system's cost  $C_{\text{cryo}}$  and its influence on the efficiency.

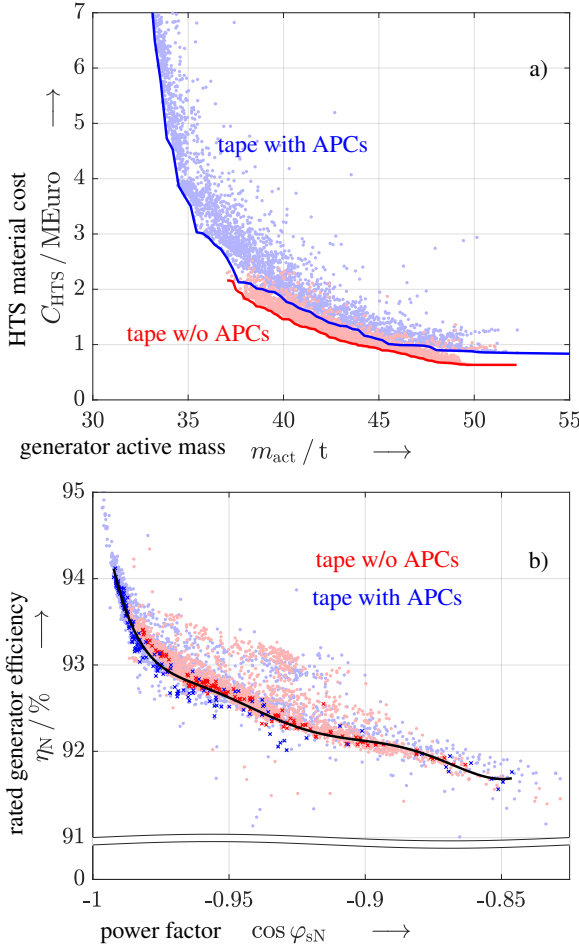


Figure 5.9.: Numerically calculated generator variants for two different tapes (ii) with APCs and (i) without APCs, Tab. 5.1. Both generator variants feature an all-iron topology  $\textcircled{A}$ ,  $V_g = 40 \text{ m}^3$ ,  $d_{\text{so}}^{\text{max}} = 6.5 \text{ m}$  and  $T_{\text{HTS}} = 30 \text{ K}$ . The lines represent fits to *Pareto* efficient variants. a) Material cost of the HTS conductors  $C_{\text{HTS}}$  versus active generator mass  $m_{\text{act}}$ . b) Rated efficiency  $\eta_N$  versus power factor  $\cos \varphi_{sN}$ . A common fit to *Pareto* efficient variants is shown as black line. Not all variants are plotted for a better visibility.

The comparison between the *Pareto* efficient designs of optimization runs, that differ only with respect to the cryogenic operating temperature  $T_{\text{HTS}}$ , reveal that a temperature of

$T_{\text{HTS}} = 25\text{K}$  is advantageous regarding maximum efficiency, Fig. 5.10 b). In this case, the sum of the stator *ohmic* loss  $P_{\text{d,Cu,s}}$  and the compressor input power  $P_{\text{compr}}$  reaches a minimum, Fig. 5.11 a). For the slightly lower cold head temperature  $T_{\text{CH}} \approx 22\text{K}$ , the coefficient of performance of the cryogenic cooling system is about  $\text{COP} \approx 0.85\%$ , since  $\dot{Q} = 55\text{W}$  at  $P_{\text{compr}} = 6.5\text{kW}$  for the *SHI* cooler in Fig. 1.10.

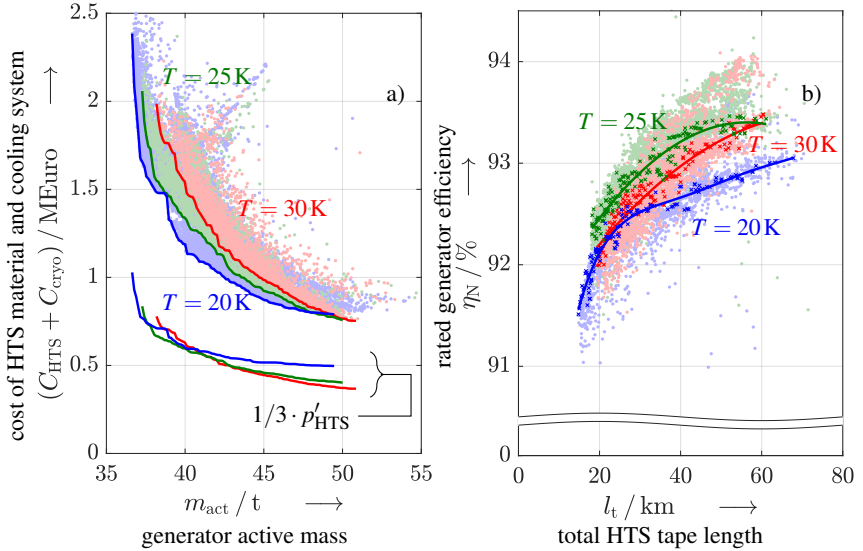


Figure 5.10.: Numerically calculated generator variants for different operating temperatures  $T = 20/25/30\text{K}$  for tape (i) in Tab. 5.1 without APCs. Generator specifications:  $V_{\text{g}} = 40\text{m}^3$ ,  $d_{\text{so}}^{\text{max}} = 6.5\text{m}$ , all-iron HTS topology  $\text{\textcircled{A}}$ . The lines represent (fits to) Pareto efficient variants. a) Combined cost of HTS material and cryogenic cooling system  $C_{\text{HTS}} + C_{\text{cryo}}$  versus active mass  $m_{\text{act}}$ . b) Rated efficiency  $\eta_{\text{N}}$  versus total HTS tape length  $l_{\text{t}}$ . Not all variants are plotted for a better visibility.

The reduction of the required amount of HTS material compared to  $T_{\text{HTS}} = 30\text{K}$  is significant and the  $\approx 15\%$  higher  $I_{\text{c}}$ -values allow for an increased rotor field and a reduction of the stator current loading. The latter effect overcompensates the moderate increase of the cooling power ( $T_{\text{HTS}} = 30\text{K}$ :  $\text{COP} \approx 1.1\%$ ). A further reduction of the operating temperature to  $T_{\text{HTS}} = 20\text{K}$  with  $\text{COP} \approx 0.45\%$  leads to a disproportionate increase of the cooling system's input power, with accordingly lower overall rated generator efficiency  $\eta_{\text{N}}$ , Fig. 5.10 b). The lowest combined investment cost of HTS material  $C_{\text{HTS}}$  and cryogenic cooling system  $C_{\text{cryo}}$  is achieved for  $T_{\text{HTS}} = 20\text{K}$ , Fig. 5.10 a). The decrease of the

### 5.3. Comparison of HTS Materials and Cryogenic Temperatures in the Field Winding

HTS material cost  $C_{\text{HTS}}$  overcompensates the more expensive cooling system  $C_{\text{cryo}}$ . If the HTS cost  $C_{\text{HTS}}$  is reduced to one third of its current value, this relation changes in favour of higher operating temperatures. At the reduced cost level, i.e. at 1/3 of the present cost, the minimum combined cost  $(C_{\text{HTS}} + C_{\text{cryo}}) < 400$  kEuro is in the order of today's NdFeB magnet costs for 7 MW PM excited generators, Sec. 3.3.

The share of the cooling system's cost  $C_{\text{cryo}}$  in the total component cost  $C_t$  depends strongly on the HTS operating temperature  $T_{\text{HTS}}$  and increases systematically towards heavier generator designs with shorter overall HTS length  $l_t$ , Fig. 5.11 b). For  $T_{\text{HTS}} = 30$  K, the cooling system accounts for less than 15 % of the total cost in the entire range of considered designs.

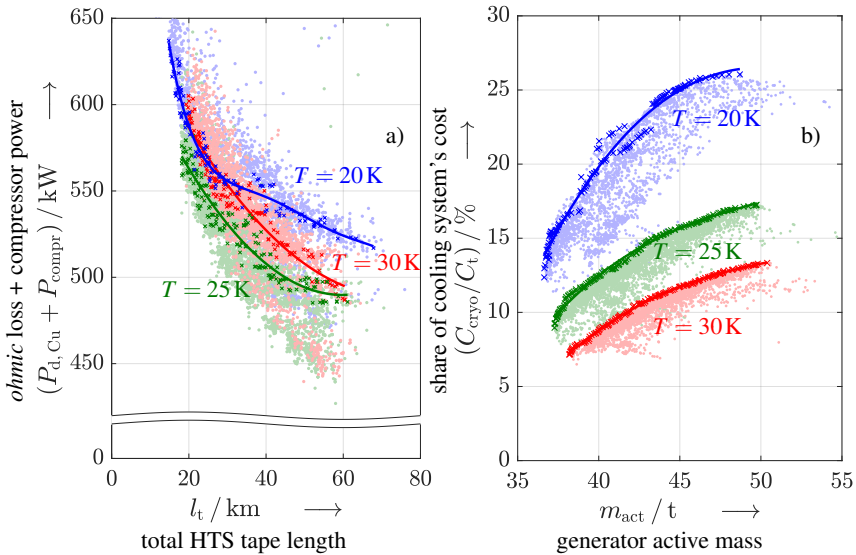


Figure 5.11.: As Fig. 5.10, but: a) Combined power of *ohmic* loss in the stator copper winding and the compressor input power  $P_{d, \text{Cu}, s} + P_{\text{compr}}$  versus total HTS tape length  $l_t$ . b) Share of the cryogenic cooling system's cost in the total system cost versus generator active mass  $m_{\text{act}}$ . Not all variants are plotted for a better visibility.

## 5.4. Exemplary Final Design of a Partially Superconducting Direct Drive Generator

For further comparisons, two exemplary designs for topologies ① and ④ are selected. The designs are *Pareto* efficient regarding low component cost and low active mass  $\{C_t, m_{act}\}$  and represent intermediate designs regarding a trade-off between the two objectives. The 2D calculated magnetic flux densities per pole at rated operation are visualized in Fig. 5.12.

The key characteristics are summarized in Tab. 5.3 - 5.10. Phasor diagrams for rated load  $I_{sN}$  and rated excitation  $I_{fN}$  are visualized in Fig. 5.13.

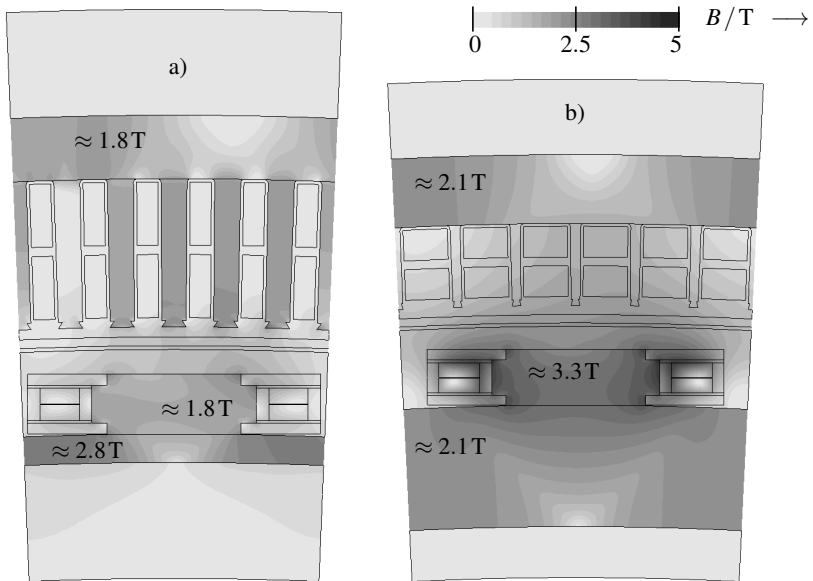


Figure 5.12.: 2D calculated magnetic flux density  $|\vec{B}|$  at rated operation for the exemplary designs, Tab. 5.3, of partially superconducting, HTS excited direct drive generators with topologies a) ① and b) ④. (software: *JMAG*)

#### 5.4. Exemplary Final Design of a Partially Superconducting Direct Drive Generator

Table 5.3.: Key characteristics of the exemplary designs of HTS excited, partially superconducting direct drive generators with topologies  $\textcircled{A}$  and  $\textcircled{D}$ . (pp: peak-to-peak, rel: reluctance)

topology	$\textcircled{A}$	$\textcircled{D}$
$P_{\text{el},N}$	-6.977 MW	-7.067 MW
$S_N$	7181 kVA	7146 kVA
$U_N$	681 V	700 V
$I_N$	6085 A	5892 A
$\cos \varphi_{sN}$	-0.972	-0.989
$n_{\text{syn}}$	8.33 rpm	8.33 rpm
$2p$	78	64
$f_s$	5.41 Hz	4.44 Hz
$M_N$	-8.526 MNm	-8.589 MNm
$M_{\text{pp}}, (M_{\text{pp}}/M_N)$	0.312 MNm, 3.7%	0.074 MNm, 0.9%
$M_{\text{rel}}$	0.507 MNm	0.009 MNm
$\sigma_t$	137.2 kN/m <sup>2</sup>	188.7 kN/m <sup>2</sup>
$A_{sN}$	179.7 kA/m	169.7 kA/m
$C_e$	21.8 kVA · min/m <sup>3</sup>	29.6 kVA · min/m <sup>3</sup>
$P'$	0.177 kW/kg	0.203 kW/kg
$M'$	216 Nm/kg	247 Nm/kg

Table 5.4.: Geometry parameters for the exemplary generator variants in Tab. 5.3.

topology	$\textcircled{A}$	$\textcircled{D}$
$V_g$	35 m <sup>3</sup>	25 m <sup>3</sup>
$\bar{l}_i$	0.986 m	0.686 m
$r_{\text{so}}$	3.240 m	3.213 m
$r_{\text{ri}}$	3.072 m	3.084 m
$r_{\text{ro}}$	3.034 m	3.047 m
$r_{\text{ri}}$	2.963 m	2.895 m
$\tau_p$	247 mm	303 mm
$\tau_Q$	41 mm	50 mm

Table 5.5.: Mass components of magnetically active generator parts for the exemplary generator variants in Tab. 5.3.

topology	$\textcircled{A}$	$\textcircled{D}$
$m_{\text{act}}$	39.5 t	34.8 t
$m_{\text{ys}}$	8.0 t	6.2 t
$m_{\text{ts}}$	8.2 t	0.3 t
$m_{\text{cs}}$	12.7 t	11.7 t
$m_{\text{yr}}$	3.6 t	11.8 t
$m_{\text{pr}}$	3.9 t	2.5 t
$m_{\text{cr}}$	3.1 t	2.2 t



Table 5.6.: SC field winding parameters for the exemplary generator variants in Tab. 5.3.

topology	Ⓐ	Ⓓ
tape	<i>THEVA</i> (i)	<i>Fujikura</i> (ii)
$I_{fN}$	487 A	1186 A
$B_{f,max}$	1.74 T	4.46 T
$N_{f,p}$	$2 \cdot 98 = 196$	$2 \cdot 110 = 220$
$T_{HTS}$	25 K	20 K
$l_t$	41.2 km	30.5 km
$I_c$	816 A	1885 A
$w_t$	12 mm	12 mm
$n_{Lf}$	2	2

Table 5.7.: Loss power components and efficiency for the exemplary generator variants in Tab. 5.3.

topology	Ⓐ	Ⓓ
$P_{d,t}$	542.6 kW	529.8 kW
$P_{d,Cu,s}$	463.5 kW	425.9 kW
$P_{d,Fe}$	14.9 kW	5.6 kW
$P_{d,Ft,damp}$	11.4 kW	0.1 kW
$P_{d,Ft,cw}$	4.1 kW	0.01 kW
$P_{compr}$	48.7 kW	98.2 kW
$Q_{cryo}$	415 W	428 W
COP	0.85 %	0.44 %
$T_{CH}$	22 K	17 K
# cryo coolers	9	16
$\eta_N$	92.8 %	93.0 %

Table 5.8.: Equivalent circuit parameters for the exemplary generator variants in Tab. 5.3 at rated operation.

topology	Ⓐ	Ⓓ
$X_d$	17.5 m $\Omega$	10.1 m $\Omega$
$X_q$	33.2 m $\Omega$	12.5 m $\Omega$
$R_s$	4.2 m $\Omega$	4.1 m $\Omega$
$L_{s\sigma b}$	0.064 mH	0.129 mH
$l_{bs}$	491 mm	736 mm
$Z_N$	64.6 m $\Omega$	68.6 m $\Omega$
$x_d$	0.271 p.u.	0.146 p.u.
$x_q$	0.513 p.u.	0.182 p.u.
$r_s$	0.065 p.u.	0.060 p.u.
$\vartheta_N$	28.9°	10.4°
$\gamma_N$	164.7°	178.2°

Table 5.9.: Cost components for the exemplary generator variants in Tab. 5.3.

topology	Ⓐ	Ⓓ
$C_t$	1.928 MEuro	4.248 MEuro
$C_{HTS}$	1.236 MEuro	3.403 MEuro
$C_{conv}$	0.215 MEuro	0.214 MEuro
$C_{cryo}$	0.225 MEuro	0.400 MEuro
$C_{Cu,s}$	0.171 MEuro	0.158 MEuro
$C_{Fe}$	0.049 MEuro	0.023 MEuro
$C'_t$	$0.276 \frac{\text{MEuro}}{\text{MW}}$	$0.601 \frac{\text{MEuro}}{\text{MW}}$

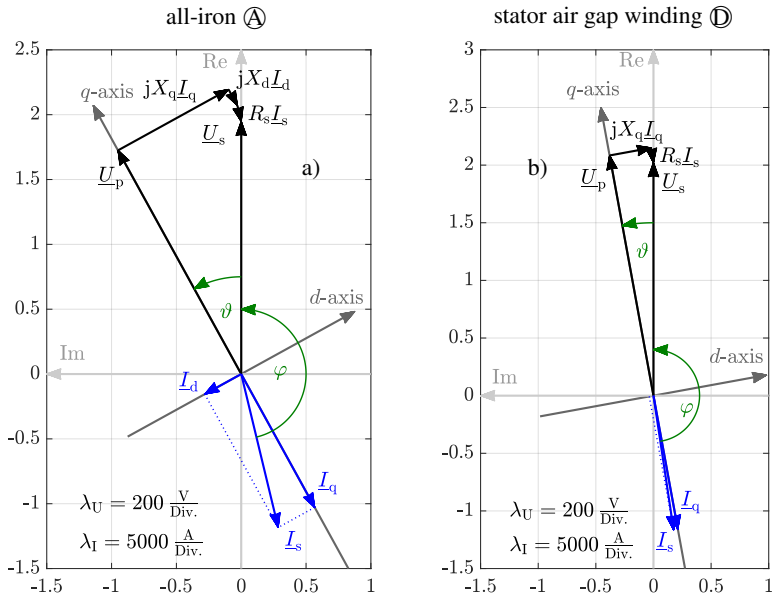


Figure 5.13.: Phasor diagrams at rated operation for the exemplary HTS excited direct drive generator variants with topologies a) ① and b) ②. The very small  $d$ -current is not shown for the stator air gap winding topology ② for better visibility. Corresponding parameters are listed in Tab. 5.8.

Table 5.10.: Stator winding parameters for the exemplary generator variants in Tab. 5.3.

topology	①	②
$m$	3	3
$q$	2	2
$W/\tau_p$	5/6	1
$a$	78	64
$N_c$	47	46
$N_s$	94	92

---

## 6. Basic Considerations on Redundancy

### Operation and Dynamics of HTS Excited Direct Drive Wind Generators

Wind turbines intended for offshore installation sites suffer from high costs of maintenance, repairs and replacements of components. Particularly in the winter period, a failure can lead to long turbine downtimes, if the wind turbine is not accessible by boat and can only be reached by helicopter. The possibility to continue operation even in case of partial component failures can therefore improve the profitability and the reliability of power supply considerably. The power converters account for a major share of the overall wind turbine failures [135, 66], since the electronic modules are exposed to harsh conditions. Today's PM excited wind turbine generators, both medium speed and direct drive, feature a grid connection with several parallel operating converters, Sec. 1.1. Therefore, a typical requirement for offshore wind installations is the possibility to operate the generator with partial feeding of the stator winding at reduced power („redundancy operation“). This accounts for the scenario, in which one of several parallel power converters fails and the corresponding stator winding section is disconnected and idling. The possibility of a redundancy operation is therefore critical regarding the competitiveness of HTS excited generators and analysed in Sec. 6.1.

The integrity of the HTS excited generator designs with respect to fault induced transients is another vital requirement. Typically, the generator experiences largest transient loads after sudden grid-side short circuits, which must be manageable regarding mechanical integrity and transient over-currents. Two additional aspects, which are unique to generators with superconducting excitation winding, are:

- The maximum short circuit torque determines the dimensioning of the cold-warm support. The latter has a strong influence on the required cryogenic cooling capacity

and therefore on the total CAPEX. The largest short circuit torque generally occurs for sudden two-phase short circuits.

- The instantaneous loss power in the cryogenic cooling system determines the transient temperature rise in the superconducting winding. This rise must be small in order to prevent a quench of the superconductor and a potential damage of the SC field winding.

To investigate these effects, Sec. 6.2 is on the analysis of sudden short circuits at the stator terminals after no-load operation. At full-load operation, the sudden short circuit currents and the peak torque values are slightly bigger due to the higher  $U_h$ . Since the difference in  $U_h$  is small as a result of rather small inductances  $L_d$ ,  $L_q$ , Fig. 5.13, the difference is neglected. A single-phase short circuit to the neutral point, a two-phase short circuit and a symmetric three-phase short circuit are considered. The analysis of the transient current responses includes the determination of sub-transient and transient parameters for an exemplary generator design. These parameters are effective when eddy currents in the damper and screening currents in the field winding occur.

### 6.1. Redundancy Operation

In order to cover the most general case, the number of feeding converters is not restricted to two, but may attain any integer number  $u$ , which is compatible with the stator winding topology. An exemplary generator with  $2p = 72$  poles and a three-phase winding with  $q = 2$ ,  $a = 24$  and  $N_c = 17$  is considered. The coils are short pitched by  $W/\tau_p = 5/6$  according to the winding selection in Sec. 4.3.3. The number of converters  $u$  must be a factor of the number of parallel branches  $a$  in order to achieve a symmetric load sharing. It is reasonable not to assign single poles but pole pairs to the different converters in order to avoid any magnetic asymmetry within one pole pair. Hence,  $u$  is also a factor of  $p$ . The number of pole pairs per inverter is  $p/u$ . The number of neighbouring pole pairs that are assigned to the same inverter is denoted by  $o$ . The integer value  $o$  must consequently be a factor of  $p/u$ , Tab. 6.1.

Table 6.1.: Possible feeding schemes of the exemplary generator stator winding with  $2p = 72$  and  $a = 24$ , which is considered for redundancy operation.  $u$  is the number of converters operating in parallel.  $o$  is the number of neighbouring pole pairs that are assigned to the same converter.

number of converters $u$	possible values of $o$	power at redundancy operation
2	1, 2, 3, 6, 9, 12	$(1/2) \cdot P_N$
3	1, 2, 3, 4, 6, 12	$(2/3) \cdot P_N$
4	1, 3, 9	$(3/4) \cdot P_N$
6	1, 2, 3, 6	$(5/6) \cdot P_N$
12	1, 3	$(11/12) \cdot P_N$

The feeding topologies in case of a failure of a single converter are visualized in Fig. 6.1 - 6.3. The encircled blue sector covers one basic scheme, i.e.  $o \cdot u$  pole pairs, which determines the spatial winding period and therefore the maximum wave length contained in the stator current loading.

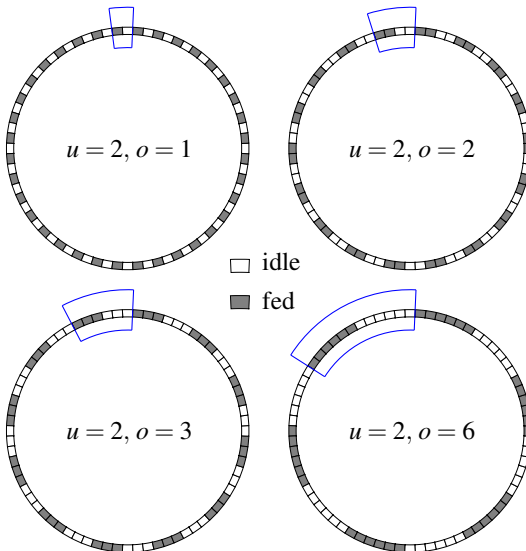


Figure 6.1.: Schematics of intermittent stator feeding patterns in case of  $u = 2$  parallel operating converters, from which one is defect. Each sector represents one basic winding scheme in the upper layer of the short-pitched two-layer winding. The schemes differ regarding the number  $o$  of neighbouring basic winding schemes, which are fed by the same converter.

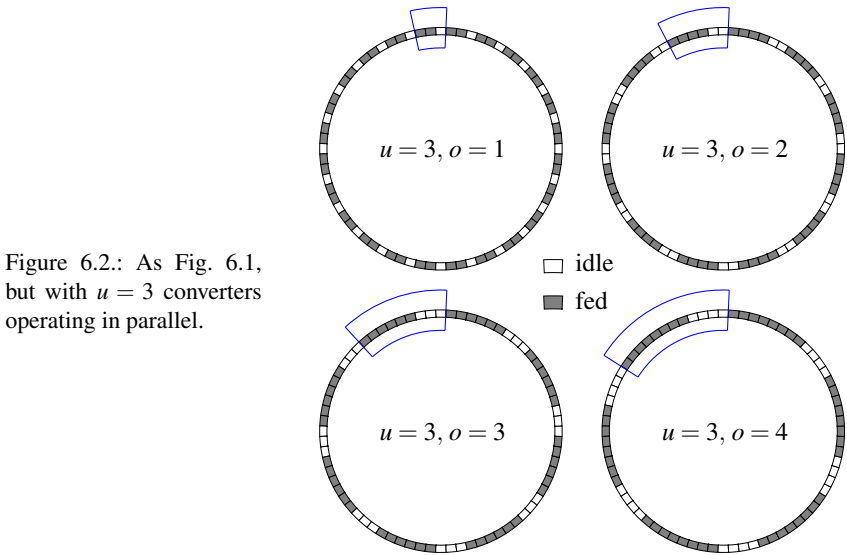


Figure 6.2.: As Fig. 6.1, but with  $u = 3$  converters operating in parallel.

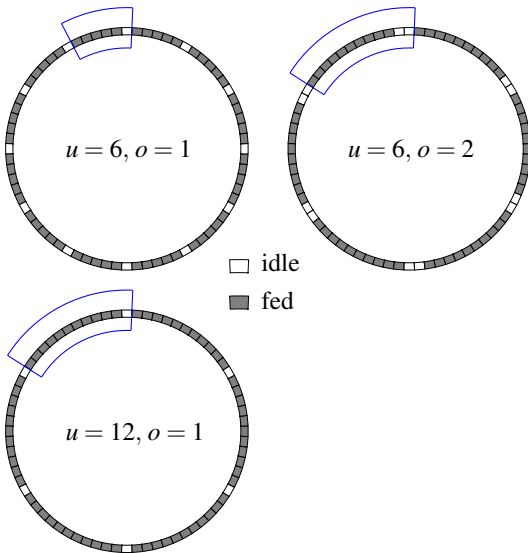


Figure 6.3.: As Fig. 6.1, but with  $u = 6$  converters operating in parallel.

In the following,  $A_{e,s}$  is used for the electrical stator current loading. The partial feeding

of the stator winding generally leads to sub-harmonics in the spectrum of the stator current loading  $A_{e,s}$ , i.e. current loading waves with a wave length  $\lambda_{v'} > 2\tau_p$ , and the stator air-gap field distribution. Moreover, additional harmonics with  $\lambda_{v'} < 2 \cdot \tau_p$  occur. The intermittent feeding corresponds to a multiplication, (6.1), of the stator current loading  $A_{e,s}(\varphi)$  with a window function  $w(\varphi)$ , (6.2).  $2\pi$  el. corresponds to an entire feeding scheme with  $o \cdot u$  pole pairs.

$$\tilde{A}_{e,s}(\varphi) = w(\varphi) \cdot A_{e,s}(\varphi) \quad (6.1)$$

$$w(\varphi) = \begin{cases} 0, & \varphi \leq \frac{2\pi}{u}, \\ 1, & \text{else} \end{cases} \quad \varphi \in [0, 2\pi) \text{ in el. deg.} \quad (6.2)$$

Due to the short-pitched coils, the window functions for the upper and the lower layer are shifted with respect to each other by one slot pitch. This shift is advantageous regarding the mitigation of additional harmonics in redundancy operation, since it leads to a smoother transition between idling and fed stator sections.

In the spectral domain with space order  $v'$ , the multiplication corresponds to a convolution of the stator current loading's spectrum  $\underline{A}_{e,v'}$  and the spectrum of the window function  $\underline{W}_{v'}$ , (6.3).

$$\tilde{\underline{A}}_{e,v'} = \underline{A}_{e,v'} * \underline{W}_{v'} \quad (6.3)$$

The spectrum of the window function features amplitudes, whose absolute values decay as  $|\underline{W}_{v'}| \sim 1/|v'|$  towards higher absolute space orders. Therefore, the convolution (6.3) leads to side bands, which are centred around the space orders that occur in the original spectrum of the healthy feeding scheme. The torque producing fundamental features the space order  $v' = u \cdot o$ . As example, the analytically calculated spectrum at intermittent feeding for  $u = 2, o = 1$  is visualized in Fig. 6.4.

The sub-harmonics with large wave lengths  $\lambda \in (2\tau_p, (u \cdot o \cdot 2\tau_p)]$  have a considerably larger outreach to the rotor parts than harmonics with  $v' > u \cdot o$ . They feature moreover comparably low time orders in the rotor frame of reference, Fig. 6.4 b), which reduces the effectiveness of the electromagnetic shielding by eddy currents in the copper damper screen. Both effects cause that air gap field sub-harmonics reach the cryogenic rotor section and produce additional losses there. In contrast, the additional harmonics with  $v' > u \cdot o$  do not reach far due to their short wave lengths. They feature higher frequencies in the rotor frame of reference and increase primarily the eddy current loss in the cryostat wall and the copper damper.

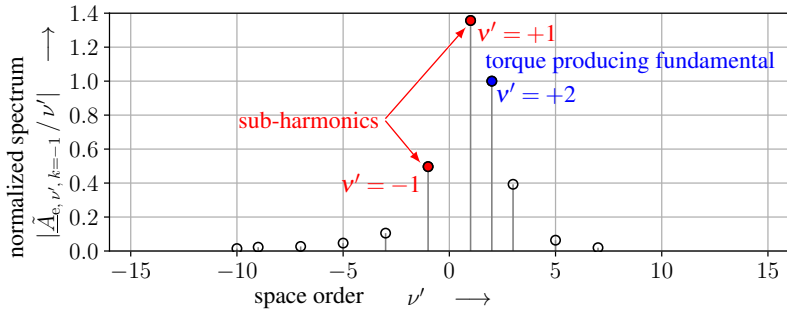


Figure 6.4.: Analytically calculated *Fourier* spectrum of the stator current loading (time order  $k^{(s)} = -1$ ), divided by the space order  $|\tilde{A}_{e,\nu',k=-1}/\nu'| \sim |\tilde{B}_{\nu',k=-1}|$  for redundancy operation with  $u = 2$  converters and  $o = 1$ . The basic winding scheme covers  $u \cdot o = 2$  pole pairs, so that the torque producing fundamental features space order  $\nu' = 2$ .

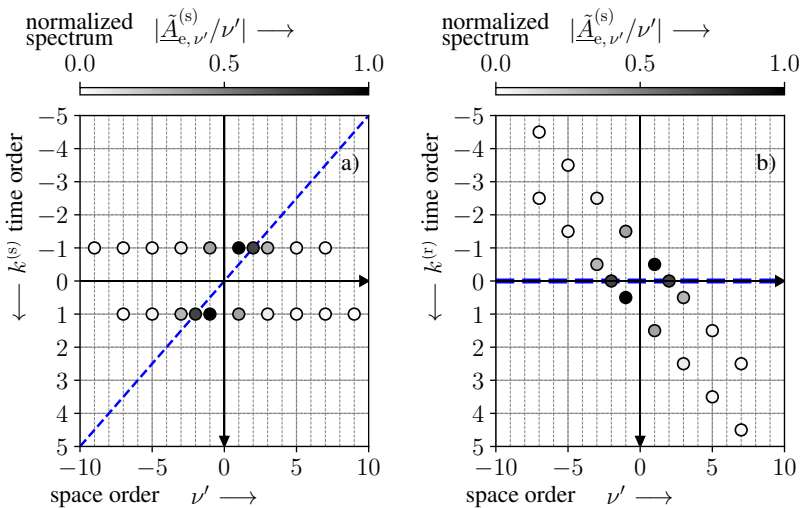


Figure 6.5.: Analytically calculated 2D *Fourier* wave spectrum of the stator current loading, divided by the space order for redundancy operation with  $u = 2$  converters and  $o = 1$ . The dashed blue lines indicate synchronously rotating waves. a) Spectrum in the stator frame of reference, where all harmonics feature the time order  $|k^{(s)}| = 1$ , since only the stator current fundamental with frequency  $f_s$  is considered. b) The same spectrum in the rotor frame of reference for synchronous rotation, where all spectral contributions, except from the fundamental, rotate asynchronously.



The comparison of the normalized *Fourier* spectra for the same size of the periodic scheme  $u \cdot o = 18$ , Fig. 6.6 a) - c), reveals a decrease of the relative sub-harmonic amplitudes towards a higher number of feeding converters  $u$ . The relative space orders  $v'$  correspond to *absolute* space orders, as  $v = v' \cdot p / (u \cdot o)$ , where  $v$  refers to the entire circumference of the generator. In contrast to the normalized amplitudes, the absolute amplitudes of sub-harmonics in the current loading's *Fourier* spectrum exhibit a similar order of magnitude for different  $u$ . The reduction of the normalized amplitudes is mainly caused by the increase of the torque producing amplitude  $|A_{e,u \cdot o}|$  in case of a higher number of feeding converters  $u$ .

The penetration depth in copper exceeds  $d_{E,v'} \gtrsim 20$  mm for all sub-harmonics, Fig. 6.6 d). Since this is much larger than a reasonable damper thickness in the range  $d_{\text{damp}} = 5 \dots 10$  mm, no effective shielding can be achieved. For an approximate estimate  $\mu_r \approx 100$  for the relative permeability of the saturated, ferromagnetic, cryogenic FeNi9 rotor iron parts (all-iron topology  $\textcircled{A}$ ), the penetration depth for  $v' = \pm 1$  is in the order of  $d_{E,v'=\pm 1} \approx 8 \dots 9$  mm, Fig. 6.6 d). The harmonics with  $v' = \pm 1$  are most critical among the sub-harmonics regarding high eddy current losses, since they feature high amplitudes  $|B_{v'}| \sim |A_{e,v'/v'}|$  and a comparably high slip  $s_{v'} \approx 1$ , Fig. 6.6 d). The outreach of the sub-harmonics into the cryogenic rotor section has generally the potential to cause also additional HTS AC losses in the superconducting field winding. The numerical calculation is however not feasible with manageable computational effort: In case of the redundancy operation, an entire periodic scheme of  $u \cdot o$  pole pairs must be modelled. In combination with the high computational effort of explicit HTS coil models in the coupled formulations, this prohibits a numerical calculation. As an alternative, the AC flux density, experienced by the field winding, is analysed in order to obtain a qualitative understanding of the criticality.

The feeding scheme with  $u = 2$ ,  $o = 1$  is regarded as the most critical case regarding the AC loss for following reasons:

- It features the highest number of transitions between fed and idling stator sections.
- In terms of spectral wave contributions, very high amplitudes of sub-harmonics in the stator air gap field occur, which even exceed the torque producing amplitude, Fig. 6.4 ( $v' = +1$ ).
- The numerically calculated rotor eddy current loss reveals a maximum for  $u = 2$ ,  $o = 1$ , e.g. in Fig. 6.13. A similar behaviour is expected for the HTS AC loss.

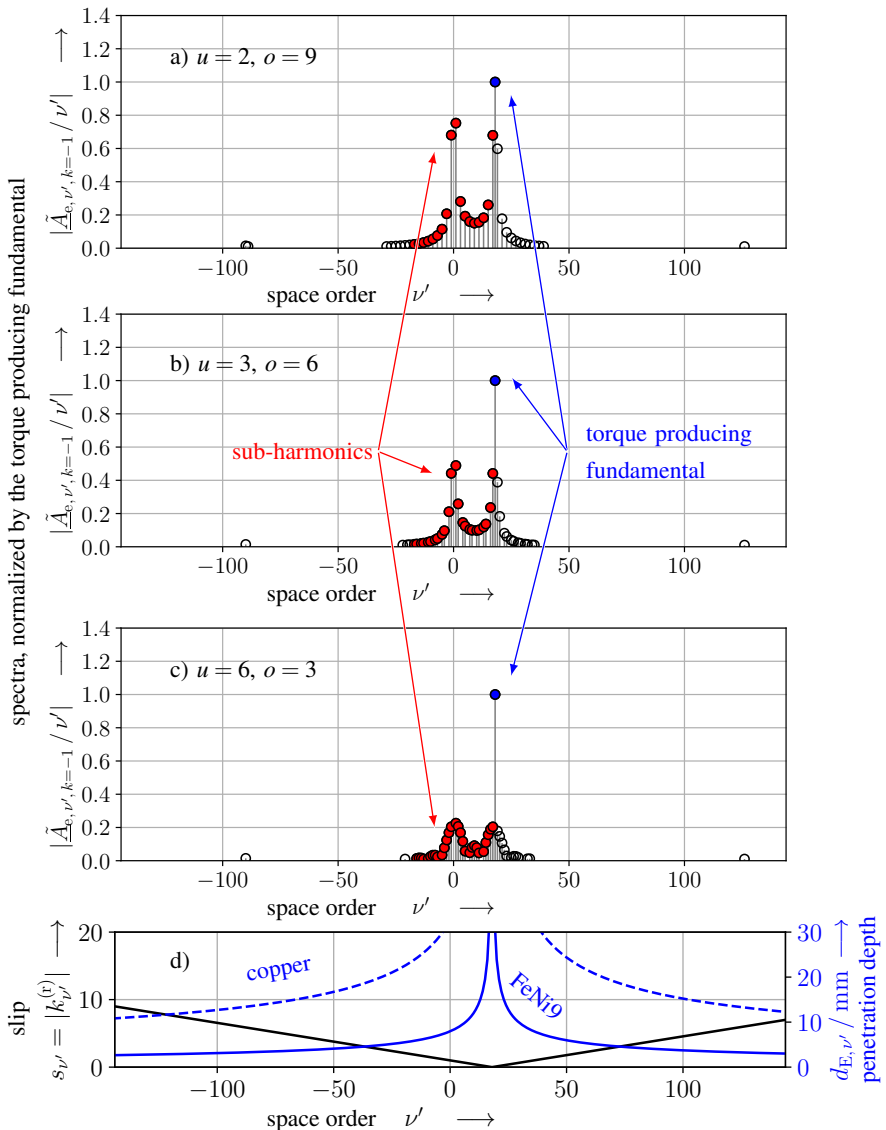


Figure 6.6.: a) - c) Analytically calculated, normalized spectra of the stator current loading, divided by the space order  $|\hat{A}_{e, \nu', k=-1} / \nu'| \sim |B_{\nu', k=-1}|$  for redundancy operation of a  $2p = 72$  pole generator with a common size of the basic winding scheme with  $o \cdot u = 18$  pole pairs: a)  $u = 2, o = 9$ , b)  $u = 3, o = 6$ , c)  $u = 6, o = 3$ . d) Slip  $s$  and penetration depth  $d_E$  in copper ( $\kappa_{Cu} = 48 \text{MS/m}$ ,  $\mu_r = 1$ ) and FeNi9 ( $\kappa_{FeNi9} \approx 8.3 \text{MS/m}$ ,  $\mu_r \approx 100$ ) as approximate average in the relevant, saturated region).

Therefore, the flux densities are evaluated for this case by means of a 2D FEM sector model in the points ① - ④ from Fig. 4.32. The AC part of the flux density's radial and circumferential components  $B_r$ ,  $B_\phi$  exhibit maximum peak-to-peak values in the order of  $\approx 100\text{mT}$ , Fig. 6.7, 6.8. The prominent AC field contribution features a time order of  $|k^{(r)}| = 0.5$  in the rotor frame of reference. It originates from the stator field sub-harmonic with relative space order  $\nu' = \pm 1$ , Fig. 6.5 b).

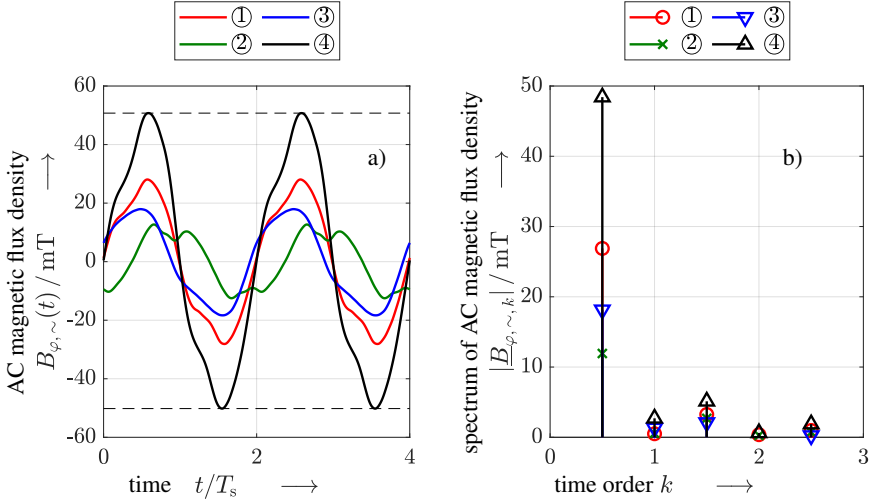


Figure 6.7.: Numerically calculated (software: *JMAG*) AC component of the circumferential flux density at points ① - ④ in Fig. 4.32. a) Magnetic flux density versus time for four electrical periods. b) *Fourier* spectrum of the magnetic flux density versus time order  $k^{(r)}$  in the rotor frame of reference. The results are shown for a feeding scheme with  $u = 2$  converters and  $o = 1$ .

An inner, warm copper damper screen with  $d_{\text{damp}} = 6\text{mm}$  is considered. The maximum amplitude is about  $\hat{B}_{\phi, \text{max}} \approx \hat{B}_{r, \text{max}} \approx 50\text{mT}$ . This value is only slightly higher than the AC field amplitudes that are experienced by the field winding in case of a  $q = 1$ ,  $W/\tau_p = 1$  stator winding in absence of a copper damper, Sec. 4.3.4. Since the numerically calculated AC loss in this case is very low, i.e.  $P_{\text{d, AC}} \lesssim 0.25\text{W}$ , Tab. 4.14, the same holds for the considered redundancy operation. In the present case, the AC loss is expected to be even lower, since the dominant flux density oscillation features only half the frequency compared to the scenario in Sec. 4.3.4. Similar to the rated operation, the AC loss in the HTS field winding plays a subordinate role in case of intermittent stator feeding.

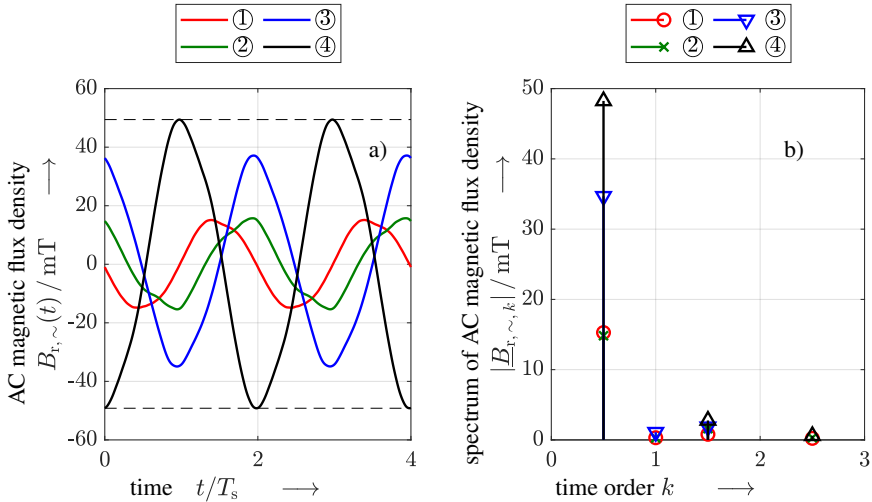


Figure 6.8.: As Fig. 6.7, but for the radial component of the magnetic flux density.

The comparison of the air gap torque for different values of  $o$ , but the same number of converters  $u = 2$ , Fig. 6.9, reveals a decrease of the torque ripple for a higher number of jointly fed, neighbouring pole pairs  $o$ . The absolute value of the average torque  $\bar{M}_e$  decreases towards higher  $o$ , since the additional eddy current loss in the rotor decreases, e.g. Fig. 6.13. The torque ripple decreases, since the number of transition zones between idling and fed stator sections is reduced. During one electrical period, two rotor poles pass each of the transition zones, which is reflected by the prominent torque pulsation with doubled stator electrical frequency for  $o = 1$ , Fig. 6.9. Even in case of  $o = 1$ , the relative peak-to-peak torque ripple is small, i.e.  $(M_{e,pp}/\bar{M}_e) \approx 4.5\%$ . It is therefore generally of minor importance regarding the choice of the feeding scheme at redundancy operation.

The eddy current loss in the cold rotor iron parts, Fig. 6.10, largely exceeds the loss in case of complete stator feeding, which is low with  $P_{d,Fi,pr} \approx 17.3 \text{ W}$  and  $P_{d,Fi,yr} < 0.01 \text{ W}$ . Similar to rated operation, the major part of the eddy current loss for intermittent feeding still occurs in the rotor pole cores (all-iron topology  $\text{\textcircled{A}}$ ), Fig. 6.10, 6.11. The eddy current loss is calculated by assuming an electrical insulation between the pole cores and the rotor yoke, since a considerable contact resistance is expected, if the pole cores are bolted to the yoke. Therefore, a zero net current is required for each of the pole cores in the 2D

model, which is imposed by additional integral constraints. The maximum instantaneous eddy current loss power in the rotor pole cores varies by a factor of  $\approx 5.5 \dots 6$  for different numbers of jointly fed, neighbouring pole pairs  $o$ , Fig. 6.10. All feeding schemes yield a dominant fluctuation of the instantaneous loss power with double stator electrical frequency  $2f_s$ . This contribution is caused by the leaving and entering of rotor poles into the fed stator sections. As the rotor reluctance in the transition region also determines the outreach of the magnetic flux to the rotor yoke, a similar variation of the eddy current loss is observed for  $P_{d, \text{Ft}, \text{yr}}$ , Fig. 6.11.

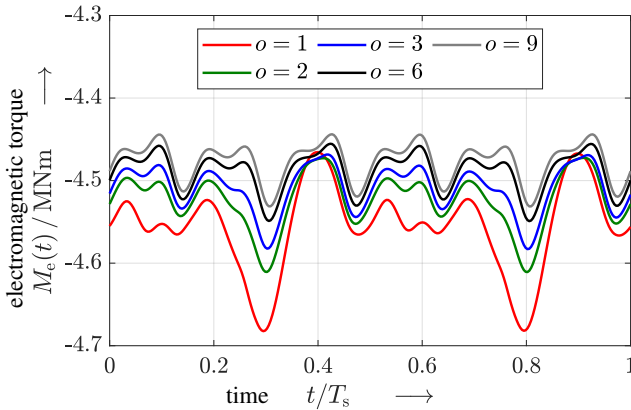


Figure 6.9.: Numerically calculated (software: *JMAG*) air gap torque for redundancy operation with  $u = 2$  converters ( $2p = 72$ ) and variation of the number of jointly fed neighbouring basic schemes  $o$ .  $o = 1$ : alternation of fed and idling pole pairs.  $o = 9$ : quadrant-wise split of fed and idling winding sections.

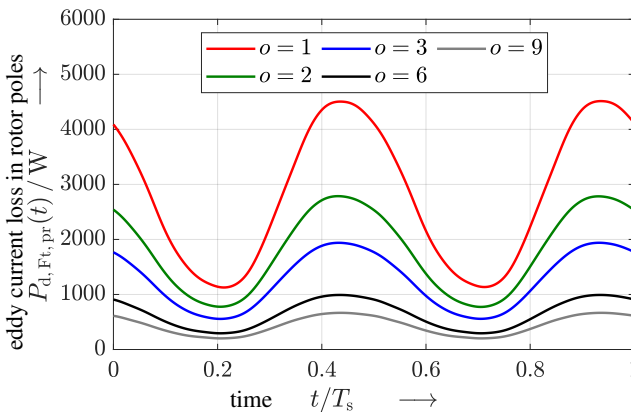


Figure 6.10.: As Fig. 6.9, but for the eddy current loss in the ferromagnetic rotor pole (all-iron topology  $\textcircled{A}$ ).

Generally, the eddy current loss is strongly decreased, if a higher number  $o$  of neighbouring pole pairs is jointly fed by one converter. The high instantaneous loss powers occur however locally in the rotor poles, which pass from idling to fed sectors or vice versa. To evaluate the criticality of the local heating, the temperature rise for adiabatic heating is approximately estimated, (6.4), for  $o = 9$ , yielding 4 poles in transition regions. An average heating power of  $\bar{P}_{d, \text{Fe}, \text{rp}} = 500/4 \approx 125 \text{ W}$ , Fig. 6.10, over half an electrical period for a stator frequency of  $f_s = 5 \text{ Hz}$  is considered. The mass of a single rotor pole core is  $m_p \approx 60 \text{ kg}$  and the specific heat capacity of FeNi9 at 30 K is  $c_{\text{th}} \approx 15 \text{ J}/(\text{kg} \cdot \text{K})$  [56].

$$\Delta T_p \approx \frac{Q_d}{C_{\text{th}}} \approx \frac{\bar{P}_{d, \text{Fe}} \cdot \Delta t}{m_p \cdot c_{\text{th}}} \approx 0.01 \dots 0.02 \text{ K} \quad (6.4)$$

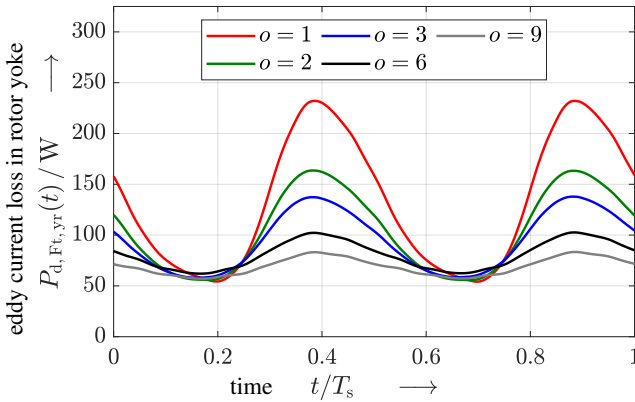


Figure 6.11.: As Fig. 6.9, but for the eddy current loss in the cold, ferromagnetic rotor yoke (all-iron topology  $\text{\textcircled{A}}$ ).

This estimate  $\Delta T_p$  for the order of magnitude of the temperature rise shows that the spatial localization of the maximum loss is of minor importance and that analyses in terms of the average, overall loss power are meaningful.

The time averaged eddy current loss in the cold rotor parts, i.e. the ferromagnetic rotor poles and the rotor yoke, increases as the total number of feeding converters  $u$ , of which one fails, is reduced, Fig. 6.12. Since the power at redundancy operation scales as  $P \sim (u - 1)/u$ , Tab. 6.1, the efficiency decrease is even stronger.

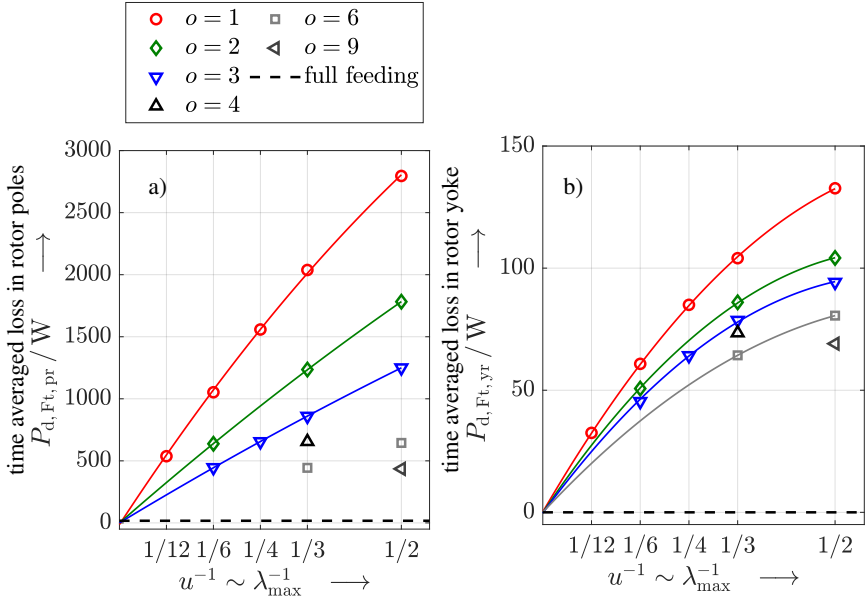


Figure 6.12.: Numerically calculated AC loss (2D FEM models, software: *JMAG*) for redundancy operation of a  $2p = 72$  pole generator. The loss is plotted versus  $u^{-1}$ , which is proportional to the inverse maximum wave length  $\lambda_{\max}$  of space harmonics in the stator current loading spectrum for fixed  $o$ . The exemplary generator features the all-iron topology  $\textcircled{A}$ . a) Eddy current loss in the massive rotor poles  $P_{d, Ft, pr}$ . b) Eddy current loss in the massive rotor yoke  $P_{d, Ft, yr}$ .

The curves for constant  $u$  in Fig. 6.13 correspond to a redundancy operation with approximately the same output power. Feeding schemes with common size of the spatial period along the circumference, i.e. comprising the same number  $u \cdot o$  of pole pairs, feature approximately the same eddy current loss in the rotor pole cores. Generally, the minimum combined additional average loss in the cold pole cores  $P_{d, Ft, pr}$  and the cold rotor yoke  $P_{d, Ft, yr}$  of  $P_{d, Ft, c} = P_{d, Ft, pr} + P_{d, Ft, yr} \approx 500 \text{ W}$  is in the order of the cryogenic heat load at rated operation. For patterns with smaller size of the spatial period of the feeding pattern  $\sim u \cdot o$ , the original cryogenic heat load is exceeded by a factor of up to  $6 \dots 7$ .

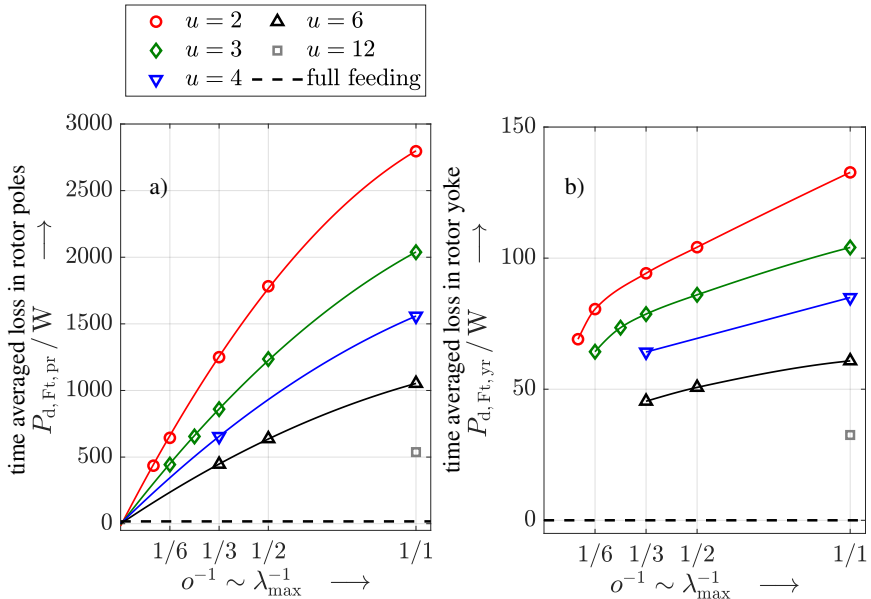


Figure 6.13.: As Fig. 6.13, but in plots versus the inverse number of jointly fed, neighbouring converters  $o^{-1}$ , which scales as the inverse maximum wave length  $\lambda_{\max}$  of space harmonics of the stator current loading for fixed  $u$ .

The relative increase of the eddy current loss in the warm copper damper  $P_{d, Ft, damp}$  and in the cryostat wall  $P_{d, Ft, cw}$  is much smaller than for the cold rotor iron parts, Fig. 6.14. The maximum loss increase factor for  $u = 2$ ,  $o = 1$  is in the order of  $\approx 3$  for  $P_{d, Ft, damp}$ , Fig. 6.14 a). As the eddy current losses in the damper and the cryostat wall are not subject to the very large cooling penalty for losses in the cryogenic section,  $P_{d, Ft, damp}$  and  $P_{d, Ft, cw}$  play a subordinate role regarding the feasibility of the redundancy operation. However, the eddy current losses in the warm parts, i.e. the damper and the cryostat wall, are also minimized for a larger number of converters  $u$  and a higher number of jointly fed, neighbouring pole pairs  $o$ .

As discussed qualitatively for the case  $u = 2$  in Fig. 6.9, the torque ripple is also smaller for larger periodic sectors of the stator feeding scheme at intermittent feeding, Fig. 6.15 a).



For  $u \cdot o = 18$ , the relative peak-to-peak torque ripple  $M_{pp}/\bar{M}$  is less than 2 %, irrespective of the number of feeding converters  $u$ . This corresponds only to a minor increase of 0.2...0.6 percentage points with respect to the torque ripple in case of a healthy feeding scheme.

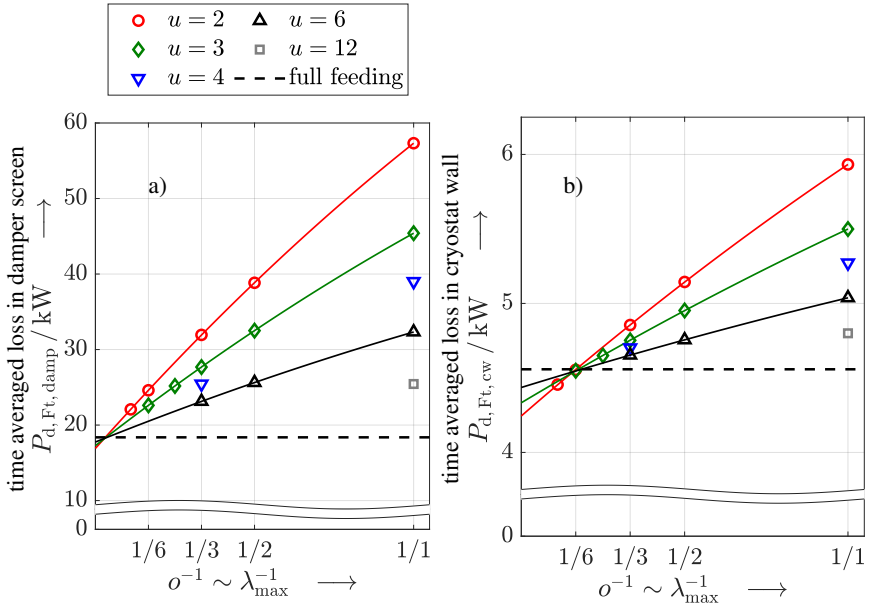


Figure 6.14.: As Fig. 6.13, but for a) the eddy current loss in the copper damper  $P_{d, Ft, damp}$  and b) the eddy current loss in the cryostat wall  $P_{d, Ft, cw}$ .

The stator iron loss  $P_{d, Fe, s}$  is generally decreased compared to the normal operation, as only parts of the stator iron stack are subject to the armature field, Fig. 6.15 b). Since the rotor field accounts for the major contribution to the stator iron loss, this decrease is only small, i.e.  $\lesssim 11\%$ . Due to the small share in the overall loss of typically  $\lesssim 3\%$ , as a result of the low fundamental frequency  $f_s \approx 5 \text{ Hz}$ , the increase of  $P_{d, Fe, s}$  towards a larger size of the periodic sector  $u \cdot o$  is not relevant regarding the choice of the inverter feeding pattern.

The high eddy current loss in the cold rotor iron (rotor poles and yoke) implies that only feeding schemes with a minimum of transitions between idling and fed sectors, i.e.  $u \cdot o = 18$  for the considered example, are reasonable. The calculated losses for these feeding schemes are summarized in Tab. 6.2.

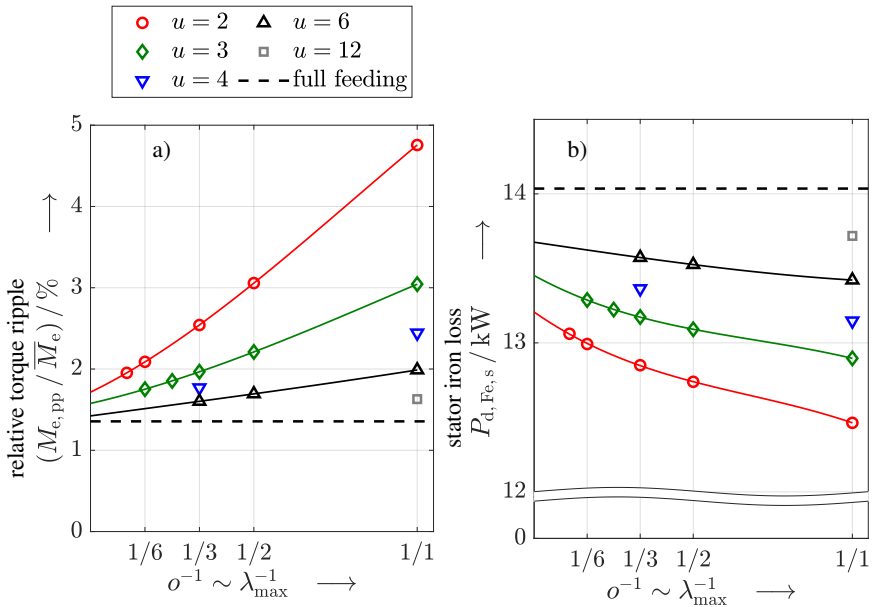


Figure 6.15.: As Fig. 6.13, but for a) the relative peak-to-peak torque ripple and b) the stator iron loss.

Two scenarios are considered as reaction to the nearly doubled cryogenic heat load:

1. The number of the cold heads  $N_{\text{CH}}$  is increased in order to maintain the original operating temperature  $T_{\text{CH}}$  of the cryo-coolers. This yields a higher cost of the cryogenic cooling system and an additional efficiency decrease.
2. The same cryogenic cooling system is used, which leads to an increase of the HTS operating temperature  $T_{\text{HTS}}$ . This is only possible, if the critical current  $I_c$  in the superconducting winding remains sufficiently high.

Following main findings are derived from the comparison:

- The additional cryogenic heat load of  $\Delta\dot{Q}_{\text{cryo}} \approx 480 \text{ W}$  is nearly independent from the feeding scheme. The number of cold heads for scenario 1) is nearly doubled compared to the original design, while the additional compressor power is in the order of 44 kW. The least impact on the overall efficiency occurs for  $u = 6$ ,  $o = 3$ , i.e.  $-0.8\%$ , as a result of the highest generator output power among the schemes.

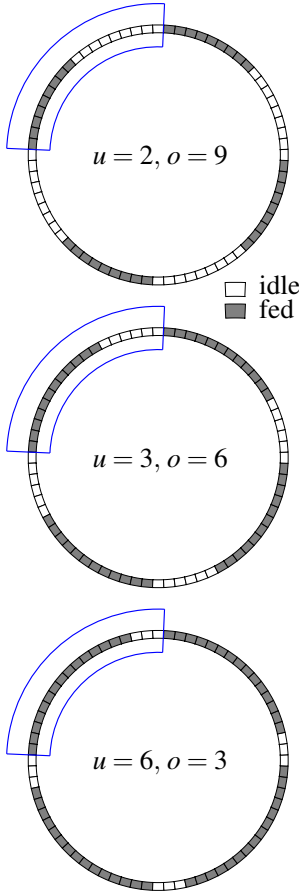


Table 6.2.: Comparison of numerically calculated losses for different feeding schemes (left) with common size of the fundamental feeding scheme with  $o \cdot u = 18$  pole pairs. Two scenarios are considered as reaction to the increased eddy current loss in the cryogenic section: 1) the number of cold heads  $N_{CH}$  is increased to maintain the original operating temperature of the cryo-coolers  $T_{CH}$ , 2) the same cooling system is used, which leads to an increase of the operating temperature  $T_{HTS}$ .

	$u = 2$	$u = 3$	$u = 6$	full
	$o = 9$	$o = 6$	$o = 3$	feeding
$P_{d, Ft, pr}$	435.5 W	443.7 W	446.0 W	17.3 W
$P_{d, Ft, yr}$	69.1 W	64.3 W	45.4 W	3.6 mW
$P_{d, Ft, damp}$	22.1 kW	22.6 kW	23.1 kW	18.4 kW
$P_{d, Ft, cw}$	4.5 kW	4.5 kW	4.7 kW	4.6 kW
$P_{d, Fe, s}$	13.1 kW	13.3 kW	13.6 kW	14.0 kW
1) increased number of cold heads $N_{CH}$				
$\Delta \dot{Q}_{cryo}$	487.3 W	490.7 W	474.1 W	-
$\dot{Q}_{cryo, t}$	896.1 W	899.5 W	882.9 W	408.8 W
$T_{HTS} - T_{CH}$	8.3 K	8.4 K	8.2 K	3.8 K
$T'_{HTS}$	34.5 K	34.6 K	34.4 K	30.0 K
$\Delta N_{CH}$	6	6	6	-
$N_{CH}$	13	13	13	7
$P_{compr}$	81.3 kW	81.6 kW	80.1 kW	37.1 kW
$\Delta P_{compr}$	44.2 kW	44.5 kW	43.0 kW	-
$\frac{\Delta P_{compr}}{P_{el, out}}$	1.3 %	0.9 %	0.7 %	-
2) same cooling system				
$COP'$	2.16 %	2.17 %	2.13 %	1.1 %
$T_{CH}$	59.4 K	59.8 K	58 K	26.2 K
$T'_{HTS}$	67.7 K	68.2 K	66.2 K	30 K
$I_c(T'_{HTS})$	0.18	0.17	0.21	1
$I_c(30K)$				

- Based on a cost per cold head of 25 kEuro, the additional cost for enabling the redundancy operation is in the order of 150 kEuro for scenario 1). This value must be compared with the opportunity cost of longer downtimes without redundancy operation in order to evaluate the economic viability.
- Without additional cold heads in scenario 2), the temperature rise is in the order of  $\Delta T_{HTS} \approx 37$  K with respect to the original operating temperature of  $T_{HTS} = 30$  K. The temperature gradient between the cold stage of the cold head and the HTS

winding is generally increased due to the higher heat load  $\dot{Q}_{\text{cryo}}$ . The COP at the elevated temperature is approximately doubled compared to the normal operation with  $T_{\text{HTS}} = 30\text{K}$ . However, the critical current  $I_c$  in the superconductor is only about  $\approx 1/5$  of the original value at  $T_{\text{HTS}} = 30\text{K}$ . Even by fully exploiting the original current margin of  $I_f/I_c = 1/1.7$ , only about one third of the rated field current  $I_f$  can be achieved. A reduction of the excitation MMF implies a further decrease in output power. Scenario 2) is therefore not possible without additional loss mitigation measures.

Since the more expensive cooling system in scenario 1) leads to an increase of  $C_l$  in the order of 10 % for *Pareto* efficient all-iron designs (topology  $\textcircled{A}$ ), Fig. 5.2, a reduction of losses in the cryogenic section is required in order to achieve economical competitiveness. Two possible loss mitigation measures are:

1. The use of non-magnetic, non-conductive pole cores eliminates the main contribution to the high eddy current loss in the cold rotor iron. For *Pareto* efficient designs, Fig. 5.2, the change from ferromagnetic to non-magnetic pole cores (topology  $\textcircled{B}$  instead of  $\textcircled{A}$ ) is accompanied by a cost increase of  $\Delta C_l \approx 300 \dots 400\text{kEuro}$  due to the higher excitation requirements. In terms of CAPEX (neglect of differences in efficiency), the up-scaling of the cryogenic cooling system represents therefore the cheaper solution owing to the current cost structure. If the HTS price decreases however, the use of non-magnetic pole cores is an economically viable measure to enable the redundancy operation.
2. The ferromagnetic pole cores can be equipped with a grooved surface in order to reduce the eddy current loss from  $P_{d,\text{Ft,orig}}$  to  $P_{d,\text{Ft,gr}}$ . The penetration depth of the relevant sub-harmonics is in the order of  $d_E \approx 10\text{mm}$ , Fig. 6.6 d). Appropriately dimensioned grooves can be used to elongate the preferred eddy current paths, leading to the reduced losses  $P_{d,\text{Ft,gr}}$ . An analytical estimate for the loss reduction factor  $\chi = P_{d,\text{Ft,gr}}/P_{d,\text{Ft,orig}}$  was derived by *Kesavamurthy* and *Basu* [113] and is discussed in App. A.4.3. As an example, the estimate for the loss reduction factor is in the order of  $\chi \approx 0.3 \dots 0.5$  for 20 grooves, which feature a depth of  $10 \dots 15\text{mm}$  and are evenly spaced in axial direction. The large penetration depth and the large wave length of the sub-harmonics generally reduce the effectiveness of the grooving. However, a loss reduction by at least 50 % could enable a redundancy operation with the original cooling system at a reduced current margin of  $I_f/I_c \approx 1$ .

## 6.2. Sudden Short Circuit Faults

The transient behaviour of HTS excited direct drive generators after sudden short circuits is analysed by means of 2D FEM time stepping simulations, implemented in the software *JMAG*. The short circuits are preceded by a generator no-load operation. The eddy current reaction in all conductive parts is directly incorporated by the numerical model. Voltage fed FEM models are used with coupling to circuit simulations of the excitation circuit and the stator circuit. The non-linear  $E(J)$ -relation of the HTS winding is not explicitly modelled in order to prevent an excessive computational effort in combination with the voltage feeding. Instead, the calculated short circuit currents are impressed in a subsequent current-fed FEM simulation using the  $H$ - $A$ -formulation (software: *COMSOL Multiphysics*) in order to quantify the AC loss. Generally, the computational effort of the short circuit simulations is high due to the multi-time scale nature of the problem: Several time constants, e.g. of the damper and of the field winding, which differ by orders of magnitude, govern the dynamic processes.

The simulations are carried out for an exemplary generator with characteristics in Tab. 6.3. Mostly per-unit values are used for the analysis, with reference quantities listed in Tab. 6.4. In a preceding analysis, the thickness of the warm, inner damper screen  $d_{\text{damp}}$  was varied with only minor impact on the general dynamic characteristics, such that the discussion is restricted to a single value of  $d_{\text{damp}} = 5$  mm here.

Due to the very high combined rotational inertia  $J_{\text{rot}}$  of the drive train and the turbine, all calculations are carried out for constant speed. To get meaningful results for the transient response, an accurate estimate for the intrinsically 3D end-winding stray reactances  $X_{s\sigma b}$  is required. It is calculated with the 3D non-linear FEM models after parametrization according to Sec. 2.4.

Three different sudden short circuit faults of the star-connected stator winding after generator no-load operation are considered:

1. symmetric three-phase short circuit at the stator terminals (3ph SC)
2. two-phase short circuit between phase U and V (2ph SC)
3. single-phase short circuit between phase U and the neutral point (1ph SC)

The symmetric three-phase short circuit represents the most common case, which essentially determines the maximum loads under real conditions. The other two cases are con-

sidered, since the single phase short circuit typically yields the highest peak values of the stator short circuit current  $\hat{I}_{k,\max}$ , while the two-phase short circuit causes the maximum short circuit torque  $\hat{M}_{k,\max}$ .

Table 6.3.: Characteristics of the exemplary direct drive HTS generator with topology  $\textcircled{A}$  and with warm, inner damper screen, for which sudden short circuit faults are analysed.

$P_{el,N} / S_N$	-6.938 MW / 7.478 MVA
$\cos \varphi_{sN} / \eta_N$	-0.928 / 93.1 %
$f_{sN} / n_N / 2p$	5.41 Hz / 8.33 rpm / 78
$d_{so} / l_i$	6.50 m / 1.2 m
$d_{cw} / d_{damp}$	10 mm / 5 mm
$m_{act} / C_t$	47.1 t / 1.54 MEuro
topology	all-iron $\textcircled{A}$
$T_{HTS} / I_{fN}$	30 K / 416.9 A
HTS tape	<i>THEVA TPL2100</i>
$m / q / (W / \tau_p)$	3 / 2 / (5 / 6)
$N_c / a / N_s$	22 / 39 / 88

Table 6.4.: Reference quantities for the conversion to per-unit values for the considered exemplary HTS excited generator with star-connected stator winding.

$M_B = \frac{S_N}{\omega_N / p}$	8.572 MNm
$I_B = \sqrt{2} \cdot I_{s,N}$	8719.3 A
$U_B = \sqrt{2} \cdot U_{ph,N}$	571.7 V
$T_B = \omega_N^{-1}$	29.4 ms
$Z_N = U_{ph,N} / I_{s,N}$	65.6 m $\Omega$
$\Psi_B = \frac{\sqrt{2} \cdot U_{N,s}}{\omega_N}$	16.8 V · s

A constant DC excitation voltage  $U_f$  is considered. For the resistance of the normal conducting part of the current leads, an estimate of  $R_{cl} \approx 20 \text{ m}\Omega$  is used from [137]. The current-dependent resistance of the brush and slip-ring system is included based on data in [43]. The inter-pole connections at cryogenic temperature feature voltage drops in the range of nanovolts [227] and their resistance is therefore neglected. Before the simulation of the sudden short circuits, equilibration runs are carried out for no-load conditions, so that the excitation current attains its rated value for the voltage feeding. Short circuits at the zero-crossing of the phase voltage in phase U are considered in order to cover the highest short-circuit current amplitude in that phase.

Irrespective of the considered short circuit type, screening currents flow mainly in the copper damper screen with very high absolute current densities of up to  $|J_z| \approx 45 \text{ A} / \text{mm}^2$ , Fig. 6.16. Due to the large magnetically effective air gap width of  $\delta_{mag} \approx 30 \text{ mm}$  and the high magnetic reluctance faced by the damper stray field, the sub-transient short circuit current  $I''_k$  is mainly limited by the stator stray reactance  $X_{s\sigma}$ . Due to the large slot height

$h_Q$ , the slot stray reactance  $X_{s\sigma Q}$  is of major importance, as reflected by the field lines in Fig. 6.16.

Over a short time period of  $\tau \leq 3$  p.u. after the sudden two-phase short circuit, maximum instantaneous loss powers of up to  $P_{d, Ft, damp} \approx 3.5$  MW occur in the damper screen and up to  $P_{d, Ft, cw} \approx 150$  kW in the cryostat wall, Fig. 6.17. The instantaneous eddy current loss powers for the single-phase and three-phase short circuits are lower, but feature the same order of magnitude, App. A.8.2. Very high instantaneous losses are also generated in the cryogenic rotor iron, Fig. 6.18. For an analysis of a potential overheating and a potential temperature-induced quench of the HTS field winding, an adiabatic temperature rise  $\Delta T$  is considered, (6.5), e.g. Fig. 6.17.

$$Q_d = c_{th} \cdot m \cdot \Delta T \Leftrightarrow \Delta T = \frac{Q_d}{c_{th} \cdot m} = \frac{Q_d}{C_{th}} \quad (6.5)$$

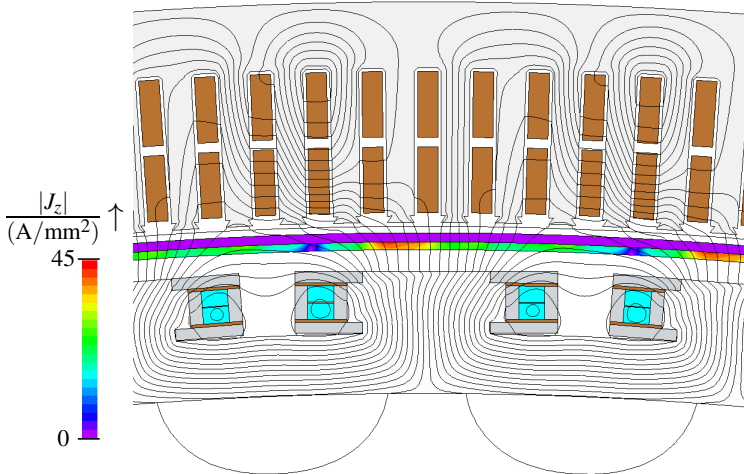


Figure 6.16.: Single-phase sudden short circuit to the neutral point: Numerically calculated magnetic field lines and color encoded absolute eddy current density  $|J_z|$  in the warm, inner copper damper screen and in the cryostat wall. Results are shown for the time instant with maximum eddy current loss in the damper screen. (software: *JMAG*)

In spite of the very high instantaneous loss power, the dissipated energy  $Q_d$  is sufficiently small due to the short period of time in the sub-transient regimes ( $\tau = 20$  p.u.  $\approx 0.59$  s). Therefore, the temperature rise in both warm and cold components is small, Tab. 6.5. The

still high eddy current loss due to the steady state 1ph and 2ph short circuit conditions requires however a rapid interruption of operation. In case of the cold rotor parts, the advantageously larger heat capacities for topology  $\textcircled{A}$  limit the increase in average temperature to  $\Delta T \approx 0.3 \dots 0.4 \text{ K}$ , Tab. 6.5.

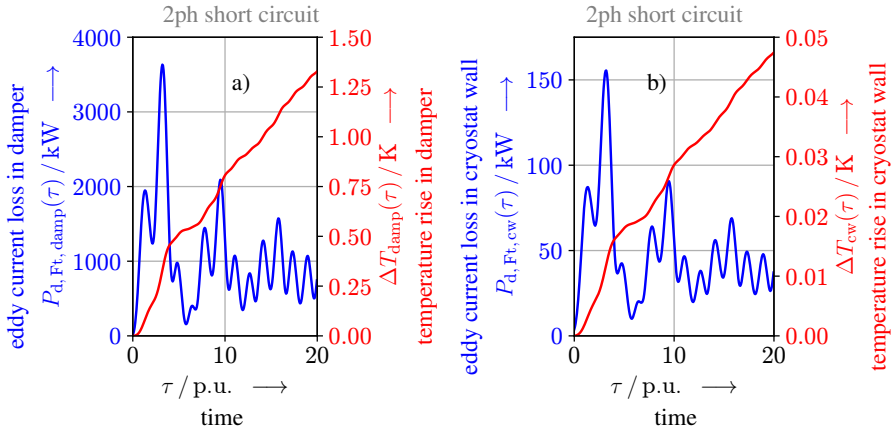


Figure 6.17.: Calculated, instantaneous loss power and temperature rise for adiabatic heating after a sudden two-phase short circuit (all-iron topology  $\textcircled{A}$ ): a) warm, inner copper damper screen, b) stainless steel cryostat wall.

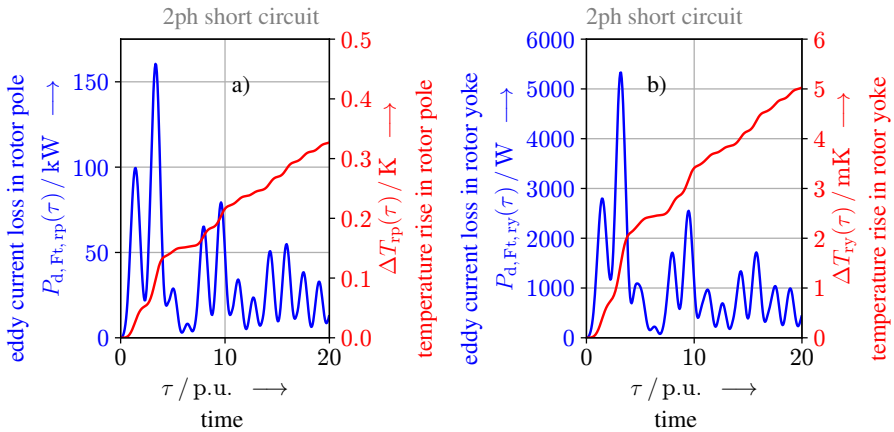


Figure 6.18.: As Fig. 6.17, but for parts in the cryogenic section (all-iron topology  $\textcircled{A}$ ): a) rotor poles, b) rotor yoke.



Table 6.5.: Calculated maximum loss power during the three different sudden short circuit (S.C.) faults. The approximate calculated temperature rise  $\Delta T$  of the rotor parts is estimated by assuming an adiabatic heating during a short time period of  $\tau = 20$  p.u. after the short circuit. After  $\tau = 20$  p.u., the sub-transient damper current has approximately decayed, e.g. Fig. 6.17.

	single-phase S.C.		two-phase S.C.		three-phase S.C.	
	$P_{d,max,1ph}$	$\Delta T_{1ph}$	$P_{d,max,2ph}$	$\Delta T_{2ph}$	$P_{d,max,3ph}$	$\Delta T_{3ph}$
warm, inner damper	1908 kW	0.84 K	3633 kW	1.33 K	1394 kW	0.35 K
$C_{th} = 466 \frac{kJ}{K}$ cryostat wall	88.4 kW	0.03 K	155.5 kW	0.05 K	61.8 kW	0.01 K
$C_{th} = 608 \frac{kJ}{K}$ rotor poles	77.9 kW	0.17 K	160.5 kW	0.33 K	68.4 kW	0.11 K
$C_{th} = 61 \frac{kJ}{K}$ rotor yoke	2019 W	2.7 mK	5329 W	5.0 mK	1849 W	1.8 mK
$C_{th} = 125 \frac{kJ}{K}$						

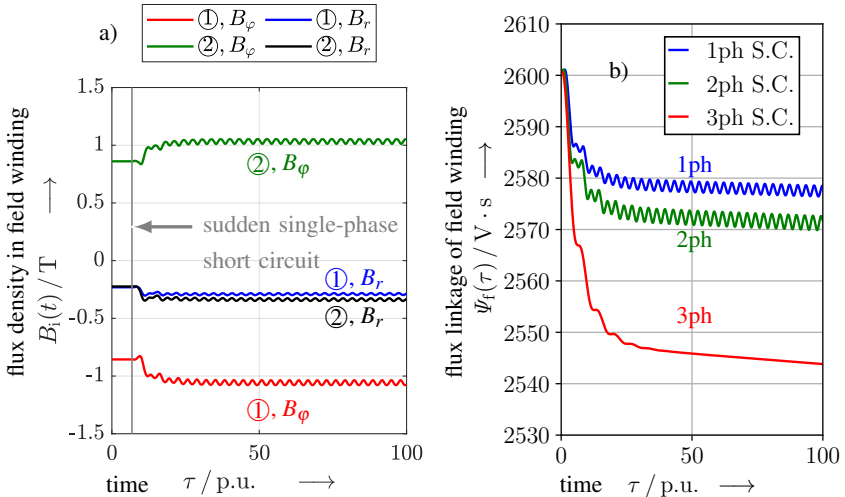


Figure 6.19.: a) Calculated, tangential and radial components  $B_r$ ,  $B_\phi$  of the magnetic flux densities in points ① and ② in Fig. 4.32 for generator topology ① and a warm, inner damper. Results are shown for a single-phase sudden short circuit to the neutral point. b) Flux linkage of the field winding  $\Psi_f$  after the three different sudden short circuit faults.

The flux density experienced by the SC field winding is only little increased during the single-phase short circuit, even in the most exposed points, Fig. 6.19 a). A slightly stronger increase of the magnetic field is found for the two- and three-phase sudden short circuits, which is caused by larger transient variations of the field current  $I_f(\tau)$ , Fig. 6.20. The symmetric, sudden three-phase short circuit current yields the highest decrease  $\Delta\psi_f(\tau)$  in the field winding's flux linkage  $\psi_f$  due to the stator short circuit current system, Fig. 6.19 b). Generally, the decrease in the flux linkage is caused by the negative  $d$ -current, which flows in the stator winding.  $\Delta\psi_f$  is small due to the additional field current  $\Delta I_f$ , which flows as to maintain the original flux linkage.

The dynamic increase  $\Delta I_f$  of the superconducting field current  $I_f$  features a maximum of about  $\Delta I_f/I_{fN} \approx 37\%$  for the sudden three-phase short circuit. Since the dynamic resistance of the HTS field winding coils  $R_{HTS,AC}$  is not directly included in the calculation, this value is just a rough estimate, as discussed in the end of this section in connection with Fig. 6.27.

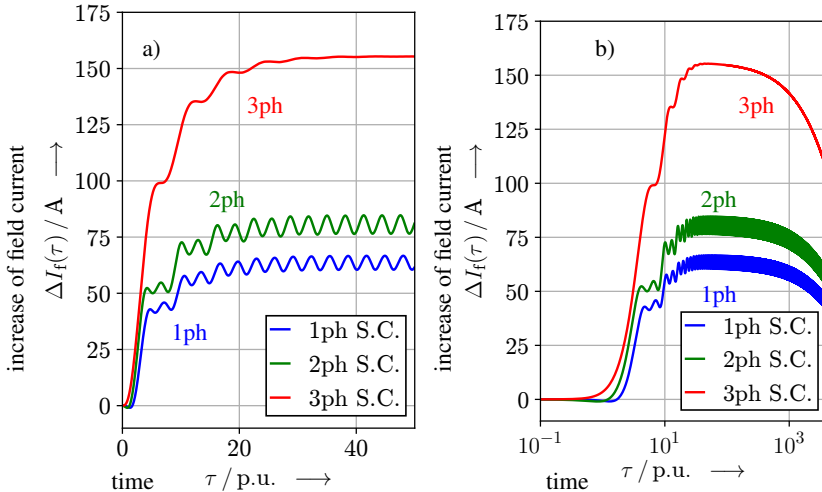


Figure 6.20.: Numerically calculated deviation of the field current from the rated value  $\Delta I_f = (I_f - I_{fN})$  after a sudden short circuit at the stator terminals. a) Initial dynamic increase of the field current  $\Delta I_f$ . b) Dynamics of the field current, including its decay for  $\tau \gtrsim 100$  p.u..

Due to the comparably large current margin of  $I_f/I_c = 1/1.7$ , the dynamic field current

peak is well below the critical current, even in case of small  $I_c$ -reductions of the SC winding ing due to a) the increase of the flux density in the field winding, Fig. 6.19, and b) the small temperature rise. Due to the large inductance  $L_f$  and the low resistance  $R_f$  in the excitation circuit, the field current decays very slowly, corresponding to a large transient time constant  $T'_d \approx 300$  s, Tab. 6.10 in the end of this section and Fig. 6.20 b).

The maximum, dynamic short circuit torque of  $m_{k,\max} \approx 2.5$  p.u., Fig. 6.21 a), is below the designed limit of three times rated torque, which is assumed for the dimensioning of the cold-warm support, App. A.9.3. For sudden single-phase and two-phase short circuits, the generator experiences a considerable torque oscillation with double fundamental frequency  $2f_s$ , with an amplitude in the order of the rated torque, Fig. 6.21 b).

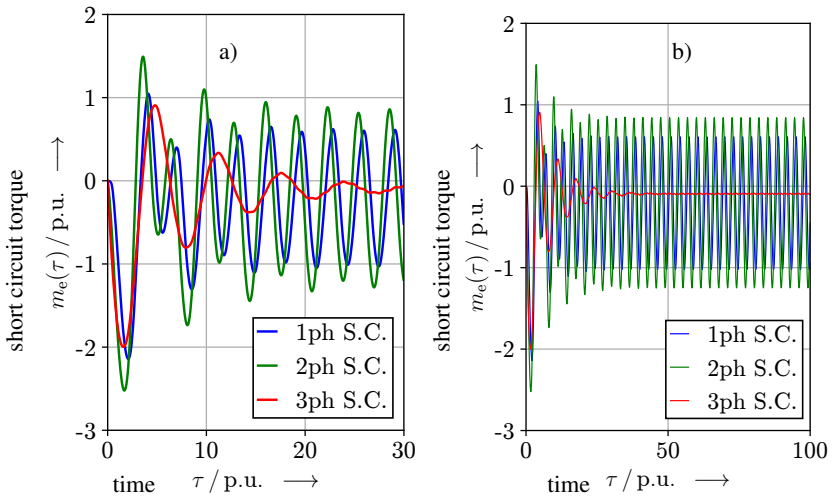


Figure 6.21.: 7 MW, 8.33 rpm HTS excited generator with topology  $\textcircled{A}$ : Numerically calculated short circuit torque after a sudden short circuit at  $\tau = 0$  (zero-crossing of phase voltage U). Results are shown for the three considered kinds of short circuits (S.C.). a) Initial course of the dynamic short circuit torque. b) Dynamic transition to the steady state short circuit torque.

This cyclic load change can generally lead to an accelerated fatigue in the GFRP structure. However, for the design value of the admissible stress  $\sigma_{\max} = 20$  MPa, a negligible fatigue degradation of mechanical strength has been reported for both compressive and tensile loads in literature [20]. The value of  $\sigma_{\max}$  is moreover well below the reported values of

tensile stress, for which G11 coupons were tested for more than  $10^6$  cycles without failure [186]. Since the short circuit failures are rather rare events, and a rapid shut-off after the sudden short circuit is assumed, the analysed generator designs are considered to fulfil mechanical requirements.

The maximum peak value of the stator short circuit current in phase U occurs for a single-phase short circuit, i.e.  $i_{k,\max} \approx 4.27$  p.u., after about half an electrical period, Fig. 6.22 a). The current envelopes, Fig. 6.22 b), reveal an initial decay of the DC component of the short circuit current at the subtransient time scale of  $\tau \approx 5 \dots 10$  p.u.. The stationary short circuit currents feature amplitudes of about  $\hat{i}_k \approx 1.8 \dots 2.4$  p.u. due to the small synchronous inductances with highest values for the single-phase short circuit. Tab. 6.6 summarizes the peak values for the dynamic stator short circuit currents  $i_{k,\max}$  and the dynamic short circuit torque  $m_{k,\max}$  as well as the maximum dynamic slope of the transient SC field current increase.

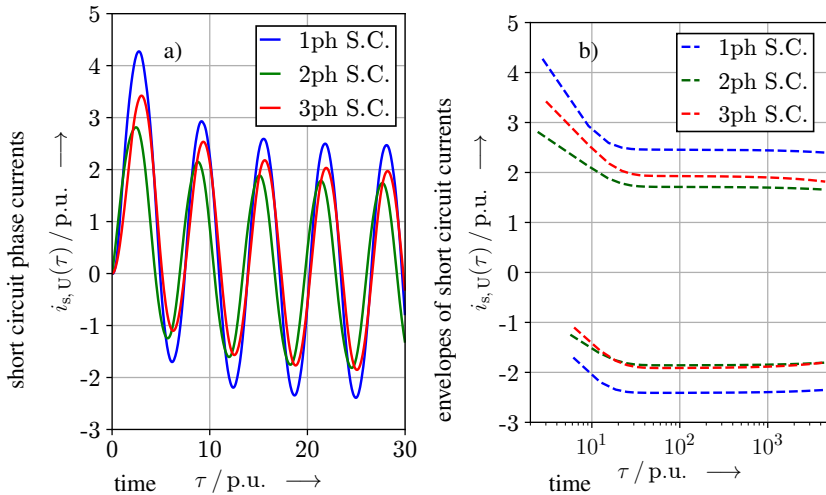


Figure 6.22.: 7 MW, 8.33 rpm HTS excited generator with topology (A): a) Numerically calculated stator short circuit currents after a sudden short circuit at  $\tau = 0$  (zero-crossing of phase voltage U). Results are shown for the three considered kinds of short circuits (S.C.). b) Envelopes of the dynamic short circuit stator currents with transition to the steady state short circuit operation.

Table 6.6.: Comparison of numerically calculated, maximum dynamic short circuit torque and maximum dynamic stator short circuit current for the three different kinds of sudden short circuits. The maximum dynamic increase in field current and the maximum slope of the field current ( $|d_t I_f|_{\max}$ ) are listed. The latter determine the maximum HTS AC loss.

	$ i_{k,\max} /\text{p.u.}$	$ m_{k,\max} /\text{p.u.}$	$(\Delta I_f)_{\max}$	$( d_t I_f )_{\max}$
1ph short circuit	4.27	2.14	66.7 A (+16 %)	728 A/s
2ph short circuit	2.81	2.52	84.7 A (+20 %)	908 A/s
3ph short circuit	3.42	2.00	155.4 A (+37 %)	991 A/s

In order to extract sub-transient and transient parameters from the numerically calculated results, the dynamic sudden short circuit stator current for the three-phase short circuit is analysed, based on following assumptions [22]:

- The stator winding resistance per phase is small,  $r_s \ll 1$ , particularly compared to the sub-transient and transient per-unit inductances. This is true for the analyzed generators (topology  $\textcircled{A}$ ), if the saturated synchronous inductances for stationary operation are considered, e.g. exemplary design  $\textcircled{1}$  in Sec. 5.4. It holds also for the sub-transient inductances that are obtained during the analysis, Tab. 6.7, so that the calculation is self-consistent in this regard.
- The generator behaves magnetically symmetric in the sub-transient regime regarding  $d$ - and  $q$ -axes. This implies  $x_d'' \approx x_q''$ . Asymmetries in the sub-transient regime between the  $d$ - and  $q$ -axes can generally be caused by asymmetries of the damper and the additional damping effect of the field winding in the  $d$ -axis. As the considered generators with topology  $\textcircled{A}$  feature a completely symmetric, warm, copper damper screen, which is located at a magnetically large distance from the ferromagnetic poles, no asymmetry regarding the damper properties occurs. The superconducting field winding has a limited damping capability due to its very long time constant as a result of the small resistance. Finally, the extracted sub-transient time constants in Tab. 6.7 point to  $x_d'' \approx x_q''$ , implying consistency with the underlying assumption.

Based on these assumptions, the analytical expression (6.6) for the dynamic per-unit short

circuit current in phase U can be derived in the *Laplace* domain [22].

$$\begin{aligned}
 i_U(\tau) = & \underbrace{+\frac{u_0}{2} \cdot \left( \frac{1}{x_d''} + \frac{1}{x_q''} \right) \cdot \cos \gamma_0 \cdot \exp \left\{ -\frac{\tau}{\tau_a} \right\}}_{=i_{U,1}(\tau)} \\
 & - \underbrace{u_0 \cdot \left[ \frac{1}{x_d} + \left( \frac{1}{x_d'} - \frac{1}{x_d} \right) \cdot \exp \left\{ -\frac{\tau}{\tau_d'} \right\} \right] \cdot \cos(\tau + \gamma_0)}_{=i_{U,2}(\tau)} \\
 & - u_0 \cdot \left( \frac{1}{x_d''} - \frac{1}{x_d'} \right) \cdot \exp \left\{ -\frac{\tau}{\tau_d'} \right\} \cdot \cos(\tau + \gamma_0) \\
 & + \frac{u_0}{2} \cdot \left( \frac{1}{x_d''} - \frac{1}{x_q''} \right) \cdot \cos(2\tau + \gamma_0) \cdot \exp \left\{ -\frac{\tau}{\tau_a} \right\}
 \end{aligned} \tag{6.6}$$

The standardized procedure described in IEC 60034-4 [51] for the experimental determination of dynamic parameters is not applicable, since the sub-transient and transient regimes are difficult to separate. Therefore, a more robust, custom multi-step fitting procedure is applied. The custom fitting routine is implemented in *Python* and uses the curve fitting functionalities of the *scipy* package. The fundamental of the no-load phase voltage is determined by a *Fourier* analysis, Fig. 6.23 a). In a first step, a fit of the form (6.7) is used for the minima and maxima of the phase current, Fig. 6.23 b).

$$f_i(\tau) = a_i \cdot \exp\{-b_i \cdot \tau\} + c_i, \quad i = \min, \max \tag{6.7}$$

The average of the fitted functions is associated with the DC part  $i_{U,1}(\tau)$  of the phase current, (6.8), i.e. the blue line in Fig. 6.23 b).

$$i_{U,1}(\tau) \equiv 0.5 \cdot (f_{\min}(\tau) + f_{\max}(\tau)) \tag{6.8}$$

A fit of the form (6.9) is applied to  $i_{U,1}(\tau)$ .

$$f_{DC}(\tau) = a_{DC} \cdot \exp\{-b_{DC} \cdot \tau\} \tag{6.9}$$

Since the short circuit at zero-crossing of the phase voltage U is considered ( $U_{U,0} = 0$ ), the expression can be simplified with  $\cos \gamma_0 = 1$ . The fit parameters directly yield the per-unit

armature time constant  $\tau_a$ , (6.10), and the expression (6.11).

$$\tau_a = b_{DC}^{-1} \quad (6.10)$$

$$\beta := \frac{1}{x_d''} + \frac{1}{x_q''} = \frac{2 \cdot a_{DC}}{u_0} \quad (6.11)$$

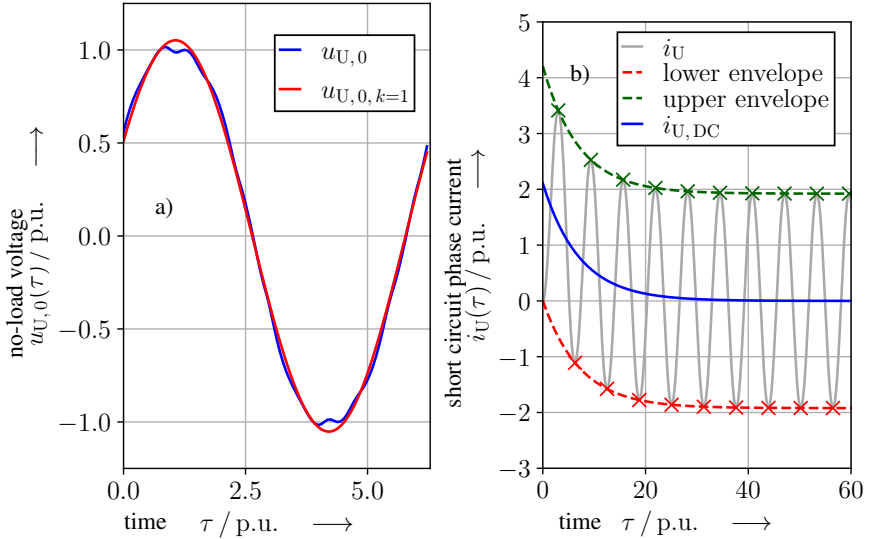


Figure 6.23.: a) Numerically calculated no-load voltage of the exemplary generator (topology  $\text{\textcircled{A}}$ , inner copper damper screen) together with its *Fourier* fundamental. b) Dynamic short circuit current in stator phase U after a three-phase sudden short circuit together with separate fits to maxima and minima (dashed lines). The blue line represents the average of both fitted envelopes and corresponds to the decaying DC part of the short circuit current.

The DC part, (6.8), is subtracted from the phase current in order to obtain the AC part of the phase current alone:  $i_{U,AC}(\tau) = i_U(\tau) - f_{DC}(\tau)$ . In the limit  $\tau \gg \tau_a, \tau_d''$ , only the contribution  $i_{U,2}(\tau)$  in (6.6) remains for the AC part, since in this limit  $\exp\{-\tau/\tau_a\} \approx \exp\{-\tau/\tau_d''\} \approx 0$  holds.

The extrema of  $i_{U,AC}(\tau)$  for  $\tau \geq 50$  p.u. are considered, with negative minima reflected across the  $\tau$ -axis, Fig. 6.24 a). These points are fitted with an envelope of the functional form (6.12), where  $\tau_0 = 50$  p.u..

$$f'(\tau) = a' \cdot \exp\{-b' \cdot (\tau + \tau_0)\} + c' \quad (6.12)$$

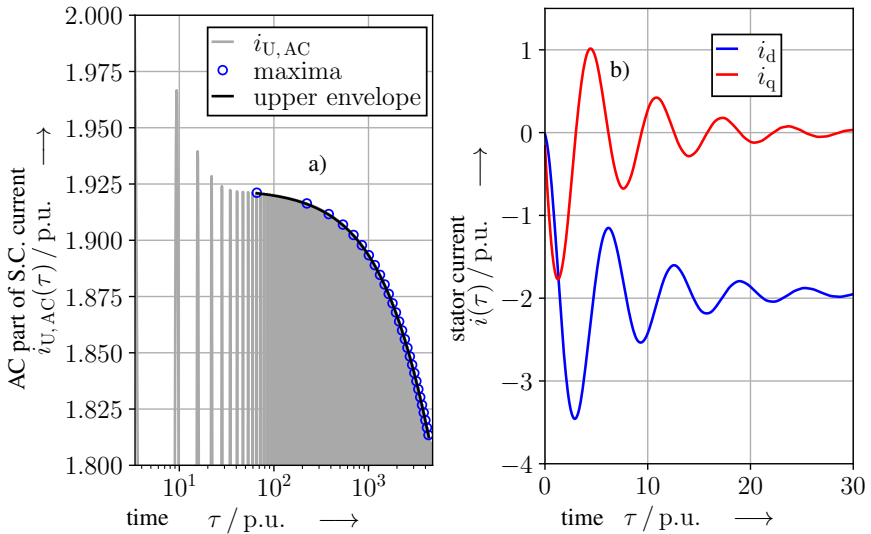


Figure 6.24.: 7 MW, 8.33 rpm generator with topology  $\textcircled{A}$  and a warm, inner copper damper screen: a) Numerically calculated decay of the AC part of the dynamic short circuit current in phase U after a three-phase short circuit for  $\tau \gtrsim 50$  p.u.. The black line represents a fitted envelope. b)  $d$ - and  $q$ -currents after a sudden three-phase short circuit at  $\tau = 0$ .

The fit parameters directly yield an estimate for the per-unit transient time constant of the  $d$ -axis  $\tau'_d$ , (6.13). Moreover, an estimate of a partially saturated synchronous inductance is obtained, (6.14). This inductance is effective in the steady state short circuit operation, when the short circuit current is largely a negative  $d$ -current, that reduces the iron saturation in the main flux path.

$$\tau'_d = \frac{1}{b'} \quad (6.13)$$

$$x_d = \frac{u_0}{|c'|} \quad (6.14)$$

$$\alpha := \frac{1}{x'_d} - \frac{1}{x_d} = \frac{|a'|}{u_0} \cdot \exp\left\{\frac{\tau_0}{\tau'_d}\right\} \quad (6.15)$$

From (6.13) and (6.15), the per-unit transient inductance of the  $d$ -axis is calculated, (6.16).

$$x'_d = \frac{1}{\alpha + x_d^{-1}} \quad (6.16)$$



The remaining analysis is carried out after transformation to the  $d$ - $q$ -frame with the *Park* transform (6.17) [22], Fig. 6.25 b).

$$\begin{pmatrix} i_d(\tau) \\ i_q(\tau) \end{pmatrix} = \frac{2}{3} \cdot \begin{pmatrix} \cos \tau & \cos(\tau - 2\pi/3) & \cos(\tau - 4\pi/3) \\ -\sin \tau & -\sin(\tau - 2\pi/3) & -\sin(\tau - 4\pi/3) \end{pmatrix} \cdot \begin{pmatrix} i_U(\tau) \\ i_V(\tau) \\ i_W(\tau) \end{pmatrix} \quad (6.17)$$

The  $d$ - and  $q$ -components of the analytically derived short circuit current after a sudden three-phase short circuit from no-load are (6.18) and (6.19) [22].

$$\begin{aligned} i_d(\tau) = & -u_0 \cdot \left[ \frac{1}{x'_d} + \left( \frac{1}{x_d} - \frac{1}{x'_d} \right) \cdot \exp \left\{ -\frac{\tau}{\tau'_d} \right\} \right. \\ & \left. + \left( \frac{1}{x''_d} - \frac{1}{x'_d} \right) \cdot \exp \left\{ -\frac{\tau}{\tau''_d} \right\} - \frac{1}{x''_d} \cdot \exp \left\{ -\frac{\tau}{\tau_a} \right\} \cdot \cos(\tau) \right] \end{aligned} \quad (6.18)$$

$$i_q(\tau) = -\frac{u_0}{x''_q} \cdot \exp \left\{ -\frac{\tau}{\tau_a} \right\} \cdot \sin \tau \quad (6.19)$$

The envelope of the  $q$ -current is fitted with relation (6.20), Fig. 6.25 a).

$$f_q(\tau) = a_q \cdot \exp \{ -b_q \cdot \tau \} \quad (6.20)$$

The fit parameters yield the per-unit sub-transient inductance of the  $q$ -axis  $x''_q$ , (6.21).

$$x''_q = \frac{u_0}{|a_q|} \quad (6.21)$$

The per-unit sub-transient inductance of the  $d$ -axis  $x''_d$  is calculated by combining (6.21) and (6.11) to (6.22).

$$x''_d = \frac{1}{\beta - x''_q^{-1}} \quad (6.22)$$

The per-unit sub-transient time constant  $\tau''_d$  is the last quantity to be determined. Since the transient time constant is much larger than the sub-transient one, i.e.  $\tau'_d \gg \tau''_d$ ,  $\tau_a$ , the decay of  $\exp \{ -\tau/\tau'_d \}$  until the end of the sub-transient regime, e.g.  $\tau \approx 20 \dots 30$  p.u., is small. This implies the approximation (6.23).

$$\begin{aligned} \Delta i_d(\tau) & := i_d(\tau) - i_d(\tau = 30 \text{ p.u.}) \\ & \approx -u_0 \cdot \left[ \left( \frac{1}{x''_d} - \frac{1}{x'_d} \right) \cdot \exp \left\{ -\frac{\tau}{\tau''_d} \right\} - \frac{1}{x''_d} \cdot \exp \left\{ -\frac{\tau}{\tau_a} \right\} \cdot \cos \tau \right] \end{aligned} \quad (6.23)$$

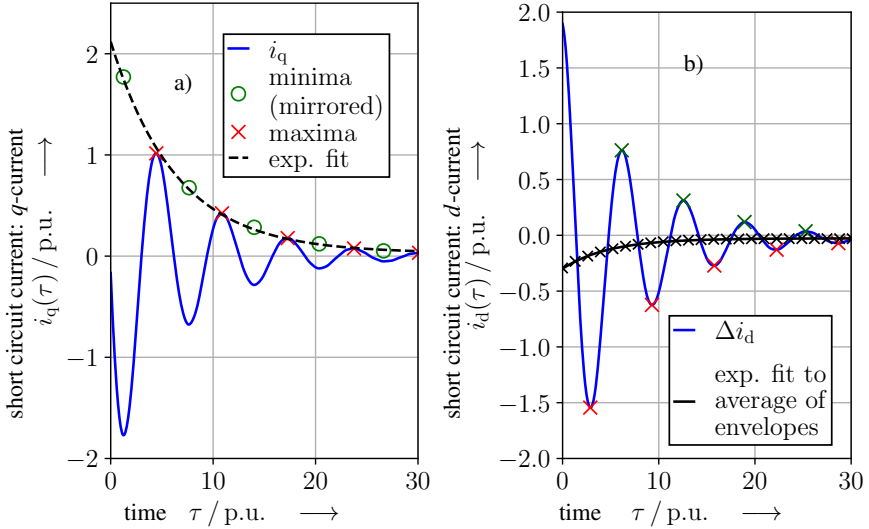


Figure 6.25.: 7 MW, 8.33 rpm HTS excited generator with topology  $\textcircled{A}$  and a warm, inner copper damper screen: a) Numerically calculated  $q$ -current after a sudden three-phase short circuit at  $\tau = 0$  (zero-crossing of phase voltage  $U$ ). The envelope is shown together with an exponential fit. b) Decaying part of the dynamic short circuit  $d$ -current  $\Delta i_d = i_d(\tau) - i_d(\tau \rightarrow \infty)$ . The minima and maxima are highlighted. The black line is an exponential fit to the average of the envelopes.

The quantity  $\Delta i_d(\tau)$  is composed of a DC and an AC part, Fig. 6.25 b). Therefore, a similar fitting procedure as for the initial separation of the DC part in  $i_U(\tau)$  can be applied.

The extrema are again fitted with expressions of the functional form (6.7). The average of the envelopes is calculated as in (6.8) and associated with the DC part of  $\Delta i_d(\tau)$ . A subsequent fit of the form (6.9) yields directly an estimate for the per-unit sub-transient time constant of the  $d$ -axis  $\tau_d'' = b_{DC}^{-1}$ .

The set of extracted parameters is summarized in Tab. 6.7 - 6.10. A comparison of the numerically calculated short circuit current in phase U and the analytical expression (6.6) is visualized in Fig. 6.26 and reveals a good agreement.

Following general findings are derived from the extracted parameters:

- Generally, the per-unit inductances differ from the typical ranges [22], due to the very large magnetically effective air gap  $\delta_{\text{mag}}$ , Tab. 6.7. The per-unit inductances of

the  $d$ - and  $q$ -axes, that are determined by the procedure in Sec. 4.2.3, are small. The  $q$ -axis inductance is larger than  $x_d$ . The salient-pole geometry has little influence, since the rotor pole cores are highly saturated and the combined reluctance of the rotor and the air gap in  $d$ - and  $q$ -axes differs only little. In contrast, the high rotor field in the  $d$ -axis leads to a strong saturation in the stator iron teeth and the flux path sections in the stator yoke. This affects both the main flux and the slot stray flux and therefore yields  $x_d < x_q$ . The calculated inductances in  $d$ - and  $q$ -axes were confirmed by means of small test coils, that were modelled in 2D FEM models. The partially saturated per-unit inductance of the  $d$ -axis, which is obtained during the short circuit analysis, is slightly larger than  $x_q$  and by about 65 % larger compared to the saturated value of  $x_d$  at rated operation.

- The per-unit transient inductance of the  $d$ -axis  $x'_d$  is larger than typical due to the limited screening capability of the excitation winding and the comparably loose magnetic coupling of stator and rotor as a consequence of the large magnetically effective air gap. Due to the large value of  $\delta_{\text{mag}}$ , and the large slot height  $h_Q$ , the slot stray reactance  $X_{s\sigma Q}$  accounts for a major part of the synchronous reactance. Since the stray reactance is not affected by the magnetic coupling with the field winding, the difference between  $x_d$  (partially saturated) and  $x'_d$  is small. The same holds for the sub-transient inductances  $x''_d, x''_q$ , as the copper damper screen is located at a comparably large distance from the stator and faces a high reluctance for any screening fields.
- Due to the very large inductance  $L_f$ , in combination with the low resistance  $R_f$  in the excitation circuit, the transient time constant  $\tau'_d$  is by about three orders of magnitude longer than the sub-transient and the armature time constants  $\tau''_d, \tau_a$ . After the sub-transient response, the field current settles to its original value on a time scale of several minutes, Tab. 6.10. This result differs considerably from normal conducting generators, where the transient regime persists on a time scale of few seconds [22]. The accuracy of the estimate for  $\tau'_d$  is limited due to the neglect of the dynamic resistance  $R_{\text{HTS,AC}}$  of the HTS field winding. However, the analysis at the end of this section reveals, that the contribution of the dynamic resistance is only significant until about  $3\tau_a \approx 21$  p.u., Fig. 6.27 b). Since the transient time constant is still by about 2.5 orders of magnitude longer, the dynamic HTS resistance has little influence on  $\tau'_d$ .

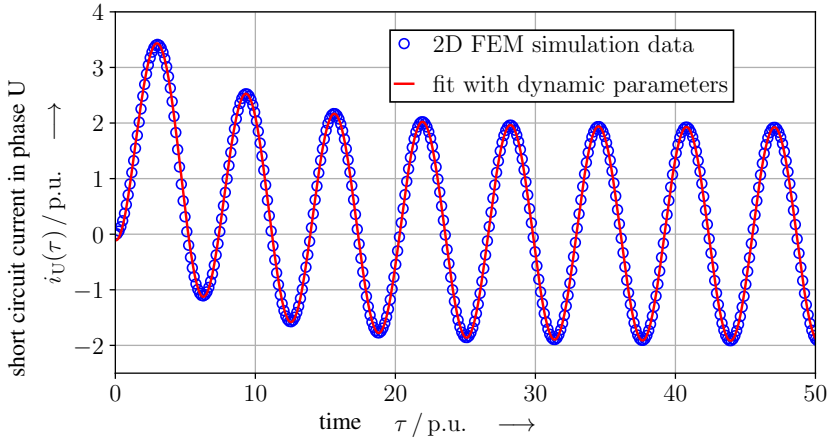


Figure 6.26.: 7 MW, 8.33 rpm HTS excited generator with topology  $\textcircled{A}$  and a warm, inner copper damper screen: Numerically calculated, dynamic short circuit current in stator phase U after a sudden three-phase short circuit at voltage zero-crossing in phase U. The numerical result is compared with the analytical relation (6.6). The transient parameters are obtained by the step-wise fitting procedure, as described in the text, and listed in Tab. 6.7 - 6.10.

- The sub-transient and armature time constants  $\tau_d''$ ,  $\tau_a$  are in the same order of magnitude. The decay of the eddy current loss in the damper screen, Fig. A.26 in App. A.8.2, allows for an exponential fit, which yields a characteristic time constant for comparison purpose. This estimate is very close to the sub-transient time constant that is obtained by the fitting procedure described above, Tab. 6.8, 6.10.

The sudden increase of the dynamic field current after the three-phase sudden short circuit causes AC losses in the HTS field winding. These losses are calculated by means of a 2D FEM model in the  $H$ - $A$ -formulation, where the previously calculated stator and field currents are impressed. The instantaneous AC loss features a maximum value of  $P_{d,AC,max} \approx 95 \text{ kW}$  during the sub-transient regime, Fig. 6.27 a). The calculated superconducting current distribution in the homogenized coil model is shown in Fig. 6.28 for the time instant with maximum AC loss. The total dissipated energy is however small due to the fast sub-transient decay on a time scale of  $3\tau_d'' \approx 14.5 \text{ p.u.}$ , when the field current has approximately already attained its maximum value.

Table 6.7.: Calculated per-unit inductances and resistance of the exemplary HTS excited direct drive generator, Fig. 6.26. The transient and sub-transient parameters are obtained by fits to the numerically calculated sudden three-phase short circuit current.

$x_d$ (partially saturated)	0.659 p.u.
saturated (rated op., Sec. 4.2.3)	
$x_d$	0.398 p.u.
$x_q$	0.613 p.u.
$x'_d$	0.547 p.u.
$x''_d$	0.479 p.u.
$x''_q$	0.504 p.u.
$r_s$	0.071 p.u.

Table 6.9.: Calculated inductances and resistance of the exemplary generator, based on Tab. 6.7, Fig. 6.26. Transient and sub-transient parameters are extracted from fits to numerical simulation data.

$L_d$ (partially saturated)	1.27 mH
$L'_d$	1.06 mH
$L''_d$	0.92 mH
$L''_q$	0.97 mH
$R_s$	4.6 m $\Omega$
$R_{f,cl}$	20.0 m $\Omega$

Table 6.8.: As Tab. 6.7, but per-unit time constants and short circuit currents of the exemplary HTS excited direct drive generator.

$\tau'_d$	10 525 p.u.
$\tau''_d$	4.834 p.u.
$\tau''_d$ from $P_{d,Ft,damp}$	4.630 p.u.
$\tau_a$	7.153 p.u.
$u_0$	1.052 p.u.
$i_k$	1.596 p.u.
$i'_k$	1.923 p.u.
$i''_k$	2.196 p.u.

Table 6.10.: As Tab. 6.8, but calculated time constants and short circuit current amplitudes. Transient and sub-transient parameters are extracted from fits to numerical simulation data.

$T'_d$	309.4 s
$T''_d$	0.142 s
$T_a$	0.210 s
$\hat{U}_0$	601 V
$I_k$	13.92 kA
$I'_k$	16.77 kA
$I''_k$	19.15 kA

An estimate for the heat capacitance of the field winding alone is  $C_{th} \approx 13.8 \text{ kJ/K}$  (mass of the entire HTS winding  $\approx 706 \text{ kg}$ ; averaged, volumetric heat capacity of the insulated HTS tapes at  $T_{HTS} \approx 30 \text{ K}$ :  $c_{th} \approx 19.5 \text{ J}/(\text{kg} \cdot \text{K})$ ), while the dissipated energy during  $3\tau_a$  after the short circuit is  $Q_{d,AC}(3\tau_a) \approx 15.9 \text{ kJ}$ . For adiabatic heating, this yields an average temperature rise of  $\Delta T_{HTS} \approx 1.2 \text{ K}$ , which is not critical regarding a temperature-induced quench of the SC. A more detailed analysis would however be required to determine the local temperature distribution in the field winding coils, in order to ensure also a sufficient limitation of the local temperature increase.

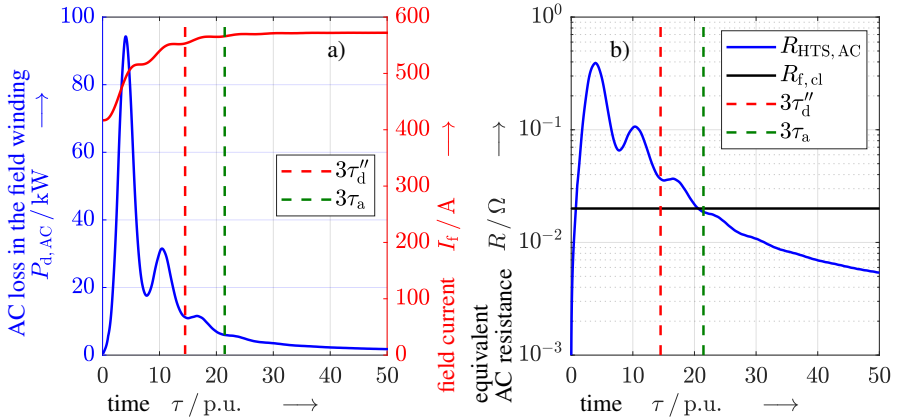


Figure 6.27.: 7 MW, 8.33 rpm HTS excited generator with topology  $\textcircled{A}$  and a warm, inner copper damper screen: a) Numerically calculated AC loss in the HTS field winding after a sudden three-phase short circuit at the stator terminals. A homogenized coil model in the coupled  $H$ - $A$ -formulation in *COMSOL Multiphysics* is used for the calculation. The dynamic field current over time is extracted from the transient simulation in *JMAG*. b) Equivalent HTS resistance during the variation of the field current after the three-phase short circuit.  $R_{f,cl}$  is the resistance of the current leads.

An equivalent HTS tape resistance is calculated as  $R_{\text{HTS,AC}} = P_{d,AC}/I_f^2$ , Fig. 6.27 b). This dynamic HTS resistance is the governing resistance in the field circuit during the sub-transient regime, but gets smaller than the normal conducting part of the current leads at  $\approx 3\tau_a$ . The higher overall resistance of the field winding circuit in the sub-transient regime has a current-limiting effect, which is generally small due to the rapid decay of  $P_{d,AC}$ . The calculated AC loss as well as the dynamic field current increase  $\Delta I_f$  are therefore regarded as upper limits for the actual values.

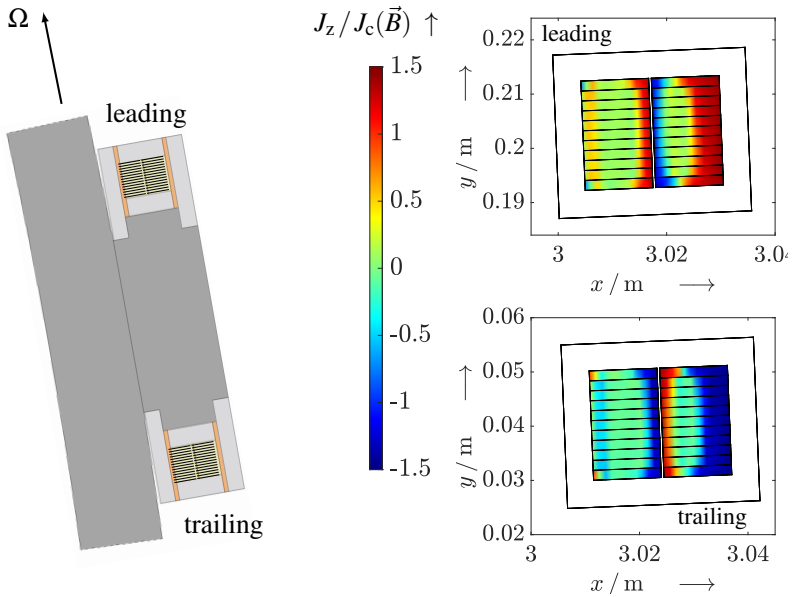


Figure 6.28.: 7 MW, 8.33 rpm HTS excited generator with topology  $\textcircled{A}$  and a warm, inner copper damper screen: Numerically calculated (software: *COMSOL Multiphysics*) superconducting field current distribution in the rotor field coils after a sudden three-phase short circuit at the stator terminals. The results are shown for the time instant with maximum instantaneous loss power in the field winding. The current density  $J_z$  is normalized by the field-dependent local critical current density  $J_c(\vec{B})$ .

---

## 7. Alternative Superconducting Wind Generator Concepts

Most of the current research projects focus on direct drive generators for offshore wind power, Ch. 1, since the absence of the gear constitutes a paramount advantage for maintenance and fire safety without requirement for gear oil. The proof of the long-time reliability of gears without failure-prone high-speed stage is vital for medium speed generators, in order to exploit the advantages of increased generator efficiency and a greatly reduced material consumption. Still, the increased maintenance requirements remain.

Besides the approach of direct drive HTS excited generators, two alternative generator concepts with superconducting windings are of particular interest for future work:

1. Medium speed wind generators with a more reliable two-stage gear and with a diode rectifier feeding of the stator winding, instead of a full converter.
2. HTS excited, fully SC gearless generators with HTS or  $\text{MgB}_2$  AC stator windings.

In the following, the major challenges and design questions, together with some basic results, are summarized.

### 7.1. HTS Medium Speed Generators with Rectifier Feeding

The rectifier feeding requires a power factor unity  $|\cos \varphi_{sN}| = 1$  at constant DC link voltage in the entire operating speed range of  $n = (0.4 \dots 0.7) \dots 1 \cdot n_N$ . A first theoretical investigation is partly published [O10] or is intended to be published soon [O16, O18]. For  $|\cos \varphi_{sN}| = 1$ , very high magnetic flux densities at lowest speeds are required, which lead to following major difficulties:

- a. A very high torque ripple, i.e.  $> 100\%$  of the average torque  $\bar{M}$ , occurs in case of a three-phase stator winding in slots, even at sinusoidal current feeding. This torque ripple occurs also at no-load and is caused by high reluctance forces, which act on the stator iron teeth, as a result of the high rotor field.
- b. Large harmonics of the induced voltage occur at low speeds and high flux densities with a maximum amplitude in the order of  $\approx 10\%$  of the fundamental.



- c. A large amount of costly HTS tape is required due to the high magnetic loading and the high required excitation MMF at the lowest speed  $n_{\min} \approx 0.4 \cdot n_N$ .
- d. The cheap rectifier feeding, e.g. in Fig. 7.1 for a B12 rectifier and a six-phase stator winding (phases A ... F), yields significant stator current harmonics, which vary between different operating points and speeds. The quantification of the stator current harmonics relies on accurate estimates for the non-linear stator inductances  $L_s$ , i.e. by means of 3D FEM models, Fig. 7.3, in order to cover the strong iron saturation. These stator current harmonics lead to following unfavourable parasitic effects:
- i. The load-dependent torque ripple increases.
  - ii. Additional eddy current losses in the outer damper, in the cryostat wall and in the electrically conductive, cold pole cores and the rotor yoke are produced.
  - iii. The DC HTS field winding experiences an additional AC loss due to increased air gap stator magnetic field harmonics.
- e. The adjustment to power factor unity  $\cos \varphi_{sN} = -1$  at different loads  $I_s$  and speeds  $n$  requires sufficient dynamics of the superconducting field current variation  $d_t I_f$ . Since the HTS medium speed generators are axially short, 3D models are required to accurately incorporate the end-winding contribution to the field winding inductance  $L_f$ , Fig. 7.4.

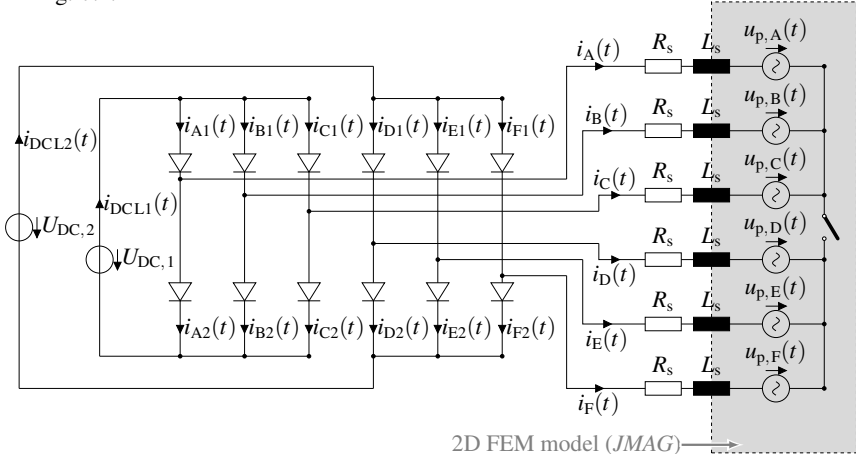


Figure 7.1.: Schematic of the coupled model for the analysis of a B12 rectifier feeding of six-phase HTS excited medium speed synchronous generators. The stator end-winding leakage inductance is calculated by means of a non-linear 3D FEM model, Fig. 7.3.  $U(I)$ -characteristics of the diodes are directly modelled. The non-linear 2D FEM model and the circuit simulation are coupled in the software *JMAG*.

Therefore, the scope of possible future work must cover following aspects:

- a. Effective torque ripple mitigation measures are vital for this generator concept with  $|\cos \varphi_{sN}| = 1$ . Possible options include asymmetric rotor pole arrangements, i.e. shifted or inclined poles, the use of magnetic stator slot wedges and a stator winding design with a higher number of turns per phase  $N_s$  to smooth the current ripple. The latter option also reduces the required flux densities for the same DC link voltage.
- b. The impact of a higher number of turns per phase  $N_s$  on following aspects is of interest:
  - i. The reduction of the required total tape length  $l_t$  of the HTS tape in the field winding.
  - ii. The limitation of the total generator loss  $P_{d,t}$  and its influence on the generator efficiency  $\eta_N$ : A higher  $N_s$  implies a higher number of turns per stator coil  $N_c$ , which yields a higher current density  $J_{Cu}$  in the stator winding for the same slot dimensions. The accordingly higher *ohmic* loss  $P_{d,Cu,s}$  is only partially compensated by the lower stator iron loss  $P_{d,Fe}$  due to the reduced magnetic flux density.

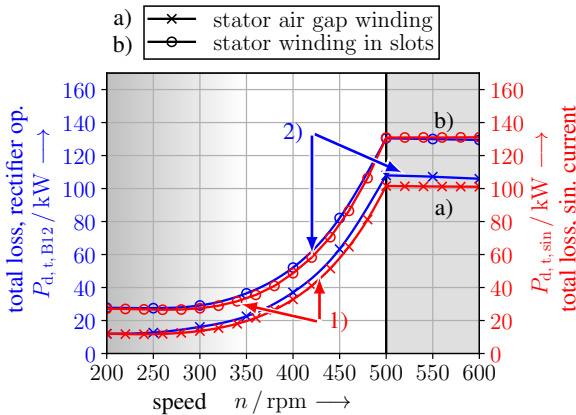


Figure 7.2.: Comparison of the total generator loss for 1) sinusoidal current and 2) six-phase rectifier feeding.  $P_{el,N} = -5\text{MW}$ ,  $U_N = 690\text{V}$ ,  $2p = 24$ ,  $n_N = 500\text{rpm}$ ,  $n = 0.4 \dots 1.2 \cdot n_N$ . A stator air gap winding a) is compared with a stator winding in slots b).

- c. The quantification of parasitic effects due to the rectifier feeding requires coupled simulations of non-linear FEM models and circuits, which incorporate the non-linear diode characteristics  $U(I)$ , e.g. Fig. 7.1. Preliminary analyses by means of such models reveal that the torque ripple and the additional rotor losses are too large in case of a three-phase stator winding in combination with a B6 rectifier. Due to the simple change from the three-phase winding to a six-phase stator winding, a B12 rectifier is a promising alternative. First investigations show that only a small increase in the total loss  $P_{d,t}$  oc-

curs for a suitably designed six-phase generator, Fig. 7.2, and that the load-dependent torque ripple is sufficiently low in the entire speed range. Future work must therefore focus on a detailed loss analysis and an optimized six-phase generator design.

- d. Preliminary analyses by means of parametric 3D models of all-iron generators, Fig. 7.3, reveal a strong saturation effect for the inductances in the stator winding  $L_s$  and the field winding  $L_f$  at full load. A good agreement with an analytical calculation is found for rated field current  $I_{fN}$  and rated stator current  $I_{sN}$ , Fig. 7.4. Based on these models, first investigations confirm that the required field current ramps of  $|d_t I_f| \approx 30 \text{ A/s}$  can be achieved with a manageable field voltage requirement of  $U_f \lesssim 250 \text{ V}$ . This enables maximum power ramps of  $|d_t P| \approx 10 \text{ kW/s}$ , which are compatible with grid codes [111]. Future work must cover a systematic analysis of different field current variation scenarios by incorporating also the AC loss in the HTS DC field winding [137]. Moreover, the extension to a topology with stator air gap winding, like in Fig. 7.2 a), is of interest due to the considerably stator inductances.

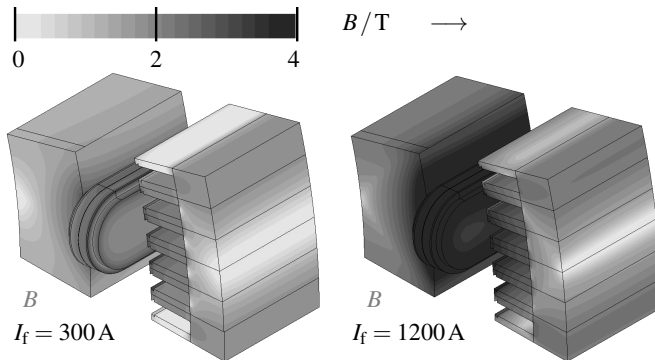


Figure 7.3.: 3D model, comprising one axial half of one pole of a medium speed generator (software: *JMAG*), like in Fig. 7.2 b) with slotted stator. The colour-encoded magnetic flux density is shown for different field currents, where  $I_f = 1200 \text{ A}$  is required for  $\cos \varphi_{sN} = -1$  operation at  $n_{\min} = 0.4 \cdot n_N = 200 \text{ rpm}$ .

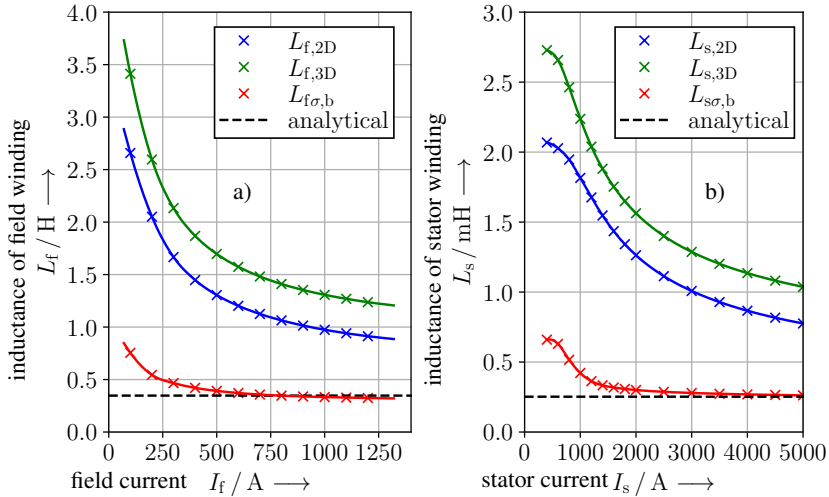


Figure 7.4.: Medium speed HTS generator, Fig. 7.3: a) Numerically and analytically calculated end-winding leakage inductance of the superconducting field winding with race-track geometry. The numerical value is calculated as difference between the inductance in a non-linear 3D FEM model and a corresponding 2D FEM model for different field currents and  $I_s = 0$ . b) Same as a) but for the end-winding leakage inductance of the distributed stator winding in slots with  $m = 3$ ,  $q = 2$ ,  $W/\tau_p = 5/6$  ( $I_s = 0 \dots 5$  kA,  $I_f = 0$ ).

## 7.2. Fully Superconducting All-HTS Direct Drive Generators

Fully superconducting rotating electrical machines feature both a superconducting DC field winding and a superconducting AC armature winding. Compared to partially superconducting machines, the superconducting poly-phase AC winding is commonly discussed in the context of following potentials:

- most compact and lightweight machines [130] with high electromagnetic utilization  $\sim A_s \cdot B_{\delta,1}$  due to an increased stator current loading  $A_s > 150$  kA/m,
- increased generator efficiency  $\eta_N$  in absence of stator *ohmic* losses  $P_{d,Cu,s}$ , that would otherwise be produced in conventional AC poly-phase copper windings.

The main challenges of fully superconducting generator concepts are:

- AC losses  $P_{d,AC}$  are produced in superconducting poly-phase windings due to the stator AC transport current: This loss can be significant and occurs in the cryogenic section.

Due to the generally low efficiency of cryogenic cooling systems, the required compressor input power  $P_{\text{compr}}$  can strongly decrease the overall efficiency  $\eta_N$ .

- b. system complexity: A second, stationary cryogenic cooling system is required to cool the superconducting stator poly-phase winding, e.g. with warm stator iron, which increases the component cost  $C_1$  and the maintenance effort.

AC HTS stator windings are discussed in literature for weight critical applications, such as wind generators and aerospace applications [151]. Most studies focus on electrically excited synchronous machines, which feature also a superconducting DC field winding [133]. In some cases, also fully superconducting DC machines are considered [130], while the slip ring system and the brushes are problematic, particularly in case of intentionally very high armature currents  $I > 1$  kA. Combinations of a PM excitation with superconducting stator windings are also discussed in literature for radial flux machines as wind generators [216] and for axial flux machines for electric aircraft propulsion (both theoretically and experimentally, [222]).

Direct drive wind turbine generators as fully superconducting synchronous generators are promising, since they feature very low stator fundamental frequencies  $f_s < 10$  Hz, which are generally beneficial regarding low AC losses  $P_{d,AC}$ . The *ohmic* loss  $P_{d,Cu,s}$  in normal conducting stator windings is the dominant loss component in direct drive generators, e.g. Ch. 3, so that even a partially decrease of the overall stator loss results in significant efficiency improvements compared to normal conducting generators. In case of medium speed generators, these aspects do not apply: The generators feature higher rated stator frequencies in the order of  $f_{sN} \approx 100 \dots 120$  Hz, which would result in higher AC losses  $P_{d,AC}$  in a poly-phase superconducting stator winding. Moreover, the share of the *ohmic* loss in the stator winding  $P_{d,Cu,s}$  in the total loss  $P_{d,t}$  is smaller than for direct drive generators due to the higher iron loss  $P_{d,Fe}$ . The already compact medium speed generators are finally subject to a weaker demand for further mass reductions.

As the cooling system's efficiency increases significantly with its cooling capacity  $\dot{Q}$  [175], it is reasonable to consider a single large cooling system for the stator of fully superconducting generators. In order to identify the admissible order of magnitude for the AC loss in a first step, a comparison to a direct drive PM generator with typical *ohmic* loss  $P_{d,Cu,s}$  in the order of 7% of the rated electrical output power  $P_{e1,N}$  is considered. This represents an upper limit for the admissible compressor input power  $P_{\text{compr}}$ , that is used for the cooling of the stator winding. By adopting the empirical scaling law for the dependence

on the cooling capacity  $\dot{Q}$  from [175], the maximum admissible AC loss  $P_{d,AC,max}$  can be estimated. Maximum values for 7MW generators are  $P_{d,AC,max} \approx 6$  kW at a cold head temperature of  $T_{CH} = 20$  K,  $P_{d,AC,max} \approx 18$  kW at  $T_{CH} = 40$  K and  $P_{d,AC,max} \approx 36$  kW at  $T_{CH} = 60$  K. Based on this considerations, numerical AC loss models are required for accurate loss estimates. As an example, the calculated AC loss in an HTS stator winding for the  $H$ - $A$ -formulation and the  $T$ - $A$ -formulation is shown in Fig. 7.5 with parametrization according to Sec. 2.2.4.

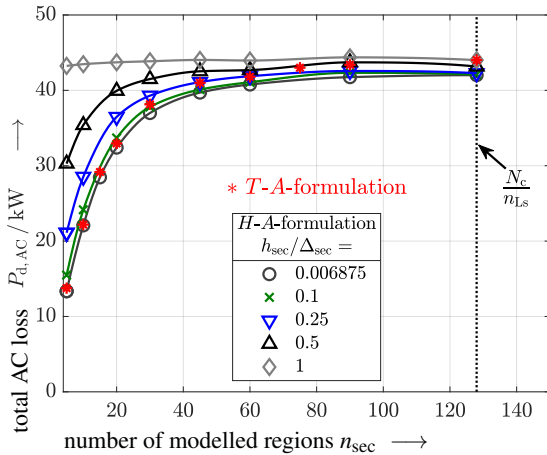


Figure 7.5.:  $P_{el,N} = -7$  MW,  $n_N = 8.33$  rpm,  $2p = 30$ : Calculated AC loss ( $H$ - $A$ -formulation) in the HTS AC stator winding for several homogenized coil models, Sec. 2.2.4.  $n_{sec}$ : number of modelled regions per layer,  $h_{sec}$ : height of the modelled regions. The AC loss calculated by means of the  $T$ - $A$ -formulation is plotted in red as reference.

The comparison in Fig. 7.5 reveals that the AC loss in the HTS AC stator windings of direct drive generators can be accurately calculated with a comparably low number of modelled regions  $n_{sec}$  in the  $H$ - $A$ -formulation, if  $h_{sec}/\Delta_{sec} = 1$  is chosen. This computationally efficient model can be used in future work for a systematic, parametric AC loss study for a large set of all-HTS fully superconducting direct drive generator designs. First results of such analyses are intended to be published in the near future [O17]. Besides the influence of the operating temperature, Fig. 7.6, the impact of following design options is of interest:

- The iron topology, i.e. stator iron „teeth“ and/or ferromagnetic rotor pole cores.
- The current margin  $\hat{I}/I_c$  of the superconducting stator current amplitude  $\hat{I}$  with respect to the critical current  $I_c$ .
- The width of the HTS tape  $w_t$  in the stator winding and the stator coil geometry [217].
- The generator active volume  $V_g$  and correspondingly the electromagnetic utilization, e.g. measured by  $C_e$ .

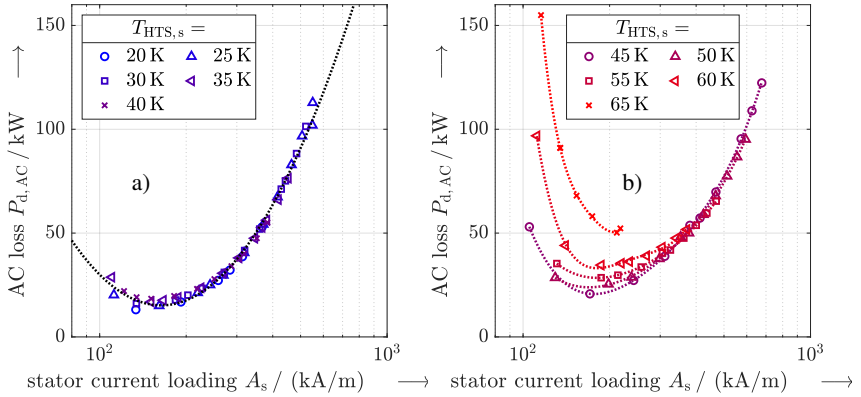


Figure 7.6.: 7 MW, 8.33 rpm all-HTS, fully superconducting direct drive generator: Numerically calculated ( $H$ - $A$ -formulation, *COMSOL Multiphysics*) HTS AC loss in the stator winding at different temperatures of the stator winding  $T_{HTS,s}$  and for a generator active volume  $V_g = 40\text{ m}^3$ . a) A master curve for the AC loss versus the stator current loading  $A_s$  is found for  $T_{HTS,s} \leq 40\text{ K}$ . b) Above this range, the minimum AC loss increases with  $T_{HTS,s}$ .

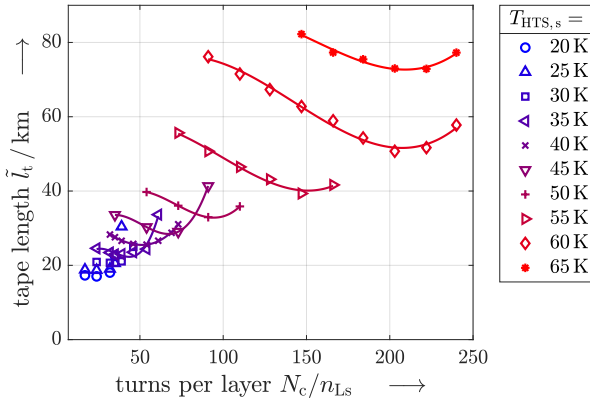


Figure 7.7.: 7 MW, 8.33 rpm, all-HTS, fully superconducting direct drive generator: Total tape length  $\tilde{l}_t$  (stator and rotor winding) of a reference tape with the same current carrying capacity per unit width and  $w_t = 12\text{ mm}$ , based on 2D non-linear FEM results.  $\tilde{l}_t$  is plotted versus the number of turns per layer of the stator racetrack coils. Lines represent cubic fits.

Preliminary analyses moreover show that a temperature-dependent, minimum total HTS tape requirement can be achieved as a result of the trade-off between a high rotor excitation MMF and a high stator current loading  $A_s$ , Fig. 7.7. This finding can also constitute the basis for future investigations of optimum designs of all-HTS fully superconducting direct drive wind generators.

### 7.3. Fully Superconducting Direct Drive Generators with HTS Excitation and MgB<sub>2</sub> AC Stator Winding

MgB<sub>2</sub> AC wires are discussed in literature, e.g. [105, 204, 134], as low AC loss superconductors, that are appropriate for AC stator windings in direct drive synchronous generators. However, several analyses of MgB<sub>2</sub> AC stator windings do not include an AC loss estimation at all [2, 133]. The studies, that provide AC loss estimates, focus mostly on aerospace or wind energy applications [105, 197]. Irrespective of the intended application, the critical temperature of  $T_{MgB_2,c} = 39\text{ K}$  at  $B = 0\text{ T}$  requires operating temperatures  $T_{MgB_2} \leq 20\text{ K}$ , in order to achieve useful critical currents  $I_c$  in external fields in the order of  $B \approx 1.5 \dots 2\text{ T}$ . The to date worse in-field performance of MgB<sub>2</sub>, compared to ReBCO coated conductors, which hampers the use of MgB<sub>2</sub> field windings ( $B \approx 3 \dots 5\text{ T}$ ), e.g. Sec. 4.3.1, is less severe for the stator winding, where typically  $B \leq 2\text{ T}$ . As a trade-off between high critical current  $I_c$  and not too low efficiency of the cryogenic cooling system, a fixed operating temperature of  $T_{MgB_2} = 20\text{ K}$  also for the AC MgB<sub>2</sub> windings is reasonable. It enables critical current densities in the order of  $J_c \approx 2 \cdot 10^3\text{ A/mm}^2$  and engineering current densities of  $J_e \approx 100\text{ A/mm}^2$  at  $B \approx 2\text{ T}$  [207].

Preliminary analyses reveal that standard MgB<sub>2</sub> conductors without twisting of filaments, with a fraction of ferromagnetic nickel and with a high volume fraction of pure copper are not suitable for the AC application in the stator winding of synchronous generators, even at lowest stator fundamental frequencies of  $f_s \approx 2\text{ Hz}$ . Therefore, minimum AC loss wires, as manufactured e.g. by *HyperTech Research*, must be considered. Here, a twisting of filaments is much easier compared to ReBCO coated conductors. The calculation of the AC loss in MgB<sub>2</sub> wires by means of numerical models is generally more challenging than for HTS tapes, since a higher degree of detail is required, Fig. 7.9.



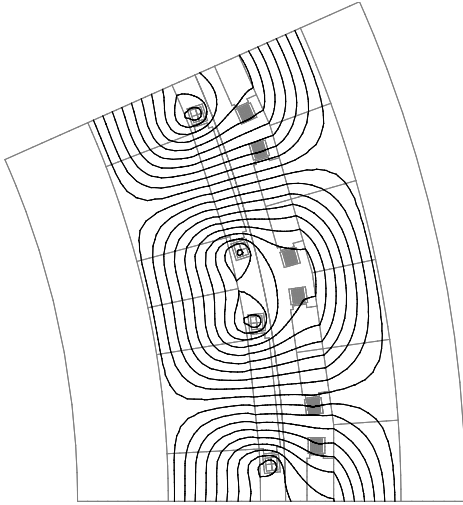


Figure 7.8.: Calculated field lines at rated power for an exemplary 7 MW, 8.33 rpm,  $2p = 30$  direct drive generator with HTS field winding and with MgB<sub>2</sub> AC stator winding. (software: *COMSOL Multiphysics*)

The basic findings of a first analysis of fully superconducting direct drive generators with MgB<sub>2</sub> stator winding, as shown in Fig. 7.8, are:

- With minimum loss MgB<sub>2</sub> wire architectures, suitably low AC losses  $P_{d,AC}$  can be achieved. Efficiency improvements compared to PM excited direct drive generators, HTS excited partially superconducting direct drive generators and all-HTS fully superconducting generators are possible.
- Lightweight 7 MW generators with a significant mass reduction of about 25% compared to PM excited direct drive generators are possible. These compact generators with  $d_{so} < 5$  m can be designed with a rather short total HTS tape length  $l_t$  for the field winding.
- Suitably high critical currents  $I_c$  of the MgB<sub>2</sub> wires can be achieved, if they are used in the stator AC winding instead of the field winding due to the lower magnetic flux density.
- Very high values of the electromagnetic specific thrust  $\sigma_t \gtrsim 100 \dots 150 \text{ kN/m}^2$  can be achieved at rated operation, leading to active mass related torque densities of  $M' = M_N/m_{act} > 200 \text{ Nm/kg}$ .

7.3. Fully Superconducting Direct Drive Generators with HTS Excitation and MgB<sub>2</sub> AC Stator Winding

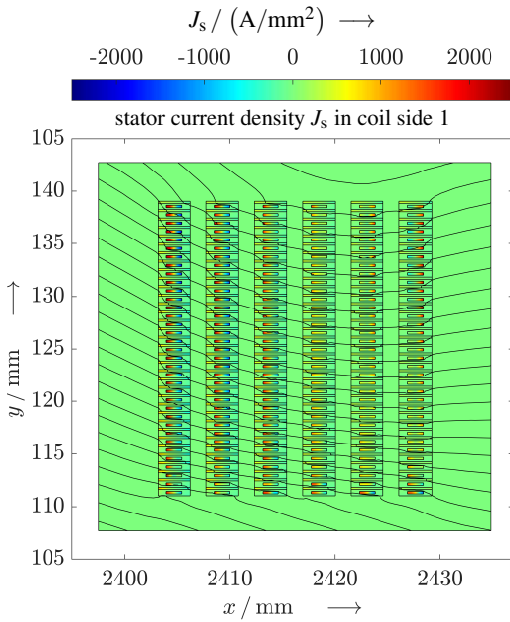


Figure 7.9.: Numerically calculated ( $H$ - $A$ -formulation, software: *COMSOL Multiphysics*) current density in the cross section of one stator coil side of the generator in Fig. 7.8, for a MgB<sub>2</sub> wire with ferromagnetic Ni matrix at nominal operation with 7 MW. Stator racetrack coils in  $n_{Ls} = 6$  layers, e.g. three double-racetrack coils, are assumed with  $N_c/n_{Ls} = 35$  turns per layer.  $N_c = 210$  conductors per coil are explicitly modelled by employing a simplified conductor geometry. The simplified model is validated against a detailed model of the filaments. A significant magnetic flux concentration in the ferromagnetic matrix occurs.

---

## 8. Summary of Main Findings and Conclusions

The scope of this last chapter consists in a summary of the main findings in Ch. 3-7. For this purpose, Sec. 8.1 answers the main research questions from Sec. 1.4. The conclusion follows in Sec. 8.2.

### 8.1. Conclusions on HTS Excited Direct Drive Generators

The largely separate analyses of the different direct drive generator concepts are brought together by addressing the main research questions, which were formulated in Sec. 1.4:

Q1: *Competitiveness of Partially SC Direct Drive Wind Generators*

For comparison, the key characteristics are listed in Tab. 8.1, which summarizes the exemplary designs from Ch. 3 and 5. Exemplary designs of fully superconducting generators from preliminary analyses, Ch. 7, are included, which are not discussed in detail in the previous chapters but will be published in detail in the near future [O17].

The component cost per power rating of installed capacity  $C'_t$  covers the generator material, the cryogenic cooling system and the full converter. In order to incorporate also the efficiency differences in a single economical performance indicator, a similar approach as in Sec. 4.3.1 is applied. Here, a cost equivalent of  $\Delta C_t \approx 700$  kEuro was derived for an efficiency decrease of  $\Delta\eta_N = -1\%$  for a 7 MW generator. The missed energy production due to a lower efficiency by  $\Delta\eta_N = -1\%$  can therefore be priced with  $p'_\eta = 100$  kEuro / MW in order to reflect the impact on the net present value (NPV) of the investment. The generator variant with highest efficiency serves as reference, so that the cost  $C'_{t,\eta}$  (8.1) incorporates both the efficiency related cost and the component cost  $C'_t$ .

$$C'_{t,\eta} = C'_t - (\Delta\eta_N \cdot p'_\eta) \quad (8.1)$$

The gravimetric torque density  $M' = M_N/m_{\text{act}}$  is increased for all superconducting generator variants, compared to direct drive PM generators, Fig. 8.1. Highest torque densi-

ties  $M' = M_N/m_{\text{act}}$  are found for HTS excited partially superconducting generators with normal conducting stator air gap copper winding. Even with all-iron partially superconducting HTS generators (topology  $\textcircled{A}$  in Fig. 4.4), an increase in  $M'$  by  $\approx 33\%$  can be achieved. The torque density  $M'$  in fully superconducting generators with HTS armature winding is limited to prevent excessive AC losses. The impact of the active mass reduction on the overall CAPEX, including the tower and foundation, is not reflected by  $C'_t$  and  $C'_{t,\eta}$ .

Table 8.1.: Comparison of key characteristics for different direct drive generator concepts. The quantity  $C'_{t,\eta}$  combines the CAPEX and the efficiency-dependent opportunity costs of missed energy production.

rotor excitation	PM	HTS	HTS	HTS	HTS
stator winding	Cu, in slots	Cu, in slots	Cu, air gap	HTS	MgB <sub>2</sub>
$\eta_N / \%$	92.22	92.80	93.00	94.87	97.50
$\Delta\eta_N / \%$	-5.28	-4.70	-4.50	-2.63	ref.
$\cos\varphi_{sN}$	-0.771	-0.972	-0.989	-0.954	-0.849
$\sigma_t / (\text{kN}/\text{m}^2)$	84.4	137.2	188.7	89.3	165.5
$C_e / (\text{kVA} \cdot \text{min}/\text{m}^3)$	16.3	21.8	29.6	15.4	31.6
$m_{\text{act}} / \text{t}$	53.2	39.5	34.8	47.5	39.2
$M' / (\text{Nm}/\text{kg})$	163	216	247	168	207
$C'_t / (\text{kEuro}/\text{MW})$	120	276	601	860	495
$C'_{t,\eta} / (\text{kEuro}/\text{MW})$	648	746	1051	1123	495

Based on current prices of superconductors, partially SC direct drive generators are not competitive to PM excited generators regarding the CAPEX, which is at least doubled for the HTS excitation and the lowest-cost, all-iron topology ( $\textcircled{A}$  in Fig. 4.4), Fig. 8.1. The CAPEX is still slightly higher than for a PM excitation, even if the HTS price is reduced to  $\approx 1/3$  of its current value. To achieve a similar value, a price reduction by  $\approx -85\%$  would be required. Alternatively, a cost-neutral increase of the critical current  $I_c$  at relevant operating conditions by a factor of  $\approx 6 \dots 7$  is required. The cost share of the cryogenic cooling system  $C_{\text{cryo}}$  in the total component cost  $C_t$  is in the range of  $10 \dots 15\%$ , which yields only a limited potential for an overall cost reduction. In turn, the price of NdFeB magnets could increase by up to nearly  $300\%$ , until a similar CAPEX as for the

HTS excitation is reached. Since both scenarios are unlikely, it is hardly realistic that HTS excited, partially superconducting direct drive generators can reach as low component costs  $C'_t$  as direct drive PM generators in the near future. Fully superconducting generators with either  $\text{MgB}_2$  or HTS AC stator winding feature a CAPEX, which is by a factor of  $\approx 5 \dots 7$  higher than for PM generators. Also partially superconducting direct drive generators with HTS excitation and a stator air gap winding are not competitive regarding the initial component cost  $C'_t$ .

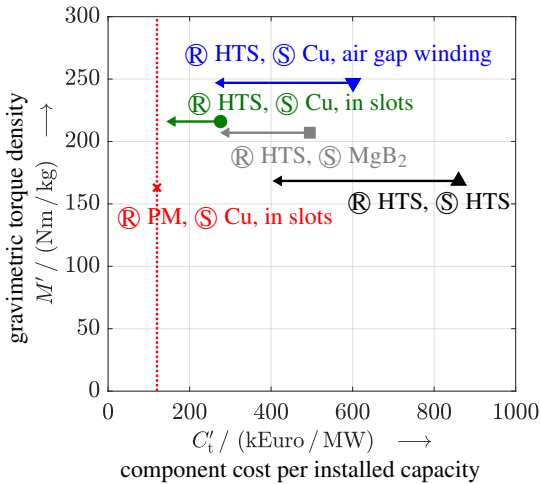


Figure 8.1.: Comparison of direct drive generator concepts in a plot of the gravimetric torque density  $M'$  versus the CAPEX per power rating of installed capacity  $C'_t$  (see Tab. 8.1).  $\textcircled{R}$ : rotor,  $\textcircled{S}$ : stator. The arrows indicate the change in component cost  $C'_t$  per rated power for a HTS price reduction to 1/3 of the present value.

The situation is different, if the impact of the increased rated efficiency  $\eta_N$  on the NPV, enabled by the HTS excitation, is included, Fig. 8.2:

- For a HTS price reduction to 1/3 of the current value, the partially superconducting direct drive generator with all-iron topology ( $\textcircled{A}$  in Fig. 4.4) is superior to the PM generator.
- The most lightweight HTS excited generator with normal conducting copper stator air gap winding features still higher costs per power rating  $C'_{t,\eta}$  than the PM generator, also for a HTS price reduction to 1/3 of the current value. Therefore, the competitiveness of this generator concept is determined by the trade-off between the generator costs, e.g. measured by  $C'_{t,\eta}$ , on one hand and by the cost savings for the tower and foundation due to a reduced tower head mass on the other hand.

- Fully superconducting generators with larger efficiency advantages get competitive: The combination of an HTS field winding and a  $MgB_2$  armature winding is competitive to the PM generator, already for the present HTS price. The all-HTS generator gets competitive for a reduced HTS cost of  $(1/3) \cdot p'_{HTS}$  and further potential is expected for optimized, minimum loss HTS conductors and coils.
- Generally, the direct drive generators with HTS excitation, which are in the focus of this thesis, suffer from the still too high HTS material prices, since a large total HTS tape length is required. In contrast, HTS excited medium speed wind generators generally allow to achieve major technological improvements, compared to the PM excitation, with only little HTS tape. For present HTS prices, the CAPEX of HTS medium speed generators is by only +11 % higher compared to the PM alternative. If a cost equivalent of the difference in rated efficiency  $\Delta\eta_N$  is included, the HTS medium speed generator is already today superior to the PM medium speed generator, i.e. yielding a reduction of  $C'_{t,\eta}$  by -21 %.

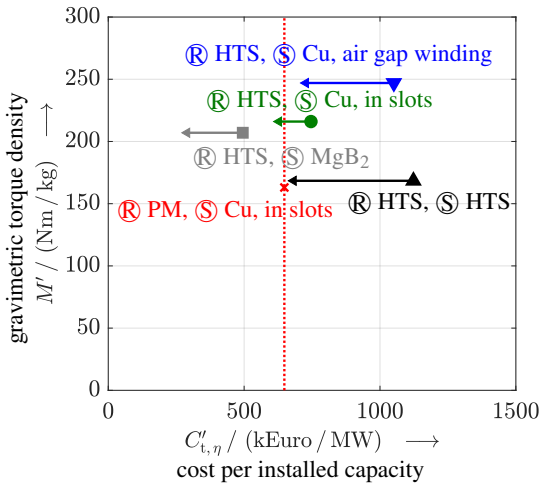


Figure 8.2.: As Fig. 8.1 but for the cost per power rating of installed capacity  $C'_{t,\eta}$  with incorporation of the difference in efficiency (opportunity costs of the missed energy production), according to Tab. 8.1.

Q2:  $MgB_2$  Field Windings in Direct Drive Synchronous Wind Generators

$MgB_2$  wires suffer mainly from the low in-field critical current  $I_c$  and the necessarily reduced operating temperature  $T_{MgB_2} \leq 20\text{K}$ . For partially superconducting generators, this limits the achievable efficiency improvements  $\Delta\eta_N$  and leads to more expensive cooling

systems. Regarding the use in DC field windings, today's  $\text{MgB}_2$  conductors are technically and economically inferior to HTS windings, in spite of the lower conductor cost.

If used in AC armature windings, these restrictions are partially relieved, as the armature winding experiences lower flux densities  $B \leq 2\text{T}$ . Moreover, the ease of filamentarization, and the accordingly low AC loss, make  $\text{MgB}_2$  wires the preferred choice for the AC armature winding. If the high efficiency increase for  $\text{MgB}_2$  AC stator windings in combination with a HTS DC excitation can be validated experimentally, this generator variant is already today superior to the PM technology. In the long-term, the successful establishment of the  $\text{MgB}_2$  technology for wind generators depends mainly on advances regarding the cryo-cooling technology, i.e. a higher COP at  $T_{\text{CH}} \leq 20\text{K}$ , and the progress of the competing low-AC-loss ReBCO conductors.

### Q3: Optimum Topology and Characteristics of HTS Direct Drive Generators

Since the total generator component cost  $C_t$  (generator active parts, converter, cryogenic cooling system) is largely dominated by the HTS material costs  $C_{\text{HTS}}$ , the lowest component costs  $C_t$  can be achieved with the all-iron topology (Ⓐ, Fig. 4.4), featuring a normal conducting copper stator winding in slots, ferromagnetic pole cores and a ferromagnetic rotor yoke. With this topology, the maximum reduction of active mass  $m_{\text{act}}$  is in the order of  $-30\%$  compared to optimum PM generators. The most lightweight generators feature a stator air gap copper winding, a rotor with ferromagnetic rotor pole cores and a ferromagnetic rotor yoke. Here, the maximum reduction of active mass  $m_{\text{act}}$  is in the order of  $-50\%$ , which requires however a very high amount of costly HTS material. The numerically optimized generators with all-iron topology (Ⓐ, Fig. 4.4) or with a stator air gap winding (Ⓓ, Fig. 4.4) dominate generators with a stator winding in slots and partially non-magnetic rotor (Ⓑ and Ⓒ, Fig. 4.4) regarding low component costs  $C_t$  and low active generator mass  $m_{\text{act}}$ . The highest power factor  $\cos \varphi_{\text{sN}}$  and the highest generator rated efficiency  $\eta_{\text{N}}$  are achieved with generator designs featuring a stator air gap winding.

### Q4: Redundancy Operation and Short Circuit Faults of HTS Direct Drive Generators

The redundancy operation is an important requirement for off-shore wind generators and is analysed for an exemplary 7 MW, 8.33 rpm HTS excited direct drive generator with the cheapest all-iron topology (Ⓐ, Fig. 4.4). The analyses reveal that the stator iron loss, which is smaller than for rated operation, and the torque ripple, i.e.  $\lesssim 2 \dots 3\%$  of the average torque, are not critical in case of partial feeding of the stator winding. Similarly,

the AC loss in the HTS DC field winding due to air gap magnetic field harmonics is low. The additional eddy current loss in warm, electrically conductive rotor parts, i.e. the damper and the cryostat wall, is sufficiently low, if a high number  $o$  of neighbouring pole pairs is jointly fed by one converter. Such feeding schemes also limit the eddy current loss in cold, electrically conductive rotor parts, i.e. the pole cores and the yoke (all-iron topology  $\textcircled{A}$ , Fig. 4.4). Still, the additional eddy current loss power in the cold rotor section is in the order of the original cryogenic heat load at rated operation. Therefore, in order to enable the redundancy operation with the all-iron topology  $\textcircled{A}$ , a higher cryogenic cooling capacity, provided by a more expensive cooling system, is required. Alternatively, the use of non-magnetic rotor poles ( $\textcircled{B}$ , Fig. 4.4) or grooved pole surfaces are suitable measures to limit the additional eddy current loss. If one of these loss mitigation measures is applied, the redundancy operation of HTS excited direct drive generators, intended for off-shore wind, is possible.

The analysis of different sudden short circuit faults reveals that the maximum dynamic peak torque  $M_{k,\max}$  is in the order of  $\approx 2.5$  times rated generator torque for a two-phase sudden short circuit after no load operation. The heat flow through the cold-warm support structure, which can withstand this peak torque  $M_{k,\max}$ , constitutes the major contribution to the cryogenic heat load. It can however be removed with an economically viable cooling system, i.e. featuring a cost fraction of  $\approx 15\%$  in the total component cost  $C_t$ . The maximum stator short circuit current after no load is in the order of  $i_{k,\max} \approx 4.3$  p.u. for a single-phase short circuit. The maximum dynamic increase of the superconducting field current occurs for a three-phase sudden short circuit and amounts to  $\approx 37\%$  of the rated field current. As the field winding is designed with a current margin of  $I_f/I_c = 1/1.7$ , the dynamic current increase does not lead to a quench in the HTS field winding. The instantaneous loss powers in the sub-transient regime in all rotor parts, i.e. the warm damper screen and the cryostat wall as well as the cold rotor poles and the cold rotor yoke, are very high. The very short time span of the sub-transient regime yields however only a small dissipated loss energy  $Q_d$ , which limits the temperature rise  $\Delta T$  in the sub-transient regime to less than  $1 \dots 2$  K. The numerically calculated sub-transient and armature time constants for a generator with  $P_{el,\text{out},N} = -7$  MW,  $n_N = 8.33$  rpm,  $U_N = 690$  V and all-iron topology ( $\textcircled{A}$ , Fig. 4.4) are in the order of  $\approx 0.15 \dots 0.2$  s. In contrast, the very low resistance in the HTS field coils leads to a transient time constant  $T'_d$  of several minutes, which is about three-times longer compared to the sub-transient time constant  $T''_d$ .



## 8.2. Summary and Outlook

Based on an overview of the current status of wind power generators and the use of superconducting windings, key research questions are developed in the first section. Several modelling approaches for superconductors, covering analytical and numerical models, are derived for the calculation of electromagnetic properties. Exemplary optimum designs are identified for the considered generator concepts and compared in Sec. 8.1.

As prerequisite for reliable comparisons, PM excited direct drive ( $n_N = 8.33$  rpm) generators are designed by parametric design studies. The main restriction for this generator concept consists in the enormous requirement of NdFeB magnets, i.e.  $\approx 0.5$  t/MW. This limits the achievable rated efficiency to about  $\eta_N \approx 92 \dots 92.5\%$  and the minimum generator active mass to  $m_{\text{act}} \approx 53$  t. The limited excitation capabilities of the permanent magnets manifest in generally low power factors of  $|\cos \varphi_{sN}| < 0.8$  for direct drive PM generators.

Based on a numerical optimization study on HTS excited partially superconducting direct drive generators, all-iron topologies and variants with stator air gap winding are identified as technologically and economically favourable. The combined component cost  $C_t$  of the generator material, the cryogenic cooling system and the full converter is reduced for a MTPA operating strategy. MgB<sub>2</sub> field windings are found to be inferior to field windings with ReBCO coated conductors. Design guidelines for the dimensioning of damper screens and for the choice of the stator winding in direct drive generators with SC excitation are developed. The AC loss  $P_{d,AC}$  due to air gap field harmonics is generally negligible for direct drive HTS generators with damper screen, even in presence of significant stator current harmonics. Basic considerations on redundancy operation show, that the additional loss in the cold parts is critical. Eddy current loss mitigation measures must be applied in order to prevent a more expensive cooling system. Analyses on different sudden short circuit faults complete the investigation of HTS excited direct drive wind generators and validate the derived generator designs regarding dynamic characteristics.

As most general finding, the use of HTS field windings in direct drive generators suffers from the large generator dimensions and the high pole counts, which require a large amount of costly HTS material. Fully superconducting generators require even larger quantities of HTS material, but may outweigh this drawback by very high efficiency improvements of  $\Delta\eta_N = 2.5 \dots 5\%$ . If the increased system complexity can be managed, the

very high efficiency could establish economical competitiveness with respect to the existing PM generators. Systematic, parametric design studies on fully superconducting direct drive wind generators with HTS DC field winding and HTS or  $\text{MgB}_2$  AC stator windings are therefore an important field of research for future work.

Preliminary investigations moreover imply that medium speed generators could be more promising for the use of HTS field windings. Here, the HTS technology is even today economically viable and superior to the PM excitation, according to fundamental investigations. Moreover, the basic calculation studies reveal no technological difficulties, which could manifest as deal-breaker. Based on this finding, additional research questions, which must be answered in future work on HTS medium speed generators, are formulated in Ch. 7. If technological and economical advantages were evident also after this further theoretical investigations, the main challenge for the future consists in an experimental validation of the advantages under real-life conditions. Proposed milestones are:

1. Systematic, parametric design studies on HTS medium speed generators, covering different topologies, HTS tape materials, operating conditions and rated speeds.
2. Theoretical analysis of HTS medium speed generator characteristics at rectifier feeding of the stator winding with quantification of the additional loss and the torque ripple due to stator current harmonics.
3. Construction and testing of a full-scale medium speed HTS excited generator ( $P \geq 5 \text{ MW}$ ) and experimental analysis in combination with a passive rectifier feeding.
4. Long-term test operation of a HTS medium speed generator in combination with an accelerated life testing, e.g. comprising a high number of cool-downs / warm ups, short circuit faults, downtimes of the cooling system and power ramps.
5. On-site installation of a HTS medium speed generator in the nacelle of on-/off-shore wind turbines, long-term operation in order to collect data on actual operating issues under real-life conditions.

A long-term experimental proof of the reliability and of the superior operating characteristics of either HTS direct drive generators or HTS medium speed generators has the potential to boost the establishment of the superconductor technology in the wind power sector.

---

## Bibliography

- [1] ABB, *ABB Wind turbine converters - Hardware Manual*, Dec. 2021, data sheet: model no. ACS880-77CC.
- [2] A. B. Abrahamsen, N. Magnusson, D. Liu, E. Stehouwer, B. Hendriks, and H. Polinder, "Design study of a 10 MW MgB<sub>2</sub> superconductor direct drive wind turbine generator." Barcelona, Spain: European Wind Energy Conference & Exhibition 2014, 10.-13. March 2014, 7 pages.
- [3] A. Abrikosov, "The magnetic properties of superconducting alloys," *Journal of Physics and Chemistry of Solids*, vol. 2, no. 3, pp. 199–208, 1957.
- [4] M. D. Ainslie, T. J. Flack, and A. M. Campbell, "Calculating transport AC losses in stacks of high temperature superconductor coated conductors with magnetic substrates using FEM," *Physica C: Superconductivity*, vol. 472, no. 1, pp. 50–56, 2012.
- [5] M. Al-Mosawi, C. Beduz, K. Goddard, J. Sykulski, Y. Yang, B. Xu, K. Ship, R. Stoll, and N. Stephen, "Design of a 100 kVA high temperature superconducting demonstration synchronous generator," *Physica C: Superconductivity*, vol. 372-376, pp. 1539–1542, 2002.
- [6] M. Al-Mosawi, C. Beduz, and Y. Yang, "Construction of a 100 kVA high temperature superconducting synchronous generator," *IEEE Transactions on Applied Superconductivity*, vol. 15, no. 2, pp. 2182–2185, 2005.
- [7] P. W. Anderson, *The Theory of Superconductivity in the High-Tc Cuprates*, 1st ed. Princeton University Press, Princeton, New Jersey, USA, 1997.
- [8] Arnold Magnetic Technologies, "Data sheet: Sintered Neodymium-Iron-Boron Magnets G44EH," March 2023. [Online]. Available: [https://www.arnoldmagnetics.com/wp-content/uploads/2018/11/N44EH\\_GBDD\\_181031.pdf](https://www.arnoldmagnetics.com/wp-content/uploads/2018/11/N44EH_GBDD_181031.pdf)

- [9] ARS Cryo, *ARS Cryocooler Series*, Macungie, PA, USA, 2023, data sheet: model no. DE110.
- [10] N. W. Ashcroft and D. N. Mermin, *Festkörperphysik*, 3rd ed. Oldenbourg Wissenschaftsverlag, Munich, Germany, 2007.
- [11] J. Bardeen, L. N. Cooper, and J. R. Schrieffer, “Microscopic Theory of Superconductivity,” *Phys. Rev.*, vol. 106, pp. 162–164, April 1957.
- [12] J. W. Barrett and L. Prigozhin, “Bean’s critical-state model as the  $p \rightarrow \infty$  limit of an evolutionary p-Laplacian equation,” *Nonlinear Analysis: Theory, Methods & Applications*, vol. 42, no. 6, pp. 977–993, 2000.
- [13] L. Bauer and S. Matysik, “Database of Wind Turbine Models,” *Accessed on: 14.04.2023*. [Online]. Available: <https://www.wind-turbine-models.com>
- [14] M. Bauer, “Supraleiter für die Energietechnik, Überblick, Technologie und Stand der Technik,” 05.03.2020, company presentation by THEVA at ZIEHL VII, Berlin, Germany. [Online]. Available: [https://ivsupra.de/wp-content/uploads/2020/03/2\\_Bauer-ZIEHL-VII-Tutorial.pdf](https://ivsupra.de/wp-content/uploads/2020/03/2_Bauer-ZIEHL-VII-Tutorial.pdf)
- [15] N. Bay and M. Nielsen, “Mechanical processing of Ag/BSCCO high temperature superconductor tape,” *Journal of Materials Processing Technology*, vol. 151, no. 1, pp. 18–26, 2004.
- [16] C. P. Bean, “Magnetization of Hard Superconductors,” *Phys. Rev. Lett.*, vol. 8, pp. 250–253, March 1962.
- [17] ———, “Magnetization of High-Field Superconductors,” *Rev. Mod. Phys.*, vol. 36, pp. 31–39, Jan. 1964.
- [18] J. G. Bednorz and K. A. Müller, “Possible high  $T_c$  superconductivity in the Ba-La-Cu-O system,” *Zeitschrift für Physik B Condensed Matter*, vol. 64, no. 2, pp. 189–193, June 1986.
- [19] T. Benkel, M. Lao, Y. Liu, E. Pardo, S. Wolfstädter, T. Reis, and F. Grilli, “T-A-Formulation to Model Electrical Machines With HTS Coated Conductor Coils,” *IEEE Transactions on Applied Superconductivity*, vol. 30, no. 6, pp. 1–7, 2020.

- [20] A. Bergen, R. Andersen, M. Bauer, H. Boy, M. ter Brake, P. Brutsaert, C. Bühler, M. Dhallé, J. Hansen, H. ten Kate, J. Kellers, J. Krause, E. Krooshoop, C. Kruse, H. Kylling, M. Pilas, H. Pütz, A. Rebsdorf, M. Reckhard, E. Seitz, H. Springer, X. Song, N. Tzabar, S. Wessel, J. Wiezoreck, T. Winkler, and K. Yagotyntsev, “Design and in-field testing of the world’s first ReBCO rotor for a 3.6 MW wind generator,” *Superconductor Science and Technology*, vol. 32, no. 12, p. 125006 (12 pages), Oct. 2019.
- [21] G. Bertotti, “General properties of power losses in soft ferromagnetic materials,” *IEEE Transactions on Magnetics*, vol. 24, no. 1, pp. 621–630, 1988.
- [22] A. Binder, *Elektrische Maschinen und Antriebe - Grundlagen, Betriebsverhalten*, 1st ed. Berlin and Heidelberg, Germany: Springer, Nov. 2012.
- [23] —, “Lecture notes: Energy Converters – CAD and System Dynamics,” 2023, Institute for Electrical Energy Conversion, Technical University Darmstadt, Germany. [Online]. Available: [https://www.ew.tu-darmstadt.de/ew\\_lehre/ew\\_vorlesungen/ew\\_lv\\_cad/index.de.jsp](https://www.ew.tu-darmstadt.de/ew_lehre/ew_vorlesungen/ew_lv_cad/index.de.jsp)
- [24] M. Boll, M. Corduan, S. Biser, M. Filipenko, Q. H. Pham, S. Schlachter, P. Rostek, and M. Noe, “A holistic system approach for short range passenger aircraft with cryogenic propulsion system,” *Superconductor Science and Technology*, vol. 33, no. 4, p. 044014 (14 pages), March 2020.
- [25] L. Bortot, B. Auchmann, I. C. Garcia, H. D. Gersem, M. Maciejewski, M. Mentink, S. Schöps, J. V. Nugteren, and A. P. Verweij, “A Coupled A–H Formulation for Magneto-Thermal Transients in High-Temperature Superconducting Magnets,” *IEEE Transactions on Applied Superconductivity*, vol. 30, no. 5, pp. 1–11, 2020.
- [26] R. Brambilla, F. Grilli, and L. Martini, “Development of an edge-element model for AC loss computation of high-temperature superconductors,” *Superconductor Science and Technology*, vol. 20, no. 1, p. 16–24, Nov. 2006.
- [27] R. Brambilla, F. Grilli, L. Martini, M. Bocchi, and G. Angeli, “A Finite-Element Method Framework for Modeling Rotating Machines With Superconducting Windings,” *IEEE Transactions on Applied Superconductivity*, vol. 28, no. 5, pp. 1–11, 2018.
- [28] E. H. Brandt, M. V. Indenbom, and A. Forkl, “Type-II Superconducting Strip in

- Perpendicular Magnetic Field,” *Europhysics Letters (EPL)*, vol. 22, no. 9, pp. 735–740, June 1993.
- [29] W. Buckel and R. Kleiner, *Supraleitung: Grundlagen und Anwendungen*, 7th ed. Wiley-VCH, Weinheim, Germany, Nov. 2012.
- [30] J. R. Bumby, *Superconducting rotating electrical machines*, 1st ed. Monographs in Electrical and Electronic Engineering, Clarendon Press, Oxford, UK, 1983.
- [31] O. Bíró and K. Preis, “On the use of the magnetic vector potential in the finite-element analysis of three-dimensional eddy currents,” *IEEE Transactions on Magnetics*, vol. 25, no. 4, pp. 3145–3159, 1989.
- [32] O. Bíró, K. Preis, and K. Richter, “On the use of the magnetic vector potential in the nodal and edge finite element analysis of 3d magnetostatic problems,” *IEEE Transactions on Magnetics*, vol. 32, no. 3, pp. 651–654, 1996.
- [33] O. Bíró, “Edge element formulations of eddy current problems,” *Computer Methods in Applied Mechanics and Engineering*, vol. 169, no. 3, pp. 391–405, 1999.
- [34] S. Carrara, P. Alves Dias, B. Plazzotta, and C. Pavel, “Raw materials demand for wind and solar PV technologies in the transition towards a decarbonised energy system,” Luxembourg, pp. 1–74, 2020, Accessed on: 13.04.2023. [Online]. Available: <https://op.europa.eu/en/publication-detail/-/publication/19aae047-7f88-11ea-aea8-01aa75ed71a1/language-en>
- [35] J. Carroll, A. McDonald, and D. McMillan, “Reliability Comparison of Wind Turbines With DFIG and PMG Drive Trains,” *IEEE Transactions on Energy Conversion*, vol. 30, no. 2, pp. 663–670, 2015.
- [36] Y. W. Chang, C. K. Jones, S. Karpathy, D. C. Litz, A. Patterson, and M. S. Walker, “Development of a 5 MVA Superconducting Generator Testing and Evaluation,” *IEEE Transactions on Power Apparatus and Systems*, vol. 93, no. 2, pp. 496–499, 1974.
- [37] J. Clarke and D. C. Larbalestier, “Wired for the future,” *Nature Physics*, vol. 2, pp. 794–796, 2006.
- [38] J. R. Clem, *Magnetic Susceptibility of Superconductors and Other Spin Systems -*

- 
- AC Losses in Type-II Superconductors*. Boston, MA, USA: Springer US, 1991, pp. 177–211.
- [39] L. N. Cooper, “Bound Electron Pairs in a Degenerate Fermi Gas,” *Phys. Rev.*, vol. 104, pp. 1189–1190, Nov. 1956.
- [40] M. Corduan, M. Boll, R. Bause, M. P. Oomen, M. Filipenko, and M. Noe, “Topology Comparison of Superconducting AC Machines for Hybrid Electric Aircraft,” *IEEE Transactions on Applied Superconductivity*, vol. 30, no. 2, pp. 1–10, 2020.
- [41] J. Coulomb and G. Meunier, “Finite element implementation of virtual work principle for magnetic or electric force and torque computation,” *IEEE Transactions on Magnetics*, vol. 20, no. 5, pp. 1894–1896, 1984.
- [42] Cryomech, *Cryorefrigerator Capacity Curve*, Syracuse, NY, USA, 2007, data sheet: model no. AL330.
- [43] R. Czepek, “Der Übergangswiderstand von Kohlenbürsten am Kollektor,” *Archiv für Elektrotechnik*, vol. 5, no. 5, pp. 161–174, May 1916.
- [44] Daily metal prices, “Database for metal prices,” *Accessed on*: 14.04.2023. [Online]. Available: <https://www.dailymetalprice.com>
- [45] E. de Vries, “MingYang ups offshore wind stakes with 16MW giant and 242-metre rotor,” *Windpower Monthly*, Haymarket Publishing, UK, Aug. 2021, *Accessed on*: 13.04.2023. [Online]. Available: <https://www.windpowermonthly.com/article/1725205/exclusive-mingyang-ups-offshore-wind-stakes-16mw-giant-242-metre-rotor>
- [46] K. Deb, A. Pratap, S. Agarwal, and T. Meyarivan, “A fast and elitist multiobjective genetic algorithm: NSGA-II,” *IEEE Transactions on Evolutionary Computation*, vol. 6, no. 2, pp. 182–197, 2002.
- [47] M. Dems, K. Komez, and J. Sykulski, “Analysis of effects of magnetic slot wedges on characteristics of large induction motor,” *Przegląd Elektrotechniczny*, vol. 88, pp. 73–77, July 2012.
- [48] D. Dezhin, R. Ilyasov, S. Kozub, K. Kovalev, and L. Verzhbitsky, “Synchronous

- motor with HTS-2G wires,” *Journal of Physics: Conference Series*, vol. 507, no. 3, p. 032011 (4 pages), May 2014.
- [49] D. Dezhin, K. Kovalev, L. Verzhbitskiy, S. Kozub, and V. Firsov, “Design and Testing of 200 kW Synchronous Motor with 2G HTS Field Coils,” *IOP Conference Series: Earth and Environmental Science*, vol. 87, no. 3, p. 032007 (7 pages), Oct. 2017.
- [50] DIN EN 60034-1, “Drehende elektrische Maschinen Teil 1: Bemessung und Betriebsverhalten,” VDE, Frankfurt, Germany, Standard, 2011.
- [51] DIN EN IEC 60034-4-1, “Drehende elektrische Maschinen Teil 4-1: Verfahren zur Ermittlung der Kenngrößen von Synchronmaschinen durch Messungen,” VDE, Frankfurt, Germany, Standard, 2019.
- [52] DTU Wind, INWIND.EU project, “Deliverable Report 3.13 - Fabrication of MgB<sub>2</sub> Coils – A superconducting generator pole demonstrator,” pp. 1–45, 2016. [Online]. Available: [http://www.innwind.eu/-/media/sites/innwind/publications/deliverables/230117/fabricationmgb2coil\\_d313\\_2november2016\\_final.pdf?la=da&hash=E1005B98F5CF0CF7C447CE4326D603E44FF963B6](http://www.innwind.eu/-/media/sites/innwind/publications/deliverables/230117/fabricationmgb2coil_d313_2november2016_final.pdf?la=da&hash=E1005B98F5CF0CF7C447CE4326D603E44FF963B6)
- [53] DTU Wind, UpWind project, “UpWind - Design limits and solutions for very large wind turbines,” pp. 1–108, 2011. [Online]. Available: [http://www.ewea.org/fileadmin/files/library/publications/reports/UpWind\\_Report.pdf](http://www.ewea.org/fileadmin/files/library/publications/reports/UpWind_Report.pdf)
- [54] P. Eckels and G. Snitchler, “5 MW High Temperature Superconductor Ship Propulsion Motor Design and Test Results,” *Naval Engineers Journal*, vol. 117, no. 4, pp. 31–36, 2005.
- [55] Eco 5, WINDSPEED project, “Abschlussbericht: Kostengünstige Supraleitergeneratoren auf MgB<sub>2</sub>-Basis für Massenmärkte der Windenergie,” pp. 1–192, 2015. [Online]. Available: <https://www.dbu.de/OPAC/ab/DBU-Abschlussbericht-AZ-31934.pdf>
- [56] J. Ekin, *Experimental Techniques for Low-Temperature Measurements: Cryostat Design, Material Properties and Superconductor Critical-Current Testing*. Oxford, UK: Oxford University Press, Oct. 2006.
- [57] M. Erbe, J. Hänisch, R. Hühne, T. Freudenberg, A. Kirchner, L. Molina-Luna, C. Damm, G. V. Tendeloo, S. Kaskel, L. Schultz, and B. Holzapfel, “BaHfO<sub>3</sub> artificial



- 
- pinning centres in TFA-MOD-derived YBCO and GdBCO thin films,” *Superconductor Science and Technology*, vol. 28, no. 11, p. 114002 (13 pages), Sept. 2015.
- [58] N. Erd and A. Binder, “Eddy Currents in the Solid Rotor Yoke of a High-Torque PMSM with Tooth-Coil Winding,” in *2022 International Symposium on Power Electronics, Electrical Drives, Automation and Motion (SPEEDAM)*, Sorrento, Italy, 22.-24. June 2022, pp. 27–34.
- [59] ———, “Optimale Auslegung von getriebelosen, permanentmagneterregten Windgeneratoren mit Zahnpulsenwicklung und massivem Rotorjoch,” *e & i Elektrotechnik und Informationstechnik*, vol. 137, no. 4, pp. 266–279, 2020.
- [60] European Commission, “The European Green Deal,” Brussels, Belgium, pp. 1–24, Dec. 2019, *Accessed on:* 13.04.2023. [Online]. Available: <https://eur-lex.europa.eu/legal-content/EN/TXT/?uri=COM%3A2019%3A640%3AFIN>
- [61] R. Fair, C. Lewis, J. Eugene, and M. Ingles, “Development of an HTS hydroelectric power generator for the Hirschaid power station,” *Journal of Physics: Conference Series*, vol. 234, no. 3, p. 032008 (12 pages), June 2010.
- [62] J. Fealey, W. Jones, T. Keim, and T. Laskaris, “Comprehence Test and Evaluation of a 20 MVA Superconducting Generator,” *IEEE Transactions on Power Apparatus and Systems*, vol. 104, no. 6, pp. 1484–1491, 1985.
- [63] K. Fischer, T. Stalin, H. Ramberg, J. Wenske, G. Wetter, R. Karlsson, and T. Thiringer, “Field-Experience Based Root-Cause Analysis of Power-Converter Failure in Wind Turbines,” *IEEE Transactions on Power Electronics*, vol. 30, no. 5, pp. 2481–2492, 2015.
- [64] B. Fomin, L. Kurilovich, G. Khutoretsky, I. Filippov, Y. Rybin, V. Varshavsky, and Y. Tyurin, “Main stages of manufacturing a 300 MW superconducting generator,” *Cryogenics*, vol. 27, no. 5, pp. 243–248, 1987.
- [65] F.-A. Fortin, F.-M. De Rainville, M.-A. Gardner, M. Parizeau, and C. Gagné, “DEAP: Evolutionary algorithms made easy,” *Journal of Machine Learning Research*, vol. 13, pp. 2171–2175, July 2012.
- [66] A. Fox and C. Hill, “System Performance, Availability and Reliability Trend Analysis - Portfolio Review 2016,” London, UK, pp. 1–9, 2017, *Accessed*
-

- on: 13.04.2023. [Online]. Available: [https://ore.catapult.org.uk/wp-content/uploads/2018/02/SPARTAbrochure\\_20March-1.pdf](https://ore.catapult.org.uk/wp-content/uploads/2018/02/SPARTAbrochure_20March-1.pdf)
- [67] M. Frank, J. Frauenhofer, B. Gromoll, P. van Haelt, W. Nick, G. Nerowski, H.-W. Neumüller, H.-U. Häfner, and G. Thummes, “Thermosyphon Cooling System for the Siemens 400 kW HTS Synchronous Machine,” in *Advances in Cryogenic Engineering: Transactions of the Cryogenic Engineering Conference*, vol. 710, no. 1, Anchorage, Alaska, USA, 22.-26. Sept. 2003, pp. 859–866.
- [68] Fraunhofer Institute for Solar Energy Systems (ISE), “Net Electricity Generation in Germany in 2022: Significant Increase in Generation from Wind and PV,” Freiburg, Germany, 2023-01-03. [Online]. Available: [https://www.ise.fraunhofer.de/content/dam/ise/en/documents/press-releases/2023/0123\\_ISE\\_e\\_PR\\_net\\_public\\_generation.pdf](https://www.ise.fraunhofer.de/content/dam/ise/en/documents/press-releases/2023/0123_ISE_e_PR_net_public_generation.pdf)
- [69] B. Gamble, S. Kalsi, G. Snitchler, D. Madura, and R. Howard, “The status of HTS motors,” in *IEEE Power Engineering Society Summer Meeting*, vol. 1, Chicago, IL, USA, 21.-25. July 2002, pp. 270–274.
- [70] B. Gamble and T. Keim, “High-Power-Density Superconducting Generator,” *Journal of Energy*, vol. 6, no. 1, pp. 38–44, 1982.
- [71] B. Gamble, G. Snitchler, and T. MacDonald, “Full Power Test of a 36.5 MW HTS Propulsion Motor,” *IEEE Transactions on Applied Superconductivity*, vol. 21, no. 3, pp. 1083–1088, 2011.
- [72] General Electric Company, “Design and Development of a 100 MVA HTS Generator for Commercial Entry,” Boston, MA, USA, pp. 1–164, 2006, NREL Final Technical Report No. DE-FC36-02GO11100.
- [73] German Environment Agency, “Seltene Erden in Permanentmagneten - Factsheet,” Dessau-Roßlau, Germany, May 2019, *Accessed on: 14.04.2023*, 10 pages. [Online]. Available: [https://www.umweltbundesamt.de/sites/default/files/medien/3521/dokumente/factsheet-magnetmaterialien\\_fi\\_barrierefrei.pdf](https://www.umweltbundesamt.de/sites/default/files/medien/3521/dokumente/factsheet-magnetmaterialien_fi_barrierefrei.pdf)
- [74] German Federal Ministry for the Environment, Nature Conservation, Nuclear Safety and Consumer Protection, “Federal Climate Change Act (Bundes-Klimaschutzgesetz),” Berlin, Germany, pp. 1–13, May 2021, *Ac-*

- cessed on: 13.04.2023. [Online]. Available: <https://www.bmu.de/en/law/federal-climate-change-act-bundes-klimaschutzgesetz>
- [75] German Federal Ministry of Economic Affairs and Climate Action, “Overview of the easter package,” 2022-04-06. [Online]. Available: [https://www.bmwk.de/Redaktion/EN/Downloads/Energy/0406\\_ueberblickspapier\\_osterpaket\\_en.pdf](https://www.bmwk.de/Redaktion/EN/Downloads/Energy/0406_ueberblickspapier_osterpaket_en.pdf)
- [76] V. L. Ginzburg, *On Superconductivity and Superfluidity: A Scientific Autobiography - On the Theory of Superconductivity*. Springer, Berlin, Heidelberg, Germany, 2009.
- [77] Global Wind Energy Council (GWEC), “Global Wind Report 2022,” Brussels, Belgium, pp. 1–158, April 2022, Accessed on: 16.04.2023. [Online]. Available: <https://gwec.net/wp-content/uploads/2022/03/gwec-global-wind-report-2022.pdf>
- [78] F. Grilli, E. Pardo, A. Stenvall, D. N. Nguyen, W. Yuan, and F. Gömöry, “Computation of Losses in HTS Under the Action of Varying Magnetic Fields and Currents,” *IEEE Transactions on Applied Superconductivity*, vol. 24, no. 1, pp. 78–110, 2014.
- [79] M. Hanif, F. Nadeem, R. Tariq, and U. Rashid, *Renewable and Alternative Energy Resources*, 1st ed. Cambridge, Massachusetts, USA: Academic Press, 2021.
- [80] K. S. Haran, S. Kalsi, T. Arndt, H. Karmaker, R. Badcock, B. Buckley, T. Haugan, M. Izumi, D. Loder, J. W. Bray, P. Masson, and E. W. Stautner, “High power density superconducting rotating machines—development status and technology roadmap,” *Superconductor Science and Technology*, vol. 30, no. 12, p. 123002 (41 pages), Nov. 2017.
- [81] E. Hidding and A. Jöckel, “Giants of the sea, the next ten years,” 05.05.2022, Flender/Winery Webcast, Flender Company, Bocholt, Germany.
- [82] F. Huber, W. Song, M. Zhang, and F. Grilli, “The T-A formulation: an efficient approach to model the macroscopic electromagnetic behaviour of HTS coated conductor applications,” *Superconductor Science and Technology*, vol. 35, no. 4, p. 043003 (14 pages), March 2022.
- [83] S. Hunklinger, *Festkörperphysik*, 3rd ed. Oldenbourg Wissenschaftsverlag, Munich, Germany, 2011.
- [84] H. Ibach and H. Lüth, *Festkörperphysik*, 5th ed. Springer, Berlin, Germany, 1999.

- [85] A. Ibi, T. Yoshida, T. Taneda, M. Yoshizumi, T. Izumi, and Y. Shiohara, “Development of Long REBCO with BMO Coated Conductors by PLD Method with High Production Rate,” *Physics Procedia*, vol. 65, pp. 121–124, 2015.
- [86] International Energy Agency, “Electricity Consumption,” Paris, France, 2021, *Accessed on:* 13.04.2023. [Online]. Available: <https://www.iea.org/reports/electricity-information-overview/electricity-consumption>
- [87] —, “Net Zero by 2050,” Paris, France, pp. 1–224, May 2021, *Accessed on:* 16.04.2023. [Online]. Available: [https://iea.blob.core.windows.net/assets/deebef5d-0c34-4539-9d0c-10b13d840027/NetZeroBy2050-ARoadmapfortheGlobalEnergySector\\_CORR.pdf](https://iea.blob.core.windows.net/assets/deebef5d-0c34-4539-9d0c-10b13d840027/NetZeroBy2050-ARoadmapfortheGlobalEnergySector_CORR.pdf)
- [88] —, “Renewable Electricity,” Paris, France, Sept. 2022, *Accessed on:* 16.04.2023. [Online]. Available: <https://www.iea.org/reports/renewable-electricity>
- [89] —, “Renewables 2022 - Analysis and forecast to 2027,” Paris, France, pp. 1–159, Dec. 2022, *Accessed on:* 16.04.2023. [Online]. Available: <https://www.iea.org/reports/renewables-2022>
- [90] —, “Wind Electricity,” Paris, France, Sept. 2022, *Accessed on:* 16.04.2023. [Online]. Available: <https://www.iea.org/reports/wind-electricity>
- [91] —, “The Role of Critical Minerals in Clean Energy Transitions,” Paris, France, pp. 1–278, April 2023, *Accessed on:* 14.04.2023. [Online]. Available: <https://iea.blob.core.windows.net/assets/ffd2a83b-8c30-4e9d-980a-52b6d9a86fdc/TheRoleofCriticalMineralsinCleanEnergyTransitions.pdf>
- [92] International Renewable Energy Agency, “Renewable Capacity Statistics 2023,” Abu Dhabi, pp. 1–69, March 2023, *Accessed on:* 16.04.2023. [Online]. Available: <https://www.irena.org/Publications/2023/Mar/Renewable-capacity-statistics-2023>
- [93] L. Intichar and D. Lambrecht, “Technical overview of the German program to develop superconducting AC generators,” *IEEE Transactions on Magnetics*, vol. 19, no. 3, pp. 536–540, 1983.
- [94] K. Ishida, T. Itaya, A. Tanaka, N. Takehira, and T. Miki, “Self-inductance of a racetrack coil,” *IEEE Transactions on Applied Superconductivity*, vol. 22, no. 4, pp. 4 905 509–4 905 509, 2012.

- [95] M. Iwakuma, Y. Hase, T. Satou, A. Tomioka, M. Konno, Y. Iijima, T. Saitoh, Y. Yamada, T. Izumi, and Y. Shiohara, "Production and Test of a REBCO Superconducting Synchronous Motor," *IEEE Transactions on Applied Superconductivity*, vol. 19, no. 3, pp. 1648–1651, 2009.
- [96] J. D. Jackson, *Klassische Elektrodynamik*, 4th ed. Berlin, Germany and Boston, USA: De Gruyter, 2014.
- [97] W. R. Johnson, "Thermal Performance of Multilayer Insulations," Cleveland, Ohio, USA, 1974, technical report NASA CR-134477, National Aeronautics and Space Administration, Lockheed Missiles & Space Company.
- [98] H. Jordan, "Die ferromagnetischen Konstanten für schwache Wechselfelder," *Elektrische Nachrichten-Technik*, vol. 1, pp. 7–29, 1924.
- [99] C. Joshi, C. Prum, R. Schiferl, and D. Driscoll, "Demonstration of two synchronous motors using high temperature superconducting field coils," *IEEE Transactions on Applied Superconductivity*, vol. 5, no. 2, pp. 968–971, 1995.
- [100] S. Kalsi, B. Gamble, G. Snitchler, and S. Ige, "The status of HTS ship propulsion motor developments," in *2006 IEEE Power Engineering Society General Meeting*, Montreal, QC, Canada, 18.-22. June 2006, pp. 1–5.
- [101] S. Kalsi, D. Madura, R. Howard, G. Snitchler, T. MacDonald, D. Bradshaw, I. Grant, and M. Ingram, "Superconducting dynamic synchronous condenser for improved grid voltage support," in *2003 IEEE PES Transmission and Distribution Conference and Exposition (IEEE Cat. No.03CH37495)*, vol. 2, Dallas, TX, USA, 7.-12. Sept. 2003, pp. 742–747.
- [102] S. Kalsi, D. Madura, G. Snitchler, M. Ross, J. Voccio, and M. Ingram, "Discussion of Test Results of a Superconductor Synchronous Condenser on a Utility Grid," *IEEE Transactions on Applied Superconductivity*, vol. 17, no. 2, pp. 2026–2029, 2007.
- [103] S. Kalsi, K. Weeber, H. Takesue, C. Lewis, H.-W. Neumueller, and R. Blaugher, "Development status of rotating machines employing superconducting field windings," *Proceedings of the IEEE*, vol. 92, no. 10, pp. 1688–1704, 2004.
- [104] S. Kalsi, "Superconducting Wind Turbine Generator Employing MgB<sub>2</sub> Windings

- Both on Rotor and Stator,” *IEEE Transactions on Applied Superconductivity*, vol. 24, no. 1, pp. 47–53, 2014.
- [105] ———, “Influence of Magnetic Iron Teeth in Motors Employing Superconductors for Field Excitation and AC Stator Windings,” *IEEE Transactions on Applied Superconductivity*, vol. 31, no. 4, pp. 1–7, 2021.
- [106] S. Kalsi, D. Madura, T. MacDonald, M. Ingram, and I. Grant, “Operating Experience of Superconductor Dynamic Synchronous Condenser,” in *2005/2006 IEEE/PES Transmission and Distribution Conference and Exhibition*, Dallas, TX, USA, 21–24. May 2006, pp. 899–902.
- [107] Y. Kamihara, H. Hiramatsu, M. Hirano, R. Kawamura, H. Yanagi, T. Kamiya, and H. Hosono, “Iron-Based Layered Superconductor: LaOFeP,” *Journal of the American Chemical Society*, vol. 128, no. 31, pp. 10012–10013, Aug. 2006.
- [108] H. Karmaker and E. Chen, “Design concepts for a direct drive wind generator using new superconductors,” in *2015 IEEE Electrical Power and Energy Conference (EPEC)*, Ottawa, Ontario, Canada, 26–28. Oct. 2015, pp. 22–25.
- [109] H. Karmaker, E. Chen, W. Chen, and G. Gao, “Stator design concepts for an 8 MW direct drive superconducting wind generator,” in *2012 XXth International Conference on Electrical Machines*, Marseille, France, 2.–5. Sept. 2012, pp. 769–774.
- [110] H. Karmaker, M. Ho, and D. Kulkarni, “Comparison Between Different Design Topologies for Multi-Megawatt Direct Drive Wind Generators Using Improved Second Generation High Temperature Superconductors,” *IEEE Transactions on Applied Superconductivity*, vol. 25, no. 3, pp. 1–5, 2015.
- [111] A. H. Kasem, E. F. El-Saadany, H. H. El-Tamaly, and M. A. A. Wahab, “Ramp rate control and voltage regulation for grid directly connected wind turbines,” in *2008 IEEE Power and Energy Society General Meeting*, Pittsburgh, Pennsylvania, USA, 20–24 July 2008, pp. 1–6.
- [112] T. Keim, T. Laskaris, J. Fealey, and P. Rios, “Design and Manufacture of a 20 MVA Superconducting Generator,” *IEEE Transactions on Power Apparatus and Systems*, vol. 104, no. 6, pp. 1474–1483, 1985.
- [113] N. Kesavamurthy and A. K. Basu, “Effects of Traveling Field on Ferromagnetic

- 
- Plates of Finite Thickness,” *IEEE Transactions on Power Apparatus and Systems*, vol. 86, no. 12, pp. 1565–1571, 1967.
- [114] A.-R. Kim, K.-M. Kim, H. Park, G.-H. Kim, T.-J. Park, M. Park, S. Kim, S. Lee, H. Ha, S. Yoon, and H. Lee, “Performance Analysis of a 10-kW Superconducting Synchronous Generator,” *IEEE Transactions on Applied Superconductivity*, vol. 25, no. 3, pp. 1–4, 2015.
- [115] C. Kim, H.-J. Sung, B.-S. Go, K. Sim, G. D. Nam, S. Kim, and M. Park, “Design, Fabrication, and Testing of a Full-Scale HTS Coil for a 10 MW HTS Wind Power Generator,” *IEEE Transactions on Applied Superconductivity*, vol. 31, no. 5, pp. 1–5, 2021.
- [116] Y. B. Kim, C. F. Hempstead, and A. R. Strnad, “Magnetization and Critical Super-currents,” *Physical Review*, vol. 129, no. 2, pp. 528–535, Jan. 1963.
- [117] C. Kingsley, G. Wilson, J. Kirtley, T. Keim, J. Smith, and P. Thullen, “Steady-state electrical tests on the MIT-EPRI 3-MVA superconducting generator,” *IEEE Transactions on Power Apparatus and Systems*, vol. 95, no. 3, pp. 887–893, 1976.
- [118] J. Kirtley, J. Smith, P. Thullen, and H. Woodson, “MIT-EEI program on large superconducting machines,” *Proceedings of the IEEE*, vol. 61, no. 1, pp. 112–115, 1973.
- [119] H. Kleinrath, *Stromrichtergespeiste Drehfeldmaschinen*. Springer Wien, Austria, 1980.
- [120] P. Komarek, *Hochstromanwendungen der Supraleitung*, 1st ed. Teubner Verlag, Stuttgart, Germany, 1995.
- [121] E. Kosuge, Y. Gocho, K. Okumura, M. Yamaguchi, K. Umemoto, K. Aizawa, M. Yokoyama, and S. Takao, “Development of helium transfer coupling of 1 MW-class HTS motor for podded ship propulsion system,” *Journal of Physics: Conference Series*, vol. 234, no. 3, p. 032032 (5 pages), June 2010.
- [122] K. Kovalev, L. Kovalev, V. Poltavets, S. Samsonovich, R. Ilyasov, A. Levin, and M. Surin, “Synchronous Generator with HTS-2G field coils for Windmills with output power 1 MW,” *Journal of Physics: Conference Series*, vol. 507, no. 3, p. 032023 (4 pages), May 2014.
-

- [123] K. Kovalev, V. Poltavets, R. Ilyasov, L. Verzhbitsky, and S. Kozub, “1 MVA HTS-2G Generator for Wind Turbines,” *IOP Conference Series: Earth and Environmental Science*, vol. 87, no. 3, p. 032018 (6 pages), Oct. 2017.
- [124] S. Krohn, P. Morthorst, and S. Awerbuch, “The Economics of Wind Energy,” Brussels, Belgium, pp. 1–156, March 2009, *Accessed on:* 14.04.2023. [Online]. Available: [https://www.ewea.org/fileadmin/files/library/publications/reports/Economics\\_of\\_Wind\\_Energy.pdf](https://www.ewea.org/fileadmin/files/library/publications/reports/Economics_of_Wind_Energy.pdf)
- [125] M. Kuczmann, “Lecture notes: Potential Formulations in magnetics Applying the Finite Element Method,” 2009, Laboratory of Electromagnetic Fields, Széchenyi István University, Győr, Hungary. [Online]. Available: <http://maxwell.sze.hu/docs/C4.pdf>
- [126] D. Lambrecht, “Status of development of superconducting AC generators,” *IEEE Transactions on Magnetics*, vol. 17, no. 5, pp. 1551–1559, 1981.
- [127] ———, “Superconducting turbogenerators: status and trends,” *Cryogenics*, vol. 25, no. 11, pp. 619–627, 1985.
- [128] D. Lambrecht, A. Grünewald, M. Liese, E. Weghaupt, L. Intichar, H.-W. Neumüller, and C. Schnapper, “Progress in the Development of Superconducting Turbogenerators at KWU/Siemens,” *Journal de Physique Colloques*, vol. 45, no. C1, pp. 713–716, 1984.
- [129] T. Laskaris and K. Schoch, “Superconducting Rotor Development for a 20 MVA Generator,” *IEEE Transactions on Power Apparatus and Systems*, vol. 99, no. 6, pp. 2031–2039, 1980.
- [130] D. Lee, T. Balachandran, H.-W. Cho, and K. Haran, “Exploring fully superconducting air-core machine topology for off-shore wind turbine applications,” *IEEE Transactions on Magnetics*, vol. 55, no. 7, pp. 1–6, 2019.
- [131] C. Lewis and J. Muller, “A Direct Drive Wind Turbine HTS Generator,” in *2007 IEEE Power Engineering Society General Meeting*, Tampa, FL, USA, 24.-28. June 2007, pp. 1–8.
- [132] F. Liang, S. Venuturumilli, H. Zhang, M. Zhang, J. Kvitkovic, S. Pamidi, Y. Wang, and W. Yuan, “A finite element model for simulating second generation high temper-



- ature superconducting coils/stacks with large number of turns,” *Journal of Applied Physics*, vol. 122, no. 4, p. 043903 (10 pages), 2017.
- [133] Y. Liang, M. D. Rotaru, and J. K. Sykulski, “Electromagnetic Simulations of a Fully Superconducting 10-MW-Class Wind Turbine Generator,” *IEEE Transactions on Applied Superconductivity*, vol. 23, no. 6, pp. 46–50, 2013.
- [134] F. Lin, R. Qu, D. Li, Y. Cheng, and J. Sun, “Electromagnetic Design of 13.2 MW Fully Superconducting Machine,” *IEEE Transactions on Applied Superconductivity*, vol. 28, no. 3, pp. 1–5, 2018.
- [135] Y. Lin, L. Tu, H. Liu, and W. Li, “Fault analysis of wind turbines in China,” *Renewable and Sustainable Energy Reviews*, vol. 55, pp. 482–490, 2016.
- [136] D. Liu, “Increasing the Feasibility of Superconducting Generators for 10 MW Direct-Drive Wind Turbines,” Ph.D. dissertation, TU Delft, 2017. [Online]. Available: <https://repository.tudelft.nl/islandora/object/uuid%3A074d4f96-e7bf-4dde-a7b4-86c9dd2e214f>
- [137] D. Liu, T. Salmi, F. Deng, and C. Ye, “Characteristics of the Superconducting Field Winding of an HTS Wind Turbine Generator During a Short Circuit Fault,” *IEEE Transactions on Applied Superconductivity*, vol. 32, no. 4, pp. 1–6, 2022.
- [138] G. Liu, G. Zhang, H. Yu, L. Jing, L. Ai, and Q. Liu, “Experimental and numerical study of frequency-dependent transport loss in YBa<sub>2</sub>Cu<sub>3</sub>O<sub>7</sub> coated conductors with ferromagnetic substrate and copper stabilizer,” *J. Appl. Phys.*, vol. 121, p. 243902 (10 pages), 2017.
- [139] Y. Liu, R. Qu, and J. Wang, “Comparative Analysis on Superconducting Direct-Drive Wind Generators With Iron Teeth and Air-Gap Winding,” *IEEE Trans. Appl. Supercond.*, vol. 24, no. 3, pp. 1–5, June 2014.
- [140] Y. Liu, “Design of a superconducting DC wind generator,” Ph.D. dissertation, Karlsruhe Institute of Technology, Karlsruhe, Germany, Nov. 2020.
- [141] Y. Liu, M. Noe, and M. Doppelbauer, “Feasibility Study of a Superconducting DC Direct-Drive Wind Generator,” *IEEE Transactions on Applied Superconductivity*, vol. 26, no. 4, pp. 1–6, 2016.

- [142] Y. Liu, J. Ou, and M. Noe, "A Large-Scale Superconducting DC Wind Generator Considering Concentrated/Distributed Armature Winding," *IEEE Transactions on Applied Superconductivity*, vol. 27, no. 4, pp. 1–5, 2017.
- [143] F. London, H. London, and F. A. Lindemann, "The electromagnetic equations of the supraconductor," *Proceedings of the Royal Society of London. Series A - Mathematical and Physical Sciences*, vol. 149, no. 866, pp. 71–88, 1935.
- [144] D. Lu, W. Qiao, and X. Gong, "Current-Based Gear Fault Detection for Wind Turbine Gearboxes," *IEEE Transactions on Sustainable Energy*, vol. 8, no. 4, pp. 1453–1462, 2017.
- [145] N. Maki, K. Yamaguchi, M. Takahashi, and T. Sanematsu, "Test results of 50 MVA superconducting generator," *IEEE Transactions on Magnetics*, vol. 23, no. 5, pp. 3536–3538, 1987.
- [146] I. Marino, A. Pujana, G. Sarmiento, S. Sanz, J. M. Merino, M. Tropeano, J. Sun, and T. Canosa, "Lightweight MgB<sub>2</sub> superconducting 10 MW wind generator," *Superconductor Science and Technology*, vol. 29, no. 2, p. 024005 (11 pages), Dec. 2015.
- [147] R. Marshall, "3000 horsepower superconductive field acyclic motor," *IEEE Transactions on Magnetics*, vol. 19, no. 3, pp. 876–879, 1983.
- [148] P. Mauceri, "Development of Superconducting MgB<sub>2</sub> Wires," in *EASITrain – European Advanced Superconductivity Innovation and Training*, Geneva, Italy, 09.10.2020, company presentation by ASG Superconductors, Geneva, Italy. [Online]. Available: [https://indico.cern.ch/event/933609/contributions/4039207/attachments/2123488/3574595/EASISchool\\_presentation.pdf](https://indico.cern.ch/event/933609/contributions/4039207/attachments/2123488/3574595/EASISchool_presentation.pdf)
- [149] E. Maxwell, "Isotope Effect in the Superconductivity of Mercury," *Phys. Rev.*, vol. 78, pp. 477–477, May 1950.
- [150] W. Meissner and R. Ochsenfeld, "Ein neuer Effekt bei Eintritt der Supraleitfähigkeit," *Naturwissenschaften*, vol. 21, no. 44, pp. 787–788, Nov. 1933.
- [151] R. Møllerud, J. Nøland, and C. Hartmann, "Preliminary Design of a 2.5-MW Superconducting Propulsion Motor for Hydrogen-Powered Aviation," in *2022 International Conference on Electrical Machines (ICEM)*, Valencia, Spain, 5.-8. Sept. 2022, pp. 1404–1410.

- 
- [152] H. Moon, Y.-C. Kim, H.-J. Park, M. Park, and I.-K. Yu, "Development of a MW-Class 2G HTS Ship Propulsion Motor," *IEEE Transactions on Applied Superconductivity*, vol. 26, no. 4, pp. 1–5, 2016.
- [153] H. Moon, Y.-C. Kim, H.-J. Park, I.-K. Yu, and M. Park, "An introduction to the design and fabrication progress of a megawatt class 2G HTS motor for the ship propulsion application," *Superconductor Science and Technology*, vol. 29, no. 3, p. 034009 (12 pages), Feb. 2016.
- [154] G. Mur, "Edge elements, their advantages and their disadvantages," *IEEE Transactions on Magnetics*, vol. 30, no. 5, pp. 3552–3557, 1994.
- [155] J. Nagamatsu, N. Nakagawa, T. Muranaka, Y. Zenitani, and J. Akimitsu, "Superconductivity at 39 K in magnesium diboride," *Nature*, vol. 410, no. 6824, pp. 63–64, 2001.
- [156] H. Nagaoka, "The inductance coefficients of solenoids," *Journal of the College of Science, Imperial University, Tokyo*, vol. 27, no. 6, p. 1 (33 pages), 1909.
- [157] S. Nakamura, T. Yamada, T. Nomura, M. Iwamoto, Y. Shindo, S. Nose, A. Ishihara, and H. Fujino, "30 MVA superconducting synchronous condenser: Design and its performance test results," *IEEE Transactions on Magnetics*, vol. 21, no. 2, pp. 783–790, 1985.
- [158] W. Nick, M. Frank, P. Kummeth, J. J. Rabbers, M. Wilke, and K. Schleicher, "Development and construction of an HTS rotor for ship propulsion application," *Journal of Physics: Conference Series*, vol. 234, no. 3, p. 032040 (9 pages), June 2010.
- [159] W. Nick, G. Nerowski, H.-W. Neumüller, M. Frank, P. van Hasselt, J. Fraunhofer, and F. Steinmeyer, "380 kW synchronous machine with HTS rotor windings—development at Siemens and first test results," *Physica C: Superconductivity*, vol. 372-376, pp. 1506–1512, 2002.
- [160] W. Nick, M. Frank, G. Klaus, J. Fraunhofer, and H.-W. Neumüller, "Operational Experience With the World's First 3600 rpm 4 MVA Generator at Siemens," *IEEE Transactions on Applied Superconductivity*, vol. 17, no. 2, pp. 2030–2033, 2007.
- [161] W. Nick, J. Grundmann, and J. Fraunhofer, "Test results from Siemens low-speed, high-torque HTS machine and description of further steps towards commercialisation

- of HTS machines,” *Physica C: Superconductivity and its Applications*, vol. 482, pp. 105–110, 2011.
- [162] W. T. Norris, “Calculation of hysteresis losses in hard superconductors carrying AC: isolated conductors and edges of thin sheets,” *Journal of Physics D: Applied Physics*, vol. 3, no. 4, pp. 489–507, April 1970.
- [163] ———, “Calculation of hysteresis losses in hard superconductors: polygonal-section conductors,” *Journal of Physics D: Applied Physics*, vol. 4, no. 9, pp. 1358–1364, 1971.
- [164] H. Ohsaki, L. Quéval, and Y. Terao, “Design and characteristic analysis of 10 MW class superconducting wind turbine generators with different types of stator and rotor configurations,” in *2013 International Conference on Clean Electrical Power (IC-CEP)*, Alghero, Italy, 11.-13. June 2013, pp. 395–398.
- [165] H. K. Onnes, “Further experiments with Liquid Helium. On the Electrical Resistance of Pure Metals. On the Sudden Change in the Rate at which the Resistance of Mercury Disappears.” *Proceedings of the Koninklijke Akademie van Wetenschappen te Amsterdam, Communications - Leiden*, vol. 124c, pp. 267 – 271, 1911.
- [166] J. Pan, S. Bala, M. Callavik, and P. Sandeberg, “Platformless DC Collection and Transmission for Offshore Wind,” in *11th IET International Conference on AC and DC Power Transmission*, Birmingham, UK, 10.-12. Feb. 2015, pp. 1–6.
- [167] E. Pardo, J. Šouc, and J. Kováč, “AC loss in ReBCO pancake coils and stacks of them: modelling and measurement,” *Superconductor Science and Technology*, vol. 25, no. 3, p. 035003 (16 pages), Jan. 2012.
- [168] E. Pardo, M. Staines, Z. Jiang, and N. Glasson, “AC loss modelling and measurement of superconducting transformers with coated-conductor Roebel-cable in low-voltage winding,” *Superconductor Science and Technology*, vol. 28, no. 11, p. 114008 (19 pages), Oct. 2015.
- [169] R. Pile, E. Devillers, and J. Le Besnerais, “Comparison of Main Magnetic Force Computation Methods for Noise and Vibration Assessment in Electrical Machines,” *IEEE Transactions on Magnetics*, vol. 54, no. 7, pp. 1–13, 2018.
- [170] Podesta, J. D., “Building a Clean Energy Economy: A Guidebook to the Inflation

- 
- Reduction Act's Investments in Clean Energy and Climate Action," Washington, USA, pp. 1–184, Jan. 2023, *Accessed on:* 13.04.2023. [Online]. Available: <https://www.whitehouse.gov/cleanenergy/inflation-reduction-act-guidebook/>
- [171] H. Polinder, J. A. Ferreira, B. B. Jensen, A. B. Abrahamsen, K. Atallah, and R. A. McMahon, "Trends in wind turbine generator systems," *IEEE Journal of Emerging and Selected Topics in Power Electronics*, vol. 1, no. 3, pp. 174–185, 2013.
- [172] L. Prigozhin, "The Bean Model in Superconductivity: Variational Formulation and Numerical Solution," *Journal of Computational Physics*, vol. 129, no. 1, pp. 190–200, 1996.
- [173] Publications Office of the European Union, "CO<sub>2</sub> emissions of all world countries - JRC/IEA/PBL 2022 Report," Luxembourg, pp. 1–261, 2022, *Accessed on:* 13.04.2023. [Online]. Available: [https://edgar.jrc.ec.europa.eu/report\\_2022](https://edgar.jrc.ec.europa.eu/report_2022)
- [174] T. Qu, P. Song, X. Yu, C. Gu, L. Li, X. Li, D. Wang, B. Hu, D. Chen, P. Zeng, and Z. Han, "Development and testing of a 2.5 kW synchronous generator with a high temperature superconducting stator and permanent magnet rotor," *Superconductor Science and Technology*, vol. 27, no. 4, p. 044026 (8 pages), March 2014.
- [175] R. Radebaugh and R. G. Ross, "Cryocooler fundamentals and space applications," in *Cryogenic Engineering Conference (The Cryogenic Society of America, NIST, NASA)*, Tucson, Arizona, USA, 28.06.2015, tutorial presentation, 252 slides.
- [176] J. Renedo Anglada, S. M. Sharkh, and M. A. Yuratic, "Calculation of rotor losses in PM machines with retaining sleeves using transfer matrices," *IET Electric Power Applications*, vol. 12, no. 8, pp. 1150–1157, 2018.
- [177] J. Röder, G. Jacobs, D. Bosse, and J. L. R. Izal, "Reduction of gearbox loads of a DFIG wind turbine during grid faults with optimized converter configurations," *Journal of Physics: Conference Series*, vol. 2265, no. 3, p. 032034 (9 pages), March 2022.
- [178] U. Sander, "Turbogenerator mit Supraleiterwicklung," *etz*, vol. 110, no. 3, pp. 114–115, 1989.
- [179] G. Sarmiento, S. Sanz, A. Pujana, J. M. Merino, I. Marino, M. Tropeano, D. Nardelli, and G. Grasso, "Design and Testing of Real-Scale MgB<sub>2</sub> Coils for

- SUPRAPOWER 10-MW Wind Generators,” *IEEE Transactions on Applied Superconductivity*, vol. 26, no. 3, p. 5203006 (6 pages), 2016.
- [180] M. Saruwatari, K. Yun, M. Iwakuma, K. Tamura, Y. Hase, Y. Sasamori, and T. Izumi, “Design Study of 15-MW Fully Superconducting Generators for Offshore Wind Turbine,” *IEEE Transactions on Applied Superconductivity*, vol. 26, no. 4, p. 5206805 (5 pages), 2016.
- [181] H. Sasa, M. Iwakuma, K. Yoshida, S. Sato, T. Sasayama, T. Yoshida, K. Yamamoto, S. Miura, A. Kawagoe, T. Izumi, A. Tomioka, M. Konno, Y. Sasamori, H. Honda, Y. Hase, M. Syutoh, S. Lee, S. Hasuo, M. Nakamura, T. Hasegawa, Y. Aoki, and T. Umeno, “Experimental Evaluation of 1 kW-class Prototype REBCO Fully Superconducting Synchronous Motor Cooled by Subcooled Liquid Nitrogen for E-Aircraft,” *IEEE Transactions on Applied Superconductivity*, vol. 31, no. 5, p. 5200706 (6 pages), 2021.
- [182] F. Schreiner, Y. Liu, and M. Noe, “Investigation of a Six-Pole Stator System Using No-Insulation 2nd Generation HTS Coils for a 10 kW Generator Demonstrator,” *IEEE Transactions on Applied Superconductivity*, vol. 31, no. 5, p. 5202405 (5 pages), 2021.
- [183] P. Seidel, *Applied Superconductivity - Handbook on Devices and Applications*. Weinheim, Germany: Wiley-VCH, 2015, vol. 2.
- [184] ———, *Applied Superconductivity - Handbook on Devices and Applications*. Weinheim, Germany: Wiley-VCH, 2015, vol. 1.
- [185] B. Shen, J. Li, J. Geng, L. Fu, X. Zhang, C. Li, H. Zhang, Q. Dong, J. Ma, and T. Coombs, “Investigation and comparison of AC losses on stabilizer-free and copper stabilizer HTS tapes,” *Physica C: Superconductivity and its Applications*, vol. 541, pp. 40–44, 2017.
- [186] Y. Shindo, S. Takano, K. Horiguchi, and T. Sato, “Cryogenic fatigue behavior of plain weave glass/epoxy composite laminates under tension–tension cycling,” *Cryogenics*, vol. 46, no. 11, pp. 794–798, 2006.
- [187] Siemens Energy, Munich, Germany, “Siemens präsentiert eine neue Gleichstrom-netzanbindung für Offshore-Windkraftwerke - Erhöhte Kosteneffizienz bei der Windstromübertragung,” 19.10.2015, protected company presentation.

- [188] N. J. Simon, E. S. Drexler, and R. P. Reed, "Properties of copper and copper alloys at cryogenic temperatures," National Institute of Standards and Technology, Gaithersburg, MD, USA, Tech. Rep. NIST MONO 177, 1992.
- [189] K. Sivasubramaniam, T. Zhang, M. Lokhandwalla, E. T. Laskaris, J. W. Bray, B. Gerstler, M. R. Shah, and J. P. Alexander, "Development of a High Speed HTS Generator for Airborne Applications," *IEEE Transactions on Applied Superconductivity*, vol. 19, no. 3, pp. 1656–1661, 2009.
- [190] J. Smith, "Overview of the development of superconducting synchronous generators," *IEEE Transactions on Magnetics*, vol. 19, no. 3, pp. 522–528, 1983.
- [191] J. Smith, J. Kirtley, and P. Thullen, "Superconducting rotating machines," *IEEE Transactions on Magnetics*, vol. 11, no. 2, pp. 128–134, 1975.
- [192] J. Smith, G. Wilson, J. Kirtley, and T. Keim, "Results from the MIT-EPRI 3-MVA superconducting alternator," *IEEE Transactions on Magnetics*, vol. 13, no. 1, pp. 751–754, 1977.
- [193] G. Snitchler, B. Gamble, and S. Kalsi, "The performance of a 5 MW high temperature superconductor ship propulsion motor," *IEEE Transactions on Applied Superconductivity*, vol. 15, no. 2, pp. 2206–2209, 2005.
- [194] G. Snitchler, B. Gamble, C. King, and P. Winn, "10 MW Class Superconductor Wind Turbine Generators," *IEEE Transactions on Applied Superconductivity*, vol. 21, no. 3, pp. 1089–1092, 2011.
- [195] M. Sommerfeld, M. Dörenkämper, J. De Schutter, and C. Crawford, "Offshore and onshore ground-generation airborne wind energy power curve characterization," *Wind Energy Science Discussions*, vol. 2020, pp. 1–39, 2020. [Online]. Available: <https://wes.copernicus.org/preprints/wes-2020-120/>
- [196] X. Song, C. Bühner, P. Brutsaert, J. Krause, A. Ammar, J. Wiezoreck, J. Hansen, A. V. Rebsdorf, M. Dhalle, A. Bergen, T. Winkler, S. Wessel, M. t. Brake, J. Kellers, H. Pütz, M. Bauer, H. Kyling, H. Boy, and E. Seitz, "Designing and Basic Experimental Validation of the World's First MW-Class Direct-Drive Superconducting Wind Turbine Generator," *IEEE Transactions on Energy Conversion*, vol. 34, no. 4, pp. 2218–2225, 2019.

- [197] X. Song, N. Mijatovic, B. B. Jensen, and J. Holbøll, “Design Study of Fully Superconducting Wind Turbine Generators,” *IEEE Transactions on Applied Superconductivity*, vol. 25, no. 3, p. 5203605 (5 pages), 2015.
- [198] T. D. Strous, X. Wang, H. Polinder, and J. A. B. Ferreira, “Brushless Doubly Fed Induction Machines: Magnetic Field Analysis,” *IEEE Transactions on Magnetics*, vol. 52, no. 11, pp. 1–10, 2016.
- [199] Sumitomo Heavy Industries - Cryogenics Division, *SHI Cryocooler Specification*, Tokio, Japan, 2013, data sheet: model no. SRDK-500B-F70H.
- [200] ———, *SHI Cryocooler Specification*, Tokio, Japan, Aug. 2019, data sheet: SRDK-500B Cold Head: Capacity Map.
- [201] J. Sun, S. Sanz, and H. Neumann, “Conceptual design and thermal analysis of a modular cryostat for one single coil of a 10 MW offshore superconducting wind turbine,” *IOP Conference Series: Materials Science and Engineering*, vol. 101, no. 1, p. 012088 (8 pages), Nov. 2015.
- [202] C. A. Swenson, “Properties of Indium and Thallium at Low Temperatures,” *Phys. Rev.*, vol. 100, pp. 1607–1614, Dec. 1955.
- [203] Tecnalia Research Company, Derio, Spain, SUPRAPOWER project, “SUPRAPOWER: Superconducting, reliable, lightweight, and more powerful offshore wind turbine - Final Report,” pp. 1–92, 2017. [Online]. Available: <https://cordis.europa.eu/docs/results/308/308793/final1-suprapower-final-report-tecnalia-20170922-rev-1.pdf>
- [204] Y. Terao, M. Sekino, and H. Ohsaki, “Electromagnetic Design of 10 MW Class Fully Superconducting Wind Turbine Generators,” *IEEE Transactions on Applied Superconductivity*, vol. 22, no. 3, p. 5201904 (4 pages), 2012.
- [205] THEVA Dünnschichttechnik, “Pro-Line Product Overview,” Ismaning, Germany, April 2022. [Online]. Available: [https://www.theva.de/wp-content/uploads/2022/09/Product\\_Overview\\_2022.pdf](https://www.theva.de/wp-content/uploads/2022/09/Product_Overview_2022.pdf)
- [206] P. Thullen, J. C. Dudley, D. L. Greene, J. L. Smith, and H. H. Woodson, “An Experimental Alternator With A Superconducting Rotating Field Winding,” *IEEE Transactions on Power Apparatus and Systems*, vol. 90, no. 2, pp. 611–619, 1971.



- [207] M. Tomsic, M. Rindfleisch, D. Doll, and M. Sumption, "Potential for superconducting stators to enable all-cryogenic motors and generators for aircraft," in *2019 AIAA Propulsion and Energy Forum, Superconducting/Cryogenic Machines and Power Systems*, Indianapolis, IN, USA, 19.-22. Aug. 2019, oral presentation, 28 slides.
- [208] D. Torrey, "High Efficiency Ultra-Light Superconducting Generator (SCG) for Offshore Wind Program," 2021, project presentation on 05.08.2021 (7 slides) by General Electric Research, *Accessed on:* 13.04.2023. [Online]. Available: <https://www.energy.gov/sites/default/files/2021-10/fy21peerreview-ge-torrey.pdf>
- [209] G. Traxler-Samek, "Zusatzverluste im Stirnraum von Hydrogeneratoren mit Roebelstabwicklung," Ph.D. dissertation, Technische Universität Wien, 2003.
- [210] M. Tropeano and G. Grasso, "MgB<sub>2</sub> development for magnets in medical application," in *Superconductivity and other new Developments in Gantry Design for Particle Therapy*, Zurich, Switzerland, 17.-19. Sept. 2015, oral company presentation, provided by ASG Superconductors.
- [211] K. Umemoto, K. Aizawa, M. Yokoyama, K. Yoshikawa, Y. Kimura, M. Izumi, K. Ohashi, M. Numano, K. Okumura, M. Yamaguchi, Y. Gocho, and E. Kosuge, "Development of 1 MW-class HTS motor for podded ship propulsion system," *Journal of Physics: Conference Series*, vol. 234, no. 3, p. 032060 (7 pages), June 2010.
- [212] United Nations, "Paris Agreement - Paris Climate Change Conference - November 2015," Paris, France, pp. 1–60, Nov. 2018, *Accessed on:* 13.04.2023. [Online]. Available: <https://unfccc.int/documents/184656>
- [213] J. A. Urbahn, R. A. Ackermann, X. Huang, E. T. Laskaris, K. Sivasubramaniam, and A. Steinbach, "The Thermal Performance of a 1.5 MVA HTS Generator," in *Advances in Cryogenic Engineering: Transactions of the Cryogenic Engineering Conference*, vol. 710, no. 1, Anchorage, Alaska, USA, 22.-26. Sept. 2003, pp. 849–858.
- [214] U.S. Department of Energy, "Rare Earth Permanent Magnets - Supply Chain Deep Dive Assessment," Washington, USA, pp. 1–82, Feb. 2022, *Accessed on:* 14.04.2023. [Online]. Available: <https://www.energy.gov/sites/default/files/2022-02/Neodymium%20Magnets%20Supply%20Chain%20Report%20-%20Final.pdf>
- [215] C. R. Vargas-Llanos, F. Huber, N. Riva, M. Zhang, and F. Grilli, "3D homoge-

- nization of the T-A formulation for the analysis of coils with complex geometries,” *Superconductor Science and Technology*, vol. 35, no. 12, p. 124001 (15 pages), Oct. 2022.
- [216] C. R. Vargas-Llanos, S. Lengsfeld, and F. Grilli, “T-A Formulation for the Design and AC Loss Calculation of a Superconducting Generator for a 10 MW Wind Turbine,” *IEEE Access*, vol. 8, pp. 208 767–208 778, 2020.
- [217] C. R. Vargas-Llanos, S. Lengsfeld, M. Noe, T. Arndt, and F. Grilli, “Influence of Coil Position on AC Losses of Stator Superconducting Windings of a Synchronous Machine for a 10 MW Wind Turbine,” *IEEE Transactions on Applied Superconductivity*, vol. 31, no. 7, pp. 1–9, 2021.
- [218] C. R. Vargas-Llanos, V. M. R. Zermeño, S. Sanz, F. Trillaud, and F. Grilli, “Estimation of hysteretic losses for MgB<sub>2</sub> tapes under the operating conditions of a generator,” *Superconductor Science and Technology*, vol. 29, no. 3, p. 034008 (13 pages), Feb. 2016.
- [219] Verein deutscher Ingenieure e.V., *VDI-Wärmeatlas*, 11th ed. Berlin, Heidelberg, Germany: Springer, 2013.
- [220] J. Voccio, B. Gamble, C. Prum, and H. Picard, “125 HP HTS motor field winding development,” *IEEE Transactions on Applied Superconductivity*, vol. 7, no. 2, pp. 519–522, 1997.
- [221] Voestalpine, Linz, Austria, “Data sheet: isovac 470-65A, Electrical Steel, Fully processed,” Jan. 2018. [Online]. Available: [https://www.voestalpine.com/division\\_stahl/content/download/34077/362807/file/DS%20isovac%C2%A9%20470-65%20A.pdf](https://www.voestalpine.com/division_stahl/content/download/34077/362807/file/DS%20isovac%C2%A9%20470-65%20A.pdf)
- [222] F. Weng, M. Zhang, T. Lan, Y. Wang, and W. Yuan, “Fully superconducting machine for electric aircraft propulsion: study of AC loss for HTS stator,” *Superconductor Science and Technology*, vol. 33, no. 10, p. 104002 (10 pages), Aug. 2020.
- [223] C. Wessels and F. W. Fuchs, “Fault ride through of DFIG wind turbines during symmetrical voltage dip with crowbar or stator current feedback solution,” in *2010 IEEE Energy Conversion Congress and Exposition*, Atlanta, GA, USA, 12.-16. Sept. 2010, pp. 2771–2777.

- [224] Westinghouse company, Pittsburgh, PA, USA, “Final report: El-577 project 429 - superconducting generator design,” *EPRI Report*, 1977, Electric Power Research Institute, Palo Alto, CA, USA.
- [225] WindEurope Industry Association, “Wind energy in Europe in 2019 - Trends and statistics,” Brussels, Belgium, pp. 1–24, Feb. 2020, *Accessed on:* 16.04.2023. [Online]. Available: <https://windeurope.org/intelligence-platform/product/wind-energy-in-europe-in-2019-trends-and-statistics>
- [226] —, “Financing and investment trends - The European wind industry in 2021,” Brussels, Belgium, pp. 1–40, April 2022, *Accessed on:* 16.04.2023. [Online]. Available: <https://windeurope.org/intelligence-platform/product/financing-and-investment-trends-2021/>
- [227] T. Winkler, “The EcoSwing Project,” *IOP Conference Series: Materials Science and Engineering*, vol. 502, no. 1, p. 012004 (9 pages), April 2019. [Online]. Available: <https://dx.doi.org/10.1088/1757-899X/502/1/012004>
- [228] H. H. Woodson, Z. J. J. Stekly, and E. Halas, “A Study of Alternators with Superconducting Field Windings: I - Analysis,” *IEEE Transactions on Power Apparatus and Systems*, vol. 85, no. 3, pp. 264–274, 1966.
- [229] World Forum Offshore Wind, BloombergNEF, “Global Offshore Wind Report 2023,” Hamburg, Germany, pp. 1–10, Feb. 2023, *Accessed on:* 16.04.2023. [Online]. Available: [https://wfo-global.org/wp-content/uploads/2023/03/WFO\\_Global-Offshore-Wind-Report-2022.pdf](https://wfo-global.org/wp-content/uploads/2023/03/WFO_Global-Offshore-Wind-Report-2022.pdf)
- [230] Y. Yamada, A. Ibi, H. Fukushima, K. Takahashi, S. Miyata, R. Kuriki, H. Kobayashi, M. Konishi, T. Kato, T. Hirayama, and Y. Shiohara, “GdBaCuO and YBaCuO Long Coated Conductors by IBAD-PLD Method—Enhancement of Production Speed and Critical Current in a Magnetic Field,” *IEEE Transactions on Applied Superconductivity*, vol. 17, no. 2, pp. 3371–3374, 2007.
- [231] K. Yamaguchi, Y. Matsunobu, N. Tada, Y. Yagi, and R. Shiobara, “Development of superconductors for a 70 MW class superconducting generator,” *IEEE Transactions on Magnetics*, vol. 27, no. 2, pp. 2399–2402, 1991.
- [232] K. Yamaguchi, M. Takahashi, R. Shiobara, T. Taniguchi, H. Tomeoku, M. Sato,

- H. Sato, Y. Chida, M. Ogihara, R. Takahashi, and H. Kusafuka, “70 MW class superconducting generator test,” *IEEE Transactions on Applied Superconductivity*, vol. 9, no. 2, pp. 1209–1212, 1999.
- [233] T. Yanamoto, M. Izumi, M. Yokoyama, and K. Umamoto, “Electric Propulsion Motor Development for Commercial Ships in Japan,” *Proceedings of the IEEE*, vol. 103, no. 12, pp. 2333–2343, 2015.
- [234] Y. Yang, S. Duan, Y. Ren, Y. Jiang, L. Feng, X. Zhang, H. Chai, M. Kuang, J. Wu, X. Yang, and Y. Zhao, “Design and Development of a Cryogen-Free Superconducting Prototype Generator With YBCO Field Windings,” *IEEE Transactions on Applied Superconductivity*, vol. 26, no. 4, pp. 1–5, 2016.
- [235] T. D. Yensen, “Magnetic and electrical properties of iron-nickel alloys,” *Transactions of the American Institute of Electrical Engineers*, vol. 39, no. 1, pp. 791–822, 1920.
- [236] S. You, M. Staines, G. Sidorov, D. Miyagi, R. A. Badcock, N. J. Long, and Z. Jiang, “AC loss measurement and simulation in a REBCO coil assembly utilising low-loss magnetic flux diverters,” *Superconductor Science and Technology*, vol. 33, no. 11, p. 115011 (11 pages), Sept. 2020.
- [237] R. Zeichfüßl, A. Jöckel, M. Deicke, D. Daners, and C. Fox, “Integrated 3-Stage Planetary Gearbox With Oil-Cooled Generator,” 2020, product presentation by Flender / winergy, Ruhstorf a.d. Rott, Germany.
- [238] H. Zhang, M. Zhang, and W. Yuan, “An efficient 3D finite element method model based on the T–A formulation for superconducting coated conductors,” *Superconductor Science and Technology*, vol. 30, no. 2, p. 024005 (7 pages), Dec. 2016.

---

## Own Publications

- [O1] R. Köster, “Redundant gespeister PMSM-Windgenerator mit Zahnspulenwicklung (engl.: Wind Turbine Generator with Intermittent Feeding and Tooth Wound Coils),” Master’s thesis, Technical University of Darmstadt, 2018.
- [O2] N. Erd, R. Köster, and A. Binder, “Computational Analysis of Air Gap Field in Electrical Machines by Fourier Coefficient Matrices,” in *2020 International Conference on Electrical Machines (ICEM)*, Online Conference (Gothenburg, Sweden), 23.-28. Aug. 2020, pp. 2479–2485.
- [O3] R. Köster and A. Binder, “Damper design in superconducting wind turbine generators by analytical and numerical models,” in *12<sup>th</sup> International Symposium on Electric and Magnetic Fields*, no. 107, Online Conference, 06.-08. July 2021, oral presentation, 15 slides.
- [O4] R. Köster and A. Binder, “Cost-Oriented Design Considerations on Direct-Drive Wind Turbine Generators with Superconducting Excitation Winding,” in *2021 International Conference on Optimization of Electrical and Electronic Equipment (OPTIM)*, Online Conference, 02.-03. Sept. 2021, pp. 115–122.
- [O5] R. Köster and A. Binder, “Multi-Objective Optimisation of a Direct-Drive Wind Turbine Generator with HTS Excitation Winding,” in *15<sup>th</sup> European Conference on Applied Superconductivity (EUCAS)*, no. 581, Online Conference, 05.-09. Sept. 2021, (13 slides).
- [O6] R. Köster, B. Deusinger, and A. Binder, “Export of Uncompressed JMAG Field Solution Data for Custom Post-Processing and Visualization,” in *2021 JMAG & PSIM Users Conference*, Online Conference, 27. Sept. - 01.Oct. 2021, (17 slides).
- [O7] R. Köster and A. Binder, “Multi-Objective Optimization of a Direct-Drive Wind

- Turbine Generator With HTS Excitation Winding,” *IEEE Transactions on Applied Superconductivity*, vol. 32, no. 4, p. 5200508 (8 pages), 2022.
- [O08] R. Köster and A. Binder, “Keynote: Trends in E-Machines Using Superconductors,” in *2022 International Symposium on Power Electronics, Electrical Drives, Automation and Motion (SPEEDAM)*, Sorrento, Italy, 2022, pp. 448–450.
- [O09] R. Köster and A. Binder, “Electromagnetic Design Considerations on HTS Excited Homopolar Inductor Alternators,” in *2022 International Symposium on Power Electronics, Electrical Drives, Automation and Motion (SPEEDAM)*, Sorrento, Italy, 22.-24. June 2022, pp. 479–484.
- [O10] R. Köster and A. Binder, “Medium-Speed Wind Turbine Generators with HTS Excitation Winding,” in *2022 International Conference on Electrical Machines (ICEM)*, Valencia, Spain, 05.-08. Sept. 2022, pp. 914–920.
- [O11] R. Köster and A. Binder, “Optimum 7 MW HTS direct-drive wind turbine synchronous generator designs with different rotor and stator iron topologies,” *e & i Elektrotechnik und Informationstechnik*, vol. 140, no. 2, pp. 324–337, April 2023.
- [O12] R. Köster and A. Binder, “Eddy current loss estimation for direct drive wind turbine generators with superconducting excitation winding by numerical and analytical models,” *International Journal of Numerical Modelling: Electronic Networks, Devices and Fields*, vol. 36, no. 3, p. e3066 (13 pages), 2023.
- [O13] R. Köster and A. Binder, “Optimum 7 MW HTS Direct-Drive Wind Turbine Synchronous Generator Designs,” in *mOre drive symposium of OVE*, Vienna, Austria, 26.-27. April 2023, (20 slides).
- [O14] R. Köster, “Technical Report: Analytical, Rotationally Symmetric Multi-Layer Model for the Electromagnetic Calculation of Fully Superconducting Wind Generators,” Institute for Electrical Energy Conversion, Technical University Darmstadt, Darmstadt, Germany, Technical Report, 2023.
- [O15] R. Köster, “Technical Report: Selected Fieldnumerical Formulations for Electromagnetics,” Institute for Electrical Energy Conversion, Technical University Darmstadt, Darmstadt, Germany, Technical Report, 2023.
- [O16] R. Köster and A. Binder, “Electromagnetic Simulation of a 6-Phase HTS Excited

- Medium Speed Wind Generator,” in *13th International Symposium on Electric and Magnetic Fields (EMF)*, Marseille, France, 29.-31. Aug. 2023, (*accepted*).
- [O17] R. Köster and A. Binder, “Parametric Design Study on 7 MW Fully Superconducting HTS Direct-Drive Wind Turbine Generators,” in *16<sup>th</sup> European Conference on Applied Superconductivity (EUCAS)*, Bologna, Italy, 3.-7. Sept. 2023, (*accepted*).
- [O18] R. Köster and A. Binder, “Performance Analysis of a HTS Excited 5 MW Medium-Speed Wind Turbine Generator with Passive Rectifier Considering Stator Current Harmonics,” in *16<sup>th</sup> European Conference on Applied Superconductivity (EUCAS)*, Bologna, Italy, 3.-7. Sept. 2023, (*accepted*).

---

# Supervised Student Theses and Seminar Topics

- [S1] S. Koch, “Konzeptionelle Untersuchung zur Kühlung der E-Maschine/n eines LKWs mit seriellem Antriebsstrang mittels kryogenem Treibstoff ohne supraleitende Materialien (engl.: Conceptual Analysis of the Cryogenic Cooling of Non-Superconducting Electrical Traction Motors in Trucks with Series Drivetrain),” Master’s thesis, Technical University of Darmstadt, 2021.
- [S2] J. Bergmann, “Optimierungsmöglichkeiten für Leistungsdichte und Wirkungsgrad von elektrischen Maschinen für elektrisches Fliegen (engl.: Approaches for Increasing the Power Density and the Efficiency of Electrical Machines for Electrical Aircrafts),” Literature Pro-Seminary, Technical University of Darmstadt, 2021.
- [S3] D. Leißner, “Zweidimensionale Wirbelstromberechnung in massiven Läuferpolen von Synchronmaschinen (engl.: Two-dimensional Eddy Current Calculation for Synchronous Machines with Massiv Rotor Poles),” Bachelor’s Thesis, Technical University of Darmstadt, 2021.
- [S4] A. Wirth, “Elektromagnetische Auslegung eines direktangetriebenen Synchrongenerators mit supraleitender  $MgB_2$ -Erreger-Wicklung für den Einsatz in einer Windkraftanlage (engl.: Electromagnetic Design of a Direct-Drive Wind Turbine Synchronous Generator with Superconducting  $MgB_2$  Excitation Winding),” Bachelor’s Thesis, Technical University of Darmstadt, 2021.
- [S5] L. Diessner, “The Road to an All Electric Aircraft - Markets and Technologies,” Literature Pro-Seminary, Technical University of Darmstadt, 2022.
- [S6] J. Bergmann, “Elektromagnetische Auslegung eines supraleitenden Homopolargenerators für elektrisches Fliegen (engl.: Electromagnetic Design of a Super-



- conducting Homopolar Inductor Alternator for Electric Aviation),” Bachelor’s Thesis, Technical University of Darmstadt, 2022.
- [S7] T. Foißner, “AC Losses in Type-II-Superconductors,” Literature Pro-Seminary, Technical University of Darmstadt, 2022.
- [S8] B. Sommer, “Elektromagnetische Auslegung eines supraleitend erregten Medium-Speed- Generators für den Betrieb mit Dioden-Gleichrichter (engl.: Electromagnetic Design of a Medium-Speed-Generator with Superconducting Excitation Winding for Operation with a Diode Rectifier),” Master’s thesis, Technical University of Darmstadt, 2022.
- [S9] D. Fabrig, “Auslegung und thermische Modellierung der Warm-Kalt-Abstützung im Rotor eines HTS-Windgenerators mit supraleitender Erregerwicklung und kaltem Rotoreisen (engl.: Design and Modelling of the Warm-Cold-Support in a HTS Excited Wind Turbine Generator),” Bachelor’s Thesis, Technical University of Darmstadt, 2022.
- [S10] T. Foißner, “Untersuchung von Wirbelstromverlusten und Drehmoment-Welligkeit in direktangetriebenen HTS-Windgeneratoren bei abschnittsweiser Speisung der Statorwicklung (engl.: Analysis of Eddy Current Losses and Torque Ripple in Direct Drive HTS Wind Turbine Generators at Intermittent Feeding of the Stator Winding),” Bachelor’s Thesis, Technical University of Darmstadt, 2022.
- [S11] S. Schumm, “Elektromagnetische Auslegung eines vollsupraleitenden, direktangetriebenen 7 MW-Windgenerators (engl.: Electromagnetic Design of a Fully Superconducting Direct-Drive 7 MW Wind Turbine Generator),” Master’s thesis, Technical University of Darmstadt, 2022.
- [S12] L. Diessner, “Konzeption und thermische Simulation einer Vorrichtung zur Vermessung von Hochtemperatur- Supraleiter-Tapes in Flüssigstickstoff (engl.: Design and thermal simulation of a test setup for critical current measurements of high temperature superconducting tapes in liquid nitrogen),” Bachelor’s Thesis, Technical University of Darmstadt, May 2023.



---

## A. Appendix

### A.1. Grid Connection Topologies for Wind Turbine Systems

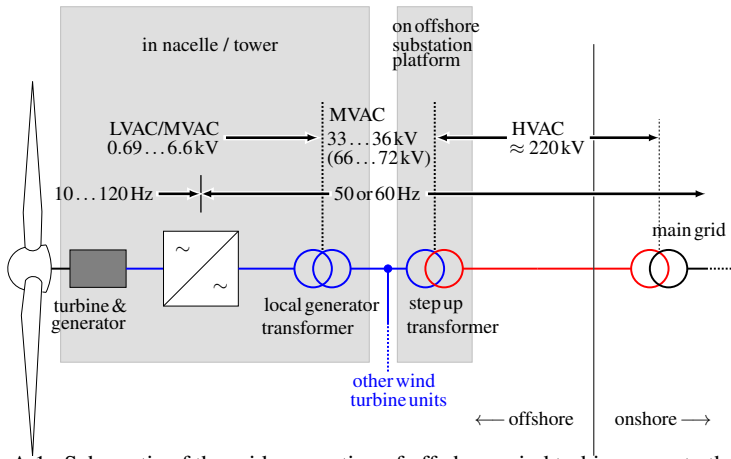


Figure A.1.: Schematic of the grid connection of off-shore wind turbines near to the coast.

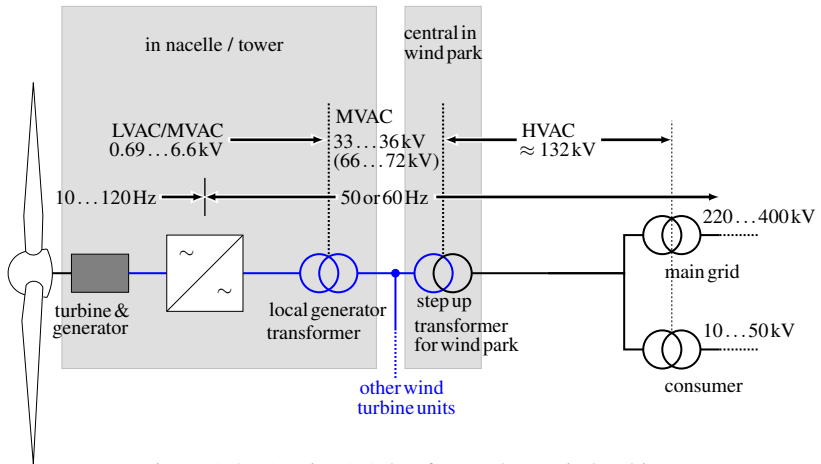


Figure A.2.: As Fig. A.1, but for on-shore wind turbines.

## A.2. Overview of Superconducting Machine Projects

Table A.1.: Summary of early projects on LTSC generators with built demonstrators. Other projects focused on LTSC machines for military applications [70, 147] with differing rotational speeds. An additional overview can be found in [127].

year	power	speed	conductor	cooling	developer	references
1971	80kVA	3600 rpm	NbTi	LHe	<i>MIT</i>	[228, 206]
1972	3MVA	3600 rpm	NbTi	LHe	<i>MIT</i>	[117, 118, 192]
1972	5MVA	3600 rpm	NbTi	LHe	<i>Westinghouse</i>	[36]
1978	20MVA	3600 rpm	NbTi	LHe	<i>GE</i>	[112, 62, 129]
1985	30MVA	3600 rpm	NbTi	LHe	<i>Mitsubishi, Fuji Electric</i>	[157]
1987	50MVA	3600 rpm	NbTi	LHe	<i>Hitachi</i>	[145]
1985	300MVA	3000 rpm	NbTi	LHe	<i>Electrosila Leningrad</i>	[64]
	(rotor tested)					
1985	300MVA	3600 rpm	NbTi	LHe	<i>Westinghouse / EPRI</i>	[224]
	(rotor tested)					
1985	400MVA/ 800MVA	3000 rpm	NbTi	LHe	<i>Siemens</i>	[126, 93, 128]
	(rotor tested)					
1996	83MVA	3600 rpm	NbTi	LHe	<i>Hitachi, SuperGM</i>	[232, 231]
1966-1972	several homopolar DC machine projects with LTSC field coils and power up to 3 MW				England, US, France, Japan	summarized in [191]
1965-1985	other synchronous machine projects with LTSC field winding, powers up to 20 MVA				i.e. Germ., US, Japan, USSR	summarized in [191, 190]

Table A.2.: Overview of built / tested superconducting machines employing 1G HTS windings. Extensive overviews are given in [69], [80] and [103].

year	power	speed	conductor	cooling	developer	ref.
1995	3.7 kW	1800 rpm	Bi-2223	81 K / liquid N	<i>Reliance El.</i>	[99]
1997	95 kW	1800 rpm	Bi-2223	27 K / Ne	<i>Reliance El.</i>	[220]
2002	380 kW	1500 rpm	Bi-2223	25...30 K / Ne	<i>Siemens</i>	[159]
2004	100 kVA	3000 rpm	Bi-2223	65 K / liquid N	<i>University of Southampton</i>	[6, 5]
2004	1.5 MVA	3600 rpm	Bi-2223	30...40 K / He	<i>GE</i>	[213, 72]
2007	4 MVA	3600 rpm	Bi-2223	25...30 K / Ne-thermosiphon	<i>Siemens</i>	[67, 160]
2005	5 MW	230 rpm	Bi-2223	$\leq 32$ K / He gas	<i>AMSC / Alstom</i>	[193, 54]
2006	8 MVA	1800 rpm	Bi-2223	35...40 K	<i>AMSC (SuperVAR)</i>	[101, 106, 102]
2008	36.5 MW	120 rpm	Bi-2223	$\approx 30$ K / He gas	<i>Northrop Grumman / AMSC</i>	[71, 100, 37]
2012	4 MW	120 rpm	Bi-2223	$\leq 30$ K, Ne	<i>Siemens</i>	[158, 161]
2010	1 MW	190 rpm	Bi-2223	30 K / He gas	<i>Kawasaki Heavy Ind.</i>	[211, 121]
2010	1.7 MW	214 rpm	Bi-2223	30 K / He gas	<i>GE / Converteam</i>	[61]
2013	3 MW	160 rpm	Bi-2223	30 K / He gas	<i>Kawasaki Heavy Ind.</i>	[233]
2014	2.5 kW	300 rpm	Bi-2223	82 K / conduction cooling	<i>Tsinghua University</i>	[174]
(HTS armature winding, PM excitation)						
2009	1.3 MW	10500 rpm	Bi-2223	30 K / Ne	<i>GE</i>	[189]
(homopolar topology with stationary field winding)						

## A.2. Overview of Superconducting Machine Projects

Table A.3.: Overview of projects on superconducting machines with 2G HTS windings. Complete demonstrators and tests of critical components are listed. An overview on recent fields of application can be found in [80].

year	power	speed	conductor	cooling	developer	ref.
2009	7.5 kW	360 rpm	GdBCO	40 K / He gas	<i>Fuji Electric / Fujikura</i>	[95]
2013	50 kW	300 rpm	YBCO	77 K / liquid N	<i>Moscow Aviation Inst.</i>	[48]
2015	10 kW	600 rpm	YBCO	30 K / liquid Ne	<i>Changwon Nat. Univ. / SuNaM</i>	[114]
2015	1 MVA	15 rpm	YBCO	77 K / liquid N	<i>Moscow Aviation Inst.</i>	[123, 122]
2016	5 MW	213 rpm	YBCO	27 K / liquid Ne	<i>Changwon Nat. Univ.</i>	[152, 153]
2017	200 kW	1500 rpm	YBCO	77 K / liquid N	<i>Moscow Aviation Inst</i>	[49]
2018	(load test only up to 200 kW) 3.6 MW	15 rpm	GdBCO	$\leq 30$ K / conduction	<i>EcoSwing consortium</i>	[196, 20]
2021	1 kW (fully superconducting)	500 rpm	EuBCO	65 K / liquid N	<i>Kyushu Univ.</i>	[181]
2011	10 MW	-	YBCO	30 K, conduction	<i>AMSC</i>	[194]
2016	(testing of single rotor pole) 10 MW	-	MgB <sub>2</sub>	20 K, conduction	<i>SUPRAPOWER consortium</i>	[179, 201]
2021	(testing of single rotor pole) 10 MW	-	GdBCO	35 K	<i>Changwon Nat. Univ.</i>	[115]
2016	(testing of single rotor pole) -	30 rpm	YBCO	30 K, conduction	<i>Dongfang El. Corp.</i>	[234]
2021	(no-load tested only) 10 kW	-	GdBCO	77 K / liquid N	<i>KIT</i>	[182]

## A.3. Material Data

### A.3.1. Material Data of Ferromagnetic Materials

The  $B(H)$ -relation of ferromagnetic materials is fitted with (A.1). This relation is also used for the extrapolation beyond available material data.

$$B(H) = B_0 \cdot \left( 1 - \exp \left\{ - \left( \frac{H}{H_1} \right)^{\beta_1} \right\} \right) \cdot \left( 1 - \exp \left\{ - \left( \frac{H}{H_2} \right)^{\beta_2} \right\} \right) + \mu_0 \cdot H \quad (\text{A.1})$$

#### A.3.1.1. Iron-Nickel Alloy FeNi9

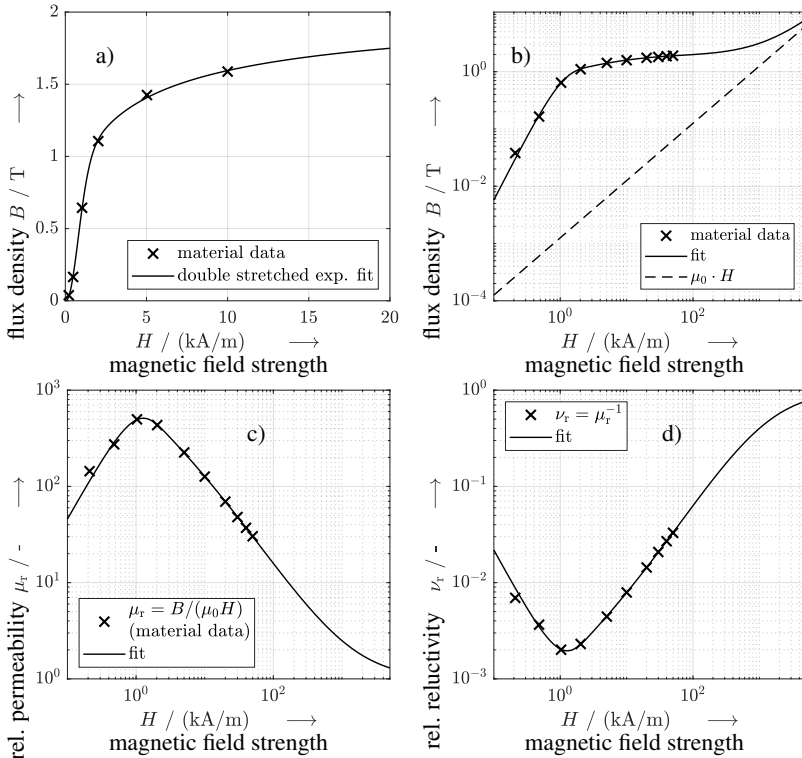


Figure A.3.: Magnetization characteristic of FeNi9 at  $T = 30\text{K}$ : a) initial  $B(H)$ -relation, b) double logarithmic plot of  $B(H)$  and extrapolation to higher flux densities with a double stretched exponential fit function, c) relative permeability, d) reluctivity [196].

A.3.1.2. Lamination Steel

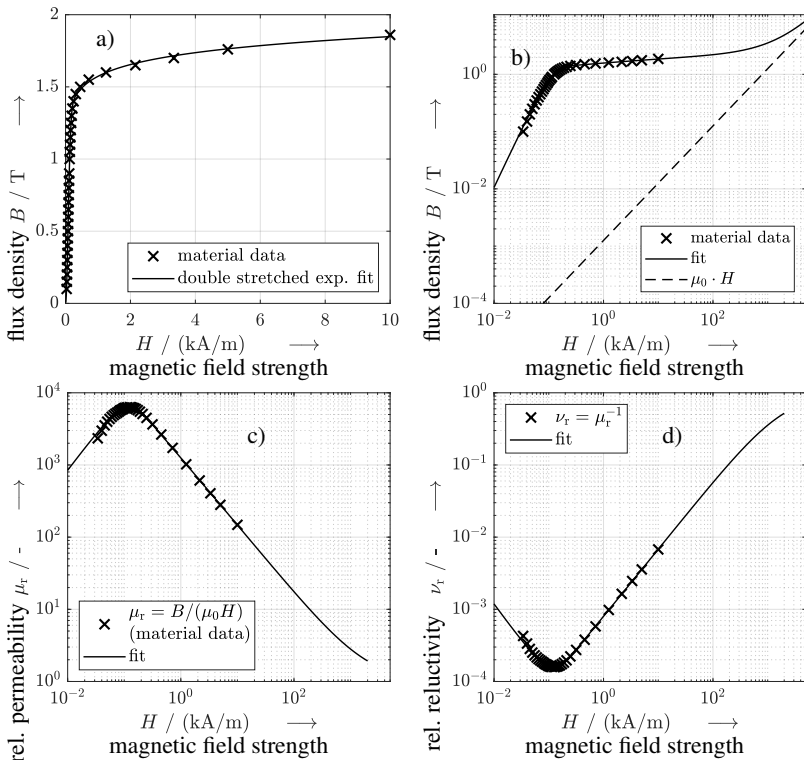


Figure A.4.: Magnetization characteristic of M470-65A electrical steel at room temperature ( $T = 300\text{K}$ ): a) initial  $B(H)$ -relation, b) double logarithmic plot of  $B(H)$  and extrapolation to higher flux densities with a double stretched exponential fit function, c) relative permeability, d) reluctivity [221].



## A.3.1.3. Nickel

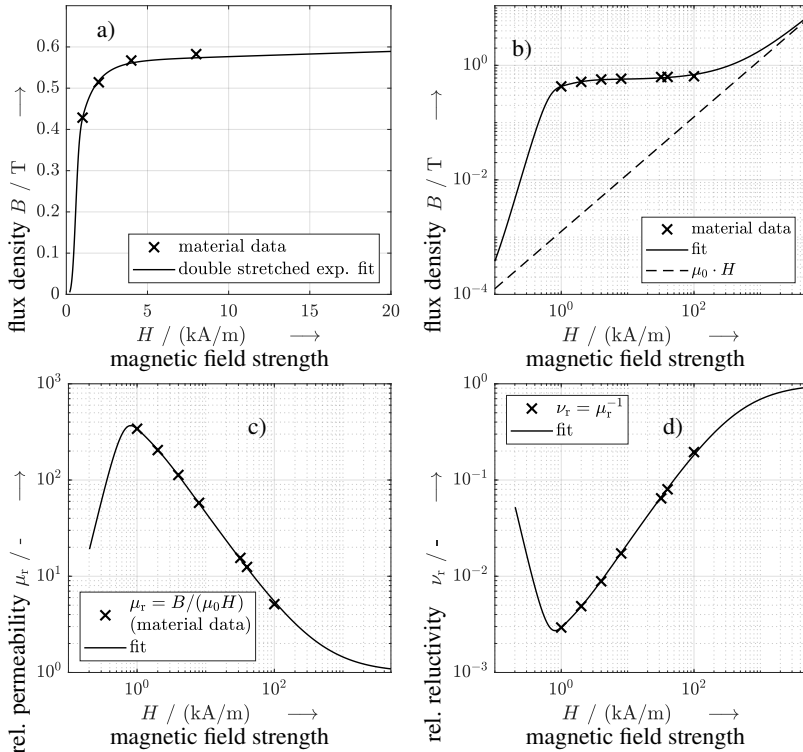


Figure A.5.: Magnetization characteristic of nickel at  $T = 300\text{K}$ : a) initial  $B(H)$ -relation, b) double logarithmic plot of  $B(H)$  and extrapolation to higher flux densities with a double stretched exponential fit function, c) relative permeability, d) reluctivity [218], weak temperature dependence reported.

A.3.1.4. Magnetic Slot Wedges

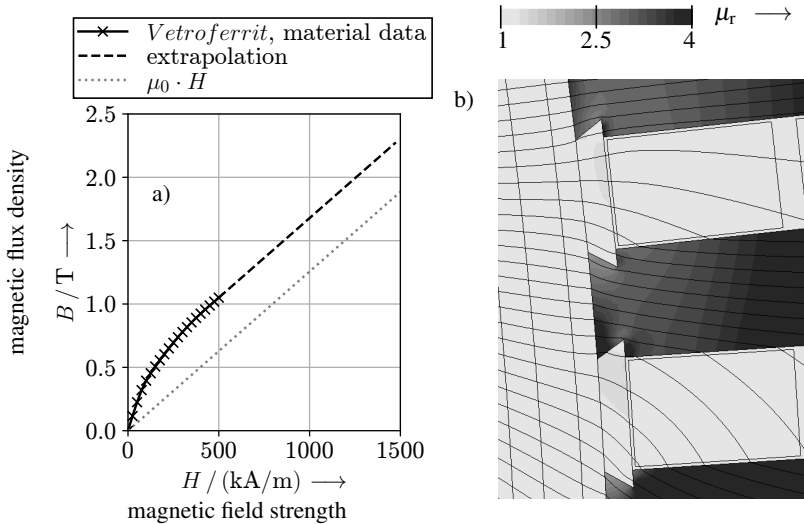


Figure A.6.: a)  $B(H)$ -relation of the considered material of the magnetic slot wedges [47], b) Numerically calculated magnetic field lines and relative permeability in the slot opening region (software: *JMAG*).

A.3.2. Material Properties of Permanent Magnets

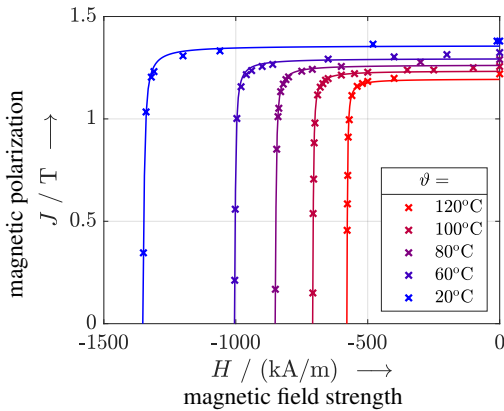


Figure A.7.: Magnet polarization versus demagnetization field for NdFeB permanent magnets of grade G44EH (*Arnold Magnetic Technologies*) [8].

### A.3.3. Thermal Material Properties

#### A.3.3.1. Thermal Conductivity of Copper

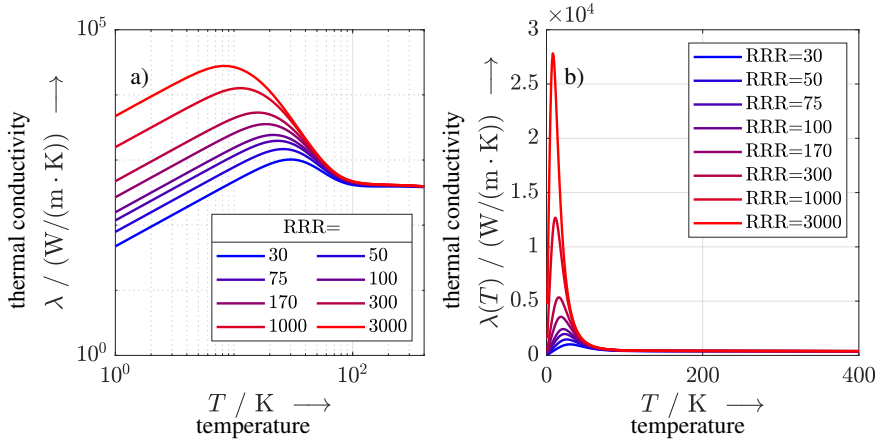


Figure A.8.: Thermal conductivity versus temperature for different values of the RRR: a) double logarithmic and b) linear plot [188].

#### A.3.3.2. Thermal Conductivity of G-10CR

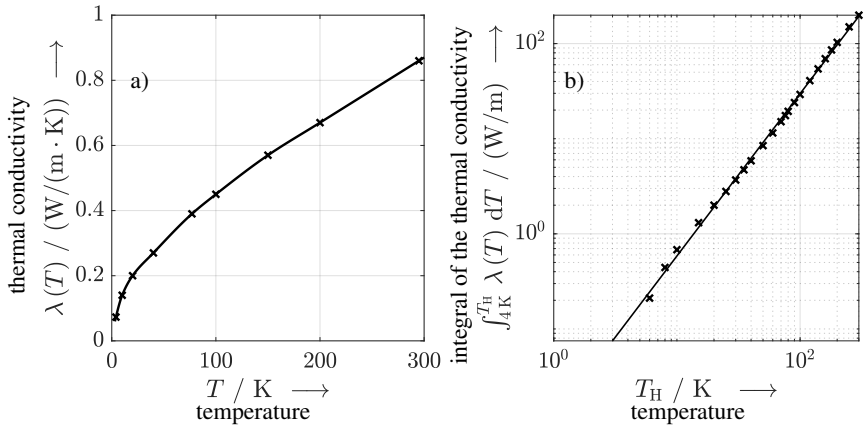


Figure A.9.: a) Thermal conductivity and b) integral of the thermal conductivity of G-10CR (warp) versus temperature [56].

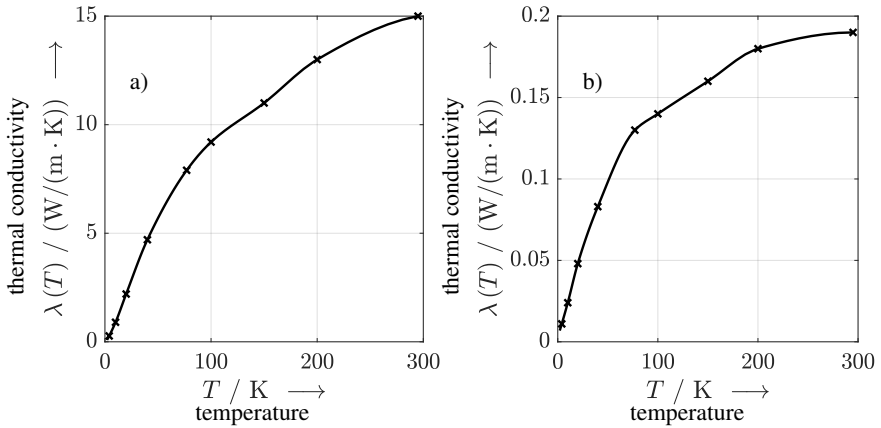


Figure A.10.: Thermal conductivity of a) stainless steel, i.e. AISI 304, 316, and b) *Kapton* versus temperature [56].

### A.3.4. Electrical Material Properties

#### A.3.4.1. Copper

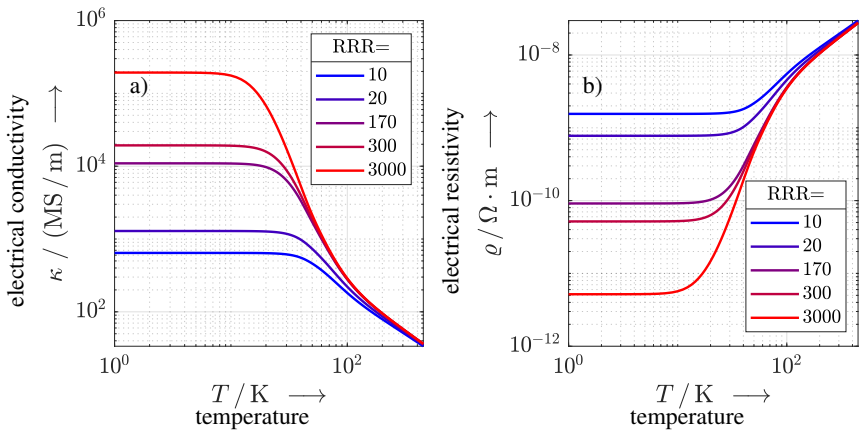


Figure A.11.: a) Electrical conductivity and b) electrical resistivity of copper versus temperature for different values of the RRR [188].

## A.3.4.2. Indium

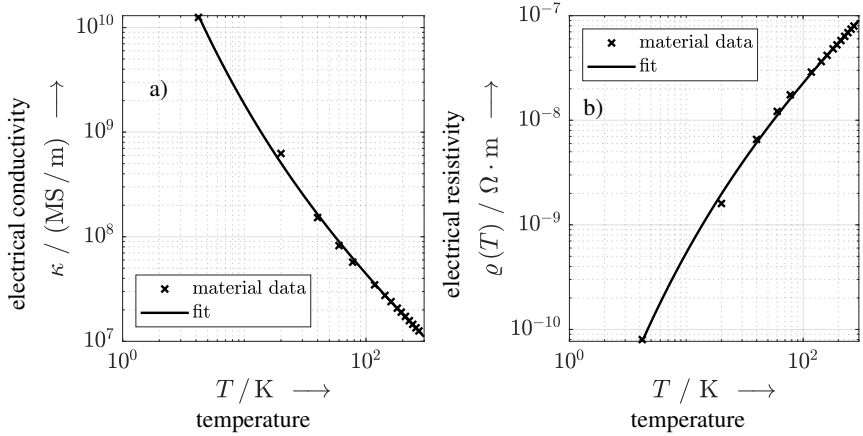


Figure A.12.: a) Electrical conductivity and b) electrical resistivity of indium versus temperature [202].

**A.3.4.3. Iron Nickel Alloys**

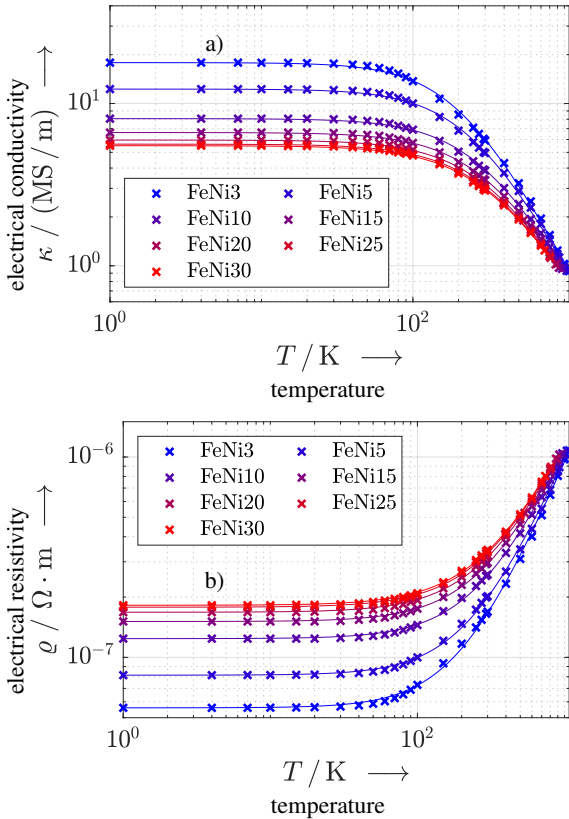


Figure A.13.: a) Electrical conductivity and b) electrical resistivity of different nickel-iron alloys [235].

**A.3.5. Alternative Parametrization of the Lift Factor of ReBCO Coated Conductors**

The modelling equation for  $I_c$  as a function of  $T$ ,  $B$  and the field orientation  $\theta$  is determined by a three-step fitting procedure. The first step consists in an approximation of the  $T$ -dependence according to (A.2), independently for several flux densities  $B$  that are oriented parallel to the  $c$ -axis.

$$\log_{10}(I_c(T)) = \log_{10}(I_{c0}) \cdot \exp \left\{ - \left( \frac{T}{a+b \cdot T} \right)^\gamma \right\} \quad (\text{A.2})$$

The parameters  $I_{c0}$ ,  $a$  and  $b$  are subsequently fitted as functions of the absolute value of the flux density  $B$  by the stretched exponentials (A.3) to (A.5).

$$\log_{10}(I_{c0}(B)) = \log_{10}(I_{c0}) \cdot \exp \left\{ - \left( \frac{B}{B_0} \right)^{\alpha_1} \right\} \quad (\text{A.3})$$

$$a(B) = a(B=0) \cdot \exp \left\{ - \left( \frac{B}{B_1} \right)^{\alpha_2} \right\} \quad (\text{A.4})$$

$$b(B) = b(B=0) \cdot \exp \left\{ - \left( \frac{B}{B_2} \right)^{\alpha_3} \right\} \quad (\text{A.5})$$

A good agreement with the considered data is achieved with a field-independent exponent  $\gamma$  in (A.2).

The dependence of  $I_c$  on the orientation  $\theta$  of the external field with respect to the normal of the tape's wide side is suitably described by the lift factor (A.6) with  $\theta^* = \theta_0 + \pi/2$ . The critical current for a given orientation  $\theta$  is then expressed as  $I_c(T, B, \theta) = I_c(T, B, \theta_0) \cdot L(T, \theta) / L(T, \theta_0)$  with the orientation angle  $\theta_0$  of the  $c$ -axis.

$$L(\theta) = a_1 \cdot \frac{1}{1 + a_2 \cdot |\sin(\theta - \theta^*)|^{a_3}} + a_4 \quad (\text{A.6})$$

The fit parameters in (A.6) are considered to be temperature dependent, (A.7).

$$\begin{aligned} a_1(T) &= c_1 + d_1 \cdot T & a_2(T) &= c_2 + d_2 \cdot T^{e_2} \\ a_3(T) &= c_3 + d_3 \cdot T & a_4(T) &= c_4 + d_4 \cdot T \end{aligned} \quad (\text{A.7})$$

## A.4. Analytical Models

### A.4.1. Derivation of Current Loading Spectra

#### Current Loading of the Field Winding

The rectangle-shaped coil cross sections are approximated by a set of current loadings at a set of radii covering the coil side's radial height. In circumferential direction (coordinate  $\varphi$ ), the current loading is described by rectangular functions, Fig. A.14.

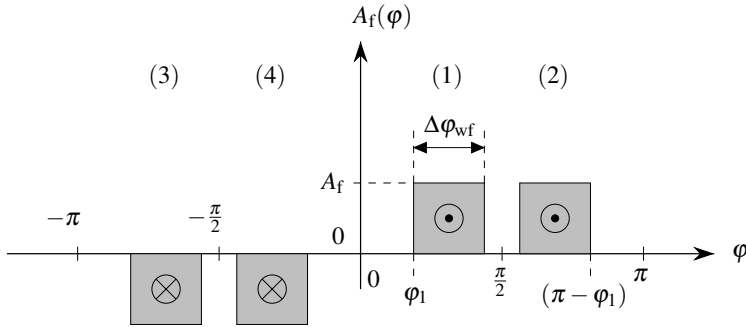


Figure A.14.: Schematic of the rotor current loading, representing the field winding for one pole pair. The  $d$ -axis is located at  $\varphi = 0$ .

The complex coefficients of the one dimensional *Fourier* series are calculated from (A.8) with relative space orders  $v'$ .

$$\underline{A}_{v'} = \frac{1}{2\pi} \cdot \int_{-\pi}^{\pi} A_f(\varphi) \cdot e^{-jv'\varphi} d\varphi \quad (\text{A.8})$$

For simplicity, only one coil side with extension from  $\varphi_1$  to  $\varphi_1 + \Delta\varphi_{wf}$  is considered first, (A.9).

$$\underline{A}_{v'}^{(1)} = \frac{1}{2\pi} \cdot \int_{\varphi_1}^{\varphi_1 + \Delta\varphi_{wf}} A_f(\varphi) \cdot e^{-jv'\varphi} d\varphi \quad (\text{A.9})$$

$$= \frac{A_f}{2\pi} \cdot \frac{j e^{-jv'\varphi}}{v'} \Big|_{\varphi_1}^{\varphi_1 + \Delta\varphi_{wf}} = \frac{j A_f}{2\pi \cdot v'} \cdot \left[ e^{-jv' \cdot (\varphi_1 + \Delta\varphi_{wf})} + e^{-jv' \cdot \varphi_1} \right] \quad (\text{A.10})$$

$$= \frac{A_f}{\pi \cdot v'} \cdot e^{-jv' \cdot \overbrace{\left( \varphi_1 + \frac{\Delta\varphi_{wf}}{2} \right)}^{=\bar{\varphi}_1}} \cdot \underbrace{\frac{1}{2j} \cdot \left[ e^{jv' \cdot \frac{\Delta\varphi_{wf}}{2}} - e^{-jv' \cdot \frac{\Delta\varphi_{wf}}{2}} \right]}_{=\sin\left(\frac{v' \cdot \Delta\varphi_{wf}}{2}\right)} \quad (\text{A.11})$$

$$= \frac{A_f}{\pi \cdot v'} \cdot \sin\left(\frac{v' \cdot \Delta\varphi_{wf}}{2}\right) \cdot e^{-j\bar{\varphi}_1} \quad (\text{A.12})$$

Here,  $\bar{\varphi}_1$  is the middle position of the considered coil side and the sin-factor accounts for



the finite width. Similar expressions are obtained for the other three coil sides per basic winding scheme. The *Fourier* coefficients are obtained by summing up, (A.13).

$$\underline{A}_{v'}^{(f)} = \frac{A_f}{\pi \cdot v'} \cdot \sin\left(\frac{v' \cdot \Delta\varphi_{wf}}{2}\right) \cdot \left[ e^{-jv'\bar{\varphi}_1} + e^{-jv'\bar{\varphi}_2} - e^{-jv'\bar{\varphi}_3} - e^{-jv'\bar{\varphi}_4} \right] \quad (\text{A.13})$$

With the MMF per coil side  $\Theta_{f,p} = N_{f,p} \cdot I_f$ , the peak value of the  $i^{\text{th}}$  current loading at radius  $r_i$  is calculated from (A.14) in the planar approximation.

$$A_f^{(i)} = \frac{\Theta_{f,p}}{w_f} \approx \frac{\Theta_{f,p}}{r_i \cdot \Delta\varphi_{wf}} \quad (\text{A.14})$$

### Current Loading of the Stator Winding

The general calculation scheme is the same as for the rotor field winding, where the contributions of coil sides are characterized by a width factor and its middle position  $\bar{\varphi}$ . The major difference consists in the variation of  $A_s$  in time, due to the AC current.

#### A.4.2. Derivation of the Transformation Relation for Time Orders

The complex 2D *Fourier* transform with respect to the circumferential coordinate  $\varphi$  (polar angle in mechanical degrees) and time  $t$  of any periodic quantity  $f(\varphi, t)$ , as seen in the reference frame of a layer  $\tilde{n}$ , is (A.15).

$$f(\varphi, t) = \sum_{k=-\infty}^{\infty} \sum_{v=-\infty}^{\infty} \underline{f}_{v,k} \cdot e^{j(v\varphi + k^{(\tilde{n})}\omega_s t)} \quad (\text{A.15})$$

The angular speed of the spectral component with orders  $\{v, k^{(\tilde{n})}\}$  is determined by requiring a constant phase in (A.15), (A.16).

$$d_t \left( v\varphi + k^{(\tilde{n})}\omega_s t \right) \stackrel{!}{=} 0 \quad \Rightarrow \quad \Omega_v^{(\tilde{n})} = \dot{\varphi} = -\frac{k^{(\tilde{n})}}{v} \cdot \omega_s \quad (\text{A.16})$$

In a layer  $n$ , featuring a relative movement with respect to the reference layer  $\tilde{n}$ , the effective time order  $k^{(n)}$  is obtained by the *Galilean* transformation for non-relativistic velocities. The angular speed of the moving layer  $n$  with respect to  $\tilde{n}$  is  $\Omega_{\text{layer}}^{(n)}$ . The angular speed, as seen from the moving layer  $n$ , can be expressed as (A.17). In the non-

relativistic case, the wave length  $\lambda_v$  of the considered harmonic is not affected by the transformation.

$$\Omega v^{(n)} = \Omega v^{(\bar{n})} - \Omega_{\text{layer}}^{(n)} \equiv -\frac{k_v^{(n)}}{v} \cdot \omega_s \quad (\text{A.17})$$

Inserting (A.16) in (A.17) and using  $\Omega_{\text{layer}}^{(n)} = 2\pi \cdot n^{(n)}$  yields the transformed time order  $k_v^{(n)}$ , as seen from the moving frame, (A.18).

$$-\frac{k^{(\bar{n})}}{v} \cdot \omega_s - 2\pi \cdot n^{(n)} = -\frac{k_v^{(n)}}{v} \cdot \omega_s \quad \Rightarrow \quad k_v^{(n)} = k^{(\bar{n})} + \frac{2\pi \cdot n^{(n)} \cdot v}{\omega_s} = k^{(\bar{n})} + v \cdot \frac{n^{(n)}}{f_s} \quad (\text{A.18})$$

### A.4.3. Loss Reduction Factor for Eddy Current Losses due to Grooves

The expression from [113] is valid for infinitely deep grooves, which requires in practice a depth that is large compared to the penetration depth.

$\tau$  is the pole pitch of the field harmonic. For sub-harmonics, where  $\lambda/2 > w_p$ , it is reasonable to use  $\tau \approx w_p$ .  $d_E$  is the penetration depth in the pole core material. Here, the frequency in the rotor frame of reference, i.e. rotor time order  $k^{(r)}$ , must be considered, which is generally low for sub-harmonics.  $h$  is the axial width of the teeth between adjacent grooves. For the considered generators, the width of the pole core is in the order of  $w_p \approx 120 \dots 150$  mm. The axial length of the partially superconducting generators is mostly in the order of  $L = 1 \dots 1.5$  m, so that a reasonable distance between e.g. 20 grooves is in the order of  $\Delta L = 45 \dots 70$  mm. This yields a ratio of  $h/\tau \approx 0.3 \dots 0.6$ . The ratio between the axial spacing of the grooves and the penetration depth of about 10 mm is in the order of  $4 \dots 7$ . The loss reduction factors, (A.19) - (A.21), are visualized in Fig. A.15. The relevant range of  $h/d_E$  and  $h/\tau$  yields a loss reduction factor of  $\chi \approx 0.3 \dots 0.5$ .

$$\chi = \frac{P_{d,\text{Ft,gr}}}{P_{d,\text{Ft,orig}}} = \frac{\sqrt{2} \cdot \pi^2}{8} \cdot \frac{\cos \varphi}{|\underline{M}|}, \quad \varphi = \angle \underline{M} \quad (\text{A.19})$$

$$\underline{M} = \frac{\pi}{4} \cdot \left(\frac{h}{\tau}\right)^{-1} \cdot \frac{1+j}{\sqrt{2}} \cdot \tanh\left(\frac{1+j}{\sqrt{2}} \cdot \frac{1}{2} \cdot \frac{h}{d_E}\right) - \underline{\Gamma} \quad (\text{A.20})$$

$$\underline{\Gamma} = \sum_{n=1,3,\dots}^{\infty} \frac{1}{n^2 \cdot \lambda_n^3}, \quad \lambda_n = \sqrt{j + \left(\frac{\pi \cdot h/\tau}{h/d_E}\right)^2 + \left(\frac{n \cdot \pi}{h/d_E}\right)^2} \quad (\text{A.21})$$

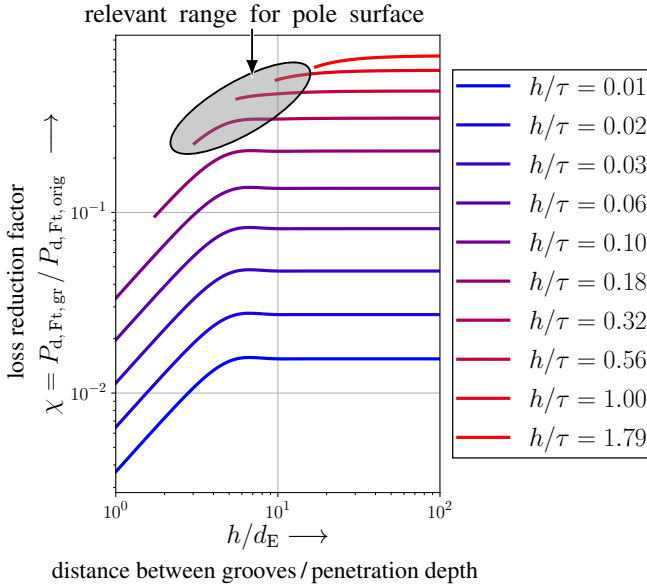


Figure A.15.: Analytically calculated loss reduction factor due to grooves in the pole surface.  $\chi$  is the ratio of the eddy current loss with and without a grooved surface.

## A.5. AC Loss in the Field Winding in Presence of Stator Current Harmonics

Besides the analysed sinusoidal current feeding, the actual stator current features stator current harmonics due to the converter feeding. A complete AC loss study therefore requires a quantification of these harmonics, which depend generally on the applied switching scheme, i.e. a PWM with switching frequency in the range 1...5kHz for wind converters [1]. However, for a general understanding of the criticality of the stator current harmonics regarding the AC loss, a six step operation is considered, where the stator voltage harmonics can approximately be calculated analytically. This switching scheme is regarded as a worst case scenario, such that the calculated AC loss in the field winding represents an upper limit of the actual additional AC loss in case of a PWM switching. The phase voltage harmonics (time order  $k$ ) of star connected generators from line to neutral point are calculated as (A.22) [119].

$$\hat{U}_{s,k} = \frac{2 \cdot U_{DC}}{\pi} \cdot \frac{(-1)^g}{k}, \quad k = 1 + 6 \cdot g, \quad g = 0, \pm 1, \pm 2, \dots \quad (\text{A.22})$$

If in a first approximation, the inductance is considered to be independent from frequency in the considered range, i.e. if inductance limiting screening currents are neglected, the amplitude of the stator current harmonics scales according to (A.23).

$$|\hat{I}_{s,k}| \sim \frac{\hat{U}_{s,k}}{|k|} \sim \frac{1}{k^2} \quad (\text{A.23})$$

The pulsating AC fields have frequency  $f_k = |k|f_s$ , while the main contribution of the AC loss in the field winding is hysteretic in nature. Therefore, the loss scales approximately linearly with frequency and correspondingly with the time order of the current harmonic. The scaling with the applied AC field  $\hat{B}_{\sim,k}$  is also approximately linear. For small superimposed current harmonics, the corresponding AC field has little influence on the iron saturation, so that in a linear approximation the scaling  $\hat{B}_{\sim,k} \sim |\hat{I}_{s,k}|$  is reasonable. The loss contribution for time order  $k$  scales therefore according to (A.24). Largest contributions occur for lowest time orders  $|k| = 5, 7$ .

$$P_{d,AC,k} \sim |k| \cdot |\hat{I}_{s,k}| \sim \frac{1}{|k|} \quad (\text{A.24})$$

Therefore, the AC loss is numerically calculated for fundamental current feeding and superimposed current harmonics of orders  $k = -5, +7$  by means of the 2D FEM model, Fig. A.17 b). The ratio of the current amplitudes are  $\hat{I}_{s,k=-5}/I_{s,1} = 1/5^2 = 1/25$  and  $\hat{I}_{s,k=+7}/I_{s,1} = 1/7^2 = 1/49$ . In presence of these current harmonics, the AC loss in the field winding is still very low, Tab. 4.15. The instantaneous loss power and the layer- and region-resolved average loss are shown in Fig. A.16. In order to elaborate on the critical order of magnitude of current harmonics regarding substantial additional AC loss, a hypothetical scaling of the current harmonics' amplitudes by a factor  $s > 1$  is considered. The numerically calculated AC loss for  $s = 1 \dots 10$  is summarized in Tab. 4.15 and visualized in Fig. A.17 a). Even for five times the current harmonics in six-step mode, low loss values  $P_{d,AC,f} < 10 \text{ W}$  are found. As main finding, the stationary AC loss in the field winding is also negligibly small in case of converter feeding.

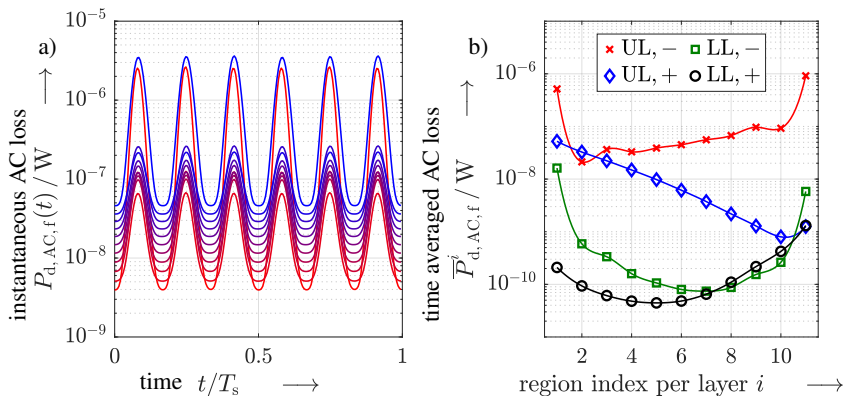


Figure A.16.: a) Instantaneous loss power in the HTS field winding of a 7 MW, 8.33 rpm generator for a stator current feeding with superimposed current harmonics of orders  $k = -5, +7$  (scaling  $s = 1$ ). Results are shown for LL  $\ominus$  in Fig. 4.32. Stator winding:  $q = 2$ ,  $W/\tau_p = 5/6$ . b) Time averaged, layer- and region-resolved AC loss power for the same operating conditions.

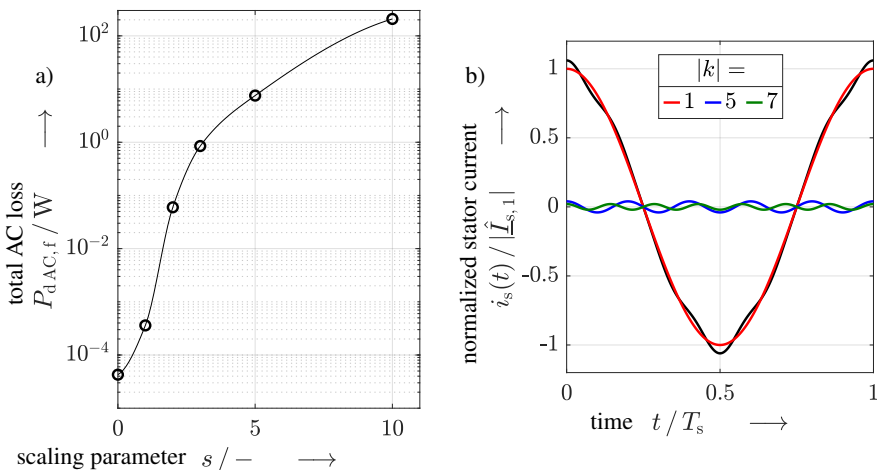


Figure A.17.: a) Total, time averaged AC loss in the HTS field winding for artificially up-scaled current harmonics of time orders  $k = -5, +7$  versus the scaling factor  $s$ . Stator winding:  $q = 2$ ,  $W/\tau_p = 5/6$ . b) Stator phase current in presence of current harmonics with  $k = -5, +7$  in six-step mode (scaling  $s = 1$ ).

### A.6. Slot Plans and Spectra of Stator Windings

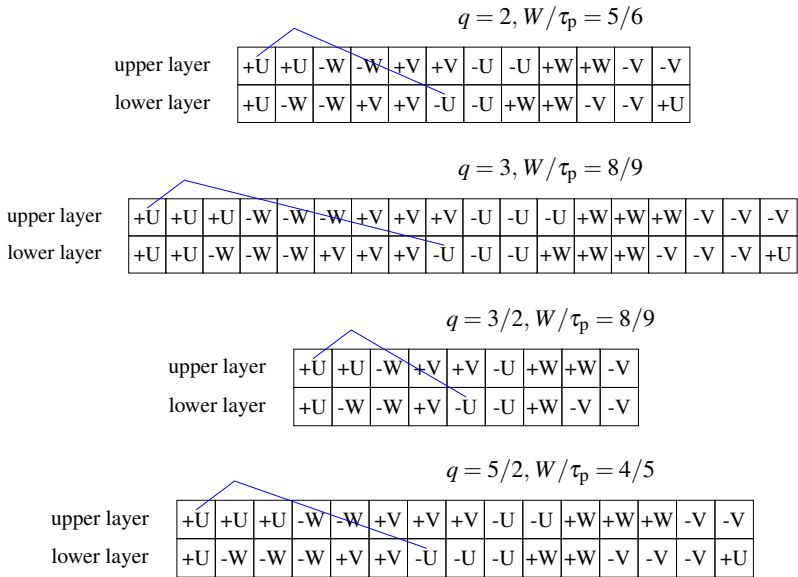


Figure A.18.: Slot plans for the considered three-phase stator windings. The spectra and properties are discussed in Sec. 4.3.3.

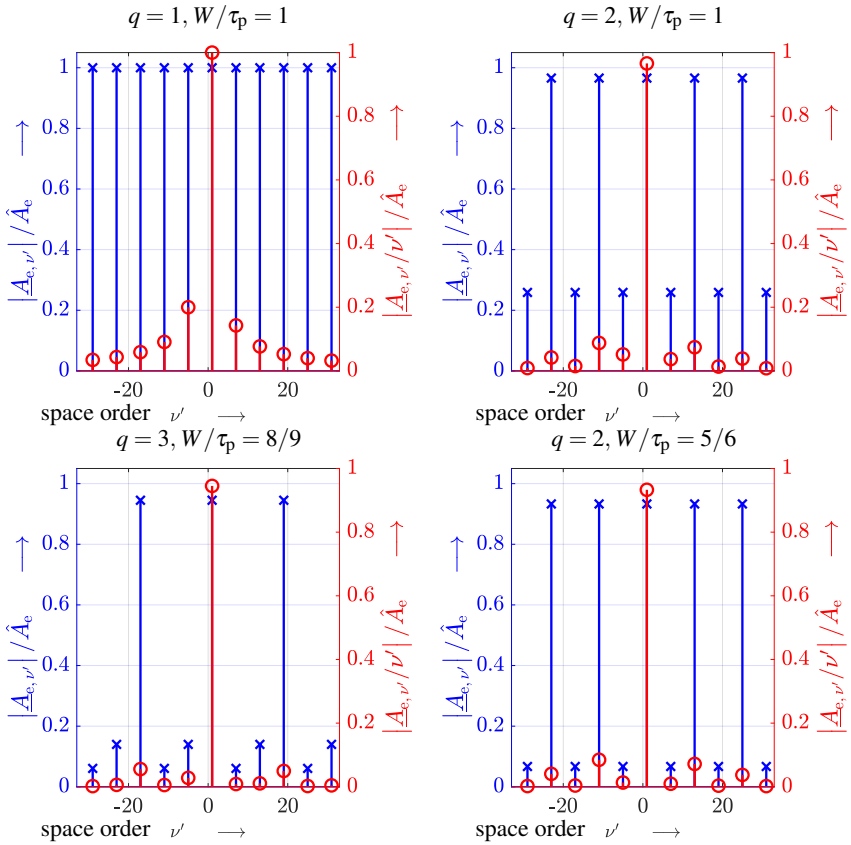


Figure A.19.: Normalized spectra of the current loading and normalized spectra of  $|\underline{A}_{\nu'} / \nu'| \sim |\underline{B}_{\nu'}|$  for different integer-slot stator windings.

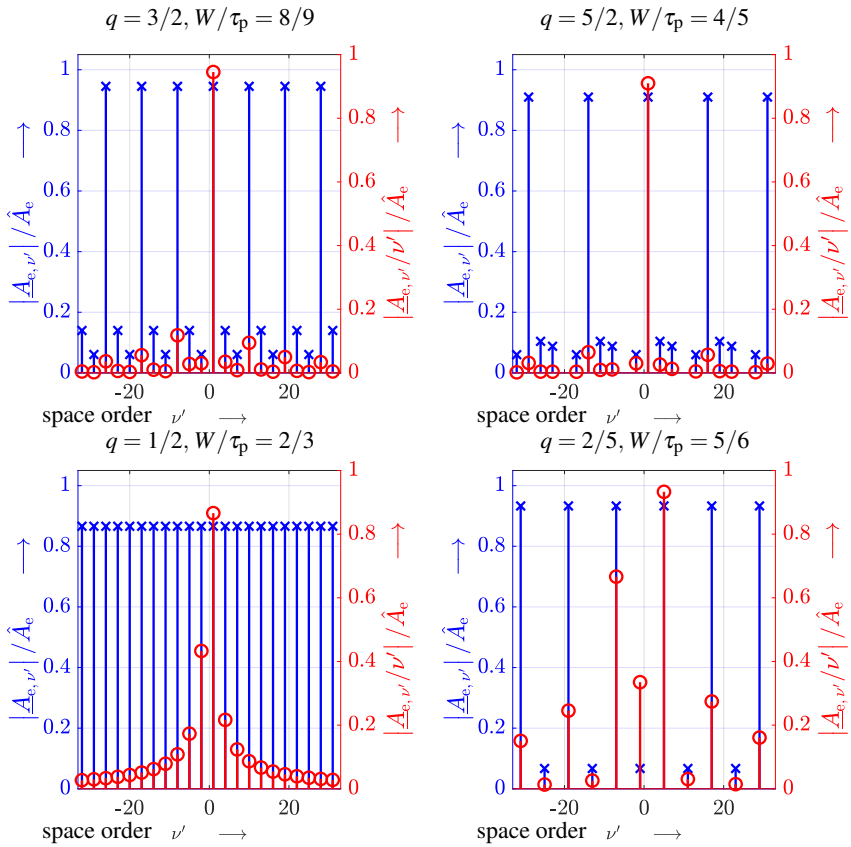


Figure A.20.: Normalized spectra of the current loading and normalized spectra of  $|\underline{A}_{\nu'}/\nu'| \sim |\underline{B}_{\nu'}|$  for different fractional-slot stator windings.



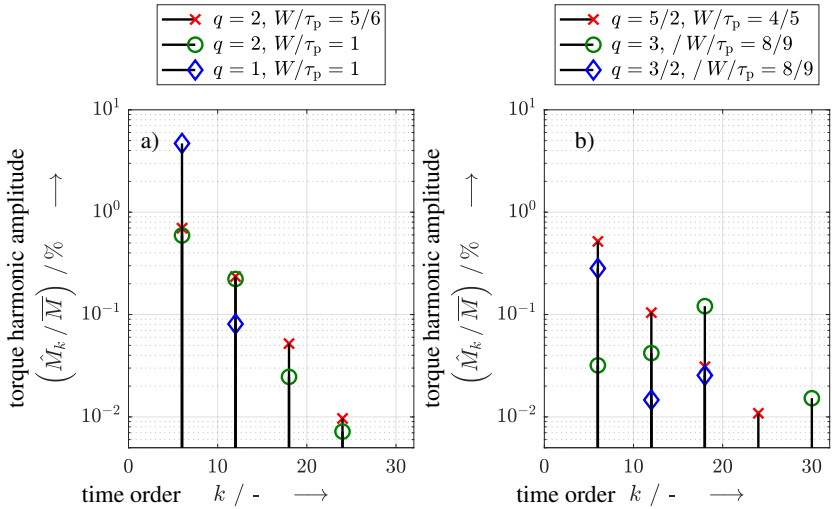


Figure A.21.: Numerically calculated, normalized spectra of the electromagnetic air gap torque, normalized by the average torque for the stator windings in Tab. 4.10. The average torque ( $k = 0$ ) is not shown for better visibility.

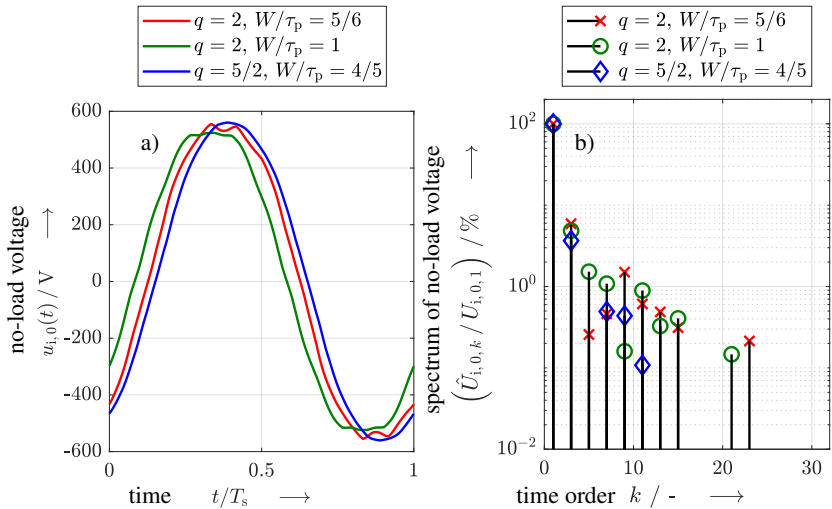


Figure A.22.: Numerically calculated no-load voltages for different stator windings in Tab. 4.10. a) No-load voltage versus time, b) normalized *Fourier* spectrum for the same windings.

## A.7. Parameter Identification

In order to determine the lead angle  $\gamma$ , the angle of the U-axis  $\bar{\alpha}_U$  (electrical degrees) of the stator winding is calculated, (A.25).  $\mathbf{Z}_{\pm}$  denote the incidence matrices of coil sides with positive (+) or negative (-) winding sense.  $\vec{\alpha}_Q$  is the vector containing all slot angles in one basic winding scheme.

$$\bar{\alpha}_U = \frac{1}{2} \cdot (\alpha_{U,+} + \alpha_{U,-}), \quad \alpha_{U,\pm} = [\mathbf{Z}_{\pm} \cdot \vec{\alpha}_Q]_1 \quad (\text{A.25})$$

The phase angle of the impressed, sinusoidal stator currents is defined in (A.26).

$$i_U(t) = \hat{I} \cdot \cos(\omega_s t + \varphi_s), \quad (\text{A.26})$$

$$i_V(t) = \hat{I} \cdot \cos\left(\omega_s t + \varphi_s - \frac{2\pi}{3}\right), \quad (\text{A.27})$$

$$i_W(t) = \hat{I} \cdot \cos\left(\omega_s t + \varphi_s - \frac{4\pi}{3}\right) \quad (\text{A.28})$$

From this, the phase angle of the armature field  $\beta_s$  at  $t = 0$  is calculated as (A.29).

$$\beta_s = \bar{\alpha}_U + \varphi_s + \pi \quad (\text{A.29})$$

As the initial angle of the  $q$ -axis and, thus, of the back-EMF in the FEM model is always chosen as  $\pi$  (el.), the lead angle from the back-EMF to the stator current  $\underline{I}_s$  is calculated as (A.30).  $\gamma = 0$  corresponds to pure positive  $q$ -current (motor operation), while  $\gamma = \pi$  denotes pure negative  $q$ -current in generator mode.

$$\gamma = \beta_s - \pi = \bar{\alpha}_U + \varphi_s \quad (\text{A.30})$$

With the RMS value of the stator current  $I_s = \hat{I}/\sqrt{2}$ , the (real valued)  $d$ - and  $q$ -currents are calculated from (A.31).

$$I_d = -I_s \cdot \sin(\gamma) \quad (\text{A.31})$$

$$I_q = +I_s \cdot \cos(\gamma) \quad (\text{A.32})$$

From the 2D FEM simulation, the phase angle  $\varphi_{i,U}$  of the induced voltage in phase U is known. The phase angle of the phasor  $\underline{U}_{i,2D,FEM}$ , i.e. the induced voltage per phase in the

2D model, is therefore calculated as (A.33).

$$\beta_i = \bar{\alpha}_U + \pi + \varphi_{i,U} \quad (\text{A.33})$$

The load angle of the 2D model  $\vartheta_{2D}$  from the 2D induced voltage to the back-EMF ( $q$ -axis with phase angle  $\pi$ ) is (A.34).

$$\vartheta_{2D} = \pi - \beta_i = \pi - (\bar{\alpha}_U + \pi + \varphi_{i,U}) = -(\bar{\alpha}_U + \varphi_{i,U}) \quad (\text{A.34})$$

The calculation of the inductance of the  $q$ -axis in the 2D model is based on the known phasor  $\underline{U}_{i,2D,FEM}$  and the assumption that the end-winding stray reactance  $X_{s\sigma b}$  is the same for the  $d$ - and  $q$ -axes. The latter assumption is reasonable, since the analysis in Sec. 4.2.2.3 implies a negligible effect of the rotor structure on the stator end-winding stray field due to the large magnetic air gap. This holds also in case of ferromagnetic pole cores. The local saturation at the axial end of the stator iron core differs between  $d$ - and  $q$ -axis, Fig. 4.10, which affects the stray field paths however only for a small fraction of the entire end-winding length  $l_{bs}$ .

The induced voltage per phase, as a result of 2D rotor and stator fields, is rewritten as (A.35).

$$\underline{U}_{i,2D,FEM} = \overbrace{\underline{U}_p + j \underbrace{(X_d - X_{s\sigma b})}_{X_{d,2D}} \cdot I_d}_{\text{in } q\text{-axis}} + j \underbrace{(X_q - X_{s\sigma b})}_{X_{q,2D}} \cdot I_q \quad (\text{A.35})$$

The projection to the  $d$ -axis can be used to calculate the  $q$ -reactance of the 2D model  $X_{q,2D}$ , (A.36), and the corresponding inductance (A.37).

$$|\underline{U}_{i,2D,FEM}| \cdot \sin(\vartheta_{2D}) = X_{q,2D} \cdot |I_q| \Leftrightarrow X_{q,2D} = \frac{|\underline{U}_{i,2D,FEM}|}{|I_q|} \cdot \sin(\vartheta_{2D}) \quad (\text{A.36})$$

$$L_{q,2D} = \frac{X_{q,2D}}{\omega_s} \quad (\text{A.37})$$

The  $d$ -axis reactance of the 2D model  $X_{d,2D}$  is calculated from the electromagnetic torque  $M_{e,2D}$ , which is extracted from the non-linear FEM simulation. For this purpose, the electromagnetic torque is expressed as (A.38).

$$M_{e,2D} = \frac{P}{\omega_s} \cdot m_s \cdot \text{Re} \{ \underline{U}_{i,2D,FEM} \cdot I_s^* \} \quad (\text{A.38})$$

$$= \frac{P}{\omega_s} \cdot m_s \cdot \operatorname{Re} \left\{ \left[ jX_{q,2D} \cdot I_q + jX_{d,2D} \cdot I_d + \underline{U}_p \right] \cdot [I_d^* + I_q^*] \right\} \quad (\text{A.39})$$

$$= \frac{P}{\omega_s} \cdot m_s \cdot \left[ U_p \cdot I_q + \underbrace{(X_{d,2D} - X_{q,2D})}_{=\Delta X_{2D}} \cdot I_d \cdot I_q \right] \quad (\text{A.40})$$

The further calculations are only valid under the assumption, that the  $d$ -current is small and particularly has no significant influence on the saturation state of the iron in the main flux path. In this case, the reluctance is little changed, if the  $d$ -current is set to  $I_d = 0$  and the remaining  $q$ -current alone is fed to the stator winding. Then, the value of the back-EMF is not affected by the change in  $I_d$ . A second simulation with pure  $q$ -current and the same rotor excitation is carried out (dashed quantities:  $I'_f = I_f$ ,  $I'_s = I_q$ ,  $\gamma' = \pi$ ). This operating mode yields a pure synchronous torque, (A.41).

$$M'_{e,2D} = \frac{P}{\omega_s} \cdot m_s \cdot U'_p \cdot I'_s \quad (\text{A.41})$$

The reluctance part of the electromagnetic torque in the 2D model is then determined as difference between the simulations with  $I_d = 0$  and  $I_d \neq 0$ , (A.42), (A.43).

$$\Delta M_{e,2D} = M_{e,2D} - M'_{e,2D} \quad (\text{A.42})$$

$$= \frac{P}{\omega_s} \cdot m_s \cdot [(U_p - U'_p) \cdot I_q + \Delta X_{2D} \cdot I_d \cdot I_q] \quad (\text{A.43})$$

With  $U'_p = U_p$ , the difference of the reactances  $X_{q,2D}$  and  $X_{d,2D}$  in the 2D model is obtained, (A.44), (A.45).

$$\Delta X_{2D} = \frac{1}{I_d \cdot I_q} \cdot \left[ \frac{\omega_s}{m_s \cdot p} \cdot \Delta M_{e,2D} - \underbrace{(U_p - U'_p)}_{\approx 0} \cdot I_q \right] \quad (\text{A.44})$$

$$\approx \frac{\omega_s}{m_s \cdot p} \cdot \frac{\Delta M_{e,2D}}{I_d \cdot I_q} \quad (\text{A.45})$$

The combination of (A.44) and (A.36) yields the reactance in the  $d$ -axis (A.46).

$$X_{d,2D} = X_{q,2D} + \Delta X_{2D} \quad (\text{A.46})$$

Actually, the considered generators feature typically a (small) negative  $d$ -current at rated load. Therefore, a stronger saturation in absence of the  $d$ -current occurs. This implies

$U'_p < U_p$ , such that  $(U_p - U'_p) > 0$ . Therefore, rather a too large value for  $\Delta X_{2D}$  is calculated with (A.44), such that the reluctance contribution of the torque is overestimated.

The absolute value of the back-EMF is calculated as (A.47).

$$U_p = |\underline{U}_{i,2D,FEM}| \cdot \cos(\vartheta_{2D}) - X_{d,2D} \cdot I_d \quad (\text{A.47})$$

The reluctance part of the total electromagnetic torque is (A.48).

$$M_{e,2D,rel} = \frac{P}{\omega_s} \cdot m_s \cdot \Delta X_{2D} \cdot I_d \cdot I_q \quad (\text{A.48})$$

After a validation against the 3D FEM model, the end-winding inductance is calculated analytically according to Sec. 2.4. The total  $d$ - and  $q$ -reactances are then determined from (A.49).

$$X_d = X_{d,2D} + X_{s\sigma b} \quad (\text{A.49})$$

$$X_q = X_{q,2D} + X_{s\sigma b} \quad (\text{A.50})$$

The calculation of the stator terminal voltage, (A.51), requires moreover the analytically calculated stator resistance  $R_s$ .

$$\underline{U}_s = \underline{U}_p + jX_d \cdot I_d + jX_q \cdot I_q + R_s \cdot (I_d + I_q) \quad (\text{A.51})$$

Since the iron loss is calculated from the 2D FEM results at a post-processing stage, the hysteretic behaviour and the loss power are not reflected in the extracted flux linkages and induced voltages.  $P_{Fe}$  is incorporated in the equivalent circuit and the phasor diagram by introducing an artificial iron loss resistance  $R_{Fe}$ . This resistance is connected in parallel to the stator terminal voltage and adds a current component  $I_{Fe}$ , which is in phase with  $\underline{U}_s$ , (A.52).

$$R_{Fe} = \frac{3 \cdot |\underline{U}_s|^2}{P_{Fe}}, \quad \Rightarrow I_{Fe} = \frac{\underline{U}_s}{R_{Fe}} \quad (\text{A.52})$$

The power factor is calculated from (A.53).

$$\cos \varphi_{sN} = \frac{\text{Re}\{\underline{U}_s \cdot \underline{I}_s^*\}}{U_s \cdot I_s} \quad (\text{A.53})$$

The actual load angle is calculated from the phase angles of the back-EMF and the stator

terminal voltage, (A.54).

$$\vartheta = \angle \underline{U}_p - \angle \underline{U}_s \quad (\text{A.54})$$

## A.8. Eddy Current Loss Calculation

### A.8.1. Eddy Current Loss in the Damper Screen for Varied Damper Temperature

The electrical resistivity in App. A.3.4 are used for the calculation.

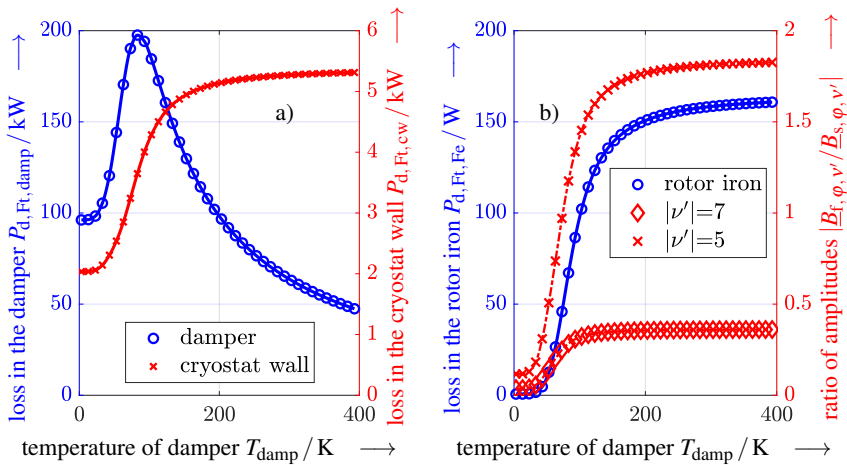


Figure A.23.: Analytically calculated eddy current loss in a partially superconducting generator at rated load  $I_{sN}$ . Damper screen thickness:  $d_{\text{damp}} = 5 \text{ mm}$ , thickness of cryostat wall:  $d_{\text{cw}} = 5 \text{ mm}$ , stator winding  $q = 1$ ,  $W = \tau_p$ . The temperature of the damper is varied in order to qualitatively evaluate the impact on the eddy current loss and on the screening of AC air gap fields. a) Eddy current loss in the damper and the cryostat wall, b) eddy current loss in the cold rotor iron and ratio between the tangential magnetic field amplitudes (space orders  $|\nu'| = 5, 7$ ) experienced by the field winding and the stator winding (indices: f - field, s - stator).

### A.8.2. Eddy Current Loss for Sudden Single-Phase and Three-Phase Short Circuits of Partially Superconducting Direct Drive Generators

#### Single-Phase Short Circuit

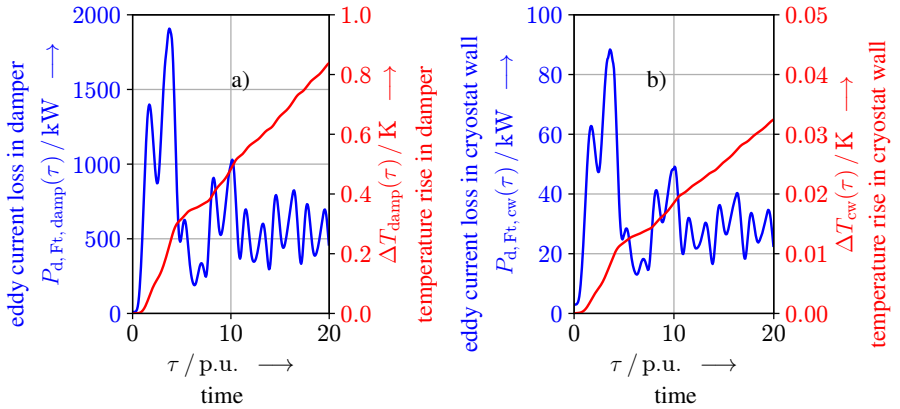


Figure A.24.: Numerically calculated (software: *JMAG*) eddy current loss in a) the warm damper screen and b) the cryostat wall after a sudden single-phase short circuit. A partially superconducting direct drive generator with all-iron topology and HTS excitation is considered. The temperature rise under the assumption of adiabatic heating is shown in red.

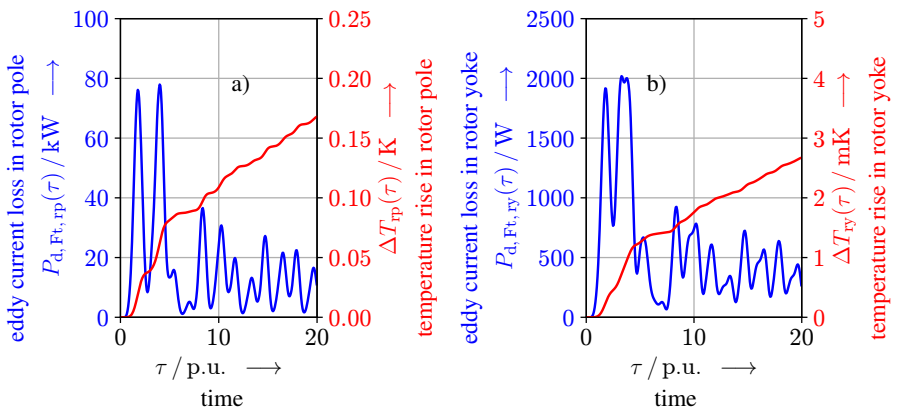


Figure A.25.: As Fig. A.24, but for the cold iron parts, i.e. rotor pole cores and rotor yoke.

**Three-Phase Short Circuit**

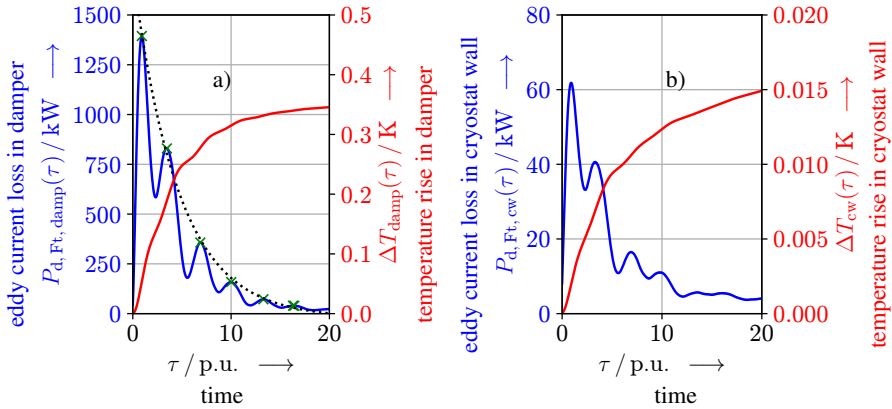


Figure A.26.: As Fig. A.24, but for a sudden, symmetrical three-phase short circuit.

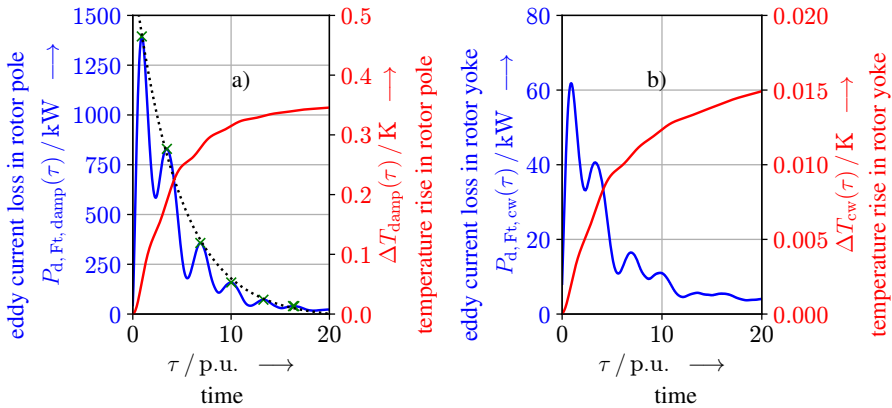


Figure A.27.: As Fig. A.26, but for the cold rotor iron parts, i.e. pole cores and yoke.



## A.9. Thermal Model of Partially Superconducting Generators

### A.9.1. Multi Layer Insulation System

Based on [56, 97], the heat transfer through the MLI system is modelled with (A.55) - (A.62).

$$\text{number of layers per cm: } \bar{N} = 33.33 \text{ cm}^{-1} \quad (\text{A.55})$$

$$\text{number of layers: } N_{\text{MLI}} = \lfloor d_{\text{MLI}} \cdot \bar{N} \rfloor \quad (\text{A.56})$$

$$\text{average temperature (approximate): } T_{\text{m}} = \frac{1}{2} \cdot (T_{\text{h}} + T_{\text{c}}) \quad (\text{A.57})$$

$$\text{equiv. therm. cond. (cond. contrib.): } \lambda_{\text{cond}} = C_{\text{s}} \cdot \left( \frac{\bar{N}}{100} \right)^{2.56} \cdot \frac{T_{\text{m}}}{N_{\text{MLI}} - 1} \cdot \frac{N_{\text{MLI}}}{\bar{N}} \quad (\text{A.58})$$

$$\text{equiv. therm. cond. (rad. contrib.): } \lambda_{\text{rad}} = C_{\text{r}} \cdot \frac{\epsilon_{\text{TR}}}{\bar{N}} \cdot \frac{T_{\text{h}}^{4.67} - T_{\text{c}}^{4.67}}{T_{\text{h}} - T_{\text{c}}} \quad (\text{A.59})$$

$$\text{overall equiv. therm. cond.: } \lambda_{\text{MLI}} = \lambda_{\text{cond}} + \lambda_{\text{rad}} \quad (\text{A.60})$$

$$\text{definition of constants: } C_{\text{s}} = 8.95 \cdot 10^{-8}, C_{\text{r}} = 5.39 \cdot 10^{-10}, \epsilon_{\text{TR}} = 0.03 \quad (\text{A.61})$$

$$\text{heat flow density: } q_{\text{MLI}} = \lambda_{\text{MLI}} \cdot (T_{\text{h}} - T_{\text{c}}) \cdot \frac{\bar{N}}{N_{\text{MLI}}} \quad (\text{A.62})$$

### A.9.2. Modelling of Thermal Resistances

#### Stator Yoke - Surrounding

$$\alpha_{\text{rad}} = 7 \frac{\text{W}}{\text{m}^2 \cdot \text{K}} \quad (\text{A.63})$$

$$\alpha_{\text{conv}} = 7 \frac{\text{W}}{\text{m}^2 \cdot \text{K}} \quad (\text{A.65})$$

$$A_{\text{y,outer}} = \pi \cdot r_{\text{so}} \cdot L \quad (\text{A.64})$$

$$R = \frac{1}{(\alpha_{\text{rad}} + \alpha_{\text{conv}}) \cdot A_{\text{y,outer}}} \quad (\text{A.66})$$

**Stator Yoke - Stator Teeth**

Conductive heat transfer in tooth:

$$b_{zo} = \frac{r_{si} + h_Q}{r_{si}} \cdot b_z \quad (\text{A.67})$$

$$l_t = \frac{h_Q}{2} \quad (\text{A.68})$$

$$\lambda_t = 33 \frac{\text{W}}{\text{m} \cdot \text{K}} \quad (\text{A.69})$$

$$A_t = \frac{b_z + 3 \cdot b_{zo}}{4} \cdot l_{\text{Fe}} \quad (\text{A.70})$$

$$R_t = \frac{l_t}{\lambda_t \cdot A_t} \quad (\text{A.71})$$

Conductive heat transfer in yoke:

$$l_y = \frac{h_{ys}}{2} \quad (\text{A.72})$$

$$\lambda_y = 33 \frac{\text{W}}{\text{m} \cdot \text{K}} \quad (\text{A.73})$$

$$R_y = \frac{l_y}{\lambda_y \cdot A_y} \quad (\text{A.74})$$

$$R_{s,y \rightarrow t} = \frac{1}{Q} \cdot R_t + R_y \quad (\text{A.75})$$

**Stator Winding - Stator Yoke**

$$l_{ys} = \frac{h_{ys}}{2} \quad (\text{A.76})$$

$$A_{ys} = \frac{1}{2} \cdot \left( Q \cdot b_z + 2\pi \cdot \left( r_{so} - \frac{h_{ys}}{2} \right) \right) \cdot l_{\text{Fe}} \quad (\text{A.79})$$

$$\lambda_{ys} = 33 \frac{\text{W}}{\text{m} \cdot \text{K}} \quad (\text{A.77})$$

$$R_{\text{Cu},y} = \frac{1}{Q} \cdot (R_{\text{Cu},\text{cond}} + R_{\text{iso},\text{cond}}) + R_{y,\text{cond}} \quad (\text{A.80})$$

$$R_{y,\text{cond}} = \frac{l_{ys}}{\lambda_{ys} \cdot A_{ys}} \quad (\text{A.78})$$

**Stator Winding - Stator Teeth**

$$l_{\text{Cu}} = \frac{b_Q - 2 \cdot d_{\text{iso},\text{main}}}{4} \quad (\text{A.81})$$

$$l_{\text{iso}} = d_{\text{iso},\text{main}} \quad (\text{A.85})$$

$$A_{\text{Cu}} = l_{\text{Fe}} \cdot 2 \cdot (h_Q - h_{\text{tt},\text{sw}}) \quad (\text{A.82})$$

$$\lambda_{\text{iso}} = 0.2 \frac{\text{W}}{\text{m} \cdot \text{K}} \quad (\text{A.86})$$

$$\lambda_{\text{Cu}} = f_{\lambda,\text{Cu}} (RRR = 80, T_{\text{Cu},s}) \quad (\text{A.83})$$

$$A_{\text{iso}} = A_{\text{Cu}} \quad (\text{A.87})$$

$$R_{\text{Cu},\text{cond}} = \frac{l_{\text{Cu}}}{\lambda_{\text{Cu}} \cdot A_{\text{Cu}}} \quad (\text{A.84})$$

$$R_{\text{iso}} = \frac{l_{\text{iso}}}{\lambda_{\text{iso}} \cdot A_{\text{iso}}} \quad (\text{A.88})$$

$$R_{\text{Cut}} = \frac{1}{Q} \cdot (R_{\text{Cu},\text{cond}} + R_{\text{iso},\text{cond}}) \quad (\text{A.89})$$

**Stator winding - radial cooling ducts**

Based on [219], the convective heat transfer from the winding insulation into the cooling

ducts is described with (A.90) - (A.117).

$$v_{\text{av},\delta} = 50 \frac{\text{m}}{\text{s}} \quad (\text{A.90})$$

$$v_{\text{av},\text{channel}} = v_{\text{av},\delta} \cdot \frac{A_{\delta}}{A_{\text{channel},\Sigma}} \quad (\text{A.98})$$

Properties of air at  $\vartheta = 50^{\circ}\text{C}$ :

$$l_{\text{conv}} = h_Q \quad (\text{A.99})$$

$$v_{\text{air}} = 18.4 \cdot 10^{-6} \frac{\text{m}^2}{\text{s}} \quad (\text{A.91})$$

$$U_v = 2 \cdot \left( l_v + \frac{1}{2} \cdot (b_z + b_{z0}) \right) \quad (\text{A.100})$$

$$\lambda_{\text{air}} = 0.027 \frac{\text{W}}{\text{m} \cdot \text{K}} \quad (\text{A.92})$$

$$d_H = 4 \cdot \frac{A_{\text{channel}}}{U_v} \quad (\text{A.101})$$

$$c_{p,\text{air}} = 1005 \frac{\text{J}}{\text{kg} \cdot \text{K}} \quad (\text{A.93})$$

$$\text{Pr} = v_{\text{air}} \cdot \rho_{\text{air}} \cdot \frac{c_{p,\text{air}}}{\lambda_{\text{air}}} \quad (\text{A.102})$$

$$\rho_{\text{air}} = 1.2041 \frac{\text{kg}}{\text{m}^3} \quad (\text{A.94})$$

$$\text{Re} = v_{\text{av},\text{channel}} \cdot \frac{d_H}{v_{\text{air}}} \quad (\text{A.103})$$

$$A_{\text{channel}} = \frac{1}{2} \cdot (b_z + b_{z0}) \cdot l_v \quad (\text{A.95})$$

$$\xi = [1.8 \cdot \log_{10}(\text{Re}) - 1.5]^{-2} \quad (\text{A.104})$$

$$A_{\text{channel},\Sigma} = A_{\text{channel}} \cdot Q \cdot n_v \quad (\text{A.96})$$

$$\alpha_{\text{Cu},\text{rcc}} = \text{Nu} \cdot \frac{\lambda_{\text{air}}}{d_H} \quad (\text{A.105})$$

$$A_{\delta} = \pi \cdot \left( r_{\text{si}}^2 - \left( r_{\text{si}} - \delta_{\text{geom}} \right)^2 \right) \quad (\text{A.97})$$

$$\text{Nu} = \frac{\frac{\xi}{8} \cdot \text{Re} \cdot \text{Pr}}{1 + 12.7 \cdot \sqrt{\frac{\xi}{8}} \cdot (\text{Pr}^{2/3} - 1)} \cdot \left( 1 + \left( \frac{d_H}{l_{\text{conv}}} \right)^{2/3} \right) \quad (\text{A.106})$$

$$A_{\text{Cu},\text{rcc}} = (h_Q - h_{\text{tt},\text{sw}}) \cdot l_v + b_Q \cdot l_v \quad (\text{A.107})$$

$$l_{\text{iso}} = d_{\text{iso},\text{main}} \quad (\text{A.112})$$

$$R_{\text{conv}} = \frac{1}{\alpha_{\text{Cu},\text{rcc}} \cdot A_{\text{Cu},\text{rcc}}} \quad (\text{A.108})$$

$$A_{\text{iso}} = (h_Q - h_{\text{tt},\text{sw}}) \cdot l_v + b_Q \cdot l_v \quad (\text{A.113})$$

$$l_{\text{Cu}} = \frac{b_Q}{2} \quad (\text{A.109})$$

$$\lambda_{\text{iso}} = 0.2 \frac{\text{W}}{\text{m} \cdot \text{K}} \quad (\text{A.114})$$

$$A_{\text{Cu}} = (h_Q - h_{\text{tt},\text{sw}}) \cdot l_v + b_Q \cdot l_v \quad (\text{A.110})$$

$$R_{\text{iso}} = \frac{l_{\text{iso}}}{\lambda_{\text{iso}} \cdot A_{\text{iso}}} \quad (\text{A.115})$$

$$\lambda_{\text{Cu}} = f_{\lambda,\text{Cu}} (\text{RRR} = 80, T_{\text{Cu},\text{s}}) \quad (\text{A.111})$$

$$R_{\text{Cu}} = \frac{l_{\text{Cu}}}{\lambda_{\text{Cu}} \cdot A_{\text{Cu}}} \quad (\text{A.116})$$

$$R_{\text{Cu},\text{rcc}} = \frac{1}{2 \cdot Q \cdot n_v} \cdot (R_{\text{conv}} + R_{\text{Cu}} + R_{\text{iso}}) \quad (\text{A.117})$$

**Stator Teeth - Radial Cooling Ducts**

$$A_{t,\text{channel}} = \frac{1}{2} \cdot (b_z + b_{zo}) \cdot h_Q \quad (\text{A.118}) \qquad \lambda_t = 0.3 \frac{\text{W}}{\text{m} \cdot \text{K}} \quad (\text{A.122})$$

$$R_{t,\text{conv}} = \frac{1}{\alpha_{t,\text{channel}} \cdot A_{t,\text{channel}}} \quad (\text{A.119}) \qquad R_{t,\text{cond}} = \frac{l_t}{\lambda_t \cdot A_t} \quad (\text{A.123})$$

$$l_t = \frac{l_{\text{seg}}}{2} \quad (\text{A.120}) \qquad R_{t,\text{rcc}} = \frac{1}{2 \cdot Q \cdot n_v} \cdot (R_{t,\text{conv}} + R_{t,\text{cond}}) \quad (\text{A.124})$$

$$A_t = A_{t,\text{channel}} \quad (\text{A.121})$$

**Stator Teeth: Middle - Surface**

$$l_t = \frac{h_Q}{2} - \frac{h_{tt,\text{sw}}}{2} \quad (\text{A.125}) \qquad R_{t,\text{cond}} = \frac{l_t}{\lambda_t \cdot A_t} \quad (\text{A.128})$$

$$\lambda_t = 33 \frac{\text{K}}{\text{m} \cdot \text{K}} \quad (\text{A.126}) \qquad R_{t,\text{m} \rightarrow \text{o}} = \frac{1}{Q} \cdot R_{t,\text{cond}} \quad (\text{A.129})$$

$$A_t = l_{\text{Fe}} \cdot \frac{3 \cdot b_z + b_{zo}}{4} \quad (\text{A.127})$$

**Stator Yoke - Radial Cooling Ducts**

Based on [219], the convective heat transfer from the winding insulation into the cooling ducts is described with (A.130) - (A.117).

$$v_{\text{av},\delta} = 50 \frac{\text{m}}{\text{s}} \quad (\text{A.130}) \qquad l_{\text{conv}} = h_{\text{ys}} \quad (\text{A.134})$$

$$A_{\text{channel,yoke}} = 2\pi \cdot \left( r_{\text{so}} - \frac{h_{\text{ys}}}{2} \right) \cdot l_{\text{seg}} \quad (\text{A.131}) \qquad d_H = 2 \cdot l_{\text{seg}} \quad (\text{A.135})$$

$$A_\delta = \pi \cdot \left( r_{\text{si}}^2 - \left( r_{\text{si}} - \delta_{\text{geom}} \right)^2 \right) \quad (\text{A.132}) \qquad \text{Pr} = v_{\text{air}} \cdot \rho_{\text{air}} \cdot \frac{c_{p,\text{air}}}{\lambda_{\text{air}}} \quad (\text{A.136})$$

$$v_{\text{av,channel}} = v_{\text{av},\delta} \cdot \frac{A_\delta}{A_{\text{channel,yoke}}} \quad (\text{A.133}) \qquad \text{Re} = v_{\text{av,channel}} \cdot \frac{d_H}{v_{\text{air}}} \quad (\text{A.137})$$

$$\xi = [1.8 \cdot \log_{10}(\text{Re}) - 1.5]^{-2} \quad (\text{A.138})$$

$$\text{Nu} = \frac{\frac{\xi}{8} \cdot \text{Re} \cdot \text{Pr}}{1 + 12.7 \cdot \sqrt{\frac{\xi}{8}} \cdot (\text{Pr}^{2/3} - 1)} \cdot \left( 1 + \left( \frac{d_H}{l_{\text{conv}}} \right)^{2/3} \right) \quad (\text{A.139})$$

$$\alpha_{y,\text{channel}} = \text{Nu} \cdot \frac{\lambda_{\text{air}}}{d_H} \quad (\text{A.140}) \quad l_y = \frac{l_{\text{seg}}}{2} \quad (\text{A.144})$$

$$A_{y,\text{channel}} = \pi \cdot \left[ r_{\text{so}}^2 - (r_{\text{so}} - h_{\text{ys}})^2 \right] \cdot n_v \quad (\text{A.141}) \quad A_y = A_{y,\text{channel}} \quad (\text{A.145})$$

$$R_{y,\text{conv}} = \frac{1}{\alpha_{y,\text{channel}} \cdot A_{y,\text{channel}}} \quad (\text{A.142}) \quad \lambda_y = 0.3 \frac{\text{W}}{\text{m} \cdot \text{K}} \quad (\text{A.146})$$

$$R_{y,\text{rcc}} = \frac{1}{2 \cdot n_v} \cdot (R_{y,\text{conv}} + R_{y,\text{cond}}) \quad (\text{A.143}) \quad R_y = \frac{l_y}{\lambda_y \cdot A_y} \quad (\text{A.147})$$

### Stator Winding - Slot Wedge

$$l_{\text{Cu}} = \frac{1}{2} \cdot (h_Q - h_{\text{tt,sw}}) \quad (\text{A.148}) \quad A_{\text{iso}} = l_{\text{Fe}} \cdot b_Q \quad (\text{A.154})$$

$$\lambda_{\text{Cu}} = f_{\lambda,\text{Cu}} (\text{RRR} = 80, T_{\text{Cu,s}}) \quad (\text{A.149}) \quad R_{\text{iso,cond}} = \frac{l_{\text{iso}}}{\lambda_{\text{iso}} \cdot A_{\text{iso}}} \quad (\text{A.155})$$

$$A_{\text{Cu}} = l_{\text{Fe}} \cdot b_Q \quad (\text{A.150}) \quad l_{\text{sw}} = h_{\text{tt,sw}} \quad (\text{A.156})$$

$$R_{\text{Cu,cond}} = \frac{l_{\text{Cu}}}{\lambda_{\text{Cu}} \cdot A_{\text{Cu}}} \quad (\text{A.151}) \quad \lambda_{\text{sw}} = 0.3 \frac{\text{W}}{\text{m} \cdot \text{K}} \quad (\text{A.157})$$

$$l_{\text{iso}} = d_{\text{iso,main}} \quad (\text{A.152}) \quad A_{\text{sw}} = l_{\text{Fe}} \cdot b_Q \quad (\text{A.158})$$

$$\lambda_{\text{iso}} = 0.2 \frac{\text{W}}{\text{m} \cdot \text{K}} \quad (\text{A.153}) \quad R_{\text{sw,cond}} = \frac{l_{\text{sw}}}{\lambda_{\text{sw}} \cdot A_{\text{sw}}} \quad (\text{A.159})$$

$$R_{\text{Cu,sw}} = \frac{1}{Q} \cdot (R_{\text{Cu,cond}} + R_{\text{iso,cond}} + R_{\text{sw,cond}}) \quad (\text{A.160})$$

**Stator Teeth - Slot Wedge**

$$l_t = \frac{h_Q}{2} - \frac{h_{tt,sw}}{2} \quad (\text{A.161})$$

$$\lambda_t = 33 \frac{\text{W}}{\text{m} \cdot \text{K}} \quad (\text{A.162})$$

$$A_t = I_{\text{Fe}} \cdot \frac{3 \cdot b_z + b_{z0}}{4} \quad (\text{A.163})$$

$$R_{t,\text{cond}} = \frac{l_t}{\lambda_t \cdot A_t} \quad (\text{A.164})$$

$$l_{t,\text{perp}} = \frac{b_z}{2} \quad (\text{A.165})$$

$$A_{t,\text{perp}} = h_{tt,sw} \cdot I_{\text{Fe}} \quad (\text{A.166})$$

$$R_{t,\text{perp}} = \frac{l_{t,\text{perp}}}{\lambda_t \cdot A_{t,\text{perp}}} \quad (\text{A.167})$$

$$l_{sw} = \frac{b_Q}{2} \quad (\text{A.168})$$

$$A_{sw} = A_{t,\text{perp}} \quad (\text{A.169})$$

$$\lambda_{sw} = 0.3 \frac{\text{W}}{\text{m} \cdot \text{K}} \quad (\text{A.170})$$

$$R_{sw} = \frac{l_{sw}}{\lambda_{sw} \cdot A_{sw}} \quad (\text{A.171})$$

$$R_{sw,t} = \frac{1}{Q} \cdot (R_t + R_{t,\text{perp}} + R_{sw}) \quad (\text{A.172})$$

**Stator Teeth - Air Gap**

$$A_{t,\delta} = b_z \cdot I_{\text{Fe}} \quad (\text{A.173})$$

$$R_{t,\text{conv}} = \frac{1}{\alpha_{t,\delta} \cdot A_{t,\delta}} \quad (\text{A.174})$$

$$l_t = \frac{h_Q}{2} \quad (\text{A.175})$$

$$A_t = \frac{3 \cdot b_z + b_{z0}}{4} \cdot I_{\text{Fe}} \quad (\text{A.176})$$

$$\lambda_t = 33 \frac{\text{W}}{\text{m} \cdot \text{K}} \quad (\text{A.177})$$

$$R_{t,\text{cond}} = \frac{l_t}{\lambda_t \cdot A_t} \quad (\text{A.178})$$

$$R_{t,\delta} = \frac{1}{Q} \cdot (R_{t,\text{conv}} + R_{t,\text{cond}}) \quad (\text{A.179})$$

**Slot Wedge - Air Gap**

$$A_{sw} = b_Q \cdot L \quad (\text{A.180})$$

$$R_{sw,\text{cond}} = \frac{1}{\alpha_{sw,\delta} \cdot A_{sw}} \quad (\text{A.181})$$

$$R_{sw,\delta} = \frac{1}{Q} \cdot R_{sw,\text{cond}} \quad (\text{A.182})$$

**Slot Wedge - Cryostat Wall Surface**

$$\sigma = 5.67 \cdot 10^{-8} \frac{\text{W}}{\text{m}^2 \cdot \text{K}^4} \quad (\text{A.183}) \quad A_{\text{cw}} = 2\pi \cdot (r_{\text{si}} - \delta_{\text{geom}}) \cdot L \quad (\text{A.187})$$

$$\varepsilon_{\text{sw}} = 0.9 \quad (\text{A.184}) \quad k = \frac{\sigma \cdot \varepsilon_{\text{sw}} \cdot \varepsilon_{\text{cw}} \cdot A_{\text{sw}}}{\varepsilon_{\text{sw}} \cdot (1 - \varepsilon_{\text{cw}}) + \varepsilon_{\text{cw}}} \quad (\text{A.188})$$

$$\varepsilon_{\text{cw}} = 0.07 \quad (\text{A.185}) \quad R_{\text{sw,cw}} = \frac{T_{\text{sw}} - T_{\text{cw,o}}}{k \cdot (T_{\text{sw}}^4 - T_{\text{cw,o}}^4)} \quad (\text{A.189})$$

$$A_{\text{sw}} = b_{\text{Q}} \cdot L \cdot Q \quad (\text{A.186})$$

**Stator Teeth Surface - Cryostat Wall Surface**

$$\varepsilon_{\text{t}} = 0.75 \quad (\text{A.190}) \quad A_{\text{cw}} = 2\pi \cdot (r_{\text{si}} - \delta_{\text{geom}}) \cdot L \quad (\text{A.193})$$

$$\varepsilon_{\text{cw}} = 0.07 \quad (\text{A.191}) \quad k = \frac{\sigma \cdot \varepsilon_{\text{t}} \cdot \varepsilon_{\text{cw}} \cdot A_{\text{t}}}{\varepsilon_{\text{t}} \cdot (1 - \varepsilon_{\text{cw}}) + \varepsilon_{\text{cw}}} \quad (\text{A.194})$$

$$A_{\text{t}} = b_{\text{z}} \cdot L \cdot Q \quad (\text{A.192}) \quad R_{\text{t,cw}} = \frac{T_{\text{t,o}} - T_{\text{cw,o}}}{k \cdot (T_{\text{t,o}}^4 - T_{\text{cw,o}}^4)} \quad (\text{A.195})$$

**Air Gap - Cryostat Wall Surface**

$$l = l_{\text{Fe}} \quad (\text{A.196}) \quad F = \frac{0.75 \cdot a^{-0.17} + (0.9 - 0.15 \cdot a^{0.6})}{1 + a} \quad (\text{A.201})$$

$$d_{\text{H}} = 2 \cdot \delta_{\text{geom}} \quad (\text{A.197})$$

$$\text{Re} = v_{\text{av},\delta} \cdot \frac{d_{\text{H}}}{\nu_{\text{air}}} \quad (\text{A.198}) \quad \text{Re}' = \text{Re} \cdot \frac{(1 + a^2) \cdot \ln(a) + (1 - a^2)}{(1 - a)^2 \cdot \ln(a)} \quad (\text{A.202})$$

$$\text{Pr} = v_{\text{air}} \cdot \rho_{\text{air}} \cdot \frac{c_{\text{p,air}}}{\lambda_{\text{air}}} \quad (\text{A.199}) \quad \xi = (1.8 \cdot \log_{10}(\text{Re}') - 1.5)^{-2} \quad (\text{A.203})$$

$$k_1 = 1.07 + \frac{900}{\text{Re}} - 0.63 \cdot \frac{1}{1 + 10 \cdot \text{Pr}} \quad (\text{A.204})$$

$$a = \frac{2 \cdot r_{\text{si}} - 2 \cdot \delta_{\text{geom}}}{2 \cdot r_{\text{si}}} \quad (\text{A.200})$$

$$\text{Nu} = \frac{\frac{\xi}{\delta_{\text{H}}} \cdot \text{Re} \cdot \text{Pr}}{k_1 + 12.7 \cdot \sqrt{\frac{\xi}{8}} \cdot (\text{Pr}^{2/3} - 1)} \cdot \left( 1 + \left( \frac{d_{\text{H}}}{l} \right)^{2/3} \right) \cdot F \quad (\text{A.205})$$

$$\alpha_{cw, \delta} = \text{Nu} \cdot \frac{\lambda_{\text{air}}}{d_H} \quad (\text{A.206})$$

$$R_{cw, \delta} = \frac{1}{\alpha_{cw, \delta} \cdot A_{cw}} \quad (\text{A.208})$$

$$A_{cw} = 2\pi \cdot (r_{si} - \delta_{\text{geom}}) \cdot L \quad (\text{A.207})$$

### Cryostat Wall Surface - Middle of Cryostat Wall

$$l_{\text{cryo}} = \frac{d_{cw}}{2} \quad (\text{A.209})$$

$$A_{\text{cryo}} = L \cdot 2\pi \cdot \left( r_{\text{cryo, outer}} - \frac{3}{4} \cdot d_{cw} \right) \quad (\text{A.212})$$

$$\lambda_{\text{StSt, cw}} = 15 \frac{\text{W}}{\text{m} \cdot \text{K}} \quad (\text{A.210})$$

$$R = \frac{l_{\text{cryo}}}{\lambda_{\text{cryo}} \cdot A_{\text{cryo}}} \quad (\text{A.213})$$

$$r_{\text{cryo, outer}} = r_{si} - \delta_{\text{geom}} \quad (\text{A.211})$$

### Middle of Cryostat Wall - Damper Screen

$$l_{cw} = \frac{d_{cw}}{2} \quad (\text{A.214})$$

$$\lambda_{\text{Cu, damper}} = f_{\lambda, \text{Cu}} (RRR = 80, T_{\text{damper}}) \quad (\text{A.220})$$

$$\lambda_{\text{StSt, cw}} = 15 \frac{\text{W}}{\text{m} \cdot \text{K}} \quad (\text{A.215})$$

$$r_{\text{damper, outer}} = r_{si} - \delta_{\text{geom}} - d_{cw} \quad (\text{A.221})$$

$$r_{cw, \text{outer}} = r_{si} - \delta_{\text{geom}} \quad (\text{A.216})$$

$$A_{\text{damper}} = L \cdot 2\pi \cdot \left( r_{\text{damper, outer}} - \frac{d_{\text{damper}}}{4} \right) \quad (\text{A.222})$$

$$A_{cw} = L \cdot 2\pi \cdot \left( r_{cw, \text{outer}} - \frac{3}{4} \cdot d_{cw} \right) \quad (\text{A.217})$$

$$R_{\text{damper}} = \frac{l_{\text{damper}}}{\lambda_{\text{Cu, damper}} \cdot A_{\text{damper}}} \quad (\text{A.223})$$

$$R_{cw} = \frac{l_{cw}}{\lambda_{\text{StSt, cw}} \cdot A_{cw}} \quad (\text{A.218})$$

$$R_{cw, \text{damp}} = R_{cw} + R_{\text{damper}} \quad (\text{A.224})$$

$$l_{\text{damper}} = \frac{d_{\text{Cu, damper}}}{2} \quad (\text{A.219})$$

### Damper - Pole Core

$$d_{\text{MLI}} = 10 \text{ mm} \quad (\text{A.225})$$

$$l_{\text{MLI, eff}} = d_{\text{MLI}} \quad (\text{A.228})$$

$$\lambda_{\text{MLI}} = f_{\lambda, \text{MLI}} (T_h = T_{\text{damper}}, T_c = T_{\text{pole}}, d_{\text{MLI}}) \quad (\text{A.226})$$

$$A_p = 2p \cdot L \cdot w_p \quad (\text{A.229})$$

$$r_{\text{damper, i}} = r_{si} - \delta_{\text{geom}} - d_{cw} - d_{\text{Cu, damper}} \quad (\text{A.227})$$

$$R_{\text{damp, pole}} = \frac{l_{\text{MLI, eff}}}{A_p \cdot \lambda_{\text{MLI}}} \quad (\text{A.230})$$



**Damper - Pressure Plate**

$$d_{\text{MLI}} = 10 \text{ mm} \quad (\text{A.231})$$

$$\lambda_{\text{MLI}} = f_{\lambda, \text{MLI}} (T_{\text{damper}}, T_{\text{pp}}, d_{\text{MLI}}) \quad (\text{A.232})$$

$$R_{\text{MLI}} = \frac{l_{\text{MLI, eff}}}{A_{\text{p}} \cdot \lambda_{\text{MLI}}} \quad (\text{A.233})$$

$$\lambda_{\text{pp}} = 1.4 \frac{\text{W}}{\text{m} \cdot \text{K}} \quad (\text{A.234})$$

$$l_{\text{pp}} = \frac{h_{\text{pp}}}{4} \quad (\text{A.235})$$

$$A_{\text{pp}} = 2p \cdot (2 \cdot w_{\text{p, side}} + 2 \cdot w_{\text{f}} + 4 \cdot w_{\text{spacer, side}}) \cdot L \quad (\text{A.236})$$

$$R_{\text{pp, cond}} = \frac{l_{\text{pp}}}{\lambda_{\text{pp}} \cdot A_{\text{pp}}} \quad (\text{A.237})$$

$$R_{\text{damp, pp}} = R_{\text{MLI}} + R_{\text{pp, cond}} \quad (\text{A.238})$$

**Damper - Rotor Yoke**

$$d_{\text{MLI}} = 10 \text{ mm} \quad (\text{A.239}) \quad \lambda_{\text{MLI}} = f_{\lambda, \text{MLI}} (T_{\text{damper}}, T_{\text{yr}}, d_{\text{MLI}}) \quad (\text{A.240})$$

$$A_{\text{dy}} = 2\pi \cdot r_{\text{ro}} \cdot L - 2p \cdot (w_{\text{p}} + 2 \cdot w_{\text{p, side}} + 2 \cdot w_{\text{f}} + 4 \cdot w_{\text{f}} \cdot w_{\text{spacer, side}}) \cdot L \quad (\text{A.241})$$

$$R_{\text{MLI}} = \frac{l_{\text{MLI}}}{A_{\text{dy}} \cdot \lambda_{\text{MLI}}} \quad (\text{A.242})$$

$$\lambda_{\text{FeNi9}} = 2.15 \frac{\text{W}}{\text{m} \cdot \text{K}} \quad (\text{A.245})$$

$$l_{\text{eff, yr}} = \frac{h_{\text{yr}}}{2} \quad (\text{A.243})$$

$$R_{\text{cond, yr}} = \frac{l_{\text{eff, yr}}}{\lambda_{\text{FeNi9}} \cdot A_{\text{dy, yr}}} \quad (\text{A.246})$$

$$A_{\text{dy, yr}} = 2\pi \cdot \left( r_{\text{ri}} + \frac{h_{\text{yr}}}{2} \right) \cdot L \quad (\text{A.244})$$

$$R_{\text{damp, yoke}} = R_{\text{MLI}} + R_{\text{cond, yr}} \quad (\text{A.247})$$

**Rotor Yoke - Pole Core**

$$l_y = \frac{h_{yr}}{2} \quad (\text{A.248})$$

$$l_p = \frac{h_p}{2} \quad (\text{A.252})$$

$$\lambda_y = 2.15 \frac{\text{W}}{\text{m} \cdot \text{K}} \quad (\text{A.249})$$

$$\lambda_p = 2.15 \frac{\text{W}}{\text{m} \cdot \text{K}} \quad (\text{A.253})$$

$$A_y = \frac{1}{2} \cdot \left( 2p \cdot w_p \cdot L + 2\pi \cdot \left( r_{ri} + \frac{h_{yr}}{2} \right) \cdot L \right) \quad (\text{A.250})$$

$$A_p = 2p \cdot w_p \cdot L \quad (\text{A.254})$$

$$R_y = \frac{l_y}{\lambda_y \cdot A_y} \quad (\text{A.251})$$

$$R_p = \frac{l_p}{\lambda_p \cdot A_p} \quad (\text{A.255})$$

$$R_{\text{yoke,pole}} = R_y + R_p \quad (\text{A.256})$$

**Pole Core - Cooling Plates**

$$l_{cp} = \frac{w_f}{2} \quad (\text{A.257})$$

$$l'_{pp} = \frac{h_{pp}}{2} \quad (\text{A.261})$$

$$A_{cp} = \frac{h_{\text{Cu,cp}}}{2} \cdot L \cdot 2 \cdot 2 \cdot 2p \quad (\text{A.258})$$

$$A_{pp} = h_{p,\text{side}} \cdot L \cdot 2 \cdot 2p \quad (\text{A.262})$$

$$\lambda_{\text{Cu,cp}} = f_{\lambda,\text{Cu}} (\text{RRR} = 170, T_{cp}) \quad (\text{A.259})$$

$$\lambda_{pp} = 1.4 \frac{\text{W}}{\text{m} \cdot \text{K}} \quad (\text{A.263})$$

$$R_{cp} = \frac{l_{cp}}{A_{cp} \cdot \lambda_{\text{Cu,cp}}} \quad (\text{A.260})$$

$$R_{pp} = \frac{l'_{pp}}{A_{pp} \cdot \lambda_{pp}} \quad (\text{A.264})$$

$$l'_{\text{pole}} = \frac{w_p}{2} + w_{p,\text{side}} \quad (\text{A.265})$$

$$R_{\text{pole}} = \frac{l'_{\text{pole}}}{A_{\text{pole}} \cdot \lambda_{\text{pole}}} \quad (\text{A.268})$$

$$A_{\text{pole}} = 2 \cdot 2p \cdot L \cdot h_p \quad (\text{A.266})$$

$$R_{\text{cp,pole}} = R_{cp} + R_{pp} + R_{\text{pole}} \quad (\text{A.269})$$

$$\lambda_{\text{pole}} = 2.15 \frac{\text{W}}{\text{m} \cdot \text{K}} \quad (\text{A.267})$$

**Pressure Plates - Cooling Plates**

$$l_{pp} = \frac{h_{pp}}{4} \quad (\text{A.270})$$

$$\lambda_{pp} = 1.4 \frac{\text{W}}{\text{m} \cdot \text{K}} \quad (\text{A.271})$$

$$A_{pp} = w_f \cdot L \cdot 2 \cdot 2p \quad (\text{A.272})$$

$$R_{pp} = \frac{l_{pp}}{\lambda_{pp} \cdot A_{pp}} \quad (\text{A.273})$$

$$l_{cp} = \frac{h_{cp}}{4} \quad (\text{A.274})$$

$$\lambda_{\text{Cu, cp}} = f_{\lambda, \text{Cu}} (\text{RRR} = 170, T_{cp}) \quad (\text{A.275})$$

$$A_{cp} = w_f \cdot L \cdot 2 \cdot 2p \quad (\text{A.276})$$

$$R_{cp} = \frac{l_{cp}}{\lambda_{cp} \cdot A_{cp}} \quad (\text{A.277})$$

$$R_{pp, cp} = R_{pp} + R_{cp} \quad (\text{A.278})$$

**Cooling Plates - Cold Heads**

$$d_{\text{Cu, conn}} = 0.02 \text{ m} \quad (\text{A.279})$$

$$w_{\text{Cu, conn}} = 0.11 \text{ m} \quad (\text{A.280})$$

$$A_{\text{Cu, conn}} = d_{\text{Cu, conn}} \cdot w_{\text{Cu, conn}} \quad (\text{A.281})$$

$$l_{\text{Cu, conn}} = w_{\text{Cu, conn}} \cdot \left(1 + \frac{\pi}{2}\right) \quad (\text{A.282})$$

$$\lambda_{\text{Cu, conn}} = f_{\lambda, \text{Cu}} (\text{RRR} = 170, T_{cp}) \quad (\text{A.283})$$

$$R_{\text{conn}, 1} = \frac{l_{\text{Cu, conn}}}{\lambda_{\text{Cu, conn}} \cdot A_{\text{Cu, conn}}} \cdot \frac{1}{2p} \quad (\text{A.284})$$

$$n'_{\text{CH, pole}} = 10 \quad (\text{A.285})$$

$$R_{\text{conn}, 2} = \frac{l_{\text{Cu, conn}}}{\lambda_{\text{Cu, conn}} \cdot A_{\text{Cu, conn}}} \cdot \frac{n'_{\text{CH, pole}}}{2p} \quad (\text{A.286})$$

$$d_{\text{Cu, bus}} = 0.05 \text{ m} \quad (\text{A.287})$$

$$w_{\text{Cu, bus}} = 0.075 \text{ m} \quad (\text{A.288})$$

$$A_{\text{Cu, bus}} = d_{\text{Cu, bus}} \cdot w_{\text{Cu, bus}} \quad (\text{A.289})$$

$$l_{\text{Cu, bus}} = n'_{\text{CH, pole}} \cdot \frac{2\pi \cdot r_{\text{rro}}}{2p} \quad (\text{A.290})$$

$$l_{\text{Cu, bus, max}} = \frac{l_{\text{Cu, bus}}}{2} \quad (\text{A.291})$$

$$R_{\text{Cu, bus}} \approx \frac{l_{\text{Cu, bus, max}}}{\lambda_{\text{Cu, conn}} \cdot A_{\text{Cu, conn}}} \cdot \frac{1}{2p} \quad (\text{A.292})$$

$$R_{cp, \text{CH}} = R_{\text{Cu, bus}} + R_{\text{conn}, 1} + R_{\text{conn}, 2} \quad (\text{A.293})$$

**Rotor Yoke - Middle of Cold-Warm Support**

$$\lambda_{G10,av} = f_{\lambda,G10}(T_{rsup}, T_{yr}) \quad (\text{A.294})$$

$$l_{G10,plate} = \frac{h_{G10}}{2} \quad (\text{A.295})$$

$$R_{yr,plate,cond} = \frac{l_{G10,plate}}{\lambda_{G10,av} \cdot A_{G10,plate}} \quad (\text{A.296})$$

$$l_{G10,bar} = \frac{\frac{h_{G10}}{2} + d_{MLI}}{\cos(\vartheta_{supp})} \quad (\text{A.297})$$

$$R_{sup,y} = R_{yr,plate,cond} + R_{yr,bar,cond} \quad (\text{A.298})$$

$$A_{G10,plate} = A_{G10,plate,single} \cdot N_{supp} \cdot \left( \frac{(n_{supp,ax} + 1)}{n_{supp,ax}} \right) \cdot 2 \quad (\text{A.299})$$

$$A_{G10,bar} = A_{G10,bar,single} \cdot N_{supp} \cdot \left( \frac{(n_{supp,ax} + 1)}{n_{supp,ax}} \right) \cdot 2 \quad (\text{A.300})$$

$$R_{yr,bar,cond} = \frac{l_{G10,bar}}{\lambda_{G10,av} \cdot A_{G10,bar}} \quad (\text{A.301})$$

**Rotor Yoke - Rotor Rim**

The dimensioning of the support is described in Sec. A.9.3.

$$d_{MLI} = 10 \text{ mm} \quad (\text{A.302})$$

$$l_{bar} = l_{G10} - \frac{h_{G10} + d_{MLI}}{\cos(\vartheta_{supp})} \quad (\text{A.304})$$

$$\lambda_{MLI} = f_{\lambda,MLI}(T_h = T_{rim}, T_c = T_{yr}, d_{MLI}) \quad (\text{A.303})$$

$$R_{rim,y} = \frac{d_{MLI}}{\lambda_{MLI} \cdot A_{MLI}} \quad (\text{A.305})$$

$$A_{MLI} = 2\pi \cdot (r_{ri} - h_{G10}) \cdot L - l_{bar} \cdot \sin(\vartheta_{supp}) \cdot d_{bar} \cdot N_{supp} \cdot \frac{n_{supp,ax} + 1}{n_{supp,ax}} \quad (\text{A.306})$$

**Middle of Rotor Support - Rotor Rim**

$$\lambda_{G10,av} = f_{\lambda,G10}(T_{rim}, T_{rsup}) \quad (\text{A.307})$$

$$R_{rim,bar,cond} = \frac{l_{G10,bar}}{\lambda_{G10,av} \cdot A_{G10,bar}} \quad (\text{A.309})$$

$$R_{rim,plate,cond} = \frac{l_{G10,plate}}{\lambda_{G10,av} \cdot A_{G10,plate}} \quad (\text{A.308})$$

$$R_{rim,cond} = R_{rim,plate,cond} + R_{rim,bar,cond} \quad (\text{A.310})$$

Radiative contribution:

$$\sigma = 5.67 \cdot 10^{-8} \frac{\text{W}}{\text{m}^2 \cdot \text{K}^4} \quad (\text{A.311}) \quad \varepsilon_{\text{rim}} = 0.07 \quad (\text{A.312}) \quad \varepsilon_{\text{G10}} = 0.9 \quad (\text{A.313})$$

$$T_{\text{supp,av}} = \left[ \frac{1}{5} \cdot \frac{T_{\text{rim}}^5 - T_{\text{rsup}}^5}{T_{\text{rim}} - T_{\text{rsup}}} \right]^{1/4} \quad (\text{A.314})$$

$$E = \frac{\varepsilon_{\text{rim}} \cdot \varepsilon_{\text{G10}}}{\varepsilon_{\text{rim}} + \varepsilon_{\text{G10}} - \varepsilon_{\text{rim}} \cdot \varepsilon_{\text{G10}}} \quad (\text{A.315})$$

$$A_{\text{proj}} = l_{\text{bar}} \cdot \sin(\vartheta_{\text{p}}) \cdot d_{\text{bar}} \cdot N_{\text{supp}} \cdot \frac{n_{\text{supp,ax}} + 1}{n_{\text{supp,ax}}} \quad (\text{A.316})$$

$$R_{\text{rim,rad}} = \frac{T_{\text{rim}} - T_{\text{sup,av}}}{\sigma \cdot E \cdot A_{\text{proj}} \cdot (T_{\text{rim}}^4 - T_{\text{sup,av}}^4)} \quad (\text{A.317})$$

### A.9.3. Approximate Dimensioning of the Rotor Support Structure

Estimation of rotor rim radius (direct drive generators):

$$r_{\text{rim}} = r_{\text{ri}} - 0.4 \text{ m} \quad (\text{A.318})$$

Maximum torque to withstand:

$$\hat{M}_{\text{max}}/M_{\text{N}} = 3 \quad (\text{A.319})$$

Maximum yield strength of G10CR:

$$\sigma_{\text{max}} = 20 \text{ MPa} = 20 \cdot 10^6 \text{ Pa} \quad (\text{A.320})$$

Number of pole pairs per support:

$$n'_{\text{pp,sup}} = 1 \quad (\text{A.321})$$

Number of supports in axial direction (2 bars take radial forces, 1 bar takes axial forces):

$$n_{\text{supp,ax}} = 3 \quad (\text{A.322})$$

$$r_1 = r_{\text{rim}} \quad (\text{A.323})$$

$$r_2 = r_{\text{ri}} \quad (\text{A.324})$$

Pole pitch at inner of rotor:

$$\tau_{\text{p}} = \pi \cdot \frac{r_{\text{ri}}}{p} \quad (\text{A.325})$$

$$\xi = 2 \cdot n'_{\text{pp, supp}} \cdot \frac{\tau_{\text{p}}}{r_2} \quad (\text{A.326})$$

$$l_{\text{G10}} = \sqrt{r_2^2 + r_1^2 - 2 \cdot r_2 \cdot r_1 \cdot \cos(\xi)} \quad (\text{A.327})$$

$$N_{\text{supp}} = n_{\text{supp, ax}} \cdot \left\lceil \frac{P}{n'_{\text{pp, supp}}} \right\rceil \quad (\text{A.328})$$

$$\vartheta_{\text{pp}} = \arccos\left(\frac{l_{\text{G10}}^2 + r_2^2 - r_1^2}{2 \cdot l_{\text{G10}} \cdot r_2}\right) \quad (\text{A.329})$$

$$\alpha = \frac{\pi}{2} - \vartheta_{\text{pp}} \quad (\text{A.330})$$

$$F_{\text{t}, \Sigma} = \left| \frac{M_{\text{N}} \cdot \hat{m}_{\text{max}}}{r_{\text{ro}}} \right| \quad (\text{A.331})$$

$$F_{\text{t}} = \frac{F_{\text{r}, \Sigma}}{N_{\text{supp}}} \quad (\text{A.332})$$

$$F_{\text{supp}} = \frac{F_{\text{t}}}{\cos(\alpha)} \quad (\text{A.333})$$

Dimensions of G10 bar:

$$A_{\text{bar}} = \frac{F_{\text{supp}}}{\sigma_{\text{max}}} \quad (\text{A.334})$$

$$d_{\text{bar}} = 2 \cdot \sqrt{\frac{A_{\text{bar}}}{\pi}} \quad (\text{A.335})$$

Dimensions of G10 plate:

$$h_{\text{G10}} = 0.15 \text{ m} \quad (\text{A.336})$$

$$d_{\text{G10}} = 0.025 \text{ m} \quad (\text{A.337})$$

$$b_{\text{G10}} = \frac{F_{\text{supp}}}{2 \cdot d_{\text{G10}} \cdot \sigma_{\text{max}}} \quad (\text{A.338})$$

$$A_{\text{G10}} = d_{\text{G10}} \cdot b_{\text{G10}} \quad (\text{A.339})$$

## A.10. Overview of Considered Direct Drive Generators

Table A.4.: Overview of considered direct drive generator designs: Topologies and key characteristics. All generators are designed for a gearless drive train with a power rating of  $P_{el,N} = -7\text{MW}$  and a rated speed of  $n_N = 8.33\text{rpm}$ . The topologies of HTS generators are named with ① - ④ according to Fig. 4.4. All considered generators feature a three-phase winding. Inner/outer damper refers to an attachment of the copper screen to the inner/outer side of the cryostat wall.

	thematic scope	topology	rotor excitation	stator winding	damper
Ch. 3	parametric design study of PMSG	all iron	PM: NdFeB	Cu in slots	no
Sec. 4.1	comparison: MTPA vs. $ \cos \varphi_{sN}  = 1$ op.	①	GdBCO	Cu in slots	warm, inner
Sec. 4.2.2.2	geom. simplifications and meshing	①(-④)	GdBCO, EuBCO	( Cu in slots )	warm, inner
Sec. 4.2.2.3	analysis of 3D effects	①(-④)	GdBCO, EuBCO	( Cu in slots )	warm, inner
Sec. 4.2.4	exemplary results for thermal calculation	①	GdBCO	Cu in slots	warm, inner
Sec. 4.3.1	comparison: $\text{MgB}_2$ , HTS field windings	①	ReBCO, $\text{MgB}_2$	Cu in slots	warm, inner
Sec. 4.3.2, Sec. 4.3.3	copper damper screen design and choice of AC winding	①, ④	GdBCO	Cu in slots/ air gap winding	warm vs. cold, inner vs. outer
Sec. 4.3.4	calculation of AC loss in the DC HTS field winding	①	GdBCO	Cu in slots	w/o or warm, inner
Ch. 5	numerical optimization: low component cost $C_t$ , low active mass $m_{act}$	① - ④	GdBCO, EuBCO	Cu in slots/ air gap winding	warm, inner
Ch. 6	analysis of redundancy operation and sudden short circuit faults	①	GdBCO	Cu in slots	warm, inner

---

# Curriculum Vitae

**Name** Robin Köster

## **Ausbildung**

Technische Universität Darmstadt

04.2017 - 06.2018 – Elektro- und Informationstechnik, Abschluss: M.Sc.  
Vertiefung: Elektrische Energietechnik

10.2016 - 03.2020 – Physik, Abschluss: M.Sc.  
Vertiefung: Festkörperphysik

10.2015 - 11.2018 – Wirtschaftsingenieurwesen, Abschluss: M.Sc.  
Vertiefung: Unternehmensfinanzierung

04.2013 - 10.2016 – Physik, Abschluss: B.Sc.

10.2012 - 09.2015 – Wirtschaftsingenieurwesen, Abschluss: B.Sc.

2004 - 2012 Taunusgymnasium, Königstein im Taunus  
Abschluss: Allgemeine Hochschulreife

## **Berufliche Praxis**

05.2019 - heute Technische Universität Darmstadt  
Institut für Elektrische Energiewandlung,  
Wissenschaftlicher Mitarbeiter

04.2017 - 01.2018 CST AG, Darmstadt  
Softwareentwicklung für Low-Frequency-Anwendungen,  
Werkstudententätigkeit

11.2016 - 02.2017 Andritz Hydro AG, Kriens (CH)  
Berechnungsabteilung Großgeneratoren, Industriepraktikum